Universität Bremen

marum

Monitoring of Deep Fluids in the Nankai Subduction Complex, SE offshore Japan

Dissertation

zur Erlangung des Doktorgrades

der Naturwissenschaften

– Doctor rerum naturalium –

(Dr. rer. nat.)

am Fachbereich Geowissenschaften

der Universität Bremen

vorgelegt von

Sebastian Hammerschmidt

Bremen, September 2014

GUTACHTER / REVIEWER

Prof. Dr. Achim J. Kopf

University of Bremen
Centre for Marine Environmental Sciences (MARUM)
Marine Geotechnics
Leobener Str./ MARUM
28359 Bremen, Germany

Prof. Dr. Wolfgang Bach

University of Bremen
Department of Geosciences
Petrology of the Ocean Crust
Postfach 330 440
28334 Bremen, Germany

Weitere Mitglieder der Prüfungskomission / Additional members of the examination board

Prof. Dr. Heinrich Villinger
Dr. Verena Heuer
Dr. Christoph Vogt
Nele Lamping

Prof. Dr. Simone Kasemann (Vertretung/substitute)
Dr. Matt Ikari (Vertretung/ substitute)
Nicole Syring (Vertretung/ substitute)

Tag des öffentlichen Kolloquiums / Day of public colloquium

03 November 2014

DECLARATION

Name: Sebastian Bernd Hammerschmidt
Address: Wegesende 7
               28195 Bremen
               Germany

Herewith I declare that

    I.   this document has been composed by myself,

    II.   I have not used any other than the stated sources and additives, and

    III.   material from the published or unpublished work of others, which is referred to in this dissertation, is credited to the author(s).

Bremen, 1 September 2014

……………………………………….
S. Hammerschmidt

EHRENWÖRTLICHE ERKLÄRUNG

Name: Sebastian Bernd Hammerschmidt

Adresse: Wegesende 7

               28195 Bremen

               Deutschland

Hiermit versichere ich, dass ich

    I.   die Arbeit ohne unerlaubte fremde Hilfe angefertigt habe,

    II.   keine anderen als die von mir angegebenen Quellen und Hilfsmittel benutzt habe und

    III.   die den benutzten Werken wörtlich oder inhaltlich entnommenen Stellen als solche kenntlich gemacht habe.

Bremen, 1 September 2014

…………………………………………

S. Hammerschmidt

七転び八起き*

TABLE OF CONTENTS

LIST OF FIGURES AND PLATES

Main Text

Appendices

LIST OF TABLES

Main Text

Appendices

PREFACE

"Nanakorobi yaoki – Fall seven times and stand up eight."
- Japanese Proverb

[1] "*Monitoring of Deep Fluids in the Nankai Subduction Complex*" – this is the title of my PhD thesis. However, this is not the topic I signed up for. Every PhD student encounters problems during his/her three years, and sometimes things simply do not work out, despite having several back-up plans. The issues I have experienced forced me to split my thesis into different sub-projects. Nonetheless, the combination of the individual topics under the terms "deep fluid" improves our understanding of fluid migration and generation in the Nankai subduction complex. The focus lies on migration pathways, temporal and spatial variations and the relationship between fluids and seismo-tectonic processes. I worked with long-term and real-time borehole measurements, and investigated paleo-fluid migration with conventional coring and laboratory techniques. Particularly for the borehole monitoring instruments, examples on how the data can be used for geological, geophysical and geochemical interpretations will be presented. Consequently, this thesis is a broad compendium rather than a highly specialized technical literature.

[2] Initially, the PhD thesis focused solely on testing and evaluation of newly developed long-term (i.e. months to years) borehole monitoring instruments, so-called MeBo-CORKs (Meeresboden-Bohrgerät-Circulation Obviation Retrofit Kit). These instruments were especially designed for installation in boreholes drilled by the MARUM drill rig MeBo. As such, this PhD thesis was planned as a follow-up project of my Master thesis entitled "*Triggering Mechanisms for Temperature and Fluid Pressure Transients in a Borehole Observatory: A Case Study from the Nankai Trough, Japan*". While both projects focused on evaluation of long-term fluid pressure and temperature data from the Nankai Trough subduction complex, SE offshore Japan, the Master thesis was embedded in the IODP (Integrated Ocean Drilling Program) NanTroSEIZE (Nankai Trough Seismogenic Zone Experiment), whereas the initial PhD thesis was planned as stand-alone project. In addition, the data used for the Master thesis were gathered by a SmartPlug borehole observatory, which, compared to the MeBo-CORKs, has a different design and uses different sensors.

[3] Two types of MeBo-CORKs were available: the MeBo-CORK A, which is screwed on top of the borehole to monitor pressure and temperature, and the MeBo-CORK B, i.e. a seafloor unit, which latches to the wellhead via a hot stab connector and which allows additional fluid sampling with an OsmoSampler. Both versions had an acoustic telemetric system, which enabled wireless communication and data download onboard the research vessel.

[4] The first MeBo-CORKs were deployed in 2012 during Expedition SO-222 (09 June – 18 July 2012; Kopf et al. 2013), on top of mud volcanoes in the Kumano forearc basin. At that time we were hoping to find co-seismic anomalies in the fluid pressure, temperature and geochemical data which might be suitable as proxies for seismogenic activity in this area.

[5] Although deployment and installation of the MeBo-CORKs succeeded, we encountered several problems. Initial data downloaded from MeBo-CORK A proved the functionality of the sensors (cf. Appendix B), but unfortunately, further data could not be gathered, probably due to a malfunction of the acoustic modem. MeBo-CORK B, on the other hand, had to be recovered shortly after its installation, because fluid pressure data indicated a problem with the hotstab connector. Consequently, no long-term data were available from the MeBo-CORKs. During Exp. SO-222, additional long-term monitoring instruments were deployed into MeBo boreholes ("MeBo Plugs") or re-designed as piezometer. However, recovery of these instruments, and MeBo-CORK A, is envisaged for 2015, i.e. after the funding for my PhD position will have expired.

[6] During Exp. SO-222, we were also hoping for long-term pressure data from the LTBMS (Long-Term Borehole Monitoring System, cf. chapter 4.2), which is a highly sophisticated CORK installed at IODP Site C0002 at the southern rom of the Kumano forearc basin. The LTBMS has no wireless data transmission system; therefore an ROV (Remotely Operated Vehicle) was necessary to download data. This time, unsolvable technical issues of the MARUM ROV "Quest" precluded any success.

[7] Since I was still working on data from the SmartPlug observatory (Hammerschmidt et al. 2013a, b, see also chapters 5.1 and 5.2), I decided to apply for IODP Expedition 338, where it was planned to recover the GeniusPlug. This instrument was installed as replacement for the SmartPlug during IODP Exp. 332 in 2010 (Kopf et al. 2011), and should provide additional pressure, temperature and geochemical data from the same borehole as the SmartPlug. The dataset was very promising, because the monitoring period of the GeniusPlug covers the 2011 M9.0 Tohoku earthquake and tsunami, which should have also affected the GeniusPlug data.

[8] My application was successful, but unfortunately, during preparation for Exp. 338, it was decided to move the recovery of the GeniusPlug to the contingency operations. As a consequence, there was again no chance to get new long-term borehole data.

[9] At this point, I realized that waiting for long-term borehole data would get my PhD thesis to nowhere. Too unsecure seemed the possibilities to get the deployed instruments back on time. Consequently, I decided to start working with another borehole monitoring technique: drilling mud gas monitoring. Due to my geochemical background and my experience in *in situ* bore-

hole data, I participated as "drilling mud gas specialist" on IODP Exp. 338, which put me in the best position to monitor, to evaluate and to sample drilling mud gas encountered during riser drilling.

[10] Prior to Exp. 338, I established the contact with Dr. Thomas Wiersberg and Prof. Dr. Jörg Erzinger, both working at the GFZ Potsdam and both being well experienced in drilling mud gas monitoring. They provided advice and equipment for sampling of drilling mud gas, and offered post-cruise gas analyses in the laboratories of Prof. Erzinger's working group "Inorganic and Isotope Geochemistry". At the same time, I got in contact with Dr. Verena Heuer from "the Organic Geochemistry" group at the MARUM, who agreed on conducting deuterium isotope analyses on the gas samples.

[11] During IODP Exp. 338 (16 October – 02 December 2012), it became apparent that the drilling mud gas monitoring system onboard drilling vessel (D/V) *Chikyu* was still in its infancy. We encountered several problems with the general configuration of the degassing system, incl. gas leaks, and malfunctions of the onboard monitoring instruments. These issues affected also the sampling of drilling mud gas. As a consequence, out of the 33 samples taken, only 4 provided sufficiently high gas concentrations to conduct noble gas analyses at the GFZ Potsdam. While the cruise was not successful in terms of sampling, it helped establishing connections to Japanese scientists. In particular, collaboration with Dr. Hidenori Kumagai from JAMSTEC would probably not have happened. He not only agreed on being a co-author on manuscript VI (see chapter 6.2), but provided also ^{222}Rn data from gas samples taken during Exp. 338.

[12] In the meanwhile, Dr. Eiichiro Araki from JAMSTEC offered his help to further investigate the SmartPlug pressure data by enabling access to seismological data from the Dense Ocean Floor Network for Earthquakes and Tsunamis (DONET). After successful application to the IMPULSE grant of Bremen University, I had enough funding to spend 2 months at JAMSTEC in Yokosuka, Japan. The collaborative work resulted in two additional manuscript, which target anomalous fluid pressure transients generated by non-volcanic tremor, distant storms and common earthquakes (cf. chapters 5.3 and 5.4).

[13] Being still highly motivated from the work at JAMSTEC and due to the need for additional drilling mud gas data from IODP Site C0002, I applied again successfully as "drilling mud gas specialist" for IODP Exp. 348 (12 November 2013 – 10 January 2014). Recovery of the GeniusPlug was again one of the objectives, and sidetracking and drilling at Site C0002 would have allowed to re-sample the depth interval drilled during IODP Exp. 338. Unfortunately, recovery of the GeniusPlug was again postponed to a later expedition. But on the positive side, most of the problems of the drilling mud gas monitoring system that were encountered during Exp.

338 were solved, which improved the gas sample quality. Thanks to a successful application to the ECORD (European Consortium for Ocean Research Drilling) grant and the ongoing collaboration with Dr. Kumagai, Dr. Heuer, Dr. Wiersberg and Prof. Dr. Erzinger, the additional work during Exp. 348 combined with data from Exp. 338 culminated in two manuscripts (see chapters 6.1 and 6.2). The first manuscript focusses on hydrocarbon gas generation and mixing in the accretionary prism, while the second uses noble gases to constrain possible migration of deep fluids.

[14] While the geochemical real-time monitoring targets the *in situ* composition of individual gases and their possible migration at depth, the work of Pape et al. (2014; chapter 7.1 in this volume) focusses on depicting the origin of gases and gas hydrates sampled from the upper few metres below seafloor at mud volcanoes investigated during MARUM Exp. SO-222. Pape et al. (2014) elucidate possible gas migration from the accretionary prism to the seafloor. As such, it ties neatly to the drilling mud gas manuscripts, because it serves as vertical extension of the fluid migration profile.

[15] Eventually, to further investigate paleo-fluid migration in the Kumano forearc basin and the underlying accretionary prism, I also worked on material from MARUM Exp. SO-222. Analyses included X-ray diffraction and illite crystallinity, thin section analyses on clasts found in gravity cores taken from mud volcanoes, and radiocarbon data of undisturbed background sediments close to intercalations of turbidites and ash layers in gravity cores. These manuscripts are still in preparation, and can be found in chapters 7.2 and 7.3. While the former relates to temporal and spatial changes of fluid expulsion and mud volcanism in the Kumano forearc basin, the latter tries again to depict the origin of the material and fluids ejected at mud volcanoes.

[16] Despite the occasional set-backs which forced me on an intricate path, this thesis turned out to be a valuable compendium for the analyses of fluids in the Nankai Subduction Zone by combining state-of-the-art borehole technology with conventional geoscientific methods. If the MeBo-CORKs would have worked in the first place, this PhD thesis would probably be much shorter and more precise in its objective and coverage. But the way it was, it allowed me to do the doctorate on a much broader scientific level and to tackle the objectives in a wider regional context. Also, I highly appreciate the opportunities I had, including the > 100 days I spend onboard *(D/V) Chikyu* and my time at JAMSTEC. These opportunities also allowed me to meet and to work with incredible smart and inspiring people from all over the world. I would not want to miss these experiences.

References

Hammerschmidt S, Davis EE, Kopf A (2013a) Fluid pressure and temperature transients detected at the Nankai Trough Megasplay Fault: Results from the SmartPlug borehole observatory. Tectonophysics 600:116 – 133. doi: 10.1016/j.tecto.2013.02.010

Hammerschmidt SB, Davis EE, Hüpers A, Kopf A (2013b) Limitation of fluid flow at the Nankai Trough megasplay fault zone. Geo-Marine Lett 33:405–418. doi: 10.1007/s00367-013-0337-z

Kopf A, Saffer DM, Davis EE, Hammerschmidt S, LaBonte A, Meldrum R, Toczko S, Lauer R, Heesemann M, Macdonald R, Wheat CG, Jannasch HW, Edwards K, Orcutt B, Haddad A, Villinger H, Araki E, Kitada K, Kimura T, Kido Y (2011) The SmartPlug and GeniusPlug: simple retrievable observatory systems for NanTroSEIZE borehole monitoring. In: Kopf A, Araki E, Toczko S, Expedition 332 Scientists, Proc IODP 332. doi:10.2204/iodp.proc.332.105.2011

Kopf A, et al. (2013) Report and Preliminary Results of R/V SONNE Cruise SO222. Berichte, MARUM – Zent für Mar Umweltwissenschaften, Fachbereich Geowissenschaften, Univ Bremen 297:121.

Pape T, Geprägs P, Hammerschmidt S, Wintersteller P, Wei J, Fleischmann T, Bohrmann G, Kopf AJ (2014) Hydrocarbon seepage and its sources at mud volcanoes of the Kumano forearc basin, Nankai Trough subduction zone. Geochemistry, Geophys Geosystems 15:2180–2194. doi: 10.1002/2013GC005057

ABSTRACT/ZUSAMMENFASSUNG

ABSTRACT

[1] Fluids, including liquids and gases, are of great importance for various geological, geochemical and geophysical processes. Generation and migration of fluids influences heat and solute transport in the earth's crust. It further plays an important role in the formation and storage of natural resources, as well as in the generation of natural hazards, including landslides and earthquakes. At the Nankai Trough subduction zone, SE offshore the Japanese Kii Peninsula, the interweaving of tectonic processes and fluids is heavily investigated. Around 15 Ma, subduction of the Philippine Sea Plate beneath the Eurasian Plate was initiated, which led to the formation of this accretionary subduction complex. Ongoing underthrusting makes this a highly earthquake-prone region, where not only normal earthquakes but also anomalous events like "episodic tremor and slip" and "very-low frequency earthquakes" occur frequently. At Nankai, seismogenic processes and the spatial and temporal variability of the seismogenic zone were repeatedly discussed in the light of pore fluid pressure and fluid migration. Of particular interest is a major splay fault, termed "Megasplay", that is supposed to be hydraulically connected to the seismogenic zone of the thrust fault boundary. If the Megasplay fault can serve as fluid conduit, it might significantly influence the stick-slip behaviour at the plate boundary and thus, would control the updip limit of the seismogenic zone. Further landward, in the Kumano forearc basin, several mud volcanoes indicate past and recent fluid and mud expulsion. However, it is unclear form what depths these fluids are derived, and what mechanisms trigger mud volcanism. The role of earthquakes and seismic waves in terms of fluid migration and expulsion is unsolved as well.

[2] In order to advance our understanding of fluid generation and migration at the Nankai Trough subduction complex, this PhD thesis combined approaches of the IODP (Integrated Ocean Drilling Program) NanTroSEIZE (Nankai Trough Seismogenic Zone Experiment and the MARUM (Marine Centre for Environmental Sciences) MeMo (MeBo Drilling and *in situ* Long-term Monitoring in the Nankai Trough Accretionary Complex, Japan) project. In the course of IODP Expedition 319, the Megasplay fault was drilled and instrument with a long-term borehole monitoring device called SmartPlug. The SmartPlug measured fluid pressure (as proxy for strain) and fluid temperature for 15 months. In the Kumano Basin, information about *in situ* composition of fluids was obtained with drilling mud gas monitoring and sampling during riser drilling with drilling vessel (D/V) *Chikyu* to ca. 3000 meter below seafloor (mbsf). Within project MeMo, paleo- and recent fluid expulsion was investigated by mapping and coring mud volcanoes in the Kumano Basin during cruise SO-222 with research vessel *Sonne.*

[3] Onshore analyses included laboratory work, modelling and time series and signal analyses. Seismic waveforms from Japanese seismological networks (e.g. Hi-Net, DONET, F-Net) were complemented with information from global seismological networks to investigate co-seismic changes in fluid migration in the accretionary prism and fluid pressure transients at the Megasplay fault. Drilling mud gas samples were subject to hydrocarbon gas and deuterium analyses, and to noble gas isotope studies with focus on helium isotopes. Post-cruise SO-222 analyses included visual core description, radiocarbon dating, thin section analyses, X-ray diffraction analyses and determination of illite crystallinity on cores from the Kumano Basin and its mud volcanoes.

[4] Evaluation of the long-term pressure and temperature data revealed that the fluid pressure data is affected by a wide range of natural signals, including seismic waves radiated by non-volcanic tremor and earthquakes, microseism, regional and distant low-pressure weather systems and tsunamis. Hydrogeological properties of the formation that are based on the pressure data and laboratory permeability tests imply the possibility of fluid migration. However, no fluid flow was observed during the monitoring period, nor was any pressure signal detected that would point to co-seismic large-scale deformation in the accretionary prism or the splay fault zone.

[5] Fluid migration in the accretionary prism is supported by drilling mud gas data which indicated thermogenic and bacterial hydrocarbon gas at depths shallower than 2000 mbsf. At these depths, time-temperature modelling implied no *in situ* generation of thermogenic gas, thus active migration of thermogenic gas and mixing with bacterial gas must take place. Noble gas isotopes suggest primordial fluids to be present as well, which, following the results of a one-dimensional fluid flow model, are related to episodic, co-seismic fluid migration.

[6] Preliminary results of radiocarbon dating and visual core description on cores from the Kumano Basin mud volcanoes point to a NW-SE gradient of mud volcanism, with mud volcanoes in the NW being inactive for at least 28000 yr cal. BP. Hydrocarbon gases that formed gas hydrates were most likely released during episodic mud volcanism. Why none of the recent earthquakes, e.g. the 1944 Tonankai M8.1 or the 1946 Nankaido M8.3 earthquake, triggered a new eruption remains unclear. Apparently, the individual ejecta are derived from different stratigraphic intervals. Thin section analyses on clasts suggests that the parent beds are located between 3000 and ca. 6000 mbsf, while hydrocarbon gases started to migrate between ca. 2000 and 4000 mbsf. Fluidized mud, the main component of the ejecta, apparently originates from depths greater 6000 mbsf.

[7] In conclusion, ongoing fluid migration in the Nankai Trough accretionary prism and the Kumano forearc basin were successfully investigated by real-time drilling mud gas monitoring. Signs for paleo-fluid expulsion of deeper fluids is indicated by ejecta and deposits of mud volcanoes in the Kumano Basin. Although fluid pressure transients at the Megasplay fault were related to earthquakes, apparently no fluid migration was initiated. Therefore, potential fluid pathways in the accretionary prism and the Kumano Basin, the co-seismicity of fluid migration, and the kind of migration (flow vs. diffusion) remain unclear at this point. In the future, ejecta of the mud volcanoes in the Kumano Basin will be subject to further investigation. In addition to that, recently developed borehole monitoring systems, namely MeBoCORKs, MeBoPLUGS and MeBoPUPPIs, will be used for long-term observation of fluid expulsion. Monitoring of *in situ* fluid pressure, temperature and geochemical parameters will improve our understanding of fluid migration its triggering mechanisms, and might help to understand the seismogenic cycle at the Nankai Trough subduction complex.

ZUSAMMENFASSUNG

[1] Fluide, inkl. Flüssigkeiten und Gase, sind von großer Bedeutung für verschiedene geologische, geochemische und geophysikalische Prozesse. Generation und Migration von Flüssigkeiten beeinflusst Wärme und Stofftransport in der Erdkruste. Darüber hinaus spielen Fluide eine wichtige Rolle bei der Bildung und Speicherung von natürlichen Ressourcen sowie bei der Entstehung von Naturkatastrophen, einschließlich Erdrutschen und Erdbeben. An der Nankai Subduktionszone, süd-östlich der japanischen Kii Halbinsel, wurde die Verflechtung von tektonischen Prozessen und Fluiden wiederholt untersucht. Vor ca. 15 Millionen Jahren begann die Subduktion der Philippinischen Platte unter die Eurasische Platte, was zur Bildung des heutigen Subduktionskomplexes führte. Die fortschreitende Subduktion macht den Nankai Trog zu einer äußerst erdbebengefährdeten Region, in der nicht nur gewöhnliche Erdbeben, sondern auch "episodic tremor and slip" und "very-low frequency" Erdbeben gehäuft auftreten. Am Nankai Subduktionskomplex wurden seismogene Prozesse und die räumliche und zeitliche Variabilität der seismogenen Zone wiederholt im Zusammenhang mit Porenfluiddruck und Fluidmigration diskutiert. Von besonderem Interesse ist ein weitläufiges Netzwerk aus Aufschiebungen, deren Hauptstörung als "Megasplay" bezeichnet wird. Diese soll hydraulisch mit der seismogenen Zone der Plattengrenze verbunden sein. Sollte dies zutreffen und die Megasplay tatsächlich als Migrationspfad für Fluide dienen, so hätte dies weitläufige Konsequenzen für die räumliche Ausbreitung der seismogenen Zone und des Verhaltens der Plattengrenze bei Stress. Weiter landwärts, im Kumano Forearc Becken, befinden sich mehrere Schlammvulkane die in der Vergangenheit aktiv waren und über die Fluide und verwässerter Schlamm ausgetreten sind. Bisher es ist jedoch unklar, von welcher Tiefe die Fluide kamen, und welche Mechanismen dem Schlammvulkanismus zu Grunde liegen. Weiterhin ungelöst ist auch, welchen Einfluss Erdbeben und seismischen Wellen auf Fluidmigration und –austritt haben.

[2] Um unser Verständnis von der Entstehung und Migration von Fluiden im Nankai Subduktionskomplex zu erweitern, kombiniert diese Doktorarbeit Ansätze des IODP (Integrated Ocean Drilling Program) NanTroSEIZE (Nankai Trough Seismogenic Zone Exerpiment) und dem MARUM (Zentrum für Marine Umweltwissenschaften) MeMo (MeBo Drilling and *in situ* Long-term Monitoring in the Nankai Trough Accretionary Complex, Japan) Projekts. im Laufe der IODP Expedition 319 wurde die Megasplay erbohrt und mit einem Bohrlochobservatorium namens „SmartPlug" instrumentiert. Der SmartPlug hat Fluiddruck (als Proxy für Deformation) und Fluidtemperatur für 15 Monate gemessen. Im Kumano Becken wurden, während einer Riserbohrung mit dem Bohrschiff *Chikyu*, Informationen über die *in situ* Zusammensetzung von Fluiden mittels Spülungsgasmessung und -probenahme bis zu einer Tiefe von 3000 Meter unter

dem Meeresboden (mbsf) gesammelt. Im Zuge von Projekt MeMo wurden Schlammvulkane im Kumano Becken kartiert und gekernt, um Rückschlüsse auf die Mechanismen vorheriger Fluid- und Schlammauswürfe ziehen zu können.

[3] Analysen an Land beinhalteten Laborarbeit, Modellierung und Zeitreihen- und Signalanalysen. Seismologische Datensätze von japanischen Erdbebennetzwerken (z.B. Hi-Net, DONET, F-Net) wurden mit Informationen aus globalen seismologischen Netzwerke kombiniert, um koseismische Veränderungen bzgl. der Fluidmigration im Akkretionskeil und des Porendrucks in der Megasplay zu identifizieren. Spülungsgasproben wurden auf Kohlenwasserstoffe, Deuterium und auf Edelgase untersucht, mit Fokus auf Helium-Isotope. Analysen der Kerne, die von Hintergrundsedimenten des Kumano Beckens und von Schlammvulkanen während Expedition SO-222 gewonnen wurden umfassen eine visuelle Kernbeschreibung, Radiokarbondatierung, Dünnschnitt-Analysen, Röntgenbeugungsanalysen und Ermittlung der Illitkristallinität.

[4] Die Auswertung der Langzeit-Druck und -Temperaturdaten ergab, dass der Fluiddruck durch verschiedene natürliche Prozesse beeinflusst wird, einschließlich seismischer Wellen, die durch nicht-vulkanischen Tremor und Erdbeben erzeugt wurden, Mikroseismizität die durch Stürme hervorgerufen wurde, und durch Tsunamiwellen. Die hydrologischen Eigenschaften der Formation, die mit Hilfe der Druckdaten und zusätzlichen Durchlässigkeitstests bestimmt wurden, implizieren dass Fluidmigration theoretisch möglich ist. Es wurden jedoch keine Drucksignale gefunden, die auf Fluidmigration oder auf weiträumige Deformation im Akkretionskeil oder der Megasplay während des Überwachungszeitraums hindeuten.

[5] Die Auswertung der Spülungsgasdaten deutet auf aktive Fluidmigration im Akkretionskeil hin. Biogene und thermogene Kohlenwasserstoffe wurden zusammen in geringen Tiefen (< 2000 mbsf) angetroffen. Zeit-Temperatur-Modellierungen lehnen die Möglichkeit einer *in situ*-Erzeugung von thermogene Gas in diesen Tiefen ab, was auf aktive Migration von thermogenen Gas und einer Vermischung mit biogenen Gas hindeutet. Edelgasisotope implizieren die Migration von Mantelfluiden durch den Akkretionskeil. Basierend auf einem eindimensionalen Fluidströmungsmodell wird das Auftreten der Mantelfluide mit episodischer, vermutlich koseismischer Fluidmigration erklärt.

[6] Vorläufige Ergebnisse der Radiokarbondatierungen und Beschreibung der Kerne aus dem Kumano-Becken und den dortigen Schlammvulkane weisen auf eine Zunahme des Schlammvulkanismus von NW nach SE hin. Schlammvulkane im NW waren mindestens für 28000 cal yr. BP inaktiv. Kohlenwasserstoffgase, die Gashydrate in den Schlammvulkanen gebildet haben, wurden wahrscheinlich während episodischen Schlammvulkanismus freigesetzt. Warum

keine der jüngsten Erdbeben, beispielsweise das 1944 Tonankai M8.1 oder das 1946 Nankaido M8.3 Erdbeben keine neue Eruption auslösten, bleibt unklar. Offenbar stammen die einzelnen Vulkanauswürfe aus verschiedenen stratigraphischen Intervallen. Dünnschnitt-Analysen der Klasten deutet darauf hin, dass die Muttergesteine zwischen 3000 und ca. 6000 mbsf liegen, während Kohlenwasserstoffgase aus Tiefen zwischen 2000 und 4000 mbsf stammen. Der verflüssigte Schlamm, der die Hauptkomponente des Schlammvulkanauswurfes darstellt, stammt jedoch offenbar aus Tiefen von über 6000 msbf.

[7] Abschließend lässt sich festhalten, dass aktive Fluidmigration im Akkretionskeil und dem Kumano forearc Becken erfolgreich mittels Echtzeit-Spülungsgasmessungen untersucht werden konnte. Die Ablagerungen der Schlammvulkanen im Kumano Becken deuten auf vormalige Fluidmigration tiefer Fluide hin. Der Porendruck, der an der Megasplay Störung gemessen wurde, zeigte zwar koseismische dynamische Veränderungen, allerdings fand offenbar keine Migration von Fluiden statt. Die Wegsamkeiten der Fluide, sowohl im Akkretionskeil als auch im Becken, der Zusammenhang mit Seismizität, sowie die Art der Migration (Strömung vs. Diffusion) bleiben ungeklärt. Die Eruptionen und die Auswürfe der Schlammvulkane im Kumano Becken werden Gegenstand weiterer Untersuchungen sein. Darüber hinaus werden vor kurzem entwickelte Bohrlochobservatorien, die MeBoCORKs, MeBoPLUGS und MeBoPUPPIs, für langfristige Beobachtung von Fluidmigration und -austritt verwendet werden. Messungen des *in situ* Fluiddrucks, der Temperatur und der Geochemie der Porenfluide werden unser Verständnis der Fluidmigration und der Auslösemechanismen verbessern, und könnten helfen, den seismogenen Zyklus in der Nankai Trog Subduktionszone zu verstehen.

CHAPTER 1
Introduction

CHAPTER 1.1

MOTIVATION

OVERVIEW AND OPEN QUESTIONS

[1] Convergent margins, particularly subduction zones, are the birth place for a wide range of catastrophic events. Ongoing tectonic processes govern mass wasting processes and earthquakes, of which can trigger tsunamis. The interplay of tectonic processes with fluids, i.e. with liquids and gases, critically influences the likelihood of these natural disasters. Compressive stresses promote fluid liberation by compaction and mineral dehydration, which increases the pore fluid pressure. Variations in fluid pressure can influence normal stresses in sediments and faults, and consequently, also the faul strength and the stick-slip-behavior of faults (e.g. Scholz 1998, Tobin and Saffer 2009). Dynamic fluid pressure osciallations further affect permeability (e.g. Elkhoury et al. 2006, 2011), and can lead to a variety of anomalous seismogenic events, including episodic tremor and slip and very-low frequency earthquakes (e.g. Rubinstein et al. 2009; Thomas et al. 2009; Saffer and Tobin 2011; Kitajima and Saffer 2012). Commonly associated with seismogenic events is the expulsion of fluids via fluid escape structures, e.g. mud volcanoes. These features are common in forearc basins, but can also form at other locations in the subduction complex (e.g. Limonov et al. 1994; Henry et al. 1996; Kopf 2002, 2008; Morita et al. 2004; Tsunogai et al. 2012).

[2] The relationship between tectonic processes and fluids is also supposed to be a major driving mechanism for seismogenesis at the Nankai Trough, SE offshore Japan (e.g. Saffer and Bekins 1998; Tobin and Saffer 2009). During the last 15 Ma, ongoing underthrusting of the Philippine Sea Plate beneath the Eurasian Plate led to the development of a > 100 km wide accretionary prism (e.g. Taira et al. 1992; Taira 2001). A major splay fault system, termed "Megasplay fault", mechanically separates the accretionary prism in an inner and a frontal part overlying the seismogenic and aseismic part of the thrust fault boundary, respectively (Wang and Hu 2006). The Megasplay fault system is suggested to be hydraulically connected to the thrust fault boundary (e.g. Tobin and Saffer 2009). If fluids can migrate along the splay fault system, the effective stress at the thrust fault boundary would increase, which influences the frictional instability and stick-slip behavior (Scholz 1998). Eventually, the Megasplay fault might control the updip limit of

the seismogenic zone (Byrne et al. 1988; Moore and Saffer 2001; Tobin and Saffer 2009). However, whether the splay fault acts as fluid conduit is not clear. Although active fluid flow can be inferred from cold seeps, heat flow measurements and seismic data (Ashi et al. 2002; Toki et al. 2004; Park et al. 2010; Hamamoto et al. 2011), recent studies based on cored material and geochemical data cannot support this hypothesis (Solomon et al. 2008; Hirono et al. 2009; Sakaguchi et la. 2011; Yamaguchi et al. 2011).

[3] At the same time, fluids are escaping further landwards in the Kumano forearc basin. The basin hosts several mud volcanoes, which were mapped and/or cored (Kuramoto et al. 2001; Sawada et al. 2002; Morita et al. 2004; Nakamura et al. 2005, 2007; Kasaya et al. 2011; Tsunogai et al. 2012). Most of the mud volcanoes seem to be inactive, and were not re-activated during recent local earthquakes, e.g. the 1944 Tonankai M8.1 or 1946 Nankaido M8.3 earthquakes. This is surprising, giving the good correspondence between earthquakes and mud volcanism worldwide (e.g. Manga et al. 2009). In the Kumano Basin, only one mud volcano emitted thermogenic methane plumes into the water column as response to an M7.5 earthquake (Tsunogai et al. 2012). Although thermogenic methane was released, the organic content of clasts ejected by the mud volcanoes seems to be too immature to be derived from the same depths as the thermogenic gas (Morita et al. 2004). Therefore, ejecta from mud volcanoes, including the fluidized mud, gases, and clasts, are assumed to be derived from different stratigraphic levels. So far, however, no study was carried out that targeted the source depth of fluids migrating through the Kumano forearc basin and the underlying accretionary prism.

[4] To summarize, fluid generation and migration in the Nankai subduction complex is not satisfactorily answered. The following questions remain:

(1) Can the Megasplay fault serve as fluid migration pathway? What are its hydrogeological characteristics? Can earthquakes and/or seismic waves dynamically influence the fluid pressure to an extent that permeability changes?

(2) What is the source depth of individual fluids? Where are hydrocarbons generated? Can fluids travel from the plate boundary through the accretionary prism and the forearc basins sediments to the seafloor?

(3) How are these fluids expelled? What information can mud volcanoes provide in terms of paleo-fluid migration? What is the source depth? Are there temporal and spatial changes in mud volcanism?

ONGOING PROJECTS AND AVAILABLE TECHNOLOGY

[5] In order to answer these questions, this PhD thesis needed to be embedded in two different projects: the IODP NanTroSEIZE (Integrated Ocean Drilling Program Nankai Trough Seismogenic

Zone Experiment) and project MeMo ("MeBo Drilling and in situ Long-term Monitoring in the Nankai Trough Accretionary Complex, Japan"). Both projects targeted the same study area, and complemented each other in terms of available technology and objectives.

[6] In the course of IODP NanTroSEIZE, a borehole transect was established with drilling vessel *Chikyu*, SE offshore the Japanese Kii Peninsula. The transect starts at the incoming Philippine Sea Plate and extends over the frontal part of the accretionary prism into the Kumano forearc basin. The overall objective of NanTroSEIZE is to understand seismogenesis at the Nankai Trough, and to access, sample and instrument the seismogenic part of the plate boundary (Kinoshita et al. 2006). As part of this overarching goal, the Megasplay fault was instrumented with a temporary long-term monitoring instrument, termed SmartPlug, during IODP Expedition 319 (Saffer et al. 2010). It measured fluid pressure, which can serve as proxy for strain and seismo-tectonic processes (Davis et al. 2006, 2009, 2013), and fluid temperature, for almost 15 months.

[7] With the goal in mind to reach the seismogenic zone, riser drilling in the Kumano forearc basin commenced at Site C0009 during Expedition 319 (Saffer et al. 2010), and at Site C0002 during IODP Expeditions 338 and 348 (Strasser et al. 2014; Expedition 348 Scientists and Scientific Participants 2014). During IODP Exps. 338 and 348, it was possible to use the newly installed drilling mud gas monitoring system, which enabled real-time gas analyses and gas sampling while drilling. It thus provided the opportunity to investigate the *in situ* gas composition at depth in the Kumano forearc basin and underlying accretionary prism.

[8] Project MeMo complemented the efforts of IODP NanTroSEIZE by mapping, coring and instrumentation of mud volcanoes in the Kumano forearc basin. Riser drilling was not possible with research vessel *Sonne*, therefore mud volcanoes were used as "tectonic windows" to deep-seated processed and fluids (Kopf 2002; Kopf et al. 2013). Consequently, the source depth of ejecta, particularly of fluids, and the spatial and temporal variation of mud volcanism could be investigated.

RESEARCH OBJECTIVES

[9] The overall objective of this thesis is to improve our understanding of fluid migration and generation at the Nankai subduction zone complex. To answer the abovementioned open questions, project NanTroSEIZE and MeMo allow the following multifaceted approach:

(1) Investigation of fluid pressure and temperature data obtained by the SmartPlug borehole observatory from the Megasplay fault to answer (i) if fluid migration along the splay fault system is possible (ii) if the pressure and temperature sensors showed coseismic changes

that might point to slip and/or deformation at the splay fault and (iii) to what extend the instrument is capable of monitoring pressure changes.

(2) Investigation of the drilling mud gas data from Site C0002 to answer (i) if the newly installed monitoring system produces reliable data (ii) at what depth thermogenic hydrocarbon generation is to be expected and whether bacterial and thermogenic hydrocarbon gas is mixing at shallow levels of the accretionary prism and (iii) if it is possible, based on helium isotope ratios and radon-222, to detect migration of primordial fluids through the accretionary prism

(3) Radiocarbon dating, X-ray diffraction analyses and determination of illite crystallinity on cores taken from mud volcanoes during project MeMo, combined with thin section analyses on clasts ejected by mud volcanoes and sampling of gas hydrates, to answer (i) if activity of mud volcanoes, and thus fluid migration, is affected by local and regional seismicity (ii) since when fluid migration via mud volcanoes has ceased and if there is a spatial and temporal variability that can be traced along the individual mud volcanoes in the Kumano forearc basin and (iii) at what depths fluidization and density inversion of the mud breccia took place and from what depths fluids and clasts were derived.

References

Ashi J, Kuramoto Si, Morita S, Tsunogai U, Goto S, Kojima S, Okamoto T, Asai S, Utsumi M (2002) Structure and cold seep of the Nankai accretionary prism off Kumano. Outline of the off Kumano survey during YK01–04 Leg 2 Cruise. J Deep Sea Res 20:1–8

Byrne DE, Davis DM, Sykes LR (1988) Loci and maximum size of thrust earthquakes and the mechanics of the shallow region of subduction zones. Tectonics 7:833–857. doi: 10.1029/TC007i004p00833

Davis EE, Becker K, Wang K, Obara K, Ito Y, Kinoshita M (2006) A discrete episode of seismic and aseismic deformation of the Nankai trough subduction zone accretionary prism and incoming Philippine Sea plate. Earth Planet Sci Lett 242:73–84.

Davis EE, Becker K, Wang K, Kinoshita M (2009) Co-seismic and post-seismic pore-fluid pressure changes in the Philippine Sea plate and Nankai decollement in response to a seismogenic strain event off Kii Peninsula, Japan. Earth, Planets Sp 61:649 – 657.

Davis E, Kinoshita M, Becker K, Wang K, Asano Y, Ito Y (2013) Episodic deformation and inferred slow slip at the Nankai subduction zone during the first decade of CORK borehole pressure and VLFE monitoring. Earth Planet Sci Lett 368:110–118. doi: http://dx.doi.org/10.1016/j.epsl.2013.03.009

Elkhoury JE, Brodsky EE, Agnew DC (2006) Seismic waves increase permeability. Nature 441:1135–1138. doi: 10.1038/nature04798

Elkhoury JE, Niemeijer A, Brodsky EE, Marone C (2011) Laboratory observations of permeability enhancement by fluid pressure oscillation of in situ fractured rock. J Geophys Res 116:B02311. doi: 10.1029/2010jb007759

Expedition 348 Scientists, Scientific Participants (2014) Expedition 348 Preliminary Report NanTroSEIZE Stage 3 : NanTroSEIZE plate boundary deep riser 3. IODP Prelim Rep 348:71. doi: 10.2204/iodp.pr.348.2014

Henry P, Le Pichon X, Lallemant S, Lance S, Martin JB, Foucher J-P, Fiala-Médioni A, Rostek F, Guilhaumou N, Pranal V, Castrec M (1996) Fluid flow in and around a mud volcano field seaward of the Barbados accretionary wedge: Results from Manon cruise. J Geophys Res Solid Earth 101:20297–20323. doi: 10.1029/96JB00953

Hamamoto H, Yamano M, Goto S, Kinoshita M, Fujino K, Wang K (2011) Heat flow distribution and thermal structure of the Nankai subduction zone off the Kii Peninsula. Geochem Geophys Geosyst 12:Q0AD20. doi:10.1029/2011GC003623

Hirono T, Ujiie K, Ishikawa T, Mishima T, Hamada Y, Tanimizu M, Soh W, Kinoshita M (2009) Estimation of temperature rise in a shallow slip zone of the megasplay fault in the Nankai Trough. Tectonophysics 478:215–220

Kasaya T, Kanamatsu T, Sawa T, Kinosita M, Tukioka S, Yamamoto F (2011) Acoustic images of the submarine fan system of the northern Kumano Basin obtained during the experimental dives of the Deep Sea AUV URASHIMA. Explor Geophys Butsuri-Tansa Jigu-Mulli-wa-Mulli-Tamsa 42:80–87.

Kinoshita M, Moore G, von Huene R, Tobin H, Ranero CR (2006) The Seismogenic Zone Experiment. Oceanography 19:28–38.

Kitajima H, Saffer DM (2012) Elevated pore pressure and anomalously low stress in regions of low frequency earthquakes along the Nankai Trough subduction megathrust. Geophys Res Lett 39:L23301. doi: 10.1029/2012GL053793

Kopf AJ (2002) Significance of mud volcanism. Rev Geophys 40:1005. doi: 10.1029/2000rg000093

Kopf AJ (2008) Volcanoes: Making calderas from mud. Nat Geosci 1:500–501.

Kopf A, Araki E, Toczko S, Expedition 332 Scientists (2011) Proc IODP 332. Integrated Ocean Drilling Program Management International, Tokyo. doi:10.2204/iodp.proc.332.2011

Kopf A, et al. (2013) Report and Preliminary Results of R/V SONNE Cruise SO222. Berichte, MARUM – Zent für Mar Umweltwissenschaften, Fachbereich Geowissenschaften, Univ Bremen 297:121.

Kuramoto S, Ashi J, Greinert J, Gulick S, Ishimura T, Morita S, Nakamura K, Okada M, Okamoto T, Rickert D, Saito S, Suess E, Tsunogai U, Tomosui T (2001) Surface Observations of Subduction Related Mud Volcanoes and Large Thrust Sheets in the Nankai Subduction Margin; Report on YK00-10 and YK01-04 Cruises. JAMSTEC J Deep Sea Res 19:131 – 139.

Limonov AF, Woodside JM, Ivanov MK (1994) Mud volcanism in the Mediterranean and Black seas and shallow structure of the Eratosthenes Seamount. Initial results Geol Geophys Investig Dur third "'Training-through-Research'"Cruise R/N Gelendzhik 64:173.

Manga M, Brumm M, Rudolph ML (2009) Earthquake triggering of mud volcanoes. Mar Pet Geol 26:1785–1798.

Moore JC, Saffer D (2001) Updip limit of the seismogenic zone beneath the accretionary prism of southwest Japan: An effect of diagenetic to low-grade metamorphic processes and increasing effective stress. Geology 29:183–186. doi: 10.1130/0091-7613(2001)029<0183:ulotsz>2.0.co;2

Morita S, Ashi J, Aoike K, Kuramoto S (2004) Evolution of Kumano Basin and Sources of Clastic Ejecta and Pore Fluid in Kumano Mud Volcanoes, Eastern Nankai Trough. Int. Symp. Methane Hydrates Fluid Flow Up. Accretionary Prism.

Nakamura Y, Ashi J, Morita S, Mochizuki K (2005) Detailed Seismic Image of Mud Volcones in Kumano Basin. Am. Geophys. Union, Fall Meet. 2005, Abstr. #T13B-0457. p #T13B–0457

Nakamura Y, Morita S, Ashi J (2007) Mini 3D seismic surveys of mud volcanoes in the Kumano Basin. Am. Geophys. Union, Fall Meet. 2007, Abstr. p #V13B–1352

Park J-O, Fujie G, Wijerathne L, Hori T, Kodaira S, Fukao Y, Moore GF, Bangs NL, Kuramoto Si, Taira A (2010) A low-velocity zone with weak reflectivity along the Nankai subduction zone. Geology 38:283–286

Rubinstein JL, Gomberg J, Vidale JE, Wech AG, Kao H, Creager KC, Rogers G (2009) Seismic wave triggering of nonvolcanic tremor, episodic tremor and slip, and earthquakes on Vancouver Island. J Geophys Res Solid Earth 114:B00A01. doi: 10.1029/2008JB005875

Saffer DM, Bekins BA (1998) Episodic fluid flow in the Nankai accretionary complex: Timescale, geochemistry, flow rates, and fluid budget. J Geophys Res Solid Earth 103:30351–30370. doi: 10.1029/98JB01983

Saffer DM, Tobin HJ (2011) Hydrogeology and Mechanics of Subduction Zone Forearcs: Fluid Flow and Pore Pressure. Annu Rev Earth Planet Sci 39:157–186. doi: doi:10.1146/annurev-earth-040610-133408

Saffer D, McNeill L, Byrne T, Araki E, Toczko S, Eguchi N, Takahashi K, Expedition 319 Scientists (2010) Proc IODP 319. Integrated Ocean Drilling Program Management International, Tokyo. doi:10.2204/iodp.proc.319.104.2010

Sakaguchi A, Chester F, Curewitz D, Fabbri O, Goldsby D, Kimura G, Li C-F, Masaki Y, Screaton EJ, Tsutsumi A, Ujiie K, Yamaguchi A (2011) Seismic slip propagation to the updip end of plate boundary subduction interface faults: vitrinite reflectance geothermometry on Integrated Ocean Drilling Program NanTro SEIZE cores. Geology 39:395–398

Sawada T, Ashi J, Murayama M, Aoike K, Ujiie Y, Kuramoto S, Kinoshita M, Tokuyama H (2002) Surface Geology and History of Mud Volcanoes in the Kumano Trough Based on Analysis of Piston Cores. Am. Geophys. Union, Fall Meet. 2002, Abstr. #T11B-1249

Scholz CH (1998) Earthquakes and friction laws. Nature 391:37–42.

Solomon EA, Hulme S, Claesson L, Tomaru H, Wheat G, Riedinger N, scientists TE (2008) Geochemical constraints on fluid-rock reactions, fluid sources, and flow pathways along the NanTroSEIZE Transect; IODP Expeditions 315/316. American Geophysical Union, Fall Meeting 2008, abstract #T21F-03

Strasser M, Dugan B, Kanagawa K, Moore GF, Toczko S, Maeda L, Kido Y, Moe KT, Sanada Y, Esteban L, Fabbri O, Geersen J, Hammerschmidt S, Hayashi H, Heirman K, Hüpers A, Jurado MJ, Kameo K, Kanamatsu T, Kitajima H, Masuda H, Milliken K, Mishra R, Motoyama I, Olcott K, Oohashi K, Pickering KT, Ramirez SG, Rashid H, Sawyer D, Schleicher A, Shan Y, Skarbek R, Song I, Takeshita T, Toki T, Tudge J, Webb S, Wilson DJ, Wu H, Yamaguchi A (2014) Site C0002. IODP Proc 338:248. doi: 10.2204/iodp.proc.338.103.2014

Taira A, Hill I, Firth J, Berner U, Brückmann W, Byrne T, Chabernaud T, Fisher A, Foucher J-P, Gamo T, Gieskes J, Hyndman R, Karig D, Kastner M, Kato Y, Lallemant S, Lu R, Maltman A, Moore G, Moran K, Olaffson G, Owens W, Pickering K, Siena F, Taylor E, Underwood M, Wilkinson C, Yamano M, Zhang J (1992) Sediment deformation and hydrogeology of the Nankai Trough accretionary prism: Synthesis of shipboard results of ODP Leg 131. Earth Planet Sci Lett 109:431–450. doi: 10.1016/0012-821X(92)90104-4

Taira A (2001) Tectonic Evolution of the Japanese Arc System. Annu Rev Earth Planet Sci 29:109–134. doi: 10.1146/annurev.earth.29.1.109

Thomas AM, Nadeau RM, Burgmann R (2009) Tremor-tide correlations and near-lithostatic pore pressure on the deep San Andreas fault. Nature 462:1048–1051.

Tobin HJ, Saffer DM (2009) Elevated fluid pressure and extreme mechanical weakness of a plate boundary thrust, Nankai Trough subduction zone. Geology 37:679–682. doi: 10.1130/g25752a.1

Toki T, Tsunogai U, Gamo T, Kuramoto S, Ashi J (2004) Detection of low-chloride fluids beneath a cold seep field on the Nankai accretionary wedge off Kumano, south of Japan. Earth Planet Sci Lett 228:37–47

Tsunogai U, Maegawa K, Sato S, Komatsu DD, Nakagawa F, Toki T, Ashi J (2012) Coseimic massive methane release from a submarine mud volcano. Earth Planet Sci Lett 341-344:79–85. doi: 10.1016/j.epsl.2012.06.004

Wang K, Hu Y (2006) Accretionary prisms in subduction earthquake cycles: The theory of dynamic Coulomb wedge. J Geophys Res 111:B06410. doi: 10.1029/2005jb004094

Yamaguchi A, Sakaguchi A, Sakamoto T, Iijima K, Kameda J, Kimura G, Ujiie K, Chester FM, Fabbri O, Goldsby D, Tsutsumi A, Li C-F, Curewitz D (2011) Progressive illitization in fault gouge caused by seismic slip propagation along a megasplay fault in the Nankai Trough. Geology 39:995–998

CHAPTER 1.2

THESIS OUTLINE

[1] This cumulative dissertation is structured in eight different main chapters, excluding the Preface, Abstract/Zusammenfassung, Acknowledgements, and Appendices. In each subchapter a list of references is provided and paragraphs are numbered consecutively. In the main text, where multiple citations were necessary, references were sorted after years in ascending order. In the following, a short overview of the different chapters and subchapters is given, and for chapters 5, 6 and 7, the contributions of the individual authors are highlighted.

[2] <u>Chapter 1</u> gives an introduction to the motivation of this thesis, and includes this thesis outline. <u>Chapter 2</u> introduces the general regional geology of the Nankai Trough subduction zone complex. The focus lies on the overall tectonic setting, age, and morphotectonic evolution. Specific information about geological and structural features are given in the individual manuscripts presented in chapters 5, 6, and 7.

[3] <u>Chapter 3</u> provides background information about the role of fluids in subduction zones. The chapter starts with a short introduction about what fluids are, what processes affect the fluid composition and where they originate from in subduction zones. In the following subchapters, the role of fault zones regarding fluid migration is reviewed, along with a summary of submarine mud volcanism as typical surface expression of escaping fluids.

[4] <u>Chapter 4</u> is a short review of the offshore borehole monitoring techniques used in this study. The chapter is separated in two subsections, including the development and recent advances of borehole observatories used in ocean scientific drilling (*Chapter 4.1*) and real-time drilling mud gas monitoring as part of mud logging services conduced on drill rigs (*Chapter 4.2*).

[5] <u>Chapter 5</u> includes all four manuscripts that are based on SmartPlug borehole observatory pressure and temperature data monitored in a borehole penetrating the Megasplay fault at IODP Site C0010. In particular:

Chapter 5.1 got published in *Tectonophysics* (Hammerschmidt et al. 2013a), and is based essentially on the Master thesis of S.B. Hammerschmidt that was written at Fachbereich 5, University of Bremen, in 2011. The manuscript, however, was reduced substantially, some figures were modified (e.g. Figures 12, 22), some figures were added (Figures 10, 16, 17, 18), and a chapter about "Seal Integrity" was included. The publication reports temperature and pressure changes

monitored at the splay fault, which are related to seismic and tsunami waves triggered by regional/distant earthquakes, and microseism generated by storms. The main work (data analyses, manuscript drafting) was done by S.B. Hammerschmidt. E.E. Davis provided Figs. 16, 17, and 18. E.E. Davis helped with drafting the manuscript, and both E.E. Davis and A. Kopf provided additional comments and suggestions.

Chapter 5.2 was published in *Geo-Marine Letters* (Hammerschmidt et al. 2013b) and elucidates the possibility of fluid migration at the Nankai Trough Megasplay fault zone using a pressure response model and laboratory permeability tests on core samples. Two results can be drawn from the analyses: the SmartPlug provides the appropriate dimensions and sensors to monitor fluid pressure transients at tidal frequencies, and fluid flow along the splay fault is unlikely. S.B. Hammerschmidt conducted the major part of the work, including permeability measurements, modelling, data analyses and drafting of the manuscript. A. Hüpers, E.E. Davis and A. Kopf provided additional comments and suggestions. A. Hüpers further helped with laboratory work.

Chapter 5.3 is a follow-up manuscript of Hammerschmidt et al. (2013a). The main work was done during a research stay of S.B. Hammerschmidt at the Japan Agency for Marine-Earth Science and Technology (JAMSTEC) in 2012. It is ready for submission to *Ocean Science*. Thorough analyses of data from the Japanese Dense Ocean Floor Network for Earthquakes and Tsunamis (DONET) revealed the presence of non-volcanic tremor signals, which caused distinctive pressure transients. The uniqueness of the signal is attributed to the low strain caused by slow slip or missing propagation of the slip and subsequent loading of the locked seismogenic zone. S.B. Hammerschmidt conducted all work, including data analyses, modelling and manuscript writing. E.E. Davis and A. Kopf provided additional comments and suggestions. E. Araki provided access to DONET and a working place at JAMSTEC. He further helped with interpretation of the seismological data.

Chapter 5.4, similar to Chapter 5.3, is based on work conducted at JAMSTEC using waveform data from DONET. The manuscript is ready for submission to *Geoscience Letters* and provides a thorough analyses of anomalous pressure transients that are not related to any obvious seismogenic or atmospheric event. Inclusion and analyses of data from DONET revealed the presence of teleseismic microseism in the pressure data. Based on DONET data and modelling of seismic wave propagation and attenuation inside the borehole, pressure transients previously interpreted as artefacts are supposed to be anomalous pressure transients caused by generic seismic waves. S.B. Hammerschmidt conducted all work, including data analyses, modelling and manuscript writing. E.E. Davis and A. Kopf provided additional comments and suggestions, E.

Araki provided access to DONET and a working place at JAMSTEC. He further helped with interpretation of the seismological data.

[6] **Chapter 6** covers all manuscripts based on real-time drilling mud gas data. In particular:

Chapter 6.1 focuses on hydrocarbon gases found in drilling mud gas sampled during IODP Expedition 348. After a comparison with shipboard data using different gas ratios, further analyses allowed estimation of in situ temperature, gas mixing and maturity. The manuscript was submitted to *Geochemical Transactions* and is currently under revision. S.B. Hammerschmidt had the lead role in all stages of data acquisition, analyses and interpretation, and drafted this manuscript. T. Wiersberg, V. Heuer and J. Wendt contributed substantially in pre- and post-cruise work, and were of tremendous help in sample analyses. The method chapter describing the deuterium analyses was drafted by V. Heuer and J. Wendt. The manuscript benefited from comments and suggestions by J. Erzinger and A. Kopf. J. Erzinger further provided the instruments to conduct shore-based analyses.

Chapter 6.2 analyses fluid migration in the accretionary prism based on noble gases and their isotopes detected in drilling mud gas data. The manuscript is still in preparation for *Geochemistry, Geophysics, Geosystems*. S.B. Hammerschmidt had the lead role in sampling, sample analyses, data evaluation and drafting of the manuscript. T. Wiersberg contributed both tables and helped with data evaluation and drafting of the manuscript. H. Kumagai provided the instrument for shipboard ^{222}Rn measurements and contributed both ^{222}Rn datasets. S. Fuchida was of tremendous help for data generation and sampling during IODP Expedition 348. J. Erzinger and A. Kopf provided comments and suggestions. It should be highlighted that the ^{222}Rn and lithological data for Holes C0002N and C0002P are still protected under IODPs moratorium regulations, thus Expedition 348 Scientists were added as co-author.

[7] **Chapter 7** covers all manuscripts that are not based on monitoring data but which further improved the understanding of deep fluid migration in the Nankai subduction complex. In particular:

Chapter 7.1 was published in *Geochemistry, Geophysics, Geosystems* (Pape et al. 2014), and reports origins of hydrocarbon gases sampled at mud volcanoes in the Kumano forearc basin. The results suggest that all investigated mud volcanoes are inactive at the moment, and that the released hydrocarbon gases originate from the Cretaceous to Tertiary Shimanto belt below the Kumano forearc basin. T. Pape conducted the main work on this manuscript, including sample collection, gas analyses, data evaluation, and interpretation. P. Geprägs, S.B. Hammerschmidt and T. Fleischmann helped with sample collection. P. Wintersteller, J. Wei and T. Fleischmann

provided additional data and figures. P. Geprägs and S.B. Hammerschmidt helped with drafting the manuscript, while G. Bohrmann and A. Kopf provided additional comments and suggestions.

In *Chapter 7.2* the temporal and spatial variability of mud volcanism in the Kumano forearc basin is investigated. The manuscript is still in preparation for submission to *Earth, Planets, Space*. S.B. Hammerschmidt had the lead role data evaluation and drafting of the manuscript. A. Kopf provided comments and suggestions, and helped with sampling and data evaluation.

Chapter 7.3 complements Chapter 7.2. While the latter focusses on the onset and termination of mud volcanism, Chapter 7.3 deals tries to depict the origin of the fluidized mud and the clasts ejected by the mud volcanoes in the Kumano forearc basin. The manuscript is still in preparation for submission to *Earth, Planets, Space*. S.B. Hammerschmidt had the lead role in sampling, thin section analyses, data evaluation and drafting of the manuscript. A. Kopf provided comments and suggestions, and helped with sampling and data evaluation.

[8] ***Chapter 8*** summarizes the main findings of this work, and provides suggestions for future studies and improvements of the individual monitoring techniques.

[9] The ***Appendices*** include supplementary material for the individual manuscripts (Appendix A), a co-authored technical manuscript about borehole observatories designed for installation with the MARUM MeBo (Meeresboden-Bohrgerät; Appendix B) and an overview of conference contributions (Appendix C) and expeditions attended in the last 3 years (Appendix D).

References

Hammerschmidt S, Davis EE, Kopf A (2013a) Fluid pressure and temperature transients detected at the Nankai Trough Megasplay Fault: Results from the SmartPlug borehole observatory. Tectonophysics 600:116 – 133. doi: 10.1016/j.tecto.2013.02.010

Hammerschmidt SB, Davis EE, Hüpers A, Kopf A (2013b) Limitation of fluid flow at the Nankai Trough megasplay fault zone. Geo-Marine Lett 33:405–418. doi: 10.1007/s00367-013-0337-z

Pape T, Geprägs P, Hammerschmidt S, Wintersteller P, Wei J, Fleischmann T, Bohrmann G, Kopf AJ (2014) Hydrocarbon seepage and its sources at mud volcanoes of the Kumano forearc basin, Nankai Trough subduction zone. Geochemistry, Geophys Geosystems 15:2180–2194. doi: 10.1002/2013GC005057

CHAPTER 2
The Nankai Trough Subduction Zone Complex

OVERVIEW

[1] The Nankai Trough Subduction Zone formed as a consequence of NW-directed subduction of the Philippine Sea Plate (PSP) beneath the Eurasian Plate at a rate of 4 – 6.5 cm yr^{-1} (Seno et al. 1993; Miyazaki and Heno 2001). The deformation front is located ca. 80 – 160 km SE offshore Japan (Moore et al. 2001), and extends roughly along the Nankaidō (meaning "southern sea circuit/region"), between the Izu Bonin Arc in the NE and the Kyushu-Palau-Ridge in the SW (Figure 1). The Shikoku Basin in the northern part of the PSP opened as a consequence of backarc spreading of the Izu Bonin Arc in the early Miocene (ca. 21 - 23 Ma; Okino et al. 1999; Marcaillou et al. 2012). Subduction of the PSP initiated at around 15 Ma, temporarily ceased at 12 Ma, and commenced again at 6 Ma (e.g. Taira 2001; Kimura et al. 2014). The hemipelagic sediments of the Shikoku basin are offscraped during subduction, which has formed a currently > 100 km-wide accretionary prism (Taira et al. 1992; Saito et al. 2009; Henry et al. 2012; Kimura et al. 2014). The slab dip increases gradually with distance from the trench, from ca. 3° within the first 30 km to >40° at distances greater 180 km landward of the trench (Nakamura et al. 1997; Cummins et al. 2002; Park et al. 2002; Marcaillou et al. 2012). The Nankai Trough is one of the most earthquake prone regions in the world, with a recurrence interval of 100 – 200 years for major earthquakes (Ando 1975).
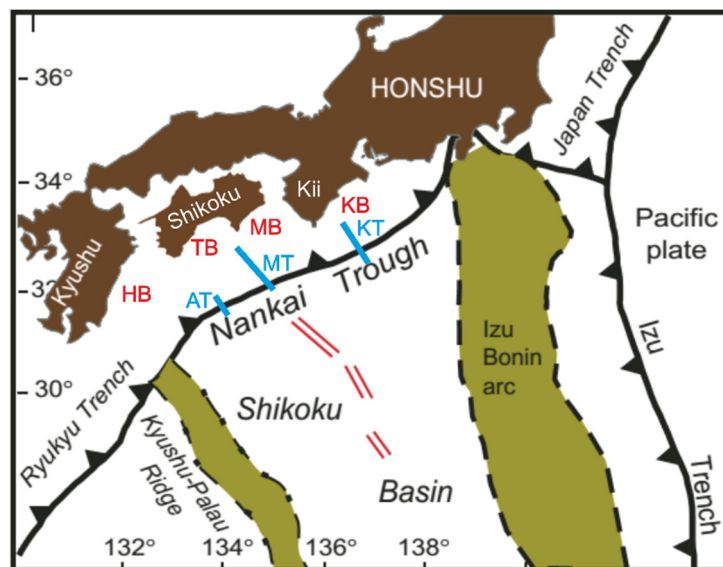
Figure 1: Regional setting of the Nankai Trough Subduction Zone (modified from Underwood and Steurer 2003). The Nankai Trough is situated between the Izu Bonin Arc and the Kyushu-Palau Ridge. To date, three different transects have been drilled (blue lines and labels): the Ashizuri transect (AT) the Muroto transect (MT) and the Kumano transect (KT). Forearc basins are, from NE to SW (red labelled): Kumano Basin (KB), Muroto Basin (MB), Tosa Basin (TB) and Hyuga Basin (HB).

[2] Further landwards, the Nankai Trough is bound by four different forearc basins, including, from NE to SW (red label in Figure 1): Kumano Basin, Muroto Basin, Tosa Basin, and Hyuga Basin. An ancient accretionary prism, the Shimanto Belt, is located landward of the forearc basins and was formed during subduction of the Kula, Pacific and Philippine Sea Plate between the

Cretaceous and the Neogene (Isozaki 1996; Kitamura and Kimura 2012). Seaward of the forearc basins, extensive drilling and coring over the course of the Deep Sea Drilling Program (DSDP), Ocean Drilling Program (ODP) and Integrated Ocean Drilling Program (IODP) was performed in three transects named the Ashizuri transect, the Muroto transect and the Kumano transect, respectively (Figure 1). Most recently, the Kumano transect was established as part of the Nankai Trough Seismogenic Zone Experiment (NanTroSEIZE), and can be separated in six morphotectonic domains (from SE to NW; Moore et al. 2009; Figure 2): the proto-thrust zone (PTZ), the frontal thrust zone (FTZ), the imbricate thrust zone (ITZ), the megasplay fault zone (MSFZ), the Kumano Basin edge fault zone (KBEFZ) and the fore-arc basin zone (FBZ).
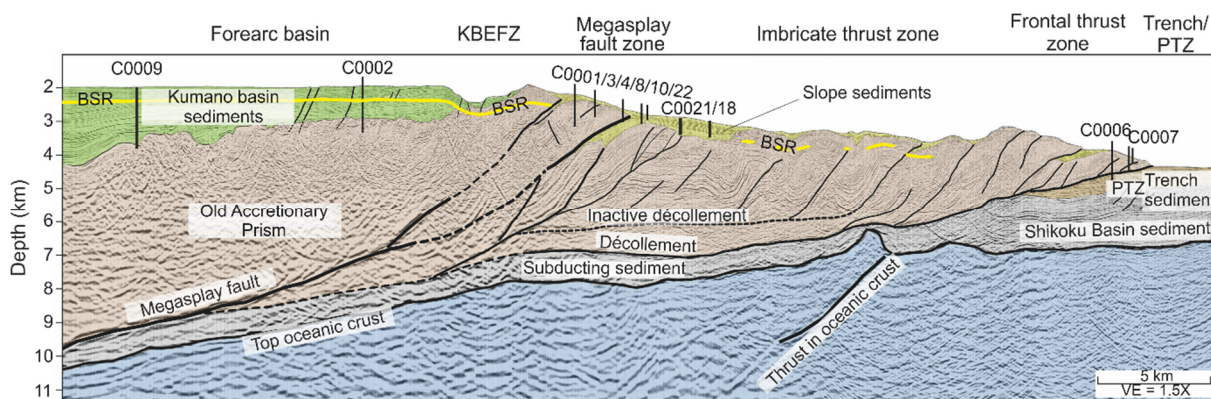
Figure 2: *Interpreted seismic cross-section of the Kumano transect offshore and south-east of the Kii peninsula (modified from Moore et al. 2009, after Moore et al. 2013). Starting with the trench, the transect is separated in six morphotectonic domains, i.e. the PTZ (proto-thrust zone), the frontal thrust zone, the imbricate thrust zone, the megasplay fault zone, the KBEFZ (Kumano Basin Edge Fault Zone) and the Kumano Forearc basin. Not shown are drill sites on the incoming Philippine Sea Plate. The cross-section has two distinct features: the Megasplay fault zone, and the BSR (bottom simulating reflector). Also shown are the underthrusted Shikoku basin sediments.*

[3] Opening of the FBZ and deposition of predominantly hemipelagic sediments started in the late Miocene (e.g., Expedition 319 Scientists 2010; Hayman et al. 2012). The basin fill is controlled by a submarine fan turbidite system, and transports material from the Miocene Kumano/Tanabe group, the Cretaceous Shimanto Supergroup and the metamorphic Sanbagawa belt, which are all disclosed on the Kii Peninsula (Morita et al. 2004; Choi et al. 2011; Kasaya et al. 2011; Takano et al. 2013; Usman et al. 2014). Rate of sedimentation increased significantly as a result of splay fault activity between 1.67 and 1.56 Ma (Strasser et al. 2009). Currently, the Kumano basin is filled with ca. 2000 m of sediments, at water depths of up to 2100 m, and comprises an area of ca. 70000 km^2. It us underlain by Miocene to Cretaceous material of the subducting Shikoku Basin and the Shimanto Belt, respectively (Taira et al. 1992; Expedition 348 Scientists and Scientific Participants 2014). The seafloor in the Kumano basin is characterized by fluid escape structures, with the most prominent being mud volcanoes that are scattered across the basin (Kuramoto et

al. 2001, Morita et al. 2004; Tsunogai et al. 2012; Pape et al. 2014). Active fluid expulsion is suggested to be episodic and related to earthquakes (Tsunogai et al. 2012).

[4] One of the most prominent features in the Nankai subduction complex is a major splay fault system cutting through the accretionary prism seaward of the Kumano basin (the MSFZ). Today, this splay fault, termed the Megasplay fault, is inferred to be inactive (Strasser et al. 2009; 2011), although recent deformation structures in the Kumano basin sediments (Moore et al. 2007) and slope sediments overlying the splay fault indicate otherwise (Kimura et al. 2011, Alves et al. 2013a). Around 50 – 55 km landward of the deformation front at around 10 km depth, the Megasplay branches upwards from the plate boundary fault, reaching the seafloor at ~25 km from the trench. The Megasplay fault is suggested to be hydraulically connected to the seismogenic zone of the thrust fault boundary. If it serves as migration pathway for fluids, it could significantly control the slip behavior of the plate boundary fault and thus, influence seismicity (Scholz 1998; Tobin and Saffer 2001; Saffer and Tobin 2011). However, whether fluid migration along this fault zone occurs remains unresolved (e.g., Screaton et al. 2009; Park et al. 2010; Sakaguchi et al. 2011; Yamaguchi et al. 2011).

[5] Another prominent feature in the Nankai subduction complex is a bottom simulating reflector (BSR), that can be traced from the Kumano basin all the way to the deformation front (Ashi et al. 2002; Foucher et al. 2002; Baba and Yamada 2004). The BSR is the seismo-acoustic manifestation of gas hydrates, which are nurtured by free gas (mainly methane) migrating through the accretionary prism, along faults at greater depths, and via diffusion in more shallow areas (Alves et al. 2013b; Yamada et al. 2014).

[6] Investigations presented in this thesis focus solely on the FTZ, MSFZ and FBZ. More detailed information about the local structural and lithological features is provided in the individual manuscripts (see chapters 5, 6 and 7, and subsequent subchapters).

References

Alves TM, Strasser M, Moore GF (2013a) Erosional features as indicators of thrust fault activity (Nankai Trough, Japan). Mar Geol. doi: 10.1016/j.margeo.2013.07.011

Alves TM, Bale S, Moore GF (2013b) Gas Hydrate Stability Zone Offshore Nankai, Japan - Is The Gas Hydrate Stable at Present ? 75th EAGE Conf. Exhib. London, UK, pp 10–13

Ando M (1975) Source Mechanisms and Tectonic Significance of Historical Earthquakes along the Nankai Trough, Japan. Tectonophysics 27:119 – 140.

Ashi J, Tokuyama H, Taira A (2002) Distribution of methane hydrate BSRs and its implication for the prism growth in the Nankai Trough. Mar Geol 187:177–191. doi: 10.1016/S0025-3227(02)00265-7

Baba T, Yamada Y (2004) BSRs and Associated Reflections as an Indicator of Gas Hydrate and Free Gas Accumulation : An Example of Accretionary Prism and Forearc Basin System along the Nankai Trough , off Central Japan. Resour Geol 54:11–24.

Choi P-Y, Nakae S, Kim H (2011) Fault tectonic analysis of Kii peninsula, Southwest Japan: Preliminary approach to Neogene paleostress sequence near the Nankai subduction zone. Isl Arc 20:455–476. doi: 10.1111/j.1440-1738.2011.00779.x

Cummins PR, Baba T, Kodaira S, Kaneda Y (2002) The 1946 Nankai earthquake and segmentation of the Nankai Trough. Phys Earth Planet Inter 132:75–87. doi: 10.1016/S0031-9201(02)00045-6

Expedition 319 Scientists (2010) Site C0010. In: Saffer D, McNeill L, Byrne T, Araki E, Toczko S, Eguchi N, Takahashi K, Expedition 319 Scientists (eds) Proc IODP 319. Integrated Ocean Drilling Program Management International, Tokyo. doi:10.2204/iodp.proc.319.104.2010

Expedition 348 Scientists and Scientific Participants (2014) Expedition 348 Preliminary Report NanTroSEIZE Stage 3 : NanTroSEIZE plate boundary deep riser 3. IODP Prelim Rep 348:71. doi: 10.2204/iodp.pr.348.2014

Foucher J-P, Nouzé H, Henry P (2002) Observation and tentative interpretation of a double BSR on the Nankai slope. Mar Geol 187:161–175. doi: 10.1016/S0025-3227(02)00264-5

Hayman NW, Timothy B. B, Lisa C. M, Kyuichi K, Toshiya K, Cassandra M. B, Anja M. S, Gary J. H (2012) Structural evolution of an inner accretionary wedge and forearc basin initiation, Nankai margin, Japan. Earth Planet Sci Lett 353–354:163–172.

Henry, P., T. Kanamatsu, Moe K, the Expedition 333 Scientists (2009) NanTroSEIZE Stage 2: Subduction Inputs and Heat Flow. Proc IODP 333. Integrated Ocean Drilling Program Management International, Tokyo.

Isozaki Y (1996) Anatomy and genesis of a subduction-related orogen: A new view of geotectonic subdivision and evolution of the Japanese Islands. Isl Arc 5:289–320. doi: 10.1111/j.1440-1738.1996.tb00033.x

Kasaya T, Kanamatsu T, Sawa T, Kinosita M, Tukioka S, Yamamoto F (2011) Acoustic images of the submarine fan system of the northern Kumano basin obtained during the experimental dives of the Deep Sea AUV URASHIMA. Copublished in Explor Geophys, Butsuri-Tansa and Jigu-Mulli-wa-Mulli-Tamsa 42:80–87.

Kimura G, Moore GF, Strasser M, Screaton E, Curewitz D, Streiff C, Tobin H (2011) Spatial and temporal evolution of the megasplay fault in the Nankai Trough. Geochem Geophys Geosyst 12:Q0A008. doi: 10.1029/2010gc003335

Kimura G, Hashimoto Y, Kitamura Y, Yamaguchi A, Koge H (2014) Middle Miocene swift migration of the TTT triple junction and rapid crustal growth in southwest Japan — A review. Tectonics 2014TC003531. doi: 10.1002/2014TC003531

Kitamura Y, Kimura G (2012) Dynamic role of tectonic mélange during interseismic process of plate boundary mega earthquakes. Tectonophysics 568–569:39–52. doi: http://dx.doi.org/10.1016/j.tecto.2011.07.008

Kuramoto S, Ashi J, Greinert J, Gulick S, Ishimura T, Morita S, Nakamura K, Okada M, Okamoto T, Rickert D, Saito S, Suess E, Tsunogai U, Tomosui T (2001) Surface Observations of Subduction Related Mud Volcanoes and Large Thrust Sheets in the Nankai Subduction Margin; Report on YK00-10 and YK01-04 Cruises. JAMSTEC J. Deep Sea Res. 19:

Marcaillou B, Henry P, Kinoshita M, Kanamatsu T, Screaton E, Daigle H, Harcouët-Menou V, Lee Y, Matsubayashi O, Kyaw Thu M, Kodaira S, Yamano M, the Expedition 333 Science Party (2012) Seismogenic zone temperatures and heat-flow anomalies in the To-nankai margin segment based on temperature data from IODP expedition 333 and thermal model. Earth Planet Sci Lett 349-350:171–185. doi: 10.1016/j.epsl.2012.06.048

Miyazaki S, Heki K (2001) Crustal velocity field of southwest Japan: Subduction and arc-arc collision. J Geophys Res 106:4305–4326. doi: 10.1029/2000jb900312

Moore GF, Taira A, Klaus A, Becker L, Boeckel B, Cragg BA, Dean A, Fergusson CL, Henry P, Hirano S, Hisamitsu T, Hunze S, Kastner M, Maltman AJ, Morgan JK, Murakami Y, Saffer DM, Sánchez-Gómez M, Screaton EJ, Smith DC, Spivack AJ, Steurer J, Tobin HJ, Ujiie K, Underwood MB, Wilson M (2001) New insights into deformation and fluid flow processes in the Nankai Trough accretionary prism: Results of Ocean Drilling Program Leg 190. Geochem Geophys Geosyst 2(10):1058. doi: 10.1029/2001gc000166

Moore GF, Bangs NL, Taira A, Kuramoto S, Pangborn E, Tobin HJ (2007) Three-Dimensional Splay Fault Geometry and Implications for Tsunami Generation. Science 318:1128–1131. doi: 10.1126/science.1147195

Moore GF, Park J-O, Bangs NL, Gulick SP, Tobin HJ, Nakamura Y, Sato S, Tsuji T, Yoro T, Tanaka H, Uraki S, Kido Y, Sanada Y, Kuramoto S, Taira A (2009) Structural and seismic stratigraphic framework of the NanTroSEIZE Stage 1 transect. Proc Integr Ocean Drill Progr. doi: doi:10.2204/iodp.proc.314315316.102.2009

Moore G, Kanagawa K, Strasser M, Dugan B, Maeda L, Toczko S, the Expedition 338 Scientists (2013) NanTroSEIZE Stage 3 : NanTroSEIZE plate boundary deep riser. IODP Prelim Rep. doi: 10.2204/iodp.pr.338.2013

Morita S, Ashi J, Aoike K, Kuramoto S (2004) Evolution of Kumano Basin and Sources of Clastic Ejecta and Pore Fluid in Kumano Mud Volcanoes, Eastern Nankai Trough. Int. Symp. Methane Hydrates Fluid Flow Up. Accretionary Prism.

Nakamura M, Watanabe H, Konomi T, Kimura S, Miura K (1997) Characteristic activities of subcrustal earthquakes along the outer zone of southwestern Japan. Annu Disaster Prev Res Inst Kyoto Univ 40:1–20.

Okino K, Ohara Y, Kasuga S, Kato Y (1999) The Philippine Sea: New survey results reveal the structure and the history of the marginal basins. Geophys Res Lett 26:2287–2290. doi: 10.1029/1999gl900537

Pape T, Geprägs P, Hammerschmidt S, Wintersteller P, Wei J, Fleischmann T, Bohrmann G, Kopf AJ (2014) Hydrocarbon seepage and its sources at mud volcanoes of the Kumano forearc basin, Nankai Trough subduction zone. Geochemistry, Geophys Geosystems 15:2180–2194. doi: 10.1002/2013GC005057

Park J-O, Tsuru T, Kodaira S, Cummins PR, Kaneda Y (2002) Splay Fault Branching Along the Nankai Subduction Zone. Science (80-) 297:1157–1160. doi: 10.1126/science.1074111

Park J-O, Fujie G, Wijerathne L, Hori T, Kodaira S, Fukao Y, Moore GF, Bangs NL, Kuramoto S, Taira A (2010) A low-velocity zone with weak reflectivity along the Nankai subduction zone. Geology 38:283–286. doi: 10.1130/g30205.1

Saffer DM, Tobin HJ (2011) Hydrogeology and Mechanics of Subduction Zone Forearcs: Fluid Flow and Pore Pressure. Annu Rev Earth Planet Sci 39:157–186. doi: doi:10.1146/annurev-earth-040610-133408

Saito S, Underwood MB, Kubo Y, the Expedition 322 Scientists (2009) NanTroSEIZE Stage 2: Subduction Inputs. Proc IODP 322. Integrated Ocean Drilling Program Management International, Tokyo.

Sakaguchi A, Chester F, Curewitz D, Fabbri O, Goldsby D, Kimura G, Li C-F, Masaki Y, Screaton EJ, Tsutsumi A, Ujiie K, Yamaguchi A (2011) Seismic slip propagation to the updip end of plate boundary subduction interface faults: Vitrinite reflectance geothermometry on Integrated Ocean Drilling Program NanTro SEIZE cores. Geology 39:395–398. doi: 10.1130/g31642.1

Scholz CH (1998) Earthquakes and friction laws. Nature 391:37–42.

Screaton EJ, Kimura G, Curewitz D, the Expedition 316 Scientists (2009) Expedition 316 Summary. In: Kinoshita M, Tobin H, Ashi J, Kimura G, Lallemant S, Screaton EJ, Curewitz D, Masago H, Moe KT, Expedition 314/315/316 Scientists (eds) Proc IODP 314/315/316. Integrated Ocean Drilling Program Management International, Washington, DC. doi:10.2204/iodp.proc.314315316.131.2009

Seno T, Stein S, Gripp AE (1993) A model for the motion of the Philippine Sea plate consistent with NUVEL-1 and geological data. J Geophys Res 98:8.

Strasser M, Moore GF, Kimura G, Kitamura Y, Kopf AJ, Lallemant S, Park J-O, Screaton EJ, Su X, Underwood MB, Zhao X (2009) Origin and evolution of a splay fault in the Nankai accretionary wedge. Nat Geosci 2:648–652. doi: 10.1038/ngeo609

Strasser M, Moore GF, Underwood MB, Guo J, Screaton EJ (2011) Slumping and mass transport deposition in the Nankai fore arc: Evidence from IODP drilling and 3-D reflection seismic data. Geochemistry Geophys Geosystems 12:1–24. doi: 10.1029/2010GC003431

Taira A (2001) Tectonic Evolution of the Japanese Arc System. Annu Rev Earth Planet Sci 29:109–134. doi: 10.1146/annurev.earth.29.1.109

Taira A, Byrne TB, Ashi J (1992) Photographic atlas of an accretionary prism: Geologic structures of the Shimanto Belt, Japan. Springer

Takano O, Itoh Y, Kusumoto S (2013) Variation in Forearc Basin Configuration and Basin- filling Depositional Systems as a Function of Trench Slope Break Development and Strike-Slip Movement : Examples from the Cenozoic Ishikari – Sanriku-Oki and Tokai-oki Kumano-nada Forearc Basins. In: Itoh Y (ed) Mech. Sediment. Basin Form. - Multidiscip. Approach Act. Plate Margins. pp 3–26

Tobin HJ, Saffer DM (2009) Elevated fluid pressure and extreme mechanical weakness of a plate boundary thrust, Nankai Trough subduction zone. Geology 37:679–682. doi: 10.1130/g25752a.1

Tsunogai U, Maegawa K, Sato S, Komatsu DD, Nakagawa F, Toki T, Ashi J (2012) Coseimic massive methane release from a submarine mud volcano. Earth Planet Sci Lett 341-344:79–85. doi: 10.1016/j.epsl.2012.06.004

Underwood M, Steurer J (2003) Composition and sources of clay from the trench slope and shallow accretionary prism of Nankai Trough. In: Mikada H, Moore GF, Taira A, et al. (eds) Proc ODP Sci Results 190/196: 1 – 28

Usman MO, Masago H, Winkler W, Strasser M (2014) Mid-Quaternary decoupling of sediment routing in the Nankai Forearc revealed by provenance analysis of turbiditic sands. Int J Earth Sci 103:1141–1161. doi: 10.1007/s00531-014-1011-z

Yamaguchi A, Sakaguchi A, Sakamoto T, Iijima K, Kameda J, Kimura G, Ujiie K, Chester FM, Fabbri O, Goldsby D, Tsutsumi A, Li C-F, Curewitz D (2011) Progressive illitization in fault gouge caused by seismic slip propagation along a megasplay fault in the Nankai Trough. Geology 39:995–998. doi: 10.1130/g32038.1

Yamada Y, Baba K, Miyakawa A, Matsuoka T (2014) Granular experiments of thrust wedges: Insights relevant to methane hydrate exploration at the Nankai accretionary prism. Mar Pet Geol 51:34–48. doi: 10.1016/j.marpetgeo.2013.11.008

CHAPTER 3

Fluids in Subduction Zones

OVERVIEW

[1] The term "fluid" is widely used as acronym for "liquid", but liquids are merely only a part of that group. In physics, fluids are objects that deform when shear stress of any magnitude is applied (Munson et al. 2013). As such, the word "fluid" also includes gases, plasma, viscoplastic (e.g. toothpaste, i.e. Bingham plastics) and viscoelastic (e.g. pitch) materials (Halliday et al. 2001). The diverse physical and chemical characteristics of fluids make them one of the most studied material groups in natural science. In Geoscience the role of fluids in the earth-ocean system, including fluid migration and fluid composition, are heavily investigated. Several studies have shown that the presence and migration of fluids through the earth's crust are essential for understanding heat and solute transport, geochemical cycles, generation and accumulation of natural resources (e.g. hydrocarbons, ores), landslide hazards and seismogenesis (see e.g. Fyfe et al. 1978; Moore and Vrolijk 1992; Manga et al. 2009; Schulz et al. 2009; Faulkner et al. 2010; Saffer and Tobin 2011; Dugan and Sheahan 2012; Tiab and Donaldson 2012; Yardley and Cleverley 2013). The diversity of fluids is based on their source, their high susceptibility to environmental changes, particularly in temperature, pressure, and chemical composition, and their interaction with surrounding geological formations and structures during migration and accumulation. The most prominent geologic fluid sources are marine and meteoric waters. While these prevail before and during the early stages of diagenesis, fluid composition is soon altered by petroleum and natural gas generation, liberated structural water from hydrous minerals during compaction and metamorphic dehydration reactions (Seewald 2003; Saffer and Tobin 2011, and references therein). With increasing depth and temperature, the importance of fluid release by dehydration/metamorphic reactions increases with respect to compaction (Saffer and Tobin 2010, and references therein; Table 1). At tectonically active margins, mantle fluids can migrate to more shallow levels and mix with the crustal fluids (e.g. Kennedy and Soest 2007; Burnard et al. 2012).

Table 1: *Temperature range of individual fluid liberation processes that alter the fluid geochemistry (after Saffer and Tobin 2011). HC = hydrocarbon*

Temperature (°C)	Reactions
< 60	HC generation
60 - 150	clay dehydration opal dehydration HC generation
100 - 225	low-grade metamorphic reactions
200 - 400	low-grade metamorphic reactions pore collapse in basalt
> 400	metamorphic reactions
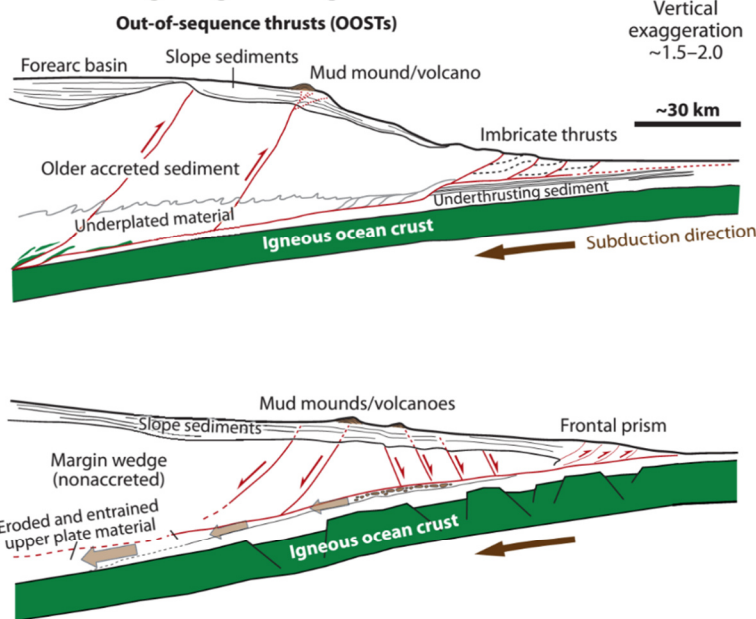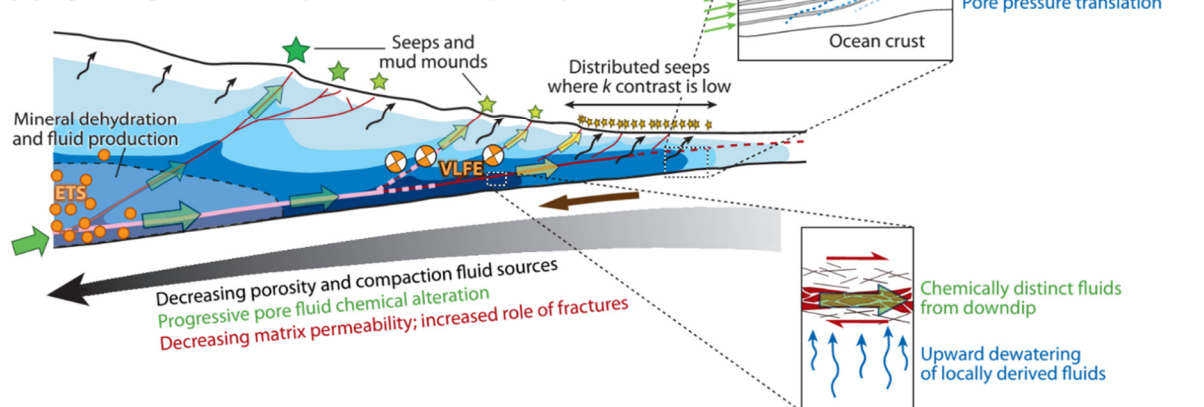
Figure 3: (A) Overview of accretionary (top) and non-accretionary subduction zones **(B)** The role of fluids set in the context of diagenetic, metamorphic and seismogenic processes (from Saffer and Tobin 2011). Blue contours denote excess pore pressure (dark blue = high pressure, light blue = less pressure). The arrows imply fluid migration along faults, where the fluids mix due to interaction with the surrounding material. The arrow color implies the degree of deviation from seawater composition (seawater = yellow). Fluids in subduction zones influence the generation of normal earthquakes and anomalous events like episodic tremor and slip (ETS) and very-low frequency earthquakes (VLFE). Areas of potential coseismic and transitional slip are highlighted by solid and dashed pink lines, respectively. Inlays show flow focused along permeable sands and in damage zones in along-fault direction, while across-fault fluid flow is prohibited. k denotes permeability.

[2] At subduction zones, and particularly in accretionary prisms, migration and accumulation of fluids and their relationship with seismo-tectonic processes have been frequently investigated (e.g. von Huene and Scholl 1991; Moore and Vrolijk 1992; Sample et al. 1996; Carson and Screaton 1998; Tryon et al. 2010; Saffer and Tobin, 2011; Arai et al. 2014; Yamada et al. 2014). Fluids in the incoming plate are sourced in the oceanic crust or the overlying sediments. Typically, they are introduced into the accretionary complex soon after the onset of subduction. The eventual

fate of the fluids depends mainly on the type of active margin. In general, subduction zones can be separated in two end-members: accretionary and erosive subduction zones (Clift and Vannucchi 2004; Figure 3A).

[3] At accretionary subduction zones, sediments from the incoming plate are offscraped or later underplated. With ongoing subduction and lateral compaction, offscraped sediments form an accretionary prism. The accretionary prism is typically characterized by imbricate thrusts, and a landward thickening due to a combination of compaction parallel to the principal horizontal stress, dewatering of accreted material, underplating, and slip on small-scale faults and out-of-sequence-thrusts (Morgan and Karig 1993; Saffer and Tobin 2011). Underthrusted sediments and their fluids are further subducted (von Huene and Scholl 1991; Moore and Vrolijk 1992), and in some cases, such as the Nankai Trough, subsequent compaction and dehydration processes are supposed to lead to a thin water layer at the surface of the subducting plate (Arai et al. 2014).

[4] At non-accretionary subduction zones almost all incoming material is underthrusted, and the ongoing subduction leads to erosion of the base of the upper plate. Both subduction zone types have in common that the underthrusted material and the wedge are separated by a décollement. Excess pore pressure can occur within and beneath the décollement, mainly as a consequence of rapid subduction and disequilibrium compaction, and mineral dehydration. Fluid migration either along faults or through inter-granular pore spaces ("diffusive flow", Baba and Yamada 2004; Yamada et al. 2014) decreases the possibility of fluid overpressure below the décollement, and thus influences slip behaviour and seismogenesis (Tobin and Saffer 2009; Saffer and Tobin 2011; cf. section "*Fluids in Fault Zones and their Influence on Seismogenesis*" in this chapter). Additionally, at accretionary margins fluids may be released from the wedge, which would not occur in erosive margins (e.g. Saffer and Tobin 2011; Ray et al. 2013). According to Yamada et al. (2014), fluid flow in accretionary prisms is subject to spatial and temporal variations, mainly as a function of faulting and changes in stress field. Their numerical and analog models suggested that fluid flow along the thrust faults at the prism toe is generally active, but in periods of inactivity, older, otherwise inactive thrust faults more landward in the prism are re-activated. Their model further implied that in the case of diffusive flow, the varying internal stresses influence inter-granular permeability in shallow parts of the prism, while diffusive flow is lower in the deeper parts, and less susceptible to fluctuations (Figures 3B, 4).

[5] Fluid migration to the surface is typically accompanied by escape structures including, but not limited to, mud volcanoes (e.g. Kopf 2002, 2008), geysers, submarine pockmarks, seeps and vents (e.g. Hovland et al. 2002; Loncke et al. 2004; Obzhirov et al. 2004; Barrick 2010; Talukder 2012). Most of these fluid escape structures can also be well identified in the subsurface using 2-D and 3-D seismic reflection surveys (e.g. Greinert and Nützel 2008). For instance, submarine

mud volcanoes show a characteristic "Christmas tree" structure, which is generated by alternating layers of erupted mud breccia and marine background sedimentation (e.g. Kopf 2008, cf. also subsection "*Submarine Mud Volcanism*" in this chapter).
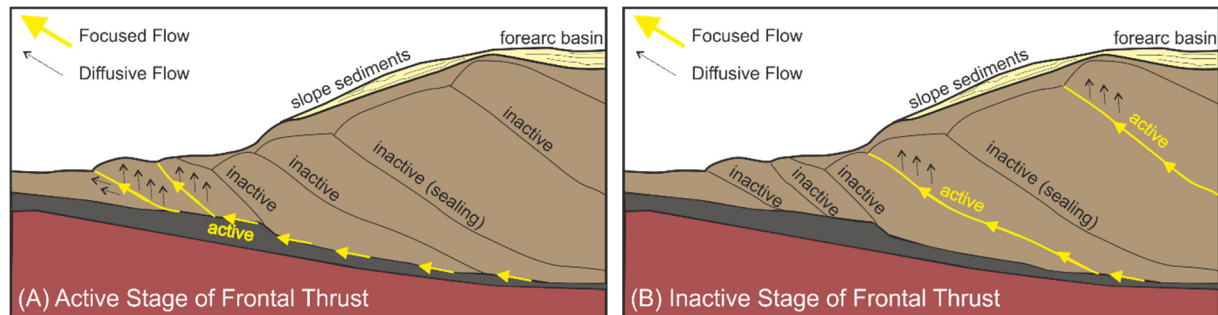
Figure 4: Fluid migration in accretionary prisms (modified form Yamada et al. 2014). **(A)** Fluids can migrate along the frontal thrusts, and at more shallow levels, also flow diffusive through the intergranular pore space. **(B)** Same as (A), but focused fluid migration occurs along re-activated, older thrust faults.

[6] While escaping gaseous components are dominated by methane and higher hydrocarbons (e.g. Judd and Hovland 2007), noble gases including CO_2 and N_2 can be released from igneous and sedimentary sources (Kroos et al. 1995; Aquilina et al. 1998; Mingram et al. 2005). Previous publications have pointed out that ^{3}He/^{4}He ratios, either alone or coupled with ^{222}Rn, can be used to detect mantle fluids migrating in divergent (e.g. Kennedy and van Soest 2007) and convergent settings (e.g. Sano et al. 2014), as well as transform plate boundaries (e.g. Kennedy et al. 1997; Wiersberg and Erzinger 2008, 2011; Burnard et al. 2012).

FLUIDS IN FAULT ZONES AND THEIR INFLUENCE ON SEISMOGENESIS

[7] Fault zones provide prominent pathways for fluid migration. They typically show temporal and spatial variations in lithology and structure. As a consequence, fault zones can prohibit, restrict or promote fluid migration (Caine et al. 1996, and references therein). Changes in hydrogeological properties (e.g. specific storage, hydraulic diffusivity) are a function of temporally and spatially variable extrinsic variables, e.g. stress state, and intrinsic controls, e.g. fluid-rock interactions and fault zone architecture and geometry (Caine et al. 1996).

[8] The most basic conceptual models of a fully developed fault zone include one or more fault cores in the centre, which are surrounded by a fracture-dominated damage zone, followed by the undamaged protolith (e.g. Caine et al. 1996; Faulkner et al. 2010; Figure 5A). In mature faults, fault cores typically act as barriers, while the damage zone allows along-fault fluid migration. At the same time, the permeability in the damage zone decreases with increasing distance from the fault core and increasing displacement (Faulkner et al. 2010; Mitchell and Faulkner 2012). Based on the architecture of the fault core and damage zone, Caine et al. (1996) defined four different end-members for permeability structures: localized conduit, distributed conduit, localized barrier,

and combined conduit-barrier structures (Figure 5B). Following this classification, modern accretionary prisms like the wedge at the Nankai Trough are classified as having a "distributed conduit permeability structure", i.e. fault cores are in their infancy and only present as discontinuous bands, while damage zones are well developed (Caine et al. 1996). Applying the end-member definition of Aydin (2000; Figure 5B) implies that fault zones in modern accretionary prisms are transmissive, and as such, theoretically allow across- and along-fault flow.
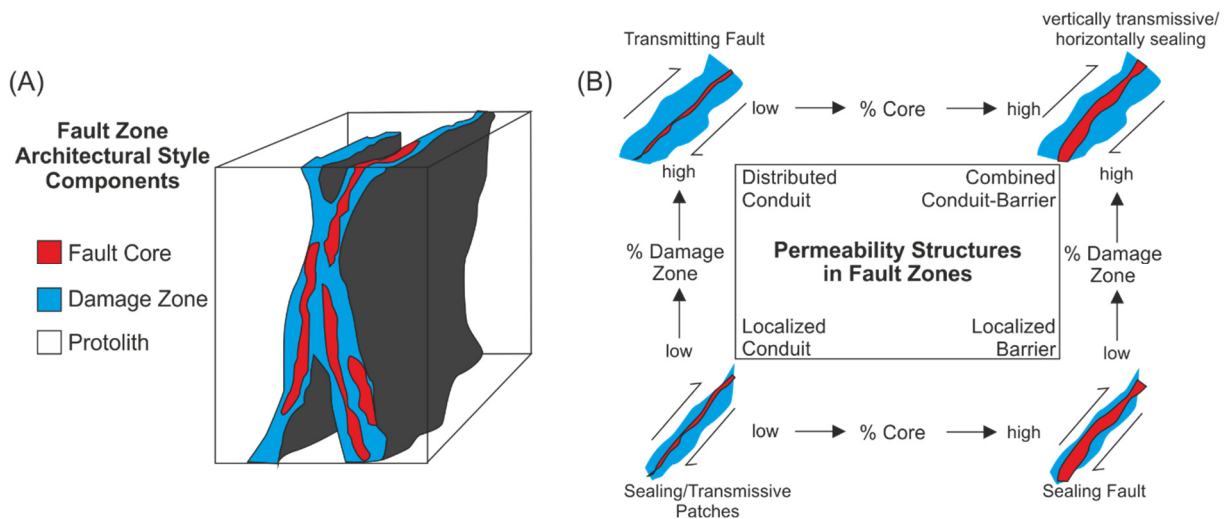
Figure 5: **(A)** Schematic, simplified model of a fully developed fault zone (modified from Caine et al. 1996). **(B)** Different end-members for permeability structures, based on the individual contribution of fault core and damage zone within a fault zone (modified from and after Caine et al. 1996; Aydin 2000).

[9] The permeability of fault zones, and particularly of fault cores, depends mainly on the lithological composition and its degree of heterogeneity, deformation mechanisms promoted during slip (shale/clay smearing vs. abrasional mixing), authigenic mineral formation, cementation, ambient temperature, and physico-chemical interactions between rock and fluids (e.g. Aydin 2000; Boles et al. 2004; Faulkner et al. 2010, and references therein; Laubach et al. 2010). The resulting sealing capacity is a function of the membrane strength and the hydraulic strength (Gluyas and Swarbrick 2004). While the former depends on the capillary entry pressure of the largest pore along the fault plane, the hydraulic strength is limited by the strength of the rock itself and the direction and magnitude of the minimum stress (Gluyas and Swarbrick 2004).

[10] The permeability in the damage zone is further controlled by initial hydrogeological properties of the undamaged host rock and the presence and distribution of fractures and deformation/compaction bands (Faulkner et al. 2010). Protoliths with low porosity tend to form damage zones with a well-developed fracture network that increases the permeability by more than three orders of magnitude (e.g., Mitchell and Faulkner 2008). In contrast, protoliths with high porosity are subject to the interplay of the fracture network and deformation/compaction bands, with the latter either lowering or enhancing the permeability (Fossen et al. 2007; Farrell et al. 2014).

[11] If fluid escape pathways are absent or blocked, fluid overpressure can develop (Figure 3B; cf. also section "*Submarine Mud Volcanism*" in this chapter), which has a significant influence on seismogenesis. Theoretical considerations (e.g. Scholz 1998) imply that elevated pore pressure reduces the effective stress, and to some extent, disables seismogenic locking of faults. Once slip is initiated, flash heating and a sudden increase in pore pressure (termed "thermal pressurization") can further promote fault weakening and slip propagation (e.g. Wibberley and Shimamoto 2005; Segall and Rice 2006). At the same time dilatancy hardening, (i.e. increase in porosity and thus, reduction in fluid pressure) transiently increases fault strength (e.g. Segall and Rice 1995; Samuelson et al. 2011).

[12] According to Saffer and Tobin (2011), elevated fluid pressure in subduction systems influences: (a) shallow seismicity (b) the depth and width of the seismogenic zone (c) the updip limit for great earthquake propagation and tsunami generation and (d) anomalous slip events, including episodic tremor and slip (ETS) and very-low frequency earthquakes (VLFE; Figure 3B). Both ETS and VLFE gained particular attention during the last decade and are attributed to elevated pore pressures and reduced effective stresses in the fault plane (e.g. Ito and Obara 2006; Obana and Kodaira 2009; Kitajima and Saffer 2012; Sugioka et al. 2012). Additional triggering mechanisms related to dynamic changes in pore fluid pressure include tidal forces (e.g. Nakata et al. 2008; Rubinstein et al. 2008; Thomas et al. 2009), climate cycles (Lowry 2006) and seismic waves (e.g., Miyazawa and Brodsky 2008; Rubinstein et al. 2009). Dynamic changes in pore pressure can further influence the permeability of fault zones (Elkhoury et al. 2006, 2011).

SUBMARINE MUD VOLCANISM

[13] Onshore and offshore, mud volcanos are among the most studied geological features worldwide. Mud volcanoes are commonly described as "*positive features constructed mainly of mud and other sedimentary constituents, which periodically or continuously vent liquid mud, including water, oil, and gas*" (Judd and Hovland 2007), or more simply as "*natural survey boreholes – free of charge*" (Hovland et al. 2014, after the Russian geologist Golubyatnicov). Together with other mud extrusives, they are typical surface emanations of fluids escaping deltaic environments (e.g. Prinzhofer and Deville 2013), divergent settings (e.g. Papatheodorou et al. 1993), transform-plate boundaries (e.g. Shakirov et al. 2004), and convergent margins, including both accretionary (e.g. Kopf et al. 2001; Schlüter et al. 2002) and erosive (e.g. Tryon et al. 2010) subduction zones. The terminology, processes of generation, and regional examples are comprehensively reviewed by Kopf (2002) and Dimitrov (2002) and the following brief outline is based on the work of these authors, if not stated otherwise.
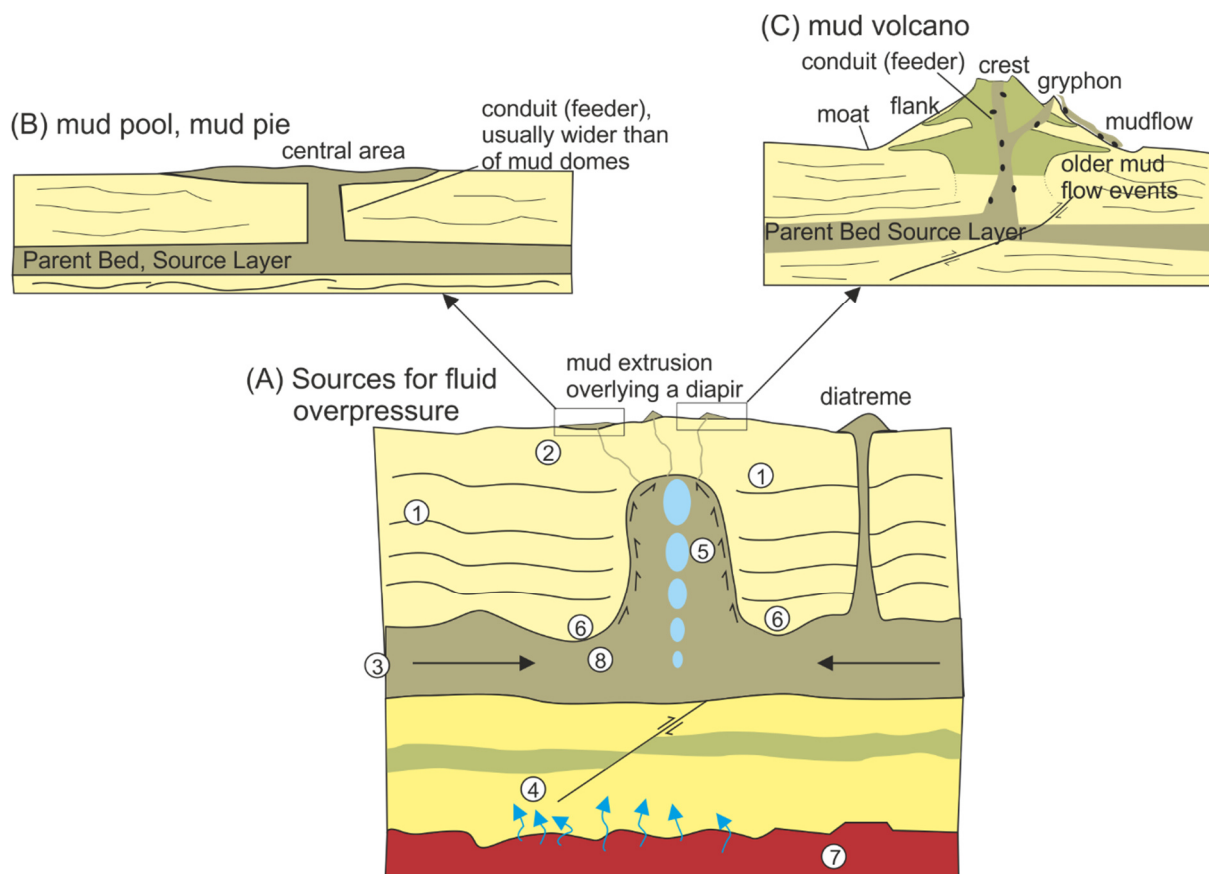
Figure 6: Examples for origins of fluids and mud extrusion (all modified from Kopf 2002). **(A)** Sources of fluid overpressure leading to diapirism and mud extrusion. 1: Pore fluid expulsion due to compaction. 2: Bacterial methane generation. 3: Lateral fluid influx. 4: Vertical fluid migration along faults. 5: Generation of thermogenic hydrocarbons. 6: Fluids from mineral dehydration. 7: Hydrothermal fluids, alteration of crustal rock. 8: Fluid expulsion caused by internal deformation of the diapiric intrusion. **(B)** Example of a mud pie, which is usually the surface expression of highly fluidized mud **(C)** Cross-section of a typical mud volcano. The conduit can diverge to create a gryphon (i.e. a smaller cone or crater) on the flank. Dark circles denote rip-up clasts from the parent bed and adjacent formations. Older mud flow lead to a typical Christmas tree structure, i.e. an interfingering of older mud flows with marine background sedimentation (after Kopf 2008).

[14] The major driving mechanism for mud extrusion is density inversion. Causes for density inversion are either of primary origin, i.e. due to grain density contrasts in the sedimentary succession, or of secondary origin, e.g. inflow, release and/or *in situ* formation of low-density fluids (e.g. hydrocarbon formation, mineral dehydration, etc.; cf. section *Overview* within this chapter; Figure 6A) and tectonic activity leading to changes in the local stress field. Although an interplay between primary and secondary processes often occurs, primary density inversion can appear without secondary processes and *vice versa*. Among the individual geological mechanisms, sedimentation has a key role in both primary and secondary processes, particularly in the marine realm. Sedimentation of clay rich material can result in porosities as high as 80%. During compaction, pore space is reduced, and hydrostatic pressure equilibrium is maintained if pore water can escape simultaneously.

[15] In subduction zones, however, the tectonically driven plate motions accelerate sediment compaction, either vertically during rapid transportation of overridden sediment deeper into the subduction zone, or by off scraping, lateral compaction and imbricate thrusting in accretionary prisms. If fluid migration pathways are absent or blocked, pore pressure soon exceeds hydrostatic levels, and the sediment reaches a so-called "undercompacted" or "overpressured" state. Together with other thermogenically and bacterially driven fluid sources, excess pore pressure can become high enough for fluids to fracture the overlying strata and/or force their way through existing geological structures ("explosive decompression"). In this case, typical surface expressions include mud volcanoes and diatremes (Figure 6A). According to Brown (1990) and Kopf (2002), both features are formed by fluidization of sediments, but fluidized mud expulsed from a diapir behaves as a single-fluid phase, while in diatremes, sediments are simply drawn upward together with escaping fluids. In the absence of density inversion, Bishop (1978) explained two further mechanisms promoting mud extrusion: either (i) unrestricted excess hydrostatic pressure release due to thin or missing overburden, which results in slowly migrating diapirs, or (ii) hydrofracturation and fragmentation due to large pressures generated under large overburden, which occurs preferentially in locked faults, shear zones and diapiric dykes. As pointed out by Moore and Byrne (1987) and Kopf (2002), violent eruptions are less likely to occur in diapiric features, because scaly fabric that develops adjacent to the diapir enhances permeability and lithostatic fluid pressures are unlikely to be reached. Natural phenomena, for example earthquakes and seismic waves, can further promote mud expulsion and even violent eruptions on certain structural features (e.g., Mellors et al. 2007; Manga et al. 2009; Kopf et al. 2010, Lupi et al 2013).

[16] Escaping aqueous and gaseous fluids are usually accompanied by solid components of the undercompacted strata, including fluidized mud and clasts from the parent bed and plucked from overlying formations during upward migration. The geometries of mud extrusions, however, vary mainly as a function of fluid composition (aqueous vs. gaseous), bulk fluid content, temperature, conduit diameter and pressure (e.g. Dupré et al. 2014). The varying petro-physical properties of the fluidized mud determine the geometric shape of the surface expressions, or more accurately, the shape of the edifice. Muds with low fluid content that results in high viscosity and low porosity (< 50%) result in mud domes and ridges, while muds with intermediate fluid content promote large scale mud volcanoes (up to 2 km in diameter and heights of > 50 m; Figure 6B). If the fluid content is high, mud pies manifest at the surface (Figure 6C). Eventually the mud reservoir gets depleted, which is followed by sinking of the central expulsion area and collapse, leading to a caldera similar to their magmatic counterparts (Kopf 2008). Active venting often promotes faunal assemblages, including clams (e.g. of the genus Calyptogena, see chapter 7.1, Pape et al. 2014), and bacterial mats (e.g. Pimenov et al. 2000). The top of mud domes is often covered by mud

breccia with > 65% lithified clasts and authigenic carbonate cement, which adds to the resistance of these features to erosion and deformation (Kopf 2002, and references therein).

[17] Gaseous components can originate from depths > 8000 mbsf (Bonini et al. 2013), and are generated during thermocatalytic reactions. Deep gases that act as driving forces can be separated into three categories: (i) mantle gases (ii) (igneous) volcanic gases and (iii) hydrocarbon gases. The contribution of the individual gases is comprehensively discussed in Kopf (2002), and can be summarized as follows: (i) the contribution of mantle gases is too small to be significant (ii) igneous sources can provide considerable amounts of CO_2 and N_2, and thus, can enhance mud volcanism, and (iii) hydrocarbons are the most prominent gases driving mud volcanism. Methane is of particular importance, because in the presence of aqueous fluids it is "*the most powerful agent for overpressuring, liquefaction and extrusion*" (Kopf 2002). While thermogenic hydrocarbons are most abundant, shallow bacterial hydrocarbon deposits (including gas hydrates) can significantly contribute to the amount of released fluids, and moreover, may serve as a trigger (but not as driving force) for mud volcanism (Kopf et al. 1998). The depth of origin of the gaseous components is often masked by secondary effects (e.g. mixing, oxidation; Whiticar 1994), and by changes in the gas composition over time, as was observed at mud volcanoes on Sakhalin Island. Shakirov et al. (2004) detected considerable variations in methane and CO_2 by comparing their data with published material from the 1960s and 1970s. They concluded that during periods without any significant eruption, the mud volcanoes emit gases derived from an intermediate reservoir. A gradual decrease of methane and increase of CO_2 in this reservoir is explained by biogeochemical reactions after the eruption. They concluded that the intermediate reservoir does not represent the composition of the main deep gas reservoir.

[18] The aqueous components of the escaping fluids vary mainly between connate and meteoric waters, and both lateral and vertical mixing between different reservoirs can occur (Judd and Hovland 2007). Connate aqueous fluids include hydrocarbons (Aliyev et al. 2002), brines (e.g. Dupré et al. 2014), and brackish water (Martinelli and Judd 2004), as well as waters released form mineral dehydration reactions and dissociation of gas hydrates (e.g. Fitts and Brown 1999; Judd and Hovland 2007, and references therein). The chemistry of aqueous fluids varies accordingly, and is a function of fluid temperature, depth of origin, the lithology of the parent bed and overlying strata, and diagenetic and early metamorphic reactions, e.g. clay dehydration and serpentinization. Volatiles, for instance B and Li isotopes, can serve as proxies for identifying deep-sourced fluids (e.g. Kopf and Deyhle 2002; Tryon et al. 2010), and have revealed the role of mud volcanoes as geochemical sinks (Kopf 2002, and references therein).

[19] Other than fluidized mud, solid components may also include clasts of various sizes, and from different stratigraphic intervals. If clasts are present, the solid components are generally referred to as mud breccia, olistostrome, or diapiric mélange (Judd and Hovland 2007). While paleontological analyses can help to reveal the stratigraphic age of the rip-up clasts, sedimentary layers which were eroded and re-deposited, including mass wasting deposits, add considerable uncertainty to biostratigraphic approaches (e.g. Kopf et al. 2000; Rabaute and Chamot-Rooke 2007). Clasts can show signs of hydrofracture (e.g. Robertson and Kopf 1998), which favors the model of "explosive decompression" for violent eruptions of mud volcanos and diatremes (cf. also paragraph 15 in this chapter).

References

Aliyev AA, Guliyev IS, Belov IS (2002) Catalog of recorded eruptions of mud volcanoes of Azerbaijan: Baku, Azerbaijan. Nafta Press

Aloisi G, Pierre C, Rouchy J-M, Foucher J-P, Woodside J (2000) Methane-related authigenic carbonates of eastern Mediterranean Sea mud volcanoes and their possible relation to gas hydrate destabilisation. Earth Planet Sci Lett 184:321–338. doi: http://dx.doi.org/10.1016/S0012-821X(00)00322-8

Aquilina L, Baubron J-C, Defoix D, Dégranges P, Disnar J-R, Marty B, Robé M-C (1998) Characterization of gases in sedimentary formations through monitoring during drilling and core leaching (Balazuc borehole, Deep Geology of France Programme). Appl Geochemistry 13:673–686. doi: 10.1016/s0883-2927(98)00008-0

Arai R, Iwasaki T, Sato H, Abe S, Hirata N (2014) Contrasting subduction structures within the Philippine Sea plate: Hydrous oceanic crust and anhydrous volcanic arc crust. Geochemistry, Geophys Geosystems 15:1977–1990. doi: 10.1002/2014GC005321

Aydin A (2000) Fractures, faults, and hydrocarbon entrapment, migration and flow. Mar Pet Geol 17:797 – 814.

Baba T, Yamada Y (2004) BSRs and Associated Reflections as an Indicator of Gas Hydrate and Free Gas Accumulation : An Example of Accretionary Prism and Forearc Basin System along the Nankai Trough , off Central Japan. Resour Geol 54:11–24.

Barrick KA (2010) Environmental review of geyser basins: resources, scarcity, threats, and benefits. Environ Rev 18:209–238. doi: 10.1139/A10-008

Bishop RS (1978) Mechanism for Emplacement of Piercement Diapirs. Am Assoc Pet Geol Bull 62:1561 – 1583.

Boles JR, Eichhubl P, Garven G, Chen J (2004) Evolution of a hydrocarbon migration pathway along basin-bounding faults: Evidence from fault cement. Am Assoc Pet Geol Bull 88:947–970. doi: 10.1306/02090403040

Bonini M, Tassi F, Feyzullayev AA, Aliyev CS, Capecchiacci F, Minissale A (2013) Deep gases discharged from mud volcanoes of Azerbaijan: New geochemical evidence. Mar Pet Geol 43:450–463. doi: 10.1016/j.marpetgeo.2012.12.003

Brown KM (1990) The Nature and Hydrogeologic Significance of Mud Diapirs and Diatremes for Accretionary Systems. J Geophys Res 95:8969–8982. doi: 10.1029/JB095iB06p08969

Burnard P, Bourlange S, Henry P, Geli L, Tryon MD, Natal'in B, Sengör a. MC, Özeren MS, Çagatay MN (2012) Constraints on fluid origins and migration velocities along the Marmara Main Fault (Sea of Marmara, Turkey) using helium isotopes. Earth Planet Sci Lett 341-344:68–78. doi: 10.1016/j.epsl.2012.05.042

Caine JS, Evans JP, Forster CB (1996) Fault zone architecture and permeability structure. Geology 24:1025-1028. doi:10.1130/0091-7613(1996)024<1025:fzaaps>2.3.co;2

Carson B, Screaton EJ (1998) Fluid flow in accretionary prisms: Evidence for focused, time-variable discharge. Rev Geophys 36:329-351. doi:10.1029/97rg03633

Clift P, Vannucchi P (2004) Controls on tectonic accretion versus erosion in subduction zones: Implications for the origin and recycling of the continental crust. Rev Geophys 42:RG2001. doi:10.1029/2003RG000127

Dimitrov LI (2002) Mud volcanoes—the most important pathway for degassing deeply buried sediments. Earth-Science Rev 59:49–76. doi: 10.1016/S0012-8252(02)00069-7

Dugan B, Sheahan TC (2012) Offshore sediment overpressures of passive margins: Mechanisms, measurement, and models. Rev Geophys 50:RG3001. doi:10.1029/2011RG000379

Dupré S, Mascle J, Foucher J-P, Harmegnies F, Woodside J, Pierre C (2014) Warm brine lakes in craters of active mud volcanoes, Menes caldera off NW Egypt: evidence for deep-rooted thermogenic processes. Geo-Marine Lett 34:153–168. doi: 10.1007/s00367-014-0367-1

Elkhoury JE, Brodsky EE, Agnew DC (2006) Seismic waves increase permeability. Nature 441:1135–1138.

Elkhoury JE, Niemeijer A, Brodsky EE, Marone C (2011) Laboratory observations of permeability enhancement by fluid pressure oscillation of in situ fractured rock. J Geophys Res 116:B02311. doi: 10.1029/2010jb007759

Farrell NJC, Healy D, Taylor CW (2014) Anisotropy of permeability in faulted porous sandstones. J Struct Geol 63:50–67. doi: 10.1016/j.jsg.2014.02.008

Faulkner DR, Jackson CAL, Lunn RJ, Schlische RW, Shipton ZK, Wibberley CAJ, Withjack MO (2010) A review of recent developments concerning the structure, mechanics and fluid flow properties of fault zones. J Struct Geol 32:1557-1575. doi:10.1016/j.jsg.2010.06.009

Fitts TG, Brown KM (1999) Stress-induced smectite dehydration: ramifications for patterns of freshening and fluid expulsion in the N. Barbados accretionary wedge. Earth Planet Sci Lett 172:179–197.

Fossen H, Schultz RA, Shipton ZK, Mair K (2007) Deformation bands in sandstone: a review. J Geol Soc 164:755-769. doi:10.1144/0016-76492006-036

Fyfe WS, Price NJ, Thompson AB (1978) Fluids in the Earth's Crust — Their Significance in Metamorphic, Tectonic and Chemical Transport Processes. In: Developments in Geochemistry. Elsevier, pp 383

Gluyas JG, Swarbrick R (2004) Petroleum Geosciences. Blackwell Science Ltd, pp. 390

Greinert J, Nützel B (2004) Hydroacoustic experiments to establish a method for the determination of methane bubble fluxes at cold seeps. Geo-Marine Lett 24:75–85. doi: 10.1007/s00367-003-0165-7

Halliday D, Resnick R, Walker J (2001) Fundamentals of Physics. John Wiley & Sons, Inc.

Hovland M, Gardner J V, Judd AG (2002) The significance of pockmarks to understanding fluid flow processes and geohazards. Geofluids 2:127–136. doi: 10.1046/j.1468-8123.2002.00028.x

Hovland M, Rueslåtten H, Johnsen HK, Al ET (2014) Buried Hydrothermal Systems : The Potential Role of Supercritical Water , " ScriW ", in Various Geological Processes and Occurrences in the Sub-Surface. Am J Anal Chem 5:128–139.

Ito Y, Obara K (2006) Very low frequency earthquakes within accretionary prisms are very low stress-drop earthquakes. Geophys Res Lett 33:L09302. doi: 10.1029/2006gl025883

Ito Y, Obara K, Shiomi K, Sekine S, Hirose H (2007) Slow Earthquakes Coincident with Episodic Tremors and Slow Slip Events. Science 315:503–506. doi: 10.1126/science.1134454

Judd AG, Hovland M (2007) Seabed fluid flow: the impact of geology, biology and the marine environment. Cambridge University Press, pp. 1 – 442.

Kitajima H, Saffer DM (2012) Elevated pore pressure and anomalously low stress in regions of low frequency earthquakes along the Nankai Trough subduction megathrust. Geophys Res Lett 39:L23301. doi: 10.1029/2012GL053793

Kennedy BM, van Soest MC (2007) Flow of mantle fluids through the ductile lower crust: helium isotope trends. Science 318:1433–6. doi: 10.1126/science.1147537

Kennedy BM, Kharaka YK, Evans WC, Ellwood A, DePaolo DJ, Thordsen J, Ambats G, Mariner RH (1997) Mantle Fluids in the San Andreas Fault System ,California. Science 278:1278 – 1281. doi: 10.1126/science.278.5341.1278

Kopf AJ (2002) Significance of mud volcanism. Rev Geophys 40:1005. doi:10.1029/2000rg000093

Kopf AJ (2008) Volcanoes: Making calderas from mud. Nature Geosci 1:500-501

Kopf A, Deyhle A (2002) Back to the roots: boron geochemistry of mud volcanoes and its implications for mobilization depth and global B cycling. Chem Geol 192:195–210.

Kopf A, Robertson AHF, Clennell MB, Flecker R (1998) Mechanisms of mud extrusion on the Mediterranean Ridge Accretionary Complex. Geo-Marine Lett 18:97–114. doi: 10.1007/s003670050058

Kopf A, Robertson AHF, Volkmann N (2000) Origin of mud breccia from the Mediterranean Ridge accretionary complex based on evidence of the maturity of organic matter and related petrographic and regional tectonic evidence. Mar Geol 166:65–82.

Kopf A, Klaeschen D, Mascle J (2001) Extreme efficiency of mud volcanism in dewatering accretionary prisms. Earth Planet Sci Lett 189:295–313.

Kopf A, Delisle G, Faber E, Panahi B, Aliyev C, Guliyev I (2010) Long-term in situ monitoring at Dashgil mud volcano, Azerbaijan: a link between seismicity, pore-pressure transients and methane emission. Int J Earth Sci 99:227–240. doi: 10.1007/s00531-009-0487-4

Kroos B, Littke R, Müiller B, Frielingsdorf J, Schwochau K, Idiz E (1995) Generation of nitrogen and methane from sedimentary organic matter : implications on the dynamics of natural gas accumulations. Chem Geol 126:291 – 318.

Laubach SE, Eichhubl P, Hilgers C, Lander RH (2010) Structural diagenesis. J Struct Geol 32:1866–1872.

Loncke L, Mascle J (2004) Mud volcanoes, gas chimneys, pockmarks and mounds in the Nile deep-sea fan (Eastern Mediterranean): geophysical evidences. Mar Pet Geol 21:669–689. doi: 10.1016/j.marpetgeo.2004.02.004

Lowry AR (2006) Resonant slow fault slip in subduction zones forced by climatic load stress. Nature 442:802–805.

Lupi M, Saenger EH, Fuchs F, Miller SA (2013) Lusi mud eruption triggered by geometric focusing of seismic waves. Nat Geosci 6:642–646.

Manga M, Brumm M, Rudolph ML (2009) Earthquake triggering of mud volcanoes. Marine and Petroleum Geology 26:1785-1798

Martinelli G, Judd AG (2004) Mud volcanoes of Italy. Geol J 39:49–61. doi: 10.1002/gj.943

Mellors R, Kilb D, Aliyev A, Gasanov A, Yetirmishli G (2007) Correlations between earthquakes and large mud volcano eruptions. J Geophys Res 112:B04304. doi: 10.1029/2006jb004489

Mitchell TM, Faulkner DR (2008) Experimental measurements of permeability evolution during triaxial compression of initially intact crystalline rocks and implications for fluid flow in fault zones. Journal of Geophysical Research: Solid Earth 113:B11412. doi:10.1029/2008JB005588

Mingram B, Hoth P, Lüders V, Harlov D (2005) The significance of fixed ammonium in Palaeozoic sediments for the generation of nitrogen-rich natural gases in the North German Basin. Int J Earth Sci 94:1010–1022. doi: 10.1007/s00531-005-0015-0

Miyazawa M, Brodsky EE (2008) Deep low-frequency tremor that correlates with passing surface waves. J Geophys Res 113:B01307. doi: 10.1029/2006jb004890

Moore JC, Byrne T (1987) Thickening of fault zones: A mechanism of melange formation in accreting sediments. Geol 15 :1040–1043. doi: 10.1130/0091-7613(1987)15<1040:TOFZAM>2.0.CO;2

Moore JC, Vrolijk P (1992) Fluids in accretionary prisms. Rev Geophys 30:113-135. doi:10.1029/92rg00201

Moore JC, Barrett M, Thu MK (2013) Fluid Pressures and Fluid Flows from Boreholes Spanning the NanTroSEIZE Transect through the Nankai Trough, SW Japan. Tectonophysics 600:108 - 115. doi: 10.1016/j.tecto.2013.01.026

Morgan JK, Karig DE (1993) Ductile strains in clay-rich sediment from Hole 808C: preliminary results using X-ray pole figure goniometry. In: IA Hill AT, JV Firth, et al., (ed) Proc Ocean Drill Program Sci Results 131: 141 - 155

Munson BR, Okiishi TH, Huebsch WW, Rothmayer AP (2013) Fundamentals of Fluid Mechanics. John Wiley & Sons, Inc.

Nakata R, Suda N, Tsuruoka H (2008) Non-volcanic tremor resulting from the combined effect of Earth tides and slow slip events. Nat Geosci 1:676–678.

Obana K, Kodaira S (2009) Low-frequency tremors associated with reverse faults in a shallow accretionary prism. Earth Planet Sci Lett 287:168–174. doi: http://dx.doi.org/10.1016/j.epsl.2009.08.005

Obzhirov A, Shakirov R, Salyuk A, Suess E, Biebow N, Salomatin A (2004) Relations between methane venting, geological structure and seismo-tectonics in the Okhotsk Sea. Geo-Marine Lett 24:135–139. doi: 10.1007/s00367-004-0175-0

Papatheodorou G, Hasiotis T, Ferentinos G (1993) Gas-charged sediments in the Aegean and Ionian Seas, Greece. Mar Geol 112:171–184. doi: 10.1016/0025-3227(93)90167-T

Pape T, Geprägs P, Hammerschmidt S, Wintersteller P, Wei J, Fleischmann T, Bohrmann G, Kopf AJ (2014) Hydrocarbon seepage and its sources at mud volcanoes of the Kumano forearc basin, Nankai Trough subduction zone. Geochemistry, Geophys Geosystems 15:2180–2194. doi: 10.1002/2013GC005057

Pimenov N V, Savvichev AS, Rusanov II, Lein AY, Ivanov M V (2000) Microbiological Processes of the Carbon and Sulfur Cycles at Cold Methane Seeps of the North Atlantic. Microbiology 69:709–720. doi: 10.1023/A:1026666527034

Prinzhofer A, Deville E (2013) Origins of hydrocarbon gas seeping out from offshore mud volcanoes in the Nile delta. Tectonophysics 591:52–61. doi: 10.1016/j.tecto.2011.06.028

Rabaute A, Chamot-Rooke N (2007) Quantitative mapping of active mud volcanism at the western Mediterranean Ridge-backstop contact. Mar Geophys Res 28:271–295. doi: 10.1007/s11001-007-9031-8

Ray JS, Kumar A, Sudheer AK, Deshpande RD, Rao DK, Patil DJ, Awasthi N, Bhutani R, Bhushan R, Dayal AM (2013) Origin of gases and water in mud volcanoes of Andaman accretionary prism: implications for fluid migration in forearcs. Chem Geol 347:102–113. doi: http://dx.doi.org/10.1016/j.chemgeo.2013.03.015

Rubinstein JL, La Rocca M, Vidale JE, Creager KC, Wech AG (2008) Tidal Modulation of Nonvolcanic Tremor. Science 319:186–189. doi: 10.1126/science.1150558

Rubinstein JL, Gomberg J, Vidale JE, Wech AG, Kao H, Creager KC, Rogers G (2009) Seismic wave triggering of nonvolcanic tremor, episodic tremor and slip, and earthquakes on Vancouver Island. J Geophys Res Solid Earth 114:B00A01. doi: 10.1029/2008JB005875

Saffer DM, Tobin HJ (2011) Hydrogeology and Mechanics of Subduction Zone Forearcs: Fluid Flow and Pore Pressure. Annu Rev Earth Planet Sci 39:157–186. doi: doi:10.1146/annurev-earth-040610-133408

Sample JC (1996) Isotopic evidence from authigenic carbonates for rapid upward fluid flow in accretionary wedges. Geology 24:897-900. doi:10.1130/0091-7613(1996)024<0897:iefacf>2.3.co;2

Samuelson J, Elsworth D, Marone C (2011) Influence of dilatancy on the frictional constitutive behavior of a saturated fault zone under a variety of drainage conditions. J Geophys Res 116:B10406. doi: 10.1029/2011jb008556

Sano Y, Hara T, Takahata N, Kawagucci S, Honda M, Nishio Y, Tanikawa W, Hasegawa A, Hattori K (2014) Helium anomalies suggest a fluid pathway from mantle to trench during the 2011 Tohoku-Oki earthquake. Nat Commun 5:1 – 6. doi: 10.1038/ncomms4084

Scholz CH (1998) Earthquakes and friction laws. Nature 391:37–42.

Schulz WH, Kean JW, Wang G (2009) Landslide movement in southwest Colorado triggered by atmospheric tides. Nat Geosci 2:863-866. doi:10.1038/ngeo659

Seewald JS (2003) Organic-inorganic interactions in petroleum-producing sedimentary basins. Nature 426:327-333

Schlüter HU, Prexl A, Gaedicke C, Roeser H, Reichert C, Meyer H, von Daniels C (2002) The Makran accretionary wedge: sediment thicknesses and ages and the origin of mud volcanoes. Mar Geol 185:219–232. doi: 10.1016/S0025-3227(02)00192-5

Segall P, Rice JR (1995) Dilatancy, compaction, and slip instability of a fluid-infiltrated fault. J Geophys Res 100:22155–22171. doi: 10.1029/95jb02403

Segall P, Rice JR (2006) Does shear heating of pore fluid contribute to earthquake nucleation? J Geophys Res 111:B09316. doi: 10.1029/2005jb004129

Shakirov R, Obzhirov A, Suess E, Salyuk A, Biebow N (2004) Mud volcanoes and gas vents in the Okhotsk Sea area. Geo-Marine Lett 24:140–149. doi: 10.1007/s00367-004-0177-y

Sugioka H, Okamoto T, Nakamura T, Ishihara Y, Ito A, Obana K, Kinoshita M, Nakahigashi K, Shinohara M, Fukao Y (2012) Tsunamigenic potential of the shallow subduction plate boundary inferred from slow seismic slip. Nat Geosci 5:414–418.

Talukder AR (2012) Review of submarine cold seep plumbing systems: leakage to seepage and venting. Terra Nov 24:255–272. doi: 10.1111/j.1365-3121.2012.01066.x

Thomas AM, Nadeau RM, Burgmann R (2009) Tremor-tide correlations and near-lithostatic pore pressure on the deep San Andreas fault. Nature 462:1048–1051.

Tiab D, Donaldson EC (2012) Petrophysics. Elsevier, pp. 950

Tobin HJ, Saffer DM (2009) Elevated fluid pressure and extreme mechanical weakness of a plate boundary thrust, Nankai Trough subduction zone. Geology 37:679-682. doi:10.1130/g25752a.1

Tryon MD, Wheat CG, Hilton DR (2010) Fluid sources and pathways of the Costa Rica erosional convergent margin. Geochem Geophys Geosyst 11:Q04S22. doi: 10.1029/2009gc002818

Yamada Y, Baba K, Miyakawa A, Matsuoka T (2014) Granular experiments of thrust wedges: Insights relevant to methane hydrate exploration at the Nankai accretionary prism. Mar Pet Geol 51:34-48. doi:10.1016/j.marpetgeo.2013.11.008

Yardley BWD, Cleverley JS (2013) The role of metamorphic fluids in the formation of ore deposits. Geological Society, London, Special Publications 393. doi:10.1144/sp393.5

von Huene R, Scholl DW (1991) Observations at convergent margins concerning sediment subduction, subduction erosion, and the growth of continental crust. Rev Geophys 29:279-316. doi:10.1029/91RG00969

Wibberley CAJ, Shimamoto T (2005) Earthquake slip weakening and asperities explained by thermal pressurization. Nature 436:689–692.

Whiticar MJ (1994) Correlation of Natural Gases with Their Sources. In: Magoon L, Dow W (eds) Pet. Syst. - From Source to Trap. AAPG, pp 261 – 283

Wiersberg T, Erzinger J (2008) Origin and spatial distribution of gas at seismogenic depths of the San Andreas Fault from drill-mud gas analysis. Appl Geochemistry 23:1675–1690. doi: 10.1016/j.apgeochem.2008.01.012

Wiersberg T, Erzinger J (2011) Chemical and isotope compositions of drilling mud gas from the San Andreas Fault Observatory at Depth (SAFOD) boreholes: Implications on gas migration and the permeability structure of the San Andreas Fault. Chem Geol 284:148–159. doi: 10.1016/j.chemgeo.2011.02.016

CHAPTER 4

In Situ Offshore Borehole Monitoring

CHAPTER 4.1

LONG-TERM BOREHOLE MONITORING USING BOREHOLE OBSERVATORIES

OVERVIEW

[1] Understanding hydrogeological processes in the ocean crust is essential for understanding thermal evolution and alteration of the oceanic lithosphere and associated changes in fluid chemistry, subseafloor microbial ecosystems, tectonic and seismogenic processes, and the generation, migration and accumulation of marine resources (e.g. petroleum, gas hydrates, ore deposits). Although investigating the (subseafloor) hydrosphere was always one of the key areas of ocean drilling research, data was often flawed by disturbance of the *in situ* conditions during the drilling and coring process. The chemistry of formation fluids can be severely disturbed by the intrusion of ambient seawater and mixing with synthetic drilling fluids (e.g. Williamson 2013). These challenges have led to the development of long-term subseafloor laboratories in which boreholes are sealed and instrumented after completion of drilling and coring operations. This allows the recovery of *in situ* conditions, and the subsequent monitoring of changes over time.

[2] Onshore, long-term borehole monitoring is a well-established technique for hydrogeological and seismological investigations (e.g. Liu et al. 1989; Woodcock and Roeloffs 1996; Roeloffs 1998), but offshore technology became available no earlier than the late 80's and early 90's (Becker and Davis 2005). Since then, long-term measurements have been conducted in boreholes ranging from a few meters (Kopf et al. 2013) to almost 1 km in depth (Kopf et al. 2011) at convergent margins, such as the Nankai Trough (Davis et al. 2013) or Costa Rica Margin (Jannasch et al. 2003; Davis et al. 2011), and divergent margins such as the Juan de Fuca ridge (e.g. Fisher et al. 1997, Davis et al. 2004). Initially deployed as stand-alone instruments, the benefits of creating local networks with real-time data access from onshore landing stations became soon apparent (e.g. NEPTUNE Canada within the Ocean Networks Canada framework, http://www.oceannetworks.ca/). However, most of the instruments still require data download via manned or unmanned submersibles.

[3] Of particular importance became the development of CORKs (Circulation Obviation Retrofit Kits), which were designed for deployment in standard ODP (Ocean Drilling Program) and IODP (Integrated Ocean Drilling/International Ocean Discovery Program) boreholes. The concept is that

the CORK allows the re-establishment and monitoring of *in situ* conditions inside the borehole by sealing off the borehole from the overlying water column. Simultaneously, fluid exchange between the uncased part of the borehole and the formation is possible. In a cased borehole, fluid circulation is governed via permeable casing screens. At the same time, most CORKs provide access to borehole and formation fluids via sampling valves at the CORK head (Table 2). The CORK head is situated on top of the wellhead (Figure 7), and hosts pressure transducers, data loggers, and battery packs, and can be accessed via an ROV. Individual sensor strings may be suspended from the CORK head, depending on the CORK system and the scientific objectives (Table 2).

SENSORS

[4] Almost all CORK systems use Paroscientific Digiquartz pressure sensors, which allow determination of absolute pressure to depths of up to 7000 m with an accuracy of ca. 0.01% (Becker and Davis 2005). Temperature measurements are carried out with a string of several thermistors or miniature temperature loggers (MTL). While pressure and temperature sensors are standard in conventional CORK systems, more recent developments include:

[5] *OsmoSampler* – An OsmoSampler uses an osmotic pump to sample fluids and to store them in a sampling coil. Suction is created by flow within the pump, where two solutions of different salinity are separated by a semipermeable membrane (Jannasch et al. 2003). Fluids migrate through the membrane from the saline to the fresher solution, with dissolved salts being held back by the membrane. The osmotic pump causes formation fluids and gases to be drawn into the sampling coil, which hosts either Teflon tubing for fluid sampling or copper tubing for gas sampling. The sampling coils can be combined to allow long-term fluid and gas sampling.

[6] *FLOCS* – These are incubation chambers for *in situ* microbiological experiments (Orcutt et al. 2010). So far, they have been deployed within a GeniusPlug (Kopf et al. 2011), a CORK lite (Wheat et al. 2012) and an L-CORK (Fisher et al. 2011). As the name implies, FLOCS (FLow-through Osmo Colonization Systems) chambers are combined with OsmoSamplers, which allow the migration of borehole fluid through the columns (Orcutt et al. 2010). Endemic microorganisms, which are present in the fluid, can colonize in the individual chambers. The substrates present in the different columns vary from case to case, and include mineral fragments, rock-chips, and substrates for concentrating biomass, e.g. glass wool (Orcutt et al. 2010).

CONVENTIONAL CORKs

[7] In the following, a short overview is given about individual CORK designs (Table 2; for more comprehensive and more technical information, see Becker and Davis 2005; Kastner et al. 2006; Wheat et al. 2011, and individual literature given in subsections):

[8] *CORK* – Initial CORK installations provided only a single-seal solution, i.e. the borehole is sealed by the CORK body itself, which sits in the casing hangar system (Figure 7). One pressure sensor and a thermistor string are located inside the borehole, while one pressure sensor sits above the seal to monitor hydrostatic reference pressure.

[9] *Advanced CORK* – Starting with A-CORKs, multilevel monitoring became available (Shipboard Scientific Party 2002). The term "multilevel" refers to the separation of individual sections in the borehole by using packers. These are "like giant tires that are inflated to fill the annulus of the borehole" (from Wheat et al. 2010), and create confined compartments within the borehole between which vertical fluid exchange is prohibited. Sensor strings and hydraulic tubing can still pass through the packers, and provide access from the data logger and sampling valves at the CORK head to the individual zones. The tubes are housed in a protective hard-plastic coating (or umbilical) (Wheat et al. 2010), which is attached to the outside of the CORK casing. The inside of the casing can host a separate sensor string, or remain empty to enable re-entry with a drill string and further deepening of the borehole. The borehole can still be sealed temporarily at its bottom with a drill- and/or wireline-removable bridge plug.

[10] *CORK II* – The CORK-II is a subsequent advancement of the A-CORK design (Jannasch et al. 2003). It is different from the A-CORK in terms of its "instrument hanger" system. After landing in the re-entry cone, a 4.5 inch diameter casing is suspended in the borehole. This casing hosts again umbilicals and packers on the outside, while the central bore serves as a structural guide for a separate sensor string.

[11] *Lateral CORK* – The design of the L-CORK is similar to the CORK-II but it has an additional ball valve, which is connected to a lateral break-out tube at the well head. A flow meter is attached to this break-out tube, and overpressurized borehole fluids can be sampled. The L-CORK works with two packers, one hydraulic packer for instantaneous sealing and one swellable packer for long-term sealing of the borehole.
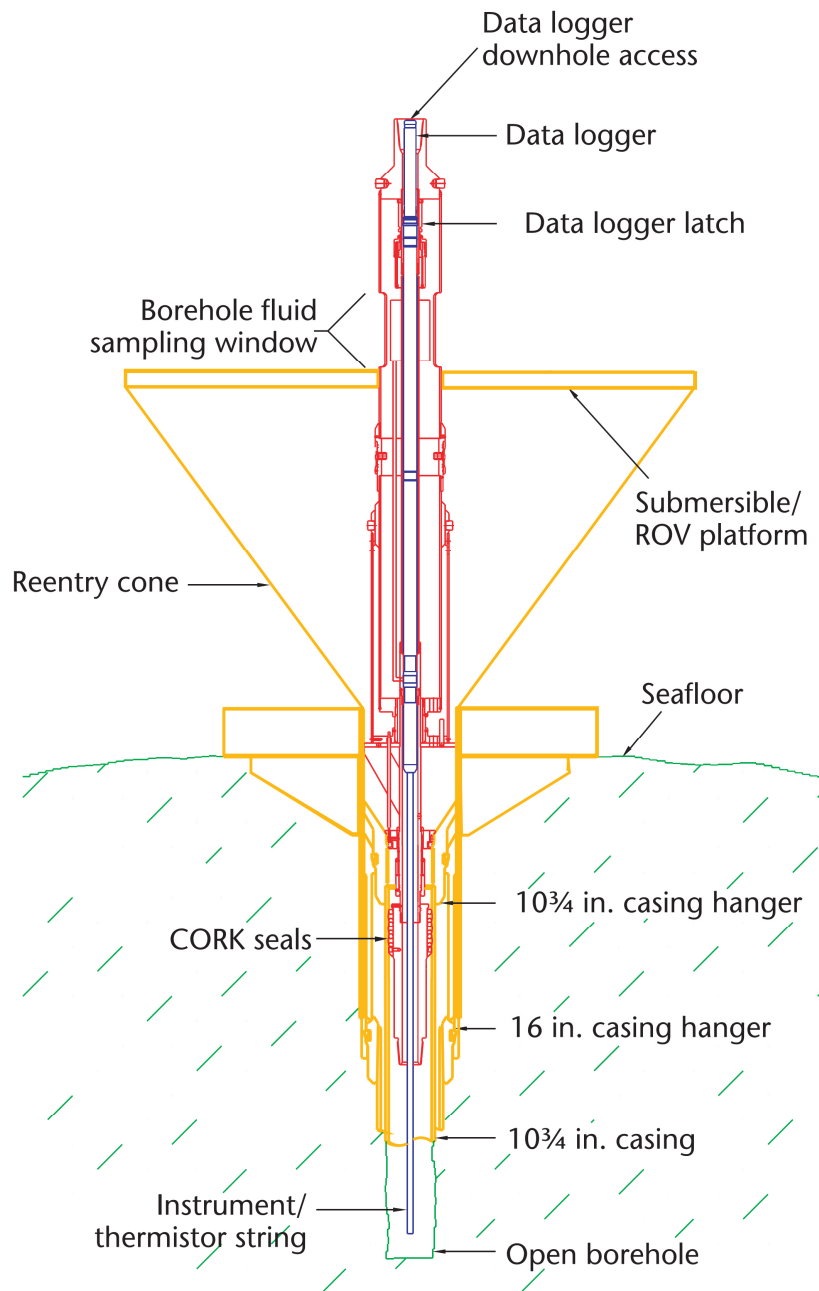
Figure 7: Configuration of a basic, single-seal CORK system. Fluid exchange between the overlying water column and the borehole is provided by the CORK body itself, which latches into the instrument hanger at the wellhead (from Becker and Davis 2005).

UNCONVENTIONAL INSTALLATIONS

[12] *CORK Lite* – The CORK Lite was designed to be installed with an ROV in so-called "legacy" boreholes (Wheat et al. 2012). These holes were drilled into the basement, and completed with a re-entry cone for potential deepening in subsequent expeditions. Only the sedimentary section was cased, leaving the lower part of the borehole open (Edwards et al. 2012; Wheat et al. 2012). The CORK Lite consists of a body with a landing seal ring at its bottom, a removable cap that seals the CORK at its top, a downhole instrument that can be deployed inside the CORK body,

4.1 Long-Term Borehole Monitoring Using Borehole Observatories

Table 2: Overview of CORK systems developed for offshore borehole monitoring. P and T denote (fluid) pressure and temperature, respectively. MS stands for "mission specific", i.e. the instrument package can be individually adjusted to specific scientific objectives. References are not comprehensive.

Name	Installation via	Year and place of first deployment	Measurements	Multilevel monitoring possible	Fluid sampling at wellhead	References
CORK	drilling vessel	1991, Juan de Fuca Ridge	P, T, OsmoSampler	no	yes	Davis et al. 1992
A-CORK	drilling vessel	2001, Nankai Trough	P	yes	yes	Shipboard Scientific Party 2002
CORK II	drilling vessel	2002, Costa Rica Margin	P, T, OsmoSampler	yes	yes	Jannasch et al. 2003
L-CORK	drilling vessel	2010. Juan de Fuca Ridge	P, T, OsmoSampler, FLOCS	yes	yes	Fisher et al. 2011
CORK lite	ROV	2012, Mid-Atlantic Ridge	P, T, OsmoSampler, FLOCS, MS	yes	yes	Wheat et al. 2012
wireline CORK	ROV/research vessel	2001, Costa Rica Rift	P, T	yes	yes	Spiess et al. 1992
LTBMS	drilling vessel	2010, Kumano Forearc Basin	P, T, seismometer, strainmeter accelerometer, tiltmeter	yes	no	Kopf et al. 2011a
JFAST Observatory	drilling vessel	2012, Japan Trench	P, T	no	no	Fulton et al. 2013
MeBo CORK/PLUG/PUPPI	MeBo/ROV	2012, Kumano Forearc Basin	P, T, OsmoSampler, MS	no	no	Kopf et al. 2013; Appendix B in this work
SmartPlug	drilling vessel	2009, Nankai Trough	P, T	no	no	Kopf et al. 2011b
GeniusPlug	drilling vessel	2010, Nankai Trough	P, T, OsmoSampler, FLOCS	no	no	Kopf et al. 2011b

and pressure gauges for borehole and hydraulic reference pressure monitoring (Wheat et al. 2012). The instrument string can be modified according to mission-specific scientific objectives.

[13] *LTBMS* – A-CORK installation in the Kumano forearc basin, SE offshore the Japanese Kii Peninsula was exceptionally successful. This so-called LTBMS (Long-Term Borehole Monitoring System) is similar to conventional A-CORKs in terms of its multilevel packer system. However, besides pressure and temperature sensors, it also includes mission-specific instruments attached to an instrument hanger, which hosts a strainmeter, seismometer, tiltmeter and accelerometer (Kopf et al. 2011a).

[14] *Wireline CORK* – This CORK system can be installed from any research vessel, i.e. a drillship is not required. It consist of an in-cone platform, which lands in the re-entry cone and from which

the instrument string is suspended. Multilevel sealing of the borehole is achieved with swellable packers, equipped with electrical and hydraulic access ports for thermistor strings and hydraulic tubing.

[15] *JFAST Observatory* – The JFAST Observatory consisted of ca. 55 MTLs, 10 of which also included pressure sensors (Expedition 343/343T Scientists 2013). The sensor string is suspended from the observatory casing hanger, which rests within the casing hanger wellhead. Unlike previous CORK designs, the JFAST Observatory does not have a CORK head where battery packs and data logger are stored. Instead, each MTL is individually powered and stores data autonomously.

[16] *MeBoCORK* – Deployment of observatories without the need for a drilling vessel was the driving motivation for developing MeBoCORKs. They are designed to be installed in boreholes drilled by the MARUM seafloor drill rig MeBo (Meeresboden-Bohrgerät), which can be deployed from any research ship (Kopf et al. 2013; cf. Appendix B). Currently, two designs are available: the MeBoCORK A (for "autonomous") and the MeBoCORK B (for "bottom"). While the former is installed by MeBo directly after drilling and coring operations are finished, the second MeBo CORK version requires an ROV for installation because it includes a seafloor unit. Both designs host pressure and temperature sensors and can transfer data via an acoustic modem. The seafloor unit of MeBo-CORK B can be modified with mission-specific sensors, e.g. OsmoSampler (Kopf et al. 2013; cf. Appendix B). A female "hotstab" receptacle on top of the well is a necessary prerequisite for installation of MeBo-CORKs. After latching into the hotstab receptacle, a PTFE coil is released, and is drawn down the borehole by a dead weight. Two other observatories are available for installation with MeBo: the MeBoPLUGs and the MeBoPUPPIs (Pop-Up Pore Pressure Instrument). While the former needs an ROV to be recovered, the MeBoPUPPI contains a pop-up telemetric unit that send the long-term data to a shorebased station (cf. Appendix B).

[17] *SmartPlug/GeniusPlug* – The SmartPlug and the GeniusPlug borehole observatories belong to a class of so-called "mini-CORKs" (Kopf and Davis 2011; Kopf et al. 2011b). Both require a drill ship for installation, are self-contained (i.e. data loggers, battery packs and instruments are all situated within a structural outer shell) and can be attached to a BakerHughes bridge plug. The SmartPlug provides temperature and pressure sensors, whereas the GeniusPlug provides also an OsmoSampler and FLOCS microbiological cells (cf. compare also chapter 5).

References

Becker K, Davis EE (2005) A review of CORK designs and operations during the Ocean Drilling Program. In: Fisher AT, Urabe T, Klaus A, the Expedtion 301 Scientists (eds) Proc IODP, 301

Davis EE, Becker, K., Pettigrew, T., Carson, B., MacDonald R (1992) CORK: a hydrologic seal and downhole observatory for deep ocean boreholes. In: Davis EE, Mottl, MJ, Fisher AT (eds) Proc ODP, Init Repts, 139

4.1 Long-Term Borehole Monitoring Using Borehole Observatories

Davis E, Becker K, Dziak R, Cassidy J, Wang K, Lilley M (2004) Hydrological response to a seafloor spreading episode on the Juan de Fuca ridge. Nature 430: 335-338

Davis E, Heesemann M, Wang K (2011) Evidence for episodic aseismic slip across the subduction seismogenic zone off Costa Rica: CORK borehole pressure observations at the subduction prism toe. Earth Planet Sci Lett 306: 299-305. doi:http://dx.doi.org/10.1016/j.epsl.2011.04.017

Edwards KJ, Becker K, Colwell F (2012) The Deep, Dark Energy Biosphere: Intraterrestrial Life on Earth. Annual Review of Earth and Planetary Sciences 40:551-568. doi:10.1146/annurev-earth-042711-105500

Expedetion 343/343T Scientists (2013) Methods. In: Chester FM, Mori J, Eguchi N, Toczko S, Expedetion 343/343T Scientists (eds) Proc IODP 343. Integrated Ocean Drilling Program Management International, Inc., Tokyo

Fisher AT, Becker K, Davis EE (1997) The permeability of young oceanic crust east of Juan de Fuca Ridge Determined using borehole thermal measurements. Geophys Res Lett 24: 1311-1314. doi:10.1029/97gl01286

Fisher AT, Wheat CG, Becker K, Cowen JP, Orcutt B, Hulme S, Inderbitzen K, Haddad A, Pettigrew TL, Davis EE, Jannasch H, Grigar K, Aduddell R, Meldrum R, Macdonald R, Edwards KJ (2011) Design, deployment, and status of borehole observatory systems used for single-hole and cross-hole experiments, IODP Expedition 327, eastern flank of Juan de Fuca Ridge. Proc IODP 327. doi:10.2204/iodp.proc.327.107.2011

Fulton PM, Brodsky EE, Kano Y, Mori J, Chester F, Ishikawa T, Harris RN, Lin W, Eguchi N, Toczko S, the Expedition 343/343T Scientists, the Expedition KR13-08 Scientists (2013) Low Coseismic Friction on the Tohoku-Oki Fault Determined from Temperature Measurements. Science 342: 1214-1217. doi:10.1126/science.1243641

Graber KK, Pollard E, Jonasson B, Schulte E (2002) Overview of Ocean Drilling Program Engineering Tools and Hardware. ODP Technical Note 31

Jannasch H, Davis E, Kastner M, Morris J, Pettigrew T, Plant JN, Solomon E, Villinger H, Wheat CG (2003) CORK-II: long-term monitoring of fluid chemistry, fluxes, and hydrology in instrumented boreholes at the Costa Rica subduction zone. In: Morris JD, Villinger HW, Klaus A (eds) Proc ODP, Initial Reports, 205

Kastner M, Becker K, Davis EE, Fisher AT, Jannasch HW, Solomon EA, Wheat CG (2006) New Insights into the Hydrogeology of the Oceanic Crust Through Long-Term Monitoring. Oceanography 19:46 – 57

Kopf A, Araki E, Toczko S, Expedition 332 Scientists (2011a) Proc IODP 332. doi:10.2204/iodp.proc.332.2011

Kopf A, Saffer DM, Davis EE, Hammerschmidt S, LaBonte A, Meldrum R, Toczko S, Lauer R, Heesemann M, Macdonald R, Wheat CG, Jannasch HW, Edwards K, Orcutt B, Haddad A, Villinger H, Araki E, Kitada K, Kimura T, Kido Y (2011b) The SmartPlug and GeniusPlug: simple retrievable observatory systems for NanTroSEIZE borehole monitoring. In: Kopf A, Araki E, Toczko S, Expedition 332 Scientists (eds), Proc IODP 332. doi:10.2204/iodp.proc.332.105.2011

Kopf A, et al. (2013). Report and Preliminary Results of SONNE Cruise SO222: Project MEMO, Berichte aus dem Fachbereich Geowissenschaften der Univ. Bremen, 297: 121pp

Liu L-B, Roeloffs, E., Zheng X-Y (1989) Seismically Induced Water Level Fluctuations in the Wali Well, Beijing, China. Journal of Geophysical Research 94: 9453 – 9462

Orcutt B, Wheat CG, Edwards KJ (2010) Subseafloor Ocean Crust Microbial Observatories: Development of FLOCS (FLow-through Osmo Colonization System) and Evaluation of Borehole Construction Materials. Geomicrobiol J 27:143 - 157

Roeloffs EA (1998) Persistent water level changes in a well near Parkfield, California, due to local and distant earthquakes. Journal of Geophysical Research 103:869-889. doi:10.1029/97jb02335

Shipboard Scientific Party (2002). Explanatory notes. In: Mikada H, Becker K, Moore JC, Klaus A, et al., Proc ODP, Init Repts, 196: 1–53

Spiess FN, Boegeman DE, Lowenstein C (1992). First ocean-research-ship-supported fly-in re-entry to a deep ocean drill hole. Mar Technol Soc J, 26: 3–10.

Wheat CG, Jannasch HW, Kastner M, Hulme S, Cowen J, Edwards K, Orcutt BN, Glazer B (2011) Fluid Sampling from Oceanic Borehole Observatories: Design and Methods for CORK Activities (1990-2010). Proc ODP 327

Wheat CG, Edwards KJ, Pettigrew T, Jannasch HW, Becker K, Davis EE, Villinger H, Bach W (2012) CORK-Lite: Bringing Legacy Boreholes Back to Life. Scientific Drilling 14: 39 - 43. doi:doi:10.2204/iodp.sd.14.05.2012

Williamson D (2013) Drilling Fluid Basics. Oilfield Review 25:63 – 64

Woodcock D, Roeloffs E (1996) Seismically-induced water level oscillations in a fractured-rock aquifer well near Grants Pass, Oregon. Oregon Geol 58:27–33.

CHAPTER 4.2

REAL-TIME DRILLING MUD GAS MONITORING

OVERVIEW

[1] Mud logging is one of the most well-established methods for real-time evaluation of formation conditions and fluids at the drill bit face. E&P companies have used mud logging since 1939, and mud loggers provided a nearly real-time description of the lithology and hydrocarbons encountered during drilling prior to the development of advanced measurement-while-drilling (MWD) and logging-while-drilling (LWD) tools (see review by Ablard et al. 2012). Mud logging utilizes two different techniques: sedimentological and petrophysical description of cuttings, and drilling mud gas monitoring. During riser drilling, cuttings (rock chips generated during drilling) and drilling mud gas (gas liberated during drilling) mix with the drilling mud and circulate upward to the drill rig, where they are again separated (Figure 8).

[2] Today, mud logging is a complementary technique to MWD and LWD. Parameters like rate-of-penetration (ROP) and total gas concentrations correlate with gamma ray and resistivity data, and the direct correlation between lithology and hydrocarbons is of substantial help for interpreting MWD/LWD logs (Ablard et al. 2012, and references therein). Moreover, mud logging becomes invaluable where borehole conditions, technical and/or financial issues preclude drilling with LWD/MWD technology. Instead of drilling ahead blindly, mud logging gives information such as ROP, lithology, hydrocarbons, weight-on-bit and mud density. In addition to the scientific merit, knowledge of these parameters is essential for running a safe operation. For instance, gas monitoring allows the detection of CO_2 and H_2S, and enables identification of overpressured intervals, i.e. intervals where the borehole pressure (= hydrostatic pressure + friction pressure loss in annulus) falls below the formation pressure (Lyons 1996; Ablard et al. 2012). These intervals are susceptible to sudden fluid influx into the borehole, commonly referred to as "gas kicks", and can lead to a blowout. With early detection using mud logging technologies, the hazard can be minimized either by increasing the mud weight, or by shutting-in the borehole.

[3] The gas encountered during riser drilling consists mainly of atmospheric gases (Ar, N_2, O_2), gases released from the pore space (e.g. He, N_2, hydrocarbons), and gases present where fault zones are penetrated (e.g. ^{222}Rn, He, hydrocarbons). Although drilling mud gas monitoring is mainly used for hydrocarbon gas identification and classification, its scientific merit has been

highlighted in several publications (e.g. Aquilina et al. 1998; Erzinger et al. 2006; Wiersberg and Erzinger 2007, 2008, 2011). Noble gases, for instance, are commonly used to identify igneous, sedimentary and primordial (mantle) sources, and isotope ratios of individual noble and hydrocarbon gases can signal active fluid migration and mixing (e.g. Aquilina et al. 1998; Ellis et al. 2003, 2007; Erzinger et al. 2006; Wiersberg and Erzinger 2011).
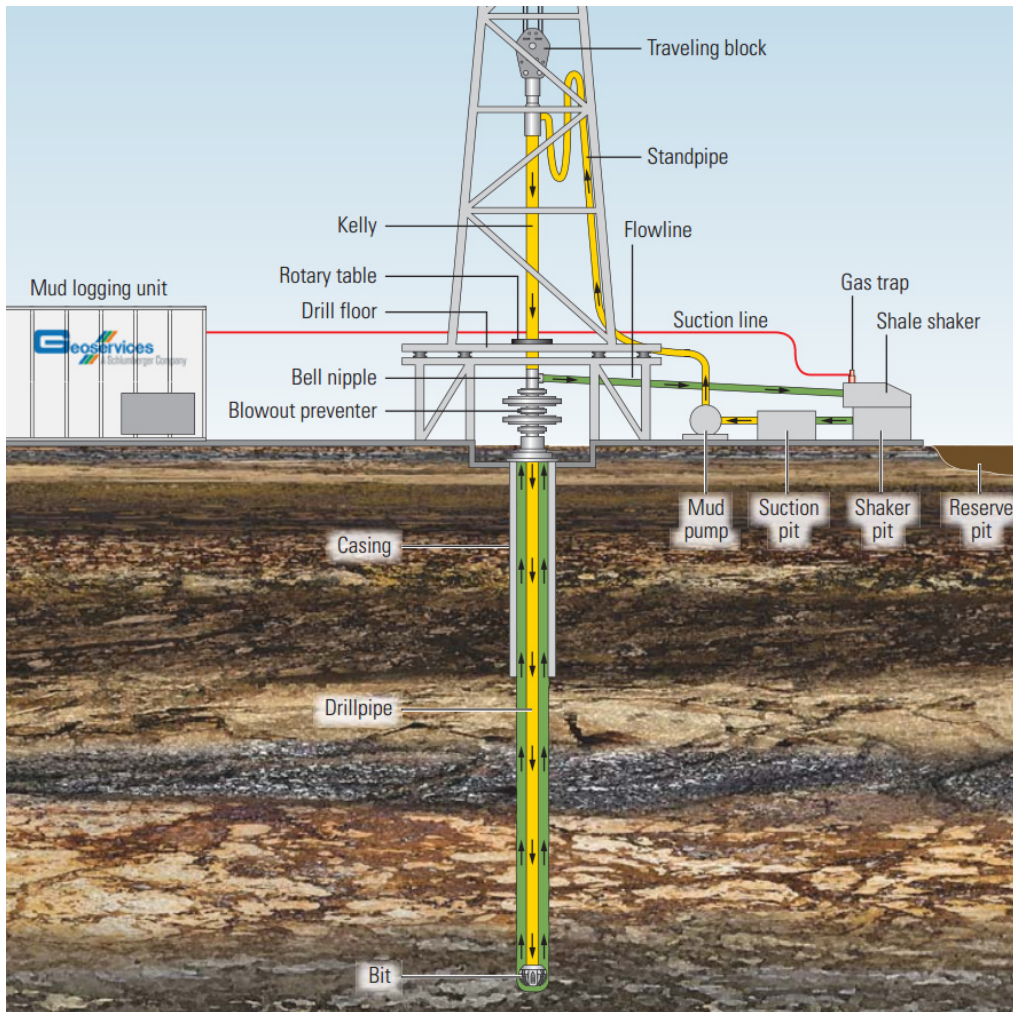
Figure 8: Example for an onshore mud circulation system (from Ablard et al. 2012). Drilling mud is drawn from the suction pit via surface pipes, and flows down the central bore of the drill string. At the drill bit, the mud serves as cooling and lubricating agent. In the annulus between borehole wall and drill string, the drilling mud then circulates back upwards along with cuttings and fluids collected at the drill bit. At the bell nipple, the drilling mud is transferred to the shale shaker pit, where the gas phase is removed by a gas trap, and the solid phase (i.e. cuttings) is removed by the shale shaker. The cleaned mud is then returned to the suction pit. The gas phase is transferred to the mud logging unit and analyzed. Cuttings are collected and may be used for petrographic analyses.

[4] Because of the large number of factors influencing the gas composition and concentration, drilling mud gas monitoring provides solely qualitative information (Erzinger et al. 2006). Since absolute values are unreliable, real-time evaluation of hydrocarbon gases commonly utilizes gas

ratios (Haworth et al. 1985), and empirical diagrams, e.g. Pixler plots (Pixler 1969) or spider/star plots (e.g. Prinzhofer et al. 2000; Dessay et al. 2011).
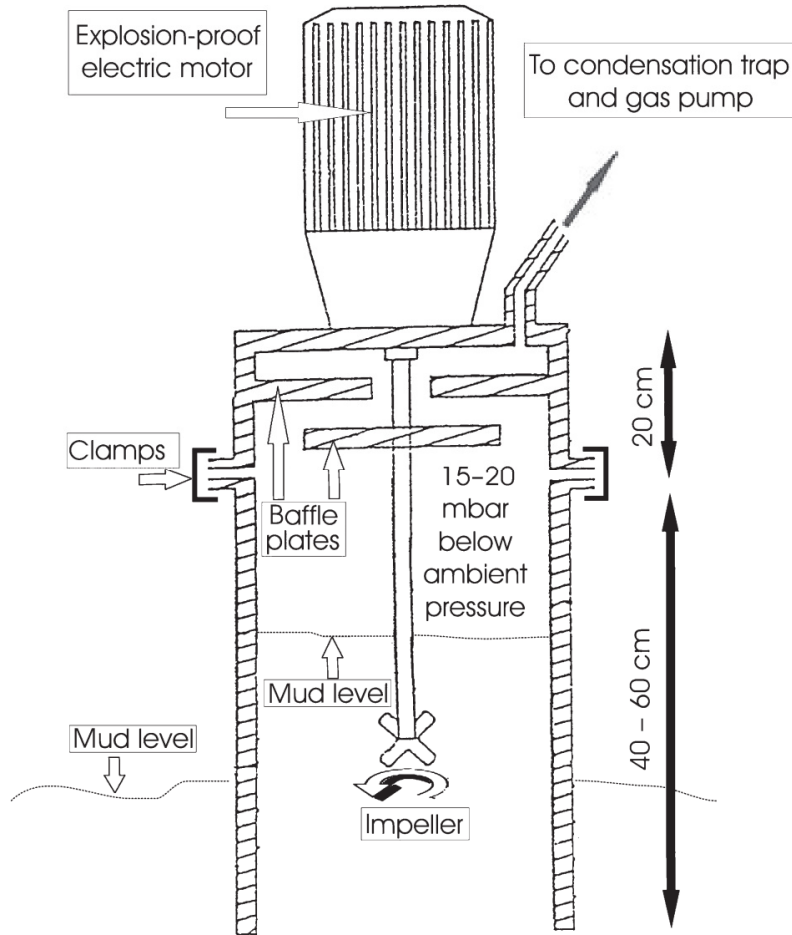
Figure 9: Schematic overview of a conventional degasser (from Erzinger et al. 2006). The impeller stirs the mud to improve gas liberation. The gas is then extracted and forwarded to the mud gas laboratory. Shown here is a fixed degasser, meaning that its height cannot be adjusted to changes in the mud level.

[5] Conventional degassing systems, however, do not adequately liberate higher hydrocarbons (C_{2+}), and therefore, the scientific value of the abovementioned methods is limited (Figure 9). Recent developments, e.g. the FLAIR system by Schlumberger, address this problem by providing a constant air-to-mud ratio (i.e. a constant gas volume) inside the gas extraction chamber, and by heating of the drilling mud during degassing (e.g. Blanc et al. 2003; Stankiewicz et al. 2007; Ablard et al. 2012; Schlumberger 2013). Consideration of thermodynamic reactions is of particular importance in deep-water environments, where mud return temperatures vary from 10°C to 15°C (Ablard et al. 2012). In this temperature range, hydrocarbons heavier than C_5 do not occur in a gaseous phase, making their detection almost impossible. Heating the mud to temperatures that can be expected at the drill bit allows not only the liberation and qualitative analyses of heavier hydrocarbons, but also the quantification of the C_1 to C_5 components.

Detection of non-hydrocarbons is improved as well. Almost 100 years after its first usage, due to the recent developments and technical inventions to come, drilling mud gas monitoring experiences a strong revival, and may again be considered "*the nerve center of the drilling rig*" (Ablard et al. 2012).

References

Ablard P, Bell C, Cook D, Fornasier I, Poyet J-P, Sharma S, Fielding K, Lawton L, Haines G, Herkommer MA, McCarthy K, Radakovic M, Umar L (2012) The Expanding Role of Mud Logging. Oilfield Review 24:24 – 41

Aquilina L, Baubron J-C, Defoix D, Dégranges P, Disnar J-R, Marty B, Robé M-C (1998) Characterization of gases in sedimentary formations through monitoring during drilling and core leaching (Balazuc borehole, Deep Geology of France Programme). Appl Geochemistry 13:673–686. doi: 10.1016/s0883-2927(98)00008-0

Blanc P, Brevière J, Laran F, Chauvin H, Boehm C, Frechin N, Capot M, Benayoun A (2003) Reducing Uncertainties In Formation Evaluation Through Innovative Mud Logging Techniques. SPE Annu. Tech. Conf. Exhib. Society of Petroleum Engineers, Denver, Colorado, p Abstract #SPE–84383–MS

Dessay J, Torres O, Sharma S (2011) Real Time Formation Characterization from Advanced Mud Gas Analyses for Improved Geological Operations Decisions. 73rd EAGE Conf. Exhib.

Ellis L, Brown A, Schoell M, Uchytil S (2003) Mud gas isotope logging (MGIL) assists in oil and gas drilling operations. Oil Gas J 101:32–41.

Ellis L, Berkman T, Uchytil S, Dzou L (2007) Integration of mud gas isotope logging (MGIL) with field appraisal at Horn Mountain Field, deepwater Gulf of Mexico. J Pet Sci Eng 58:443–463. doi: 10.1016/j.petrol.2007.03.001

Erzinger J, Wiersberg T, Zimmer M (2006) Real-time mud gas logging and sampling during drilling. Geofluids 6:225–233. doi: 10.1111/j.1468-8123.2006.00152.x

Haworth J, Sellens M, Whittaker A (1985) Interpretation of Hydrocarbon Shows Using Light (C1-C5) Hydrocarbon Gases from Mud-Log Data. Am Assoc Pet Geol Bull 69:1305–1310.

Lyons W (1996) Standard Handbook of Petroleum and Natural Gas Engineering, 1st ed, pp 1456.

Pixler BO (1969) Formation Evaluation by Analysis of Hydrocarbon Ratios. J Pet Technol 21:665 – 670. doi: 10.2118/2254-PA

Prinzhofer A, Mello MR, Takaki T (2000) Geochemical Characterization of Natural Gas : A Physical Multivariable Approach and its Applications in Maturity and Migration Estimates. Am Assoc Pet Geol Bull 84:1152–1172.

Schlumberger (2013) FLAIR - Fluid Logging and Analysis in Real Time Service. pp 8.

Stankiewicz BA, McKinney D, Breviere J, Lessi J, Jaulneau P, the FEAST Team (2007) Advanced Mud Logging Technology "FLAIR" - New Horizons in Petroleum Geochemistry (abstract). Int. Meet. Org. Geochemistry. Torquay, United Kingdom, p Abstract #O85

Wiersberg T, Erzinger J (2007) A helium isotope cross-section study through the San Andreas Fault at seismogenic depths. Geochem Geophys Geosyst 8:Q01002. doi: 10.1029/2006gc001388

Wiersberg T, Erzinger J (2008) Origin and spatial distribution of gas at seismogenic depths of the San Andreas Fault from drill-mud gas analysis. Appl Geochemistry 23:1675–1690. doi: 10.1016/j.apgeochem.2008.01.012

Wiersberg T, Erzinger J (2011) Chemical and isotope compositions of drilling mud gas from the San Andreas Fault Observatory at Depth (SAFOD) boreholes: Implications on gas migration and the permeability structure of the San Andreas Fault. Chem Geol 284:148–159. doi: 10.1016/j.chemgeo.2011.02.016

CHAPTER 5
Long-term Borehole Monitoring at the Megasplay Fault

CHAPTER 5.1 – MANUSCRIPT I

FLUID PRESSURE AND TEMPERATURE TRANSIENTS DETECTED AT THE NANKAI TROUGH MEGASPLAY FAULT: RESULTS FROM THE SMARTPLUG BOREHOLE OBSERVATORY

Sebastian B. Hammerschmidt[1]*, Earl E. Davis[2], Achim Kopf[1]

published 2013 in

Tectonophysics, 600, pp. 116 – 166, doi: 10.1016/j.tecto.2013.02.010

* corresponding author: shammerschmidt@marum.de

[1] MARUM, University of Bremen, Bremen, Germany

[2] Pacific Geoscience Center, Geological Survey of Canada, Sidney, B.C., Canada

Abstract The SmartPlug is the first borehole observatory in the IODP Nankai Trough Seismogenic Zone Experiment (NanTroSEIZE). It comprises a retrievable bridge plug with an autonomous instrument for pressure (P) and temperature (T) monitoring. The borehole observatory was installed at Site C0010 of the Integrated Ocean Drilling Program (IODP) Kumano transect crossing the Nankai Trough, SE offshore Japan, to obtain fluid pressure and temperature data from where the borehole penetrates one of the shallow branches of the subduction Megasplay fault at 410 mbsf. In this manuscript, a 15 month-long P-T record collected by the SmartPlug is evaluated. Despite the 1 min sampling interval, pressure variations related to local storms and to tsunami and seismic waves from regional and distant earthquakes are observed. Seismic waves of one regional earthquake appear to have led to a drop in formation pressure that may be the consequence of a seismic-wave-induced increase in permeability. Pressure variations related to Rayleigh waves are typically larger in the formation than in the inadvertently sealed casing above, whereas seafloor loading signals imposed by tides, tsunamis, and storm-generated waves are larger in the casing than in the formation. This difference presumably reflects the different response to strain generated by formation deformation vs. strain caused by loading at the seafloor. No seismogenic or aseismic deformation event at the Megasplay fault or within the accretionary prism was observed during this initial 15-month-long recording period.

INTRODUCTION

[1] Globally, the most destructive earthquakes are generated at subduction zones (e.g. Lay et al. 1989; Hyndman et al. 1997), including the Nankai Trough region offshore south-western Japan. The most recent large and destructive earthquakes in this region occurred in 1944 (Tonankai M8.1) and 1946 (Nankaido M8.3) (e.g. Ando 1975; Satake 1993; Ichinose et al. 2003) (Figure 10). In order to investigate the mechanisms responsible for earthquake and tsunami generation at subduction zones, the Nankai Trough Seismogenic Zone Experiment (NanTroSEIZE) is being established by the Integrated Ocean Drilling Program (IODP). NanTroSEIZE represents a northward extension of previous projects (Figure 10) investigating seismogenesis SE off the Ashizuri Peninsula (Deep Sea Drilling Project Legs 31, 87; Karig and Ingle 1975; Kagami et al. 1987) and off Cape Muroto (Ocean Drilling Program Legs 131, 190, 196; Taira et al. 1991; Moore et al. 2001). To be within the operational limits of riser drilling with drilling vessel (D/V) Chikyu, a location SE off the Kii Peninsula was chosen for the NanTroSEIZE transect (Saffer et al. 2009). During NanTroSEIZE stage 1, the so-called Kumano transect was initiated by three drilling campaigns including the frontal thrust region (Site C0006, C0007), the Megasplay fault region (Sites C0001, C0003, C0004, C0008) and the Kumano forearc basin region (C0002), which are summarized in Kinoshita et al. (2009). The transect is shown in Figure 11. The Megasplay fault region is one of the main study areas in NanTroSEIZE because this major splay fault may have hosted coseismic slip during the 1944 Tonankai event and played a role in tsunamigenesis (Satake 1993; Sagiya and Thatcher 1999; Cummins et al. 2001; Park et al. 2002).

[2] Several studies suggest that the Megasplay fault acts as a fluid conduit, allowing the pore fluid pressure in the surrounding sediments and especially in the deeper part of the plate boundary to escape and subsequently increase effective stress there. Elevated effective stress may in turn enhance consolidation, cementation and lithification (e.g. Byrne et al. 1988; Scholz

1998; Moore and Saffer 2001; Park et al. 2002; Tobin and Saffer 2009). Increased effective stress also favours frictional instability and stick-slip behaviour and thus potential earthquake generation underneath the inner accretionary wedge (Byrne et al. 1988; Scholz 1998). The Megasplay fault branches from the main décollement at ~8 km depth, and reaches shallow
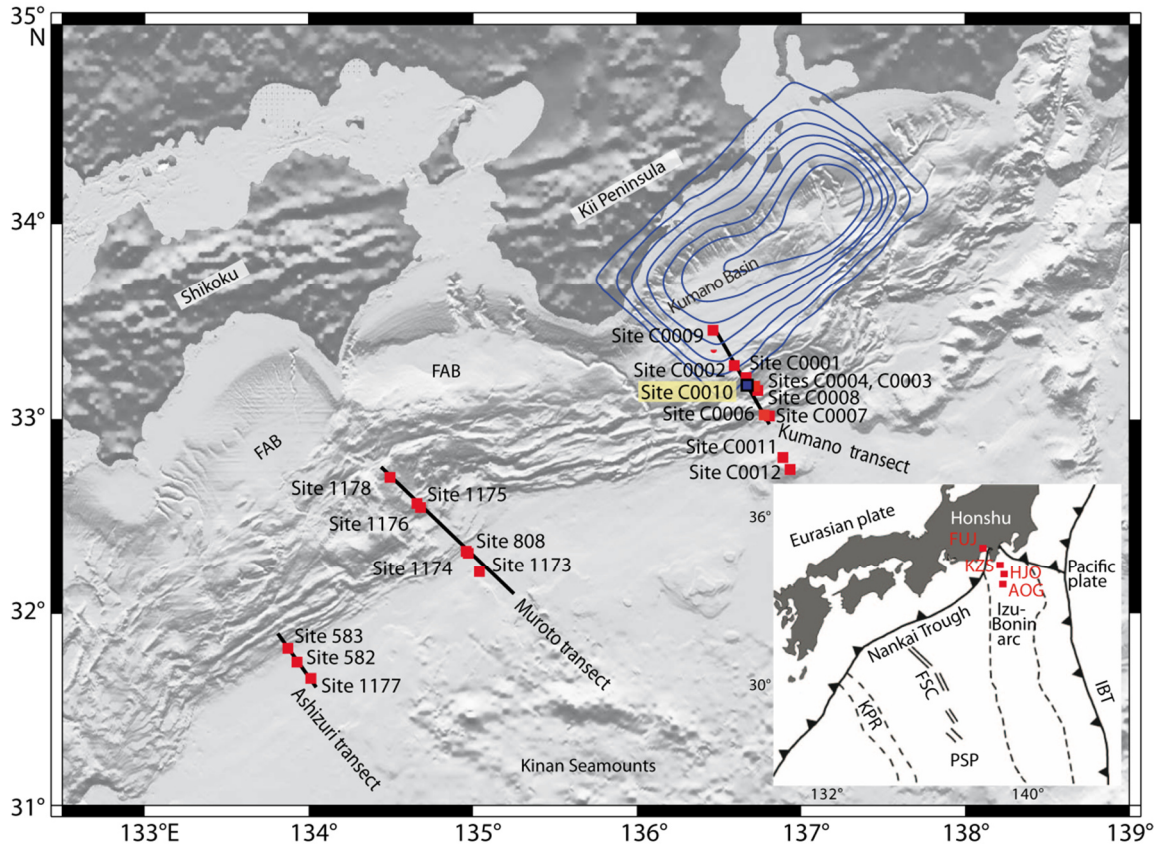
Figure 10: Overview of the DSDP Ashizuri, the ODP Muroto and IODP Kumano transects (modified from Moore et al. 2009). The inlay shows the tectonic map of the study area as well as the spatial distribution of F-Net stations (red labelled) from which waveform data was used in this study. Site C0010 is situated at the Nankai Trough, south-east off the Kii Peninsula, where the Philippine Sea Plate is subducted beneath the Eurasian Plate with a rate of 4 – 6.5cm/a. This area is suggested to have shown coseismic slip during the 1944 Tonankai earthquake (unlabelled contours) and was therefore chosen as the main study area of NanT-roSEIZE. FAB: forearc basin; IBT: Izu-Bonin Trench, KPR: Kyushu-Palau Ridge, FSC: fossil spreading center, PSP: Philippine Sea plate.

depths at Site C0010, making it easily accessible for drilling and logging. The borehole at Site C0010 is scheduled for deepening at a later time for a permanent deeper observatory installation, and in the interim it was to be sealed with grout. To capitalize on the potential for an earlier phase of monitoring, a first simple observatory was conceived using a retrievable instrument referred to here as the "SmartPlug", designed and constructed to provide an interim seal and to allow rudimentary monitoring to begin. The installation of permanent borehole observatories (or CORKs, i.e. Circulation Obviation Retrofit Kits) near this fault was one of the main objectives over the last years, with the goal of making *in situ* measurements including strain, seismic ground motion, temperature and fluid pressure. After successful deployment during IODP Expedition 319 (Saffer et al. 2009), the SmartPlug was recovered during Expedition 332 (Kopf et

al. 2011a) and replaced with a second unit capable of fluid sampling as well as temperature and pressure monitoring. The data downloaded in 2010 provide a 15-month record from four temperature (T) sensors and two pressure (P) sensors.

[3] In this article pressure and temperature measurements are presented and evaluated regarding the average state of formation fluid pressure at this site, and how pressure is influenced by oceanographic and seismic loading (e.g. in a manner discussed by Cooper et al. 1965; Wang and Davis 1996; Woodcock and Roeloffs 1996; Roeloffs 1998; Davis et al. 2000; Brodsky et al. 2003; Wang 2004; Elkhoury et al. 2006).
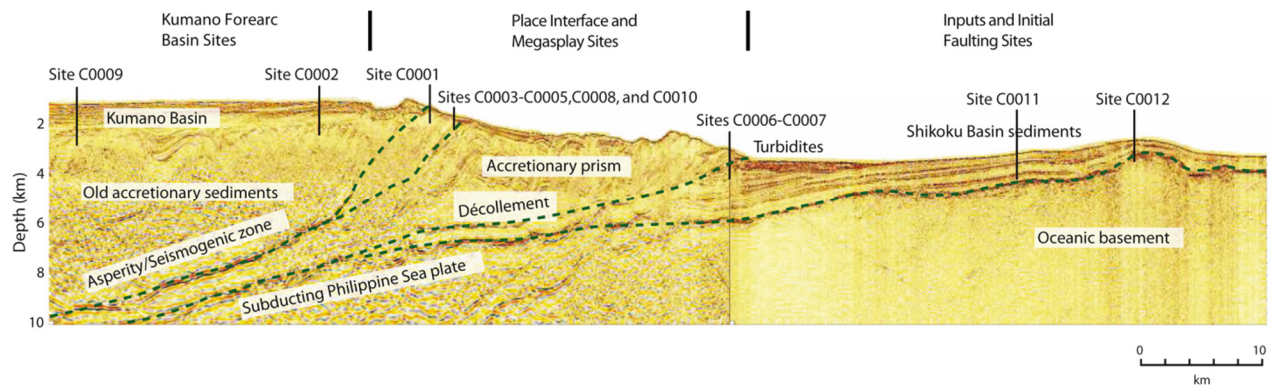
Figure 11: *Seismic cross-section of the NanTroSEIZE Kumano transect (modified from Kopf et al. 2011a). The Megasplay fault extends from the plate boundary up to the seafloor separating the accretionary prism into an inner and an outer part. At Site C0010, a borehole is penetrating one of the shallow branches of the Megasplay fault, and was therefore chosen as primary location for long-term borehole monitoring.*

GEOLOGICAL BACKGROUND

[4] The Nankai Trough area is a subduction zone along the SW coast of Japan, where the ~15 Ma old Philippine Sea plate (PSP) is subducting beneath the Eurasian Plate at a rate between 4 and 6.5 cm/yr, forming a thick sediment accretionary prism (Figures 10, 11). Underthrusting occurs along an azimuth of 300°- 315°N (Seno et al. 1993; Miyazaki and Heki 2001).

[5] Common along subduction zones are upward branching thrust faults, often termed "splay faults", and displacement along them during major subduction thrust earthquakes may be important in creating earthquake-triggered tsunamis (Fukao 1979). The Nankai Trough Megasplay fault was detected within a major out-of-sequence-thrust (OOST) fault system, branching from the main plate bounding décollement into several smaller faults in the accretionary prism seaward of the Kumano forearc basin (Figure 11). This splay fault probably serves as a mechanical boundary dividing an (i) inner, stronger accretionary wedge overlying the seismogenic part of the subduction thrust and (ii) a weaker outer wedge situated over the shallower, aseismic part of the plate boundary (Wang and Hu 2006). Based on combined 3-D seismic data and age determinations from cored material, Strasser et al. (2009) reported an onset of accretion at this location at around 2.87 Ma. The subduction of the PSP led to in-sequence forward imbrication

of accreted strata. As a consequence, a trench-slope basin system with abundant mass wasting deposits evolved. At around 1.95 Ma, the splay fault system started as an OOST in the lower part of the prism, followed by uplift and reactivation from approx. 1.5 Ma until 1.24 Ma (Strasser et al. 2009). Recent episodic activity of the splay fault is indicated by seismic data from this area showing young, truncated sedimentary bedding (Moore et al. 2007). According to Moore et al. (2009), the activity of the splay varies spatially, and different branches of the splay fault can slip independently from each other. Strain induced by recent activity of the Megasplay fault system is indicated by the deformation of overlying slope sediments (Kimura et al. 2011). This is supported by earlier studies reporting seismogenic activity of the Megasplay fault based on investigations of the tectono-stratigraphy of the Kumano forearc basin (e.g. Satake 1993; Sagiya and Thatcher 1999; Cummins et al. 2001; Park et al. 2002).

[6] At Site C0010, the top ~200 m of the drilled section are characterized by slope apron deposits consisting mainly of silty mudstone with some intercalated thin sand and ash layers. These deposits are underlain by a ~210 m thick wedge of fractured mudstone surrounding a thrust sheet in the hanging wall of the Megasplay fault (Kopf et al. 2011b, and references therein). The fault displacement moves the thrust sheet over the slope apron sediments (Kimura et al. 2008; Moore et al. 2009). Although geologically similar and only a few kilometres away, the Megasplay fault at Site C0004 shows an apparently different architecture, having a ~50 m thick "fault bounded package", whereas the fault at Site C0010 is imaged as single sharp reflector (Kimura et al. 2008; Saffer et al. 2009). This well-defined zone was targeted for pressure monitoring.

INSTRUMENTATION AND METHODS

The SmartPlug

[7] The SmartPlug represents the first effort in the history of NanTroSEIZE to monitor *in situ* pressure and temperature. The 1.3 m-long instrument includes a CrMo alloy steel shell mounted below a mechanically set retrievable Baker Hughes bridge plug that seals the deeper part of the borehole from the overlying ocean. The bridge plug prevents the flow of seawater into or out of the perforated section of casing below, and creates a hydrologically isolated interval at the zone of interest. The water filling the hollow body of the packer and SmartPlug shell communicates directly with the water within the cased section of borehole above the plug (Figure 12). Below the plug, the borehole at Site C0010 is cased with a c. 22 m-long interval of screens (two sections of perforated casing wrapped with filter screens each c. 11 m long, see also Fig. 13) that allow hydraulic connection to the fault zone for pressure observations (Araki et al. 2010).
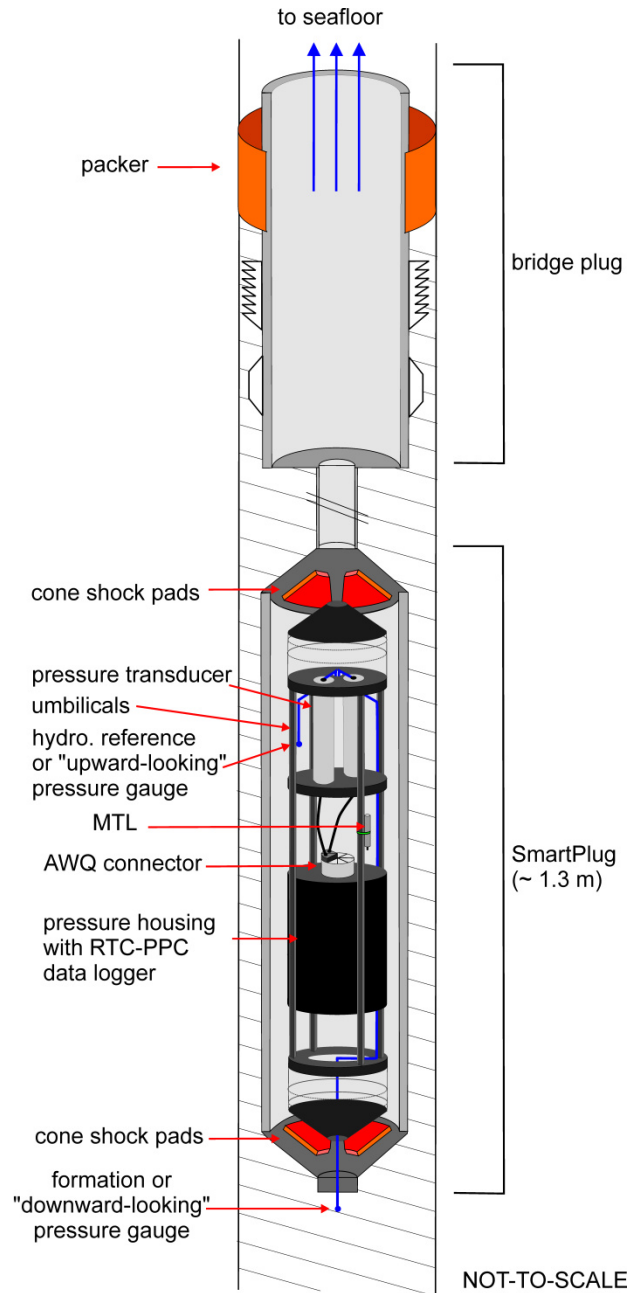
Figure 12: *Schematic drawing of the SmartPlug and the bridge plug (modified from Toczko et al. 2012). Seawater can enter both of them allowing the determination of hydrostatic reference fluid pressure and temperature. The packer as well as the bottom seal at the SmartPlug prevents the inflow of seawater into the borehole itself (see also Fig. 24). Thus, it is possible to measure formation pressure and temperature with the lowermost pressure gauge, which is influenced by fluids from the Megasplay fault and the formation entering via the casing screens.*

The shell interior houses two Digiquartz pressure transducers (Paroscientific Inc.), two Precision Period Counters (Bennest Enterprises Ltd.) providing 0.7 Pa resolution pressure measurements, a data logger recording at a 1 min interval, and four temperature sensors (one as an integral part of each pressure transducer, one stand-alone miniature temperature logger (MTL) and one platinum thermometer in the data logger, Figure 12). The temperature sensors also have a sampling interval of 1 min, except for the MTL, which collects data every 30 min. Temperature measurement precision is roughly 0.5 mK, and accuracy is a few tenths of 1°C.

5.1 Fluid Pressure and Temperature Transients Detected at the Megasplay Fault
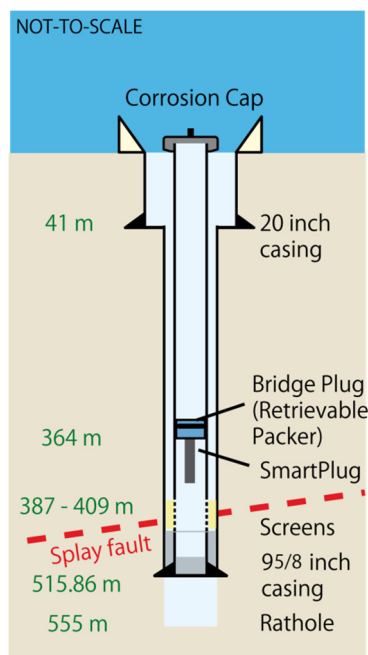
Figure 13: Schematic drawing of the deployment configuration at Site C0010. The borehole sensor of the SmartPlug is in contact with the formation and the splay fault via casing screens and hydraulically separated from the overlying water column via a Baker Hughes bridge plug (modified from Kopf et al. 2011a)

[8] The pressure and temperature sensors are located at the upper end of the in-shell assembly, and the data logger and pressure period counter at the lower end (Figure 12; see Kopf et al. (2011b) for comprehensive technical details). In the isolated zone below the SmartPlug, formation pressure is monitored by the "downward-looking" pressure transducer via 1/16 inch hydraulic tubing that is passed through the solid bottom bulkhead of the instrument shell (Figures 12, 13). At Site C0010, the SmartPlug was set at ~364 mbsf to create an isolated interval below the plug that includes one of the shallow branches of the Megasplay fault at 410 mbsf (Figure 13), as was identified by comprehensive suite of logging-while-drilling (LWD) data combined with seismic reflection data (Saffer et al. 2010). A hydrostatic reference fluid pressure was intended to be measured by the "upward-looking" pressure transducer with its port in the instrument shell above the bottom bulkhead. Unfortunately, a corrosion cap used at the wellhead (Figure 13) unintentionally included o-ring seals, isolating the cased section above the SmartPlug from the ocean above; hence pressures measured by the hydrostatic reference sensor is a "casing pressure", not an open-ocean reference pressure, for most of the recording period. [9] After 15 months of continuous monitoring, the SmartPlug was recovered during IODP Expedition 332 (Kopf et al. 2011a). The downloaded time series were complete for each of the temperature and fluid pressure sensors from 23 August 2009 until 07 November 2009.

5.1 Fluid Pressure and Temperature Transients Detected at the Megasplay Fault
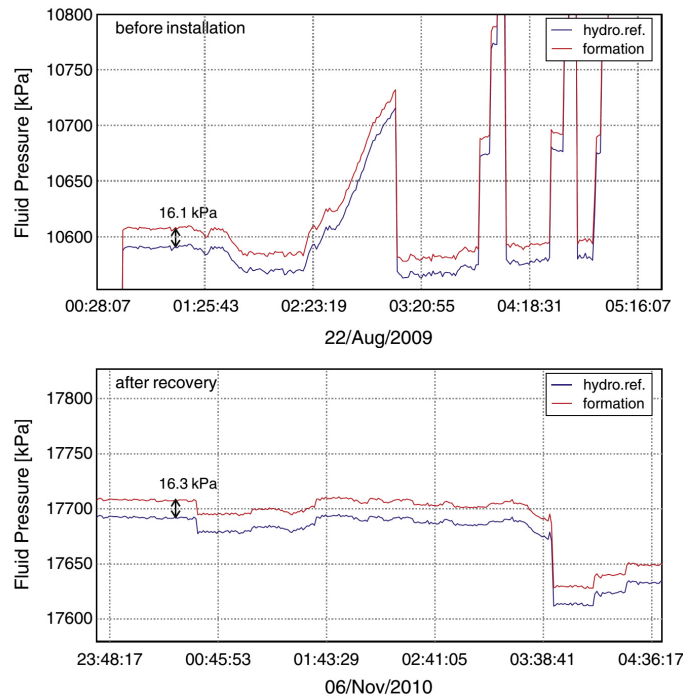
Figure 14: *Hydrostatic checks for the HR and formation pressure sensors. The tests were made in the water column during the deployment and recovery procedures, showing a drift of 0.2 kPa after the monitoring period.*
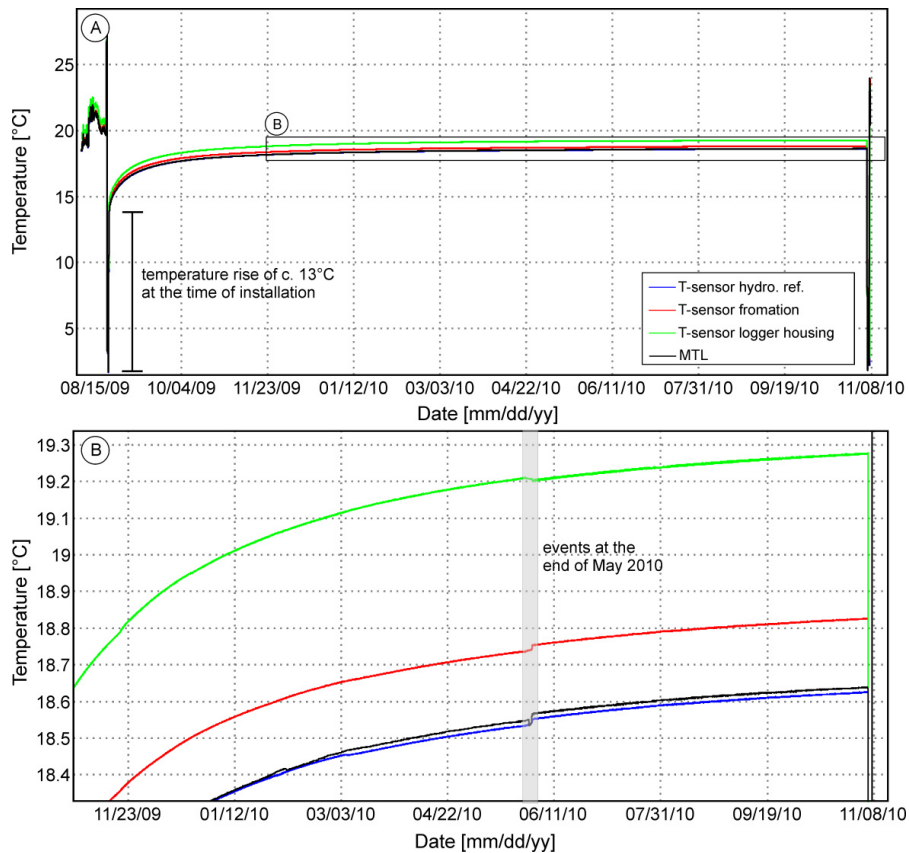
Figure 15: *(A) Overview of the temperature data obtained during the monitoring period. The latter was not sufficient to allow the temperature to reach in situ conditions. The data are free of any disturbance, except for the period shown in (B). The strong variations and high amplitudes at the beginning and at the end of the data are caused by deployment and recovery procedures, respectively. See text for further explanation.*

Data Processing

[9] Pressure readings made by the Paroscientific pressure sensors are influenced by temperature changes. In order to remove these effects, a method called "temperature compensation" is applied, i.e. different calibration coefficients provided by Paroscientific Inc. are used to compensate the influence of temperature variations.

[10] Beside changes in temperature, pressure data obtained in the marine environment are also easily affected by a great number of periodic and aperiodic signals (e.g. Wearn and Lrson 1982; McPhaden and Picaut 1990; Watts and Kontoyiannis 1990; Niiler et al. 1993; Fischer et al. 1997; Fujimoto et al. 1998, 2003; Pawlowicz et al. 2002; Becker et al. 2004; Chadwick et al. 2006; Ballu et al. 2009; Nooner and Chadwick 2009). In the SmartPlug pressure data, ocean tidal signals range up to 18 kPa in amplitude, and while the formation response to seafloor tidal loading is interesting, the tidal signals mask more subtle geodynamic signals of interest. Removal of the interfering signals was done using a slightly modified version of the MatLab routine *t_tide* from Pawlowicz et al. (2002), where a harmonic analysis is performed. One disadvantage of this method is that usually, non-harmonic and some harmonic signals remain in the data. For instance, amplitude and phase for each tidal constituent were assumed to stay constant, which might be a problem for tidal constituents with months-lasting periods (Foreman et al. 1995).
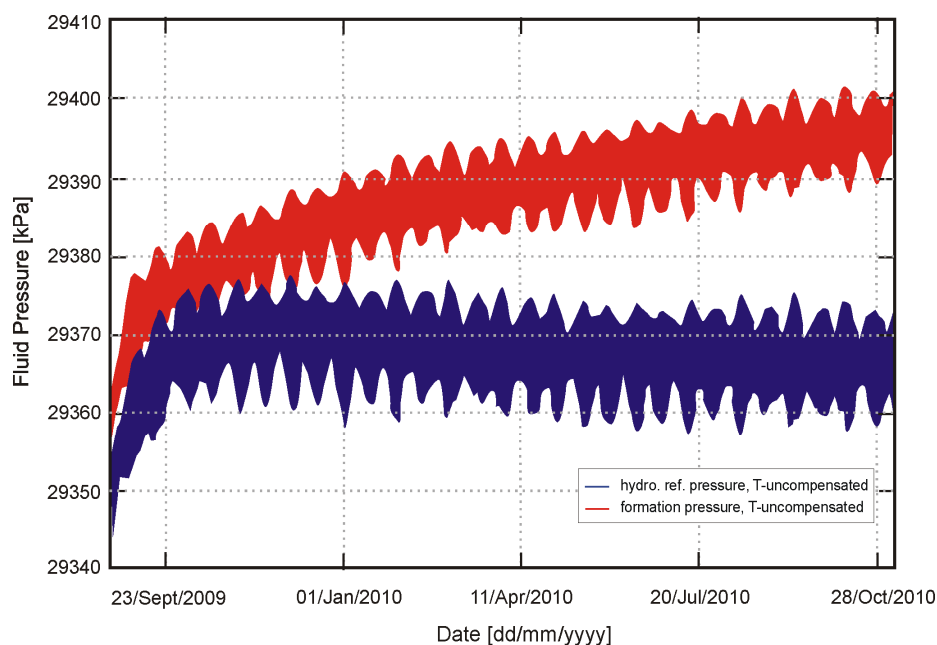
Figure 16: *Overview of the raw pressure data, i.e. without any T-compensation, de-tiding and filtering applied. The raw pressure data is heavily influenced by tidal signals.*

Therefore, the harmonic analysis was followed by filtering of the data to remove remaining harmonic and non-harmonic components (e.g. Foreman et al. 1995; Polster et al. 2009). A high-pass butterworth filter was applied, with a cut-off frequency depending on the signals to be investigated. For tsunami wave-induced anomalies, a cut-off frequency of 1.7×10^{-5} Hz was cho-

sen (corresponding to a period of 17 hours), whereas for seismic waves and storm-induced signals a frequency of 0.002 Hz (corresponding to a period of 8.35 min) was applied.

[11] Each pressure sensor has a temperature-sensitive quartz oscillator used to compensate for temperature sensitivity of the pressure-sensitive oscillator. After this correction, a small calibration-limited offset remains between the formation and reference sensors. This offset (formation sensor - hydrostatic reference sensor = ca. 16 kPa) was determined by examining data during deployment and recovery when the SmartPlug was hanging stable in the water column (e.g., Figure 14). Unfortunately, because of the effect of the corrosion cap, the hydrostatic reference was of limited utility.
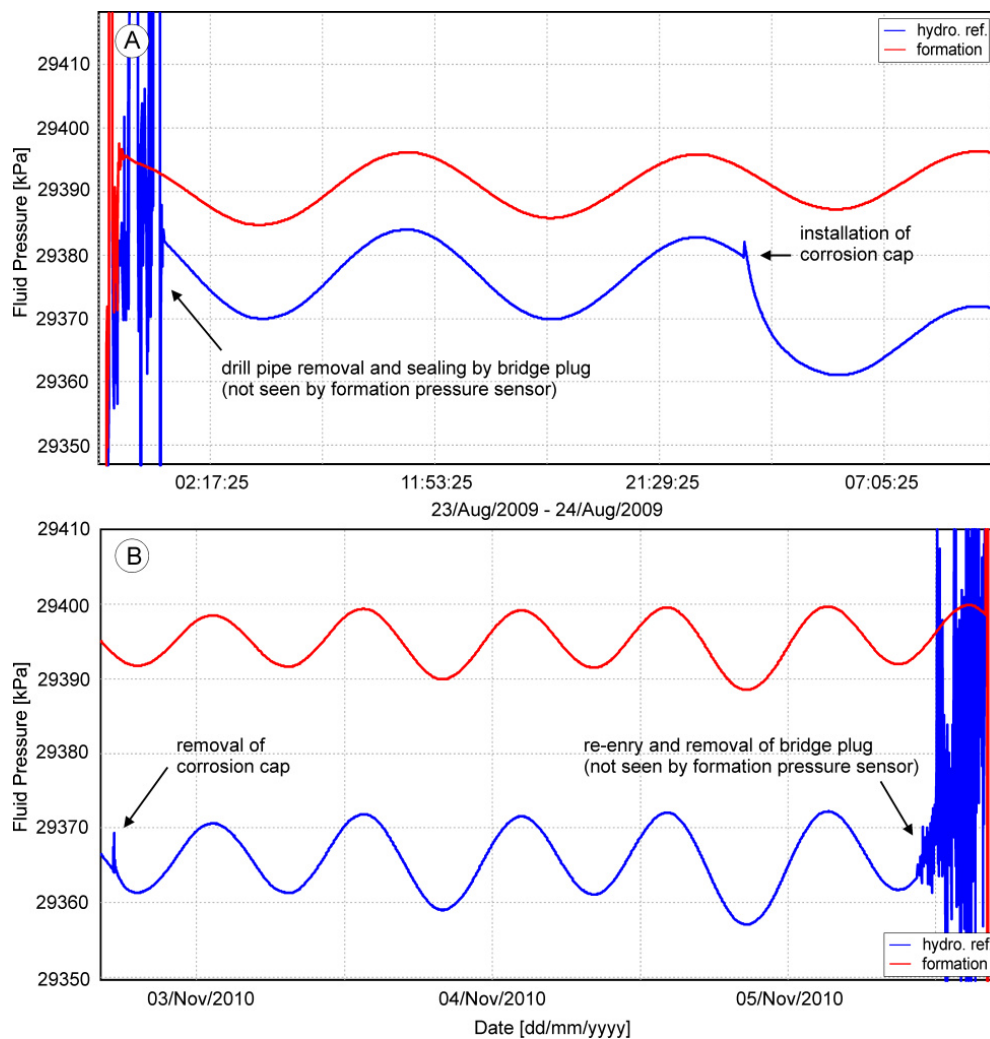
Figure 17: *(A) Initial monitoring period showing pressure transients caused by the deployment and installation of the SmartPlug as well as by the sealing of the borehole with the corrosion cap. In this figure, the pressure was not de-tided. Whereas the formation pressure is not affected, the hydrostatic reference pressure drops by almost 10 kPa. See text for explanations. (B) Period in where the corrosion cap was removed, followed by re-entering of the hole with the drill string and recovery of the SmartPlug and bridge plug. The formation pressure was not affected before the bridge plug was removed. See text for further explanations.*

[12] After the data were de-tided and filtered, detection of hydrological transients was possible, and these were compared to online earthquake catalogues of the International Seismological

Centre (ISC) and the USGS as well as to local Japanese earthquake catalogues (i.e. F-Net broadband and Hi-Net high-sensitivity seismograph networks, see Okada et al. (2004) and inlay in Fig. 10 for location of the F-Net stations from which waveforms were obtained). To validate the arrival times of seismic waves of events listed by the catalogues, theoretical travel time calculations by the USGS were used (http://neic.usgs.gov/neis/travel_times/ compute_tt.html.). This allowed a clear distinction of the type of seismic waves (i.e. surface waves, body waves) which caused the pressure transients. Hours- to days- lasting periods of pressure variations were attributed to meteorological events and tsunami waves as was indicated by data from the Japan Meteorological Agency (JMA, www.jma.go.jp) and the U.S. National Geophysical Data Centre (NGDC, see http://www.ngdc.noaa.gov/hazard/recenttsunamis.shtml). In addition to that, the P-T-evolution was compared with the aforementioned seismological and meteorological data to be able to detect earthquake related strain anomalies.

RESULTS AND DISCUSSION

Temperature data

[13] Raw temperature data are shown for the 15 month recording period in Fig. 15. Temperatures measured by the various sensors track one another within a few tenths of °C. The sensors are essentially collocated; offsets are probably caused by inaccuracies in calibration. Temperature rises smoothly from roughly 13 °C at the time of installation and approaches 19 °C at the time of recovery.
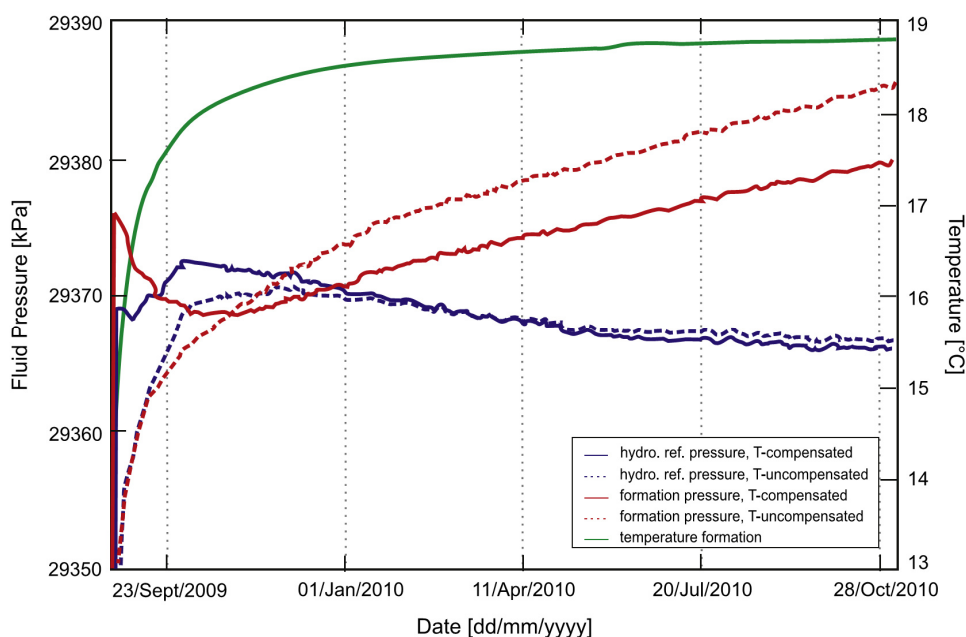
Figure 18: Composite plot of the whole monitoring period showing the temperature (red), as well as the temperature-compensated (solid) and –uncompensated (dashed), de-tided hydrostatic reference (blue) and formation (brown) data. On the x-axis, the datum point is defined as 01 January 2010. The first two months of the compensated data might not show the true pressure development. See text for further explanations.

[14] The initial temperature at the time of installation reflects the perturbation caused by circulation of cold water during drilling. The natural formation temperature had not been achieved at the end of the deployment phase of 15 months. Assuming a 1/t recovery behaviour which is appropriate for times well after the thermal time constant of the borehole itself (Villinger and Davis 1987), extrapolation of the MTL record yields an natural formation temperature of roughly 19 °C (Figure 15A), which is consistent with the local geothermal gradient of c. 52 °C /km (Tobin et al. 2009).

[15] A few small (~ 0.01 °C) steps in temperature are present during the monitoring phase, most notably at the end of May, 2010, when MTL and pressure sensor temperatures rose and the logger platinum sensor temperature fell (Figure 15B, grey-shaded stripe). The cause of these changes is unknown, but may be related to changes in thermal coupling caused by shifts in debris within the SmartPlug or around the exterior of the casing. No associated changes in either formation or reference pressures are observed.

Pressure Data

Seal integrity

[16] Shown in Fig. 16 are raw, T-uncompensated pressure data, with no corrections or filtering applied. During the monitoring period, signals are dominated by tides which range up to 18 kPa in peak-to-peak amplitude, and long-term trends, the origins of which are explored below. At times of deployment and recovery (Figure 17), large, relatively high frequency variations are caused by accelerations of the SmartPlug and hydrodynamic effects. With the bridge plug set, formation tidal variations are smooth and attenuated relative to the reference signal, and differential pressures are maintained over the full history of the deployment; these characteristics lend confidence to the quality achieved by the seal, as does the absence of any signal in the formation record associated with drill string withdrawal and re-entry during installation and recovery operations while the SmartPlug was set (Figure 17).

[17] An unanticipated result is that effects are seen in the reference signal associated with both installation and removal of the corrosion cap. A c. -8 kPa offset in pressure occurred at the time of installation (with no contemporary change of the formation signal), and changes in the tidal signal amplitude were seen at both deployment and recovery times (Figure 17). With the corrosion cap on, the amplitude ratio was constant at 0.80, whereas prior to corrosion cap installation and after removal, the formation-to-reference ratio was 0.73. Tidal signals are in phase at all times, suggesting that there were no leaks in either the bridge plug or the corrosion cap. Thus it is reasonable to conclude that the amplitude ratio for the brief periods with no corrosion cap provides a reliable estimate of the 1-D loading efficiency for the formation at the level of the perforated and screened casing. The unwanted seal at the corrosion cap is unfortunate in that a

reliable seafloor loading reference (e.g., for analysing the formation response to tidal and non-tidal ocean loading) is not available for the bulk of the recording period. The volume inside the casing that is confined by the corrosion cap and SmartPlug does, however, constitute a volumetric strain gauge, albeit with an relatively high effective loading efficiency of 0.91 and low implied strain-to-pressure conversion efficiency (e.g., see Figure 6 in Davis et al. 2009).
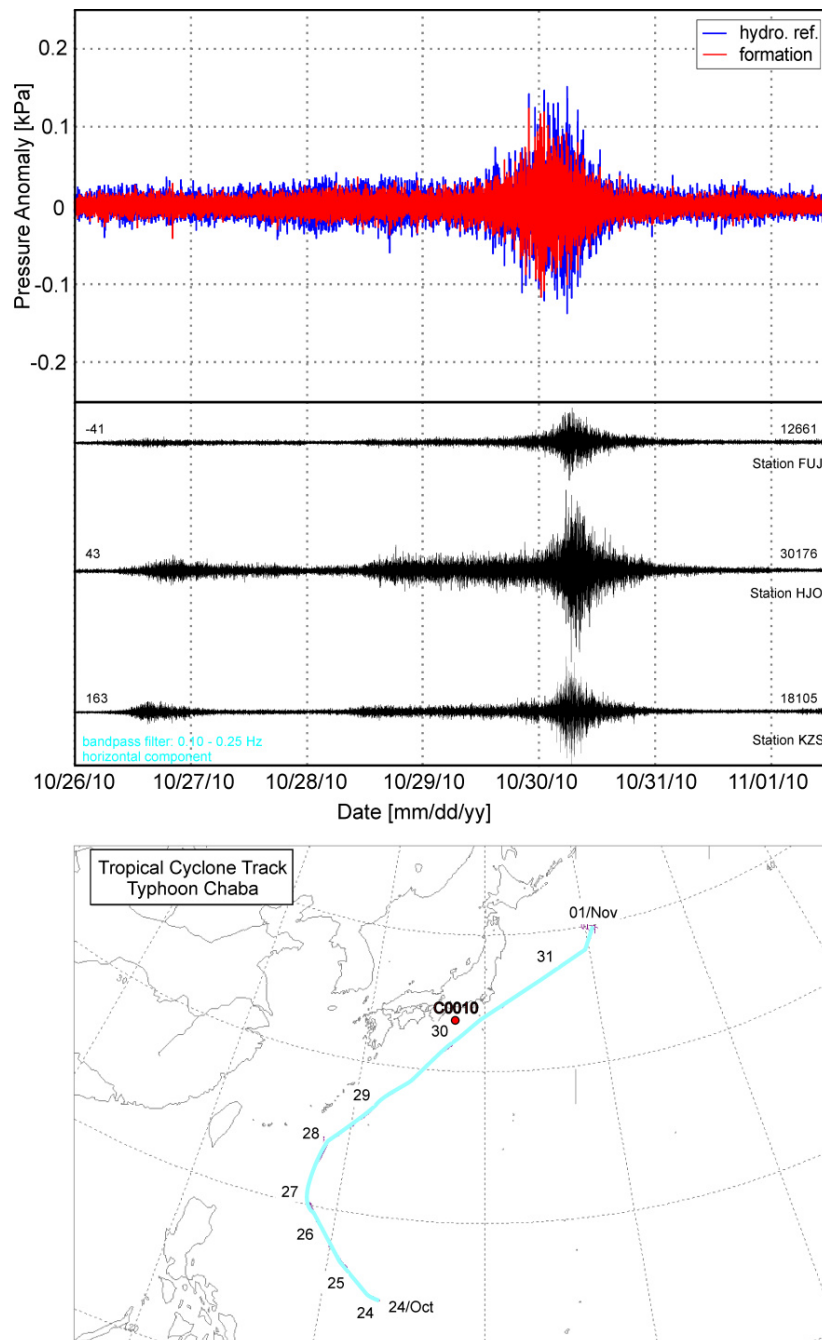
Figure 19: Onset of microseism in the de-tided and highpass filtered pressure data caused by the approach of typhoon Chaba. From the F-net waveform data, only frequencies between 0.10 and 0.25 Hz are shown, i.e. the range of microseismic frequency. A steady increase in amplitude is observable in both datasets, which reached its maximum when the typhoon arrived at the south-eastern Japanese coast. The map (lower panel) is modified from http://www.jma.go.jp. For location of the onshore F-Net stations, please see Fig. 10.

Long-term variations

[18] Long-term variations, i.e. months-lasting variations, in formation and casing pressures are made clear when tidal frequency variations have been removed. Results with two levels of processing are presented here, with and without compensation for temperature variation using sensor manufacturer's calibration coefficients (Figure 18). There is a fundamental difference between the compensated and uncompensated values during the first 1-2 months of recording, when temperature rose by more than 5 °C. During that period, compensated formation pressure values decrease by c. 10 kPa, whereas uncompensated values
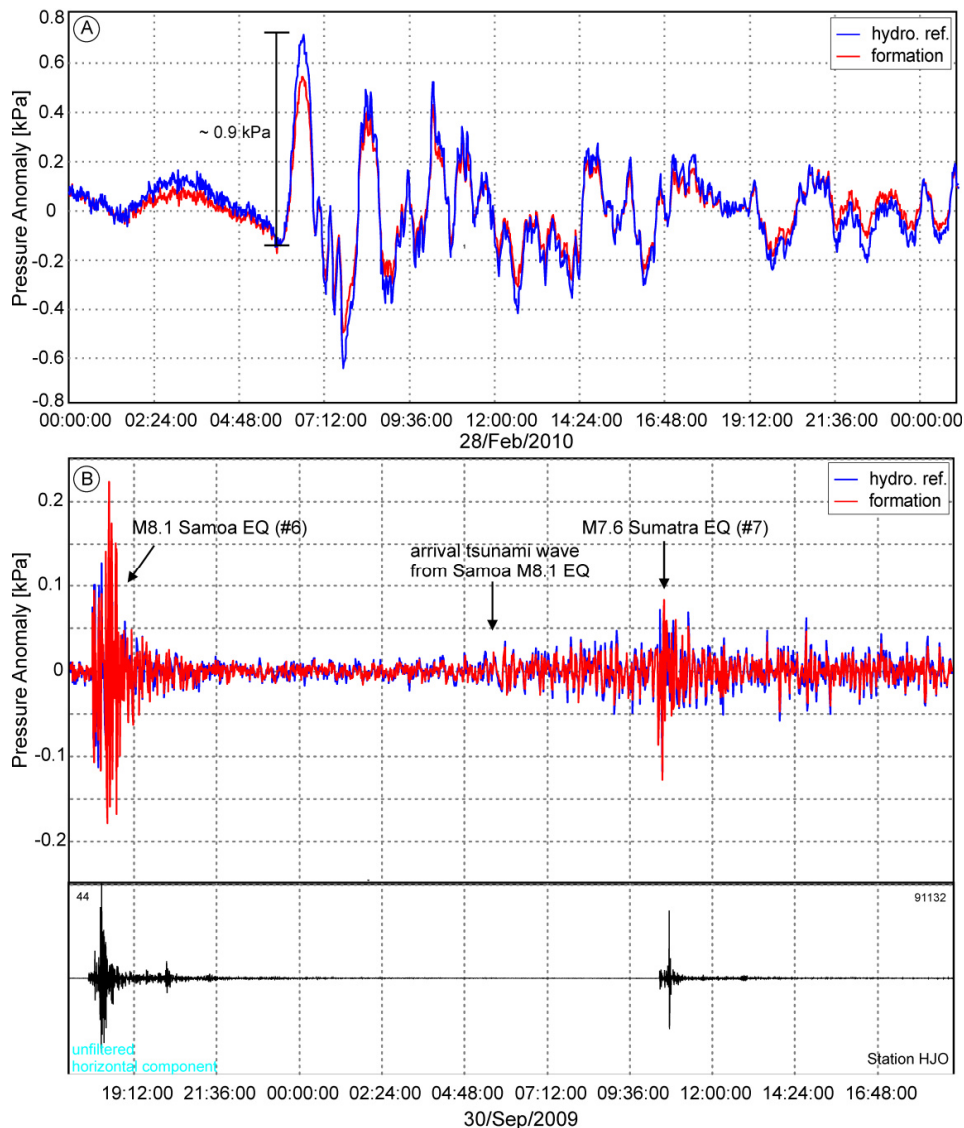
Figure 20: **(A)** Arrival of the tsunami wave caused by the Maule M8.8 Earthquake in Chile, which is visible as tremor-like signal in the pressure data. Nearly 24 h after the earthquake occurred, the tsunami waves arrived at Site C0010. **(B)** Pressure oscillations caused by an M8.1 EQ close to the Samoa Islands region and an M7.6 EQ close to Sumatra with corresponding waveform data from F-Net station HJO. The Samoa M8.1 EQ triggered a tsunami which arrived at Site C0010 almost 12 h later. The tsunami waves do not occur in the F-net data because station HJO is based onshore. The identification numbers refer to the ones listed in Table 5 and displayed in Fig. 22.

increase by roughly the same amount. In the case of the casing sensor, the difference in the early compensated and uncompensated records is about half this amount. In both cases, it may be that the compensation is simply not correct at this level of precision (10 kPa being only 0.01% of the full sensor range); hence the details of the early parts of the records should not be trusted. In contrast, sensitivity of pressure to sensor temperature change is seen to be insignificant over the remainder of the record, i.e., when temperature was changing slowly and by less than 1 °C. During this time, long-term pressure trends can be accepted with confidence.
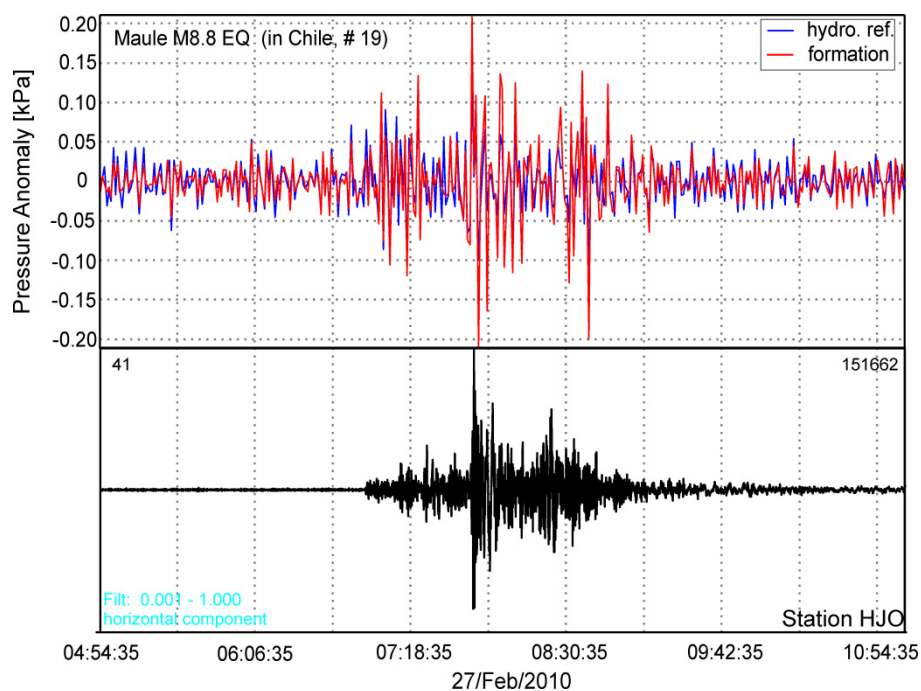
Figure 21: *Pressure transients caused by the Maule M8.8 earthquake compared with the F-Net waveform data from station HJO. The "#19" refers to the identification number in Table 5 and Fig. 22. The waveform data was band-pass filtered between 0.001 and 1 Hz to highlight the arrival of low-frequent seismic waves, in particular surface waves.*

[19] The gradual rise (continuous from the time of installation if the true pressure is close to the uncompensated values) is most likely associated with recovery of the formation after the release of natural super-hydrostatic pressure at the time of drilling. The rate of increase declined through the record, but only by about a factor of two from the beginning of 2010 to the end of the record, when pressure was continuing to rise at c. 2 kPa/month. This far exceeds typical rates of sensor drift (i.e. up to 2 kP/a, see Polster et al. 2009; Gennerich and Villinger 2011; Davis et al. 2012), so it can be concluded that the natural formation state is superhydrostatic by an amount more than that observed at the end of the monitoring period (c. +15 kPa), but currently not by more than a few tens of kPa. Extrapolation of the record to equilibrium conditions and estimation of the formation hydraulic diffusivity may be possible under certain assumptions, but would be difficult given the uncertainties of the early part of the record and are beyond the scope of this paper. Uncertainties notwithstanding, the likely overpressure is clearly a small

fraction of the lithostatic potential at the depth of the casing screens, given the cumulative mass of the overburden (hydrostatic effective stress of c. 3.0 MPa). The long-time constant of the recovery (> 1 year) suggests a relatively low permeability for the section intersected by the casing screen (c. 22m), which is consistent with determinations of the hydraulic diffusivity based on the tidal signal in the SmartPlug pressure data which are in the range of $10^{-8}\,m^2s^{-1}$ (i.e. an intrinsic permeability of $10^{-19}\,m^2s^{-1}$, see Hammerschmidt et al. (2013) for further information).
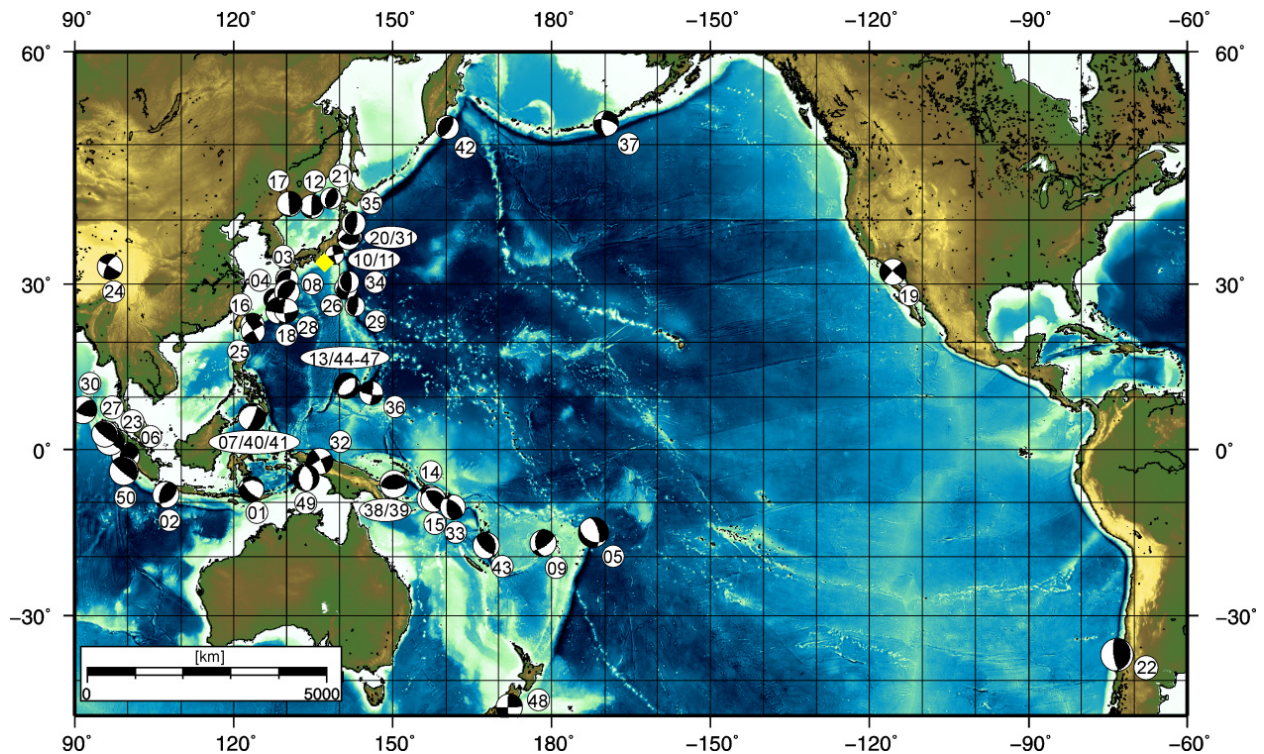
Figure 22: *Overview of earthquakes during the monitoring period, which can be correlated to the pulse-like pressure transients. Fluid pressure transients are independent of the focal mechanism and only events with magnitude > 4.8 were detected. The yellow diamond indicates the position of the SmartPlug, the identification numbers are given according to Table 5.*

[20] Both temperature-compensated and -uncompensated casing pressure records show an initial pressure increase followed by a slow decrease (Figures 16, 18). Uncompensated hydrostatic reference pressure averaged 29356 kPa prior to installation, dropped to 29348 kPa after, rose to a peak of 29370 kPa roughly two months later, then declined to 29367 kPa at the time of removal of the corrosion cap (when the tidal signal increased to the full open ocean amplitude but there was virtually no change in average pressure). While the cause of the initial pressure drop at the time of corrosion cap installation is unknown, the remainder of the history is consistent with thermal expansion of the water trapped inside the warming cased borehole, combined with slow leakage, either via the corrosion cap or through casing joints, back to an average state very close to hydrostatic.

5.1 Fluid Pressure and Temperature Transients Detected at the Megasplay Fault

Short-term variations

[21] Signals anticipated to be superimposed on long-term and tidal pressure variations (signals with periods ranging from seconds to weeks) are those associated with storms, tsunamis, seismic waves, volumetric strain, and hydrologic transients. Examples of all but the last two are present in the data and discussed in this section.

[22] *Storms* – Energy from ocean waves reaches the deep seafloor over a broad frequency range, with dominant sources being infragravity waves at one- to several-minute period, and ocean swell at periods of 5-10 s, double the frequency of the swell source. Storm-related microseisms are a well-known phenomenon which is caused by the non-linear interaction of opposite propagating oceanic waves of the same wavelength (e.g. Longuet-Higgins 1950; Hasselmann 1963; Tabulevich 1992; Webb 1998, 2007).
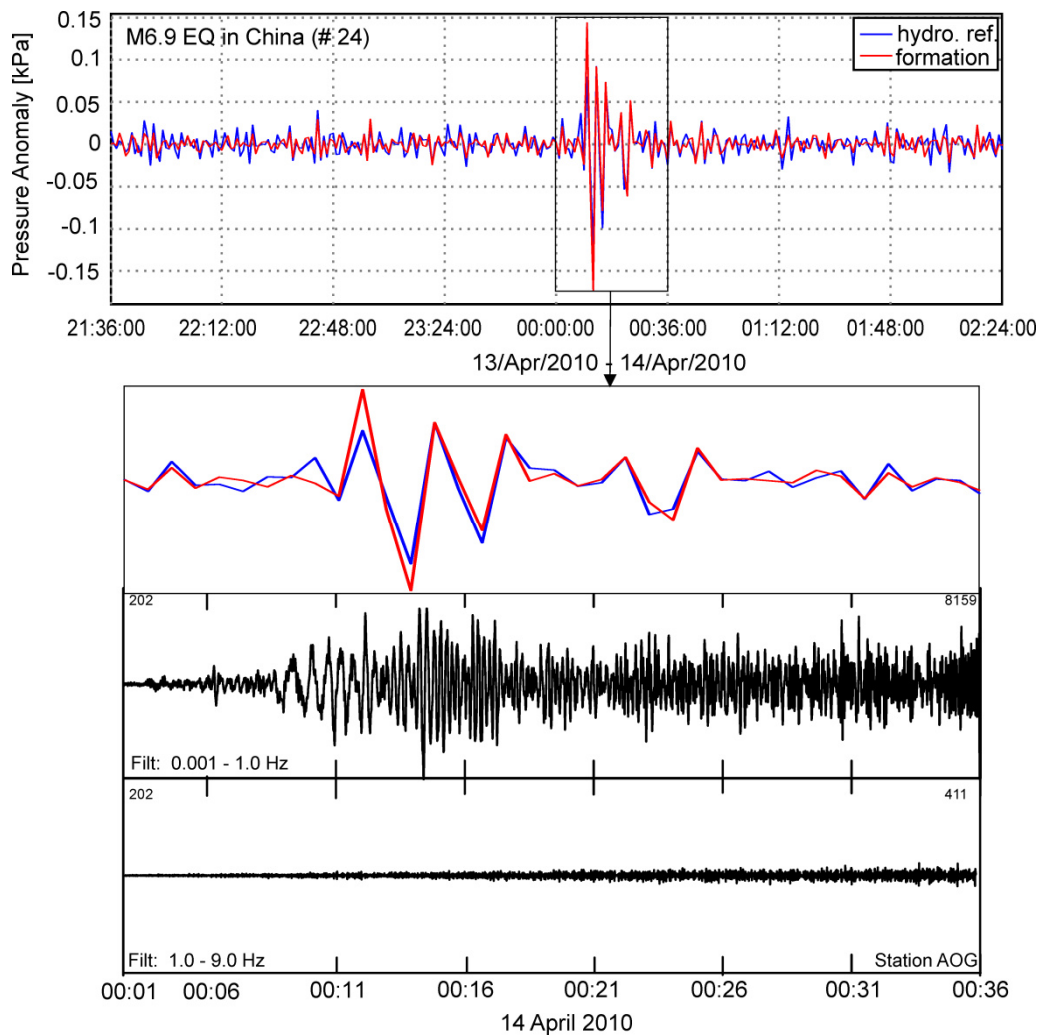
Figure 23: *Fluid pressure anomalies caused by the YushuM6.9 EQ, with the arrival of the surface waves indicated by the high formation pressure amplitudes relative to the HR pressure amplitudes (see inlay). The "#24" refers to the identification number in Table 5 and Fig. 22. The inlay is compared with corresponding bandpass filtered waveform data from F-Net station AOG. The numbers at the beginning and the end of each seismogram indicate the lowest and highest count of an amplitude within this time section, respectively. The absence of high-frequent energy is obvious when comparing the filtered waveform datasets.*

In seismic noise spectra, there is a significant peak at 0.1-0.25 Hz, which is termed the double frequency (microseism) peak or secondary peak. Another peak, although much smaller but still distinct, is the primary or single-frequency peak which occurs between 0.05 and 0.12 Hz. Although both peaks are related to storms, they have different origins. The primary peak is produced by teleseismic microseisms, i.e. seismic waves which travel up to thousands of km from distant coastal sources, whereas the secondary microseism peak is generated locally in deep water by local swell (Babcock et al. 1995; Webb 1998; Gerstoft et al. 2008). Bromirski et al. (2005) further divided the secondary peak into a long-period double frequency (LPDF) and a short-period double frequency (SPDF) microseism. The former is usually generated near the coast by interaction of storm-driven ocean waves with reflected or scattered waves at the shoreline, whereas the SPDF originates from a local source at the open ocean. Both lead to the excitation of Rayleigh wave modes (Webb 1998; Bromirski et al. 2005), but local storms produce the largest signals in seafloor and formation pressure records.

[23] The 1 minute sampling period of the SmartPlug precludes resolution of microseismic energy, but infragravity waves are resolved. This is well illustrated by the example shown in Fig. 19, where a signal generated by typhoon Chaba is seen in both the formation and casing. That this signal is storm-generated is consistent with the F-Net waveform data which show a simultaneous increase in the frequency range 0.1 – 0.25 Hz when the storm is approaching the area (Figure 19). Amplitudes of variations rose above background levels by more than a factor of five as the storm passed near the observatory site. Like tides, infragravity waves have a sufficiently long wavelength (few tens of km) to impose a spatially uniform load on the seafloor, so the physics of the loading response in both the formation and casing is the same over this frequency (wavelength) range. Signals at this frequency are generally larger in the cased section than in the formation, and the amplitude ratio is close to that seen at tidal frequencies. If LPDF or SPDF microseism is responsible for the observed anomalies, one would expect an amplified formation pressure signal compared to the HR pressure signal, similar to that observed for approaching Rayleigh waves from teleseismic and regional earthquakes. However, this is not the case here. In fact, based on the findings of several authors (e.g. Gerstoft et al. 2008; Landès et al. 2010; Zhang et al. 2010), the wavefield of secondary microseism is also influenced by P-waves, especially the SPDF. Tanimoto et al. (2006) showed that above 0.2 Hz the dominance of Rayleigh wave modes apparently decreases, probably due to an increasing contribution of P-wave phases.

[24] In summary, the correspondence of storms with the microseisms in the data excludes a high amount of teleseismic energy, i.e. single frequency microseisms. The great water depth and the great distance to the adjacent shoreline, and the apparent absence of Rayleigh waves,

5.1 Fluid Pressure and Temperature Transients Detected at the Megasplay Fault

Table 3: Overview of the 40 days-lasting transients that are either caused by low-pressure weather systems or typhoons. Most of the transients are not relatable to any event and are marked by "N/A". See text for further explanations.

Date Start [dd.mm.yyyy]	Date End [dd.mm.yyyy]	Correlation possible with
30.08.2009	31.08.2009	Severe Tropical Storm Krovanh
07.09.2009	08.09.2009	Severe Tropical Storm Dujuan
13.09.2009	13.09.2009	local low-pressure system [QuickScat]
16.09.2009	22.09.2009	Typhoon Choi-wan
05.10.2009	09.10.2009	Typhoon Melor
19.10.2009	27.10.2009	Typhoon Lupit
01.11.2009	04.11.2009	local low; probably influenced by tropical depression, east of Manila, Phillipines
07.11.2009	09.11.2009	N/A, perhaps related to tropical depression 810 km SE of Pohnpei
10.11.2009	14.11.2009	N/A, perhaps related to tropical depression 810 km SE of Pohnpei
17.11.2009	17.11.2009	N/A
11.12.2009	11.12.2009	N/A
04.01.2010	06.01.2010	N/A
20.01.2010	24.01.2010	N/A, perhaps related to tropical depression 320 km NW of Bandar Seri Begawan, Brunei
27.01.2010	29.01.2010	N/A
30.01.2010	03.02.2010	N/A
11.02.2010	12.02.2010	N/A
15.02.2010	16.02.2010	N/A
26.02.2010	26.02.2010	N/A
27.02.2010	27.02.2010	N/A
01.03.2010	10.03.2010	N/A
15.03.2010	17.03.2010	N/A
20.03.2010	22.03.2010	N/A
24.03.2010	26.03.2010	N/A, probably related to Tropical Storm Omais
01.04.2010	02.04.2010	N/A
12.04.2010	13.04.2010	N/A
20.04.2010	21.04.2010	N/A
22.04.2010	22.04.2010	N/A
27.04.2010	28.04.2010	N/A
23.05.2010	24.05.2010	N/A
08.06.2010	10.06.2010	N/A
13.06.2010	14.06.2010	N/A
17.06.2010	19.06.2010	N/A
28.07.2010	30.07.2010	N/A
08.08.2010	12.08.2010	N/A, perhaps to related Severe Tropical Storm Dianmu
13.08.2010	14.08.2010	N/A, perhaps to related Severe Tropical Storm Dianmu
04.09.2010	07.09.2010	Severe Tropical Storm Malou
18.09.2010	19.09.2010	Typhoon Fanapi
24.09.2010	26.09.2010	Typhoon Malakas
07.10.2010	10.10.2010	N/A, probably related to Tropical Depression in the South China Sea
17.10.2010	04.11.2010	Typhoon Chaba

exclude LPDF microseisms to account mainly for the observed oscillations. Therefore, these and other similar oscillations are assumed to be caused by storm-induced SPDF microseism, which is dominated by P-waves. Higher frequency data (e.g., 1 Hz) will be available once observatory sites are cable-connected, and this will remove uncertainties in this conclusion. [26] Although some of the days-lasting periods of high-frequency energy can clearly be attributed to the occurrence of low-pressure weather systems and typhoons approaching the study area, most anomalies show no strong correspondence to any meteorological event (Table 3). Another triggering mechanism for these pressure transients could be tectonically induced tremor, which is usually correlated in time and space with slow slip events (Beroza and Ide 2011). On seismograms, tremor occurs with no abrupt onset, has frequencies in the range of 1-8 Hz and seismic waves are usually hard to identify (Beroza and Ide 2011). A potential source could be the Megasplay fault itself, but also the seismogenic zone beneath the Kumano forearc basin as well as other convergent and strike-slip boundaries in up to 300 km distance (Beroza and Ide 2011). However, when investigating the F-Net waveform data, the periods when tremor-like signals are observable in the pressure data are usually depleted in frequencies over 1 Hz but show increasing energy in the range of 0.1 – 0.25 Hz. Furthermore, no VLFE (i.e. very-low frequency earthquake, see e.g. review by Beroza and Ide 2011) activity is observed beneath the outer accretionary prism over this period. Therefore, slow-slip events can be excluded as a potential source.

Table 4: *During the monitoring period, only two of the days-lasting anomalies in the pressure data could be correlated with the arrival of tsunami waves.*

Date Start [dd.mm.yyyy]	Date End [dd.mm.yyyy]	Correlation possible with
30.09.2009	30.09.2009	tsunami wave released by Samoa M8.1 EQ on 29.09.2009
28.02.2010	28.02.2010	tsunami wave released by Maule M8.8 EQ on 27.02.2009

[25] Another explanation for the apparent absence of corresponding storms can be explained by the results of Gerstoft et al. (2008) and Landès et al. (2010). Storms occurring above deep water can produce high energetic body waves, in particular P, PP and PKP phases (i.e. a P-wave phase traveling through the mantle, a P-wave phase in the mantle which gets reflected from the surface, and a P-wave phase which passes the mantle – outer core – mantle boundaries, respectively) which can then be detected at distant seismological observatories. However, the energy of p-wave phases excited by distant storms is probably not high enough to be detected by the pressure sensors. Indeed, swell of distant storms reaching Site C0010 might be responsible for the observed pressure oscillations.

[26] *Tsunamis* – While infrequent, tsunamis constitute another source of seafloor loading signal (Table 4). During the SmartPlug monitoring epoch, two tsunamigenic earthquakes occurred, one M8.1 normal-slip event in the Samoa Islands Region and the Maule M8.8 subduction earthquake offshore Chile (Figure 20A, #6 and #19, respectively, in Table 5 and Fig. 22). The tsunami generated by the latter event produced signals in the formation and casing of up to 0.9 kPa peak-to-peak amplitude at an initial period of 50 min, which corresponds to a strain of 1.9×10^{-7} (assuming a strain sensitivity of 4.8 kPa/μstrain, see Hammerschmidt et al. 2013). The amplitude ratio was virtually identical to that determined by tidal loading, consistent again with the long tsunami wavelength (o. 100 km). Given the information discussed in Section "Seal Integrity" (see paragraph 16), the inferred maximum peak-to-peak amplitude of the ocean pressure variation was 1 kPa, reflecting a wave amplitude of 10 cm (Table 5). The inferred amplitude of the Samoa tsunami is smaller, roughly 1 cm, and the initial period is only 8 min, although a proper characterization of this tsunami is difficult due to the interference of oscillations caused by the arrival of seismic waves radiated from a Sumatra M7.6 earthquake, which occurred one day later on 30 September 2009 (Figure 20B, #7 in Table 5 and Figure 22). Before the Sumatra M7.6 event appears in the data, once again, the amplitude of the signal is smaller in the formation than in the casing, although interference from other oceanographic signals, probably infragravity waves, precludes an accurate determination of the amplitude ratio.

[27] *Seismic waves* – The aforementioned Chile earthquake generated large seismic surface waves, and these, primarily the Rayleigh waves, are also resolved in the SmartPlug records (Figure 21). In general, the arrival of seismic waves causes volume changes in the rock, leading to hydroseismograms similar to common seismograms (e.g. Eaton and Takasaki 1959; Rexin et al. 1962; Woodcock and Roeloffs 1996; Kano and Yanagidani 2006). In fact, all phases that impose volumetric change, i.e. P-phases, Love and Rayleigh Waves as well as S-phases consisting of SV- and converted P-phases, may also cause pressure fluctuations (Kano and Yanagidani 2006; Kitagawa et al. 2006; Wang et al. 2009; Geballe et al. 2011).

[28] During the monitoring period, a total of 50 similar hydroseismograms can be confidently assigned to earthquakes, based on travel-time calculations provided by the USGS (Figure 22, Table 5). Assuming a strain sensitivity of 4.8 kPa/μstrain for the formation surrounding the SmartPlug (Hammerschmidt et al. 2013), the seismic waves caused strain in the range of $10^{-7} - 10^{-9}$ (Table 5, Figure 22). All hydroseismograms are highly aliased, due to the low sampling frequency of the SmartPlug. No local events were detected, which might be due to local heterogeneities, the low sampling frequency as well as the duration and magnitude of local earthquakes which occurred during the monitoring period.
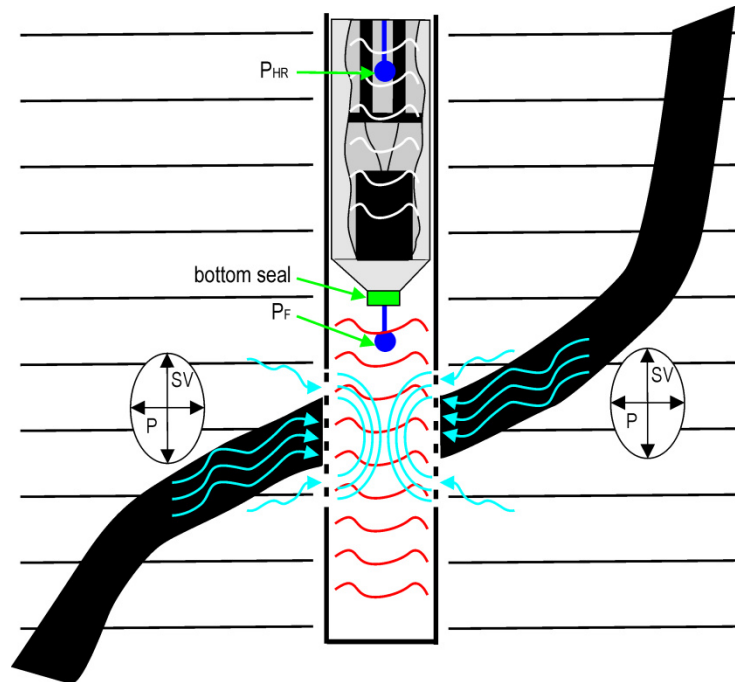
Figure 24: *Schematic drawing for the pressure pulses at the borehole pressure sensor induced by Rayleigh waves. The areas with white and red lines indicate hydrostatic and borehole pressure, respectively. The HR pressure sensor (PHR) is only affected by the incoming Rayleigh waves. By contrast, the formation pressure sensor (PF) experiences stronger oscillations due to the additional fluid flow from the Megasplay fault through the casing screens (blue arrows) into the borehole.*

[29] The focal mechanism of the different earthquakes seemed to be of no importance for the pressure anomalies, both dip-slip and strike-slip mechanisms were observed. For instance, the Yushu M6.9 strike-slip earthquake in China (Figure 23, #24 in Table 5 and Fig. 22), which occurred on 14 April 2010, caused strain of up to 3.6×10^{-8}, leading to a significant amplification of the formation compared to the HR pressure signal. In all instances, except for deep earthquakes (see below), the formation-to-casing amplitude ratio is greater than 1. In general, shear waves have no effect on water, which should lead to similar amplitudes, since both sensors are located inside a water column. However, the Rayleigh waves lead to volumetric strain at the Megasplay fault and the surrounding formation, which subsequently contracted and dewatered, influencing the formation pressure sensor solely (Figure 24). Although other phases, in particular Love waves and body waves, might contribute to this process, a clear distinction is hardly possible because of pressure waves and other phases generally having frequencies too high and/or amplitudes too small to be resolved in the 1-min-interval pressure data.

[30] For earthquakes at depths greater 200 km, the most pronounced oscillations are amplified in the casing relative to the formation (Figure 25). This is not surprising due to a deep-sourced by body wave phases (Kennett 2002, and references therein). Additionally, deep sourced surface waves have lower amplitudes and occur widespread in time (Frohlich 1989), aiding to the dominance of the body waves in seismograms and hydroseismograms. As shown in Fig. 25, on 23 July 2010, a series of earthquakes occurred near Mindanao, Philippine Islands, of which a

5.1 Fluid Pressure and Temperature Transients Detected at the Megasplay Fault

Table 5: *Overview of the earthquakes (EQ) which occurred during the monitoring period and which were correlated to pressure transients in the SmartPlug data. See also Fig. 23 for identification number, location and focal mechanism. The strain induced by the arrival of seismic waves was calculated assuming a strain sensitivity of 4.8 kPa/μstrain (Hammerschmidt et al. 2013).*

Running Nr.	Date Start [dd.mm.yyyy]	Lat. [°]	Lon. [°]	Orig. Time [hh:mm:ss]	Start in Pressure Data [hh:mm:ss]	Theoretical Arrival Time based on USGS [hh:mm:ss]	Max. Peak-to-Peak Pressure Transient [kPa]	Inferred Max. Strain	Depth [km]	Magn.	Location	focal mechanism
1	28.08.2009	-7.0876	123.2562	01:51:20	02:01:00	01:58:22	0.14	2.92E-08	642	6.9	Banda Sea	oblique-slip (normal)
2	02.09.2009	-7.4692	107.1782	07:55:01	08:02:34	08:03:49	0.44	9.17E-08	46	7.0	Java, Indonesia	oblique-slip (thrust)
3	03.09.2009	31.14	130.01	13:26:17	13:27:14	13:27:53	0.38	7.92E-08	163	6.2	Kyushu, Japan	oblique-slip (thrust)
4	28.09.2009	27.5212	127.5418	19:22:56	19:24:53	19:25:17	0.09	1.88E-08	9	5.8	Ryuku Islands, Japan	dip-slip (thrust)
5	29.09.2009	-15.2934	-172.057	17:48:11	17:59:19	17:59:17	0.42	8.75E-08	18	8.1	Samoa Islands Region	oblique-slip (normal)
6	30.09.2009	-0.432	99.5202	10:16:09	10:23:57	10:24:48	0.22	4.58E-08	81	7.6	Sumatra, Indonesia	oblique-slip (thrust)
7	04.10.2009	6.444	123.2268	10:58:00	11:07:19	11:03:25	0.06	1.25E-08	620	6.6	Mindanao, Philippine Islands	oblique-slip (normal)
8	30.10.2009	28.97	130.22	07:03:38	07:06:00	07:05:37	0.49	1.02E-07	34	6.8	near Amami-Oshima Island	dip-slip (thrust)
9	09.11.2009	-17.1416	178.201	10:44:55	10:53:07	10:54:28	0.10	2.08E-08	595	7.3	Fiji Islands	dip-slip (thrust)
10	17.12.2009	34.934	139.179	14:45:24	14:49:00	14:45:49	0.06	1.25E-08	13.6	4.8	east off Izu Peninsula	Strike-slip
11	17.12.2009	34.921	139.261	23:45:36	23:42:20	23:46:02	0.10	2.08E-08	6.9	5.0	east off Izu Peninsula	Strike-slip
12	24.12.2009	41.5694	135.2834	00:23:31	00:25:19	00:25:18	0.21	4.38E-08	38	6.1	Sea of Japan	oblique-slip (thrust)
13	02.01.2010	12.2544	141.573	08:45:32	08:54:58	08:50:23	0.07	1.46E-08	2	6.1	South of the Marianas	dip-slip (normal)
14	03.01.2010	-8.4794	157.2076	22:36:27	22:45:09	22:44:43	0.19	3.96E-08	25	7.1	Solomon Islands	dip-slip (thrust)
15	05.01.2010	-9.0114	157.3306	12:15:32	12:34:41	12:23:58	0.06	1.25E-08	15	6.8	Solomon Islands	oblique-slip (thrust)
16	07.02.2010	23.1921	123.4167	06:10:00	06:13:18	06:13:51	0.06	1.25E-08	10	6.4	near Ishigakijima Island	Strike-slip
17	18.02.2010	42.3722	131.0381	01:13:17	01:17:00	01:15:33	0.31	6.46E-08	43	6.8	near Vladivostok	oblique-slip (thrust)
18	26.02.2010	25.85	128.59	20:31:26	20:30:20	20:33:57	0.63	1.31E-07	18	7.0	near Okinawajima Islands	Strike-slip
19	27.02.2010	-36.0732	-72.5388	06:34:12	06:51:13	06:51:15	0.42	8.75E-08	22	8.8	West off Chile	dip-slip (thrust)
20	14.03.2010	37.4345	141.4908	08:08:04	08:08:57	08:09:17	0.57	1.19E-07	59.6	6.4	East off Fukushika Pref.	dip-slip (thrust)
21	30.03.2010	43.115	138.347	01:02:55	01:06:01	01:05:10	0.12	2.50E-08	20	5.6	Eastern Sea of Japan	dip-slip (thrust)
22	04.04.2010	32.1	115.05	22:50:17	23:03:56	23:02:55	0.08	1.67E-08	10	5.4	NW Mexico	Strike-slip
23	06.04.2010	2.2298	97.0288	22:15:02	22:24:06	22:23:45	0.29	6.04E-08	31	7.8	Sumatra, Indonesia	dip-slip (thrust)
24	14.04.2010	33.17	96.55	23:49:38	00:09:59	23:56:19	0.31	6.46E-08	17	6.9	China	Strike-slip
25	26.04.2010	22.1262	123.4954	02:59:49	03:06:11	03:03:40	0.11	2.29E-08	44	6.4	far south off Ishigakijima	Strike-slip
26	03.05.2010	29.4363	141.2944	10:27:43	10:28:09	10:29:01	0.35	7.29E-08	98	6.4	near Torishima Island	dip-slip (thrust)
27	09.05.2010	3.4488	96.0108	05:59:42	06:07:51	06:08:23	0.06	1.25E-08	38	7.2	Sumatra, Indonesia	dip-slip (thrust)
28	26.05.2010	25.4454	129.5938	08:53:07	08:56:47	08:55:38	0.30	6.25E-08	10	6.3	near Minami-Daitojima Islands	Strike-slip
29	11.06.2010	26.3889	143.0938	16:37:46	16:42:56	16:39:53	0.11	2.29E-08	7	5.4	near Chichijima Island	dip-slip (thrust)
30	12.06.2010	7.5286	91.5616	19:26:50	19:37:03	19:35:37	0.18	3.75E-08	35	7.5	Nicobar Islands	oblique-slip (thrust)
31	13.06.2010	37.2376	141.4774	03:32:57	03:33:08	03:34:08	0.13	2.71E-08	33.8	5.6	East off Fukushika Pref.	oblique-slip (thrust)
32	16.06.2010	-2.1044	136.3258	03:16:28	03:23:09	03:23:24	0.19	3.96E-08	18	7.0	Irian Jaya, Indonesia	Strike-slip
33	26.06.2010	-10.3762	161.2682	05:30:19	05:45:16	05:39:11	0.04	8.33E-09	35	6.7	Solomon Islands	oblique-slip (thrust)
34	28.06.2010	30.4466	142.0228	12:07:23	12:09:55	12:08:40	0.19	3.96E-08	7	5.8	near Torishima Island	dip-slip (thrust)
35	04.07.2010	39.3934	142.3917	21:55:52	21:57:04	21:57:26	0.09	1.88E-08	27	6.3	east off Iwate Pref.	dip-slip (thrust)
36	10.07.2010	11.0858	145.5994	11:43:32	11:47:36	11:48:43	0.10	2.08E-08	13	6.3	South of the Marianas	Strike-slip
37	18.07.2010	52.5256	-169.5088	05:56:45	06:16:01	06:04:38	0.05	1.04E-08	14	6.6	Fox Islands, Aleutian Islands	oblique-slip (normal)
38	18.07.2010	-5.5796	150.2568	13:04:09	13:11:15	13:11:43	0.12	2.50E-08	28	6.9	New Britain, P.N.G.	dip-slip (thrust)
39	18.07.2010	-5.586	150.354	13:34:59	13:44:16	13:42:32	0.11	2.29E-08	35	7.2	New Britain, P.N.G.	dip-slip (thrust)
40	23.07.2010	6.4308	123.2454	22:08:11	22:16:40	22:13:33	0.05	1.04E-08	607	7.3	Mindanao, Philippine Islands	oblique-slip (normal)
41	23.07.2010	6.486	123.467	22:51:13	22:55:41	22:56:33	0.42	8.75E-08	585	7.6	Mindanao, Philippine Islands	oblique-slip (normal)
42	30.07.2010	52.2988	159.5058	03:56:19	04:01:52	04:01:31	0.07	1.46E-08	23	6.3	off east coast of Kamchatka	dip-slip (thrust)
43	10.08.2010	-17.3246	168.0414	05:23:45	05:34:07	05:33:39	0.17	3.54E-08	25	7.3	Vanuatu (New Hebrides)	oblique-slip (thrust)
44	13.08.2010	12.2904	141.2856	21:19:33	21:23:58	21:24:22	0.80	1.67E-07	10	6.9	South of the Marianas	oblique-slip (normal)
45	14.08.2010	12.2088	141.2922	07:30:17	07:34:50	07:35:07	0.08	1.67E-08	10	6.2	South of the Marianas	oblique-slip (normal)
46	14.08.2010	12.1638	141.2574	23:01:04	23:08:58	23:05:54	0.16	3.33E-08	13	6.6	South of the Marianas	dip-slip (normal)
47	18.08.2010	12.1404	141.3084	16:28:15	16:33:10	16:33:06	0.09	1.88E-08	10	6.3	South of the Marianas	dip-slip (normal)
48	03.09.2010	-43.52	171.83	16:35:27	16:54:42	16:48:12	0.04	8.33E-09	12	7.0	South Island, New Zealand	Strike-slip
49	29.09.2010	-4.5454	133.4272	17:10:51	17:20:10	18:18:06	0.10	2.08E-08	10	6.2	Irian Jaya, Indonesia	dip-slip (normal)
50	25.10.2010	-3.2929	100.0504	14:42:22	14:49:53	14:51:19	0.14	2.92E-08	20	7.8	Sumatra, Indonesia	dip-slip (thrust)
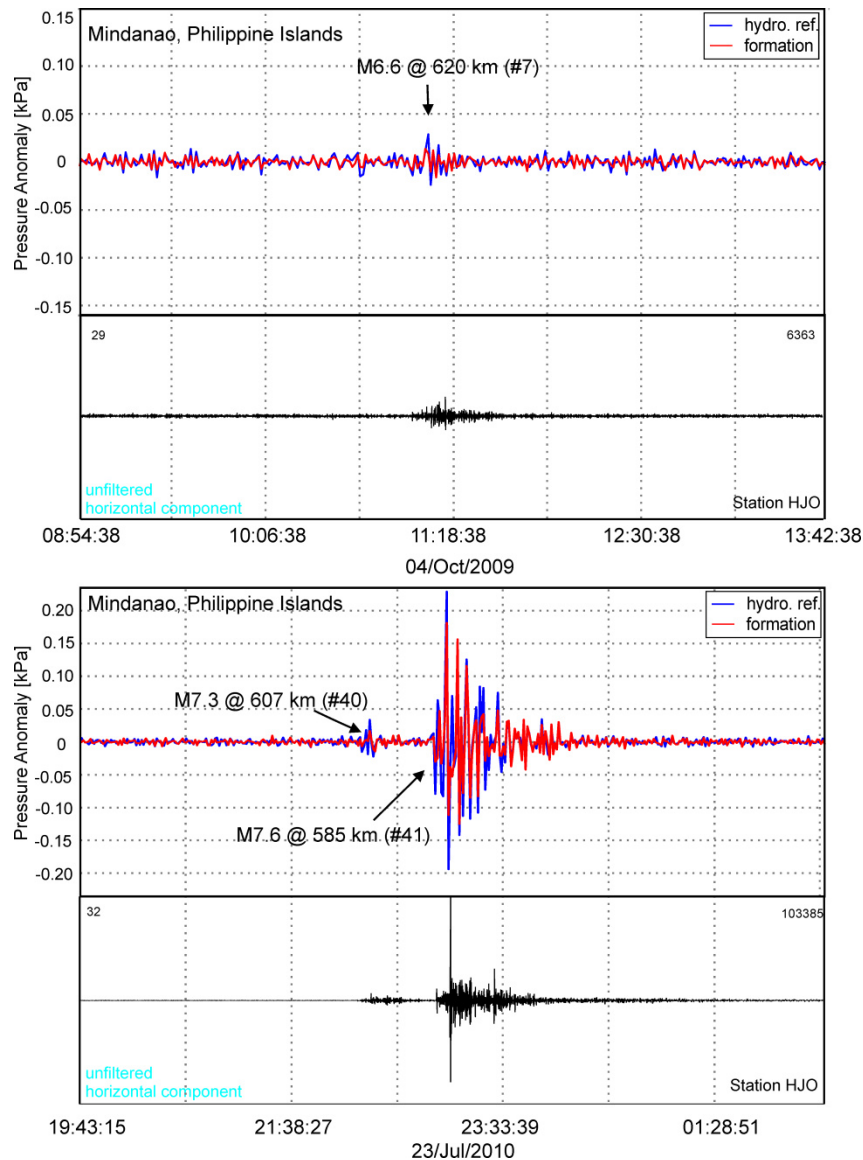
Figure 25: *Examples for fluid pressure oscillations induced by earthquakes from over 550 km depth near Mindanao, Philippine Islands, with corresponding unfiltered waveform data from F-Net station HJO. (A) AM6.6 earthquake (# 7 in Table 5 and Figure 22), originating from around 620 km depth near Mindanao, Philippine Islands; (B) Two earthquakes from near Mindanao, Philippine Islands, with the hypocentres being in 607 and 585 km depth (#40 and #41 in Table 5 and Figure 22, respectively). The deeper earthquake, although of similar magnitude, is hardly recognizable in the pressure data.*

M7.6 event having its hypocentre at ~580 km depth led to significant pressure oscillations, showing the previously described pattern. The onset of a slightly weaker earthquake (M7.3) occurring around 40 minutes earlier in ~610 km depth can only be assumed by theoretical travel time calculations (online service provided by the USGS).

[31] *Strain* – The largest earthquake near the SmartPlug observatory site was a magnitude 6.2 earthquake roughly 720 km to the southwest, which occurred on 03 September 2009 (Figure 26; #3 in Table 5 and Figure 22). While highly aliased, surprisingly large (several tens of kPa) surface waves from this relatively shallow event are seen by both sensors, and in this instance, the amplitude of the signal in the formation is smaller than that in the casing. Most notable

about this event is a 0.2 kPa decrease in formation pressure roughly 20 minutes after the arrival of surface waves. There is no corresponding change in the casing, which argues against this pressure step reflecting large-scale volumetric strain as has been observed in many CORK installations (e.g., Davis et al. 2009). This is supported by there being no contemporaneous signals observed at either Holes 1173B or 808I (roughly 200 km closer to the earthquake epicentre; see Site 1173 and Site 808, respectively, in Fig. 10, and Fig. 26). The formation anomaly may reflect local strain in the fault zone in the range of 10^{-8} (Table 5), not seen in the cased interval. Alternatively, the offset may be hydrologic in origin, similar to ones documented in land boreholes and attributed to increases in formation permeability (e.g. Cooper et al. 1965; Woodcock and Roeloffs 1996; Roeloffs 1998; Brodsky et al. 2003; Elkhoury et al. 2006; Kano and Yanagidani 2006); in this case an increase within the splay fault that allowed the formation pressure to drop by a small amount.

[32] While there are a few small steps in pressure seen early in the record in the hydrostatic reference section, no other anomalies are seen that point to discrete volumetric strain events. This is not surprising, as the SmartPlug monitoring period falls within a period of no observed strain-related events at Holes 808I and 1173B, and virtually none of the very low frequency earthquakes that have been found to accompany strain event at those observatories (Davis et al. 2012).

CONCLUSIONS

[33] Although the thermal re-equilibration of the borehole was still underway at the end of the SmartPlug recording period, the *in situ* temperature could be well constrained to 19°C. For the fluid pressure, the first 1-2 months of the compensated pressure cannot be trusted, as the coefficients used for temperature compensation are insufficiently accurate at this level of sensor precision. Like the temperature, the pressure showed an exponential increase for the rest of the monitoring period, indicating recovery of the formation whose rate exceeds typical rates of sensor drift. Interpolation to the *in situ* formation pressure is not possible here, but the pressure is superhydrostatic by an amount close to 15 kPa. The pressure monitoring was influenced by the inadvertent seal created by the corrosion cap at the top of the casing string, which undermined the utility of the reference sensor for open-ocean monitoring. The interval did serve as a sealed "strain gauge", however, but with a loading efficiency of 0.91 and a correspondingly low-strain-to-pressure conversion efficiency.

[34] While the short-term transients in the temperature data remain unclear, most of the ones detected in the pressure data are related either to seismological, tsunamigenic or meteorological events. The arrival of seismic waves influenced the hydrogeological regime by inducing

strain, which was, at least in one case, followed by a drop in formation pressure indicating a possible increase in permeability.
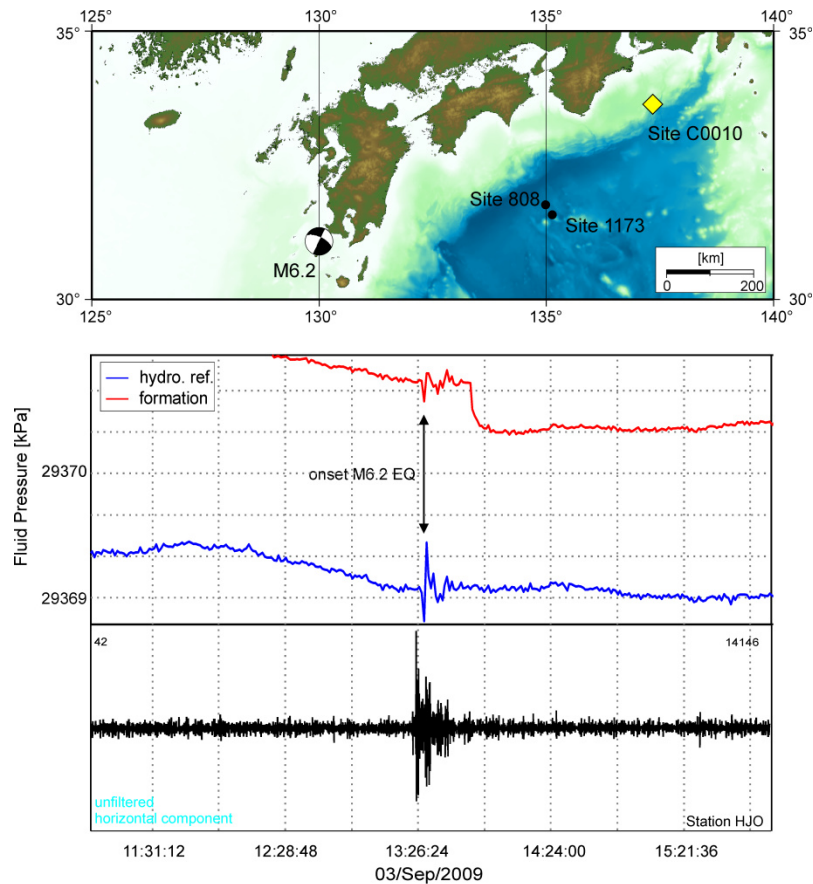
Figure 26: *Pressure step by arrival of seismic waves from a regional M6.2 earthquake (#3 in Table 5 and Figure 22) with corresponding unfiltered waveform data from F-Net station HJO. The pressure step occurs only in the formation fluid pressure and subsequently in the excess pressure. The drop is probably caused by increased permeability due to the arrival of the seismic waves.*

[35] Future studies should compare the datasets of several different borehole observatories from the Nankai Trough, including those installed much earlier and still operational off Cape Muroto, and ones of the Kumano Basin transect to be connected to the Japanese DONET observatory network. The latter will provide data from pressure sensors, strainmeters, seismometers, tiltmeters and accelerometers. A combination of these datasets, together with data from the F-Net and Hi-Net stations, will allow a better understanding of the role of the fluid pressure and temperature in the seismogenic cycle of the Nankai Trough and in particular, of the Megasplay fault.

Acknowledgments

References

Ando M (1975) Source Mechanisms and Tectonic Significance of Historical Earthquakes along the Nankai Trough, Japan. Tectonophysics 27:119 – 140.

Amante C, Ealkins BW (2009) ETOPO1 1 Arc-Minute Global Relief Model: Procedures, Data Sources and Analysis. NOAA Tech Memo NESDIS NGDC-24:19 pp.

Araki E, Byrne T, McNeill L, Saffer DM, Eguchi N, Moe KT, Toczko S, the Expedition 319 Scientists (2010) Proc. IODP, 319: 410 pp. doi:10.2204/iodp.proc.319.2009

Babcock JM, Kirkendall BA, Orcutt JA (1995) Relationships between ocean bottom noise and the environment. Bull Seismol Soc Am 84:1991–2007.

Ballu V, Ammann J, Pot O, de Viron O, Sasagawa G, Reverdin G, Bouin M-N, Cannat M, Deplus C, Deroussi S, Maia M, Diament M (2009) A seafloor experiment to monitor vertical deformation at the Lucky Strike volcano, Mid-Atlantic Ridge. J Geod 83:147–159. doi: 10.1007/s00190-008-0248-3

Becker K, Davis EE, Spiess FN, deMoustier CP (2004) Temperature and video logs from the upper oceanic crust, Holes 504B and 896A, Costa Rica Rift flank: implications for the permeability of upper oceanic crust. Earth Planet Sci Lett 222:881–896.

Beroza GC, Ide S (2011) Slow Earthquakes and Nonvolcanic Tremor. Annu Rev Earth Planet Sci 39:271–296. doi: doi:10.1146/annurev-earth-040809-152531

Brodsky EE, Roeloffs E, Woodcock D, Gall I, Manga M (2003) A mechanism for sustained groundwater pressure changes induced by distant earthquakes. J Geophys Res 108:2390. doi: 10.1029/2002jb002321

Bromirski PD, Duennebier FK, Stephen RA (2005) Mid-ocean microseisms. Geochem Geophys Geosyst 6:Q04009. doi: 10.1029/2004gc000768

Byrne DE, Davis DM, Sykes LR (1988) Loci and maximum size of thrust earthquakes and the mechanics of the shallow region of subduction zones. Tectonics 7:833–857. doi: 10.1029/TC007i004p00833

Chadwick WW, Nooner SL, Zumberge MA, Embley RW, Fox CG (2006) Vertical deformation monitoring at Axial Seamount since its 1998 eruption using deep-sea pressure sensors. J Volcanol Geotherm Res 150:313–327.

Cooper Jr. HH, Bredehoeft JD, Papadopulos IS, Bennett RR (1965) The Response of Well-Aquifer Systems to Seismic Waves. J Geophys Res 70:3915–3926. doi: 10.1029/JZ070i016p03915

Cummins PR, Hori T, Kaneda Y (2001) Splay fault and megathrust earthquake slip in the Nankai Trough. Earth Planets Sp 53:243–248.

Davis EE, Wang K, Becker K, Thomson RE (2000) Formation-scale hydraulic and mechanical properties of oceanic crust inferred from pore pressure response to periodic seafloor loading. J Geophys Res 105:13423–13435. doi: 10.1029/2000jb900084

Davis EE, Becker K, Wang K, Kinoshita M (2009) Co-seismic and post-seismic pore-fluid pressure changes in the Philippine Sea plate and Nankai decollement in response to a seismogenic strain event off Kii Peninsula, Japan. Earth, Planets Sp 61:649 – 657.

Davis EE, Kinoshita M, Wang K, Asano Y, Ito Y, Becker K (2012) Slip at the Nankai subduction zone triggered by the 2011 Tohoku earthquake, Earth Plan Sci Lett, in review.

Eaton JP, Takasaki KJ (1959) Seismological interpretation of earthquake-induced water-level fluctuations in wells. Bull Seismol Soc Am 49:227–245.

Elkhoury JE, Brodsky EE, Agnew DC (2006) Seismic waves increase permeability. Nature 441:1135–1138.

Fisher AT, Becker K, Davis EE (1997) The permeability of young oceanic crust east of Juan de Fuca Ridge Determined using borehole thermal measurements. Geophys Res Lett 24:1311–1314. doi: 10.1029/97gl01286

Foreman MGG, Crawford WR, Marsden RF (1995) De-tiding: Theory and Practice. In: Lynch DR, Davis AM (eds) Quant. Ski. Assess. Coast. Ocean Model. American Geophysical Union, Washington D.C., p 510

Frohlich C (1989) The Nature of Deep-Focus Earthquakes. Annu Rev Earth Planet Sci 17:227–254.

Fukao Y (1979) Tsunami Earthquakes and Subduction Processes Near Deep-Sea Trenches. J Geophys Res 84:2303–2314. doi: 10.1029/JB084iB05p02303

Fujimoto H, Koizumi K, Osada Y, Kanazawa T (1998) Development of instruments for seafloor geodesy. Earth, Planets Sp 50:905–911.

Fujimoto H, Mochizuki M, Mitsuzawa K, Tamaki T, Sato T (2003) Ocean bottom pressure variations in the southeastern Pacific following the 1997–98 El Niño event. Geophys Res Lett 30:1456. doi: 10.1029/2002gl016677

Geballe ZM, Wang CY, Manga M (2011) A permeability-change model for water-level changes triggered by teleseismic waves. Geofluids 11:302–308. doi: 10.1111/j.1468-8123.2011.00341.x

Gerstoft P, Shearer PM, Harmon N, Zhang J (2008) Global P, PP, and PKP wave microseisms observed from distant storms. Geophys Res Lett 35:L23306. doi: 10.1029/2008gl036111

Gennerich H-H, Villinger H (2011) Deciphering the ocean bottom pressure variation in the Logatchev hydrothermal field at the eastern flank of the Mid-Atlantic Ridge. Geochem Geophys Geosyst 12:Q0AE03. doi: 10.1029/2010gc003441

Hammerschmidt SB, Davis EE, Hüpers A, Kopf A (2013) Limitation of fluid flow at the Nankai Trough Megasplay fault zone. Geo-Marine Lett 33:405–418. doi: 10.1007/s00367-013-0337-z

Hasselmann K (1963) A statistical analysis of the generation of microseisms. Rev Geophys 1:177–210. doi: 10.1029/RG001i002p00177

Hino R, Tanioka Y, Kanazawa T, Sakai S, Nishino M, Suyehiro K (2001) Micro-tsunami from a local interplate earthquake detected by cabled offshore tsunami observation in northeastern Japan. Geophys Res Lett 28:3533–3536. doi: 10.1029/2001gl013297

Hyndman RD, Yamano M, Oleskevich DA (1997) The seismogenic zone of subduction thrust faults. Isl Arc 6:244–260. doi: 10.1111/j.1440-1738.1997.tb00175.x

Ichinose GA, Thio HK, Somerville PG, Sato T, Ishii T (2003) Rupture process of the 1944 Tonankai earthquake (M s 8.1) from the inversion of teleseismic and regional seismograms. J Geophys Res 108:2497. doi: 10.1029/2003jb002393

Kagami H, Karig DE, Coulbourn WT, the Expedition 87 Scientists (1987) Initial Reports of the Deep Sea Drilling Project 87: 985pp.

Kano Y, Yanagidani T (2006) Broadband hydroseismograms observed by closed borehole wells in the Kamioka mine, central Japan: Response of pore pressure to seismic waves from 0.05 to 2 Hz. J Geophys Res 111:B03410. doi: 10.1029/2005jb003656

Karig DE, Ingle Jr JC (1975) Initial Reports of the Deep Sea Drilling Project 31: 927pp.

Kennett BLN (2002) The Seismic Wavefield - Volume II: Interpretation of Seismograms on Regional and Global Scales. Cambridge University Press, Cambridge

Kimura G, Screaton EJ, Curewitz D, the Expedition 316 Scientists (2008) NanTroSEIZE Stage 1A: NanTroSEIZE Shallow Megasplay and Frontal Thrusts. IODP Prel Rep 316.

Kimura G, Moore GF, Strasser M, Screaton E, Curewitz D, Streiff C, Tobin H (2011) Spatial and temporal evolution of the Megasplay fault in the Nankai Trough. Geochem Geophys Geosyst 12:Q0A008. doi: 10.1029/2010gc003335

Kinoshita M, Tobin H, Ashi J, Kimura G, Lallement S, Screaton EJ, Curewitz D, Masago H, Moe KT, the Expedition 314/3159/316 Scientists (2009). Proc IODP 314/315/316.

Kitagawa Y, Koizumi N, Takahashi M, Matsumoto N, Sato T (2006) Changes in groundwater levels or pressures associated with the 2004 earthquake off the west coast of northern Sumatra (M9.0). Earth Planets Sp 58:173–179.

Kopf A, Araki E, Toczko S, the Expedition 332 Scientists (2011a). NanTroSEIZE Stage 2: Riserless Observatory. IODP Prel Rep 332.

Kopf A, Saffer DM, Davis EE, Hammerschmidt S, LaBonte A, Meldrum R, Toczko S, Lauer R, Heesemann M, Macdonald R, Wheat CG, Jannasch HW, Edwards K, Orcutt B, Haddad A, Villinger H, Araki E, Kitada K, Kimura T, Kido Y (2011b). The SmartPlug and GeniusPlug: Simple retrievable observatory systems for NanTroSEIZE borehole monitoring. In: Kopf A, Araki E, Toczko S, the Expedition 332 Scientists (eds) Proc IODP, 332: Tokyo (Integrated Ocean Drilling Program Management International, Inc.).

Landès M, Hubans F, Shapiro NM, Paul A, Campillo M (2010) Origin of deep ocean microseisms by using teleseismic body waves. J Geophys Res 115:B05302. doi: 10.1029/2009jb006918

Lay T, Astiz L, Kanamori H, Christensen DH (1989) Temporal variation of large intraplate earthquakes in coupled subduction zones. Phys Earth Planet Inter 54:258–312.

Longuet-Higgins MS (1950) A Theory of the Origin of Microseisms. Philos Trans R Soc London Ser A, Math Phys Sci 243:1–35. doi: 10.1098/rsta.1950.0012

McPhaden MJ, Picaut J (1990) El Niño-Southern Oscillation Displacements of the Western Equatorial Pacific Warm Pool. Science 250:1385–1388. doi: 10.1126/science.250.4986.1385

Miyazaki S, Heki K (2001) Crustal velocity field of southwest Japan: Subduction and arc-arc collision. J Geophys Res 106:4305–4326. doi: 10.1029/2000jb900312

Moore JC, Saffer D (2001) Updip limit of the seismogenic zone beneath the accretionary prism of southwest Japan: An effect of diagenetic to low-grade metamorphic processes and increasing effective stress. Geology 29:183–186. doi: 10.1130/0091-7613(2001)029<0183:ulotsz>2.0.co;2

Moore GF, Taira A, Klaus A, Becker L, Boeckel B, Cragg BA, Dean A, Fergusson CL, Henry P, Hirano S, Hisamitsu T, Hunze S, Kastner M, Maltman AJ, Morgan JK, Murakami Y, Saffer DM, Sánchez-Gómez M, Screaton EJ, Smith DC, Spivack AJ, Steurer J, Tobin HJ, Ujiie K, Underwood MB, Wilson M (2001) New insights into deformation and fluid flow processes in the Nankai Trough accretionary prism: Results of Ocean Drilling Program Leg 190. Geochem Geophys Geosyst 2:1058. doi: 10.1029/2001gc000166

Moore GF, Bangs NL, Taira A, Kuramoto S, Pangborn E, Tobin HJ (2007) Three-Dimensional Splay Fault Geometry and Implications for Tsunami Generation. Science 318:1128–1131. doi: 10.1126/science.1147195

Moore GF, Park J-O, Bangs NL, Gulick SP, Tobin HJ, Nakamura Y, Sato S, Tsuji T, Yoro T, Tanaka H, Uraki S, Kido Y, Sanada Y, Kuramoto S, Taira A (2009) Structural and seismic stratigraphic framework of the NanTroSEIZE Stage 1 transect. Proc Integr Ocean Drill Progr. 314/315/316. doi:10.2204/iodp.proc.314315316.102.2009

Niiler PP, Filloux J, Liu WT, Samelson RM, Paduan JD, Paulson CA (1993) Wind-Forced Variability of the Deep Eastern North Pacific: Observations of Seafloor Pressure and Abyssal Currents. J Geophys Res 98:22589–22602. doi: 10.1029/93jc01288

Nooner SL, Chadwick Jr. WW (2009) Volcanic inflation measured in the caldera of Axial Seamount: Implications for magma supply and future eruptions. Geochem Geophys Geosyst 10:Q02002. doi: 10.1029/2008gc002315

Okada Y, Kasahara K, Hori S, Obara K, Sekiguchi S, Fujiwara H, Yamamoto A (2004) Recent progress of seismic observation networks in Japan: Hi-net, F-net, K-NET and KiK-net. Earth Planets Sp 56:15–28.

Park J-O, Tsuru T, Kodaira S, Cummins PR, Kaneda Y (2002) Splay Fault Branching Along the Nankai Subduction Zone. Science 297:1157–1160. doi: 10.1126/science.1074111

Pawlowicz Bearsley, B. R, Lentz S (2002) Classical Tidal Harmonic Analysis Including Error Estimates in MATLAB using T_TIDE. Comput Geosci 28:929–937.

Polster A, Fabian M, Villinger H (2009) Effective resolution and drift of Paroscientific pressure sensors derived from long-term seafloor measurements. Geochem Geophys Geosyst 10:Q08008. doi: 10.1029/2009gc002532

Rexin EE, Oliver J, Prentiss D (1962) Seismically-induced fluctuations of the water level in the Nunn-Bush well in Milwaukee. Bull Seismol Soc Am 52:17–25.

Roeloffs EA (1998) Persistent water level changes in a well near Parkfield, California, due to local and distant earthquakes. J Geophys Res 103:869–889. doi: 10.1029/97jb02335

Saffer D, McNeill L, Araki E, Byrne T, Eguchi N, Toczko S, Takahashi K, the Expedition 319 Scientists (2009) NanTroSEIZE Stage 2: NanTroSEIZE Riser/Riserless Observatory. IODP Prel Rep 319: 83 pp.

Saffer D, McNeill L, Byrne T, Araki E, Toczko S, Eguchi N, Takahashi K, the Expedition 319 Scientists (2010) NanTroSEIZE Stage 2: NanTroSEIZE Riser/Riserless Observatory. Proc IODP, 319: 83 pp.

Sagiya T, Thatcher W (1999) Coseismic slip resolution along a plate boundary megathrust: The Nankai Trough, southwest Japan. J Geophys Res 104:1111–1129. doi: 10.1029/98jb02644

Satake K (1993) Depth Distribution of Coseismic Slip Along the Nankai Trough, Japan, From Joint Inversion of Geodetic and Tsunami Data. J Geophys Res 98:4553–4565. doi: 10.1029/92jb01553

Scholz CH (1998) Earthquakes and friction laws. Nature 391:37–42.

Seno T, Stein S, Gripp AE (1993) A model for the motion of the Philippine Sea plate consistent with NUVEL-1 and geological data. J Geophys Res 98:8.

Strasser M, Moore GF, Kimura G, Kitamura Y, Kopf AJ, Lallemant S, Park J-O, Screaton EJ, Su X, Underwood MB, Zhao X (2009) Origin and evolution of a splay fault in the Nankai accretionary wedge. Nat Geosci 2:648–652.

Tabulevich VN (1992) Microseismic and Infrasound waves. Springer-Verlag, Berlin Heidelberg

Taira A, Hill I, Firth JV, the Expedition 131 Scientists (1991) Init Rep ODP 131.

Tanimoto T, Ishimaru S, Alvizuri C (2006) Seasonality in particle motion of microseisms. Geophys J Int 166:253–266. doi: 10.1111/j.1365-246X.2006.02931.x

Tobin HJ, Saffer DM (2009) Elevated fluid pressure and extreme mechanical weakness of a plate boundary thrust, Nankai Trough subduction zone. Geology 37:679–682. doi: 10.1130/g25752a.1

Tobin HJ, Kinoshita M, Ashi J, Lallemant S, Kimura G, Screaton E, Moe KT, Masago H, Curewitz D, the Expedition 314/315/316 Scientists (2009) NanTroSEIZE Stage 1 expeditions: Introduction and synthesis of key results. In: Kinoshita M, Tobin HJ, Ashi J, Kimura G, Lallemant S, Screaton E, Curewitz D, Masago H, Moe KT, the Expedition 314/315/316 Scientists, Proc IODP, 314/315/316: Washington, DC (Integrated Ocean Drilling Program Management International, Inc.). doi:10.2204/iodp.proc.314315316.101.2009

Toczko ST, Kopf AJ, Araki E, the IODP Expedition 332 Scientific Party (2012) The IODP Expedition 332 : Eyes on the Prism, The NanTroSEIZE Observatories. Sci Drill 14: 34–38. doi: 10.2204/iodp.sd.14.04.2012

Villinger H, Davis EE (1987) A New Reduction Algorithm for Marine Heat Flow Measurements. J Geophys Res 92:12846–12856. doi: 10.1029/JB092iB12p12846

Wang K (2004) Applying fundamental principles and mathematical models to understand processes and estimate parameters. In: Davis E, Elderfield H (eds) Hydrogeol Ocean Lithosph, Cambridge University Press, p 706

Wang K, Davis EE (1996) Theory for the Propagation of Tidally Induced Pore Pressure Variations in Layered Subseafloor Formations. J Geophys Res 101:11483 – 11495.

Wang K, Hu Y (2006) Accretionary prisms in subduction earthquake cycles: The theory of dynamic Coulomb wedge. J Geophys Res 111:B06410. doi: 10.1029/2005jb004094

Wang C, Chia Y, Wang P, Dreger D (2009) Role of S waves and Love waves in coseismic permeability enhancement. Geophys Res Lett 36:L09404. doi: 10.1029/2009gl037330

Watts DR, Kontoyiannis H (1990) Deep-ocean bottom pressure measurement: Drift removal and performance. J Atmos Ocean Technol 7:296–306.

Wearn JRB, Larson NG (1982) Measurements of the sensitivities and drift of Digiquartz pressure sensors. Deep Sea Res Part A Oceanogr Res Pap 29:111–134.

Webb SC (1998) Broad seismology and noise under the ocean. Rev Geophys 36:105–142. doi: 10.1029/97RG02287

Webb SC (2007) The Earth's `hum' is driven by ocean waves over the continental shelves. Nature 445:754–756.

Wessel P, Smith WHF (1991) Free software helps map and display data. Eos Trans AGU 72:441 – 446.

Woodcock D, Roeloffs E (1996) Seismically-induced water level oscillations in a fractured-rock aquifer well near Grants Pass, Oregon. Oregon Geol 58:27–33.

Zhang J, Gerstoft P, Bromirski PD (2010) Pelagic and coastal sources of P-wave microseisms: Generation under tropical cyclones. Geophys Res Lett 37:L15301. doi: 10.1029/2010gl044288

CHAPTER 5.2 – MANUSCRIPT II

LIMITATION OF FLUID FLOW AT THE NANKAI TROUGH MEGASPLAY FAULT ZONE

Sebastian B. Hammerschmidt[1]*, Earl E. Davis[2], Andre Hüpers[1], Achim Kopf[1]

* corresponding author: shammerschmidt@marum.de

[1] MARUM, University of Bremen, Bremen, Germany

[2] Pacific Geoscience Center, Geological Survey of Canada, Sidney, B.C., Canada

Abstract Along the Nankai Trough Megasplay fault off SE Japan, the effect of fluid migration on subduction-related seismogenesis and tsunamigenesis remains unresolved. To investigate the existence and role of fluid flow, a SmartPlug borehole observatory was installed at Site C0010 of the Integrated Ocean Drilling Program NanTroSEIZE Kumano transect, where a shallow branch of the fault was intersected and *in situ* fluid pressure monitored from August 2009 - November 2010. The tidal signal in the formation showed no phase shift relative to seafloor loading. The attenuation of 0.73 reflects the loading efficiency accurately, and enabled calculation of a formation compressibility of 1.0×10^{-9} Pa^{-1} and a hydraulic diffusivity (HD) of 1.5×10^{-5} m^2 s^{-1}. A similar HD is predicted by a tidal response model based on SmartPlug pressure data. By contrast, permeability measurements on intact samples from Site C0004 SE along-strike the splay fault and from Site C0006 at the frontal thrust zone were found similar and one magnitude smaller, respectively, despite having a higher porosity. This is explained by the presence of fractures, which are covered by the larger scale of *in situ* measurements at Site C0010. Consequently, HD can be set to be at least 10^{-5} m^2 s^{-1} for the splay fault and 10^{-6} m^2 s^{-1} for the frontal thrust fault zone. Considering recent publications makes fluid flow at the splay fault unlikely, despite the presence of fractures. If the influence of fractures is limited, processes leading to fault weakening may be enhanced.

INTRODUCTION

[1] Japan experiences numerous earthquakes each year, with one main earthquake-prone area being the Nankai Trough off its southeast coast (Figure 27), where large subduction thrust earthquakes have occurred at intervals of 100 - 200 years (Ando 1975; Satake 1993; Ichinose et al. 2003). To unravel the mechanisms driving the regional seismogenic and tsunamigenic processes, the Nankai Trough Seismogenic Zone Experiment (NanTroSEIZE) was initiated as part of the Integrated Ocean Drilling Program (IODP), a follow-up program to the DSDP (Deep Sea Drilling Project) and the ODP (Ocean Drilling Program) during which seismogenic processes at the Nankai Trough were investigated by drilling the Ashizuri and Muroto transects (Figure 27). In the course of the IODP NanTroSEIZE project, those earlier investigations were complemented by the Kumano transect. Here, the Megasplay fault region (IODP sites C0001, C0003, C0004, C0008, C0010, C0018, C0021 and C0022, see Figure 27) is of particular interest.

[2] In order to understand its permeability structure better, the Megasplay fault has been investigated by coring (IODP Exp. 316, Site C0004, Screaton et al. 2009) as well as logging-while-drilling (LWD), and by deployment of a SmartPlug borehole observatory (IODP Exp. 319, Site C0010, Expedition 319 Scientists 2010). The temperature and particularly the fluid pressure data obtained from Site C0010 showed several anomalies, but none could be attributed to recent fluid flow and/or deformation events in this sector of the Megasplay fault (Hammerschmidt et al. 2013).

[3] Indeed, it has long been suggested that the Megasplay fault can act as conduit which facilitates drainage and enables pore fluid pressure to decrease in ambient sediments, especially in the deeper parts of the plate boundary (e.g. Byrne et al. 1988; Moore and Saffer 2001; Park et al. 2002; Tobin and Saffer 2009). The associated increase in effective stress could subsequently promote consolidation, cementation and lithification (Scholz 1998). This would increase the

frictional instability, favouring stick-slip behaviour and potential earthquake generation below the inner accretionary wedge (Byrne et al. 1988). By contrast, the outer wedge is considered to experience steady slip due to the overpressurized and thus underconsolidated weak sediment below the décollement (Rice 1992; Tobin and Saffer 2009). This would suggest a lack of fluid pathways seawards of the Megasplay fault, which is supported by findings from ODP Leg 131 along the Muroto transect of the Nankai Trough. There, the composition of fluids from the megathrust fault at Site 808 did not indicate any recent active fluid flow (Gieskes et al. 1993).
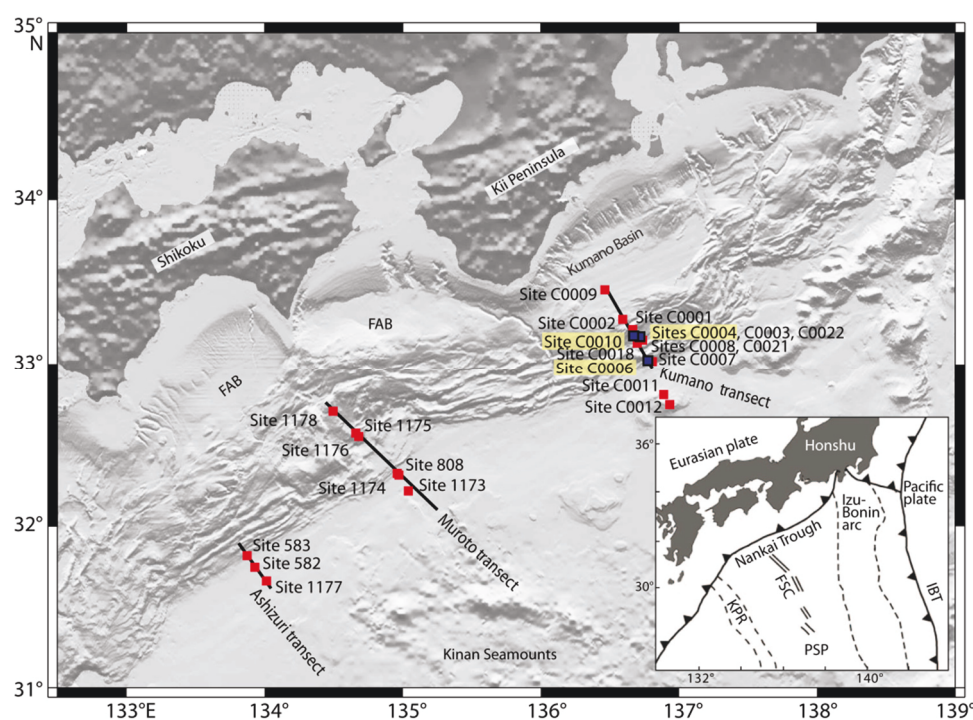
Figure 27: *Overview of study sites along the Ashizuri, Muroto and Kumano transects across the Nankai Trough (modified from Moore et al. 2009), and regional tectonic map (inset). The present work evaluates data from sites C0004, C0006 and C0010 (yellow) of the Kumano transect, drawing upon novel and published information from long-term in situ pressure measurements (Site C0010), LWD (sites C0004, C0010) and coring (sites C0004, C0006). Of particular interest is the seismo- and tsunamigenic potential of a splay fault system in the accretionary prism, which was penetrated at sites C0004 and C0010. FAB Forearc basin, IBT Izu-Bonin Trench, KPR Kyushu-Palau Ridge, FSC fossil spreading centre, PSP Philippine Sea plate*

[4] It is also possible that faults can serve as combined conduit/barrier systems for fluid flow (e.g. Caine et al. 1996). Fault zones can be differentiated into a fractured, permeable damage zone, a highly permeable transition zone, and a core zone comprising fault gouge and/or breccia which usually impede across- and/or along-fault fluid migration (for example, see review of internal fault zone architecture by Wibberley et al. 2008). Permeability might vary temporally and spatially (along-strike and along-dip), which is of particular importance for the seismogenic potential of a fault zone (e.g. Sibson 1992; Wibberley and Shimamoto 2003, 2005; Boutareaud et al. 2008; Faulkner et al. 2008; Wibberley et al. 2008). Low permeabilities can create an undrained setting in which fault slip can either be hindered by dilatancy hardening or be enhanced

by thermal pressurization (e.g. Rudnicki and Chen 1988; Segall and Rice 1995, 2006; Wibberley and Shimamoto 2005).

[5] Along the Kumano transect (Figure 28), previous studies have led to a highly equivocal hydrogeologic model for the Megasplay fault. Although along-fault fluid flow has been suggested on the basis of seismic data (Park et al. 2010), cold seeps with chemosynthetic communities (Ashi et al. 2002; Toki et al. 2004) and heat-flow anomalies observed in places where shallow branches reach the seafloor (Hamamoto et al. 2011), no supporting evidence was found in cores (Screaton et al. 2009) or by *in situ* monitoring (Hammerschmidt et al. 2013). Additionally, geochemical analyses of the fluids (Solomon et al. 2008; Hirono et al. 2009) and vitrinite reflectance analysis (Sakaguchi et al. 2011) argue against any contribution of deep-sourced fluids. Indeed, independent chemical and mineralogical data point to frictional heating during slip, rather than migration of deep-sourced fluids along the fault zone (Yamaguchi et al. 2011). In attempting to clarify the impact of the Megasplay fault on the hydrogeology of the Nankai subduction system, the present study further explores the hydrogeological properties of splay fault material along the Kumano transect based on the following multifaceted approach:
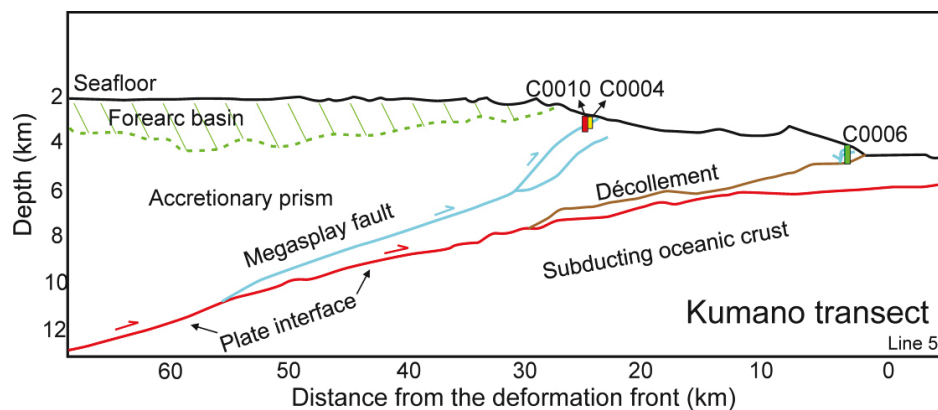
Figure 28: Cross-section of the Kumano transect (modified from Tobin et al. 2009). Sites C0010 and C0004 cross-cut a shallow branch of the splay fault system, site C0004 being located along-strike immediately northeast of site C0010. Site C0006 intersects several branches of a frontal thrust fault system further seawards.

1. Investigation of the tidal signal in the SmartPlug fluid pressure data from Site C0010. By calculating the tidal loading efficiency, i.e. the total fraction of pressure change caused by seafloor loading which is elastically taken up by the fluid (Wang 2004), it should be possible to compute the poroelastic properties of the splay fault zone.

2. Calculation of a tidal response model following the approach of Sawyer et al. (2008). By comparing the theoretical formation- instrument compliance ratio with this model, qualitative estimation of the permeability of the fault zone material in the immediate vicinity of the SmartPlug casing screens should be possible.

3. Conducting permeability measurements on fault zone material cored at Site C0004 and on material from a frontal thrust fault zone further seawards at Site C0006. Note that for Site C0010 no cores were available for analyses in the present case.

GEOLOGICAL SETTING

Geological overview

[6] At the Nankai Trough, SE Japan, subduction of the ca. 15-Ma-old Philippine Sea plate (PSP) beneath the Eurasian plate takes place at a rate of 4–6.5 cm year^{-1}, forming a large accretionary prism. Underthrusting occurs at very shallow angles along an azimuth of 300–315°N (Seno et al. 1993; Miyazaki and Heki 2001). Starting at about 2.87 Ma, the ongoing subduction of the PSP has caused an in-sequence forward imbrication of the accreted material, leading to a trench-slope basin system where massive mass-wasting events occurred (Strasser et al. 2009). At about 1.95 Ma, one of the major features in this accretionary prism, the so-called Megasplay fault, was initiated. This splay fault system started as an out-of-sequence thrust in the lower part of the prism, and is considered to have been temporarily active between 1.50 and 1.24 Ma (Strasser et al. 2009). Multichannel seismic data revealed that the ca. 30-km-long Megasplay fault migrates upwards from the décollement through the whole accretionary prism (Park et al. 2002). The splay fault mechanically separates the wedge into an inner stronger part and an outer weaker part, which overlie the seismogenic zone and the more shallow aseismic zone of the plate boundary, respectively (Wang and Hu 2006).

[7] In contrast to the findings of Strasser et al. (2009), Moore et al. (2007) proposed that recent activity of the Megasplay fault can be inferred from truncated sediments identified in seismic data, and Kimura et al. (2011) concluded that deformation structures in the overlying slope sediments might be caused by recent splay fault activity. Coseismic slip along the Megasplay fault was also proposed by other authors (e.g. Satake 1993; Sagiya and Thatcher 1999; Cummins et al. 2001; Park et al. 2002). Moore et al. (2009) suggest that the activity of the splay fault varies spatially, and that the branches can slip asynchronously. Park et al. (2010) have concluded that future slip behaviour of the Megasplay fault may be influenced by a zone of elevated fluid pressure in the outer accretionary prism. With ongoing subduction, this zone may reach the splay fault system and cause fluids to migrate along the fault, leading to mineral precipitation and faster healing of the fault (Park et al. 2010). Consequently, activation of the splay fault would be favoured by elevated pore pressure. Such slip would have a high tsunamigenic potential once the slip along the high-angle fault reached the seafloor (Fukao 1979; Moore and Saffer 2001; Park et al. 2002, 2010).

Fault zone properties

[8] Shallow branches of the Megasplay fault were intersected by four boreholes at sites C0003, C0004, C0010 and C0022 along the Kumano transect (Expedition 314 Scientists 2009; Expedition 316 Scientists 2009a; Expedition 319 Scientists 2010; Moore et al. 2013a). The uppermost 151 m (C0003), 260 m (C0004) and 200 m at (C0010) consist mainly of slope apron deposits characterized by silty mudstone with intercalations of thin sand and ash layers. These are followed by a ca. 210-m-thick pile of fractured mudstone surrounding the thrust sheet in the hanging wall of the splay fault (Expedition 332 Scientists 2011, and references therein). The thrust sheet itself has moved over the slope apron deposits (Kimura et al. 2008; Moore et al. 2009) during the last active phase between 1.50 and 1.24 Ma (Strasser et al. 2009).

[9] At Site C0003 the splay fault – indicated by washouts between 381 and 470 mbsf (metres below seafloor) – is associated with low gamma ray values and is also visible in 3-D seismic data (Expedition 314 Scientists 2009). At Site C0010 the fault can be identified as a sharp, single reflector in seismic data, whereas at Site C0004 the fault zone comprises a ca. 50-m-thick "fault bounded package" (Kimura et al. 2008; Expedition 319 Scientists 2010). In contrast, at Site C0022, the position of the splay fault is only inferred by logging-while-drilling resistivity data at around 100 mbsf. Bad core recovery at this interval precluded any detailed lithological investigation, but indicated that the missing material must be heavily fractured and/or deformed (Moore et al. 2013a). Compared to Site C0004, there is evidence of generally coarser-grained sediments at Site C0010. At the latter site, however, logging-while-drilling revealed higher gamma ray and resistivity values in the thrust wedge than recorded in the over- and underlying slope sediments. By contrast, the thrust wedge at C0004 shows porosities similar to the over- and underlying slope sediments (Expedition 319 Scientists 2010).

[10] Further seaward at the prism toe, a set of frontal thrust faults was detected by Moore et al. (2009) and subsequently logged and cored at Site C0006 (Expedition 316 Scientists 2009b), where a maximum depth of 603 mbsf was reached. Most of the thrust faults were identified by visual core description within a major interval of heavily fractured and brecciated material at ca. 230–545 mbsf. The fault zones appeared to be tectonically more brecciated than the surrounding material (Expedition 316 Scientists 2009b), and showed distinct deformation bands and mudstone (micro-)breccia. Between 526 and 545 mbsf, an 8-cm-thick layer of fault gouge was detected. Moore et al. (2009) successfully correlated these thrust faults with sharp seismic reflectors visible in 3-D multichannel seismic data.

[11] For the Nankai accretionary prism (Figure 27), strong variations in permeability were recorded along the Kumano transect as well as the Muroto transect located to the southwest. At

Site 808 of the Muroto transect, a major thrust fault had permeabilities of about 10^{-17} m^2 (Taylor and Fisher 1993; see also Gamage and Screaton 2003; Adatia and Maltman 2004). Coring along the Kumano transect, including sites C0004 and C0006 but not focused on fractured fault zone material, revealed permeabilities of 10^{-14}–10^{-20} m^2 for the accretionary prism (Ikari et al. 2009; Dugan and Daigle 2011; Ekinci et al. 2011; Rowe et al. 2011, 2012; Ikari and Saffer 2012; Kitajima et al. 2012) and of 10^{-14}–10^{-19} m^2 for the Kumano forearc basin and underlying accretionary prism (Boutt et al. 2012; Saffer et al. 2013; Guo et al. 2013).

MATERIALS AND METHODS

The SmartPlug borehole observatory

[12] The SmartPlug is the first borehole observatory in a series of recently developed mini-CORKs, and is characterized by a relatively simple design compared to that of conventional CORKs (Circulation Obviation Retrofit Kits; for reviews, see Becker and Davis 2005; Kastner et al. 2006; Wheat et al. 2010). The SmartPlug is a self-contained instrument of almost 1 m length and designed to be compatible with standard industry mechanically set bridge plugs. In the upper part of the SmartPlug, one of these plugs seals the borehole, preventing the exchange of water between the overlying water column and the borehole. The interior of the SmartPlug includes a battery, a data logger, pressure transducers and temperature sensors (for more comprehensive technical details, see Kopf et al. 2011). One pressure gauge is hydraulically connected to the cased hole above the SmartPlug to monitor the hydrostatic reference pressure. Another pressure transducer is connected through the solid end of the plug into the borehole to monitor the formation pressure (Figure 29). In the present case, pressure measurements were conducted at a sampling interval of 1 minute and a resolution of 10 ppb (i.e. ~0.7 Pa, equivalent to 0.07 mm of seawater head; see also Kopf et al. 2011).

[13] In August 2009 during IODP Exp. 319, the SmartPlug was installed at Site C0010 along the Kumano transect (Expedition 319 Scientists 2010). The casing screens were located at the fault zone, enabling pressure variations in the splay fault to be monitored by the lower pressure gauge (see Figure 3). The instrument was recovered in November 2010 during IODP Exp. 332 (Expedition 332 Scientists 2011), providing a continuous 15-month record of fluid pressure and temperature measurements. Initial data analysis revealed that both hydrostatic reference and formation pressures were strongly influenced by seismic and tsunami waves (Hammerschmidt et al. 2013) and, most significantly, by tidal signals (Kopf et al. 2011).
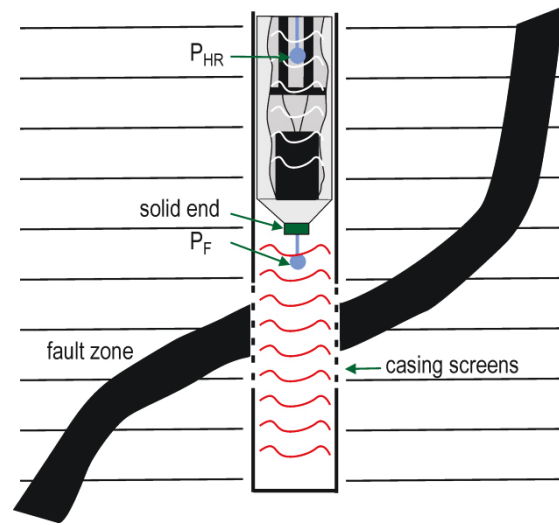
Figure 29: *Schematic of the SmartPlug borehole observatory (modified from Hammerschmidt et al. 2013): P_{HR} hydrostatic reference pressure sensor, P_F formation pressure sensor, white lines unconfined hydrostatic depth interval, red lines confined depth interval influenced only by fluids entering through the casing screens*

Determining the tidal loading efficiency and formation properties

[14] Calculating the tidal loading efficiency (sometimes also termed the Skempton coefficient) can serve to constrain the elastic and hydrogeologic properties of the formation (Wang and Davis 1996; Wang 2004). Assuming negligible effects of diffusion and drainage boundaries like the seafloor, the 1-D loading efficiency is determined by the ratio of long wavelength pressure variations (e.g., tides) between the formation and seafloor. For this purpose, it is necessary to choose an appropriate subset of the dataset, which is free of any anomalies caused by seismic waves or microseismic signals. Moreover, for much of the recording period at Site C0010 the borehole was sealed by a corrosion cap, which precluded observations of seafloor pressure variations (see discussion in Hammerschmidt et al. 2013). Therefore, in this study, a period of pressure data was chosen when the bridge plug had been removed (i.e., 2–5 November 2010; for raw data, see Figure S.1 in Appendix A.1).

[15] A discrete Fourier transformation was applied to this selected dataset. The Fourier coefficient magnitude M, which is composed of the real and complex numbers a and bi respectively, is then squared to gain the power:

$$M^2 = a^2 + bi^2 \tag{1}$$

Only frequencies below 8.3×10^{-3} s^{-1} (i.e. half the SmartPlug sampling frequency) are considered here. Dividing M^2 by the frequency gives the power spectral density which, in turn, enables the calculation of the 1-D loading efficiency as a function of frequency:

$$\gamma'(f) = \sqrt{\frac{M_{form}^2 f}{f M_{hr}^2}} \tag{2}$$

where M_{hr}^2 and M_{form}^2 are the power of the selected hydrostatic reference and formation pressures respectively, and f is the frequency.

[16] With the 1-D tidal loading efficiency γ', it is possible to compute the poroelastic and hydrogeologic properties of the fault zone material. By taking the mean value of the tidal loading efficiency, the 1-D matrix compressibility is determined as:

$$m_f' = \frac{\beta_w n}{(\frac{1}{\overline{\gamma'}} - 1)} \tag{3}$$

where the subscript f denotes the formation, and β_w and n are the fluid compressibility and the porosity respectively (Wang and Davis 1996). Here, the latter was taken as 0.38, based on the porosity estimated from logging-while-drilling data from Site C0010 (Expedition 319 Scientists 2010). According to Davis et al. (2009), the unconfined matrix compressibility can then be expressed as:

$$m_f = 3m_f' \frac{(1 - v)}{(1 + v)} \tag{4}$$

with v being the Poisson's ratio of the matrix. In this case, a Poisson's ratio of 0.1 was used, because the pore fluid does not contribute to the elastic modulus of the matrix frame (Wang and Davis 1996).

[17] The specific storage S, the hydraulic conductivity K and the hydraulic diffusivity c can then be calculated as:

$$S = \rho g (m_f + n\beta_w) \tag{5}$$

$$K = \frac{k\rho g}{\mu} \tag{6}$$

and

$$c = \frac{K}{S} \tag{7}$$

with

$$\log k = -18 + 3.45n \tag{8}$$

$$\mu = 0.01688 T^{-0.8987} \tag{9}$$

where T is the temperature in °C measured at the borehole sensor, μ the viscosity in Pa s (after Gartling 1977) and k the intrinsic permeability in m². Eq. 8 was taken from Rowe et al. (2012),

who considered this permeability-porosity relationship to be suitable for the frontal tip of the Nankai Trough accretionary prism. The latter is assumed to be permeable, due to the presence of fractures and a décollement that allows fluid migration. No other verified relationship is available for the Nankai prism; therefore Eq. 8 was applied to determine the intrinsic permeability in the present case.

[18] To calculate the relationship between strain and a sudden pore fluid pressure change in a poroelastic medium, the approach of Davis et al. (2009) was used. The strain sensitivity S_f is defined as a function of the elastic properties of a fluid-saturated formation by the following equation:

$$S_f = \frac{\theta}{P} = m_f(\frac{1}{\gamma} - \alpha_m) \tag{10}$$

with

$$\alpha_m = 1 - \frac{\beta_s}{m_f} \tag{11}$$

$$\gamma = \alpha_m m_f \frac{1}{\zeta} \tag{12}$$

$$\zeta = \alpha_m m_f + n\alpha_f \beta_w \tag{13}$$

and

$$\alpha_f = 1 - \frac{\beta_s}{\beta_w} \tag{14}$$

where θ is the strain induced by the pressure transient P, α_f and α_m the effective stress coefficients for the fluid and the matrix respectively, γ the 3-D loading efficiency, ζ the storage compressibility and β_s the solid compressibility (see also Wang 2004, and references therein). An overview of defined variables can be found in Table S.1 in Appendix A.1.

Calculating the tidal response model

[19] When a pressure change occurs in the formation, the signal is transmitted to the formation sensor inside the casing via the casing screens (see Figure 29). A small amount of fluid flow is required to accommodate the difference between the compressibility of the formation and of the measurement system, primarily the water filling the casing plus any fractured material surrounding the casing screens. This is broadly referred to here as the "formation-instrument compliance ratio" following the definition of Sawyer et al. (2008), who presented the theory behind the "tidal response model". With increasing formation-instrument compliance ratio β, pressure equilibrates faster and the hydraulic diffusivity of the surrounding formation is of less im-

portance. The "instrument compliance" depends on the total confined volume of the cased borehole, and this directly influences the fidelity of the measurements (Davis and Becker 2007; Sawyer et al. 2008). The higher the borehole volume, the more compliant becomes the measurement system and the smaller is the formation-instrument compliance ratio (see also Section "*Tidal Response Model*" in Appendix A.1).

[20] Following the approach of Sawyer et al. (2008) and also Hsieh et al. (1987), it was possible to model the amplitude and the phase response to the sinusoidal change of diurnal tidal signals as a function of different formation-instrument compliance ratios, as well as the dimensionless frequencies and hydraulic diffusivities. Ignoring any effects of fracturing in the sediment volume outside the casing, an instrument-specific formation-instrument compliance ratio can be inferred from the casing and screen "system" design (Sawyer et al. 2008). The calculations are comprehensively shown in the section "*Tidal Response Model*" in Appendix A.1. The hydraulic diffusivity of the zone of interest can then be inferred by plotting the SmartPlug-specific formation-instrument compliance ratio versus the observed amplitude damping and phase shift in the tidal response model.

Permeability experiments

[21] Permeability measurements were conducted on mini-cores (i.e. cylindrical sample with a diameter of 1 inch) from sites C0004 and C0006 using a pressure permeameter. The operational setup is described in detail in the section "*Permeability Measurements*" and Fig. S.2 in Appendix A.1. All mini-cores are classified as silty claystone. The data reported in the present study account for the orientation of mini-cores relative to the main core axis, i.e. either perpendicular or parallel to the core (labelled horizontal and vertical, respectively). An overview of the sample codes and raw data is given in Table S.2 in Appendix A.1. These were compared with the findings of Rowe et al. (2011), who reported permeabilities of other mini-cores from sites C0004 and C0006.

RESULTS

Formation properties at Site C0010

[22] A power spectral density analysis of the raw SmartPlug fluid pressure data for the period 2–5 November 2010 shows the diurnal (O_1, K_1) and semidiurnal (S_2, M_2) tidal frequencies to have the largest energy (see Figure S.3 in Appendix A.1). The tidal loading efficiency was determined by taking the average tidal loading efficiency for frequencies $\leq 4 \times 10^{-5}$ s^{-1}; higher frequencies show a large decrease in power and coherence between the seafloor and formation signals. The loading efficiency below this frequency averages roughly 0.73.

[23] Based on the tidal loading efficiency, a formation compressibility of 1.0×10^{-9} Pa^{-1} is inferred. Following the approach of Sawyer et al. (2008) and using the dimensions of the cased hole below the SmartPlug, this leads to a compliance ratio of $\beta_D = 15$ and a wellbore storage of $\beta V = 1.6 \times 10^{-10}$ m^3 Pa^{-1}. Based on the compressibilities inferred from the observed fluid pressure variations in the SmartPlug data, the sector of the fault zone enclosed by the casing screens has a strain sensitivity of 6 kPa μstrain^{-1}. An overview of all results is given in Table 6.

Table 6: *Overview of calculated poroelastic properties for Site C0010, as well as instrument response and sensitivity to pressure and strain changes respectively. FI = formation-instrument*

Variable	Definition	Dimension
γ'	tidal loading efficiency	0.73
γ	3-D loading efficiency	0.87
α_m	eff. stress coeff. matrix	0.98
α_f	eff. stress coeff. fluid	0.95
ζ	storage compress.	1.2×10^{-9} Pa^{-1}
S_f	sensitivity	6.0 kPa μstrain^{-1}
m_v	formation compress.	1.0×10^{-9} Pa^{-1}
S	specific storage	1.2×10^{-5} m^{-1}
μ	fluid viscosity	1.2×10^{-3} Pa s
k	intrinsic permeability	2.1×10^{-17} m^2
K	hydraulic conductivity	1.7×10^{-10} m s^{-1}
c	hydraulic diffusivity	1.5×10^{-5} m^2 s^{-1}
β_d	FI compliance ratio	15
βV	wellbore storage	1.6×10^{-10} m^3 Pa^{-1}
β	system compressibility	5.2×10^{-10} Pa^{-1}

Tidal response model for Site C0010

[24] An overview of tidal response modelling results for Site C0010 is shown in Fig. 30 and can be summarized as follows:

(i)   At a given formation-instrument compliance ratio, the signal response improves with decreasing frequency or increasing hydraulic diffusivity, i.e. the phase shift is decreased and the amplitude response becomes closer to be purely elastic.

(ii) For a given dimensionless frequency or hydraulic diffusivity, the signal response improves with increasing formation-instrument compliance ratio.

(iii) Plotting the formation-instrument compliance ratio $\beta_D = 15$ at an amplitude response and phase shift near 100 % and 0° respectively suggests a hydraulic diffusivity of roughly 10^{-5} m^2 s^{-1} for Site C0010 (red stars in Figure 30). This corresponds to the value calculated from porosity and tidal loading efficiency-inferred formation compressibility via equations

(5), (7) and (8) (1.5×10^{-5} m^2 s^{-1}; see also Table 6). It also lies in the range of hydraulic diffusivities determined by permeability tests at sites C0004 and is one magnitude higher than at C0006, although the sediments at Sites C0004 and C0006 have higher porosities (cf. next chapter; see also Figures 31, 32).
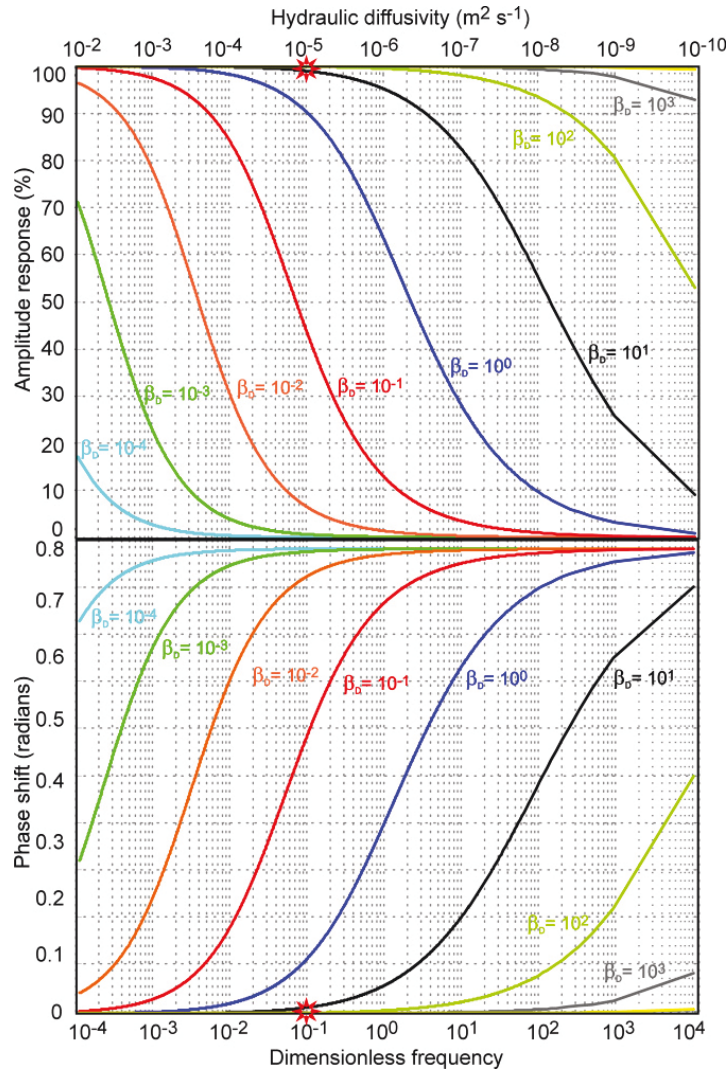
Figure 30: *Amplitude response and phase shift of tidal noise-induced peaks in SmartPlug pressure data from Site C0010, versus dimensionless frequency (bottom x-axis) and hydraulic diffusivity (top x-axis). This model is based on a solar tidal signal (i.e. 24 h). Red stars Formation-instrument compliance ratio in terms of the SmartPlug design and borehole dimensions at the observed amplitude response and phase shift in the fluid pressure data.*

Hydraulic diffusivity at sites C0004 and C0006

[25] An overview of the results of the high-pressure permeability tests for sites C0004 and C0006 is shown in Figs. 31 and 32 (for the data, see Table S.2 in Appendix A.1). Regarding the measurements conducted on "vertical" mini-cores taken parallel to the core axis, the hydraulic diffusivities show no clear correlation with the applied effective stress of 0.5 to 1.5 MPa. However, almost all hydraulic diffusivities are in the range of 10^{-5} m^2 s^{-1} to 10^{-6} m^2 s^{-1} for sites C0004

and C0006. Varying effective stresses applied by Rowe et al. (2011) were below 1 MPa, and resulted in hydraulic diffusivities in the same order of magnitude. Elevated hydraulic diffusivity of the fault-bounded package at Site C0004 was found only on one vertically oriented mini-core (ca. 7.7×10^{-5} m^2 s^{-1}, see Figure 31) tested by Rowe et al. (2011). This suggests that variation in the transmissivity between the underthrust sediment and the fault zone material is small. Vertically oriented mini-cores of heavily brecciated and fractured material from above and within the interval from ca. 230–545 mbsf at Site C0006 show similar hydraulic diffusivities (Figure 32). Horizontally (i.e. parallel to bedding or structural grain) oriented mini-cores of both sites have hydraulic diffusivities in the same order of magnitude as their vertically oriented counterparts, but show a better correlation when plotted versus confining pressure. One of the horizontally oriented mini-cores from Site C0004 has a significantly higher hydraulic diffusivity of up to 10^{-3} m^2 s^{-1} (i.e. up to two orders of magnitude higher, Figure 31) and a stronger dependence on the applied effective stress. However, this is not surprising given the poor condition of the sample: its cylindrical geometry was not perfect, and an artificially created fracture made it easier for the fluid to migrate through the specimen during the permeability test.

[26] Comparing the permeability results with porosity derived from moisture and density (MAD) measurements conducted during IODP Exp. 316 (Expedition 316 Scientists 2009a) showed that the slightly higher hydraulic diffusivities of the fault-bounded package at Site C0004 correspond well with elevated porosity values. Porosities scatter from 0.37 to 0.57 and with the lowest values being found in the same depth interval as that characterized by the lowest hydraulic diffusivities. At Site C0006, there is no clear correlation between the porosity trend and the derived hydraulic diffusivities.

DISCUSSION

[27] The tidal loading efficiency of 0.73 determined at Site C0010 of the Nankai Trough Megasplay fault zone (Table 6) is smaller than CORK-based values observed for sediments of similar porosities in similar settings elsewhere in the world - e.g. the Barbados accretionary prism (0.85; Becker et al. 1997) and the Costa Rica forearc wedge (0.86; Davis and Villinger 2006). At the Barbados accretionary prism, the perforated casing screens of the CORK system were located between 400 and 440 mbsf, comprising radiolarian-rich claystone above and hemipelagic claystone and turbidites below a décollement with an average porosity of 60% (Underwood and Deng 1997; Becker et al. 1997). At the Costa Rica margin, fluid flow was monitored in accreted pelagic and hemipelagic sediments of 55 % porosity at a depth of ca. 127 mbsf (Davis and Villinger 2006). In the Nankai Trough region, Davis et al. (2009) reported a

5.2 Limitation of Fluid Flow at the Nankai Trough Megasplay Fault Zone
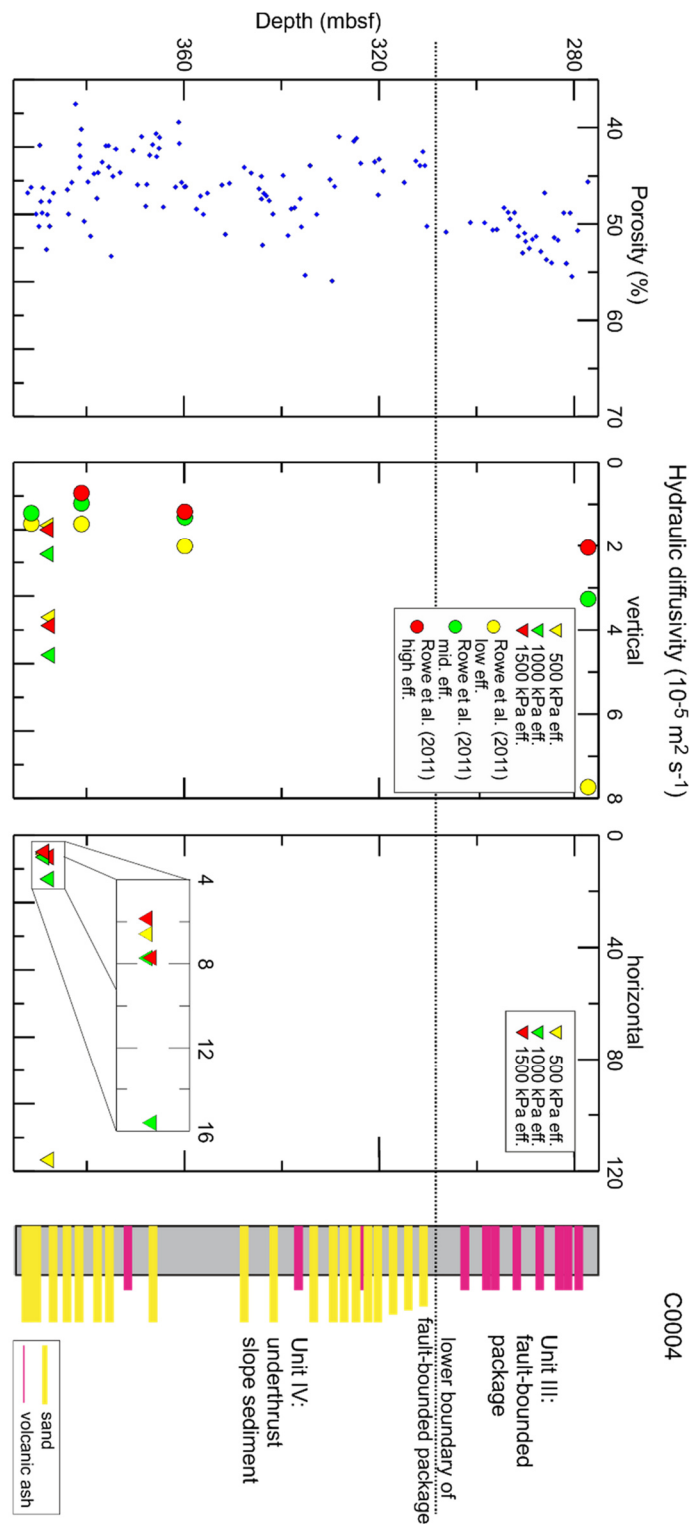
Figure 31: Overview of permeability measurements conducted on samples from Site C0004. Left column Highly scattered porosity values derived from moisture and density measurements during IODP Exp. 316 (Expedition 316 Scientists 2009a). Middle columns Hydraulic diffusivity of vertically and horizontally oriented mini-cores: triangles present study, circles extracted from Rowe et al. (2011). Right column Lithostratigraphic log recorded during IODP Exp. 316 (modified from Expedition 316 Scientists 2009a). See text for further explanation.

5.2 Limitation of Fluid Flow at the Nankai Trough Megasplay Fault Zone
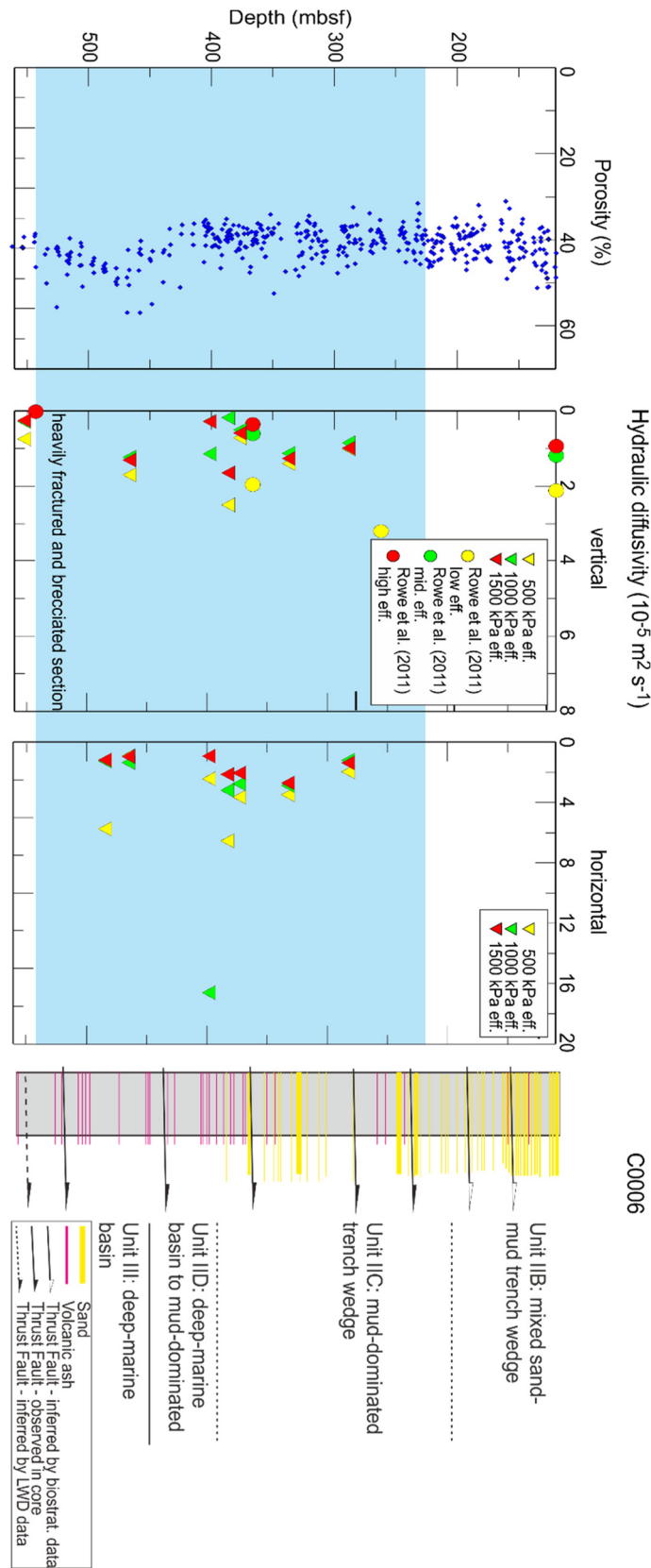
Figure 32: Overview of permeability measurements conducted on samples from Site C0006. Left column Porosity values derived from moisture and density measurements during IODP Exp. 316 (Expedition 316 Scientists 2009b). Middle columns Hydraulic diffusivity of vertically and horizontally oriented mini-cores: triangles present study, circles extracted from Rowe et al. (2011). Right column Lithostratigraphic log recorded during IODP Exp. 316 (modified from Expedition 316 Scientists 2009b). See text for further explanations.

tidal loading efficiency ranging from 0.6 to 0.9 for sediments of the Shikoku Basin facies pene-trated by an ACORK at Site 1173 (Figure 27, Muroto transect), where tidal loading efficiency decreased with increasing depth. The relatively low tidal loading efficiency of 0.73 recorded in the present study might be related to the low porosity caused by overcompaction of fault zone material at Site C0010 (Expedition 319 Scientists 2010; Figure 33).

[28] The absence of any phase shift is not surprising given the depth of the screened interval below the seafloor. Pressure variations migrate from a hydrologic boundary as a damped pressure wave, and the induced response of the formation can be separated into an elastic and a diffusive component (e.g. Davis et al. 2000; Wang and Davis 2003). In contrast to the instantaneous elastic response, which is responsible for the amplitude damping, diffusion needs more time and leads to a phase lag within the formation (Wang and Davis 2003). The characteristic diffusion scale for 1/e attenuation, q, is defined as

$$q = \sqrt{\pi c T} \tag{15}$$

where c and t are the hydraulic diffusivity and the period of the loading signal respectively (Wang and Davis 2003). Substituting $t=24$ h and $c=1.5\times10^{-5}$ m^2 s^{-1} into Eq. 15 yields a q of roughly 2 m, which is in the typical range of 1–10 m for low-permeability seafloor sediments (Davis et al. 2000; Wang 2004). Clearly, this penetration length is negligible when compared to the C0010 monitoring depth of the SmartPlug (cf. the distance from the seafloor to the sensor is almost 370 m). Therefore, pressures are unaffected by tidal pressure wave-induced diffusion from the seafloor, and the response of the formation would be purely elastic. However, phase lags can still be caused either by the so-called borehole storage effect (Wang and Davis 2003) or by limited diffusion between the sealed section of the borehole and the formation in the direct vicinity of the screened section. The borehole storage depends on the volume of the borehole and the compressibility of the fluid. With increasing volume, the borehole storage increases, as does the possibility for phase lags. Fortunately, the wellbore storage of the SmartPlug is already low (i.e. 1.6×10^{-10} m^3 Pa^{-1}, see Table 6), and with c being in the range of 10^{-5} m^2 s^{-1}, a good hydraulic communication is given, which further supports the tidal signals being in phase. Hydraulic diffusivities below 10^{-5} m^2 s^{-1} are unlikely, because these would result in amplitude damping and phase shifts when the tidal response model is considered (see also Figure 30). The lower limit of 10^{-5} m^2 s^{-1} is verified by the here applied porosity-permeability relationship (Eq. 8), which considers a permeable accretionary prism by taking the presence of fractures into account (Rowe et al. 2012). Fractures would further increase the hydraulic communication, allowing faster pressure equilibration between the borehole and the formation, and hence reduce the possibility of phase lags. Consequently, the hydraulic diffusivity can be constrained to at least ca. 1.0×10^{-5} m^2 s^{-1}, and might fractures would also explain why the tidal response model leads to a hydraulic diffusivity which is

similar higher when compared to the laboratory-derived results from Site C0004 and Site C0006, respectively, although the porosity at Site C0010 is up to 19 % lower (Expedition 319 Scientists 2010). That a fracture network close to the main fault might be developed is supported from recent drilling and coring at Site C0022, where the tip of a shallow splay fault branch was intersected. During coring, recovery of the fault itself failed, most likely due to the presence of intensively fractured and/or disturbed material (Moore et al. 2013a). Additionally, around 20 m above the suggested location of the fault, a dense network of minor fractures was detected. In the interval between 93 and 95 mbsf, Expedition 338 Scientists (personal communication, 2013) further detected planar fabrics, which bear be higher depending on the ramification and extension of the fracture network. The presence of striations with rakes of 90°, indicating dip-slip faulting. These features were interpreted to be secondary branches of the main fault branch.
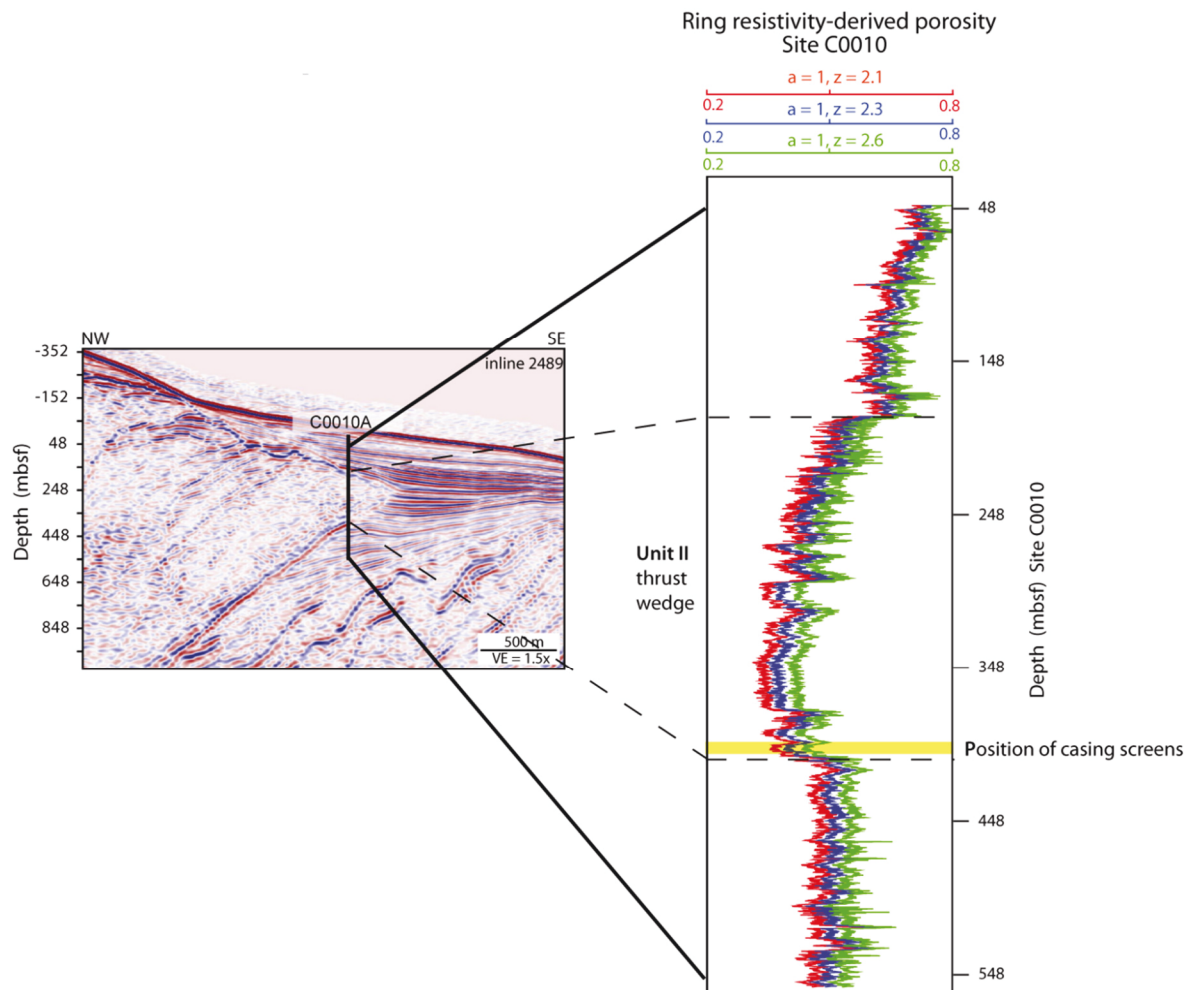
Figure 33: Left: *Seismic profile including Hole A of Site C0010 (inline 2489).* **Right:** *Corresponding ring resistivity-derived porosity (both plots modified from Expedition 319 Scientists 2010). Testing for various cementation factors (z) revealed only minor effects on porosity ("a" denotes tortuosity; see Expedition 319 Scientists (2010) for information on calculations). Note the significant decline in porosity in the thrust wedge of the accretionary prism. The location of the casing screens is highlighted by the yellow box.*

[29] Although one sample from the fault-bounded package at Site C0004 as well as most samples from Site C0006 were taken from a zone characterized by strong brecciation (Expedition 316 Scientists 2009a, 2009b; see also Figures 31 and 32), only bigger clasts were subsampled for permeability determination. Thus, the influence of fractures is neglected, and these measurements are representative for protolith rock only. Consequently, the smallest possible value for hydraulic diffusivity is settled to 10^{-5} m^2 s^{-1} and 10^{-6} m^2 s^{-1} for sites C0004 and C0006 respectively.

[30] The different influence of porosity in laboratory- and *in situ*-derived hydraulic diffusivities is not surprising, giving the larger scale of *in situ* methods (e.g. Boutt et al. 2012). Although earlier studies suggest that scale effects in argillaceous rock are of minor importance (e.g., Neuzil 1994), Boutt et al. (2012) and Saffer et al. (2013) assumed that scale effects in the Nankai Trough Kumano forearc basin (sites C0002, C0009; see Figure 27) are the cause for the differences between *in situ* and laboratory measurements. The effect of fractures is only covered by *in situ* methods, which is supported by the findings presented here.

[31] Unfortunately, the interconnection of these fractures and their spatial extension (lateral and vertical) remain speculative. That recent across- and along-fault flow at the Megasplay fault is unlikely can be supported by elevated fluid pressures inferred from seismic p-wave velocities, porosities and mean effective stresses in the outer wedge and directly below deeper sections (i.e., 4500 – 6500 mbsf) of the Megasplay fault (Park et al. 2010; Kitajima and Saffer 2012). In contrast, further updip of the splay fault, at sites C0004 and C0010, fluid pressures were only slightly above hydrostatic values (Kopf et al. 2011; Moore et al. 2013b). If recent (deep-sourced) fluid flow would have occurred, fluid pressure at Site C0004 and Site C0010 must be significantly higher. This effect of active fluid flow was apparent in annular pressure data from sites C0001, C0003 and from the boundary thrust fault at Site C0006, where the baseline pressure is suddenly increased by 1 – 3 MPa when a fluid-rich zone was penetrated (Moore et al. 2012, 2013b).

[32] If the real hydraulic diffusivities at sites C0004 and C0010 are close to the lowest values estimated above, the mechanisms of rupture slip nucleation and propagation along the Megasplay fault could be influenced significantly. For instance, Tsutsumi et al. (2004) investigated the permeability of the Nobi fault system, onshore SW Japan. They found values as low as 10^{-17} m^2 for the fault zone and concluded that these were sufficiently low to support thermal pressurization causing fault weakening (cf. Wibberley and Shimamoto 2005). Similar arguments apply to the Nankai Trough Megasplay fault: if diffusion of pore pressure is limited, then shear heating leads to an increase in pressure and thereby to a reduction in fault strength (cf. Segall

and Rice 2006). The presence of a fractured damage zone might decrease this effect, since fluids could escape from the Megasplay fault zone at sites C0004 and C0010. In addition to that, the effect of dilatancy hardening has to be considered, whereby an increase in slip velocity leads to transient changes in pore pressure and to an increase in shear strength (Rudnicki and Chen 1988; Segall and Rice 1995; Garagash and Rudnicki 2003; Samuelson et al. 2009, 2011). The question whether and when thermal pressurization and dilatancy hardening dominate and how these interact can be answered by examining the complex interplay amongst various key parameters, in particular fault zone permeability (e.g. Segall and Rice 1995, 2006; Andrews 2002; Tsutsumi et al. 2004; Rice 2006). As was shown here, fault zone permeability can be constrained on a scale appropriate for the fault zone by long-term *in situ* measurements, which should help to validate future models addressing Megasplay fault slip behaviour at the Nankai Trough.

CONCLUSIONS

[33] Based on the results and interpretations presented above, the following main conclusions are drawn: (1) the SmartPlug is capable of accurately monitoring pressure changes at tidal frequencies in formations with hydraulic diffusivities of $\geq 10^{-5} \, \mathrm{m^2 \, s^{-1}}$, (2) the hydraulic diffusivities at the shallow branch of the Megasplay fault (sites C0004, C0010) and the thrust fault zone at Site C0006 are limited to be at least $10^{-5} \, \mathrm{m^2 \, s^{-1}}$ and $10^{-6} \, \mathrm{m^2 \, s^{-1}}$ respectively, and might be enhanced by a fracture network; (3) if fractures are present, the possibility of recent across- and or along-fault fluid flow at the Megasplay fault at greater depth remains speculative, and is less likely when recent publications are considered, and (4) observations made with the SmartPlug and other observatory installations can constrain hydraulic diffusivity of the splay fault and other structures at a scale much larger than those made on core samples. Such constraints should improve hydraulic and thermal models for fault rupture and slip.

remarks. Comments from an anonymous reviewer and the journal editors further improved the paper.

References

Adatia RH, Maltman AJ (2004) Initial permeability determination on sediments from the Nankai Trough Accretionary Prism, ODP Sites 1173 and 1174. Proc ODP Sci Results 190/196. doi:10.2973/odp.proc.sr.190196.2005

Ando M (1975) Source mechanisms and tectonic significance of historical earthquakes along the Nankai Trough, Japan. Tectonophysics 27:119–140

Andrews DJ (2002) A fault constitutive relation accounting for thermal pressurization of pore fluid. J Geophys Res 107:2363. doi:10.1029/2002JB001942

Ashi J, Kuramoto Si, Morita S, Tsunogai U, Goto S, Kojima S, Okamoto T, Asai S, Utsumi M (2002) Structure and cold seep of the Nankai accretionary prism off Kumano. Outline of the off Kumano survey during YK01–04 Leg 2 Cruise. J Deep Sea Res 20:1–8

Becker K, Davis EE (2005) A review of CORK designs and operations during the Ocean Drilling Program. In: Fisher AT, Urabe T, Klaus A, Expedition 301 Scientists (eds) Proc IODP. doi:10.2204/iodp.proc.301.104.2005

Becker K, Fisher AT, Davis EE (1997) The CORK experiment in Hole 949C: long-term observations of pressure and temperature in the Barbados accretionary prism. Proc ODP 156:247–252

Boutareaud S, Wibberley CAJ, Fabbri O, Shimamoto T (2008) Permeability structure and co-seismic thermal pressurization on fault branches: insights from the Usukidani Fault, Japan. In: Wibberley CAJ, Kurz W, Imber J, Holdsworth RE, Collettini C (eds) The internal structure of fault zones: implications for mechanical and fluid-flow properties. Geol Soc Lond Spec Publ 299, pp 341–361

Boutt DF, Saffer D, Doan M-L, Lin W, Ito T, Kano Y, Flemings P, McNeill LC, Byrne T, Hayman NW, Moe KT (2012) Scale dependence of in-situ permeability measurements in the Nankai accretionary prism: The role of fractures. Geophys. Res. Lett. 39:L07302. doi: 10.1029/2012gl051216

Byrne DE, Davis DM, Sykes LR (1988) Loci and maximum size of thrust earthquakes and the mechanics of the shallow region of subduction zones. Tectonics 7:833–857

Caine JS, Evans JP, Forster CB (1996) Fault zone architecture and permeability structure. Geology 24:1025–1028

Cummins PR, Hori T, Kaneda Y (2001) Splay fault and megathrust earthquake slip in the Nankai Trough. Earth Planets Space 53:243–248

Davis EE, Becker K (2007) On the fidelity of "CORK" Borehole Hydrologic Observatory pressure records. Sci Drilling 5:54–59

Davis EE, Villinger HW (2006) Transient formation fluid pressures and temperatures in the Costa Rica forearc prism and subducting oceanic basement: CORK monitoring at ODP Sites 1253 and 1255. Earth Planet Sci Lett 245:232–244

Davis EE, Wang K, Becker K, Thomson RE (2000) Formation-scale hydraulic and mechanical properties of oceanic crust inferred from pore pressure response to periodic seafloor loading. J Geophys Res 105:13423–13435

Davis EE, Becker K, Wang K, Kinoshita M (2009) Co-seismic and post-seismic pore-fluid pressure changes in the Philippine Sea plate and Nankai decollement in response to a seismogenic strain event off Kii Peninsula, Japan. Earth Planets Space 61:649–657

Dugan B, Daigle H (2011) Data report: permeability, compressibility, stress state, and grain size of shallow sediments from Sites C0004, C0006, C0007, and C0008 of the Nankai accretionary complex. In: Kinoshita M, Tobin H, Ashi J, Kimura G, Lallement S, Screaton EJ, Curewitz D, Masago H, Moe KT, Expedition 314/315/316 Scientists (eds) Proc IODP 314/315/316. Integrated Ocean Drilling Program Management International, Tokyo. doi: 10.2204/iodp.proc.314315316.211.2011

Ekinci MK, Likos WJ, Guo J, Underwood MB (2011) Permeability of mud(stone) samples from IODP Sites C0004, C0006, C0007, and C0008 Nankai Trough Seismogenic Zone Experiment. AGU Fall Meeting 2011, San Francisco, abstract #1190471

Expedition 314 Scientists (2009) Expedition 314 Site C0003. In: Kinoshita M, Tobin H, Ashi J, Kimura G, Lallement S, Screaton EJ, Curewitz D, Masago H, Moe KT, Expedition 314/315/316 Scientists (eds) Proc IODP 314/315/316. Integrated Ocean Drilling Program Management International, Tokyo. doi:10.2204/iodp.proc.314315316.115.2009

Expedition 316 Scientists (2009a) Expedition 316 Site C0004. In: Kinoshita M, Tobin H, Ashi J, Kimura G, Lallement S, Screaton EJ, Curewitz D, Masago H, Moe KT, Expedition 314/315/316 Scientists (eds) Proc IODP 314/315/316. Integrated Ocean Drilling Program Management International, Tokyo. doi:10.2204/iodp.proc.314315316.133.2009

Expedition 316 Scientists (2009b) Expedition 316 Site C0006. In: Kinoshita M, Tobin H, Ashi J, Kimura G, Lallement S, Screaton EJ, Curewitz D, Masago H, Moe KT, Expedition 314/315/316 Scientists (eds) Proc IODP 314/315/316. Integrated Ocean Drilling Program Management International, Tokyo. doi:10.2204/iodp.proc.314315316.134.2009

Expedition 319 Scientists (2010) Site C0010. In: Saffer D, McNeill L, Byrne T, Araki E, Toczko S, Eguchi N, Takahashi K, Expedition 319 Scientists (eds) Proc IODP 319. Integrated Ocean Drilling Program Management International, Tokyo. doi:10.2204/iodp.proc.319.104.2010

Expedition 332 Scientists (2011) Expedition 332 summary. In: Kopf A, Araki E, Toczko S, Expedition 332 Scientists (eds) Proc IODP 332. Integrated Ocean Drilling Program Management International, Tokyo. doi:10.2204/iodp.proc.332.101.2011

Faulkner DR, Mitchell TM, Rutter EH, Cembrano J (2008) On the structure and mechanical properties of large strike-slip faults. In: Wibberley CAJ, Kurz W, Imber J, Holdsworth RE, Collettini C (eds) The internal structure of fault zones: implications for mechanical and fluid-flow properties. Geol Soc Lond Spec Publ 299, pp 139–150

Fukao Y (1979) Tsunami earthquakes and subduction processes near deep-sea trenches. J Geophys Res 84:2303–2314

Gamage K, Screaton E (2003) Data report: permeability, compressibility, and friction coefficient measurements under confining pressure and strain, Leg 190, Nankai Trough. Proc ODP Sci Results 190/196:1–22

Garagash DI, Rudnicki JW (2003) Shear heating of a fluid-saturated slip-weakening dilatant fault zone: 2. Quasi-drained regime. J Geophys Res 108:2472. doi:10.1029/2002JB002218

Gartling DK (1977) Convective heat transfer analysis by the finite element method. Computer Methods in Applied Mechanics and Engineering 12:365-382

Gieskes JM, Toshitaka G, Kastner M (1993) Major and minor element geochemistry of interstitial waters of Site 808, Nankai Trough: an overview. In: Hill IA, Taira A, Firth JV et al. (eds) Proc ODP Sci Results 131:387–396

Guo J, Underwood MB, Likos WJ, Saffer DM (2013) Apparent overconsolidation of mudstones in the Kumano Basin of southwest Japan: Implications for fluid pressure and fluid flow within a forearc setting. Geochemistry, Geophysics, Geosystems (in press). doi: 10.1002/ggge.20042

Hamamoto H, Yamano M, Goto S, Kinoshita M, Fujino K, Wang K (2011) Heat flow distribution and thermal structure of the Nankai subduction zone off the Kii Peninsula. Geochem Geophys Geosyst 12:Q0AD20. doi:10.1029/2011GC003623

Hammerschmidt S, Davis EE, Kopf A (2013) Fluid pressure and temperature transients detected at the Nankai Trough Megasplay Fault: results from the SmartPlug Borehole Observatory. Tectonophysics (in press). doi:10.1016/j.tecto.2013.02.010

Hirono T, Ujiie K, Ishikawa T, Mishima T, Hamada Y, Tanimizu M, Soh W, Kinoshita M (2009) Estimation of temperature rise in a shallow slip zone of the Megasplay fault in the Nankai Trough. Tectonophysics 478:215–220

Hsieh PA, Bredehoeft JD, Farr JM (1987) Determination of aquifer transmissivity from Earth tide analysis. Water Resour Res 23:1824–1832

Ichinose GA, Thio HK, Somerville PG, Sato T, Ishii T (2003) Rupture process of the 1944 Tonankai earthquake (M_s 8.1) from the inversion of teleseismic and regional seismograms. J Geophys Res 108:2497. doi:10.1029/2003JB002393

Ikari MJ, Saffer DM (2012) Permeability contrasts between sheared and normally consolidated sediments in the Nankai accretionary prism. Mar Geol 295/298:1–13

Ikari MJ, Saffer DM, Marone C (2009) Frictional and hydrologic properties of a major splay fault system, Nankai subduction zone. Geophys Res Lett 36:L20313. doi:10.1029/2009GL040009

Kastner M, Becker K, Davis EE, Fisher AT, Jannasch HW, Solomon EA, Wheat G (2006) New insights into the hydrogeology of the oceanic crust through long-term monitoring. Oceanography 19:46–57

Kestin J, Khalifa HE, Correia RJ (1981) Tables of the dynamic and kinematic viscosity of aqueous NaCl solutions in the temperature range 20-150 °C and the pressure range 0.1-35 MPa. Journal of Physical and Chemical Reference Data 10: 71-88

Kimura G, Screaton EJ, Curewitz D, Expedition 316 Scientists (2008) NanTroSEIZE Stage 1A: NanTroSEIZE shallow Megasplay and frontal thrusts. IODP Prelim Rep 316. doi:10.2204/iodp.pr.316.2008

Kimura G, Moore GF, Strasser M, Screaton E, Curewitz D, Streiff C, Tobin H (2011) Spatial and temporal evolution of the Megasplay fault in the Nankai Trough. Geochem Geophys Geosyst 12:Q0A008. doi:10.1029/2010GC003335

Kitajima H, Saffer DM (2012) Elevated pore pressure and anomalously low stress in regions of low frequency earthquakes along the Nankai Trough subduction megathrust. Geophys Res Lett 39:L23301. doi:10.1029/2012GL053793

Kitajima H, Chester FM, Biscontin G (2012) Mechanical and hydraulic properties of Nankai accretionary prism sediments: effect of stress path. Geochem Geophys Geosyst 13:Q0AD27. doi:10.1029/2012GC004124

Kopf A, Saffer DM, Davis EE, Hammerschmidt S, LaBonte A, Meldrum R, Toczko S, Lauer R, Heesemann M, Macdonald R, Wheat CG, Jannasch HW, Edwards K, Orcutt B, Haddad A, Villinger H, Araki E, Kitada K, Kimura T, Kido Y (2011) The SmartPlug and GeniusPlug: simple retrievable observatory systems for NanTroSEIZE borehole monitoring. In: Kopf A, Araki E, Toczko S, Expedition 332 Scientists, Proc IODP 332. doi:10.2204/iodp.proc.332.105.2011

Miyazaki S, Heki K (2001) Crustal velocity field of southwest Japan: subduction and arc-arc collision. J Geophys Res 106:4305–4326

Moore JC, Saffer D (2001) Updip limit of the seismogenic zone beneath the accretionary prism of southwest Japan: an effect of diagenetic to low-grade metamorphic processes and increasing effective stress. Geology 29:183–186

Moore GF, Bangs NL, Taira A, Kuramoto S, Pangborn E, Tobin HJ (2007) Three-dimensional splay fault geometry and implications for tsunami generation. Science 318:1128–1131

Moore GF, Park J-O, Bangs NL, Gulick SP, Tobin HJ, Nakamura Y, Sato S, Tsuji T, Yoro T, Tanaka H, Uraki S, Kido Y, Sanada Y, Kuramoto S, Taira A (2009) Structural and seismic stratigraphic framework of the NanTroSEIZE Stage 1 transect. Proc IODP 314/315/316. doi:10.2204/iodp.proc.314315316.102.2009

Moore JC, Barrett M, Thu MK (2012) High fluid pressures and high fluid flow rates in the Megasplay Fault Zone, NanTroSEIZE Kumano Transect, SW Japan. Geochemistry, Geophysics, Geosystems 13: Q0AD25. doi: 10.1029/2012gc004181

Moore GF, Kanagawa K, Strasser M, Dugan B, Maeda L, Toczko S, and the Expedition 338 Scientists (2013a). NanTroSEIZE Stage 3: NanTroSEIZE Plate Boundary Deep Riser IODP Preliminary Report, 338. doi: 10.2204/iodp.pr.338.2013

Moore JC, Barrett M, Thu MK (2013b) Fluid Pressures and Fluid Flows from Boreholes Spanning the NanTroSEIZE Transect through the Nankai Trough, SW Japan. Tectonophysics (in press). doi: 10.1016/j.tecto.2013.01.026

Neuzil CE (1994) How permeable are clays and shales? Water Resour. Res. 30:145 – 150

Park J-O, Tsuru T, Kodaira S, Cummins PR, Kaneda Y (2002) Splay fault branching along the Nankai Subduction Zone. Science 297:1157–1160

Park J-O, Fujie G, Wijerathne L, Hori T, Kodaira S, Fukao Y, Moore GF, Bangs NL, Kuramoto Si, Taira A (2010) A low-velocity zone with weak reflectivity along the Nankai subduction zone. Geology 38:283–286

Rice JR (1992) Fault stress states, pore pressure distributions, and the weakness of the San Andreas Fault. In: Evans B, Wong T-F (eds) Fault mechanics and transport properties of rocks. Academic Press, San Diego, CA, pp 475–503

Rice JR (2006) Heating and weakening of faults during earthquake slip. J Geophys Res 111:B05311. doi:10.1029/2005JB004006

Rowe K, Screaton E, Guo J, Underwood MB (2011) Data report: permeabilities of sediments from the Kumano Basin transect off Kii Peninsula, Japan. In: Kinoshita M, Tobin H, Ashi J, Kimura G, Lallemant S, Screaton EJ, Curewitz D, Masago H, Moe KT, Expedition 314/315/316 Scientists, Proc IODP 314/315/316. Integrated Ocean Drilling Program Management International, Washington, DC. doi:10.2204/iodp.proc.314315316.211.2011

Rowe KT, Screaton EJ, Ge S (2012) Coupled fluid flow and deformation modeling of the frontal thrust region of the Kumano Basin transect, Japan: implications for fluid pressures and décollement downstepping. Geochem Geophys Geosyst 13:Q0AD23. doi:10.1029/2011GC003861

Rudnicki JW, Chen C-H (1988) Stabilization of rapid frictional slip on a weakening fault by dilatant hardening. J Geophys Res 93:4745–4757

Saffer DM, Flemings PB, Boutt D, Doan ML, Ito T, McNeill L, Byrne T, Conin M, Lin W, Kano Y, Araki E, Eguchi N, Toczko S (2013) In Situ Stress and Pore Pressure in the Kumano Forearc Basin, offshore SW Honshu from Downhole Measurements During Riser Drilling. Geochemistry, Geophysics, Geosystems (in press). doi: 10.1002/ggge.20051

Sagiya T, Thatcher W (1999) Coseismic slip resolution along a plate boundary megathrust: the Nankai Trough, southwest Japan. J Geophys Res 104:1111–1129

Sakaguchi A, Chester F, Curewitz D, Fabbri O, Goldsby D, Kimura G, Li C-F, Masaki Y, Screaton EJ, Tsutsumi A, Ujiie K, Yamaguchi A (2011) Seismic slip propagation to the updip end of plate boundary subduction interface faults: vitrinite reflectance geothermometry on Integrated Ocean Drilling Program NanTro SEIZE cores. Geology 39:395–398

Samuelson J, Elsworth D, Marone C (2009) Shear-induced dilatancy of fluid-saturated faults: experiment and theory. J Geophys Res 114:B12404. doi:10.1029/2008JB006273

Samuelson J, Elsworth D, Marone C (2011) Influence of dilatancy on the frictional constitutive behavior of a saturated fault zone under a variety of drainage conditions. J Geophys Res 116:B10406. doi:10.1029/2011JB008556

Satake K (1993) Depth distribution of coseismic slip along the Nankai Trough, Japan, from joint inversion of geodetic and tsunami data. J Geophys Res 98:4553–4565

Sawyer AH, Flemings P, Elsworth D, Kinoshita M (2008) Response of submarine hydrologic monitoring instruments to formation pressure changes: theory and application to Nankai advanced CORKs. J Geophys Res 113:B01102. doi:10.1029/2007JB005132

Scholz CH (1998) Earthquakes and friction laws. Nature 391:37–42

Screaton EJ, Kimura G, Curewitz D, the Expedition 316 Scientists (2009) Expedition 316 Summary. In: Kinoshita M, Tobin H, Ashi J, Kimura G, Lallemant S, Screaton EJ, Curewitz D, Masago H, Moe KT, Expedition 314/315/316 Scientists (eds) Proc IODP 314/315/316. Integrated Ocean Drilling Program Management International, Washington, DC. doi:10.2204/iodp.proc.314315316.131.2009

Segall P, Rice JR (1995) Dilatancy, compaction, and slip instability of a fluid-infiltrated fault. J Geophys Res 100:22155–22171

Segall P, Rice JR (2006) Does shear heating of pore fluid contribute to earthquake nucleation? J Geophys Res 111:B09316. doi:10.1029/2005JB004129

Seno T, Stein S, Gripp AE (1993) A model for the motion of the Philippine Sea plate consistent with NUVEL-1 and geological data. J Geophys Res 98:17941–17948

Sibson RH (1992) Implications of fault-valve behaviour for rupture nucleation and recurrence. Tectonophysics 211:283–293

Solomon EA, Hulme S, Claesson L, Tomaru H, Wheat G, Riedinger N, scientists TE (2008) Geochemical constraints on fluid-rock reactions, fluid sources, and flow pathways along the NanTroSEIZE Transect; IODP Expeditions 315/316. American Geophysical Union, Fall Meeting 2008, abstract #T21F-03

Strasser M, Moore GF, Kimura G, Kitamura Y, Kopf AJ, Lallemant S, Park J-O, Screaton EJ, Su X, Underwood MB, Zhao X (2009) Origin and evolution of a splay fault in the Nankai accretionary wedge. Nature Geosci 2:648–652

Taylor E, Fisher A (1993) Sediment permeability at the Nankai accretionary prism, Site 808. Proc ODP Sci Results 131:235–245

Tobin HJ, Saffer DM (2009) Elevated fluid pressure and extreme mechanical weakness of a plate boundary thrust, Nankai Trough subduction zone. Geology 37:679–682

Tobin H, Kinoshita M, Ashi J, Lallemant S, Kimura G, Screaton E, Moe KT, Masago H, Curewitz D, the Expedition 314/315/316 Scientists (2009) NanTroSEIZE Stage 1 expeditions: introduction and synthesis of key results. In: Kinoshita M, Tobin H, Ashi J, Kimura G, Lallement S, Screaton EJ, Curewitz D, Masago H, Moe KT, Expedition 314/315/316 Scientists (eds) Proc IODP 314/315/316. Integrated Ocean Drilling Program Management International, Tokyo. doi:10.2204/iodp.proc.314315316.101.2009

Toki T, Tsunogai U, Gamo T, Kuramoto S, Ashi J (2004) Detection of low-chloride fluids beneath a cold seep field on the Nankai accretionary wedge off Kumano, south of Japan. Earth Planet Sci Lett 228:37–47

Tsutsumi A, Nishino S, Mizoguchi K, Hirose T, Uehara S, Sato K, Tanikawa W, Shimamoto T (2004) Principal fault zone width and permeability of the active Neodani fault, Nobi fault system, Southwest Japan. Tectonophysics 379:93–108

Underwood MB, Deng X (1997) Clay Mineralogy and Clay Geochemistry in the Vicinity of the Décollement Zone, Northern Barbados Ridge. Proceedings of the Ocean Drilling Program 156:1 - 30

Wang K (2004) Applying fundamental principles and mathematical models to understand processes and estimate parameters. In: Davis E, Elderfield H (eds) Hydrogeology of the oceanic lithosphere. Cambridge University Press, Cambridge, pp 376–413

Wang K, Davis EE (1996) Theory for the propagation of tidally induced pore pressure variations in layered subseafloor formations. J Geophys Res 101:11,483–11,495

Wang K, Davis EE (2003) High permeability of young oceanic crust constrained by thermal and pressure observations. In: Taniguchi M, Wang K, Gamo T (eds) Land and marine hydrogeology. Elsevier, Amsterdam, pp 165–188

Wang K, Hu Y (2006) Accretionary prisms in subduction earthquake cycles: the theory of dynamic Coulomb wedge. J Geophys Res 111:B06410. doi:10.1029/2005JB004094

Wheat CG, Jannasch HW, Kastner M, Hulme S, Cowen J, Edwards K, Orcutt BN, Glazer B (2010) Fluid sampling from oceanic borehole observatories: design and methods for CORK activities (1990-2010). Proc ODP 327. doi:10.2204/iodp.proc.327.109.2011

Wibberley CAJ, Shimamoto T (2003) Internal structure and permeability of major strike-slip fault zones: the Median Tectonic Line in Mie Prefecture, Southwest Japan. J Struct Geol 25:59–78

Wibberley CAJ, Shimamoto T (2005) Earthquake slip weakening and asperities explained by thermal pressurization. Nature 436:689–692

Wibberley CAJ, Yielding G, DiToro G (2008) Recent advances in the understanding of fault zone internal structure: a review. In: Wibberley CAJ, Kurz W, Imber J, Holdsworth RE, Collettini C (eds) The internal structure of fault zones: implications for mechanical and fluid-flow properties. Geol Soc Lond Spec Publ 299, pp 5–33

Yamaguchi A, Sakaguchi A, Sakamoto T, Iijima K, Kameda J, Kimura G, Ujiie K, Chester FM, Fabbri O, Goldsby D, Tsutsumi A, Li C-F, Curewitz D (2011) Progressive illitization in fault gouge caused by seismic slip propagation along a Megasplay fault in the Nankai Trough. Geology 39:995–998

CHAPTER 5.3 – MANUSCRIPT III

BOREHOLE FLUID PRESSURE RESPONSE
TO NON-VOLCANIC TREMOR

Sebastian B. Hammerschmidt[1]*, Earl E. Davis[2], Achim Kopf[1], Eiichrio Araki[3]

ready for submission to

Ocean Science

* corresponding author: shammerschmidt@marum.de

[1] MARUM, University of Bremen, Bremen, Germany

[2] Pacific Geoscience Center, Geological Survey of Canada, Sidney, B.C., Canada

[3] Japan-Agency for Marine-Earth Science and Technology, Yokosuka, Japan

Abstract Fluid pressure changes as proxy for strain can provide valuable information about tectonic processes. In the Nankai Trough accretionary prism, SE Japan, pressure was monitored at a shallow branch of a splay fault using a SmartPlug borehole observatory. The instrument was installed at 370 mbsf in IODP (Integrated Ocean Drilling Program) borehole C0010A. Anomalous pressure transients (APTs) were detected and compared with seismic waveforms from DONET (Dense Ocean Floor Network for Earthquakes and Tsunamis). One non-volcanic tremor episode was found to correspond with one APT on 14 August 2010. The APT resembles oscillations caused by seismic waves from local earthquakes, but has longer periods and higher amplitudes. The latter is attributed to intensification of seismic waves along the splay fault or inside the SmartPlug. Other NVT caused no pressure transients, probably because the induced strain at Site C0010 was either too small ($< 10^{-10}$) or too slow ($< 10^{-10}\,min^{-1}$).

INTRODUCTION

[1] During the last decade, slow earthquakes were repeatedly detected along the thrust faults in the Nankai Trough accretionary prism, SE offshore Japan (Ito and Obara 2006a,b; Obana and Kodaira 2009; Sugioka et al. 2012). The term "slow earthquake" includes non-volcanic tremor (NVT), slow slip events, and very low frequency earthquakes (Ide et al. 2007a; Beroza and Ide 2011; Obara 2011). NVT is composed of a swarm of low-frequency earthquakes (LFE; Shelly et al. 2006, 2007), which are a consequence of shear or plate boundary slip (Brown et al. 2009; Ide et al. 2007a).
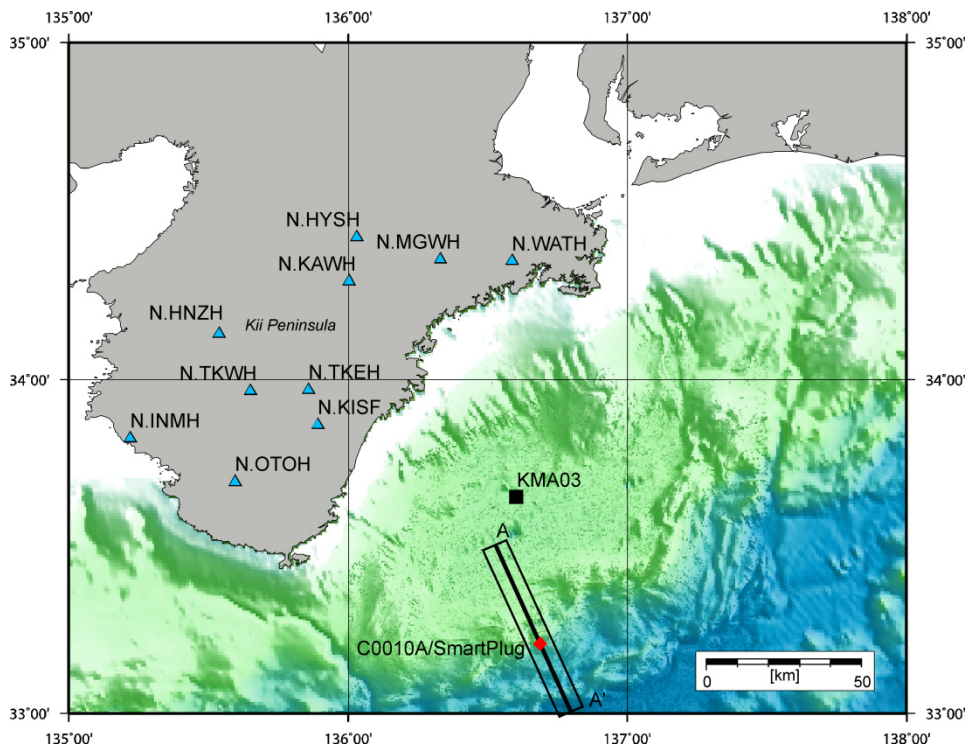
Figure 34: Overview of the study area. The SmartPlug (red diamond) is installed in IODP borehole C0010A, around 50 km SE of DONET station KMA03 (black square). For localization of tremor, additional data from Hi-Net and F-Net stations (blue triangle) onshore Kii Peninsula were used. The profile A-A′ is shown in Fig. 35.

[2] To test if thrust faults in or below the Nankai accretionary complex currently experience slip, a borehole observatory was deployed to conduct *in situ* measurements (Kopf et al. 2011). The

so-called "SmartPlug" monitored in a borehole that was instrumented during Integrated Ocean Drilling Program (IODP) Expedition 319 at Site C0010 (Figures 34, 35) (Expedition 319 Scientists 2010), where a shallow branch of a major out-of-sequence thrust fault, termed "megasplay fault" (Park et al. 2002; Tobin and Kinoshita 2006), is penetrated. Models based on seismic and tsunamigenic inversions suggest that the megasplay may have experienced coseismic slip during the 1944 M_W 8.2 Tonankai earthquake (Cummins et al. 2001; Park et al. 2002; Ichinose et al. 2003; Baba et al. 2006).
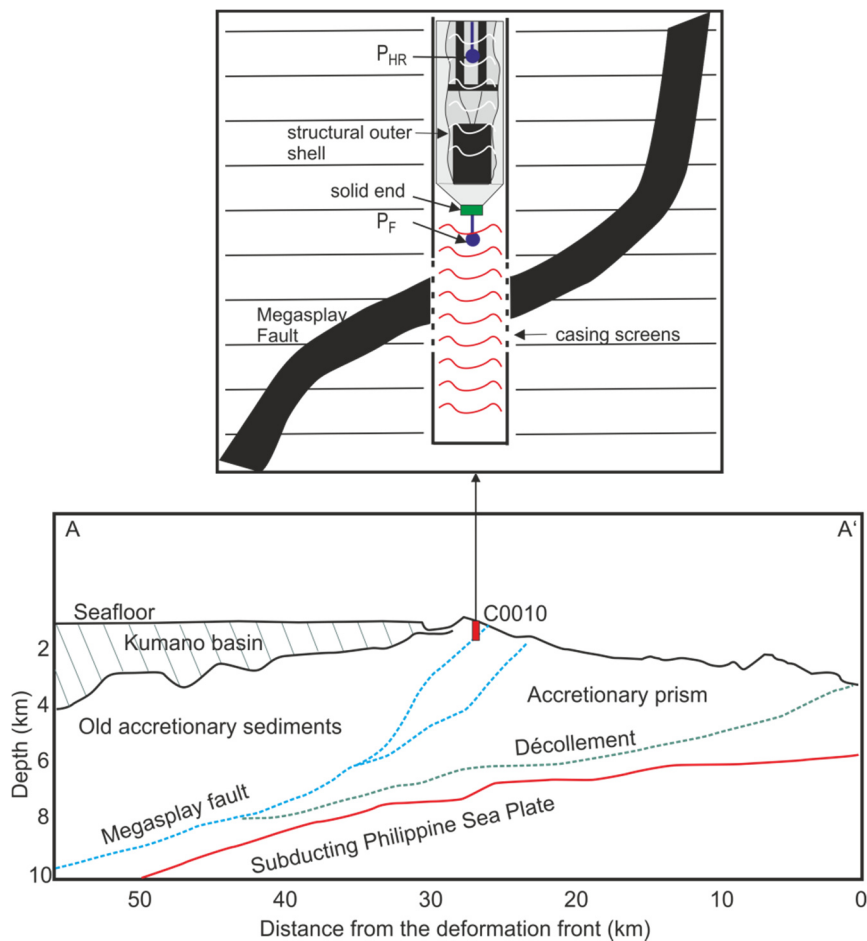
Figure 35: *Cross-section of the frontal part of the Nankai Trough subduction complex (after Moore et al. 2013). Site C0010 is positioned at a shallow branch of the Megasplay fault. The Inlay shows a schematic diagram of the installation and instrument configuration inside Hole C0010A, where it has direct access to the Megasplay fault (modified from Hammerschmidt et al. 2013a). P_{HR}: pressure sensor located in the upper sealed casing interval. P_F: Pressure sensor located in the formation section of the borehole, where fluid exchange between the formation and the borehole is possible via the casing screens.*

[3] Slip at the fault and subsequent deformation of the accretionary prism would result in pressure changes in the formation, which influence the pressure measurements in the borehole. During the monitoring period from August 2009 until October 2010, however, no indications for slip along the splay or underlying thrust boundary fault were found (Hammerschmidt et al. 2013a).

The pressure transients were attributed to the arrival of seismic or tsunami waves and micro-seisms caused by earthquakes and storms, respectively. A small group of anomalous pressure transients (APT) remained, which are unrelated to any obvious seismo-tectonic, meteorological or oceanographic event (Hammerschmidt et al. 2011).

[4] In this article, we further explore mechanisms triggering APTs by comparing them with wave-form data from one station of the Dense Ocean-floor Network for Earthquakes and Tsunamis (DONET) (Kawaguchi et al. 2008). Our results suggest that NVT may be a previously unrecognized cause of fluid pressure transients in marine boreholes.

GEOLOGICAL SETTING

[5] At the Nankai Trough, the Philippine Sea Plate (PSP) subducts beneath the Eurasian Plate with a convergence rate of 4 – 6.5 cm/a and an azimuth of 300° - 315°N (Miyazaki and Heki 2001; Seno et al. 1993) (Figures 34, 35). The splay fault was temporarily active between 1.95 and 1.24 Ma, with a phase of major activity starting at 1.50 Ma (Strasser et al. 2009). Today, the megasplay diverts from the plate boundary décollement ca. 25 km landward of the trench and branches again near the seafloor (Park et al. 2000, 2002; Moore et al. 2007).

[6] At Site C0010, the upper 200 m are characterized by slope apron deposits consisting of silty mudstone with intercalations of sand and minor ash layers. The hanging wall wedge is located between 200 and 410 mbsf (meter below seafloor), consists of a thick pile of fractured mudstone, and is underlain by overthrust slope apron deposits (Expedition 332 Scientists 2011, and references therein). The splay fault was identified in seismic reflection data at around 370 mbsf (Expedition 319 Scientists 2010), at the base of the thrust wedge. Logging-while-drilling (LWD) during IODP Exp. 319 revealed an increase in natural gamma ray radiation and electrical resistivity which is interpreted to correlate with the wedge, accompanied with a drop in LWD-derived porosity of up to 10% (Expedition 319 Scientists 2010). Laboratory friction experiments using samples from ∼260 – 310 mbsf in a shallow branch of the megasplay fault at nearby Site C0004 show that the frictional behavior of the fault material favors aseismic creep, earthquake afterslip, or slow earthquakes (Ikari and Saffer 2011; Ikari et al. 2013).

MATERIALS AND METHODS

The SmartPlug

[7] The SmartPlug is a borehole observatory for implementation in IODP boreholes, which is attached to a Baker Hughes bridge plug. The bridge plug seals off the borehole, creating a confined space where water exchange is solely possible between the formation and the borehole. Fluid pressure is monitored continuously by two Paroscientific pressure transducers, which have

a resolution of 0.7 Pa. One transducer determines formation pressure below the plug via casing screens, which were located at the splay fault. Hydrostatic pressure is sensed in the casing above the plug (Figure 35). Data were recorded at a sampling frequency of 0.017 Hz (i.e. 1 min^{-1}) (Kopf et al. 2011). The instrument was recovered during IODP Exp. 332 (Expedition 332 Scientists 2011), and provides a complete pressure record from August 2009 to October 2010.

Table 7: Overview of the variables used for applying the envelope correlation method

Variables	Definition
dt_i^{obs}	travel time difference between the *i*th station pair
w_i^t	correlation coefficient
dt_i^{calc}	theoretical travel time difference between the *i*th station pair
r_k	theoretical epicentral distance *k*th station
r_i	theoretical epicentral distance *i*th station
V_0	seismic s-wave speed (here: 3500 ms^{-1})

Seismological Networks

[8] The DONET adds to a broad seismological network across Japan, including the Hi-Net and F-Net (Okada et al. 2004). Hi-Net stations consist of onshore three-component high-frequency velocity seismometers, which are placed in a borehole in at least 100 m depth, whereas F-Net stations use broadband seismographs. Suda et al. (2009) developed a system for automatic detection of NVT in SW Japan, the Automatic Tremor Monitoring System (ATMOS) (http://tremor.geol.sci.hiroshima-u.ac.jp/), using the Japanese networks (excl. DONET).

[9] While Hi-net and F-Net are operating onshore, DONET is located in the Kumano forearc basin, offshore Japan (Kawaguchi et al. 2008; Kaneda 2010; Nakano et al. 2013). Five different "science nodes" are connected to an onshore landing station via a backbone cable system. Branching from each node are four different stations. Each station includes a broadband (Guralp CMG-3T, flat velocity response from 100 Hz to 360 s) and a strong-motion seismometer (Metrozet TSA-100S). The seismometers are buried at 1 mbsf to minimize the influence of signals from both artificial (e.g. ships) and natural, non-geologic (e.g. animals) sources.

[10] In this study, the SmartPlug pressure data were compared with data from ATMOS and DONET, which were sampled at 200 Hz per channel. DONET started monitoring on May 2010, thus only data from one station ("KMA03") and for the period from May to October 2010 were available (Figure 34). NVT/LFE were detected by band-pass filtering with a Butterworth filter with cut-off frequencies between 2 – 8 Hz, and by calculating an envelope using a Hilbert transform (Obara et al. 2004; Beroza and Ide 2011).

Localization of Tremor

[11] Localization of NVT/LFE followed the general procedure outlined in previous publications, using the envelope correlation method (ECM) (Obara 2002; Obara et al. 2004; Maeda and Obara 2009; Obana and Kodaira 2009). Data from proximal Hi-Net and F-Net stations were included to improve the localization (Figure 34). In general, the ECM uses the different onset times of the LFE within a defined area. A pre-defined misfit function is minimized (variables are described in Table 7):

$$\sigma_t^2 = \frac{\sum_{i=1}^{M}\{w_t^i(dt_i^{obs} - dt_i^{calc})\}^2}{\sum_{i=1}^{M}(w_i^t dt_i^{obs})^2} \tag{16}$$

where

$$dt_i^{calc} = t_k - t_l = \frac{r_k}{V_0} - \frac{r_l}{V_0} \tag{17}$$

[12] Epicentral distances and theoretical travel times for each station were calculated for a rectangular grid of 0.02° spacing between (33.645°N, 135.645°E) and (34.705°N, 136.720°E). A homogeneous medium with $V_0 = 3500$ ms^{-1} was assumed (Maeda and Obara 2009). If the maximum w_i^t was below 0.7, the travel time difference was disregarded. Detailed information is available in Appendix A.2.

Table 8: *Low frequency earthquakes, which correlate with anomalous pressure transients in the SmartPlug data from 14 August 2010*

ID number	Time Start Pressure UTC [hh:mm:ss]	Time End Pressure UTC [hh:mm:ss]	Max. Amplitude in 2- 8 Hz band in the DONET data [counts/(ms⁻¹)]	explicit positive tremor identification by ATMOS
1	00:23:12	00:25:19	1.17E+13	yes
2	00:31:35	00:33:48	2.09E+13	yes
3	00:43:12	00:46:14	2.80E+13	yes
4	00:51:05	00:52:30	2.74E+13	no
5	00:53:25	00:56:37	2.53E+13	no
6	00:56:37	00:59:49	1.85E+13	no
7	01:01:31	01:03:23	2.57E+13	no
8	01:03:23	01:05:09	1.82E+13	no
9	01:25:36	01:27:23	2.29E+13	no

RESULTS

[13] One prominent APT began on 14 August 2010, lasted for ca. four hours, and cannot be attributed to individual earthquakes (Figure 36). Comparing our data with earthquakes and NVT detected by ATMOS reveals that: (1) the onset of the pressure transients in the SmartPlug and

bursts in the band-pass filtered KMA03 data correlate well with the occurrence of nine LFEs between 00:20 a.m. and 01:30 a.m., of which three correspond to NVT episodes identified by AT-MOS (Table 8), followed by (2) local and regional earthquakes which may have extended the duration of the APT on 14 August 2010 (Figure 36). NVT-related pressure transients have 5 min periods, whereas normal earthquakes are characterized by 3 min periods (Figure 36). Consequently, this is the first successful identification of NVT in pressure data from an instrumented marine borehole.

[14] Although some uncertainties arose due to the weak signals, for all LFE except for events 3 and 8 (Table 8; see supporting information, Figures S.4 – S.12 in Appendix A.2), the ECM led to an epicenter east of F-Net station N.KISF and Hi-Net station N.TKEH, and around 100 km NW of Site C0010 (Figure 37).

[15] Assuming that NVT is related to slow slip along the plate boundary megathrust (Ide et al. 2007a), and following previous estimations of the hypocenter for NVT (e.g., Ide et al. 2007b; Katayama et al. 2012; Katsumata and Kamaya 2003; Obara 2002), normal earthquakes located SE of the Kii Peninsula (e.g. Shiomi et al. 2008) and the depth distribution of the surface of the subducting PSP (Baba et al. 2002, 2006), the hypocenter is most likely located between 25 and 30 km depth.

DISCUSSION

[16] Recent publications related step-like transients in borehole pressure to strain caused by normal (Davis et al. 2009; Hammerschmidt et al. 2013a) and by VLF earthquakes (Davis et al. 2006, 2013; Walter et al. 2013). Strain triggered by slip along the fault should result in a similar anomaly in the SmartPlug data. For Nankai, this assumption is assessed using a simple first-order model for faulting-related deformation (Cohen 1996, 1999) (Figure 38A). The model assumes crustal deformation following a uniform slip of 10 cm on a rectangular fault patch at a depth of 30 km and a dip of 40° (Saiga et al. 2013) in a homogenous elastic half space, leading to strain of ca. 0.5×10^{-7} (Figure 38A; see also section "*First Order Modeling of Crustal Deformation*" in Appendix A.2). Given a strain sensitivity of 6 kPa μstrain^{-1} for the formation (Hammerschmidt et al. 2013b) and the position of Hole C0010A, a pressure transient of ca. 3 kPa is expected in our pressure data. However, this value was never exceeded.

[17] The absence of a large pressure transient suggests seismic waves to be responsible, and that seismo-tectonic deformation at the borehole is insignificant. Surprisingly, contrary to the signals found in KMA03 data (Figure 36), the pressure transients are larger than anomalies caused by normal earthquakes. This could be related to a fault-guiding effect leading to signals of higher intensity (Ben-Zion et al. 2003; Calderoni et al. 2010). For example, recent findings by Lupi et al.

(2013) indicated that trapped S-waves increased seismic energies in faults beneath a mud volcano. At Nankai, entrapment at the splay fault is supported by low-velocity zones at shallow parts of the megasplay fault (Park et al. 2010; Figure 1b in Kitajima and Saffer 2012), and amplification inside the fault zone is further enhanced due to non-linear effects of the low-strain seismic waves (Karabulut and Bouchon 2007). Alternatively, refraction of incoming seismic waves at the casing and subsequent generation and amplification of wave modes inside the borehole (Paillet and Cheng 1991) might also be responsible.

Table 9: *Variables for calculating the minimum strain rate necessary to cause fluid pressure transients at Site C0010 (based on Hammerschmidt et al. 2013b)*

Variable	Description	Value
β	matrix compressibiliy [Pa-1]	1.0×10^{-9}
β_w	water compressibility [Pa^{-1}]	4.0×10^{-10}
β_s	grain compressibility [Pa^{-1}]	2.0×10^{-11}
v	Poisson's Ratio	0.4
ρ_w	density of seawater [kg/m^3]	1025
ρ_b	average density of bulk rock [kg/m^3]	2650
k	intrinsic permeability [m^2]	2.1×10^{-17}
H	max. crustal thickness involved in thrusting [m]	4000
g	acceleration due to gravity [m/s2]	9.81
μ	dynamic viscosity [Pa s]	1.2×10-3

[18] It remains unclear why other NVT/LFE were undetected by the SmartPlug (for examples, see section "*Relationship Distance – Pressure Transients*" in Appendix A.2), similar to the selective manifestation of common earthquakes in the pressure data (Hammerschmidt et al. 2013a). We quantitatively address this issue by defining threshold values for (i) strain at the borehole and (ii) the seismic energy density *e*:

(i)   Strain θ is assessed using a strain sensitivity S_f of 6 kPa μstrain^{-1} for the formation, which is based on the Skempton coefficient and formation properties provided by Hammerschmidt et al. (2013b) (see Table 9). Our results are shown in Fig. 38B and suggest that minimum strain of 10^{-10} is required to cause pressure transients > 0.7 Pa, i.e. above the pressure sensors' resolution (Figure 38B). A strain rate θ_T is defined following Cello and Deiana (1995)(see Table 9 for variables):

$$\theta_T = -\frac{kg\,(\rho_g - \rho_f)}{\mu H}\left[2(\beta - \frac{\beta_S}{\beta_W})\frac{(1 - 2v)}{(1 - v)}\right]^{-1} \tag{18}$$

5.3 Borehole Fluid Pressure Response to Non-volcanic Tremor
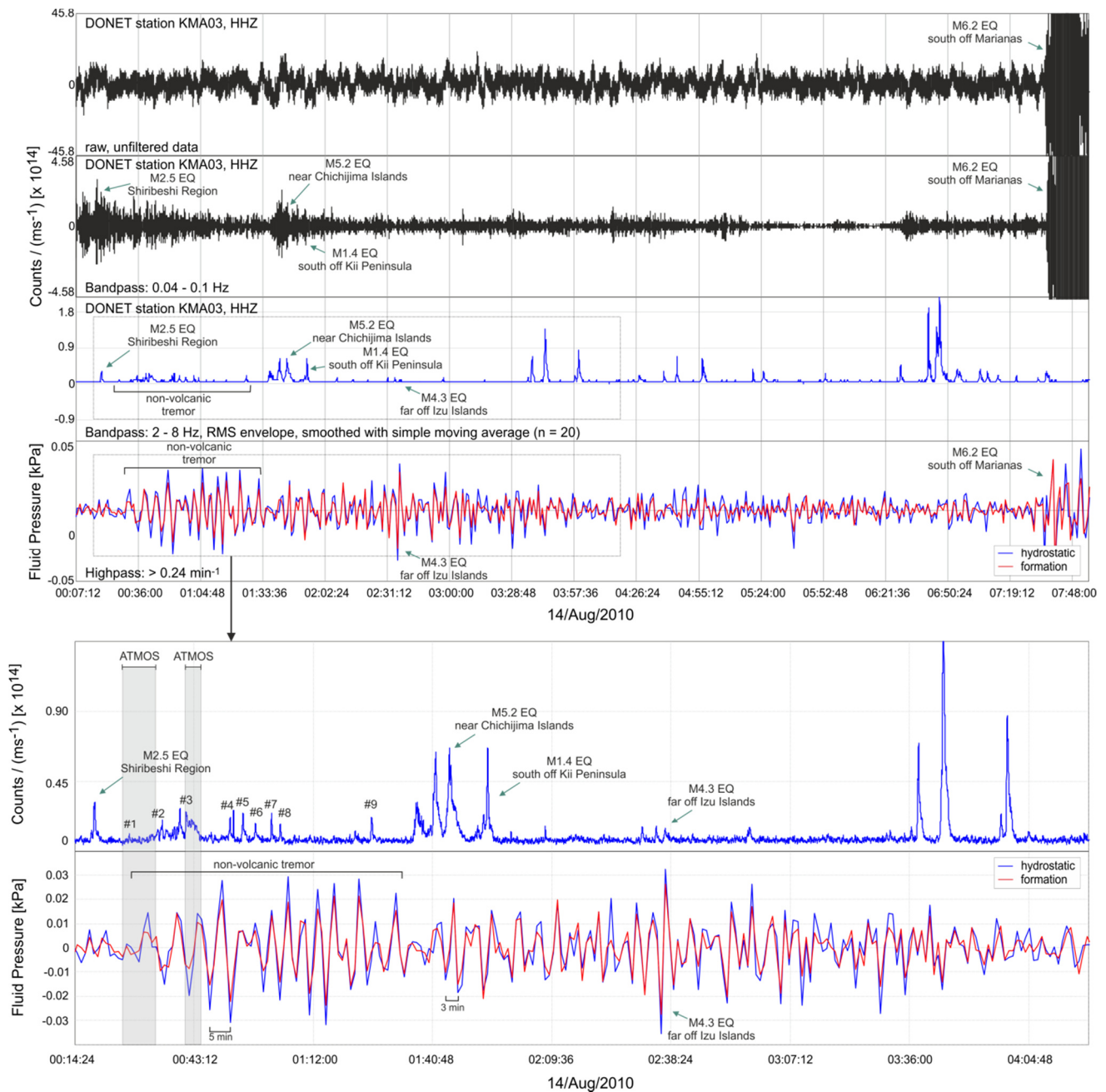
Figure 36: *Overview of data from DONET station KMA03 and the SmartPlug from the first 8 hours on 14 August 2010. The upper panel shows the unfiltered DONET data, followed by the same data band-pass filtered between 0.04 and 0.1 Hz and as root-mean-square envelope band-pass filtered between 2 and 8 Hz. The fourth panel displays SmartPlug pressure data, where a large APT is visible between ca. 00:20 a.m. and 03:50 a.m.. Considering the DONET data and the Hi-Net catalogue, it becomes clear that the APT falls in a period of several smaller regional and local earthquakes. The onset, however, corresponds with increased non-volcanic tremor, and lasts until ca. 01:30 a.m.. The inlay highlights the APTs which correspond to NVT. In total, nine different tremor bursts were identified and localized. Grey boxes indicate the time intervals where NVT was detected by ATMOS. During the tremor, the pressure amplitudes have 5 min-periods, whereas normal earthquakes cause only 3 min-periods. See text for further explanations.*

5.3 Borehole Fluid Pressure Response to Non-volcanic Tremor
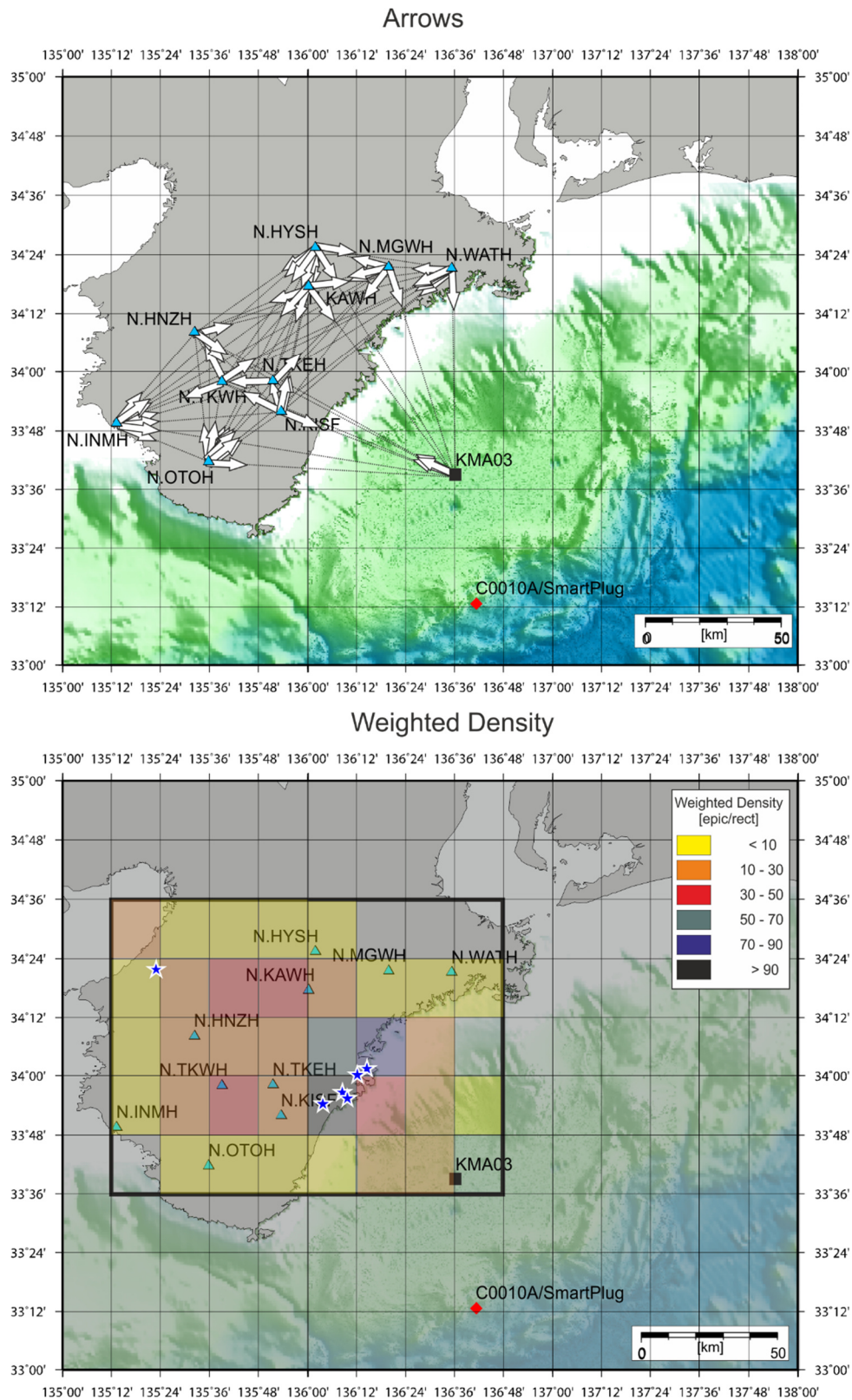
Figure 37: *Summary plot for the localization of tremor between ca. 00:20 a.m. and 1:30 a.m. on 14 August 2010.* **Upper panel:** *Arrows are drawn for each station pair, and point to the station where the tremor signal arrived first.* **Lower panel:** *Colored rectangles denote the weighted density ρ_w based on the number of successful epicenter determinations ≥ 3 between different station pairs. The higher ρ_w, the higher the number of epicenters per rectangle. For simplicity, only successful correlations ≥ 5 are shown (blue stars). The localization points clearly to an epicenter east of stations N.KISF and N.TKEH, around 100 km NW of the SmartPlug (red diamond). Black square shows the position of DONET station KMA03, whereas the Hi- and F-Net stations used for the localization are drawn with blue triangles. See text for further explanations.*

Assuming a constant temperature gives a minimum threshold of ca. 10^{-10} min^{-1}, which corresponds to a pressure rate of 0.76 Pa min^{-1} (i.e. close to the sensitivity of the pressure sensors: 0.7 Pa).

(ii)   Following the empirical relationship published by Wang (2007) and Wang and Manga (2010), seismic energy density e is related to magnitude M and distance D by

$$\log D = 0.48M - 0.33 \log e - 1.4 \tag{19}$$

Table S.3 in Appendix A.2 shows e for pressure transients induced by seismic waves from normal earthquakes. Applying equation (19) results in a threshold value of $e \geq 10^{-7}$ J m^{-3}. Solving equation (19) for M with $D = 100$ km and $e = 10^{-7}$ J m^{-3}, we assume that earthquakes of $M \geq 1.4$ are necessary to induce pressure transients.

[19] Consequently, we suggest that previous LFE had M < 1.4, or that NVT- or seismic wave-induced strain was too weak ($\theta < 10^{-10}$) and/or too slow ($\theta_T < 10^{-10}$ min^{-1}) to be detected by the pressure sensors. Even if these values could be exceeded, shear wave anisotropy close to a LFE-generating zone beneath the Kii Peninsula (Saiga et al. 2013) could favor attenuation of the seismic waves.

[20] The absence of any tectonic signal like those observed SE offshore Shikoku (Davis et al. 2013) could also imply stress accumulation in deeper portions of the thrust-boundary fault. Low energy release by weak slow slip at around 25 – 30 km depth and along one fault patch of the thrust boundary fault (Ide et al. 2007a; Shelly 2010) would hinder slip propagation into neighboring fault patches updip and subsequently, stress build-up in deeper portions of the seismogenic zone is possible.

CONCLUSIONS

[21] One APT, which occurred on 14 August 2010, corresponds with NVT located close to the SE coast of the Kii Peninsula. This is the first successful observation of NVT in an offshore borehole instrumented with a borehole observatory. The pressure transients have larger periods and similar amplitudes compared to pressure transients related to seismic waves radiated by common earthquakes. This may be explained by trapping and amplification of seismic waves inside the fault zone and/or the borehole itself. The absence of other LFE implies that the earthquakes were too weak or that the strain rate was too slow. Alternatively, slow slip did not propagate beyond the deeper portion of the plate boundary megathrust, possibly contributing to stress accumulation in the seismogenic zone.

5.3 Borehole Fluid Pressure Response to Non-volcanic Tremor
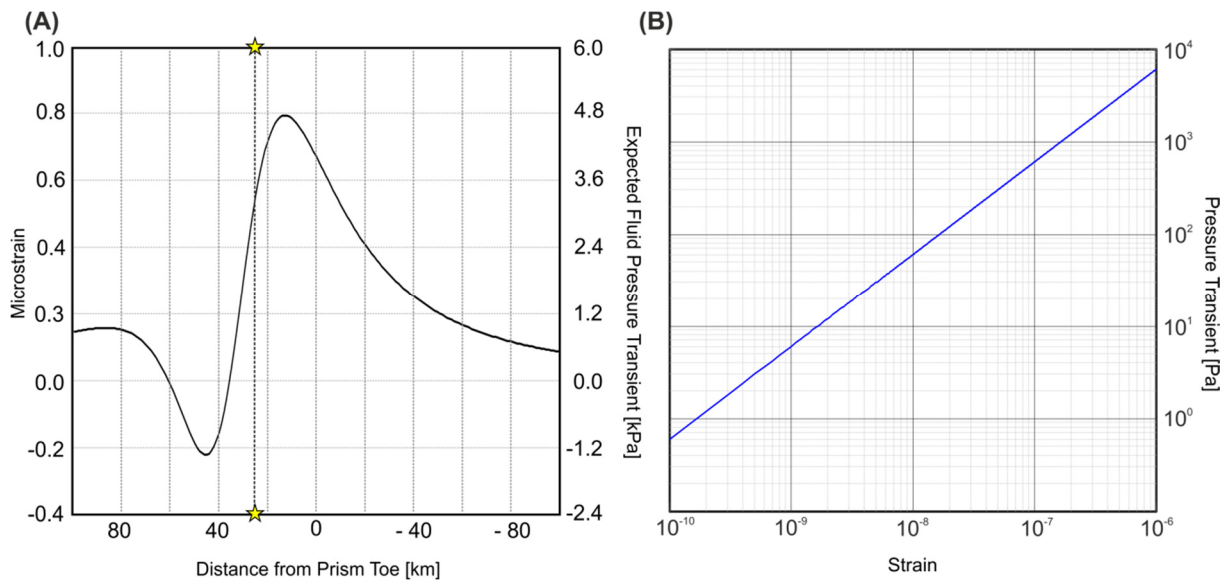
Figure 38: ***(A)*** *Simple first-order model for faulting-related deformation (based on Cohen 1996, 1999). Positive and negative x-values mark the landward and seaward distance from the prism toe, respectively. The stars indicate the position of the SmartPlug in relation to the prism toe. A slip of 10 cm at around 30 km depth and at a dip angle of 40° should already cause pressure transients of ca. 3 kPa. See text for further explanations.* ***(B)*** *Strain-pressure relationship based on a constant strain sensitivity for the formation of 6 kPa μstrain^{-1} (based on Hammerschmidt et al. 2013b). Strain of 10^{-10} still leads to pressure transients above the pressure sensor resolution of 0.7 Pa.*

References

Baba T, Tanioka Y, Cummins PR, Uhira K (2002) The slip distribution of the 1946 Nankai earthquake estimated from tsunami inversion using a new plate model. Phys Earth Planet Inter 132:59–73. doi: 10.1016/S0031-9201(02)00044-4

Baba T, Cummins PR, Hori T, Kaneda Y (2006) High precision slip distribution of the 1944 Tonankai earthquake inferred from tsunami waveforms: Possible slip on a splay fault. Tectonophysics 426:119–134. doi: 10.1016/j.tecto.2006.02.015

Ben-Zion Y, Peng Z, Okaya D, Seeber L, Armbruster JG, Ozer N, Michael AJ, Baris S, Aktar M (2003) A shallow fault-zone structure illuminated by trapped waves in the Karadere–Duzce branch of the North Anatolian Fault, western Turkey. Geophys J Int 152:699–717. doi: 10.1046/j.1365-246X.2003.01870.x

Beroza GC, Ide S (2011) Slow Earthquakes and Nonvolcanic Tremor. Annu Rev Earth Planet Sci 39:271–296. doi: doi:10.1146/annurev-earth-040809-152531

Brown JR, Beroza GC, Ide S, Ohta K, Shelly DR, Schwartz SY, Rabbel W, Thorwart M, Kao H (2009) Deep low-frequency earthquakes in tremor localize to the plate interface in multiple subduction zones. Geophys Res Lett 36:L19306. doi: 10.1029/2009GL040027

Calderoni G, Rovelli A, Di Giovambattista R (2010) Large amplitude variations recorded by an on-fault seismological station during the L'Aquila earthquakes: Evidence for a complex fault-induced site effect. Geophys Res Lett 37:L24305. doi: 10.1029/2010GL045697

Cello G, Deiana G (1995) Role and effects of pore fluid pressure in thrusting : The case history of the Umbria-Marche Apennines, central Italy. Tectonics 14:848–854.

Cohen SC (1996) Convenient Formulas for Determining Dip-Slip Fault Parameters from Geophysical Observables. Bull Seismol Soc Am 86:1642–1644.

Cohen SC (1999) Numerical Models of Crustal Deformation in Seismic Zones. Adv Geophys 41:133 – 231.

Cummins PR, Hori T, Kaneda Y (2001) Splay fault and megathrust earthquake slip in the Nankai Trough. Earth Planets Sp 53:243–248.

Davis EE, Becker K, Wang K, Obara K, Ito Y, Kinoshita M (2006) A discrete episode of seismic and aseismic deformation of the Nankai trough subduction zone accretionary prism and incoming Philippine Sea plate. Earth Planet Sci Lett 242:73–84.

Davis EE, Becker K, Wang K, Kinoshita M (2009) Co-seismic and post-seismic pore-fluid pressure changes in the Philippine Sea plate and Nankai decollement in response to a seismogenic strain event off Kii Peninsula, Japan. Earth, Planets Sp 61:649 – 657.

Davis E, Kinoshita M, Becker K, Wang K, Asano Y, Ito Y (2013) Episodic deformation and inferred slow slip at the Nankai subduction zone during the first decade of CORK borehole pressure and VLFE monitoring. Earth Planet Sci Lett 368:110–118. doi: http://dx.doi.org/10.1016/j.epsl.2013.03.009

Expedition 319 Scientists (2010) Site C0010. In: Saffer D, McNeill L, Byrne T, Araki E, Toczko S, Eguchi N, Takahashi K, Expedition 319 Scientists (eds) Proc IODP 319. Integrated Ocean Drilling Program Management International, Tokyo. doi:10.2204/iodp.proc.319.104.2010

Expedition 332 Scientists (2011) Expedition 332 summary. In: Kopf A, Araki E, Toczko S, Expedition 332 Scientists (eds) Proc IODP 332. Integrated Ocean Drilling Program Management International, Tokyo. doi:10.2204/iodp.proc.332.101.2011

Hammerschmidt S, Kopf A, the Expedition 332 Scientists (2011) Fluid Pressure and Temperature Response at the Nankai Trough Megasplay Fault: Initial Results of the SmartPlug Borehole Observatory. Poster presented at the AGU Fall Meeting, San Francisco, CA, abstract# OS11A-1456

Hammerschmidt S, Davis EE, Kopf A (2013a) Fluid pressure and temperature transients detected at the Nankai Trough Megasplay Fault: Results from the SmartPlug borehole observatory. Tectonophysics 600:116 – 133. doi: 10.1016/j.tecto.2013.02.010

Hammerschmidt SB, Davis EE, Hüpers A, Kopf A (2013b) Limitation of fluid flow at the Nankai Trough megasplay fault zone. Geo-Marine Lett 33:405–418. doi: 10.1007/s00367-013-0337-z

Ichinose GA, Thio HK, Somerville PG, Sato T, Ishii T (2003) Rupture process of the 1944 Tonankai earthquake (M s 8.1) from the inversion of teleseismic and regional seismograms. J Geophys Res 108:2497. doi: 10.1029/2003jb002393

Ide S, Shelly DR, Beroza GC (2007a) Mechanism of deep low frequency earthquakes: Further evidence that deep non-volcanic tremor is generated by shear slip on the plate interface. Geophys Res Lett 34:L03308. doi: 10.1029/2006GL028890

Ide S, Beroza GC, Shelly DR, Uchide T (2007b) A scaling law for slow earthquakes. Nature 447:76–79.

Ikari MJ, Saffer DM (2011) Comparison of frictional strength and velocity dependence between fault zones in the Nankai accretionary complex. Geochem Geophys Geosyst 12:Q0AD11. doi: 10.1029/2010gc003442

Ikari MJ, Marone C, Saffer DM, Kopf AJ (2013) Slip weakening as a mechanism for slow earthquakes. Nat Geosci 6:468–472.

Ito Y, Obara K (2006a) Very low frequency earthquakes within accretionary prisms are very low stress-drop earthquakes. Geophys Res Lett 33:L09302. doi: 10.1029/2006gl025883

Ito Y, Obara K (2006b) Dynamic deformation of the accretionary prism excites very low frequency earthquakes. Geophys Res Lett 33:L02311. doi: 10.1029/2005gl025270

Kaneda Y (2010) The advanced ocean floor real time monitoring system for mega thrust earthquakes and tsunamis-application of DONET and DONET2 data to seismological research and disaster mitigation. Ocean. 2010. pp 1–6

Karabulut H, Bouchon M (2007) Spatial variability and non-linearity of strong ground motion near a fault. Geophys J Int 170:262–274. doi: 10.1111/j.1365-246X.2007.03406.x

Katayama I, Terada T, Okazaki K, Tanikawa W (2012) Episodic tremor and slow slip potentially linked to permeability contrasts at the Moho. Nat Geosci 5:731–734.

Katsumata A, Kamaya N (2003) Low-frequency continuous tremor around the Moho discontinuity away from volcanoes in the southwest Japan. Geophys Res Lett 30:1020. doi: 10.1029/2002GL015981

Kawaguchi K, Kaneda Y, Araki E (2008) The DONET: A real-time seafloor research infrastructure for the precise earthquake and tsunami monitoring. Ocean. 2008 - MTS/IEEE Kobe Techno-Ocean. pp 1–4

Kitajima H, Saffer DM (2012) Elevated pore pressure and anomalously low stress in regions of low frequency earthquakes along the Nankai Trough subduction megathrust. Geophys Res Lett 39:L23301. doi: 10.1029/2012GL053793

Kopf A, Saffer DM, Davis EE, Hammerschmidt S, LaBonte A, Meldrum R, Toczko S, Lauer R, Heesemann M, Macdonald R, Wheat CG, Jannasch HW, Edwards K, Orcutt B, Haddad A, Villinger H, Araki E, Kitada K, Kimura T, Kido Y (2011) The SmartPlug and GeniusPlug: simple retrievable observatory systems for NanTroSEIZE borehole monitoring. In: Kopf A, Araki E, Toczko S, Expedition 332 Scientists, Proc IODP 332. doi:10.2204/iodp.proc.332.105.2011

Lupi M, Saenger EH, Fuchs F, Miller SA (2013) Lusi mud eruption triggered by geometric focusing of seismic waves. Nat Geosci 6:642–646.

Maeda T, Obara K (2009) Spatiotemporal distribution of seismic energy radiation from low-frequency tremor in western Shikoku, Japan. J Geophys Res Solid Earth 114:B00A09. doi: 10.1029/2008JB006043

Miyazaki S, Heki K (2001) Crustal velocity field of southwest Japan: Subduction and arc-arc collision. J Geophys Res 106:4305–4326. doi: 10.1029/2000jb900312

Moore GF, Bangs NL, Taira A, Kuramoto S, Pangborn E, Tobin HJ (2007) Three-Dimensional Splay Fault Geometry and Implications for Tsunami Generation. Science 318:1128–1131. doi: 10.1126/science.1147195

Moore GF, Kanagawa K, Strasser M, Dugan B, Maeda L, Toczko S, and the Expedition 338 Scientists (2013). NanTroSEIZE Stage 3: NanTroSEIZE Plate Boundary Deep Riser, IODP Prel Rep, 338. doi: 10.2204/iodp.pr.338.2013.

Nakano M, Nakamura T, Kamiya S, Ohori M, Kaneda Y (2013) Intensive seismic activity around the Nankai trough revealed by DONET ocean-floor seismic observations. Earth Planets Sp 65:5 – 15.

Obana K, Kodaira S (2009) Low-frequency tremors associated with reverse faults in a shallow accretionary prism. Earth Planet Sci Lett 287:168–174.

Obara K (2002) Nonvolcanic Deep Tremor Associated with Subduction in Southwest Japan. Science 296:1679–1681. doi: 10.1126/science.1070378

Obara K, Hirose H, Yamamizu F, Kasahara K (2004) Episodic slow slip events accompanied by non-volcanic tremors in southwest Japan subduction zone. Geophys Res Lett 31:L23602. doi: 10.1029/2004gl020848

Obara K (2011) Characteristics and interactions between non-volcanic tremor and related slow earthquakes in the Nankai subduction zone, southwest Japan. J Geodyn 52:229–248. doi: 10.1016/j.jog.2011.04.002

Okada Y, Kasahara K, Hori S, Obara K, Sekiguchi S, Fujiwara H, Yamamoto A (2004) Recent progress of seismic observation networks in Japan: Hi-net, F-net, K-NET and KiK-net. Earth Planets Sp 56:15–28.

Paillet FL, Cheng CH (1991) Acoustic Waves in Boreholes. 264.

Park J-O, Tsuru T, Kodaira S, Nakanishi A, Miura S, Kaneda Y, Kono Y, Takahashi N (2000) Out-of-sequence thrust faults developed in the coseismic slip zone of the 1946 Nankai Earthquake (Mw=8.2) off Shikoku, southwest Japan. Geophys Res Lett 27:1033–1036. doi: 10.1029/1999GL008443

Park J-O, Tsuru T, Kodaira S, Cummins PR, Kaneda Y (2002) Splay Fault Branching Along the Nankai Subduction Zone. Science 297:1157–1160. doi: 10.1126/science.1074111

Park J-O, Fujie G, Wijerathne L, Hori T, Kodaira S, Fukao Y, Moore GF, Bangs NL, Kuramoto S, Taira A (2010) A low-velocity zone with weak reflectivity along the Nankai subduction zone. Geology 38:283–286. doi: 10.1130/g30205.1

Saiga A, Kato A, Kurashimo E, Iidaka T, Okubo M, Tsumura N, Iwasaki T, Sakai S, Hirata N (2013) Anisotropic structures of oceanic slab and mantle wedge in a deep low-frequency tremor zone beneath the Kii Peninsula, SW Japan. J Geophys Res Solid Earth 118:1091–1097. doi: 10.1002/jgrb.50069

Seno T, Stein S, Gripp AE (1993) A model for the motion of the Philippine Sea plate consistent with NUVEL-1 and geological data. J Geophys Res 98:17941–17948.

Shelly DR (2010) Migrating tremors illuminate complex deformation beneath the seismogenic San Andreas fault. Nature 463:648–652.

Shelly DR, Beroza GC, Ide S (2007) Non-volcanic tremor and low-frequency earthquake swarms. Nature 446:305–307.

Shelly DR, Beroza GC, Ide S, Nakamula S (2006) Low-frequency earthquakes in Shikoku, Japan, and their relationship to episodic tremor and slip. Nature 442:188–191.

Shiomi K, Matsubara M, Ito Y, Obara K (2008) Simple relationship between seismic activity along Philippine Sea slab and geometry of oceanic Moho beneath southwest Japan. Geophys J Int 173:1018–1029. doi: 10.1111/j.1365-246X.2008.03786.x

Strasser M, Moore GF, Kimura G, Kitamura Y, Kopf AJ, Lallemant S, Park J-O, Screaton EJ, Su X, Underwood MB, Zhao X (2009) Origin and evolution of a splay fault in the Nankai accretionary wedge. Nat Geosci 2:648–652.

Suda N, Nakata R, Kusumi T (2009) An automatic monitoring system for nonvolcanic tremors in southwest Japan. J Geophys Res Solid Earth 114:B00A10. doi: 10.1029/2008JB006060

Sugioka H, Okamoto T, Nakamura T, Ishihara Y, Ito A, Obana K, Kinoshita M, Nakahigashi K, Shinohara M, Fukao Y (2012) Tsunamigenic potential of the shallow subduction plate boundary inferred from slow seismic slip. Nat Geosci 5:414–418.

Tobin HJ, Kinoshita M (2006) NanTroSEIZE: The IODP Nankai Trough Seismogenic Zone Experiment. Sci Drill 2:23–27. doi: 10.2204/iodp.sd.2.06.2006

Walter JI, Schwartz SY, Protti M, Gonzalez V (2013) The synchronous occurrence of shallow tremor and very low frequency earthquakes offshore of the Nicoya Peninsula, Costa Rica. Geophys Res Lett 40:1517–1522. doi: 10.1002/grl.50213

Wang C-Y (2007) Liquefaction beyond the Near Field. Seismol Res Lett 78 :512–517. doi: 10.1785/gssrl.78.5.512

Wang C-Y, Manga M (2010) Hydrologic responses to earthquakes and a general metric. Geofluids 10:206–216. doi: 10.1111/j.1468-8123.2009.00270.x

Wessel P, Smith WHF (1991) Free software helps map and display data. Eos Trans AGU 72:441 – 446.

CHAPTER 5.4 – MANUSCRIPT IV

BOREHOLE FLUID PRESSURE ARTIFACTS STIMULATED BY SEISMIC WAVES

Sebastian B. Hammerschmidt[1]*, Earl E. Davis[2], Achim Kopf[1], Eiichrio Araki[3]

ready for submission to

Geoscience Letters

* corresponding author: shammerschmidt@marum.de

[1] MARUM, University of Bremen, Bremen, Germany

[2] Pacific Geoscience Center, Geological Survey of Canada, Sidney, B.C., Canada

[3] Japan-Agency for Marine-Earth Science and Technology, Yokosuka, Japan

Abstract Fluid pressure data is easily influenced by tidal, oceanographic, seismo-tectonic and atmospheric processes. Here we report data from a SmartPlug long-term borehole observatory that was installed in IODP (Integrated Ocean Drilling Program) borehole C0010A at the Nankai Trough, SE offshore Japan. The SmartPlug monitored a shallow branch of an out-of-sequence splay fault at ca. 370 mbsf from August 2009 to October 2010. We observe anomalous pressure transients (APTs) in the de-tided and filtered data, which we compared with seismic waveforms from the DONET (Dense Ocean Floor Network for Earthquakes and Tsunamis). We found that: (i) discrete APTs, which are only present in the upper sealed casing interval of the borehole, correlate with the arrival of seismic waves from local, regional and distant earthquakes. The distinct APTs are interpreted to be caused by seismic wave propagation in the cased part of the borehole, and varying attenuation in different levels of the borehole. (ii) APTs which have durations on the order of hours to days correlate well with waveform data from DONET. Power spectral density analyses point to teleseismic microseism caused by distant storms to be responsible. The low sampling frequency of the SmartPlug precludes a thorough analysis of the seismic wave modes, but allows a clear distinction between atmospheric, seismo-tectonic and tidal phenomena.

INTRODUCTION

[1] The Nankai Trough subduction zone, SE offshore Japan, repeatedly hosts a wide variety of earthquakes (e.g. Ando 1975; Obara 2002; Sugioka et al. 2012). Borehole observatories located in the Nankai Trough accretionary prism and the incoming Philippine Sea Plate were able to observe the subsequent deformation and stepwise pressure changes of several kPa in the formation (cf. Davis et al. 2006, 2009, 2013). Coseismic activity of a major out-of-sequence thrust fault cutting through the accretionary prism ("Megasplay" fault; Park et al. 2002; Tobin and Kinoshita 2006), e.g. during the 1944 M_W 8.2 Tonankai earthquake, is further indicated by tsunami and seismic waveform inversion (Cummins et al. 2001; Park et al. 2002; Ichinose et al. 2003; Baba et al. 2006). In order to test if the Megasplay fault experiences slip, in situ observations were conducted using a temporary borehole observatory termed "SmartPlug" (Kopf et al. 2011). The SmartPlug monitored a borehole that was drilled and instrumented during Integrated Ocean Drilling Program (IODP) Expedition 319 at Site C0010 (Figures 39, 40) (Expedition 319 Scientists 2010), where a shallow branch of the Megasplay fault is penetrated.

[2] During the monitoring period from August 2009 – October 2010, no indications for co-seismic or aseismic slip along the splay or underlying thrust boundary fault were found (Hammerschmidt et al. 2013a). Most of the pressure transients can be attributed to the arrival of seismic or tsunami waves radiated by regional or distant earthquakes, and microseisms excited by local storms. In general, seismic waves lead to expansion/contraction of the formation matrix, and cause dynamic pressure changes (e.g. Cooper et al. 1965; Wang and Davis 1996; Woodcock and Roeloffs 1996; Roeloffs 1998; Brodsky et al. 2003; Kano and Yanagidani 2006). By conrast, microseism is generated by opposing oceanic waves of the same wavelength generated during storms or by swell (Longuet-Higgins 1950). The subsequent generation of standing waves causes a pressure anomaly at the seafloor, where several acoustic phases are excited (Ardhuin and Herbers 2013).
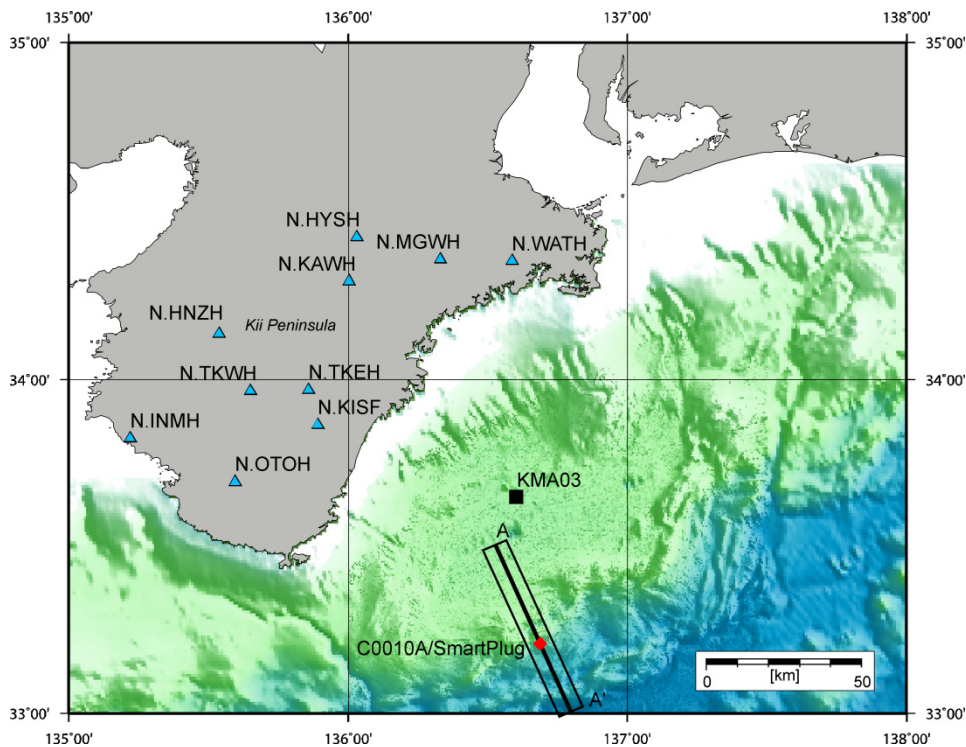
Figure 39*: Location of the SmartPlug (red diamond), SE offshore the Kii Peninsula, Japan (cf. chapter 5.3). The instrument is installed in IODP borehole C0010A, around 50 km SE of DONET station KMA03 (black square). The box indicates the location of the profile shown in Fig. 40.*

[3] Understanding what mechanisms lead to dynamic fluid pressure perturbations is essential, because dynamic transients can influence fault zone permeability and fault behaviour during slip (e.g. Scholz 1998; Elkhoury 2006, 2011; Miyazawa and Brodsky 2008; Rubinstein et al. 2008). One anomalous pressure transient (APT) was already attributed to episodic tremor and slip (cf. chapter 5.3), while the other APT were initially interpreted as artefacts (Hammerschmidt et al. 2011). In this article, we further investigated the origin of the APTs by including data from the Dense Ocean-floor Network for Earthquakes and Tsunamis (DONET) (Kawaguchi et al. 2008). Our results suggest that APTs are caused by microseism from distant storms, and seismic wave refraction, amplification and attenuation inside the borehole.

GEOLOGICAL SETTING

[4] The Nankai Trough subduction zone was initiated around 15 Ma, when the Philippine Sea Plate (PSP) started to subduct beneath the Eurasian Plate (Taira 2001). Nowadays, subduction occurs with 4 – 6.5 cm/a and an azimuth of 300° - 315°N (Seno et al. 1993; Miyazaki and Heki 2001) (Figures 39, 40). The incoming part of the PSP includes the ca. 23 Ma old Shikoku Basin which is filled mainly by hemipelagic sediments (Okino et al. 1999; Marcaillou et al. 2012).
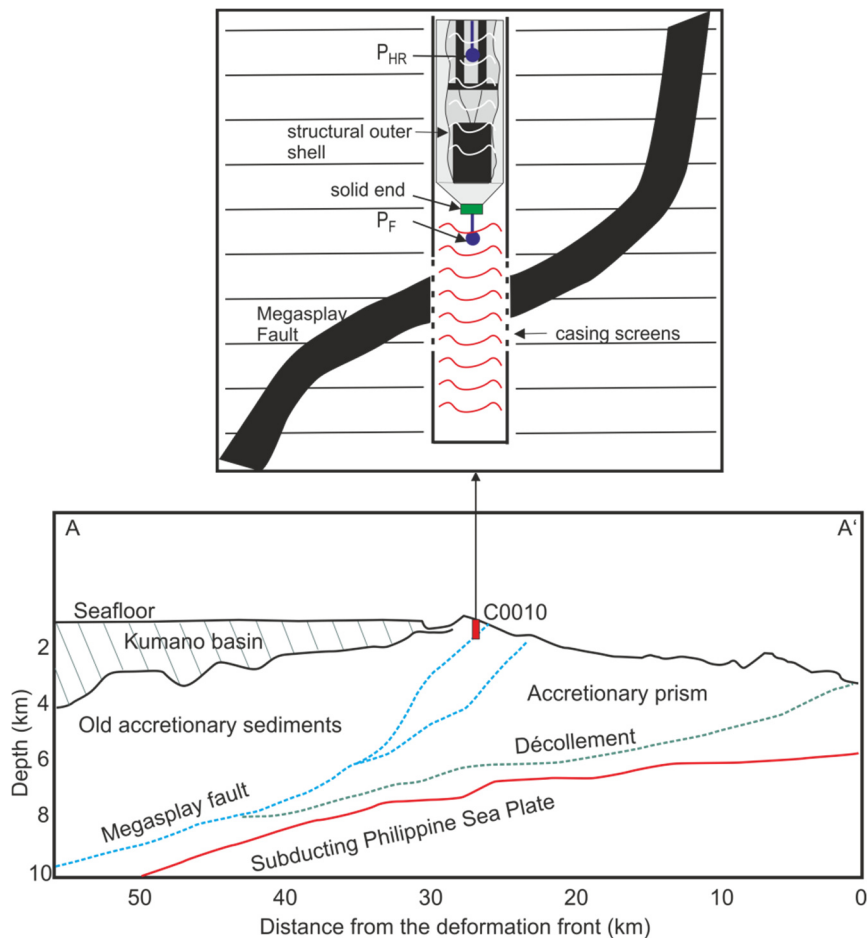
Figure 40: Cross-section of the box shown in Figure 39 (after Moore et al. 2013). The SmartPlug sits inside a borehole at Site C0010, where a shallow branch of the Megasplay fault is intersected at around 370 mbsf. The in-hole instrument configuration is shown in the inlay. The borehole was cased except for casing screens where the Megasplay fault is intersected (modified from Hammerschmidt et al. 2013a). P_{HR}: pressure sensor located in the upper sealed casing interval. P_F: Pressure sensor located in the formation section of the borehole, where fluid exchange between the formation and the borehole is possible via the casing screens.

[5] Today, a prominent splay fault, the "Megasplay", cuts through the accretionary prism (Park et al. 2000, 2002; Wang and Hu 2006; Moore et al. 2007). The splay fault is rooted at the décollement at around 10 km depth and ca. 50 – 55 km landward from the frontal prism toe. At around 30 – 35 km and 6 km depth, the splay fault starts to diverge in different branches. Active faulting probably commenced at ca. 1.95 Ma, and ceased after 1.24 Ma (Strasser et al. 2009). Whether the Megasplay fault was active after 1.24 Ma is still debated. Fault slip at ages < 1 Ma is supported by truncated and deformed overlying slope sediments (Moore et al. 2007; Kimura et al. 2011; Alves et al. 2013).

[6] At Site C0010, the hanging wall wedge starts at ca. 200 mbsf and extends to 410 mbsf. The wedge sits between slope apron deposits, which are characterized by silty mudstone intercalated by sand and minor ash layers. The wedge itself is a thick pile of fractured mudstone (Expedition 332 Scientists 2011, and references therein), and is characterized by a 10%-drop in porosity and

an increase in natural gamma ray radiation and electrical resistivity determined during logging-while-drilling (Expedition 319 Scientists 2010). The Expedition 319 Scientists (2010) attributed the splay fault to a sharp, single seismic reflector with negative polarity at around 370 mbsf.
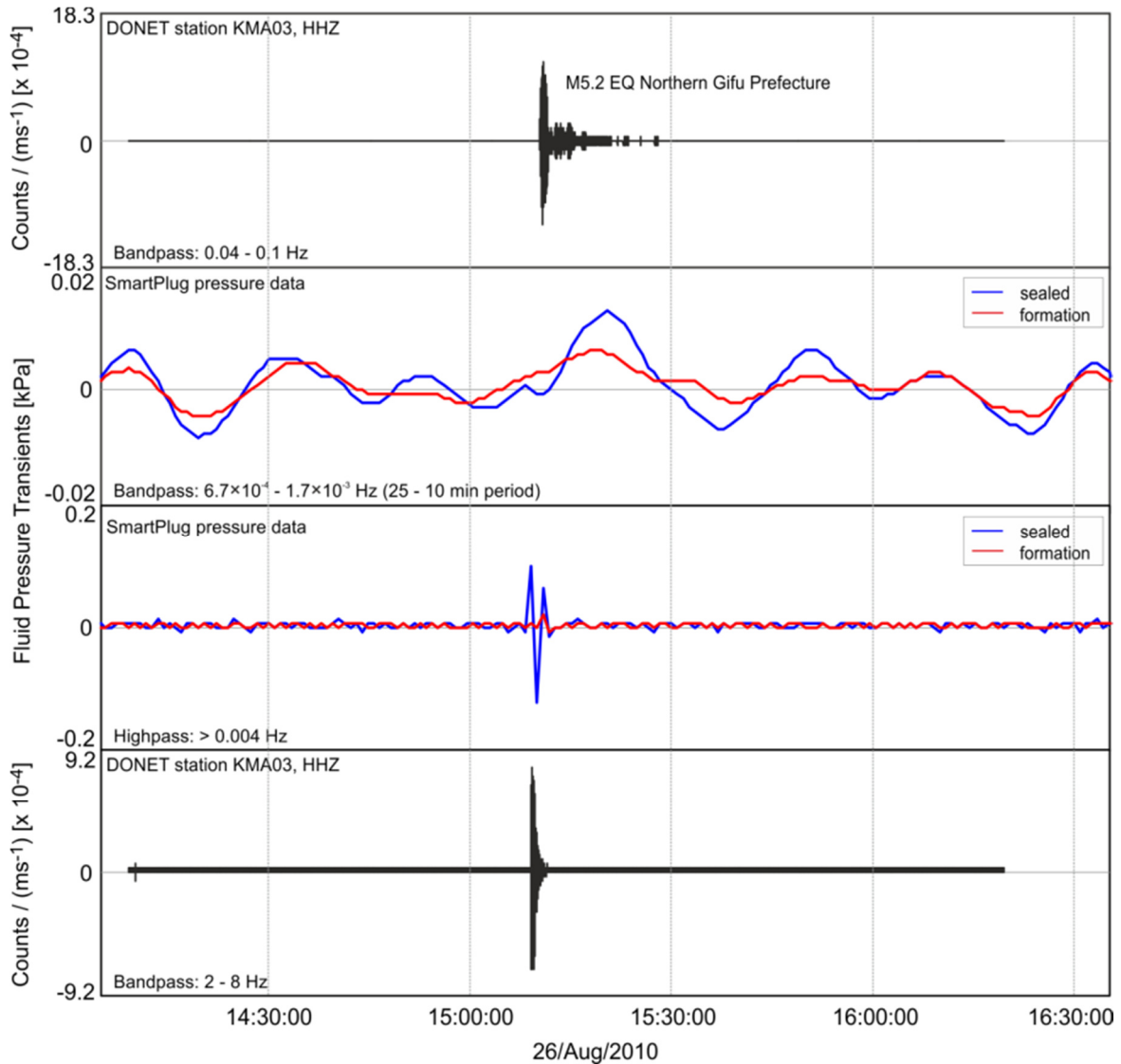
Figure 41: *Example for an anomalous pressure transient (APT) from 26 August 2010, which only occurs in the upper sealed casing interval (blue curve). This APT is visible in different frequency bands, and when compared to the DONET data, corresponds to a waveform typical for earthquakes. Following the information given by the Hi-Net (Okada et al. 2004), this event was identified as an M5.2 earthquake which occurred in the Northern Gifu Prefecture, central Japan.*

MATERIALS AND METHODS

The SmartPlug Borehole Observatory

[7] The SmartPlug borehole observatory belongs to the CORK (Circulation Obviation Retrofit Kit; e.g. Becker and Davis 2005) family, which are all designed to fit in boreholes of the IODP and the
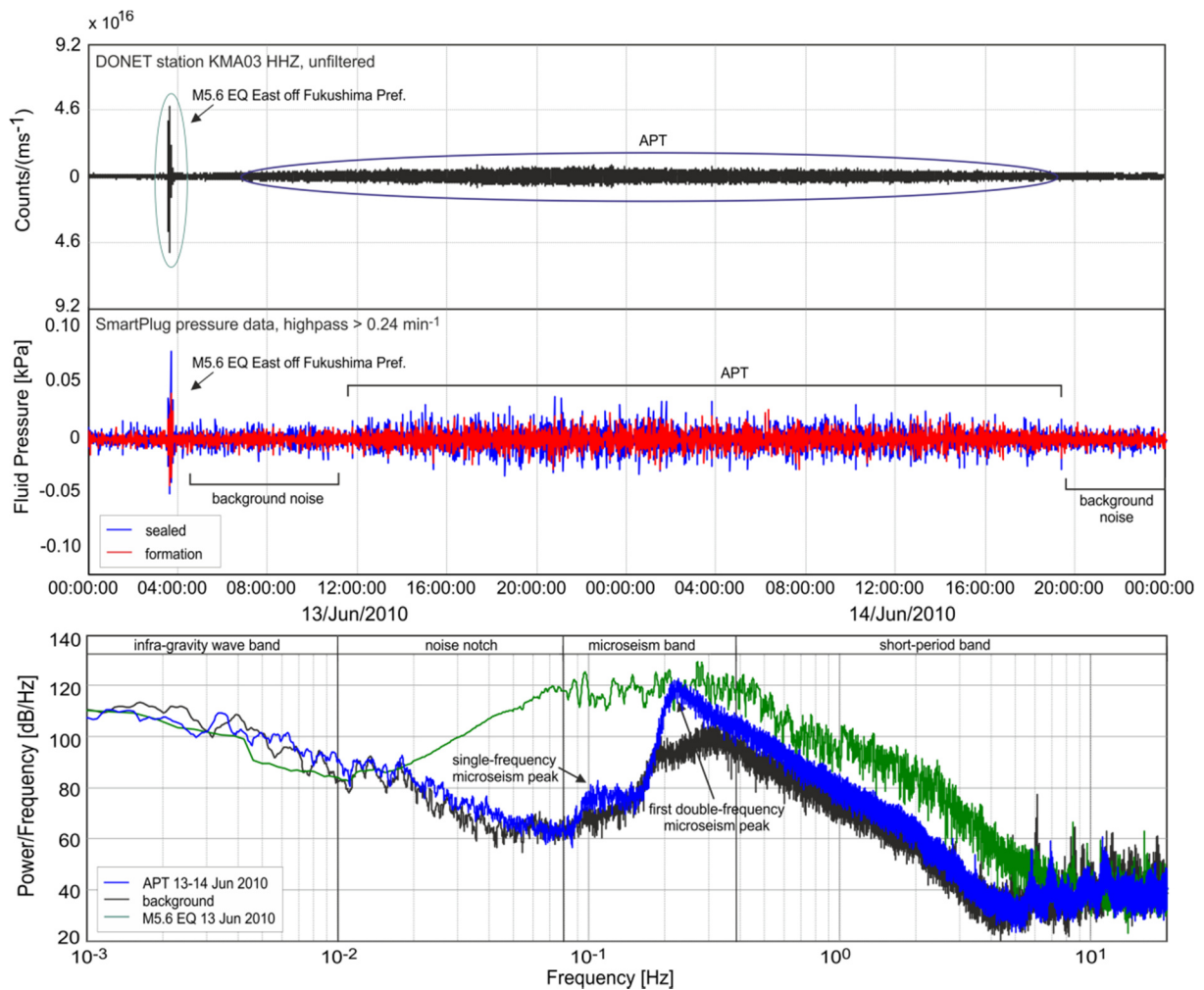
Figure 42: *Example for typical pressure transients related to the arrival of seismic waves from a regional earthquake (here: M5.6 EQ east off Fukushima Prefecture) and by a several hours lasting anomalous pressure transient (APT). The upper panel shows these features in waveform data from DONET station KMA03, whereas the middle panel belongs to the SmartPlug pressure data. The lower panel shows a power spectral density analysis of the APT (blue line), the M5.6 EQ (green line) and the background noise (black line) visible in DONET data. Compared to the background noise, the APT is clearly characterized by long-period-double- and single-frequency peaks. See text for further information.*

Ocean Drilling Program (ODP). The SmartPlug is attached to a Baker Hughes bridge plug, which shuts down water circulation between the screened part of the borehole and the overlying water body in the cased part. At the casing screens, water exchange is possible between the formation and the borehole. Strain and/or fluid pressure changes are monitored continuously by two Paroscientific pressure transducers, which have a resolution of 0.7 Pa and are plumbed to sense formation pressure below the plug via a casing screen, and seafloor hydrostatic pressure in the casing above the plug (Figure 40). Use of a corrosion cap at the top of the hole resulted in the upper interval being completely sealed, and as such, that interval appears to have become sensitive to volumetric strain (here we call that "upper sealed casing interval", because it is completely isolated from the ocean; Figure 40). Until its recovery during IODP Exp. 332, the instrument

continuously monitored fluid pressure from August 2009 to October 2010, with a sampling frequency of 0.017 Hz (i.e. 1 min⁻¹) (Kopf et al. 2011).

The Dense Ocean Floor Network for Earthquake and Tsunamis (DONET)

[8] The Dense Ocean-floor Network for Earthquake and Tsunamis is a recently completed seismological network offshore Japan which spans the Kumano forearc basin (Kawaguchi et al. 2008; Kaneda 2010; Nakano et al. 2013). The network originates from an onshore landing station, and connects to 5 different "science nodes" via a backbone cable system. Branching from each science node are four different stations. Each station includes a broadband (Guralp CMG-3T, flat velocity response from 100 Hz to 360 s) and a strong-motion seismometer (Metrozet TSA-100S). The seismometers are installed at 1 mbsf to minimize the influence of non-geologic signals.

[9] In this study, we used seismic waveform data from DONET Station KMA03, which was sampled at 200 Hz per channel by an on-site 24-bit A/D converter. When APTs corresponded to prominent energy bursts in the waveform data, local (Hi-Net, F-Net) (Okada et al. 2004) and global (International Seismological Centre 2013; US Geological Survey, www.usgs.com) catalogues were consulted. If applicable, theoretical travel times of seismic waves were determined using TauP (Crotwell et al. 1999).

RESULTS

Anomalous Pressure Transients and Seismic Waves

[10] From the different APTs detected, one group occurs in the upper sealed casing interval only. These anomalies appear in all frequency bands, and can lead to pressure transients with an amplitude up to 0.5 kPa (Hammerschmidt et al. 2011). Comparing the transients with waveforms from DONET station KMA03, some of these events correspond with the arrival of seismic waves from local, regional and distant earthquakes (Figure 41). Based on travel time calculations, these transients are most likely related to regional earthquakes with magnitudes between 0.2 and 5.3 (Table 1). For small earthquakes (<M3.0), the correlation remains unclear. Onsets of P-waves are hardly detectable in the waveform data, therefore, correlations are based on travel time calculations only. Earthquakes with M>3.0 were well identified using the Hi-Net catalog (Okada et al. 2004) and correspond well with timing and onset in the upper sealed casing interval. The sampling frequency of 1 min⁻¹ of the SmartPlug aliased the seismic signals (Figure 41). Some of the other distinct APTs in the upper sealed casing interval are apparently unrelated to any excursion in the DONET data and any event in the Hi-Net catalogue, but a relation with seismo-tectonic processes cannot be fully excluded.

Anomalous Pressure Transients and Microseism

[11] APTs which last up to several hours or days occur in the DONET waveforms as well (Figure 42). Detection was possible without filtering and the transients show durations similar to the ones in the pressure data. Hammerschmidt et al. (2013a) showed that some of these pressure transients can be related to local and regional low-pressure weather systems and storms, but did not perform a power spectral density (PSD) analysis due to the low sampling frequency of the SmartPlug. Here, this information gap is filled with a PSD analyses of DONET data from station KMA03 (Figure 42). Compared to the background values, the single- and double-frequency microseism peaks are significantly enhanced at 0.11 Hz and 0.22 Hz, respectively. The most striking feature is the long-period component of the microseism peak, which is almost 30dB/Hz higher than the background values.

Table 10: *Anomalous pressure transients related to local, regional and teleseismic earthquakes (based on Hi-Net catalogue)*

Date [dd.mm.yyyy]	Time Start Pressure UTC [hh:mm:ss]	Time End Pressure UTC [hh:mm:ss]	Start Time JST [hh:mm:ss]	Arrival Time JST [hh:mm:ss]	Magnitude	Depth [km]	Lat. [°]	Long.[°]	Epicentral Distance to Hole C0010A [km]
12.05.2010	18:01:55	18:05:14	03:01:55	03:03:19	2.1	44.0	26.011	129.416	1064.60
17.05.2010	10:47:03	10:57:59	19:45:35	19:50:53	4.2	74.0	39.077	144.464	954.96
27.05.2010	04:48:57	04:54:26	13:47:19	13:49:34	2.7	98.2	36.170	139.321	407.82
27.05.2010	05:10:04	05:13:53	14:08:39	14:10:54	3.6	0.0	32.550	140.987	408.20
30.05.2010	18:37:09	18:47:15	03:36:10	03:38:35	3.6	467.0	29.930	139.259	438.60
01.06.2010	06:24:17	06:33:50	15:24:10	15:25:17	0.2	36.0	34.851	137.679	204.11
10.06.2010	19:04:59	19:07:57	04:06:00	04:06:17	3.4	56.2	33.138	137.256	53.60
20.07.2010	21:18:19	21:21:00	07:09:21	07:09:39	1.0	34.9	33.631	136.370	55.27
18.08.2010	23:32:59	23:37:06	08:33:12	08:34:18	5.3	395.5	32.050	138.328	200.65
26.08.2010	15:09:08	15:14:49	00:08:04	00:09:55	5.2	285.8	36.192	136.967	332.58
07.09.2010	11:11:00	11:18:40	20:11:26	20:12:41	0.6	9.8	35.080	135.716	226.31
07.09.2010	11:35:31	11:40:07	20:30:50	20:41:22	5.1	30.0	45.778	151.735	1896.35

DISCUSSION

Seismic Waves and Induced Strain

[12] Pressure and head fluctuations in confined and unconfined aquifers in response to the arrival of seismic waves are a well-known phenomenon (e.g. Cooper et al. 1965; Wang and Davis 1996; Woodcock and Roeloffs 1996; Roeloffs 1998; Brodsky et al. 2003; Kano and Yanagidani 2006). Recently, Hammerschmidt et al. (2013a) reported hydroseismograms monitored by the SmartPlug borehole observatory inside Hole C0010A. The most prominent transients were

caused by the arrival of surface waves from regional and distant earthquakes, with the formation pressure being amplified compared to the pressure in the upper sealed casing interval (Hammerschmidt et al. 2013a). The arrival of seismic waves, particularly of surface waves, causes compression and dilation in the rock matrix. The induced strain ultimately leads to a pressure change, which migrates through the formation and which is monitored by the borehole instrument in dependence of its formation-instrument compliance ratio (Sawyer et al. 2008; Hammerschmidt et al. 2013b). For a constant instrument compliance ratio of 15 and a constant hydraulic diffusivity of around $10^{-5}\,ms^{-2}$ (Hammerschmidt et al. 2013b), the instrument response to changes in formation pressure is shown in Fig. 43. With increasing frequency, the instrument has difficulties to recognize the pressure disturbance in the formation, which results in smaller pressure amplitudes and higher phase shifts. At the same time, strain close to 10^{-10} is already sufficient to cause pressure transients above the resolution of the SmartPlug pressure sensors (given a strain sensitivity of 6 kPa/μstrain, see Hammerschmidt et al. (2013b) for more information).

[13] The only sensor connected to the formation is the formation pressure gauge. Therefore, it is expected that the strongest transients occur in the formation pressure data. By contrast, the behavior of the discrete APTs is completely opposing. Magnitudes, focal mechanisms and epicenters of the earthquakes can hardly serve as an explanation, because there is no apparent relationship between these properties and the seismic wave-induced pressure transients (Hammerschmidt et al. 2013a). In the upper sealed casing interval, however, seismic waves propagating along the borehole wall could have caused the observed APT. If incident seismic waves are refracted parallel to the casing, refracted body and surface wave modes can travel along the interface and up- and downward migrating head waves are generated (Haldorsen et al. 2006). At the same time, generation of trapped waves inside the upper sealed casing interval is possible (e.g., Paillet and Cheng 1991). P- and surface wave modes are partly reflected inside the casing and interfere constructively, resulting in an amplified signal. In contrast to the completely sealed upper interval, seismic wave modes in the formation interval are subject to attenuation at the casing screens, where fluid can be pressed into the formation, leading to energy loss (Norris 1993). Fig. 44 shows a simple model based on the work of Rubino et al. (2008) and Rubino and Holliger (2013) (see Appendix A.3 for calculation). Here, it is assumed that the viscous fluid is forced into an elastic sediment body with the properties listed in Table 4. Our calculations show that the attenuation inside the upper sealed casing interval is less sensitive to higher frequencies than attenuation in the formation. Also attenuation inside the instrument is around five orders of magnitude smaller than the attenuation at the casing screens.
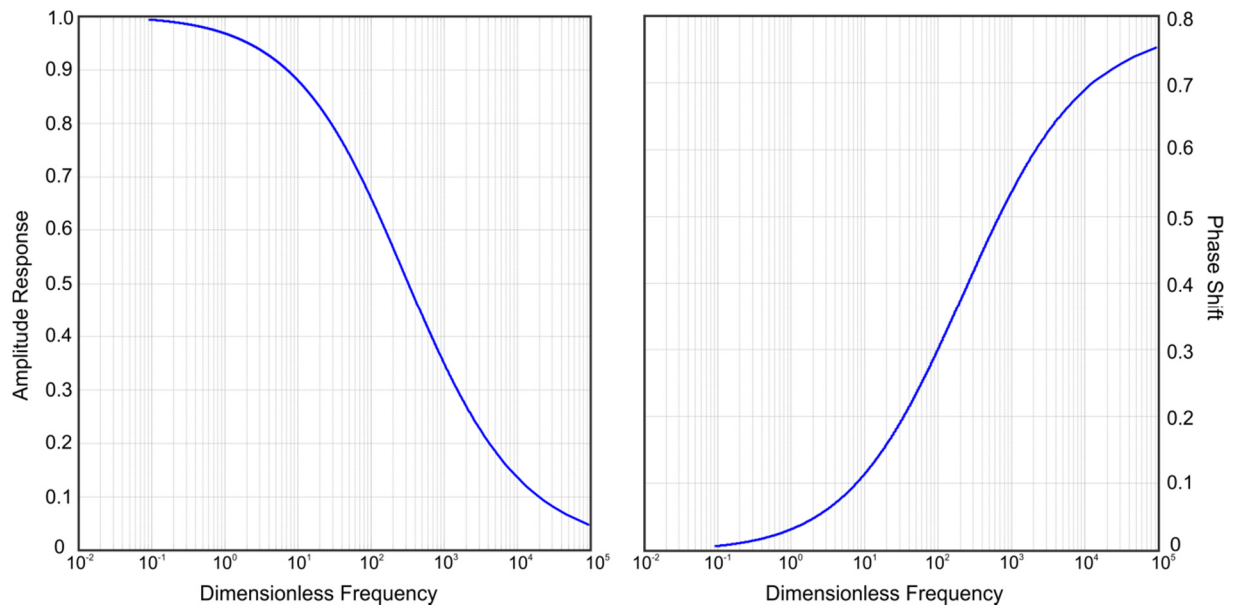
Figure 43: *Expected amplitude response (left) and phase shift (right) of the monitored pressure signal compared to the one in the formation. Calculations were made for a hydraulic diffusivity of 10^{-5} $m^2 s^{-1}$ and an instrument-compliance ratio of 15. With increasing frequency, the SmartPlug has difficulties keeping pace with the pressure changes in the formation, resulting in damped amplitudes and phase shifts in the pressure data. See text for further explanations.*

[14] The case of seismic waves being attenuated at the casing screens is exemplified by Stoneley waves in Fig. 44. Stoneley waves occur when body waves are refracted at a solid-solid (Stoneley 1924) or at a fluid-solid boundary (Scholte 1948). For our borehole configuration, Stoneley waves could be generated either at the solid-solid interface between borehole casing and the structural outer shell of the SmartPlug, or at the interface between structural outer shell and the seawater (Figure 43). The resulting surface waves travel along the interface in an expanding/contracting motion (Figure 43) (Bradley et al. 1994; Qobi et al. 2001) and with increasing permeability of the solid body and decreasing frequency, Stoneley waves experience stronger attenuation (e.g., Winkler et al. 1989; Pfender and Villinger 2006). The confined upper sealed casing interval of the SmartPlug has virtually no permeability, thus Stoneley waves remain unattenuated and lead to pressure transients. Based on our data, however, it is not possible to depict a discrete seismic wave mode to be responsible.

Microseism

[15] Recently, many publications addressed the origin of microseism energies (e.g., Cessaro 1994; Bromirski et al. 2005, 2013; Gerstoft and Tanimoto 2007; Gerstoft et al. 2008; Landès et al. 2010; Obrebski et al. 2012). When applying a PSD, microseism can be easily identified by characteristic single-frequency and double-frequency peaks. Whereas the former indicates a more distant source (e.g., Babcock et al. 1995; Bromirski et al. 1999), the double-frequency peak is either generate by swell reflected at the coastline (long-period component, LPDF) or from storms

over the open ocean (short-period component) (Bromirski et al. 2005, 2013). Similar to LPDF, the single-frequency peak is also generated due to interaction of swells with the coastline (Cessaro 1994; Bromirski et al. 2013), and together with LDPF, is accountable for most of the microseism (Gerstoft and Tanimoto 2007). Since no local storms and/or low pressure weather systems are observed for the day-long APTs, it seems most likely that waves excited from distant sources and interacting with the coastline caused the transients. Alternatively, microseism could be triggered by P-wave phases excited by distant storms, which travel through the earth's interior (Gerstoft et al. 2008; Landès et al. 2010). Teleseismic body-wave phases particularly add to the double-frequency microseism energy (Landès et al. 2010; Zhang et al. 2010) and might therefore contribute as well to the observed APTs.
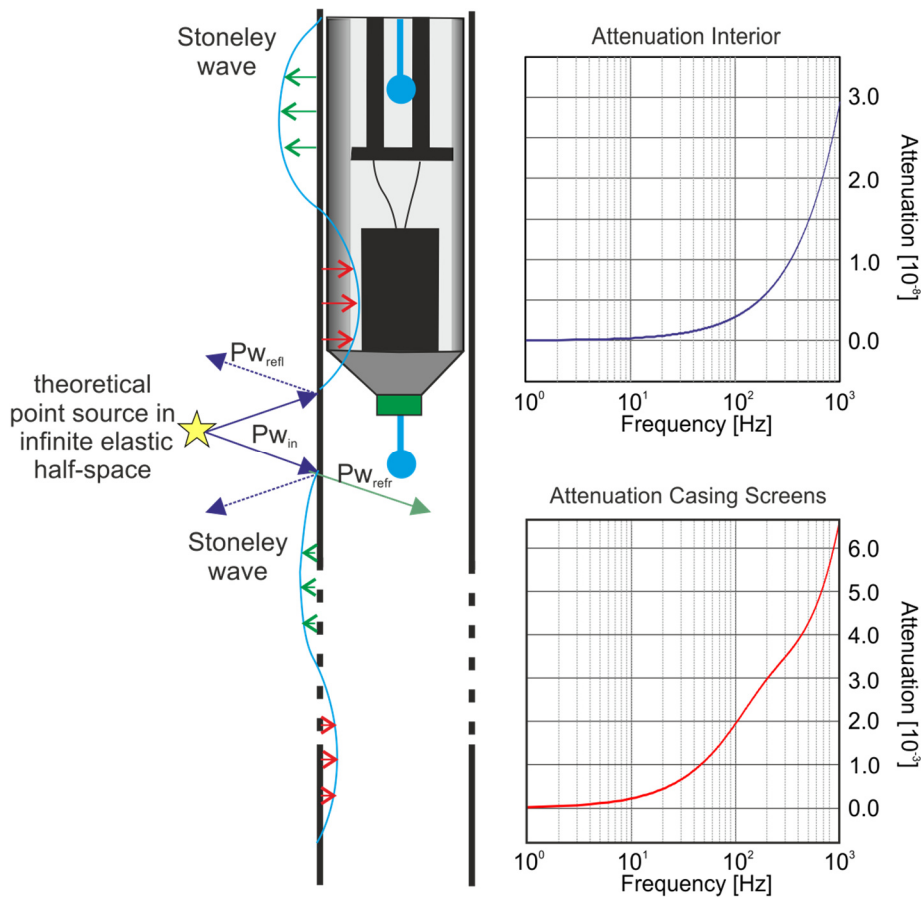
Figure 44: *Schematic diagram of body waves being reflected and refracted at the solid-fluid interface (modified from Hammerschmidt et al. 2013b, and after Bradley 1994; Haldorsen et al. 2006; Qobi et al. 2001) and calculated attenuation inside the upper sealed casing interval ("attenuation interior") and at the casing screens (after Rubino et al. 2008). The hypothesis is exemplified by Stoneley-waves. The latter are travelling along the interface in a contracting/expanding motion, and are attenuated where the SmartPlug casing allows fluid exchange with the permeable formation (i.e., at the casing screens). Please be aware of the different scales on the y-axis of the attenuation diagrams Pw_{in}: incident P-wave. Pw_{refl}: reflected P-wave. Pw_{refr}: refracted P-wave.*

CONCLUSIONS

[16] We compared anomalous pressure transients (APT) monitored in a shallow branch of the Nankai Trough megasplay fault with initial datasets from the DONET cabled network. The main findings are summarized as follows:

1. The discrete APTs in the upper sealed casing interval correlate well with regional and local earthquakes, and are probably caused by refracted seismic waves and/or trapped and amplified seismic wave modes within the casing. Attenuation occurs only at the casing screens, due to interaction of the borehole fluid with the formation and subsequent energy loss.

2. Almost all of the several hours- to days-lasting APTs can also be found in DONET data, and applying a power spectral density analysis to the waveforms clearly revealed an increase in the primary and long-period secondary microseism. This suggests that swells and/or teleseismic phases generated by a remote source are probably responsible for the observed transients.

[17] Future efforts will focus on installing a CORK system at Site C0010 similar to the LTBMS at Site C0002. Once connected to the DONET, sampling frequencies of at least 1 Hz will be available, which enable us to properly study wave propagation inside the monitoring instrument, as well as trapped waves inside the splay fault zone. The higher sampling frequency will further elucidate the contribution of natural signals to pressure transients.

References

Alves TM, Strasser M, Moore GF (2013) Erosional features as indicators of thrust fault activity (Nankai Trough, Japan). Mar Geol. doi: 10.1016/j.margeo.2013.07.011

Ando M (1975) Source Mechanisms and Tectonic Significance of Historical Earthquakes along the Nankai Trough, Japan. Tectonophysics 27:119 – 140.

Ardhuin F, Herbers THC (2013) Noise generation in the solid Earth, oceans and atmosphere, from nonlinear interacting surface gravity waves in finite depth. J Fluid Mech 716:316–348.

Baba T, Cummins PR, Hori T, Kaneda Y (2006) High precision slip distribution of the 1944 Tonankai earthquake inferred from tsunami waveforms: Possible slip on a splay fault. Tectonophysics 426:119–134. doi: 10.1016/j.tecto.2006.02.015

Babcock JM, Kirkendall BA, Orcutt JA (1995) Relationships between ocean bottom noise and the environment. Bull Seismol Soc Am 84:1991–2007.

Becker K, Davis EE (2005) A review of CORK designs and operations during the Ocean Drilling Program. Proc. Integr. Ocean Drill. Progr. 301.

Bradley CR (1994) Very Low Frequency Seismo-Acoustic Noise Below the Sea Floor (0.2-10 Hz). Woodshole Oceanogr. Inst. MA

Brodsky EE, Roeloffs E, Woodcock D, Gall I, Manga M (2003) A mechanism for sustained groundwater pressure changes induced by distant earthquakes. J Geophys Res 108:2390. doi: 10.1029/2002jb002321

Bromirski PD, Flick RE, Graham N (1999) Ocean wave height determined from inland seismometer data: Implications for investigating wave climate changes in the NE Pacific. J Geophys Res Ocean 104:20753–20766. doi: 10.1029/1999JC900156

Bromirski PD, Duennebier FK, Stephen RA (2005) Mid-ocean microseisms. Geochem Geophys Geosyst 6:Q04009. doi: 10.1029/2004gc000768

Bromirski PD, Stephen RA, Gerstoft P (2013) Are deep-ocean-generated surface-wave microseisms observed on land? J Geophys Res Solid Earth 118:3610–3629. doi: 10.1002/jgrb.50268

Cessaro RK (1994) Sources of primary and secondary microseisms. Bull Seismol Soc Am 84:142–148.

Cooper Jr. HH, Bredehoeft JD, Papadopulos IS, Bennett RR (1965) The Response of Well-Aquifer Systems to Seismic Waves. J Geophys Res 70:3915–3926. doi: 10.1029/JZ070i016p03915

Crotwell HP, Owens TJ, Ritsema J (1999) The TauP Toolkit: Flexible Seismic Travel-time and Ray-path Utilities. Seismol Res Lett 70 :154–160. doi: 10.1785/gssrl.70.2.154

Cummins PR, Hori T, Kaneda Y (2001) Splay fault and megathrust earthquake slip in the Nankai Trough. Earth Planets Sp 53:243–248.

Davis EE, Becker K, Wang K, Obara K, Ito Y, Kinoshita M (2006) A discrete episode of seismic and aseismic deformation of the Nankai trough subduction zone accretionary prism and incoming Philippine Sea plate. Earth Planet Sci Lett 242:73–84.

Davis EE, Becker K, Wang K, Kinoshita M (2009) Co-seismic and post-seismic pore-fluid pressure changes in the Philippine Sea plate and Nankai decollement in response to a seismogenic strain event off Kii Peninsula, Japan. Earth, Planets Sp 61:649 – 657.

Davis E, Kinoshita M, Becker K, Wang K, Asano Y, Ito Y (2013) Episodic deformation and inferred slow slip at the Nankai subduction zone during the first decade of CORK borehole pressure and VLFE monitoring. Earth Planet Sci Lett 368:110–118.

Elkhoury JE, Brodsky EE, Agnew DC (2006) Seismic waves increase permeability. Nature 441:1135–1138. doi: http://www.nature.com/nature/journal/v441/n7097/suppinfo/nature04798_S1.html

Elkhoury JE, Niemeijer A, Brodsky EE, Marone C (2011) Laboratory observations of permeability enhancement by fluid pressure oscillation of in situ fractured rock. J Geophys Res 116:B02311. doi: 10.1029/2010jb007759

Expedition 319 Scientists (2010) Site C0010. In: Saffer D, McNeill L, Byrne T, Araki E, Toczko S, Eguchi N, Takahashi K, Expedition 319 Scientists (eds) Proc IODP 319. Integrated Ocean Drilling Program Management International, Tokyo. doi:10.2204/iodp.proc.319.104.2010

Expedition 332 Scientists (2011) Expedition 332 summary. In: Kopf A, Araki E, Toczko S, Expedition 332 Scientists (eds) Proc IODP 332. Integrated Ocean Drilling Program Management International, Tokyo. doi:10.2204/iodp.proc.332.101.2011

Gerstoft P, Tanimoto T (2007) A year of microseisms in southern California. Geophys Res Lett 34:L20304. doi: 10.1029/2007gl031091

Gerstoft P, Shearer PM, Harmon N, Zhang J (2008) Global P, PP, and PKP wave microseisms observed from distant storms. Geophys Res Lett 35:L23306. doi: 10.1029/2008gl036111

Haldorsen JBU, Johnson DL, Plona T, Sinha B, Valero H-P, Winkler K (2006) Borehole Wcoustic Waves. Oilf Rev Spring:34–43.

Hammerschmidt S, Kopf A, the Expedition 332 Scientists (2011) Fluid Pressure and Temperature Response at the Nankai Trough Megasplay Fault: Initial Results of the SmartPlug Borehole Observatory. Poster presented at the AGU Fall Meeting, San Francisco, CA, abstract# OS11A-1456

Hammerschmidt S, Davis EE, Kopf A (2013a) Fluid pressure and temperature transients detected at the Nankai Trough Megasplay Fault: Results from the SmartPlug borehole observatory. Tectonophysics 600:116 – 133. doi: 10.1016/j.tecto.2013.02.010

Hammerschmidt SB, Davis EE, Hüpers A, Kopf A (2013b) Limitation of fluid flow at the Nankai Trough megasplay fault zone. Geo-Marine Lett 33:405–418. doi: 10.1007/s00367-013-0337-z

Ichinose GA, Thio HK, Somerville PG, Sato T, Ishii T (2003) Rupture process of the 1944 Tonankai earthquake (M s 8.1) from the inversion of teleseismic and regional seismograms. J Geophys Res 108:2497. doi: 10.1029/2003jb002393

Kaneda Y (2010) The advanced ocean floor real time monitoring system for mega thrust earthquakes and tsunamis-application of DONET and DONET2 data to seismological research and disaster mitigation. Ocean. 2010. pp 1–6

Kano Y, Yanagidani T (2006) Broadband hydroseismograms observed by closed borehole wells in the Kamioka mine, central Japan: Response of pore pressure to seismic waves from 0.05 to 2 Hz. J Geophys Res 111:B03410. doi: 10.1029/2005jb003656

Kawaguchi K, Kaneda Y, Araki E (2008) The DONET: A real-time seafloor research infrastructure for the precise earthquake and tsunami monitoring. Ocean. 2008 - MTS/IEEE Kobe Techno-Ocean. pp 1–4

Kimura G, Moore GF, Strasser M, Screaton E, Curewitz D, Streiff C, Tobin H (2011) Spatial and temporal evolution of the megasplay fault in the Nankai Trough. Geochem Geophys Geosyst 12:Q0A008. doi: 10.1029/2010gc003335

Kopf A, Saffer DM, Davis EE, Hammerschmidt S, LaBonte A, Meldrum R, Toczko S, Lauer R, Heesemann M, Macdonald R, Wheat CG, Jannasch HW, Edwards K, Orcutt B, Haddad A, Villinger H, Araki E, Kitada K, Kimura T, Kido Y (2011) The SmartPlug and GeniusPlug: simple retrievable observatory systems for NanTroSEIZE borehole monitoring. In: Kopf A, Araki E, Toczko S, Expedition 332 Scientists, Proc IODP 332. doi:10.2204/iodp.proc.332.105.2011

Landès M, Hubans F, Shapiro NM, Paul A, Campillo M (2010) Origin of deep ocean microseisms by using teleseismic body waves. J Geophys Res 115:B05302. doi: 10.1029/2009jb006918

Longuet-Higgins MS (1950) A Theory of the Origin of Microseisms. Philos Trans R Soc London Ser A, Math Phys Sci 243:1–35. doi: 10.1098/rsta.1950.0012

Kyaw Thu M, Kodaira S, Yamano M, the Expedition 333 Science Party (2012) Seismogenic zone temperatures and heat-flow anomalies in the To-nankai margin segment based on temperature data from IODP expedition 333 and thermal model. Earth Planet Sci Lett 349-350:171–185. doi: 10.1016/j.epsl.2012.06.048

Marcaillou B, Henry P, Kinoshita M, Kanamatsu T, Screaton E, Daigle H, Harcouët-Menou V, Lee Y, Matsubayashi O, Kyaw Thu M, Kodaira S, Yamano M, Party IE 333 S (2012) Seismogenic zone temperatures and heat-flow anomalies in the To-nankai margin segment based on temperature data from IODP expedition 333 and thermal model. Earth Planet Sci Lett 349-350:171–185. doi: 10.1016/j.epsl.2012.06.048

Miyazaki S, Heki K (2001) Crustal velocity field of southwest Japan: Subduction and arc-arc collision. J Geophys Res 106:4305–4326. doi: 10.1029/2000jb900312

Miyazawa M, Brodsky EE (2008) Deep low-frequency tremor that correlates with passing surface waves. J Geophys Res 113:B01307. doi: 10.1029/2006jb004890

Moore GF, Bangs NL, Taira A, Kuramoto S, Pangborn E, Tobin HJ (2007) Three-Dimensional Splay Fault Geometry and Implications for Tsunami Generation. Science 318:1128–1131. doi: 10.1126/science.1147195

Moore GF, Kanagawa K, Strasser M, Dugan B, Maeda L, Toczko S, and the Expedition 338 Scientists (2013). NanTroSEIZE Stage 3: NanTroSEIZE Plate Boundary Deep Riser, IODP Prel Rep, 338. doi: 10.2204/iodp.pr.338.2013.

5.4 Borehole Fluid Pressure Artifacts Stimulated by Seismic Waves

Nakano M, Nakamura T, Kamiya S, Ohori M, Kaneda Y (2013) Intensive seismic activity around the Nankai trough revealed by DONET ocean-floor seismic observations. Earth Planets Sp 65:5 – 15.

Norris AN (1993) Low-frequency dispersion and attenuation in partially saturated rocks. J Acoust Soc Am 94:359 – 370. doi: 10.1121/1.407101

Obara K (2002) Nonvolcanic Deep Tremor Associated with Subduction in Southwest Japan. Science 296:1679–1681. doi: 10.1126/science.1070378

Obrebski MJ, Ardhuin F, Stutzmann E, Schimmel M (2012) How moderate sea states can generate loud seismic noise in the deep ocean. Geophys Res Lett 39:L11601. doi: 10.1029/2012GL051896

Okada Y, Kasahara K, Hori S, Obara K, Sekiguchi S, Fujiwara H, Yamamoto A (2004) Recent progress of seismic observation networks in Japan: Hi-net, F-net, K-NET and KiK-net. Earth Planets Sp 56:15–28.

Okino K, Ohara Y, Kasuga S, Kato Y (1999) The Philippine Sea: New survey results reveal the structure and the history of the marginal basins. Geophys Res Lett 26:2287–2290. doi: 10.1029/1999gl900537

Paillet FL, Cheng CH (1991) Acoustic Waves in Boreholes. 264.

Park J-O, Tsuru T, Kodaira S, Nakanishi A, Miura S, Kaneda Y, Kono Y, Takahashi N (2000) Out-of-sequence thrust faults developed in the coseismic slip zone of the 1946 Nankai Earthquake (Mw=8.2) off Shikoku, southwest Japan. Geophys Res Lett 27:1033–1036. doi: 10.1029/1999GL008443

Park J-O, Tsuru T, Kodaira S, Cummins PR, Kaneda Y (2002) Splay Fault Branching Along the Nankai Subduction Zone. Science 297:1157–1160. doi: 10.1126/science.1074111

Pfender M, Villinger H (2006) Estimating fracture density in oceanic basement: an approach using Stoneley wave analysis. Proc IODP 205:1 - 22. doi:10.2973/odp.proc.sr.205.206.2006

Qobi L, de Kuijper A, Tang XM, Strauss J (2001) Permeability determination from Stoneley waves in the Ara group carbonates, Oman. GeoArabia 6:649 – 666.

Roeloffs EA (1998) Persistent water level changes in a well near Parkfield, California, due to local and distant earthquakes. J Geophys Res 103:869–889. doi: 10.1029/97jb02335

Rubino JG, Holliger K (2013) Research note: Seismic attenuation due to wave-induced fluid flow at microscopic and mesoscopic scales. Geophys Prospect 61:882–889. doi: 10.1111/1365-2478.12009

Rubino J, Ravazzoli C, Santos J (2008) Equivalent viscoelastic solids for heterogeneous fluid-saturated porous rocks. Geophysics 74:N1–N13. doi: 10.1190/1.3008544

Rubinstein JL, La Rocca M, Vidale JE, Creager KC, Wech AG (2008) Tidal Modulation of Nonvolcanic Tremor. Science 319:186–189. doi: 10.1126/science.1150558

Sawyer AH, Flemings P, Elsworth D, Kinoshita M (2008) Response of submarine hydrologic monitoring instruments to formation pressure changes: Theory and application to Nankai advanced CORKs. J Geophys Res 113:B01102. doi: 10.1029/2007jb005132

Scholte JG (1948) On the large displacements commonly regarded as caused by Love waves and similar dispersive surface waves. Proc Konink Ned Akad Wetench 51:533 – 543, 642 – 649, 828 – 835, 969.

Scholz CH (1998) Earthquakes and friction laws. Nature 391:37–42.

Seno T, Stein S, Gripp AE (1993) A model for the motion of the Philippine Sea plate consistent with NUVEL-1 and geological data. J Geophys Res 98:17941–17948.

Stoneley R (1924) Elastic Waves at the Surface of Separation of Two Solids. Proc R Soc London Ser A, Contain Pap a Math Phys Character 106:416–428 CR – Copyright © 1924 The Royal Socie. doi: 10.2307/94262

Strasser M, Moore GF, Kimura G, Kitamura Y, Kopf AJ, Lallemant S, Park J-O, Screaton EJ, Su X, Underwood MB, Zhao X (2009) Origin and evolution of a splay fault in the Nankai accretionary wedge. Nat Geosci 2:648–652.

Sugioka H, Okamoto T, Nakamura T, Ishihara Y, Ito A, Obana K, Kinoshita M, Nakahigashi K, Shinohara M, Fukao Y (2012) Tsunamigenic potential of the shallow subduction plate boundary inferred from slow seismic slip. Nat Geosci 5:414–418.

Taira A (2001) Tectonic Evolution of the Japanese Arc System. Annu Rev Earth Planet Sci 29:109–134. doi: 10.1146/annurev.earth.29.1.109

Tobin HJ, Kinoshita M (2006) NanTroSEIZE: The IODP Nankai Trough Seismogenic Zone Experiment. Sci Drill 2:23–27. doi: 10.2204/iodp.sd.2.06.2006

Wang K, Davis EE (1996) Theory for the Propagation of Tidally Induced Pore Pressure Variations in Layered Subseafloor Formations. J Geophys Res 101:11483 – 11495.

Wang K, Hu Y (2006) Accretionary prisms in subduction earthquake cycles: The theory of dynamic Coulomb wedge. J Geophys Res 111:B06410. doi: 10.1029/2005jb004094

Wessel P, Smith WHF (1991) Free software helps map and display data. Eos Trans AGU 72:441 – 446.

Winkler K, Liu H, Johnson D (1989) Permeability and borehole Stoneley waves: Comparison between experiment and theory. Geophysics 54:66–75. doi: 10.1190/1.1442578

Woodcock D, Roeloffs E (1996) Seismically-induced water level oscillations in a fractured-rock aquifer well near Grants Pass, Oregon. Oregon Geol 58:27–33.

Zhang J, Gerstoft P, Bromirski PD (2010) Pelagic and coastal sources of P-wave microseisms: Generation under tropical cyclones. Geophys Res Lett 37:L15301. doi: 10.1029/2010gl044288

CHAPTER 6
Real-time Drilling Mud Gas Monitoring beneath the Kumano Basin

CHAPTER 6.1 – MANUSCRIPT V

REAL-TIME DRILLING MUD GAS MONITORING FOR QUALITATIVE EVALUATION OF SUBSURFACE HYDROCARBON GAS COMPOSITION

Sebastian B. Hammerschmidt[1]*, Thomas Wiersberg[2], Verena Heuer[1], Jenny Wendt[1], J. Erzinger[2], A. Kopf[1]

Submitted in June 2014 to

Geochemical Transactions

Currently in revision

* corresponding author: shammerschmidt@marum.de

[1] MARUM, University of Bremen, Leobener Str., 28359 Bremen, Germany

[2] GFZ German Research Centre for Geosciences, Telegrafenberg, 14473 Germany

Abstract Integrated Ocean Drilling Program Expedition 338 was the second scientific expedition with *D/V Chikyu* during which riser drilling was conducted as part of the Nankai Trough Seismogenic Zone Experiment. Riser drilling enabled sampling and real-time monitoring of drilling mud gas with the onboard drilling mud gas monitoring ("SciGas") system. A stand-alone system was provided by Geoservices. Both systems allowed the determination of (non-) hydrocarbon gas, while the SciGas system also monitored the methane carbon isotope ratio ($\delta^{13}C_{CH4}$). The gas composition was predominated by methane (> 10000 ppmv), while ethane and propane were up to two orders of magnitude lower. $\delta^{13}C_{CH4}$ values suggested an onset of thermogenic gas starting with 1700 meter below seafloor. This study aims on evaluating the onboard data and subsequent geological interpretations by conducting shore-based analyses of drilling mud gas samples. 23 gas samples were taken from the SciGas system and analyzed onshore for hydrocarbon gas composition with a gas chromatograph (GC; methane, ethane, propane) and a quadrupole mass spectrometer (QMS; methane only). The individual datasets were compared with Geoservices data using the Bernard parameter (i.e. methane/(ethane + propane)) and the total wet gas ratio (i.e., [(ethane + propane) / (methane - propane)] × 100). The onshore measurements revealed concentrations for methane from ca. 134 to 10346 ppmv in the GC data and 440 to 49800 ppmv in the QMS data, while ethane and propane remained between 2 – 18 ppmv and 2 – 4 ppmv, respectively. Deuterium concentrations were uniform downhole, with values between -171‰ and -164‰. Based on these results, all three datasets imply an immature gas composition. The apparent increase in thermogenic gas is probably caused by mixing. In situ thermogenic gas production at depths shallower 2000 mbsf is unlikely based on *in situ* temperature estimations between 81°C and 85°C and a cumulative time-temperature index of 0.23. In conclusion, the onboard SciGas data acquisition helps to provide a preliminary, qualitative evaluation of the gas composition, the *in situ* temperature and the possibility of gas migration.

INTRODUCTION

[1] Beginning in the 1930s, mud logging became a standard technique on drill rigs worldwide (Ablard et al. 2012). Besides improving safety during riser drilling, mud logging focuses on formation and reservoir evaluation in real-time. These objectives are accomplished by characterizing the cuttings (i.e. small pieces of the formation) and by analyses of the drilling mud gas composition. Cuttings and drilling mud gas circulate upwards with the drilling mud, where the cuttings are collected at the shale shaker and investigated under the microscope. The gas component is removed from the drilling mud by a degasser, and is then forwarded to the mud gas monitoring unit, where the gas composition is analyzed.

[2] Causes for varying gas concentrations in the drilling mud gas data are difficult to assess, because drilling mud gas is a function of the *in situ* gas composition, physical and chemical properties of the formation and the drilling mud, and the drilling operation. Gas sources include liberated gas (i.e. gas that is released when the drill bit crushes the rock), produced gas (i.e. gas inflow caused by borehole pressure lower than hydrostatic), atmospheric gas (O_2, N_2, Ar), and recycled gas (i.e. gas not liberated at the surface when the mud is collected in the mud pits). The amount of liberated gas strongly depends on the porosity and permeability of the penetrated formation, but also on parameters like rate-of-penetration, mud weight, mud flow rate, bit and borehole diameter, and degasser efficiency (Hammerschmidt et al. 2014; cf. Appendix C.2).

[3] During the last decades, the scientific value of drilling mud gas monitoring was repeatedly highlighted (Hilton and Craig 1989; Aquilina et al. 1998; Ellis et al. 2003, 2007; Erzinger et al.
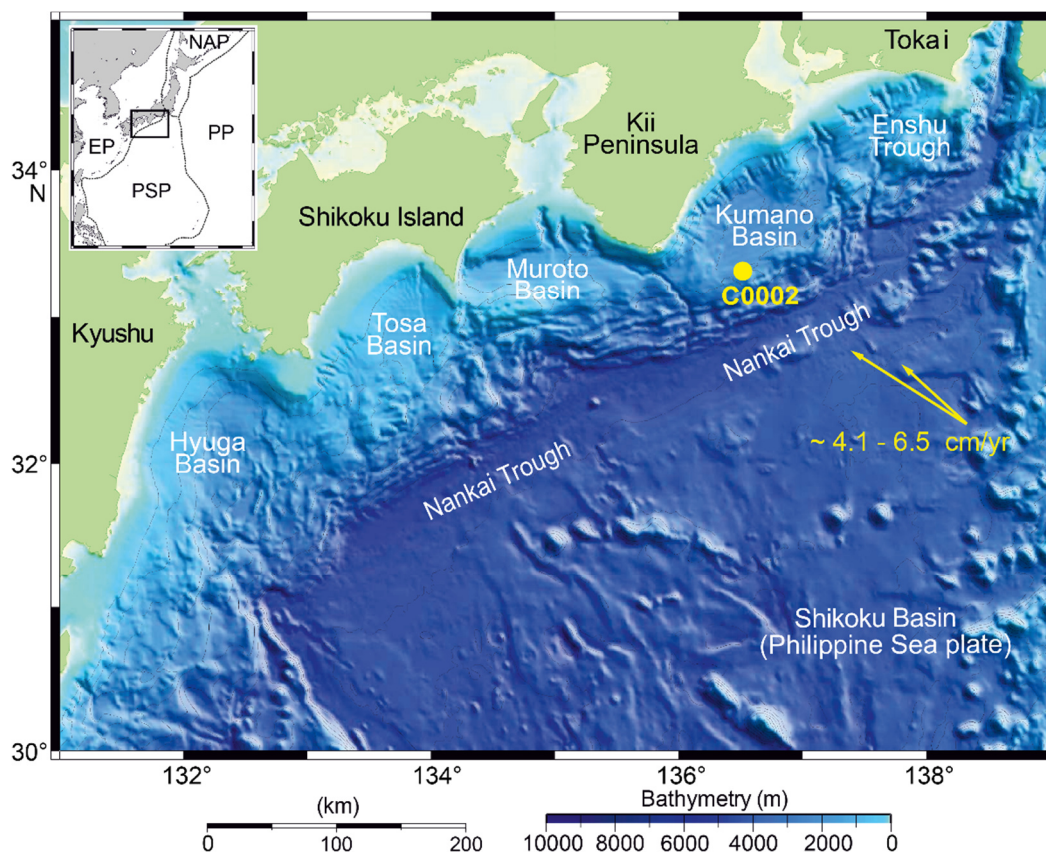
Figure 45: *Overview of the Nankai Trough area (modified from Screaton et al. 2009), where the Philippine Sea plate subducts beneath the Eurasian plate with a rate of 4.1 to 6.5 cm/yr. Site C0002 is situated at the southern rim of the Kumano forearc basin, which is located between the Muroto Basin in the south-west and the Enshu trough in the north-east. The inlay gives an overview of the tectonic situation in this area, with EP = Eurasian Plate, PSP = Philippine Sea Plate, PP = Pacific Plate, NAP = North American Plate.*

2004, 2006; Wiersberg and Erzinger 2007, 2008, 2011; Ablard et al. 2012), and also found its way into the Integrated Ocean Drilling Program (IODP) Nankai Trough Seismogenic Zone Experiment (NanTroSEIZE). Drilling mud gas monitoring was first conducted with third-party tools on IODP Expedition 319 during riser drilling with *D/V Chikyu* (Expedition 319 Scientists 2010). The third-party installation was later replaced by an onboard scientific drilling mud gas monitoring system (hereafter termed "SciGas system"), which was tested successfully during IODP Exp. 337 for the first time (Inagaki et al. 2013). The SciGas system allows determination of hydrocarbons (methane, ethane, propane, *i-* and *n-*butane), methane carbon isotope ratios ($\delta^{13}C_{CH4}$), and non-hydrocarbons (e.g., amongst others, O_2, N_2, Ar, H_2, Xe, He) gases. Verena Heuer and colleagues (personal communication, 2013) evaluated the quality of real-time results by sampling the drilling mud gas during IODP Exp. 337 and subsequent shore-based analysis focusing on $\delta^{13}C_{CH4}$ variations. Both offshore and shore-based results show good correlations, pointing to the scientific value of real-time analyses using isotope ratios.

[4] The SciGas system was again used during IODP NanTroSEIZE Exp. 338, where a borehole was successfully drilled to 2007 meter below seafloor (mbsf) at Site C0002 in the Kumano forearc

basin, SE offshore the Kii Peninsula (Figure 45). In an approach similar to the one of V. Heuer and colleagues, we evaluated the scientific value of the current SciGas system (Figure 46). We use hydrocarbon gas contents from samples taken from Hole C0002F drilling mud gas, which were analyzed onshore, and compare those with shipboard drilling mud gas data. Analyses focused on methane (C_1), ethane (C_2) and propane (C_3), as well as different gas ratios and temperature estimations using shore-based and shipboard datasets.

GEOLOGICAL SETTING

[5] North-west directed subduction of the Philippine Sea plate (PSP) beneath the Eurasian Plate at a rate of ca. 4.1 – 6.5 cm/yr formed the Nankai Trough accretionary complex (Seno et al. 1993; Miyazaki and Heki 2001). The northern part of the PSP comprises sediments from the Shikoku Basin, which formed during backarc spreading of the Izu Bonin Arc ca. 23 Ma ago (Okino et al. 1999). Subduction and accretion started around 15 Ma, stopped at ca. 12 Ma and continued ca. 6 Ma (Taira et al. 1992; Taira 2001; Kimura et al. 2014). Site C0002 is situated in the Kumano forearc basin, which is the most intensely studied area among the Nankai forearc basins (i.e. from SW to NE: Hyuga basin, Tosa basin, Muroto basin, Kumano Basin, Enshu trough; Figure 45). It opened up not earlier than 1.67 Ma ago as a consequence of splay fault activity in the accretionary prism (Strasser et al. 2009). Nowadays, the Kumano Basin extends around 100 km from west to east and ca. 80 km from north to south. At Site C0002, the upper four lithological units were fully investigated by drilling and coring 7 boreholes (C0002B, C0002D, C0002H, C0002J, C0002K, C0002L, C0002F; Table 11). The upper ca. 826 m are separated in two units, with Unit I from 0 – 126 mbsf and Unit II from 126 – 826 mbsf (Expedition 315 Scientists 2009) (Figures 47, 48). While both units are dominated by hemipelagic mudstone, intercalations of silty-sandy turbidites and ash layers are more abundant in Unit I. Unit II is followed by basal forearc basin sediments (Unit III), which comprise silty claystone with scattered bioturbation and glauconite-rich zones. Further downhole, in Hole C0002F, the upper accretionary prism (Unit IV) was encountered at ca. 1025.5 mbsf (Strasser et al. 2014a). The boundary was defined based on a pronounced increase in interbedding of sand-, silt- and mudstone. The varying sand content was used to differentiate individual subunits from 1025.5 – 1140.5 mbsf, 1140.5 – 1270.5 mbsf, 1270.5 – 1420.5 mbsf, 1420.5 – 1600.5 mbsf and 1600.5 – 1740.5 mbsf. Below 1740.5 mbsf, sediments of Unit V consist mainly of silty to fine silty claystone. Beginning with Unit IV, all boundaries include an uncertainty of 50 – 70 m, which is caused by the underreamer borehole assembly (BHA) that was used for widening the borehole during riser drilling (Strasser et al. 2014b).

Table 11: *Overview of depth intervals for Units I to V and subunits at Site C0002.*

Unit	Sub-units	C0002B (mbsf)	C0002D (mbsf)	C0002F (mbsf)	C0002H (mbsf)	C0002J (mbsf)	C0002K (mbsf)	C0002L (mbsf)
I			0 - 135.8					
II		135.8 - 826.3	135.8 - 826.3				200 – 505	200 – 505
III		834.0 - 921.7		875.5 – 1025.5		902 - 926.7		
IV		921.7 - 1052.5		1025.5 – 1740.5	1100.5 - 1120			
	IVA			1025.5 – 1140.5				
	IVB			1140.5 – 1270.5				
	IVC			1270.5 – 1420.5				
	IVD			1420.5 – 1600.5				
	IVE			1600.5 – 1740.5				
V				1740.5 – 2004.5				

MATERIALS AND METHODS

Shipboard Analyses

[6] Generation of shipboard data is comprehensively explained in Strasser et al. (2014b) and will be briefly summarized in the following (Figure 46). Shipboard data were compiled in real-time by the SciGas and Geoservices systems, of which each uses an individual degasser to extract gas from the drilling mud. Compared to the SciGas system (Figure 46, position D1), the degasser from Geoservices was placed further downstream the flow line (Figure 46, position D2) and was adjustable in height in case the mud level dropped. This instrument provides an agitator stirring the mud to maximize separation of the gas phase from the fluid phase. Afterwards, the gas travelled through a ca. 50 m long PVC tubing with ca. 3 mm inner diameter, causing a time difference of ca. 6 minutes between gas extraction and arrival at the mud gas monitoring laboratories. At the Geoservices mud logging laboratory, total gas concentration and gas composition were determined separately using two individual gas chromatographs.

[7] Compared to the Geoservices logging unit, position and configuration of the SciGas degasser precluded any height adjustment (Figure 46, position D1), but the extracted drilling mud gas was subject to a broader range of measurements. After having bypassed the sampling line, the gas composition was first analyzed by a methane carbon isotope analyzer (MCIA), followed by a GC-natural gas analyzer (GC-NGA), a ^{222}Rn detector and a process gas mass spectrometer (PGMS).
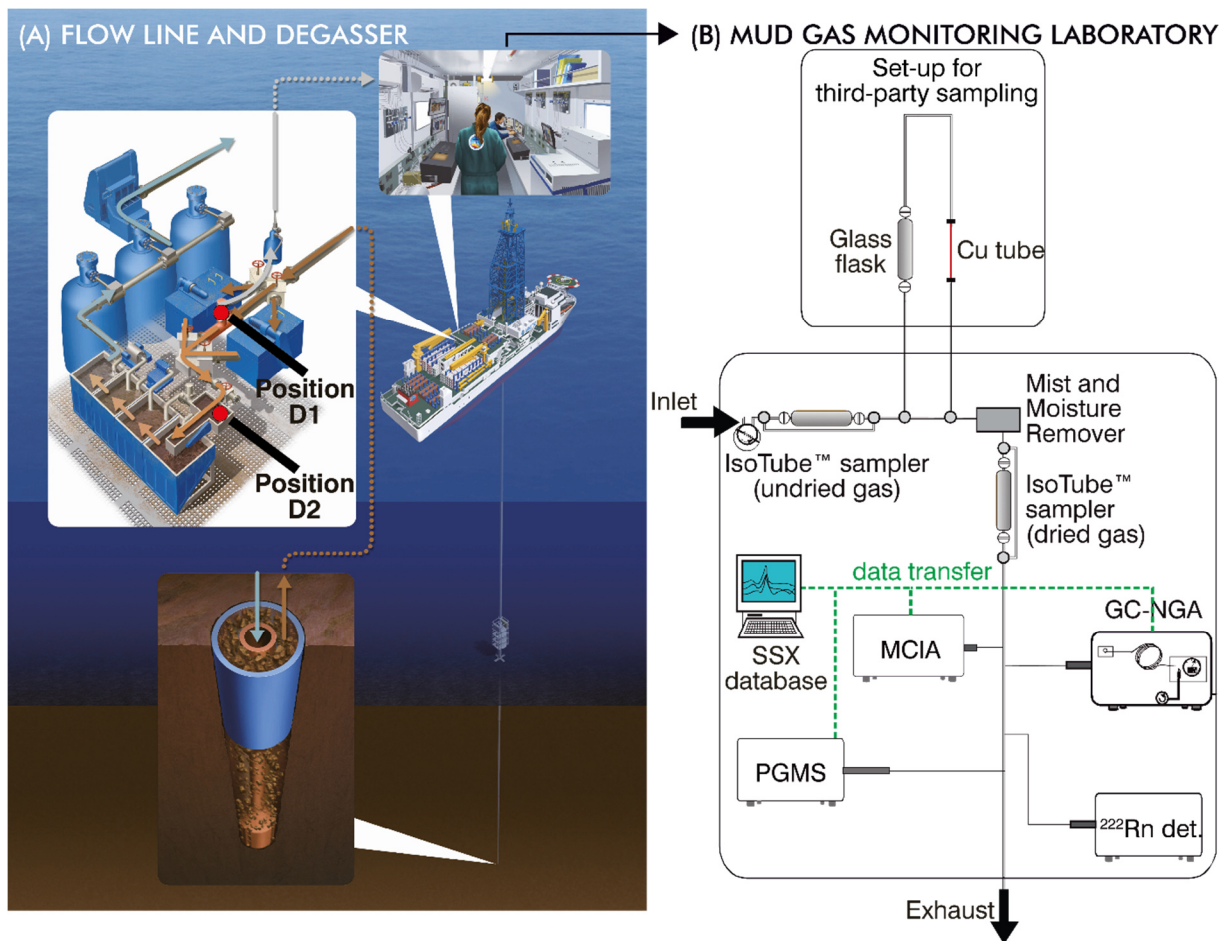
Figure 46: *Drilling mud gas monitoring set-up during IODP Exp. 338 (modified from Strasser et al., 2014b; 3D schematic © JAMSTEC). "Position D1" denotes the position of the SciGas degasser, whereas "Position D2" indicates the position of the Geoservices degasser.*

[8] In this manuscript, shipboard data used for further evaluation of and comparison with the shore-based data include the MCIA and GC-NGA datasets. The data generated by Geoservices will be included as well to highlight the differences of the Geoservices and SciGas monitoring systems. $\delta^{13}C_{CH4}$ values are reported in notion to the Vienna Peedee belemnite (VPDB) standard in parts per mil (‰) (Strasser et al. 2014b).

Drilling Mud Gas Sampling and Analyses

[9] During IODP Exp. 338, before being analyzed by onboard instruments, the gas phase flowed through a third-party sampling line and the onboard Isotube sampling system (Strasser et al. 2014b). Sampling took place between 850 and 1998.5 mbsf using glass flasks and copper (Cu) tubes for the third-party flow line, and Isotubes for the Isotube system (Figure 46). All samples were taken before the gas passed the mist and moisture remover.
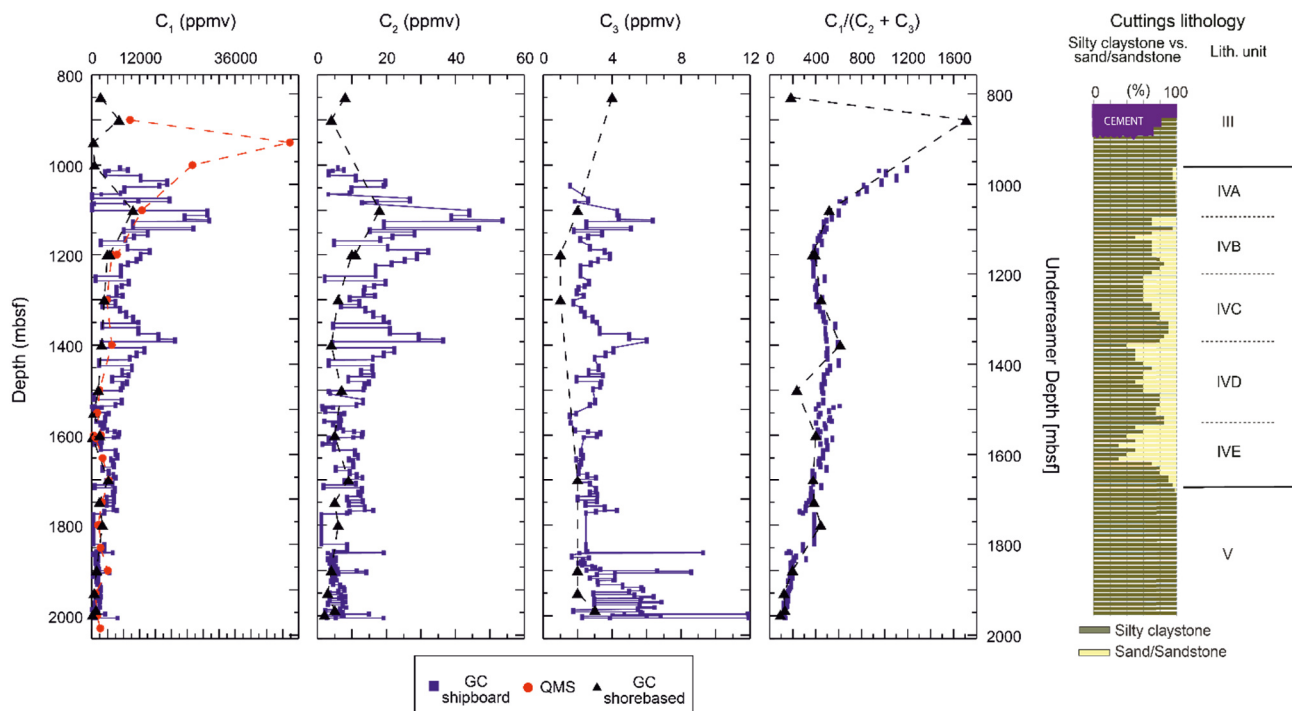
Figure 47: *Hydrocarbon gas components in drilling mud gas samples analyzed onshore with a gas chromatograph (GC shore-based; black triangles) and quadrupole mass spectrometer (QMS; red dots) compared to shipboard GC-NGA real-time data (GC shipboard, blue squares; Strasser et al. 2014a). C_1 = methane, C_2 = ethane, C_3 = propane, $(C_1/(C_2 + C_3))$ = Bernard parameter). The lithological column on the right side was modified from (Strasser et al. 2014a).*

[10] In total, 23 of the drilling mud gas samples collected during IODP Exp. 338 (Strasser et al. 2014a) were subject to shore-based analyses by a quadrupole mass spectrometer (QMS; Pfeiffer Omnistar) and a gas chromatograph (GC SRI-8610) equipped with a Haysep D column and a flame ionization detector. While the QMS only detected methane (hereafter termed $C_{1\text{-QMS}}$), the GC allowed identification and quantification also higher hydrocarbons in addition to methane, i.e. C_2H_6 and C_3H_8 (hereafter termed $C_{1\text{-GC}}$, $C_{2\text{-GC}}$, $C_{3\text{-GC}}$). For both the QMS and the GC, the detection limit for hydrocarbon gases was set to 1 part per million by volume (ppmv).

Deuterium Determination

[11] Out of the 23 samples taken, 14 were subject to hydrogen isotope analysis. Prior to the analysis, samples were given time to adjust to room temperature. The stable hydrogen isotopic composition of CH_4 was analyzed by isotope ratio monitoring gas chromatography/mass spectrometery (irm-GC/MS) using a Thermo Finnigan Trace Ultra GC, connected to a Thermo Finnigan DELTA V Plus mass spectrometer via Thermo Finnigan GC-Isolink interface as reported previously (Inagaki et al. 2013). The analysis involved online transfer of samples from a high temperature conversion reactor (containing an empty ceramic tube covered with graphite layer that was kept at a temperature of 1440°C) in which compounds were pyrolyzed to molecular hydrogen, carbon, and carbon monoxide, prior to their transfer into the mass spectrometer via Conflow IV interface. The Trace Ultra GC was equipped with a Carboxen column (30 m length, 0.32 mm

Table 12: *Results for shore-based analyses of drilling mud gas samples (iso = isotube, glass = glass flask, iso event = event gas sampled with isotube). NA = not available, BD = below detection limit, mBRT = meters below rotary table, mbsf = meters below seafloor*

Sample ID 338-C0002F-00	Sampling Vial	Total Depth (mBRT)	Lag Depth (mbsf)	$C_{1\text{-QMS}}$ (ppmv)	$C_{1\text{-GC}}$ (ppmv)	$C_{2\text{-GC}}$ (ppmv)	$C_{3\text{-GC}}$ (ppmv)	δD_{CH4} (‰, SMOW)
244GMW-WR	glass	2817.5	850	NA	2215	8	4	NA
013GMW-WR	glass	2867.5	900	9610	6834	4	BD	BD
023GMW-WR	glass	2917.5	950	49800	416	BD	BD	-164
033GMW-WR	glass	2967.5	1000	25300	96	BD	BD	-167
033GMW-WR	iso	2967.5	1000	NA	689	BD	BD	NA
070GMW-WR	glass	3067.5	1100	12600	10346	18	2	-170
079GMW-WR	glass	3167.5	1200	6360	4489	11	1	NA
079GMW-WR	iso	3167.5	1200	5080	3936	10	BD	-166
128GMW-WR	glass	3267.5	1300	3800	3124	6	1	-167
129GMW-WR	iso	3367.5	1400	5040	2457	4	BD	-167
146GMW-WR	glass	3467.5	1500	1940	1647	7	BD	NA
180GMW-WR	glass	3517.5	1550	1380	563	BD	BD	ND
181GMW-WR	glass	3567.5	1600	2300	439	2	3	NA
181GMW-WR	iso	3567.5	1600	440	2000	5	BD	-164
197GMW-WR	iso event	3572.3	1604.8	960	186	BD	BD	BD
225GMW-WR	glass	3667.5	1700	4340	4144	9	2	-166
226GMW-WR	glass	3717.5	1750	2580	1928	5	BD	NA
243GMW-WR	glass	3767.5	1800	1580	2664	6	BD	-169
263GMW-WR	iso	3767.5	1800	1890	43	BD	BD	NA
277GMW-WR	glass	3867.5	1900	4050	1192	4	2	-171
278GMW-WR	glass	3917.5	1950	946	625	3	2	NA
305GMW-WR	iso	3955	1987.5	1360	1058	5	3	-166
391GMW-WR	glass	3965.7	1998.2	2140	184	2	BD	NA

inner diameter). The carrier gas was helium (1.2 mL min^{-1}), the split ratio 1:8, and the temperature of the GC oven and injector were 60°C (isotherm) and 200°C, respectively. The primary standardization of the DELTA V Plus was based on multiple (three to six) injections of reference H_2 from a lab tank (δD= -96.4 ± 0.3‰ vs VSMOW, 3.2 ± 0.3 V at m/z 2) at the beginning and end of the analysis of each sample. Lab tank H_2 was calibrated against the certified CH_4 standard T-iso2 (2.5 vol% CH_4 in a balance of dry, synthetic air; $\delta^{13}C_{CH4}$ = -38.3 ± 0.2‰ vs VPD; δD_{CH4} = -138‰ vs SMOW). We assessed the precision of our analysis by repeated analysis of the standard. The precision was better than 2‰ (1σ). Stable hydrogen isotope analysis of methane requires a peak amplitude of 1 V or higher at m/z 2. Depending on CH_4 concentration, ~300 μL- ~3000 μL of sample were injected per analysis. All analyses were carried out in duplicate.

[12] Stable hydrogen isotope ratios are reported in δD notation (per mil, ‰) relative to the Vienna Standard Mean Ocean Water (VSMOW), with $\delta D = [(R_{sample}-R_{VSMOW})/R_{VSMOW}] \cdot 10^3$, where $R = {}^2H/{}^1H$ and $R_{VSMOW} = (155.76 \pm 0.05) \times 10^{-6}$ (Gonfiantini 1978).

RESULTS

Results of Shipboard Analyses

[13] The results of the measurements are displayed in Figs. 47 – 50. The results of the shipboard measurements are comprehensively documented in Strasser et al. (2014a), and will only be reviewed briefly. Both the GC dataset from the SciGas system and the Geoservices dataset were dominated by C_1, with concentrations of up to 86400 ppmv and 164000 ppmv, respectively. C_2 and C_3 were only found in minor concentrations, with up to 300 ppmv and 900 ppmv for C_2, and 130 ppmv and 2300 ppmv for C_3, in the Geoservices and GC datasets, respectively. Shipboard values for $\delta^{13}C_{CH4}$ stayed below – 60‰ at depths shallower than 1700 mbsf, and gradually increase farther downhole (Figure 50).
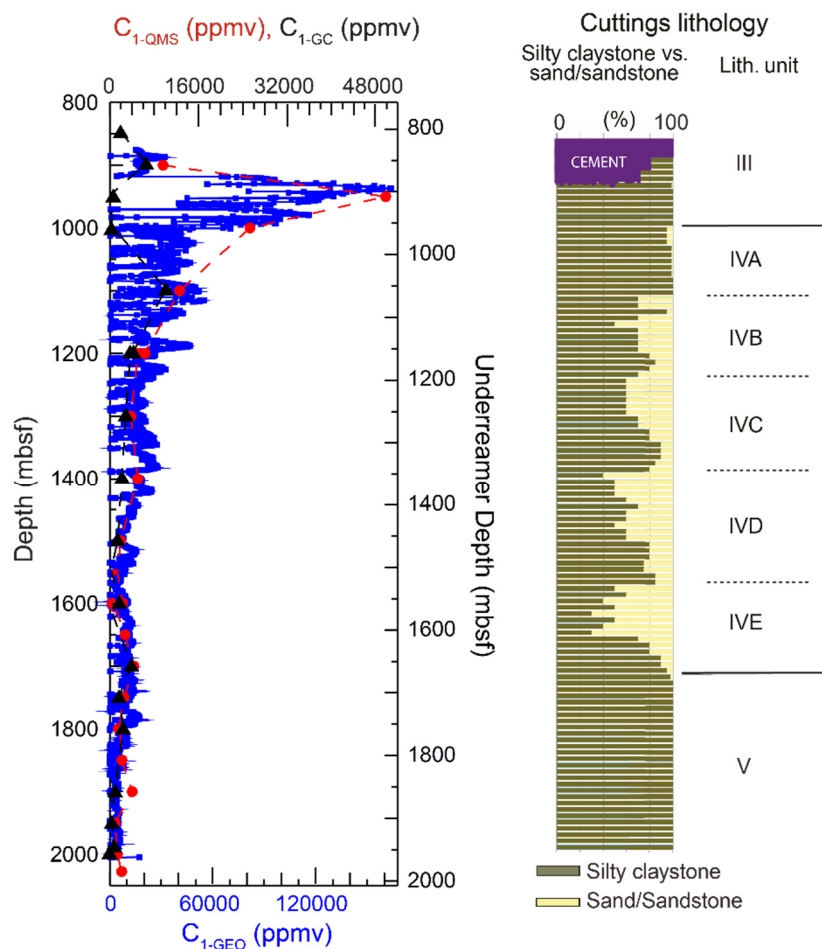
Figure 48: *Methane determined by the QMS ($C_{1\text{-}QMS}$; red dots) and by GC ($C_{1\text{-}GC}$, black triangles) compared with shipboard methane data from Geoservices ($C_{1\text{-}Geo}$; blue squares and line). Please be aware of the different scales of the individual x-axis at the bottom and at the top. The lithological column on the right side was modified from Strasser et al. (2014a).*

Results of Shore-based Analyses

[14] With values between 134 and 10346 ppmv in the GC data and 440 to 49800 ppmv in the QMS data, C_1 was also the dominant gas species in the shore-based data, followed by C_{2-GC} (2 – 18 ppmv) and C_{3-GC} (2 – 4 ppmv) (Table 12). Higher homologues were not detected. Although concentrations of C_{2-GC} are up to four orders of magnitude smaller compared to the concentrations of C_{1-GC}, both components show a similar distribution with depth (Figure 47) and are positively correlated with R = 0.94 (Figure 49). The highest values for C_{1-GC} and C_{2-GC} were found at 1100 mbsf, with 10346 and 18 ppmv, respectively. Both components experience an overall decrease downhole. C_{1-GC} is hardly correlated with C_{3-GC} (R = 0.25), and shows a slightly negative trend (Figure 47) with minor variations downhole. After C_{3-GC} decreases from 4 to 1 ppmv between 850 and 1200 msbf, it slightly increases again with depth to 3 ppmv.
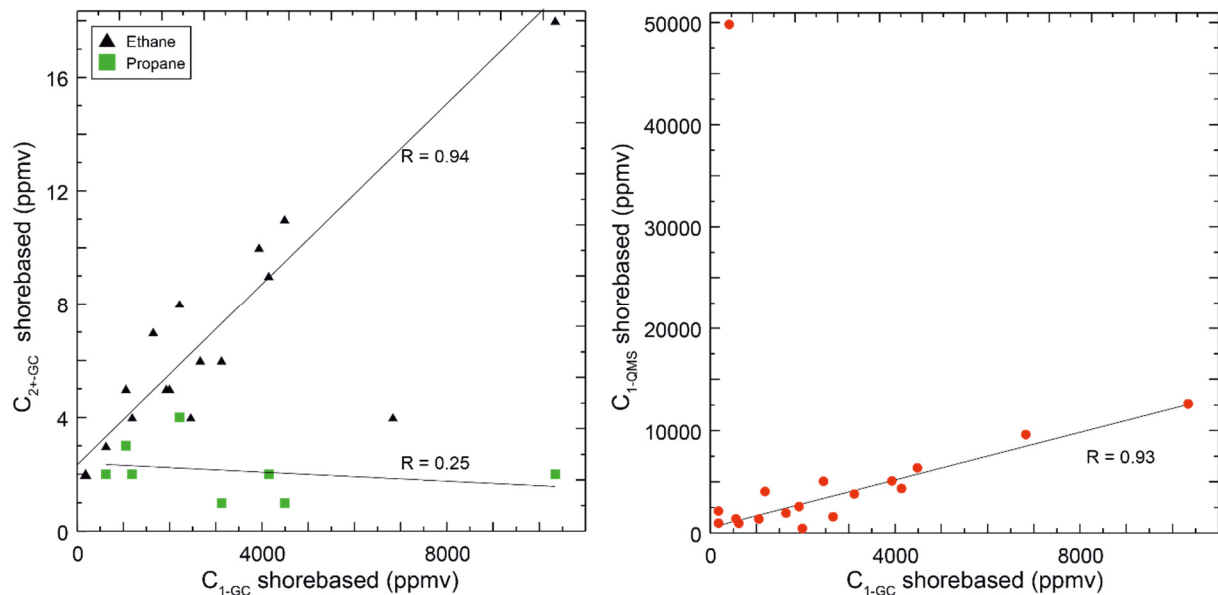
Figure 49: Left: *Methane (C_{1-GC}) vs. higher hydrocarbon components ($C_{2+-GC;}$ ethane: black triangle; propane: green square), all determined by shore-based analyses with a gas chromatograph.* **Right**: *Methane following shore-based analyses with a gas chromatograph (C_{1-GC}) vs. methane following shore-based analyses with a quadrupole mass spectrometer (C_{1-QMS}).*

[15] C_{1-QMS} shows a positive correlation with C_{1-GC} (R = 0.93), and at depths greater 1000 mbsf, both C_{1-QC} and C_{1-QMS} experience similar variations and concentrations with depth (Figures 48, 49). In the depth interval between 900 and 1000 mbsf, however, C_{1-QMS} dominates the gas show with almost 50000 ppmv, whereas C_{1-GC} decreases to 416 ppmv. This deviation might result from gas depletion in the sample vial after the initial total gas analyses carried out with the QMS. The Bernard parameter (Bernard et al. 1978) varies between 1708 at 900 mbsf and 92 at 1998.2 mbsf, indicating a relative increase in thermogenic components downhole.

[16] Methane concentrations were high enough for reliable stable hydrogen isotope analysis in 12 of the 14 samples taken (Table 12). The hydrogen isotopic composition of CH_4 was uniform;

δD-values ranged from -171‰ to -164‰ and averaged around -167 ± 2‰ (Figure 50). The standard deviation of duplicate measurements was on average 2‰.

Comparison between shipboard and shore-based drilling mud gas data

[17] A comparison between the GC, QMS and onboard GC-NGA and Geoservices data (Strasser et al. 2014a) is shown in Figs. 47, 48, 50 and Figure S.17 in the Appendix A.4). Above 1300 mbsf, concentrations of C_{1-GC}, C_{1-QMS} (both on the upper x-axis in Figure 48) and C_{2-GC} are well below the concentrations of the shipboard data. Below 1300 mbsf, concentrations correspond to the real-time values. The small data coverage for C_{3-GC} prevents a thorough comparison, but the available concentrations are in the same order of magnitude as the shipboard measurements.
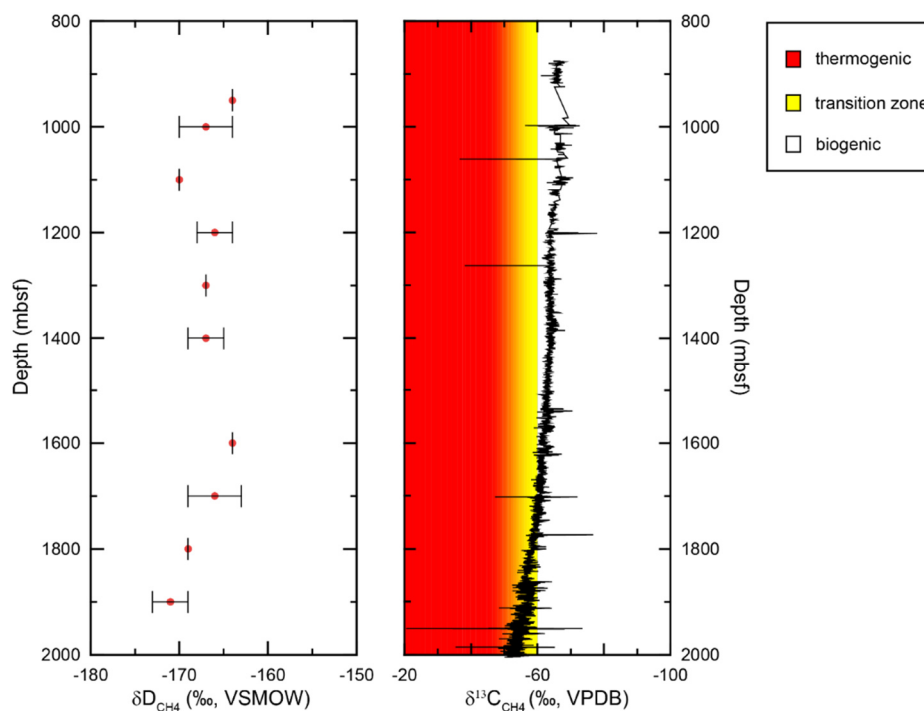
Figure 50: Left panel: δD_{CH4} values determined for different gas samples from IODP Expedition 338 (2014a). Horizontal bars indicate the standard deviation of duplicate measurements. **Right panel**: $\delta^{13}C_{CH4}$ data obtained during drilling borehole C0002F (modified from Strasser et al. 2014a). Starting at 1700 mbsf, the $\delta^{13}C_{CH4}$ data indicate a shift to methane of thermogenic origin (boundaries after Whiticar 1994).

[18] Despite the different concentrations, overall trends are similar and resemble the online data. This gets obvious when comparing the Bernard parameter based on online GC-NGA data with the Bernard parameter from shore-based measurements (Figure 47). Except for an outlier at 1500 mbsf, relative changes in the gas composition are well reproduced by onshore measurements. A comparison between the C_1/C_2, C_1/C_3 and C_2/C_3 ratios of the shipboard (GC-NGA only) and shore-based measurements is given in the Appendix A.4 (Figure S.17). C_1/C_2 ratios correspond well with a correlation coefficient R of 0.87, whereas ratios with C_3 experience a worse correlation and/or large scatter (R of C_1/C_3 and C_2/C_3 are both ≤ 0.4). Similar findings arise when comparing the Geoservices data with the shore-based GC data. While the C_1/C_2 ratios correspond well with

a correlation coefficient of R = 0.95, C_2/C_3 ratios have a negative correlation with R = -0.5, and C_1/C_3 ratios show data scatter with R = 0.16 (see Figure S.18 in the Appendix A.4).

[19] Plotting δD_{CH4} vs. $\delta^{13}C_{CH4}$, following the classification of Whiticar (1999) clearly indicates microbial CO_2 reduction to be responsible for methanogenesis at depths shallower than 1600 mbsf (Figure S.19 in the Appendix A.4). Thermogenic gas is not indicated for depths shallower 1987.5 mbsf.

DISCUSSION

Technical Considerations

[20] During IODP Exp. 338, the mud-gas monitoring system from Geoservices recorded distinctly higher absolute hydrocarbon gas concentrations than the recently installed SciGas system (Strasser et al. 2014a). The lower gas recovery of the latter are likely due to the technical configuration (Strasser et al. 2014b) that can only be adjusted and optimized during riser drilling operations. As a consequence, relative changes are less pronounced, and differentiation between formation- and/or drilling-related artefacts is more difficult (e.g. Ablard et al. 2012).

[21] Hydrocarbon ratios are commonly used to evaluate relative variations, e.g. pixler plots (Pixler 1969), star/spider diagrams (e.g. Prinzhofer et al. 2000; Dessay et al. 2011; Ablard et al. 2012) and parameters such as hydrocarbon wetness, balance and character (Haworth et al. 1985). Most of these methods require reliable estimations of higher hydrocarbons (i.e. C_{5+}), which cannot be derived by conventional degassing methods due to inefficient liberation of higher hydrocarbons. These are in gas phase at *in situ* temperature and pressure, but only C_1 to C_4 remain in gas phase at atmospheric conditions due to their boiling points < 0°C. Efficient extraction of C_{5+} requires heating of the drilling mud during degassing. Although such instruments exist (e.g., FLAIR, see Ablard et al. 2012) none were available during IODP Expedition 338 (Strasser et al. 2014b).

[22] Our results suggest that simple gas-to-gas ratios are not sufficient to orderly evaluate the SciGas system. The relatively good correlation with the Geoservices system with respect to the C_1/C_2 ratios is contrasted with a bad correspondence of C_2/C_3 and C_1/C_3 ratios, and thus, the comparison is ambiguous. Therefore, for a qualitative evaluation, we focus also on the Bernard parameter (Bernard et al. 1976) and the hydrocarbon wetness, which is expressed as total wet gas fraction (TWG), i.e. $(\sum C_2 + C_3)/(\sum C_1 - C_3) \times 100)$ (Bernard et al. 1976; James 1983; Schoell 1983; Haworth et al. 1985; Abrams 2005). At a TWG $\leq$ 5.0%, the gas composition is dominated by methane, either because temperature and time were insufficient to produce higher-order hydrocarbons, or the hydrocarbons are overmature (e.g. Schoell 1980). Our samples show a TWG

of $\leq$ 1.15 % and are in good agreement with the TWG derived from shipboard GC-NGA measurements (Appendix A.4, Table S.6). TWG for the Geoservices data is, with up to 2.4%, more than twice as high as the shore-based GC data, but still below the 5.0% threshold. At depths > 1950 mbsf, all three datasets show an increase in TWG (Appendix A.4, Table S.6). Individual TWG values imply a good correlation (see Appendix A.4, Figure S.20A, R = 0.81, Figure S.20B, R = 0.95) and all three datasets confirm the overall absence of wet gas, despite being generated by different instruments.

[23] When comparing the different Bernard parameters (i.e. $C_1/(C_2+C_3)$, Bernard et al. 1976) in a Bernard diagram (i.e. Bernard parameter vs. $\delta^{13}C_{CH4}$, Figure 51), both shipboard and shore-based GC measurements are again in good agreement. In contrast, Geoservices data show larger scatter and a relatively higher amount of ethane and propane. As a consequence, in the Bernard Diagram, Geoservices samples from depths > 1950 mbsf clearly plot in the thermogenic regime (Figure 51).

[24] Following the results for the TWG and the Bernard parameter, the SciGas as well as the Geoservices datasets allow us to qualitatively evaluate the gas composition data despite the different degassing systems. Nonetheless, both the TWG and the Bernard parameter point to generally higher ethane and propane concentrations using the Geoservices degassing system. Reasons for the underestimation of ethane and propane with the SciGas system are manifold and cannot solely be explained by boiling temperatures. Most likely, the configuration of the Sci Gas degasser caused insufficient gas liberation from the drilling mud (Strasser et al. 2014a). At times of low or absent mud pump activity, the mud level in the flow line declined. Contrary to degassing system from Geoservices, it was impossible to adjust the SciGas degasser in height in real-time. This caused insufficient stirring of the drilling mud, thus the gas phase was less efficiently liberated and more likely to be contaminated by atmospheric gases. Consequently, the SciGas only detected concentrated gases, which degass readily without further stimulation.

Origin of Gases

[25] At depths greater 1950 mbsf, the Bernard parameter, the δD-$\delta^{13}C_{CH4}$ plot and the TWG ratios point to a relative increase in thermogenic gases in all datasets (Figures 50, 51, and Figure S.19 in Appendix A.4). At the same time, no wet gas composed of C_{2+} > 5 % (i.e., > 50000 ppmv; e.g., Schoell 1980) was encountered. Wet gas is generated at elevated thermal maturity, which can be evaluated using vitrinite reflectance R_o. The latter is estimated by the shipboard $\delta^{13}C_{CH4}$ values using the empirical relationship $\delta^{13}C_{CH4}$ (‰) = 15.4 $\log_{10}$ %R_o - 41.3 (Whiticar 1994, and references therein). Computing the vitrinite reflectance led to values below 0.6, i.e. below a maturation indicative for the onset of the oil and gas window (Appendix A.4, Table S.6).
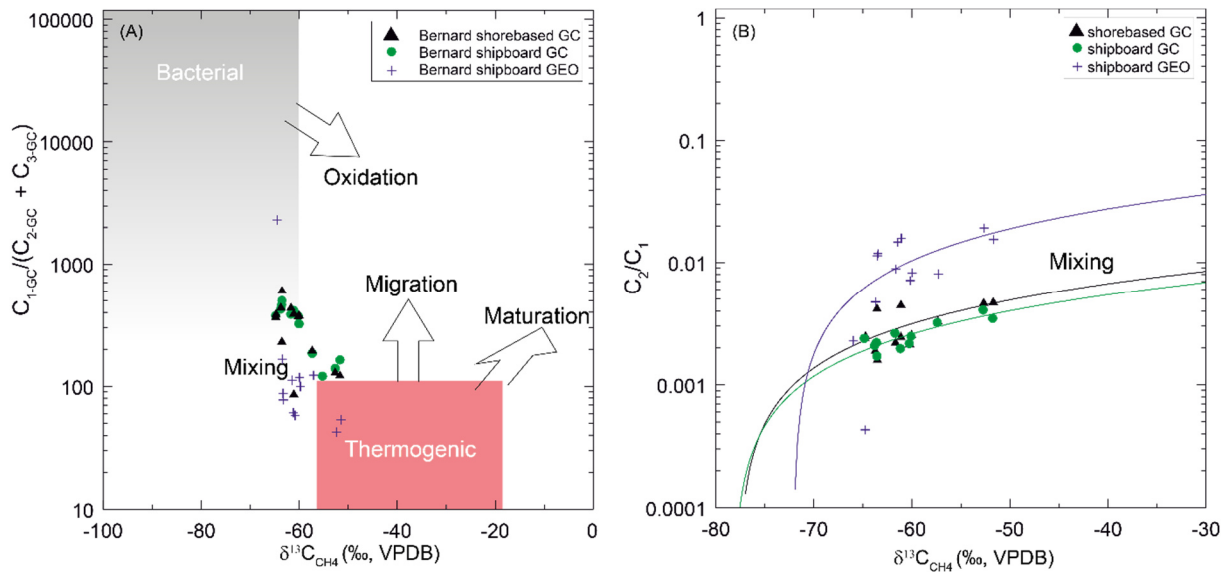
Figure 51: (A) *Bernard diagram based on the Bernard parameter (based on shipboard and shore-based data) and the shipboard $\delta^{13}C_{CH4}$ data (after Bernard et al. 1976). All three datasets clearly plot in the mixing regime.* **(B)** *C_2/C_1 ratios vs. shipboard $\delta^{13}C_{CH4}$ data (after Prinzhofer and Pernaton 1997). All datasets clearly point to a mixed gas regime, rather than diffusion fractionation.*

[26] In general, thermal maturity is influenced by the geothermal gradient and the time available for maturation. For the Kumano forearc basin, following the heat flow determination of Harris et al. (2011), the geothermal gradient is estimated to be ca. 40°C/km. This gradient was already corrected for sedimentation rate and subsidence (Harris et al. 2011). Giving a bottom water temperature of 2.4°C at Site C0002 (Harris et al. 2011), an *in situ* temperature of 82.4°C can be concluded for a thermal conductivity of 1.5 W m^{-1} K^{-1} at a depth of 2000 mbsf. This estimate is confirmed by using an empirically determined C_1/C_2-TOC-temperature relationship originally compiled for safety purposes by the JOIDES PPSP (1992). Plotting TOC data from Expedition 338 (Strasser et al. 2014a) and the C_1/C_2 ratios based on the shore-based and shipboard GC measurements shows a rather large scatter (Figure S.21 in the Appendix A.4), which is understandable giving the uncertainties in drilling mud gas monitoring and the limitations of the empirical C_1/C_2-TOC-temperature relationship (JOIDES PPSP 1992). In particular, this relationship is only valid for hydrocarbon gases that are strictly produced *in situ*. Nonetheless, a simple linear fit applied to both datasets points to an *in situ* temperature between 81°C and 85°C (Figure 52) at 2000 mbsf, which is in agreement with the estimations provided by Harris et al. (2011). Although hydrocarbon generation already starts at 50°C (Seewald 2003), higher hydrocarbons are usually encountered at temperatures > 100 °C. At the same time, in addition to the low temperature, the geological timescale for hydrocarbon generation at these temperatures was probably too short.

6.1 Drilling Mud Gas Monitoring for Evaluation of Hydrocarbon Gas Composition

Table 13: *Overview of the different temperature and time intervals for which a time-temperature index (TTI) was calculated.*

Temp. Interval (°C)	r^n	δt (Ma)	Interval TTI	Total TTI
0 - 10	2^{-10}	0.53	0.0005	0.0005
10 - 20	2^{-9}	0.76	0.0015	0.0020
20 - 30	2^{-8}	0.76	0.0030	0.0050
30 - 40	2^{-7}	0.76	0.0059	0.0109
40 - 50	2^{-6}	0.76	0.0119	0.0228
50 - 60	2^{-5}	0.76	0.0237	0.0465
60 - 70	2^{-4}	0.76	0.0475	0.0940
70 - 80	2^{-3}	0.76	0.0949	0.1889
80 - 82	2^{-2}	0.15	0.0380	0.2269

[27] A simple quantitative measure for the time-temperature-related maturity is the time-temperature index (TTI; Lopatin 1971; Waples 1980), which can be calculated as follows:

$$TTI = \Sigma \, (\delta t_i) \, (r_i^n) \tag{20}$$

where δt_i denotes the time interval spent in the *i-th* 10°C temperature interval, and r_i^n is the temperature factor related to the individual temperature interval (Waples 1980). The TTI is based on the assumption that the rate of the chemical reaction responsible for hydrocarbon generation from kerogen doubles for every interval of 10°C, while variations in kerogen composition are neglected (Killops and Killops 2005). In addition, we make the following assumptions: (i) the material at ca. 2000 mbsf at Site C0002 is similar to the material encountered in Unit III at NanTroSEIZE Sites C0011 and C0012, and thus, has a maximum age of 9 Ma (Expedition 348 Scientists, in preparation); (ii) if the material was deposited at 9 Ma, than it falls in the period where subduction ceased and thus, it was only subject to diagenesis between 9 and 6 Ma (Kimura et al. 2014) (iii) following Underwood et al. (2010), we assume that the material was not buried deeper than 100 mbsf, and thus, the material experienced temperatures of up to 3°C (based on a temperature gradient of ca. 100°C/km, and a seafloor temperature of ca. 2°C; Underwood et al. 2010; Marcaillou et al. 2012) (iv) the material was subducted at 6 Ma (Kimura al. 2014), and (v) experienced an increase in temperature by 79°C, leading to 82°C at 2000 mbsf based on the work of Harris et al. (2011). These estimates result in two different heating rates: a pre-subduction heating rate of 2.3°C/Ma and a post-subduction heating rate of 20°C/Ma. Based on these rates, we calculated a cumulative TTI of 0.23 (Table 13). This value is slightly above the onset of petroleum production (TTI ≥ 15), but far too low to indicate wet gas (TTI ≥ 1500) (Waples 1980).
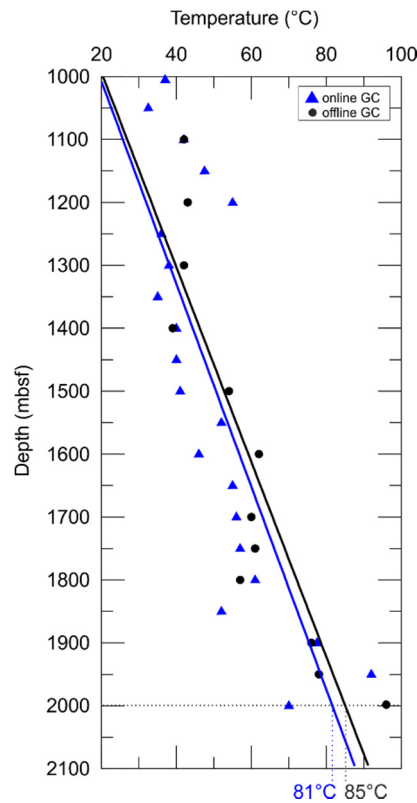
Figure 52: *Temperature estimation following the C$_1$/C$_2$-Temperature-TOC relationship shown in Fig. S.21 in the Appendix A.4. Geothermal gradients are similar, with 39.3 °C and 42.5 °C for the shipboard and shore-based data, respectively*

[28] Consequently, following our estimations for R$_0$, *in situ* temperature and the TTI, *in situ* production of significant amounts of higher hydrocarbons is unlikely at depths < 2000 mbsf. Beside *in situ* production, gases tend to follow the pressure gradient and migrate in adjacent rocks along faults or fractures, or via inter-granular diffusion. For shallower gas accumulations, this can lead to mixing of biogenic and thermogenic gas. The TWG allows first qualitative estimations, but identifying secondary effects such as mixing or oxidation remains difficult. Indeed, the Bernard diagram points to a gas composition, which is affected by mixing rather than showing a clear biogenic or thermogenic signal (Figure 51A). Mixing can occur in different ways, either due to active gas migration along faults or fractures, or the gas mixture was derived by diffusive migration leading to isotope fractionation (Prinzhofer and Pernaton 1997). For methane, diffusive migration would lead to an enrichment of the light carbon isotope, and thus, the migrated gas would plot in the biogenic or mixed regime despite being derived from a thermogenic source.

[29] To differentiate between pure mixing and diffusive migration, Prinzhofer and Pernaton (1997) developed a two-endmember mixing model using C$_2$/C$_1$ vs. $\delta^{13}C_{CH4}$ mixing diagrams. The authors concluded that, on a semi-logarithmical scale, a negatively curved line would point to pure mixing, whereas a straight line indicates the prevalence of diffusion fractionation. Applying this method

to all three datasets results in negatively curved fits, which indicate mixing to be responsible for the observed hydrocarbon gas composition (Figure 51B).

[30] At Site C0002, a fault zone is indicated between 1500 and 1640 mbsf based on resistivity data obtained during logging-while-drilling (Strasser et al. 2014a). This corresponds to an increase in TWG of the Geoservices and the shore-based dataset at 1600 mbsf, pointing to active or recently active migration of higher hydrocarbons from greater depths and subsequent mixing. Detailed analyses of possible gas migration and mixing will be covered in future studies evaluating data from the recently finished IODP Exp. 348 using noble gas isotopes from Holes C0002F, C0002N and C0002P (cf. chapter 6.2).

CONCLUSIONS

[31] In conclusion, shipboard and shore-based analyses allow the same qualitative estimation about the genetic origin of the drilling mud gas. Differences in absolute concentrations of the SciGas and Geoservices degassing systems are most likely caused by the different configurations of the individual degassers. Comparison of the individual datasets by simple gas ratio analysis was ambiguous, therefore we chose the Bernard parameter and the total wet gas ratio to qualitatively analyze and compare the individual datasets. Following theses evaluations, we showed that, beside the technical problems encountered during IODP Exp. 338, the SciGas system produced reliable data, which helped to qualitatively estimate temperature, maturity, and possible mixing of the hydrocarbon gases. Consequently, the SciGas system onboard *D/V Chikyu* is suitable for detecting qualitative changes, and allows a first estimation of the contribution of biogenic and thermogenic hydrocarbon gas.

References

Ablard P, Bell C, Cook D, Fornasier I, Poyet J-P, Sharma S, Fielding K, Lawton G, Haines G, Herkommer MA, Mccarthy K, Radakovic M, Umar L (2012) The Expanding Role of Mud Logging. Oilf Rev 24:24–41.

Abrams MA (2005) Significance of hydrocarbon seepage relative to petroleum generation and entrapment. Mar Pet Geol 22:457–477. doi: 10.1016/j.marpetgeo.2004.08.003

Aquilina L, Baubron J-C, Defoix D, Dégranges P, Disnar J-R, Marty B, Robé M-C (1998) Characterization of gases in sedimentary formations through monitoring during drilling and core leaching (Balazuc borehole, Deep Geology of France Programme). Appl Geochemistry 13:673–686. doi: 10.1016/s0883-2927(98)00008-0

Bernard BB, Brooks JM, Sackett WM (1976) Natural gas seepage in the Gulf of Mexico. Earth Planet Sci Lett 31:48–54. doi: 10.1016/0012-821X(76)90095-9

Dessay J, Torres O, Sharma S (2011) Real Time Formation Characterization from Advanced Mud Gas Analyses for Improved Geological Operations Decisions. 73rd EAGE Conf. Exhib.

Ellis L, Brown A, Schoell M, Uchytil S (2003) Mud gas isotope logging (MGIL) assists in oil and gas drilling operations. Oil Gas J 101:32–41.

Ellis L, Berkman T, Uchytil S, Dzou L (2007) Integration of mud gas isotope logging (MGIL) with field appraisal at Horn Mountain Field, deepwater Gulf of Mexico. J Pet Sci Eng 58:443–463. doi: 10.1016/j.petrol.2007.03.001

Erzinger J, Wiersberg T, Dahms E (2004) Real-time mud gas logging during drilling of the SAFOD Pilot Hole in Parkfield, CA. Geophys Res Lett 31:L15S18. doi: 10.1029/2003gl019395

Erzinger J, Wiersberg T, Zimmer M (2006) Real-time mud gas logging and sampling during drilling. Geofluids 6:225–233. doi: 10.1111/j.1468-8123.2006.00152.x

Expedition 315 Scientists (2009) Site C0002. In: Kinoshita M, Tobin H, Ashi J, Kimura G, Lallemant S, Screaton EJ, Curewitz D, Masago H, Moe KT, the Expedition 314/315/316 Scientists (eds) Proc IODP 315. Integrated Ocean Drilling Program Management International, Inc., Washington D.C. doi:10.2204/iodp.proc.314315316.124.2009

Expedition 319 Scientists (2010) Site C0009. In: Saffer D, McNeill L, Byrne T, Araki E, Toczko S, Eguchi N, Takahashi K, Expedition 319 Scientists (eds) Proc IODP 319. Integrated Ocean Drilling Program Management International, Tokyo. doi:10.2204/iodp.proc.319.103.2010

Gonfiantini R (1978) Standards for stable isotope measurements in natural compounds. Nature 271:534–536.

Hammerschmidt S, Toczko S, Kubo Y, Wiersberg T, Fuchida S, Kopf A, Hirose T, Saffer D, Tobin H, the Expedition 348 Scientists (2014) Influence of drilling operations on drilling mud gas monitoring during IODP Exp. 338 and 348 [abstract], EGU General Assembly 2014, abstract # EGU2014-5904

Harris RN, Schmidt-Schierhorn F, Spinelli G (2011) Heat flow along the NanTroSEIZE transect: Results from IODP Expeditions 315 and 316 offshore the Kii Peninsula, Japan. Geochemistry, Geophys Geosystems 12:Q0AD16. doi: 10.1029/2011GC003593

Haworth J, Sellens M, Whittaker A (1985) Interpretation of Hydrocarbon Shows Using Light (C1-C5) Hydrocarbon Gases from Mud-Log Data. Am Assoc Pet Geol Bull 69:1305–1310.

Hilton DR, Craig H (1989) The Siljan Deep Well: Helium isotope results. Geochim Cosmochim Acta 53:3311–3316. doi: 10.1016/0016-7037(89)90110-5

Inagaki F, Hinrichs K-U, Kubo Y, the Expedition 337 Scientists (2013) Deep Coalbed Biosphere off Shimokita - Microbial processes and hydrocarbon system associated with deeply buried coalbed in the ocean. IODP Prel Report, 337. doi: 10.2204/iodp.pr.337.2012

James AT (1983) Correlation of natural gas by use of carbon isotopic distribution between hydrocarbon components. Am Assoc Pet Geol Bull 67:1176 – 1191.

JOIDES PPSP (1992) Ocean Drilling Guidelines for Pollution Prevention and Safety. JOIDES J 18

Killops SD, Killops VJ (2005) Introduction to Organic Geochemistry. 406.

Kimura G, Hashimoto Y, Kitamura Y, Yamaguchi A, Koge H (2014) Middle Miocene swift migration of the TTT triple junction and rapid crustal growth in southwest Japan — A review. Tectonics 2014TC003531. doi: 10.1002/2014TC003531

Lopatin NV (1971) Temperature and Geologic Time as Factors in Coalification. Izv Akad Nauk SSSR, Ser Geol 3:95 – 106.

Marcaillou B, Henry P, Kinoshita M, Kanamatsu T, Screaton E, Daigle H, Harcouët-Menou V, Lee Y, Matsubayashi O, Kyaw Thu M, Kodaira S, Yamano M, the Expedition 333 Sientific Party (2012) Seismogenic zone temperatures and heat-flow anomalies in the To-nankai margin segment based on temperature data from IODP expedition 333 and thermal model. Earth Planet Sci Lett 349-350:171–185. doi: 10.1016/j.epsl.2012.06.048

Miyazaki S, Heki K (2001) Crustal velocity field of southwest Japan: subduction and arc-arc collision. J Geophys Res 106:4305–4326

Okino K, Ohara Y, Kasuga S, Kato Y (1999) The Philippine Sea: New survey results reveal the structure and the history of the marginal basins. Geophys Res Lett 26:2287–2290. doi: 10.1029/1999gl900537

Pixler BO (1969) Formation Evaluation by Analysis of Hydrocarbon Ratios. J Pet Technol 21:665 – 670. doi: 10.2118/2254-PA

Prinzhofer A, Pernaton É (1997) Isotopically light methane in natural gas: bacterial imprint or diffusive fractionation? Chem Geol 142:193 – 200. doi: 10.1016/S0009-2541(97)00082-X

Prinzhofer A, Mello MR, Takaki T (2000) Geochemical Characterization of Natural Gas : A Physical Multivariable Approach and its Applications in Maturity and Migration Estimates. Am Assoc Pet Geol Bull 84:1152–1172.

Schoell M (1980) The hydrogen and carbon isotopic composition of methane from natural gases of various origins. Geochim Cosmochim Acta 44:649–661. doi: 10.1016/0016-7037(80)90155-6

Schoell M (1983) Genetic characterization of natural gases. Am Assoc Pet Geol Bull 67:2225 – 2238.

Screaton EJ, Kimura G, Curewitz D, the Expedition 316 Scientists (2009) Expedition 316 Summary. In: Kinoshita M, Tobin H, Ashi J, Kimura G, Lallemant S, Screaton EJ, Curewitz D, Masago H, Moe KT, the Expedition 314/315/316 Scientists (eds) IODP Proc 316. Integrated Ocean Drilling Program Management International, Inc., Washington D.C. . doi: 10.2204/iodp.proc.314315316.131.2009

Seewald JS (2003) Organic-inorganic interactions in petroleum-producing sedimentary basins. Nature 426:327–333.

Seno T, Stein S, Gripp AE (1993) A model for the motion of the Philippine Sea plate consistent with NUVEL-1 and geological data. J Geophys Res 98:17941–17948

Strasser M, Moore GF, Kimura G, Kitamura Y, Kopf AJ, Lallemant S, Park J-O, Screaton EJ, Su X, Underwood MB, Zhao X (2009) Origin and evolution of a splay fault in the Nankai accretionary wedge. Nat Geosci 2:648–652.

Strasser M, Dugan B, Kanagawa K, Moore GF, Toczko S, Maeda L, Kido Y, Moe KT, Sanada Y, Esteban L, Fabbri O, Geersen J, Hammerschmidt S, Hayashi H, Heirman K, Hüpers A, Jurado Rodriguez MJ, Kameo K, Kanamatsu T, Kitajima H, Masuda H, Milliken K, Mishra R, Motoyama I, Olcott K, K. O, Pickering KT, Ramirez SG, Rashid H, Sawyer D, Schleicher A, Shan Y, Skarbek R, Song I, Takeshita T, Toki T, Tudge J, Webb S, Wilson DJ, Wu H-Y, Yamaguchi A (2014a) Site C0002. In: Strasser et al. (eds) IODP Proc 338:92. doi: 10.2204/iodp.proc.338.102.2014

Strasser M, Dugan B, Kanagawa K, Moore GF, Toczko S, Maeda L, Kido Y, Moe KT, Sanada Y, Esteban L, Fabbri O, Geersen J, Hammerschmidt S, Hayashi H, Heirman K, Hüpers A, Jurado MJ, Kameo K, Kanamatsu T, Kitajima H, Masuda H, Milliken K, Mishra R, Motoyama I, Olcott K, Oohashi K, Pickering KT, Ramirez SG, Rashid H, Sawyer D, Schleicher A, Shan Y, Skarbek R, Song I, Takeshita T, Toki T, Tudge J, Webb S, Wilson DJ, Wu H, Yamaguchi A (2014b) Methods. In: Strasser et al. (eds) IODP Proc 338:248. doi: 10.2204/iodp.proc.338.103.2014

Taira A (2001) Tectonic Evolution of the Japanese Arc System. Annu Rev Earth Planet Sci 29:109–134. doi: 10.1146/annurev.earth.29.1.109

Taira A, Byrne TB, Ashi J (1992) Photographic atlas of an accretionary prism: Geologic structures of the Shimanto Belt, Japan. Springer

Underwood MB, Saito S, Kubo Y, the Expedition 322 Scientists (2010) Expedition 322 Summary. In: Saito S, Underwood MB, Kubo Y, the Expedition 322 Scientists (eds) Proc IODP 322. Integrated Ocean Drilling Program Management International, Inc., Tokyo; 2010. doi:10.2204/iodp.proc.322.101.2010

Waples D (1980) Time and Temperature in Petroleum Formation: Application of Lopatin's Method to Petroleum Exploration. Am Assoc Pet Geol Bull 64:916 – 926.

Whiticar MJ (1994) Correlation of Natural Gases with Their Sources. In: Magoon L, Dow W (eds) Pet. Syst. - From Source to Trap. AAPG, pp 261 – 283

Whiticar MJ (1999) Carbon and hydrogen isotope systematics of bacterial formation and oxidation of methane. Chem Geol 161:291 – 314.

Wiersberg T, Erzinger J (2007) A helium isotope cross-section study through the San Andreas Fault at seismogenic depths. Geochem Geophys Geosyst 8:Q01002. doi: 10.1029/2006gc001388

Wiersberg T, Erzinger J (2008) Origin and spatial distribution of gas at seismogenic depths of the San Andreas Fault from drill-mud gas analysis. Appl Geochemistry 23:1675–1690. doi: 10.1016/j.apgeochem.2008.01.012

Wiersberg T, Erzinger J (2011) Chemical and isotope compositions of drilling mud gas from the San Andreas Fault Observatory at Depth (SAFOD) boreholes: Implications on gas migration and the permeability structure of the San Andreas Fault. Chem Geol 284:148–159. doi: 10.1016/j.chemgeo.2011.02.016

CHAPTER 6.2 – MANUSCRIPT VI

GAS MIGRATION IN THE NANKAI TROUGH ACCRETIONARY PRISM

Sebastian B. Hammerschmidt[1], Thomas Wiersberg[2], Shigeshi Fuchida[3], Jörg Erzinger[2], Achim Kopf[1], Expedition 348 Scientists

In preparation for submission to

Geochemistry, Geophysics, Geosystems

* corresponding author: shammerschmidt@marum.de

[1] MARUM, University of Bremen, Leobener Str., 28359 Bremen, Germany

[2] GFZ German Research Centre for Geosciences, Telegrafenberg, 14473 Potsdam, Germany

[3] Osaka City University, Osaka, Japan

6.2 Gas Migration in the Nankai Trough Accretionary Prism

Abstract During Integrated Ocean Drilling Program (IODP) Expeditions 338 and 348, riser drilling at Site C0002 close to the southern rim of the Kumano forearc basin, offshore SE Japan, enabled drilling mud gas monitoring and sampling to up to 3050 meters below seafloor (mbsf). Drilling mud gas samples collected during these drilling campaigns were investigated for helium (He) concentrations and He isotope ratios and combined with shipboard radon-222 (^{222}Rn) data to investigate possible fluid migration in the accretionary prism beneath the Kumano Basin. Despite the high amount of atmospheric gases, He isotope ratios are on average twice as high as atmospheric values and thus imply a strong contribution of primordial helium. The highest values of ^{3}He/^{4}He isotopes and ^{222}Rn were found during Exp. 338 in the upper part of the accretionary prism (950 – 1200 mbsf), and are accompanied by high methane concentrations. At depths greater than 2000 mbsf (Exp. 348), ^{222}Rn shows a steady increase, while He isotope ratios, concentrations and methane values remain uniform. A steady-state one-dimensional fluid flow model based on ^{3}He/^{4}He and neon isotopes predicts velocities of 0.2 to 3.9 mm yr^{-1}, which are too low to explain the elevated gas concentrations. We suggest that increased gas concentrations in the upper part of the accretionary prism are caused by episodic fluid flow during Exp. 338, probably triggered by seismo-tectonic events in SW Japan.

INTRODUCTION

[1] The Kumano forearc basin, which is located SE of the Kii Peninsula (Figure 53), is one of the most studied forearc basins in the Nankai Trough region, and has been explored in several riser and non-riser drilling operations over the course of the Integrated Ocean Drilling Program (IODP) Nankai Trough Seismogenic Zone Experiment (NanTroSEIZE). Recent 3-D seismic reflection surveys report the presence of several normal faults cutting through the forearc basin (Moore et al. 2009), which could serve as possible migration pathways for fluids and gases. Common migration features at convergent margins, and particularly in the Kumano forearc basin, are mud volcanoes, through which fluids and gases are expelled to the hydro- and atmosphere. Mud volcanoes can serve as "tectonic windows" to processes operating at greater depths (e.g., Kopf 2002), where the presence of gases significantly enhance mud mobilization. Gas samples taken from mud volcanoes in the Kumano forearc basin showed a clear thermogenic signal (δ^{13}C $\geq$ -40‰) indicating that they are derived from source rocks of the Cretaceous to Tertiary Shimanto Belt underlying the basin sediments at ca. 2.3 – 4.3 km depth (Pape et al. 2014). In contrast, Inagaki et al. (2008) found mixed signatures at the diapiric centre of one of the studied MVs and previous IODP expeditions found no convincing evidence for upward migration of deep-sourced gases (Expedition 315 Scientists 2009; Expedition 319 Scientists 2010). Previously, drilling mud gas monitoring and headspace sampling at IODP Site C0002 at the southern rim of the Kumano forearc basin revealed the overall dominance of bacterial methane to depths of up to 1700 mbsf (Strasser et al. 2014a, b). Follow-up research confirmed the increasing contribution of thermogenic gas with depth, although *in situ* generation of thermogenic gas at depths shallower than 2000 mbsf is unlikely (see chapter 6.1). Instead, the mixing of deep-sourced gas with shallow bacterial hydrocarbon gas is likely.

[2] Noble gases like ^{222}Rn and He can be used to distinguish between active circulation through permeable strata and trapping of pore fluids in pore space. Both helium (He) and radon-222

(^{222}Rn) are products of uranium (U) and uranium plus thorium (U + Th) radioactive decay chains. They are soluble in water and can be easily transported by fluid flow through permeable features. However, the most stable isotope of radon, ^{222}Rn, has a half-life of 3.8 days, and contrary to He, ^{222}Rn is characterized by a low diffusivity. As a consequence, high concentrations of He and low concentrations of ^{222}Rn suggest high porosity and low permeability, whereas high concentrations of ^{222}Rn and He point to rapid fluid flow. High permeability can be further identified using the ^{3}He/^{4}He isotope ratio (e.g., Aquilina et al. 1998; Kennedy et al. 1997; Wiersberg and Erzinger 2011; Burnard et al. 2012), which can even indicate active crustal deformation and enhancement in local permeability (Kennedy et al. 2007). The ^{3}He/^{4}He ratio is normalized to the atmospheric value (Ra = 1.386 × 10^{-6}). An endmember value of 0.02 Ra indicates fluids derived from crustal sources (Ballentine and Burnard 2002), whereas ratios of ≥ 8 Ra, are significantly affected by primordial (i.e. mantle) He sources (Graham 2002). ^{3}He/^{4}He have been investigated in several active margins, e.g. from mud volcanoes at the Caucasian continental collision zone (Kopf et al. 2003), the San Andreas fault zone (Wiersberg and Erzinger 2011), the Büyük Menderes Graben (Wiersberg et al. 2011) and in SW Japan (see data compilation and review by Umeda et al. 2012). In southwest Japan, as expected, higher He isotope ratios are found in the back-arc region, with values similar to the average ratio of 5.4 ± 1.9 Ra for arc-related volcanism (Hilton et al. 2002; Umeda et al. 2012). He isotope ratios generally decrease to crustal and atmospheric values in forearc regions, except for the Shikoku Island and Kii Peninsula forearcs. In these areas, ^{3}He/^{4}He ratios between 1 and 5.4 Ra are associated with the subduction of young and warm oceanic lithosphere (Shikoku Basin; Umeda et al. 2012). At the Kii Peninsula, elevated He isotope ratios show a spatial distribution approximately parallel to the Nankai Trough itself, and are explained by the upward flow of mantle volatiles originating from the mantle wedge overlying the subducting Philippine Sea plate, or from the hydrated mantle of the subducting slab (Matsumoto et al. 2003; Umeda et al. 2007a; 2012).

[3] Here we report results from helium isotope ratios (^{3}He/^{4}He) from drilling mud gas samples taken during IODP Expeditions 338 and 348 (Strasser et al. 2014a, b; Expedition 348 Scientists and Scientific Participants 2014). During both expeditions, riser drilling was conducted in the Kumano forearc basin, southeast offshore the Kii Peninsula (Site C0002; Figure 53). The drilling operation commenced in Kumano Basin sediments at around 850 mbsf (meter below seafloor), and stopped at around 3050 mbsf in the accretionary prism. The entire interval was subjected to drilling mud gas monitoring and sampling during riser drilling. We explore possible contribution from mantle helium at depths as low as 950 mbsf, and whether fluid migration through the accretionary prism is active. Our data also provide a seaward extension of previously compiled He isotope ratio dataset for southeast Japan (Umeda et al. 2012).

GEOLOGICAL BACKGROUND

[4] The Nankai Trough, located southeast of the eastern coast of southern Japan, started to form around 15 Ma with the subduction of the Philippine Sea Plate (PSP) beneath the Eurasian Plate. Except for a quiescence period between 12 and 6 Ma, ongoing subduction led to the formation of > 100 km wide accretionary prism (Kimura et al. 2014). Today, the northwest directed subduction occurs at rate of ca. 4.1 – 6.5 cm/yr (Seno et al. 1993; Miyazaki and Heki 2001). As a consequence of ongoing subduction, the Kumano forearc basin formed in the late Miocene (Hayman et al. 2012). Splay fault activity in the accretionary prism significantly promoted sedimentation in the Kumano forearc basin at around 1.67 – 1.56 Ma (Strasser et al. 2009). Site C0002 is situated at the southern rim of the Kumano forearc basin, in the so-called "forearc basin zone" (Moore et al. 2009, 2013; Ashi et al. 2009; Kopf et al. 2011).
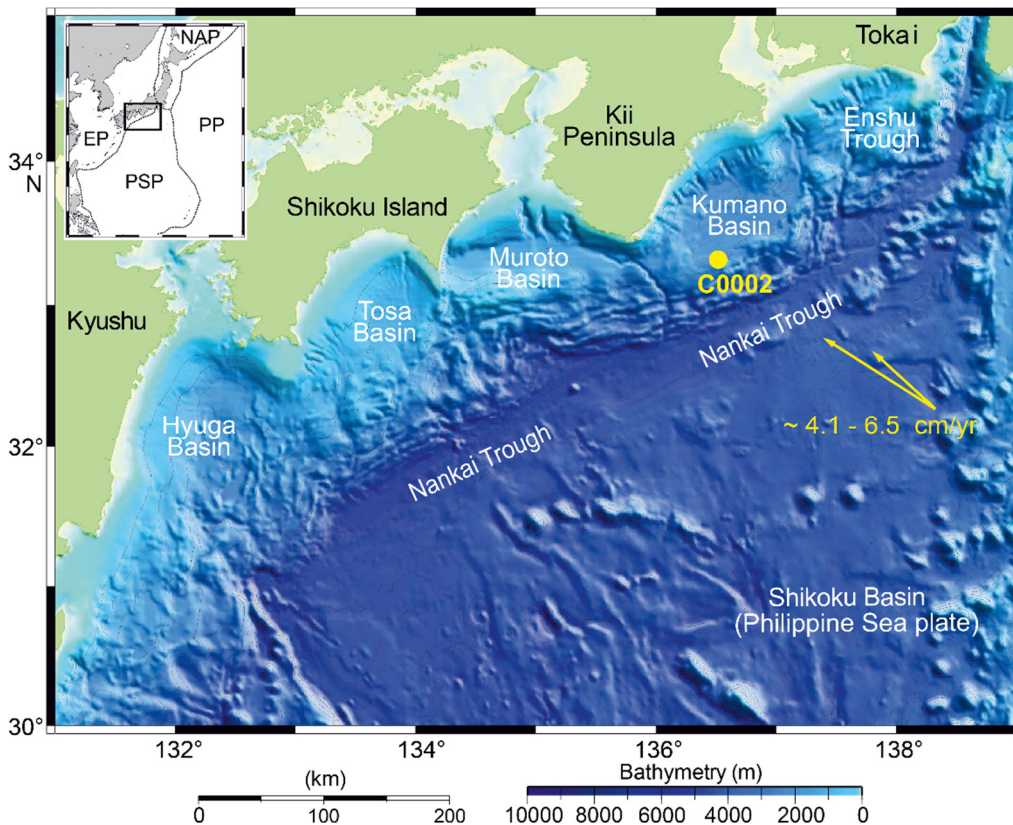
Figure 53: *Map showing the complete Nankai Trough area (modified from Screaton et al. 2009). Subduction of the Philippine Sea plate occurs at a rate of 4.1 to 6.5 cm/yr. Site C0002 is situated at the southern rim of the Kumano forearc basin, which is located between the Muroto Basin in the southwest and the Enshu trough in the northeast. The regional tectonic setting is displayed in the inset, where EP = Eurasian Plate, PSP = Philippine Sea Plate, PP = Pacific Plate, NAP = North American Plate.*

[5] Based on coring and logging data, the Expedition 315 Scientists (2009; Hole C0002B), Strasser et al. (2014b; Holes C0002F, H, J, K, L) and the Expedition 348 Scientists (2014, Holes C0002N, P) recognized five different lithological units in the southern part of the Kumano forearc basin at Site C0002: Unit I is comprised of mud of clayey silt to silty clay, which is partially enriched

in foraminifera. Unit II is also dominated by mud (clayey silt to silty clay), with silty to sandy inter-beds and is generally coarser than Unit I, and is interpreted to be distal basin deposits (Expedition 315 Scientists 2009). Unit III is interpreted to be basal forearc basin sediments, and is character-ized by silty claystone with abundant occurrence of calcareous nannofossils and dewatering structures as well as scattered bioturbation and glauconite-rich zones (Expedition 315 Scientists 2009). The lower part of Unit III hosts several moderately dipping faults, with one cluster occurring between 920 – 950 mbsf. Unit IV is interpreted to be the upper accretionary prism, based on a remarkable increase in interbedding of mud-, silt- and sandstone in an otherwise mudstone dom-inated interval. Unit IV is further characterized by a decrease in calcareous nannofossils and in-tense tectonic deformation. Based on sand content, Unit IV was further divided in five different subunits (Strasser et al. 2014b). A fault cluster is present between 1000 – 1050 msbf in Unit III. Between 1665 mbsf and 1701 mbsf, the lithology becomes predominantly silty claystone, which defines the top boundary Unit V. In Hole C0002P, the Unit V top and bottom boundaries are located at 1965.5 and 3058.5 mbsf respectively, therefore the top boundary is 300 m deeper than in Hole C0002B. Based on calcareous assemblages, Unit V is most likely of Miocene age. Strasser et al. (2014b) and Expedition 348 Scientists and Scientific Participants (2014) concluded that Unit V is either trench or Shikoku Basin sediment that might be correlatable with the Miocene Unit III at reference Sites C0011 and C0012 seaward of the trench. The cored interval within Unit V (2163 – 2219 mbsf) revealed a prominent fault zone at 2205 – 2206 mbsf.

METHODS AND DATASETS

[6] We integrate four different datasets for this study: two ^{222}Rn datasets, which were collected shipboard during IODP Exp. 338 (Hole C0002F) and 348 (Holes C0002N, C0002P; Strasser et al. 2014a; Expedition 348 Scientists, in preparation), and two datasets which were obtained from shore-based analyses on gas samples taken during Exps. 338 and 348. Samples from Expedition 338 were all taken during riser drilling of Hole C0002F (875.5 – 2005.6 mbsf), while samples from Expedition 348 were obtained from Hole C0002N (875.5 – 2325.5 mbsf) and C0002P (1965.5 – 3058.5 mbsf). The lateral distance between Hole C0002F and C0002N is 16 m, and 39 m between Hole C0002N and Hole C0002P. Holes C0002F and C0002P are 55 m apart.
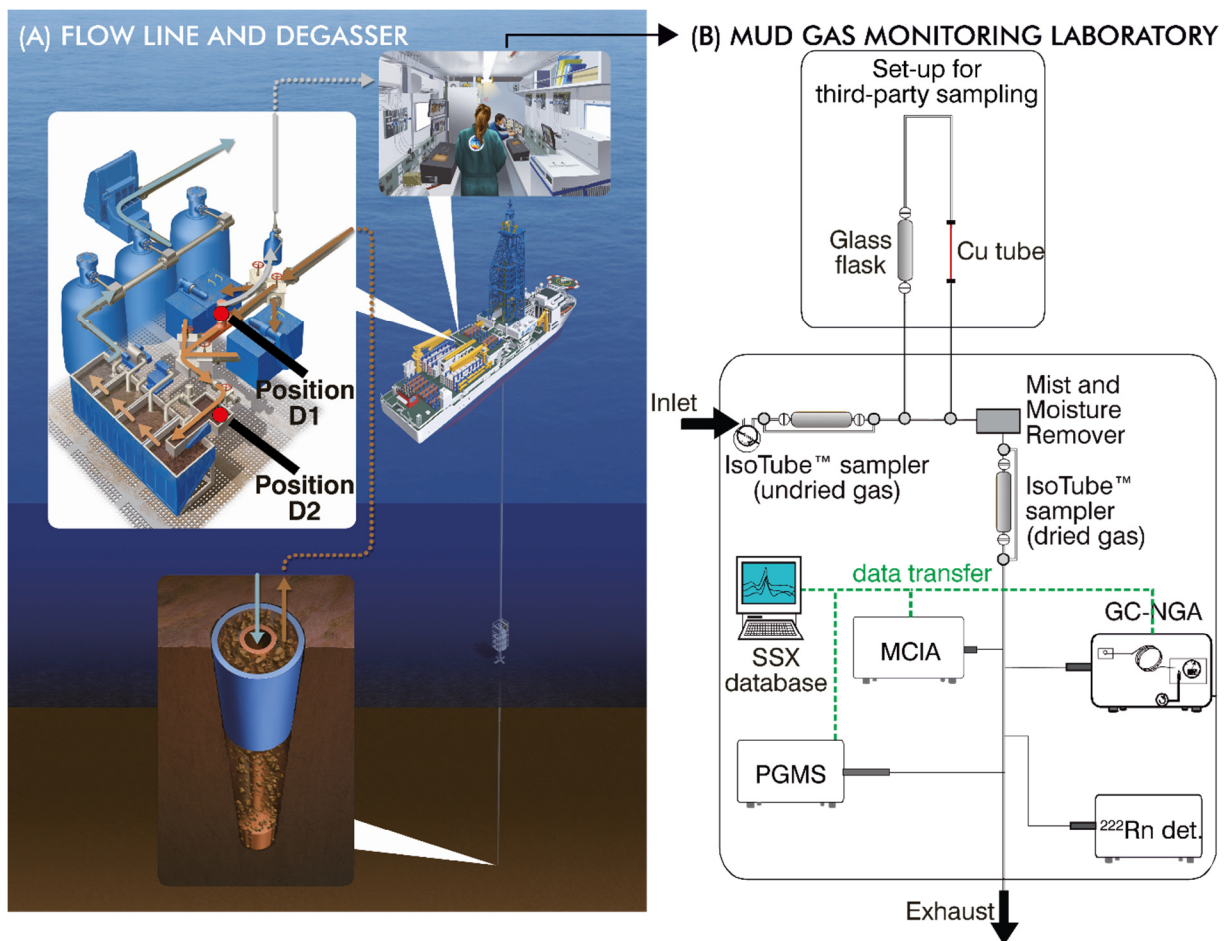
Figure 54: *Drilling mud gas monitoring set-up during IODP Exps. 338 and 348 (modified from Strasser et al. 2014a; 3D schematic © JAMSTEC). "Position D1" denotes the position of the SciGas degasser for drilling holes C0002F and C0002N. For drilling Hole C0002P, the degasser was moved to "Position D2".*

Real-time Drilling Mud Gas Monitoring

[7] Riser drilling uses drilling mud circulation along the drill string in order to cool the bit, to stabilize the borehole and to remove cuttings. While the drill bit is crushing the rock, gases in pore space or which are migrating along permeable features (e.g. faults, fractures) are released into the drilling mud. Circulation of the drilling mud transports the cuttings and gases upwards to the drilling ship (Figure 54). At the degasser, the gas phase is extracted from the drilling mud, and forwarded to the drilling mud gas monitoring laboratory. During drilling Holes C0002F (Exp. 338) and C0002N (Exp. 348), the degasser was located at the uppermost point of the flow line (Position D1, Figure 54), whereas for Hole C0002P (Exp. 348), the degasser was positioned further downstream (Position D2, Figure 54).

[8] During IODP Expeditions 338 and 348, the gas passes through an IsoTube sampling system, and a third-party flow line where gas was sampled with copper (Cu) tubes and glass flasks (Strasser et al. 2014a; Expedition 348 Scientists and Scientific Participants 2014). ^{222}Rn monitoring was conducted in real time by counting ^{222}Rn decay, which occurs every 3.8 days, inside a

650 mL ion-counting chamber. The sampling rate was 10 min, with 5 counts per minute (cpm) and a sensitivity of 100 Bq/m^3 for a concentration range between 2 and 2×10^6 Bq/m^3 (Strasser et al. 2014a; Expedition 348 Scientists and Scientific Participants 2014).

Shorebased Analyses

[9] Determination of gas concentrations and isotopic composition of He, Ne, Ar, Kr, and Xe were carried out at the German Research Centre for Geosciences (GFZ) Potsdam. Total gas analysis was performed with a quadrupole mass spectrometer (QMS, Pfeiffer Omnistar) for N_2, O_2, CH_4, He, and Ar with detection limits of 1 parts per million by volume (ppmv) for CH_4, Ar, and He as well as 10 ppmv for O_2 and N_2. Repeated measurements show that values are reproducible with repeatabilities 5% for He, 2% for CH_4, and 1% for Ar, N_2 and O_2.

[10] The procedure for noble gas isotope analyses includes purification, a mass spectrometric analysis using a VG 5400 mass spectrometer and data processing (see Niedermann et al. (1997) for a comprehensive explanation and statistical evaluation of the procedure). An aliquot with a predefined volume is introduced in the system under a constant pressure. The gas split is transferred to the purification line, where vaporized water is extracted by a dry-ice cooled cold trap. Removal of nitrogen, oxygen and carbon dioxide is accomplished by passing the sample to two titanium sponge getters, which are heated to ca. 1024 K and 674 K, respectively. The setup also comprises two Zr-Al getters, which extract hydrogen, hydrocarbons and remaining carbon dioxide. Prior to the helium and neon analyses, argon, krypton and xenon are separated from the gas phase by two nitrogen-cooled charcoal fingers.

[11] The remaining gas is transferred to two cryogenic cold heads that have temperatures of 50 K and 11 K, respectively. The former allows adsorption of remaining argon, krypton and xenon. Helium and neon are collected with the second cold head. Temperature-controlled release is used to determine noble gases concentrations. For He, the second cryogenic cold head is heated to 35 K, which is followed by a step-wise increase in temperature of the first cold head (80 K → 100 K → 190 K) to measure argon, krypton and xenon. Afterwards, Ne is released by heating the second cold head to 120 K. For He and Ne measurements, background concentrations of argon and hydrocarbons were suppressed by a stainless steel frit and an activated charcoal finger that was cooled with liquid nitrogen.

[12] The measurements in this study were corrected for initial ("blank") gas concentrations and influences of atmospheric gas following Niedermann et al. (1997, and references therein). Concentrations of the blanks were typically (in cm^3 STP): ^{4}He $\sim 5 \times 10^{-12}$, ^{20}Ne $\sim 0.5 \times 10^{-12}$, ^{40}Ar $\sim 5 \times 10^{-10}$, ^{84}Kr $\sim 0.05 \times 10^{-12}$ and ^{132}Xe $\sim 0.02 \times 10^{-12}$ (Niedermann et al. 1997; Wiersberg et al. 2011).

These concentrations were all well below the concentrations in the samples, therefore a correction was not necessary. The influence of isobaric interferences is minimized by correlating the mass spectrometer background values with the efficiency for double charged ion production (Niedermann et al. 1997). N_2/Ar ratios were found to be < 100 during IODP Exp. 338 and Exp. 348 (Strasser et al. 2014a, b; Expedition 348 Scientists and Scientific Participants 2014), which indicate a strong contribution of atmospheric gases (Jenden et al. 1988; Kroos et al. 1995). Therefore, further corrections for the contribution of atmospheric helium were necessary. The helium correction is very sensitive to the $^4He/^{20}Ne$ ratio (Wiersberg and Erzinger 2007) and consequently, the ^{20}Ne was used as an additional measure for air contamination. The low N_2/Ar ratio already indicates that atmospheric air is a major contributor, thus the atmospheric $^4He/^{20}Ne$ ratio of 0.319 was used for the correction (Hilton and Craig 1989).
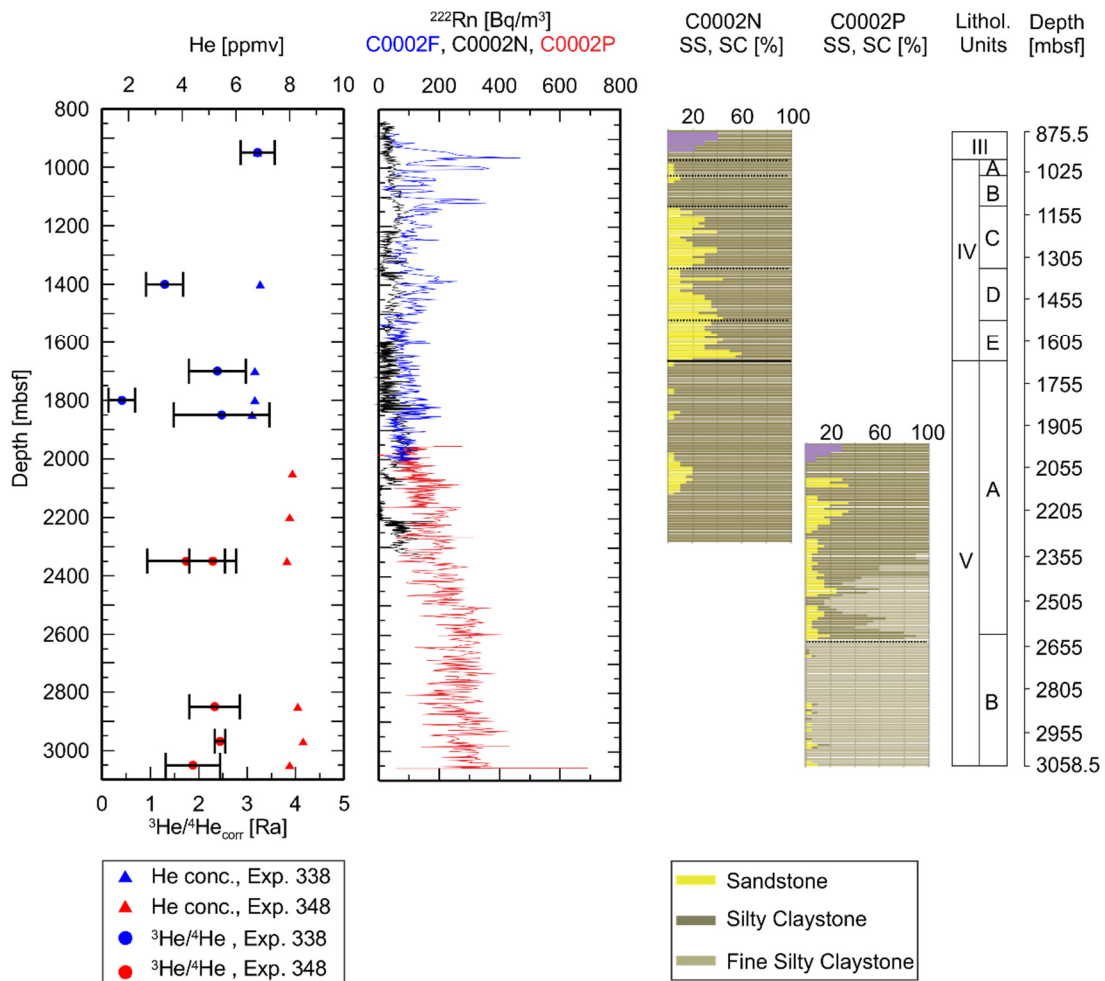
Figure 55: *Results for air-corrected He isotope ratios (circles, bottom x-axis) and He concentrations (triangles, upper x-axis) in drilling mud gas samples from IODP Expeditions 338 and 348, compared to shipboard ^{222}Rn data and lithological information from cuttings (SS = sandstone; SC = silty claystone; from Strasser et al. 2014b; Expedition 348 Scientists and Scientific Participants 2014). Lithological information of C0002F is not shown, because it resembles the one of C0002N.*

RESULTS

Concentrations of He, ^{222}Rn and ^{3}He/^{4}He ratios

[13] Shipboard results, including ^{222}Rn, are comprehensively outlined in Strasser et al. (2014b) and Expedition 348 Scientists and Scientific Participants (2014). Here, the main findings will be briefly reviewed (Figure 55). In Hole C0002F, the highest values of ^{222}Rn were present at ca. 966 mbsf, with 468 Bq/m^3. Further downhole, the data show no clear trend, and vary between 5 and 362 Bq/m^3. Surprisingly, during re-drilling this interval in Hole C0002N, the concentrations of ^{222}Rn remained below 100 Bq/m^3 at depths $\leq$ 2200 mbsf. At depths greater 2200 mbsf, concentrations up to 180 Bq/m^3 were encountered. For Hole C0002P, concentrations > 100 Bq/m^3 were present at depths $\leq$ 2200 mbsf, and showed an overall increase downhole to values up to > 300 Bq/m^3 at ca. 2500 mbsf. At depths greater 2500 mbsf, the concentrations vary between 56 and 692 Bq/m^3, with an average of 269 Bq/m^3.

Table 14: *Results for air-corrected He isotope values and quadrupole mass spectrometer analyses. Bracketed He isotope ratios are not further considered for data valuation due to bad sample quality. Helium components: A = atmospheric, S = subduction (i.e. mantle), R = radiogenic (i.e. crustal)*

Depth [mbsf]	File #	Expedition, Hole	(^{3}He/^{4}He)$_{corr.}$ [Ra]	He [ppmv]	Ar [%]	N$_2$ [%]	O$_2$ [%]	CH$_4$ [%]	He comp. [%] A	S	R
950	M461A	338, C0002F	3.26 ± 0.28	6.8	0.93	74.8	19.2	4.98	14	34	52
1400	M460A	338, C0002F	1.33 ± 0.34	6.9	0.98	77.9	20.5	0.50	8	5	87
1700	M462A	338, C0002F	2.46 ± 0.49	6.7	1.00	78.2	20.3	0.43	10	21	68
1800	M458A	338, C0002F	0.44 ± 0.24	6.7	0.96	78.6	20.3	0.19	20	6	74
1850	M459A	338, C0002F	**	6.6	1.01	78.2	20.4	0.22	15	23	62
2050	M480A	348, C0002N	-	8.1	0.93	78.8	20.1	0.07	8	5	87
2050	M480B	348, C0002N	(1,99 ± 1,36)*	8.1	0.93	78.8	20.1	0.07	10	21	68
2200	M484A	348, C0002N	(2,17 ± 0,99)*	8.0	0.92	80.0	19.8	0.12	20	6	74
2349.5	M482A	348, C0002P	2,29 ± 0,48	7.9	0.93	78.8	20.1	0.20	15	23	62
2349.5	M486A	348, C0002P	(1,74 ± 0,80)*	n.d.	n.d.	n.d.	n.d.	n.d.	8	5	87
2850	M481A	348, C0002P	2,33 ± 0,52	8.3	0.91	79.3	19.5	0.25	10	21	68
2968.5	M479A	348, C0002P	2,44 ± 0,11	8.5	0.90	78.2	18.9	1.91	20	6	74
2968.5	M487A, Cu	348, C0002P	(0.29 + 0.44, - 0.29)	n.d.	n.d.	n.d.	n.d.	n.d.	15	23	62
3050	M485A	348, C0002P	1,88 ± 0,56	8.0	0.92	79.3	19.5	0.23	8	5	87

- not determined due to fractionation
n.d. not determined
* air content > 95%
** not determined, air content >> 95%

[14] QMS measurements indicated the predominance of atmospheric gas components, namely Ar, N$_2$, and O$_2$, with an average of 0.94 %, 78.4 % and 19.9 %, respectively. Of the non-atmospheric gases, methane shows the highest concentrations with an average of 0.76 %, while He ranged only between 6.6 and 8.5 ppmv. Values of He show only minor variations with depth. The distinct increase to overall higher concentrations at ~2000 mbsf is due to differences between the Exp. 338 and Exp. 348 datasets.

[15] The results of the noble gas isotope analyses are listed in Table 14, Table S.7 (see Appendix A.5) and shown in Figs. 55 and 56. Values for ^{4}He/^{20}Ne vary between 0.330 and 0.500, and thus,

are only slightly higher than atmospheric ratios (i.e. 0.319 for air; Wiersberg et al. 2011; Table S.7 in Appendix A.5, Figure 56A), indicating a contribution of atmospheric gases. $^3He/^4He$ ratios (corrected for air) were normalized to the atmospheric value (i.e. Ra = 1.4 × 10^{-6}) and average 2.05. The highest value, 3.22 Ra, was observed for the shallowest sample at ~ 950 msbf. Except for the sample at 1800 mbsf (0.44 Ra), all samples have $^3He/^4He$ ratios higher than 0.7 Ra, which is to be expected for regions that have been tectonically active for less than 50 Ma, such as the Nankai Trough subduction zone (Ballentine and Burnard 2002, after Polyak and Tolstikhin 1985).

[16] According to Sano and Wakita (1985), He concentrations are composed of subduction-related helium (i.e. mantle helium), radiogenic helium and atmospheric helium. The individual contributions can be estimated using the $^3He/^4He$ - $^4He/^{20}Ne$ couple:

$$(^3He/^4He) = (^3He/^4He)_A \times A + (^3He/^4He)_S \times S + (^3He/^4He)_R \times R \tag{21}$$

$$(^4He/^{20}Ne)^{-1} = (^4He/^{20}Ne)_A^{-1} \times A + (^4He/^{20}Ne)_S^{-1} \times S + (^4He/^{20}Ne)_R^{-1} \times R \tag{22}$$

$$1 = A + S + R \tag{23}$$

where A, S, and R are the variables for atmospheric, subduction-related and radiogenic He, respectively. This set of linear equations can be solved for A, S, and R assuming that $(^3He/^4He)_A$ = 1.4 × 10^{-6}, $(^3He/^4He)_S$ = 1.1 × 10^{-5}, $(^3He/^4He)_R$ = 1.5 × 10^{-8}, $(^4He/^{20}Ne)_A$ = 0.318, $(^4He/^{20}Ne)_S$ = 1000, and $(^4He/^{20}Ne)_R$ = 1000 (Sano and Wakita 1985). Our results indicate a strong contribution of atmospheric gases, with a mean value of 71%, while mantle- and crustal-derived He average 17.7 and 11.2%, respectively (Table 14).
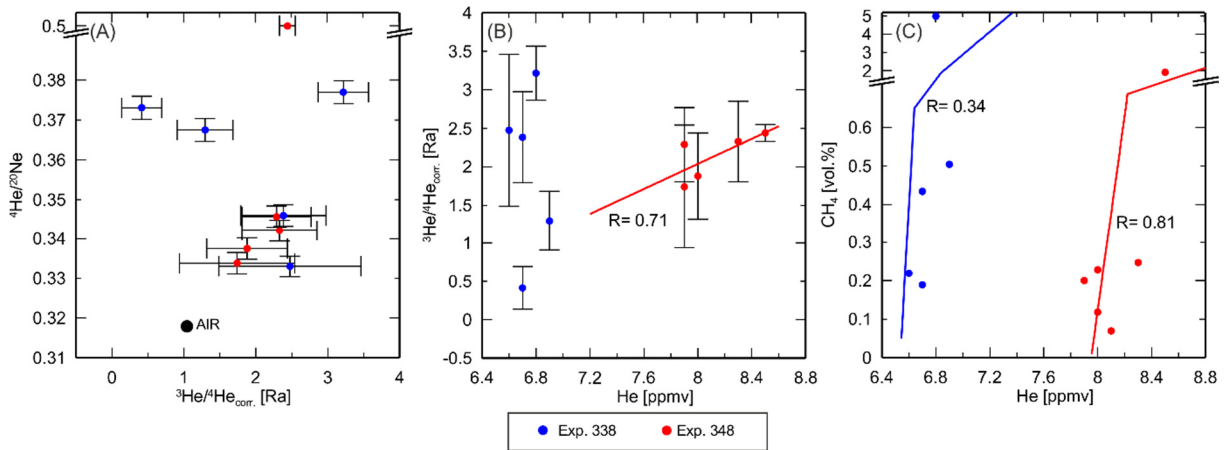
Figure 56: **(A)** $^4He/^{20}Ne$ plotted against air-corrected $^3He/^4He$ ratios. $^4He/^{20}Ne$ ratios are only slightly above atmospheric concentrations, while most $^3He/^4He$ ratios are clearly indicating contribution of primordial helium. The ordinate was broken between 0.39 and 0.5. **(B)** Air-corrected $^3He/^4He$ ratios vs. He concentrations. While no clear trend is visible in data from Ex. 338, He concentrations increase with air-corrected $^3He/^4He$ ratios in samples from Exp. 348. **(C)** CH_4 vs. He concentrations in samples from Expedition 338 (blue, R = 0.34) and Expedition 348 (red, R = 0.81). The ordinate was broken between 0.7 and 2.0.

[17] He isotope ratios found in Exp. 348 increase with increasing He concentrations (R = 0.71), while ^{3}He/^{4}He ratios from Exp. 338 show no corresponding changes with the overall He concentration (Figure 56B). Similarly, methane and helium concentrations in samples from Expedition 348 show a good positive correlation with R = 0.81, in contrast with the data from Expedition 338 (R = 0.34) (Figure 56C).

[18] The overall increase in He concentrations and the improved correlations with methane concentrations and ^{3}He/^{4}He ratios is related to the different degassing systems used during Exp. 338 and 348. The Exp. 338 dataset was generated with a different degasser further upstream the flow line, which caused air contamination (Strasser et al. 2014; Hammerschmidt et al. 2014, see chapter 6.1 in this volume; Expedition 348 Scientists and Scientific Participants 2014). Although the new degassing system improved the sample quality, contamination of samples with atmospheric gases is still an issue, as is implied by the overall strong atmospheric He content (Table 14).

DISCUSSION

Fluid Flow in the Accretionary Prism

[19] The elevated ^{222}Rn concentrations and ^{3}He/^{4}He ratios suggest active fluid migration through the accretionary prism, which are at least partially sourced by a mantle-derived fluid reservoir. In order to assess fluid flow through the accretionary prism, we assume that during upward migration, ^{3}He/^{4}He ratios are constantly altered by radiogenic ^{4}He. In this case, a depth-dependent increase in ^{3}He/^{4}He ratios should be expected. Assuming a constant radiogenic ^{4}He production rate in the host rock, the following steady-state one-dimensional solution for upward fluid flow rate q can be formulated (Johnson and DePaolo 1994; Kennedy et al. 1997):

$$q = \frac{H_{cr}\rho_s P(He)}{\rho_f [^4He]_{f,ma}} \times \left[\frac{(R/Ra)_{meas} - (R/Ra)_{cr}}{(R/Ra)_{ma} - (R/Ra)_{meas}} \right] \tag{24}$$

where H_{cr} is the thickness of the crust (30 km), the density of the solid rock ρ_s =2.6 g/cm^3, and the fluid density ρ_f =1.025 g/cm^3, assuming that He is in solution with seawater following the "particle-in-the-box" model (e.g. Benson and Krause 1980). $[^4He]_{f, ma}$ is the primordial concentration of ^{4}He in the mantle fluid (5 $\times$ 10^{-6} cm^3 STP/g; Porcelli and Wasserburg 1995; Burnard and Polya 2004), $(R/Ra)_{meas, ma, cr}$ are the ^{3}He/^{4}He ratio related to the atmospheric value in the gas samples in the mantle (8 Ra, Umeda et al. 2012) and the crust (0.02 Ra), respectively, and $P(He)$ is the radiogenic production rate of ^{4}He in the crust. $P(He)$ depends on U and Th concentrations, and is calculated by (e.g. Craig and Lupton 1976):

$$P(He) = 0.2355 \times 10^{-12} U [(1 + 0.123(Th/U - 4)] \tag{25}$$

[20] For average concentrations of U = 1.2 ppm and Th = 7 ppm for clay-rich deep-sea sediments (Turekian and Wedepohl 1961), $P(He)$ = 3.46 × 10^{-13} cm^3 STP ^{4}He g^{-1} yr^{-1}. For the Nankai Trough accretionary prism, the subsequent fluid flow rate q ranges between 0.19 and 3.5 mm/yr (i.e. 0.5 – 9.6 μm/d; Figure 57). Contrary to the theoretical expectation that upward fluid flow should lead to increasing ^{3}He/^{4}He ratios with depth, our samples show a rather uniform distribution of ^{3}He/^{4}He ratios. Similarly, fluid flow rates associated with the ^{3}He/^{4}He ratios do not vary with depth, except for the samples from IODP Exp. 338 (Figure 57).
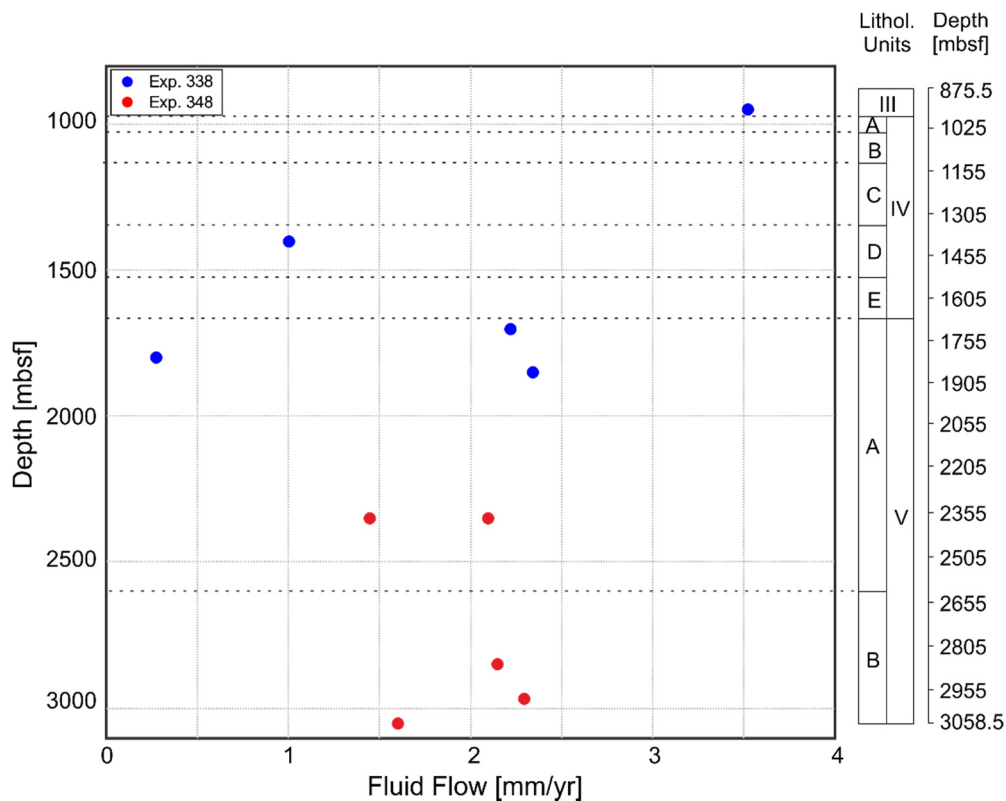
Figure 57: *Fluid flow calculated for different He isotope ratios at different stratigraphic levels within the accretionary prism. Except for some outliers, the fluid flow remains uniform downhole.*

[21] Actual flow rates can be significantly higher than those calculated here, because the one-dimensional model does not include mixing with ^{4}He-rich fluids from the adjacent crust, hydrodynamic dispersion, and neglects episodic flow events (Kennedy et al. 1997). Moreover, for the Exp. 348 dataset, the increase in ^{3}He/^{4}He with He concentration implies that the input of primordial helium must have outpaced the radiogenic ^{4}He production. If the increase in He concentration was caused by ^{4}He, the He isotope ratio should decrease simultaneously. Coseismic, episodic fluid flow events is one possible source of ^{3}He, as has been previously reported for active margins (e.g. Wakita et al. 1987; Sano et al. 1986, 1998, 2014; Lupton et al. 1999; Bräuer et al. 2003; Umeda et al. 2007a,b; 2012). Decreases in ^{3}He/^{4}He have been attributed to the sudden release of crustal helium, e.g. during the Kobe 1995 earthquake (Sano et al. 1998) and an earthquake swarm beneath the western Eger rift (Bräuer et al. 2003). Examples for an increase in

mantle helium were observed after the Tohoku M9.0 rupture in 2011 (Sano et al. 2014), and the 1984 western Nagano earthquake (Sano et al.1986). Sano et al. (2014) reported fluid flow rates of 4 km/d, which is 9 orders of magnitude higher than our steady-state flow velocity. The Nankai Trough area is highly earthquake prone, and indeed, between October 2012 and December 2012 (during Exp. 338) and November 2013 and January 2014 (during Exp. 348) the region [30°-35°N], [131°-139°E] experienced ca. 82 and 34 earthquakes, respectively, with moment magnitudes between 3.0 and 5.5 (International Seismological Centre 2014). Deformation is not only caused by the actual rupture, but also by radiated seismic waves leading to pore fluid pressure oscillations (Hammerschmidt et al. 2013) which can contribute to fluid migration (e.g. Elkhoury et al. 2006, 2011; Lupi et al. 2013). Therefore we suggest that elevated flow during earthquakes caused the observed helium signal during IODP Exp. 338.

[22] Episodic fluid flow can also help explain the elevated ^{222}Rn concentrations encountered during Exp. 338, and why 12 months later during Exp. 348, concentrations never exceeded 100 Bq/m^3. Assuming a maximum q of 9.6 μm/d and a half-life 3.8 days for ^{222}Rn means that ^{222}Rn would be able to travel a maximum vertical travel distance of ca. 36.5 μm before decaying, suggesting that the high concentrations of ^{222}Rn found in the upper part of Hole C0002F (Exp. 338) cannot be explained by steady-state flow. If episodic flow is not a factor, elevated ^{222}Rn concentrations must be related to local enrichments of U and Th, and are thus produced *in situ*. Local enrichments of U in the upper part of the accretionary prism were reported for interstitial waters sampled at Site C0002 (Expedition 315 Scientists 2010; Strasser et al. 2014b; Expedition 348 Scientists and Scientific Participants 2014).

[23] However, local enrichments of U in the upper part of the prism and subsequent production of radiogenic ^{4}He and ^{222}Rn are not supported by the high He isotope ratios. The strong variation of ^{3}He/^{4}He found during Exp. 338 in Hole C0002F, with the highest value in the uppermost sample, point to episodic flow causing temporary accumulation of mantle fluids within the upper part of the accretionary prism. That this episodic flow is accompanied by more shallow fluids is supported by elevated methane concentrations with decreasing depth in Hole C0002F, which were absent in Holes C0002N and C0002P (Expedition 348 Scientists and Scientific Participants 2014).

[24] The small variations in the He isotope ratios observed during Exp. 348 imply diffusion and/or steady-state fluid flow of fluids. Possible sources include the subducting Philippine Sea Plate, the overlying mantle wedge and/or dehydration of the slab mantle between 30 and 60 km depth (Umeda et al. 2006; 2007a; 2012). Fractures present in the oceanic crust could serve as conduits for fluid migration from the oceanic mantle (Umeda et al. 2006, 2012).

PRELIMINARY CONCLUSIONS AND FUTURE WORK

[25] Although the drilling mud gas samples obtained from Site C0002 during IODP Expeditions 338 and 348 indicate a strong contribution of mantle helium, the atmospheric component is dominant, which is to be expected based on previous reports regarding the efficiency of the drilling mud gas monitoring system onboard drilling vessel (D/V) *Chikyu* (Strasser et al. 2014a; Expedition 348 Scientists and Scientific Participants 2014; cf. also chapter 6.1). Steady-state one-dimensional fluid flow through the accretionary prism is estimated to be 0.19 and 3.5 mm/yr (0.5 – 9.6 μm/d). Given these values, the elevated ^{222}Rn concentrations in the upper part of Hole C0002F could not have been derived by steady-state flow from a deep reservoir, because ^{222}Rn would decay after travelling 36.5 μm. One possible explanation for elevated ^{222}Rn observed during Exp. 338 is episodic fluid flow triggered by regional earthquakes. In addition to elevated concentrations of ^{222}Rn and high He isotope ratios, increased methane concentrations also suggest episodic fluid flow and accumulation in the shallow part of the accretionary prism, near the deepest Kumano Basin sediments.

[26] Future work will try to constrain the possibility of earthquake-triggered fluid flow by investigating epicentral distances of the earthquakes that occurred during IODP Exp. 338 and subsequent strain analyses at Site C0002, possibly with contribution from pressure data from the long-term borehole monitoring system installed in Hole C0002G (cf. chapter 4). Of particular interest is the question whether peak ground velocity and peak ground acceleration caused by these earthquakes were high enough to affect permeability. Further investigation will include estimation of heat flux from the mantle based on ^{3}He/^{4}He ratios, as was proposed by Polyak and Tolstikhin (1985) and further outlined by Ballentine and Burnard (2002). If the primordial helium component is derived from the subducting slab, then may be possible to estimate the impact that flow rate has on the pressurization of the fault zone (Kennedy et al. 1997). Both heat flow and the influence of fluids at the thrust fault boundary would significantly advance the understanding of seismogenic processes at the Nankai Trough subduction zone.

References

Aquilina L, Baubron J-C, Defoix D, Dégranges P, Disnar J-R, Marty B, Robé M-C (1998) Characterization of gases in sedimentary formations through monitoring during drilling and core leaching (Balazuc borehole, Deep Geology of France Programme). Appl Geochemistry 13:673–686. doi: 10.1016/s0883-2927(98)00008-0

Ashi J, Lallement S, Masago H, the Expedition 315 Scientists (2009) Expedition 315 Summary. In: Kinoshita M, Tobin H, Ashi J, Kimura G, Lallement S, Screaton EJ, Curewitz D, Masago H, Moe KT, Expedition 314/315/316 Scientists (eds) Proc IODP 314/315/316: Tokyo (Integrated Ocean Drilling Program Management International, Inc.). doi: 10.2204/iodp.proc.314315316.121.2009

Ballentine CJ, Burnard PG (2002) Production, Release and Transport of Noble Gases in the Continental Crust. Rev Mineral Geochemistry 47:481–538. doi: 10.2138/rmg.2002.47.12

Benson BB, Krause Jr. D (1980) Isotopic fractionation of helium during solution: A probe for the liquid state. J Solution Chem 9:895–909. doi: 10.1007/BF00646402

Bräuer K, Kämpf H, Strauch G, Weise SM (2003) Isotopic evidence (^{3}He/^{4}He, of fluid-triggered intraplate seismicity. J Geophys Res Solid Earth 108:2070. doi: 10.1029/2002JB002077

Burnard PG, Polya DA (2004) Importance of mantle derived fluids during granite associated hydrothermal circulation: He and Ar isotopes of ore minerals from Panasqueira. Geochim Cosmochim Acta 68:1607–1615. doi: 10.1016/j.gca.2003.10.008

Burnard P, Bourlange S, Henry P, Geli L, Tryon MD, Natal'in B, Sengör a. MC, Özeren MS, Çagatay MN (2012) Constraints on fluid origins and migration velocities along the Marmara Main Fault (Sea of Marmara, Turkey) using helium isotopes. Earth Planet Sci Lett 341-344:68–78. doi: 10.1016/j.epsl.2012.05.042

Craig H, Lupton JE (1976) Primordial neon, helium, and hydrogen in oceanic basalts. Earth Planet Sci Lett 31:369–385. doi: 10.1016/0012-821X(76)90118-7

Elkhoury JE, Brodsky EE, Agnew DC (2006) Seismic waves increase permeability. Nature 441:1135–1138. doi: 10.1038/nature04798

Elkhoury JE, Niemeijer A, Brodsky EE, Marone C (2011) Laboratory observations of permeability enhancement by fluid pressure oscillation of in situ fractured rock. J Geophys Res 116:B02311. doi: 10.1029/2010jb007759

Expedition 315 Scientists (2009) Expedition 315 Site C0002. In: Kinoshita M, Tobin H, Ashi J, Kimura G, Lallemant S, Screaton EJ, Curewitz D, Masago H, Moe KT, the Expedition 314/315/316 Scientists (eds) Proc IODP 315. Integrated Ocean Drilling Program Management International, Inc., Washington D.C.

Expedition 319 Scientists (2010) Expedition 319 Summary. In: Saffer D, McNeill L, Byrne T, Araki E, Toczko S, Eguchi N, Takahashi K, Expedition 319 Scientists (eds) Proc IODP 319. Integrated Ocean Drilling Program Management International, Tokyo.

Expedition 348 Scientists and Scientific Participants (2014) Expedition 348 Preliminary Report NanTroSEIZE Stage 3 : NanTroSEIZE plate boundary deep riser 3. IODP Prelim Rep 348:71. doi: 10.2204/iodp.pr.348.2014

Graham DW (2002) Noble Gas Isotope Geochemistry of Mid-Ocean Ridge and Ocean Island Basalts: Characterization of Mantle Source Reservoirs. Rev Mineral Geochemistry 47 :247–317. doi: 10.2138/rmg.2002.47.8

Hammerschmidt S, Davis EE, Kopf A (2013) Fluid pressure and temperature transients detected at the Nankai Trough Megasplay Fault: Results from the SmartPlug borehole observatory. Tectonophysics 600:116 – 133. doi: 10.1016/j.tecto.2013.02.010

Hayman NW, Timothy B. B, Lisa C. M, Kyuichi K, Toshiya K, Cassandra M. B, Anja M. S, Gary J. H (2012) Structural evolution of an inner accretionary wedge and forearc basin initiation, Nankai margin, Japan. Earth Planet Sci Lett 353–354:163–172.

Hilton DR, Craig H (1989) The Siljan Deep Well: Helium isotope results. Geochim Cosmochim Acta 53:3311–3316. doi: 10.1016/0016-7037(89)90110-5

Hilton DR, Fischer TP, Marty B (2002) Noble Gases and Volatile Recycling at Subduction Zones. Rev Mineral Geochemistry 47 :319–370. doi: 10.2138/rmg.2002.47.9

Inagaki F, Eguchi N, Aioike K, Kubo Y, Toczko S, the Expedition CK09-01 Scientists (2008) Kumano Mud-Volcano Drilling: A Window to the Deep-Biosphere. JAMSTEC Cruise Report, Chikyu Training Cruise Leg 1.

International Seismological Centre (2014) On-line Bulletin, http://www.isc.ac.uk, Internatl Seis Cent, Thatcham, United Kingdom.

Jenden PD, Newell KD, Kaplan IR, Watney WL (1988) Composition and stable-isotope geochemistry of natural gases from Kansas, Midcontinent, U.S.A. Chem Geol 71:117–147. doi: 10.1016/0009-2541(88)90110-6

Johnson TM, DePaolo DJ (1994) Interpretation of isotopic data in groundwater-rock systems: Model development and application to Sr isotope data from Yucca Mountain. Water Resour Res 30:1571–1587. doi: 10.1029/94WR00157

Kennedy BM, van Soest MC (2007) Flow of mantle fluids through the ductile lower crust: helium isotope trends. Science 318:1433–6. doi: 10.1126/science.1147537

Kennedy BM, Kharaka YK, Evans WC, Ellwood A, DePaolo DJ, Thordsen J, Ambats G, Mariner RH (1997) Mantle Fluids in the San Andreas Fault System ,California. Science 278:1278 – 1281. doi: 10.1126/science.278.5341.1278

Kimura G, Hashimoto Y, Kitamura Y, Yamaguchi A, Koge H (2014) Middle Miocene swift migration of the TTT triple junction and rapid crustal growth in southwest Japan — A review. Tectonics 2014TC003531. doi: 10.1002/2014TC003531

Kopf AJ (2002) Significance of mud volcanism. Rev Geophys 40:1005. doi:10.1029/2000rg000093

Kopf A, Deyhle A, Lavrushin VY, Polyak BG, Gieskes JM, Buachidze GI, Wallmann K, Eisenhauer A (2003) Isotopic evidence (He, B, C) for deep fluid and mud mobilization from mud volcanoes in the Caucasus continental collision zone. Int J Earth Sci 92:407–425. doi: 10.1007/s00531-003-0326-y

Kopf A, Araki E, Toczko S, the Expedition 332 Scientists (2011) Proc IODP, 332: Tokyo (Integrated Ocean Drilling Program Management International, Inc.)

Kopf A, Hammerschmidt S, Freudenthal T, Ratmeyer V, Tryon M, Toczko S, Ashi Y (2012) Extending NanTroSEIZE landwards: Long-term observatories in the Kumano Basin mud volcanoes to monitor EQ precursors. Poster presented at the International Conference on a New Perspective of Great Earthquakes along Subduction Zones 2012, Kochi, Japan

Kopf A, et al. (2013). Report and Preliminary Results of SONNE Cruise SO222: Project MEMO, Berichte aus dem Fachbereich Geowissenschaften der Univ. Bremen, 297: 121pp

Kroos B, Littke R, Müller B, Frielingsdorf J, Schwochau K, Idiz E (1995) Generation of nitrogen and methane from sedimentary organic matter : implications on the dynamics of natural gas accumulations. Chem Geol 126:291 – 318.

Lupi M, Saenger EH, Fuchs F, Miller SA (2013) Lusi mud eruption triggered by geometric focusing of seismic waves. Nat Geosci 6:642–646.

Lupton JE, Baker ET, Massoth GJ (1999) Helium, heat, and the generation of hydrothermal event plumes at mid-ocean ridges. Earth Planet Sci Lett 171:343–350. doi: 10.1016/S0012-821X(99)00149-1

Manga M, Brumm M, Rudolph ML (2009) Earthquake triggering of mud volcanoes. Mar Pet Geol 26:1785–1798.

Matsumoto T, Kawabata T, Matsuda J, Yamamoto K, Mimura K (2003) 3He/4He ratios in well gases in the Kinki district, SW Japan: surface appearance of slab-derived fluids in a non-volcanic area in Kii Peninsula. Earth Planet Sci Lett 216:221–230. doi: 10.1016/S0012-821X(03)00479-5

Moore GF, et al. (2009), Structural and seismic stratigraphic framework of the NanTroSEIZE Stage 1 transect. Proc IODP 314/315/316. doi:10.2204/iodp.proc.314315316.102.2009

Moore G, Kanagawa K, Strasser M, Dugan B, Maeda L, Toczko S, the Expedition 338 Scientists (2013) NanTroSEIZE Stage 3: NanTroSEIZE Plate Boundary Deep Riser. IODP Prelim Rep 338. doi:10.2204/iodp.pr.338.2013

Miyazaki S, Heki K (2001) Crustal velocity field of southwest Japan: Subduction and arc-arc collision. J Geophys Res 106:4305–4326. doi: 10.1029/2000jb900312

Niedermann S, Bach W, Erzinger J (1997) Noble gas evidence for a lower mantle component in MORBs from the southern East Pacific Rise: Decoupling of helium and neon isotope systematics. Geochim Cosmochim Acta 61:2697–2715. doi: 10.1016/S0016-7037(97)00102-6

Pape T, Geprägs P, Hammerschmidt S, Wintersteller P, Wei J, Fleischmann T, Bohrmann G, Kopf AJ (2014) Hydrocarbon seepage and its sources at mud volcanoes of the Kumano forearc basin, Nankai Trough subduction zone. Geochemistry, Geophys Geosystems 15:2180–2194. doi: 10.1002/2013GC005057

Polyak BG, Tolstikhin IN (1985) Isotopic composition of the earth's helium and the problem of the motive forces of tectogenesis. Chem Geol Isot Geosci Sect 52:9–33. doi: 10.1016/0168-9622(85)90005-3

Porcelli D, Wasserburg GJ (1995) Mass transfer of helium, neon, argon, and xenon through a steady-state upper mantle. Geochim Cosmochim Acta 59:4921–4937. doi: 10.1016/0016-7037(95)00336-3

Sano Y, Nakamura Y, Wakita H, Notsu K, Kobayashi Y (1986) ^{3}He/^{4}He ratio anomalies associated with the 1984 Western Nagano Earthquake: Possibly induced by a diapiric magma. J Geophys Res Solid Earth 91:12291–12295. doi: 10.1029/JB091iB12p12291

Sano Y, Takahata N, Igarashi G, Koizumi N, Sturchio NC (1998) Helium degassing related to the Kobe earthquake. Chem Geol 150:171–179. doi: 10.1016/S0009-2541(98)00055-2

Sano Y, Hara T, Takahata N, Kawagucci S, Honda M, Nishio Y, Tanikawa W, Hasegawa A, Hattori K (2014) Helium anomalies suggest a fluid pathway from mantle to trench during the 2011 Tohoku-Oki earthquake. Nat Commun 5:1 – 6. doi: 10.1038/ncomms4084

Sano Y, Wakita H (1985) Geographical distribution of ^{3}He/^{4}He ratios in Japan: Implications for arc tectonics and incipient magmatism. J Geophys Res Solid Earth 90:8729–8741. doi: 10.1029/JB090iB10p08729

Seno T, Stein S, Gripp AE (1993) A model for the motion of the Philippine Sea plate consistent with NUVEL-1 and geological data. J Geophys Res 98:17941–17948.

Strasser M, Dugan B, Kanagawa K, Moore GF, Toczko S, Maeda L, Kido Y, Moe KT, Sanada Y, Esteban L, Fabbri O, Geersen J, Hammerschmidt S, Hayashi H, Heirman K, Hüpers A, Jurado Rodriguez MJ, Kameo K, Kanamatsu T, Kitajima H, Masuda H, Milliken K, Mishra R, Motoyama I, Olcott K, K. O, Pickering KT, Ramirez SG, Rashid H, Sawyer D, Schleicher A, Shan Y, Skarbek R, Song I, Takeshita T, Toki T, Tudge J, Webb S, Wilson DJ, Wu H-Y, Yamaguchi A (2014a) Methods. In: Strasser et al. (eds) IODP Proc 338:92. doi: 10.2204/iodp.proc.338.102.2014

Strasser M, Dugan B, Kanagawa K, Moore GF, Toczko S, Maeda L, Kido Y, Moe KT, Sanada Y, Esteban L, Fabbri O, Geersen J, Hammerschmidt S, Hayashi H, Heirman K, Hüpers A, Jurado MJ, Kameo K, Kanamatsu T, Kitajima H, Masuda H, Milliken K, Mishra R, Motoyama I, Olcott K, Oohashi K, Pickering KT, Ramirez SG, Rashid H, Sawyer D, Schleicher A, Shan Y, Skarbek R, Song I, Takeshita T, Toki T, Tudge J, Webb S, Wilson DJ, Wu H, Yamaguchi A (2014b) Site C0002. In: Strasser et al. (eds) IODP Proc 338:248. doi: 10.2204/iodp.proc.338.103.2014

Turekian KK, Wedepohl KH (1961) Distribution of the Elements in Some Major Units of the Earth's Crust. Geol Soc Am Bull 72:175–192. doi: 10.1130/0016-7606(1961)72[175:DOTEIS]2.0.CO;2

Umeda K, Ogawa Y, Asamori K, Oikawa T (2006) Aqueous fluids derived from a subducting slab: Observed high 3He emanation and conductive anomaly in a non-volcanic region, Kii Peninsula southwest Japan. J Volcanol Geotherm Res 149:47–61. doi: 10.1016/j.jvolgeores.2005.06.005

Umeda K, McCrank GF, Ninomiya A (2007a) Helium isotopes as geochemical indicators of a serpentinized fore-arc mantle wedge. J Geophys Res Solid Earth 112:B10206. doi: 10.1029/2007JB005031

Umeda K, Sakagawa Y, Ninomiya A, Asamori K (2007b) Relationship between helium isotopes and heat flux from hot springs in a non-volcanic region, Kii Peninsula, southwest Japan. Geophys Res Lett 34:L05310. doi: 10.1029/2006GL028975

Umeda K, Kusano T, Asamori K, McCrank GF (2012) Relationship between ^{3}He/^{4}He ratios and subduction of the Philippine Sea plate beneath southwest Japan. J Geophys Res Solid Earth 117:B10204. doi: 10.1029/2012JB009409

Wakita H, Sano Y, Mizoue M (1987) High ^{3}He emanation and seismic swarms observed in a nonvolcanic, forearc region. J Geophys Res Solid Earth 92:12539–12546. doi: 10.1029/JB092iB12p12539

Wiersberg T, Erzinger J (2007) A helium isotope cross-section study through the San Andreas Fault at seismogenic depths. Geochem Geophys Geosyst 8:Q01002. doi: 10.1029/2006gc001388

Wiersberg T, Erzinger J (2011) Chemical and isotope compositions of drilling mud gas from the San Andreas Fault Observatory at Depth (SAFOD) boreholes: Implications on gas migration and the permeability structure of the San Andreas Fault. Chem Geol 284:148–159. doi: 10.1016/j.chemgeo.2011.02.016

Wiersberg T, Süer S, Güleç N, Erzinger J, Parlaktuna M (2011) Noble gas isotopes and the chemical composition of geothermal gases from the eastern part of the Büyük Menderes Graben (Turkey). J Volcanol Geotherm Res 208:112–121. doi: 10.1016/j.jvolgeores.2011.09.009

CHAPTER 7
Mud Volcanoes as Windows to Paleo-Fluid Migration

CHAPTER 7.1 – MANUSCRIPT VII

HYDROCARBON SEEPAGE AND ITS SOURCES AT MUD VOLCANOES OF THE KUMANO FOREARC BASIN

Thomas Pape[1]*, Patrizia Geprägs[1], Sebastian B. Hammerschmidt[1], Paul Wintersteller[1],

Jiangong Wei[1], Timo Fleischmann[1], Gerhard Bohrmann[1], Achim Kopf[1]

published 2014 in

* corresponding author: tpape@marum.de

[1] MARUM, University of Bremen, Bremen, Germany

Abstract Twelve submarine mud volcanoes (MV) in the Kumano forearc basin within the Nankai Trough subduction zone were investigated for hydrocarbon origins and fluid dynamics. Gas hydrates diagnostic for methane concentrations exceeding solubilities were recovered from MVs 2, 4, 5, and 10. Molecular ratios (C_1/C_2 <250) and stable carbon isotopic compositions ($\delta^{13}C_{CH4}$ > -40‰ V-PDB) indicate that hydrate-bound hydrocarbons (HCs) at MVs 2, 4, 41 and 10 are derived from thermal cracking of organic matter. Considering thermal gradients at the nearby IODP Sites C0009 and C0002, the likely formation depth of such HCs ranges between 2,300 and 4,300 m below seafloor (mbsf). With respect to basin sediment thickness and the minimum distance to the top of the plate boundary thrust we propose that the majority of HCs fueling the MVs is derived from sediments of the Cretaceous to Tertiary Shimanto belt below Plio-/Pleistocene to recent basin sediments. With respect to sizes and appearances hydrates are suggested to be relicts of higher MV activity in the past, although the sporadic presence of vesicomyid clams at MV 2 showed that fluid migration is sufficient to nourish chemosynthesis-based organisms in places. Distributions of dissolved methane at MVs 3, 4, 5, and 8 pointed at fluid supply through one or few MV conduits and effective methane oxidation in the immediate subsurface. The aged nature of the hydrates suggests that the major portion of methane immediately below the top of the methane-containing sediment interval is fueled by current hydrate dissolution rather than active migration from greater depth.

INTRODUCTION

[1] Submarine mud volcanoes (MVs) are seafloor expressions of localized outflow of sediment and warm fluids mobilized in the subsurface typically several km in depth (Dimitrov 2002; Kopf 2002). Subduction-related liquid and gaseous fluids form in the deep subsurface as a consequence of sediment consolidation, mineral alteration and organic matter decomposition (Moore and Vrolijk 1992; Moore et al. 2001). Light hydrocarbons are typically formed during thermal cracking of organic matter at temperatures exceeding about 100°C in the deep subsurface (Selley 1998; Seewald 2003). In contrast, microbial methane formation is thought to occur at temperatures less than ca. 90°C which usually occur at shallower sediment depths. It is well documented that MVs can show transient fluid discharge activities, which may be evaluated by interpreting concentration profiles of fluids having migrated into the pore space of shallow sediments. For instance, the depth of the sulfate-methane interface (SMI), i.e. the zone where upward migrating methane and seawater-derived sulfate are converted through the anaerobic oxidation of methane (e.g. Hoehler et al. 1994) was proposed as a measure for the relative methane flux intensity (Borowski et al. 1996; Castellini et al. 2006; Bhatnagar et al. 2011).

[2] Submarine MVs are widespread at active continental margins because the buoyant upward migration of fluids is promoted by high pore-fluid pressure at depth caused by the overburden of overlying sediments and the general compressional regime induced by plate convergence. Subduction-related MVs predominantly located in forearc basins were reported from various regions including the Makran accretionary wedge (Schlüter et al. 2002), the Mediterranean accretionary wedge (Camerlenghi et al. 1995; Kopf 1999), off Costa Rica (Bohrmann et al. 2002), the Barbados Ridge complex (Westbrook and Smith 1983), the eastern Indonesian accretionary

complex (Barber et al. 1986), and the Nankai accretionary wedge of Japan (Kuramoto et al. 2001; Morita et al. 2004).
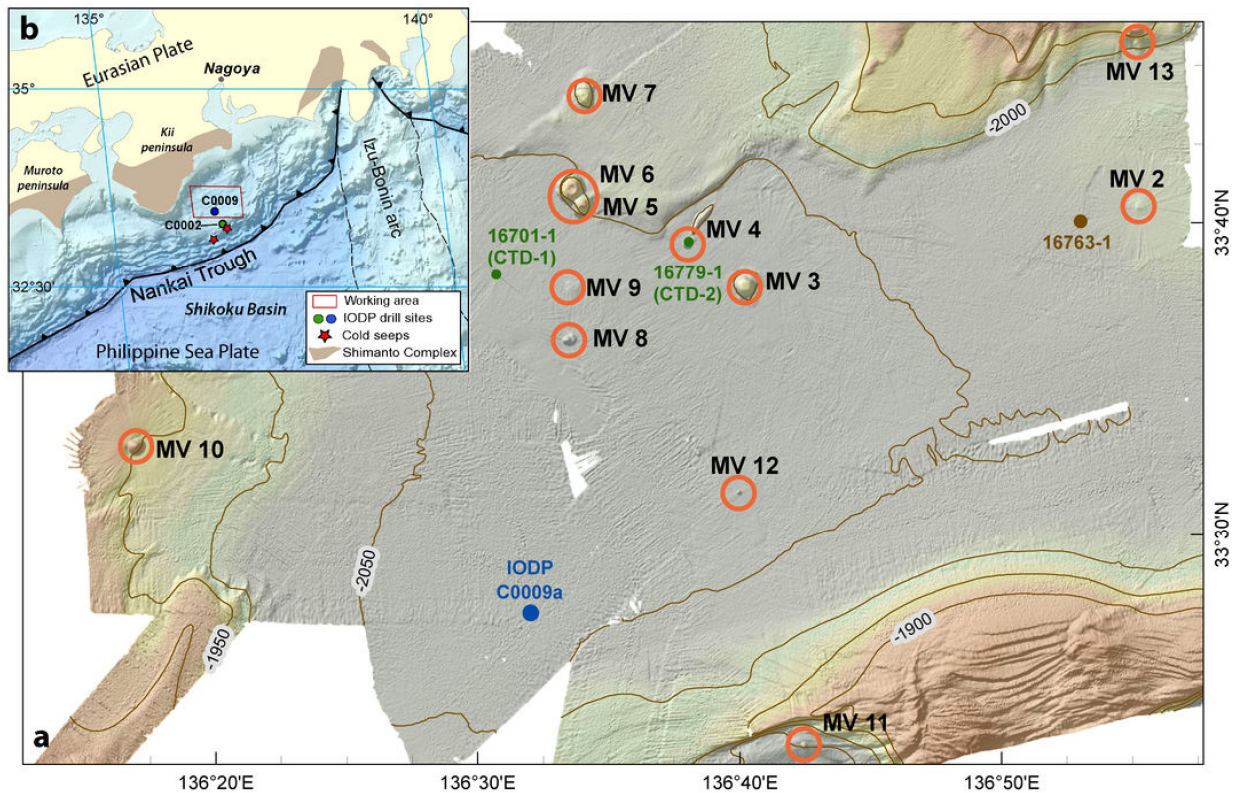
Figure 58: (A) Bathymetric map of the study area indicating positions of individual mud volcanoes investigated in this study. **(B)** Relief map and regional tectonic setting of the subduction zone of southwest Japan indicating the position of the study area in the Kumano forearc basin. Distributions of the Shimanto complex according to Moore and Saffer (2001).

[3] In case the MV is located within the gas hydrate stability zone (GHSZ), hydrates might form a capacious reservoir of light hydrocarbons from the ascending fluids in shallow sediments (e.g. Milkov 2000; Bohrmann et al. 2003; Feseker et al. 2009; Sahling et al. 2009; Pape et al. 2010b; Pape et al. 2011b). Despite biotic and abiotic molecular and isotopic modifications known to occur during fluid migration and hydrate formation (e.g. James and Burns 1984; Sassen et al. 1999; Hachikubo et al. 2007; Pape et al. 2010a), the chemical characteristics of those hydrates bear information on the geochemistry of the hydrocarbon source. For instance, a predominance of thermogenic hydrocarbons was reported from MVs in the Nile deep sea fan (Mastalerz et al. 2007), the Anaximander Mountains (Pape et al. 2010b), or in the Gulf of Cadiz (Hensen et al. 2007). A prevalence of microbial hydrocarbons was proposed for the Dvurechenskii and Vodyanitskii MV in the Black Sea (Feseker et al. 2009; Sahling et al. 2009), and the Håkon Mosby MV in the Barents Sea (Pape et al. 2011b).

[4] More than a dozen of MVs are known from above the seismogenic zone in the Kumano forearc basin at the Nankai Trough subduction zone offshore SW Japan (Figure 58a). The re-

gion is characterized by destructive and tsunamigenic earthquakes and non-volcanic tremors (Ito and Obara 2006; Shelly et al. 2006; Obana and Kodaira 2009). Although several sites at the Nankai Trough subduction zone have already been explored in the frame of IODP drilling campaigns (see Kinoshita et al. 2009; Saito 2009; Saffer et al. 2010; Kopf et al. 2011; Henry et al. 2012; Moore et al. 2013), causes for the MV activity in the Kumano forearc basin and the fluid sources have been poorly constraint so far.

[5] In the present study we analyzed hydrate-bound gases and dissolved methane in shallow deposits of twelve MVs in order to assign fluid formation depths and processes, and potential source rocks, respectively. Current stages of activity at individual MVs were evaluated by conducting hydroacoustic water column surveys, seafloor inspections, and geochemical profiling.

TECTONIC AND GEOLOGICAL SETTING

Geological overview

[6] The Nankai Trough accretionary subduction zone is the active convergent plate boundary between the subducting Shikoku basin on the Philippine Sea Plate and the Eurasian Plate (Figure 58b). For the Philippine Sea Plate, minimum ages of 20–21 Myr (early Miocene) were estimated (Marcaillou et al. 2012). Nowadays, the deformation front is located about 80–160 km southeast off the Kii Peninsula, SW Japan (Moore et al. 2001). In our study area in the Kumano forearc basin the top of the subducting plate was proposed to be located at depths between about 10 and 20 kmbsf (Moore and Saffer 2001; Marcaillou et al. 2012).

[7] The landward subduction zone margin consists of the >100 km-wide Nankai accretionary prism (e.g. Taira et al. 1992). At present predominantly hemipelagic sediments of the Shikoku basin are being accreted (Saito, 2009; Henry et al. 2012). The landward succession of the toe of the prism is formed by sediments underlying the Kumano basin fill that are believed to belong to the Cretaceous and Tertiary Shimanto Belt (Figures 57a and 57b); (Taira et al. 1992). The Kumano forearc basin is located east of the Kii peninsula and extends about 100 km in E–W and 70 km in N–S direction. It forms a low-topography seafloor basin approaching water depths of approx. 2,100 m. Terrigenous and hemipelagic sediments in that basin are up to 2 km in thickness (Morita et al. 2004; Tobin and Kinoshita, 2006). Age assignments for rocks at the bases of IODP Sites C0002 and C0009, that penetrated the boundary between basin sediments and old accreted sediments, suggest that basin formation commenced in the late Miocene (Kinoshita et al. 2009; Hayman et al. 2012; McNeill et al. 2010; Saffer et al. 2010).

[8] A landward dipping system of out-of-sequence splay (OOSS) faults commences from the plate boundary thrust fault at ca. 50–55 km landward of the prim toe, migrates through the accretionary prism and surfaces at the seafloor (Park et al. 2002; Moore et al. 2007). A

megasplay, which apparently intersects the Nankai accretionary prism between the currently formed accretionary prism and the older accreted belt (Moore et al. 2007), branches upward from the plate-boundary interface at a depth of about 10 kmbsf and about 50 to 55 km landward to the deformation front (Strasser et al. 2009; Gulick et al. 2010). The OOSSs are believed to branch from the up-dip limit of the seismogenic zone, and thus, to potentially serve as migration pathway for rapid fluid ascent to the seafloor (Park et al. 2002; Tobin and Saffer, 2009), but indications for deep-sourced fluids are missing yet (e.g. Screaton et al. 2009).

[9] In the Kumano forearc basin more than a dozen of MVs evolved with basal diameters of up to two km (Kuramoto et al. 2001; Kopf 2002; Morita et al. 2004) (Figure 58a). Typically they form conically-shaped domes indicative for a relatively low viscosity of the expelled mud with several MVs protruding more than 100 m into the water column. Clasts ejected from the MVs are predominantly Late early Miocene to Early middle Miocene in age (Morita et al. 2004).

[10] Seismic studies show that the MVs are situated above anticlines (Morita et al. 2004). Also, most bottom-simulating seismic reflectors indicative for the presence of hydrates and free gas were associated with buried anticlines in our study area (Baba and Yamada 2004). Seismic studies, seafloor observations, as well as sedimentological and microbial investigations suggested different and varying dynamics of the individual MVs (Kuramoto et al. 2001; Morita et al. 2004). For instance, enrichments in dissolved methane above MV 5 in 2004 were attributed to methane release into the water column (Tsunogai et al. 2012). Indications for elevated methane concentrations in shallow sediments and/or methane seepage from the summit area were also reported for MV 8 in 2006 (Miyazaki et al. 2009).

MATERIALS AND METHODS

[11] The twelve MVs in the Kumano forearc basin (Figures 57 and 58; see Table S.7 in Appendix A.6) were inspected in summer 2012 by means of hydroacoustic surveys, visual seafloor inspections and groundtruthing (Kopf et al. 2013). For methodological details refer to Appendix A.6.

Seafloor inspection, sampling and sample preparation

[12] Bathymetric mapping was conducted with the hull-mounted Kongsberg EM120 multibeam echosounder. A TV-grab was used for on-line seafloor inspection and sampling of near-surface sediments at MVs 2, 3, 4, and 10. Additional seafloor inspections and hydroacoustic bottom water investigations were carried out with the remotely operated vehicle (ROV) 'QUEST4000m' (MARUM) equipped with a forward-looking sonar (Nikolovska et al. 2008) at MVs 3 and MV 4.

[13] In total, 34 non-pressurized gravity cores of shallow sediments from twelve MVs were investigated (Appendix A.6, Table S.7). Hydrate-bound gas was prepared from hydrate pieces (Pape et al. 2010a) and transferred into glass serum vials prefilled with saturated NaCl solution for storage until analysis. For vertical profiling of methane concentrations in gravity cores, a modified headspace technique (Kvenvolden and McDonald 1986) was used. 3 ml of sediment were taken with cut-off syringes immediately after core recovery, when concentrations of light hydrocarbons have still not equilibrated to atmospheric pressure, at defined depths and transferred into 20 ml glass vials prefilled with 5 ml of 1 M NaOH. The samples were stored at $+4°C$ until analysis onshore.

Analytical Methods

[14] Gas samples were analysed for their molecular compositions and methane concentrations by gas chromatography (GC) (Pape et al. 2010a). Stable carbon isotope ratios ($^{13}C/^{12}C$) of CH_4 in hydrate-bound gas and in lowermost headspace samples were determined by GC–isotope ratio mass spectrometry (GC–IRMS). Carbon isotopic ratios are reported in δ-notation in parts per mil (‰) relative to the Vienna PeeDee Belemnite (V-PDB).

RESULTS

Sediments and associated gas hydrates

[15] For all gravity core stations conducted at MVs, a penetration less than 6 m (Figure 60) indicated the presence of relatively hard substrate such as mud clasts, stiff sediments and/or gas hydrates. The main lithologies detected were mud breccia with mud-, silt- and sandstone clasts and background sediment, including shell fragments and nanno- and microfossils. The background sediment had intercalations of layers with varying grain size, which, due to their fining upward behavior, were interpreted as turbidites. Background sediment overlying the mud breccia at the investigated MVs remained undetected, indicating their (sub-) recent activity. Several gas escape structures (i.e. voids, perforated appearance, smell of H_2S) indicated gas enrichments. In places, the mud breccia had regular gas voids, giving the entire lithology a mousse-like texture. The majority of the clasts were mudstones, most likely derived from within the old accreted sediments underlying the basin fill.

[16] Hydrates were sampled in multiple gravity cores recovered from MVs 2, and 4, and in single cores each from MVs 5 and 10 (Figure 58; Table 15). They were present in cores from the summit areas and in cores GeoB16772-1 and 16722-2 that were taken from the slopes of MVs 2 and 4, respectively. In all cores hydrates occurred below about 0.5 mbsf as disseminated specimen less than ca. 1 cm in diameter (Figures 58a and 58b).

[17] Gases prepared from hydrates recovered from MVs 2, 4, and 10 were strongly dominated by methane ($CH_4 \geq 92.787$ mol% Σ (C_1 to n-C_4 + CO_2); Table 15), followed by CO_2 (3.837 – 4.509 mol%) and C_2H_6 (≤ 2.725 mol%). Higher hydrocarbons occurred in much smaller portions or were below detection limit (ca. 2 ppm). For all hydrate pieces, $\delta^{13}C$-ratios of hydrate-bound methane were ≥ -40.5‰ V-PDB.

Table 15: *Distributions of light hydrocarbons and CO_2 (in mol-% $\sum[C_1$ to n-C_4 + CO_2]), C_1/C_2 ratios, and stable C isotope signatures of CH_4 (in ‰ V-PDB and SMOW, respectively) in hydrate-bound gas (hyd.) and dissolved gas (diss.). Values of $\delta^{13}C$-CH_4 (diss.) are given for lowermost sample in profile.*

GeoB	C_1	C_2	C_3	i-C_4	C_4 n. i-dent.	CO_2	n	C_1/C_2	$\delta^{13}C$-CH_4 (hyd.)	$\delta^{13}C$-CH_4 (diss.)	$\Delta\delta^{13}C$ (CH_4 hyd.-diss.)
MV #2											
16764-1	95.4837	0.4230	tr.	tr.	tr.	3.9944	1	226			
16771-1	95.3569	0.6120	tr.	tr.	tr.	3.9336	2	156	−39.5	−38.8	−0.7
16772-1	95.4521	0.5860	tr.	tr.	tr.	3.8649	2	163	−40.5	−37.2	−3.3
16788-1	95.5311	0.4318	tr.	tr.	tr.	3.9408	2	221	−39.7		
16788-2	95.5640	0.4854	tr.	tr.	tr.	3.8534	2	197	−39.9		
average	*95.4776*	*0.5076*	*tr.*	*tr.*	*tr.*	*3.9174*		*188*	*−39.9*		
MV #4											
16722-2	92.7873	2.7252	tr.	tr.	tr.	4.3911	2	34	−39.4	−41.1	+1.7
16725-1	93.7949	1.7243	tr.	tr.	tr.	4.3817	2	54	−38.9	−37.3	−1.6
16736-1	94.0164	1.3663	0.0412	tr.	tr.	4.5087	4	69	−39.3		
average	*93.5329*	*1.9386*	*tr.*	*tr.*	*tr.*	*4.4275*		*48*	*−39.2*		
MV #5											
16746-1	95.9588	0.1065	tr.	tr.	tr.	3.8371	6	901	−37.6	−36.7	−0.9
MV #10											
16716-2	94.7519	0.8170	0.4285	0.1107	tr.	3.8565	7	116	−38.0	−39.6	+1.6

n = number of samples analyzed for molecular composition (mean value)
tr. = trace (≤ 0.04 mol%)

Vertical distributions and stable carbon isotope ratios of dissolved methane

[18] Vertical *ex situ* concentration profiles of methane dissolved in pore waters of shallow sediments recovered from the summit areas and partially from the slopes were established for all MVs investigated (Figure 60). These profiles signify considerable methane enrichments with the top of the methane-bearing sediment interval ('methane zone') being situated shallower than ca. 350 cm below seafloor (cmbsf) in central areas of several MVs (Table 16). The shallowest sulfate-methane interface (SMI) was found for MV 5 (ca. 15 cmbsf), which also showed highest *ex situ* concentrations of dissolved methane (ca. 35 mmol L-1 at 230 cmbsf). This was followed by MVs 2, 4, and 13. As exemplified for MVs 3 and 4 (Figure 60), methane concentrations decreased significantly with increasing distance to the summit and the SMI could not be penetrated at the edges of the MVs. At stations positioned at the slopes of certain MVs (e.g. 3, 4, 5, 8) concentrations were at least one order of magnitude higher compared to those measured at a station in the NE part of the study area (Figure 58a), where background samples were taken (GeoB16763-1; <1.0 μmol L-1 throughout the core). Methane was virtually absent in cores from MVs 6 and 7.

[19] Stable carbon isotope ratios of dissolved methane in lowermost headspace samples varied from –59.0‰ (MV 10) to –29.3‰ (MV 2; Figure 60). Differences in stable carbon isotope signatures ($\delta^{13}C$) between dissolved methane in lowermost samples and of hydrate-bound methane ranged between –1.7‰ to +3.3‰ (Table 15). For cores from MVs 2 and 5 relative enrichments in ^{13}C with decreasing depth were observed for dissolved methane, while for cores from MVs 4 and 10 depletions in ^{13}C were found for shallower samples.
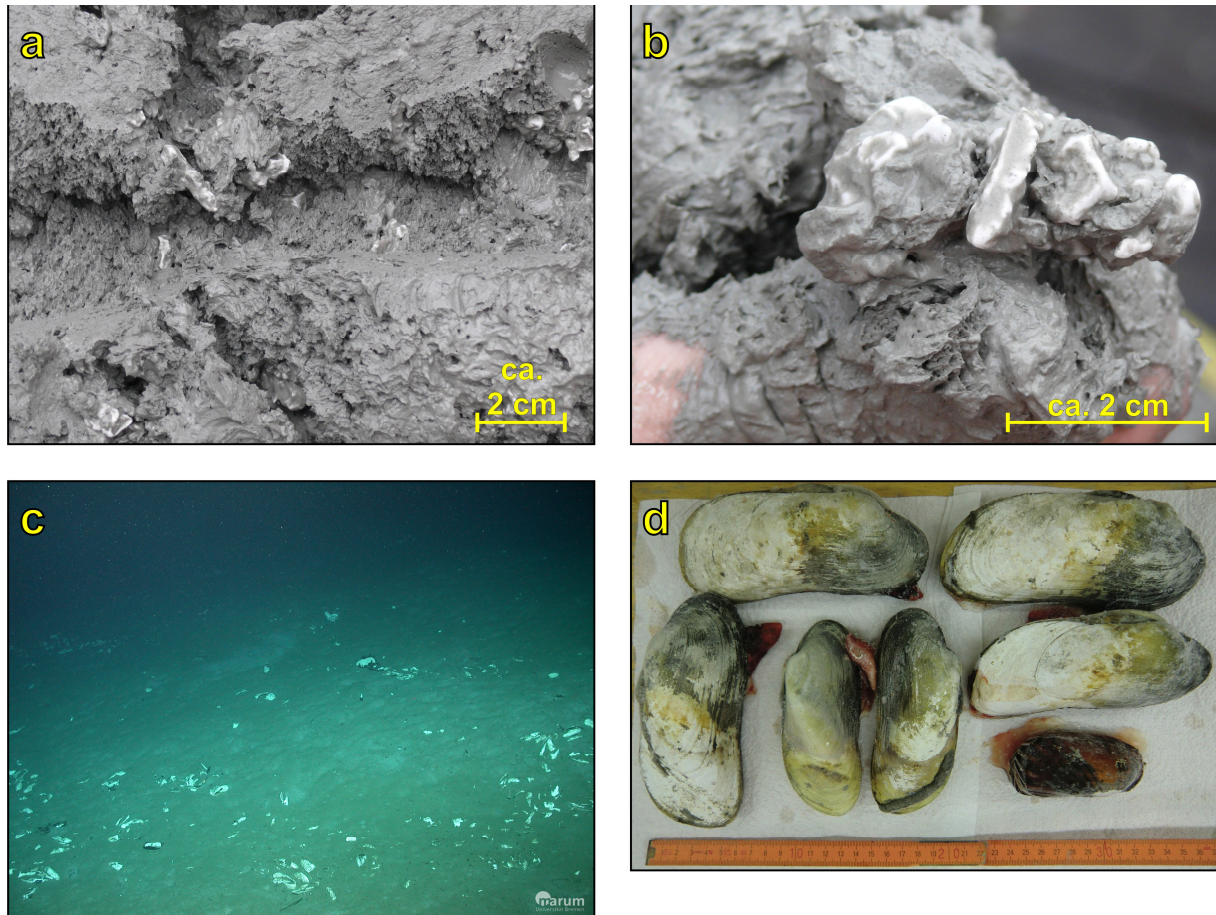
Figure 59: (a)+(b): *Disseminated, mm-sized gas hydrate specimen in homogenous sediments (mud breccia) retrieved from MV 2. (c)+(d): Seafloor picture showing clam shells tentatively assigned to the genus Calyptogena at MV 3 taken during ROV dive 321 (GeoB16767-1). Picture of live clams sampled from MV 2 during station TVG-5 (GeoB16793-1).*

Water column and seafloor characteristics

[20] During SO-222 hydroacoustic anomalies in the water column ('gas flares') diagnostic for gas bubble release from the seafloor were not observed above the MVs using the hull-mounted ATLAS Hydrographic PARASOUND sediment echosounder P70 (Kopf et al. 2013). During the five TV-grab surveys and two ROV dives at MVs 2, 3, 4, and 10, gas bubble emissions were neither observed visually nor detected with the ROV-mounted sonar. During the ROV dive at MV 3 relative bottom water temperature elevations by up to ca. 1.75°C indicative for heat flow through MV activity, were recorded. Dense microbial mats, usually observed at active hydrocar-

bon-seeps, became not obvious. However, shells of clams inferred to belong to the genus Calyptogena (Vesicomyidae) and thought to indicate H2S enrichments in the immediate subsurface (Sahling et al. 2002) were sporadically observed on the seafloor at the summit areas of MVs 2, 3, 4, and 10 (e.g. Figure 59c). On the summit of MV 2 live Calyptogena clams were sticking in the sediment in places (Figure 59d).

DISCUSSION

Origin of Volatiles

[21] Although molecular and isotopic compositions of gases might be altered during migration through the sediment and incorporation into gas hydrates, hydrates provide information on sources of hydrocarbons formed at greater depth (e.g. Sassen et al. 1999; Hachikubo et al. 2007; Pape et al. 2010a). Relatively low C_1/C_2 ratios of hydrate-bound hydrocarbons ranging between 35 and 254 and $\delta^{13}C_{CH4}$ signatures $>-40‰$ V-PDB (Table 15) substantiate that light hydrocarbons expelled from MVs 2, 4, and 10 are predominantly generated by thermal cracking of type II kerogen, which typically originates from marine organic matter (Figure 61). In contrast, a significantly higher C_1/C_2 ratio of approx. 1,630 determined for hydrocarbons bound in the single hydrate piece recovered from MV 5 may be explained by microbial production as additional hydrocarbon source and/or preferred incorporation of methane into the hydrate phase. A microbial hydrocarbon source would be consistent with stronger enrichments in ^{12}C ($\delta^{13}C = -52.0 \pm 2‰$) determined for dissolved methane in shallow pore waters at the centre of MV 5 in 2000/2001 (Tsunogai et al. 2012). By contrast, preferential incorporation of methane into hydrates (Pape et al. 2010a) causing the comparably high C1/C2 ratios would be plausible with respect to the similarities in $\delta^{13}C_{CH4}$ (Table 15, Figure 61) for all MVs investigated.

[22] Thermogenic gases are typically characterized by much higher proportions of C_{3+} hydrocarbons (Claypool and Kvenvolden 1983; Sassen et al. 1999), which in our study were only found in detectable amounts at MVs 4 and 10 (Table 15). In previous studies depletions of hydrate-bound gases in C_{3+} hydrocarbons relative to the source gas were attributed to selective removal during migration or to size exclusion during hydrate precipitation (James and Burns 1984; Sassen et al. 2000; Pape et al. 2010a). With respect to the comparably low C_1/C_2 ratios and the likely formation of sII hydrates at least at MV 10 (chapter 5.2) that would allow for incorporation of C_{3+} hydrocarbons (Sloan and Koh 2007), we assume higher amounts in the source gas, which have been depleted during migration. However, as migrated gas was not analysed
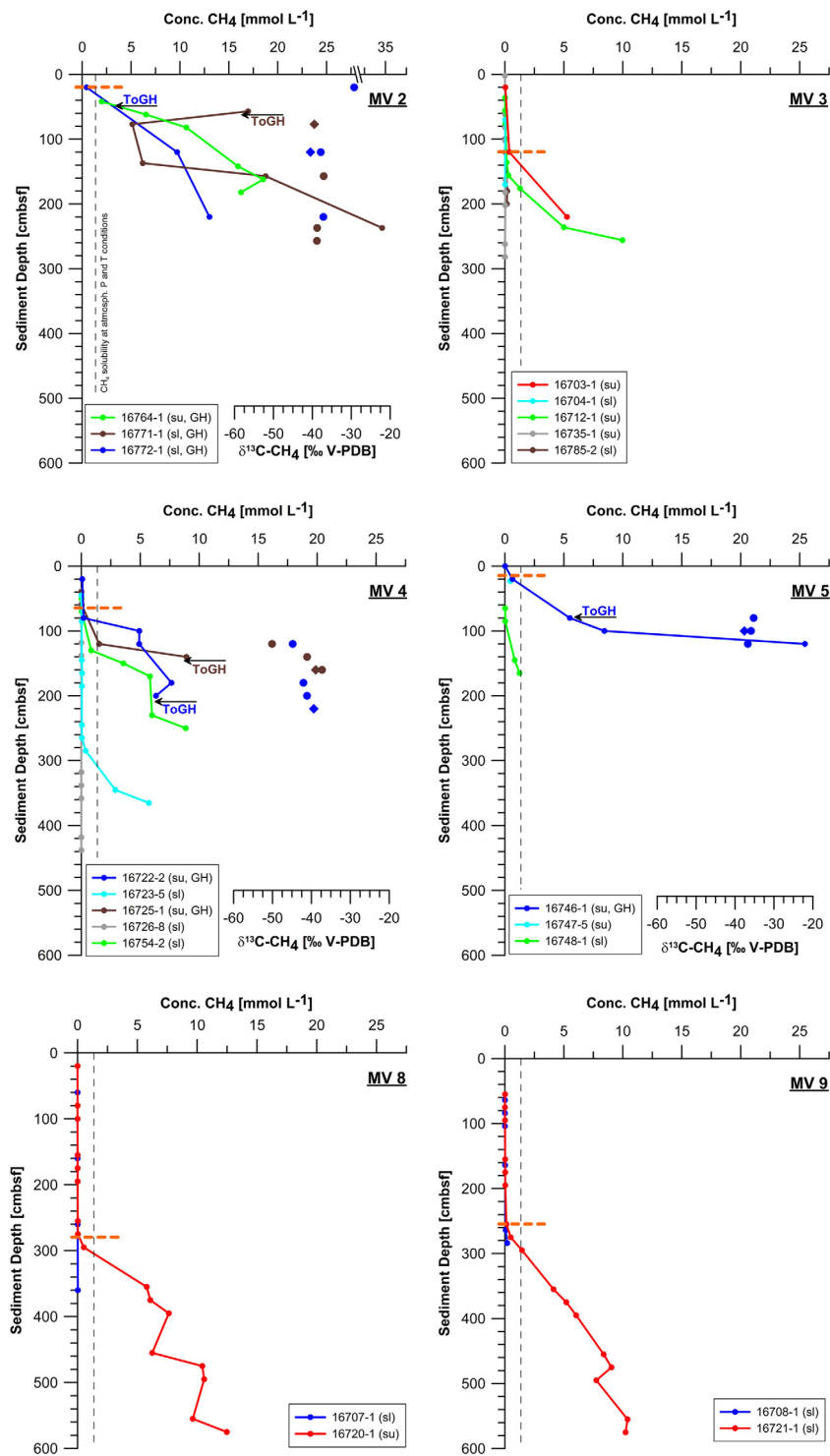
Figure 60: *Vertical concentration profiles of methane dissolved in pore waters (solid line and filled circles) recovered from the MVs. Gas hydrate presence ('GH') in cores from MVs 2, 4, and 5 as well as positions of cores at the summit ('su') or slope ('sl') of individual MVs are indicated (except for MVs 11 and 12). For cores from MVs 2, 4, 5, and 10, $\delta^{13}C$-values of dissolved methane (filled circles) and of hydrate-bound methane (filled diamonds) are added. The dashed horizontal orange-colored lines indicate the shallowest top of the methane zone observed at an individual MV during cruise SO-222. Because of rapid sample preparation upon core recovery on ship's deck, methane concentrations in deeper core sections still exceeded methane solubility under atmospheric pressure (ca. 1.35 mmol L-1, dashed vertical line; Duan and Mao 2006). Irregularly shaped methane concentration profiles in the bottom parts of some cores, as observed for e.g. MVs 4, 11, and 13 are due to inhomogenous degassing at atmospheric pressure and/or dissociation of tiny hydrate pieces. In situ methane solubility under presence of a sl hydrate phase would be ca. 55.5 mmol L-1 (at 1.7°C and 30 PSU salinity; Kopf et al. 2013).*

7.1 Hydrocarbon Seepage and its Sources at Mud Volcanoes of the Kumano Forearc Basin
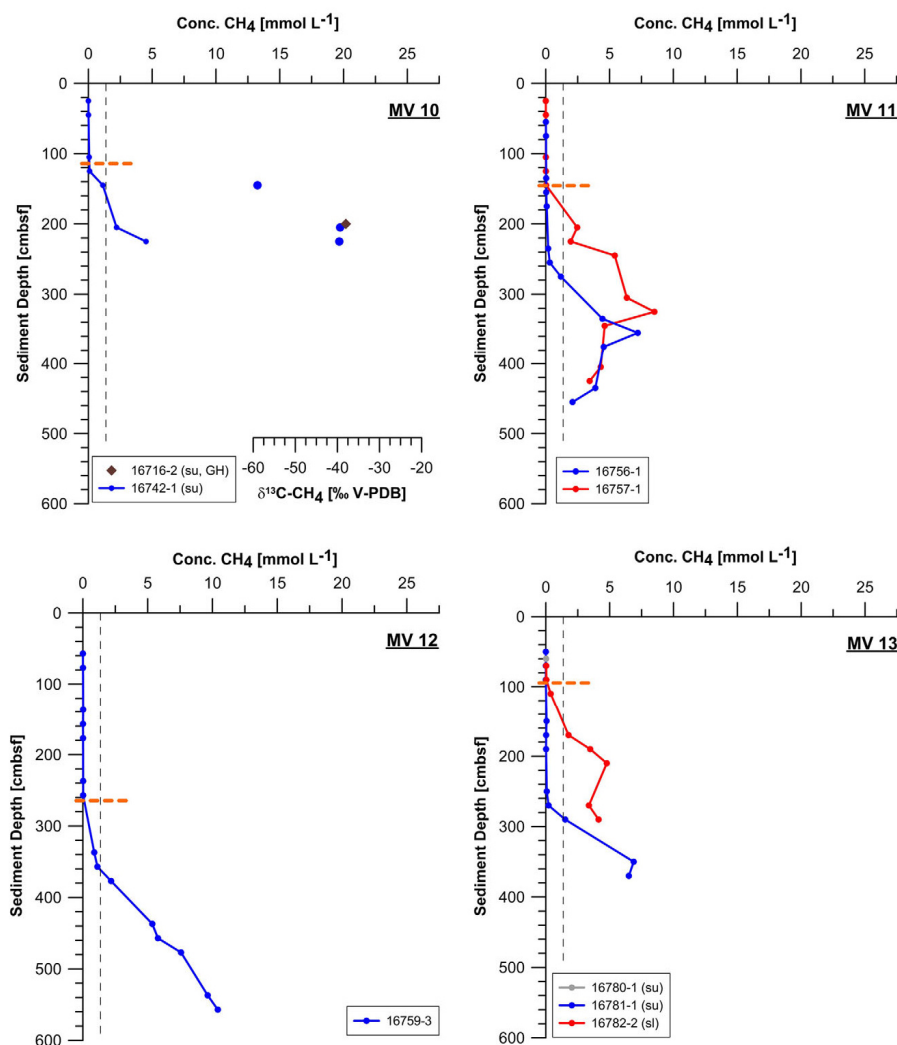
Figure 60: (continued)

in this study, the specific effects of processes having led to potential removal of C_{3+} hydrocarbons are undetermined yet.

[23] Whereas microbial light hydrocarbons are believed to be formed at temperatures below about 90°C (Orphan et al. 2000), formation of thermogenic hydrocarbons peaks in the 100°C to 150°C-range (Claypool and Kvenvolden 1983; Selley 1998; Seewald 2003). Analysis of in situ temperatures in shallow sediments at MVs 2, 3, 4, 9, 10, and 13 concurrent to our present study revealed slightly elevated temperature gradients compared to background values in shallow sediments only at the centres of MV 2 (max. 0.29°C/m) (Kopf et al. 2013) and MV 3 (max. 0.12°C/m). Therefore, the temperature gradients determined at IODP Holes C0009 (approx. 0.035°C/m) (Saffer et al. 2010) and C0002 (ca. 0.043°C/m) (Kinoshita et al. 2009; Harris et al. 2011), which are located close to our study area, were used for a depth estimate of the hydrocarbon source rocks fuelling the MVs. Assuming that the gradient follows a linear trend with depth, temperatures required to induce thermogenic hydrocarbon formation likely occur at

depths between about 2,300 mbsf (100°C, 43°C/km) and 4,300 mbsf (150°C, 35°C/km). The higher C_1/C_2 ratio observed for hydrate-bound hydrocarbons at MV 5 compared to those from MVs 2, 4, and 10 might be explained by additional microbial hydrocarbon generation in the upper 2,100 to 2,600 mbsf.
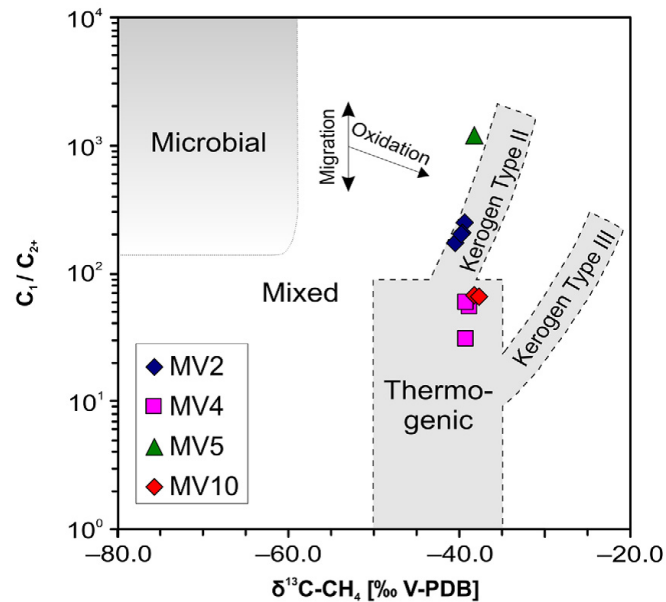
Figure 61: *"Bernard diagram" modified after Whiticar (1989) showing $\delta^{13}C$ values of methane vs. molecular hydrocarbon ratios in hydrate-bound gas at MVs 2, 4, 5, and 10 and inferred hydrocarbon sources.*

[24] The minimum formation depths calculated here for light hydrocarbons expelled from MVs 2, 4, and 10 imply that the fluids are mainly generated below the ca. max. 2 km thick Pliocene to recent basin sediments (Tobin and Kinoshita 2006; Hayman et al. 2012). Consequently, the MVs should root either in the old accretionary wedge or even deeper. This assumption is corroborated by the exclusive occurrence of thermogenic hydrocarbons (as interpreted from C_1/C_{2+} ratios) in accreted sediments (Sites C0002, 1176, 1178), hemipelagic sediments (Site 808), and the oceanic basement (Sites C0011, C0012, 1173, 1174) drilled within the frame of ODP and IODP campaigns off the Kii Peninsula and off Cape Muroto, respectively (Figures 58b and 62) (Hill et al. 1993; Mikada et al. 2005). Moreover, recent drilling mud gas monitoring at Hole C0002F revealed a prevalence of thermogenic hydrocarbons below approx. 1700 mbsf with $\delta^{13}C_{CH4} \geq -60‰$ and C_1/C_{2+} ratios ranging between 300 and 400 (Moore et al. 2013). In contrast, at Hole C0009A that is positioned close to the MVs studied herein (Figure 62) and likely was drilled through the forearc basin sediments into the top of the old accretionary prism (total depth ca. 1,600 mbsf), a predominance of microbial hydrocarbons (C_1/C_{2+} ratios >100) was found at all depths investigated (Saffer et al. 2010).

7.1 Hydrocarbon Seepage and its Sources at Mud Volcanoes of the Kumano Forearc Basin
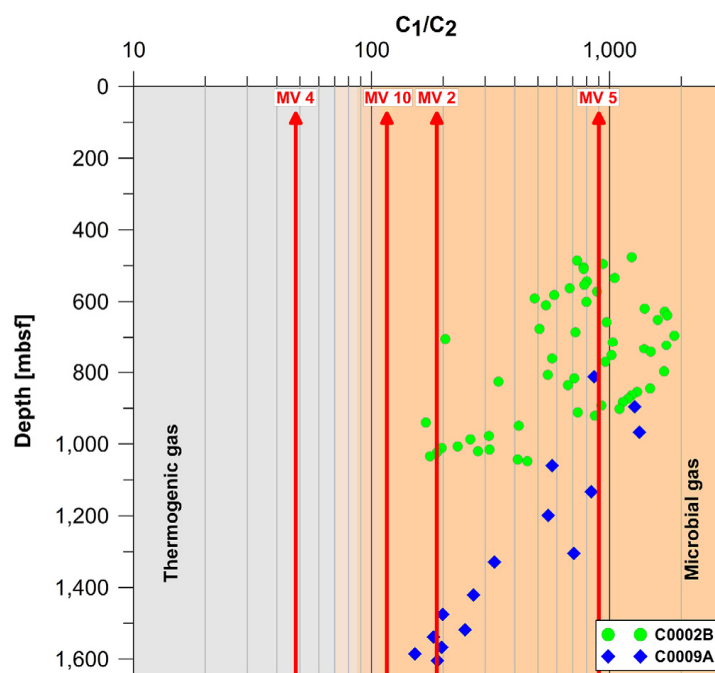
Figure 62: *Depth profiles of C_1/C_2 ratios in headspace samples from IODP Holes C0002B and C0002D (green circles; Tobin and Kinoshita 2006) and in drilling cuttings from Hole C0009A (blue diamonds; Saffer et al. 2010). C_1/C_2 ratios of hydrate-bound hydrocarbons at MVs 2, 4, 5, and 10 (red vertical lines) are shown for comparison.*

[25] In our study area the plate boundary thrust dips from about 10 km depth (SE edge) to more than 20 km depth (NW edge) and thermal modelling revealed temperatures between about 150 and 350°C at respective depths (Moore and Saffer 2001; Marcaillou et al. 2012). With respect to i) temperatures at the interplate boundary, ii) the distance between its top and the seafloor, and iii) the assumed preferential non-vertical transport of fluids generated at the inter-plate boundary via OOSSs to more seaward sites, it appears most probable that hydrocarbons mobilized during MV activity are derived from the old accreted sediments overlying the seismo-genic zone (Figure 63). A supportive conclusion was drawn by Moore and Saffer (2001) who proposed that the fluid production potential is vastly reduced at burial depths exceeding about 4000 mbsf. With respect to age assignments for the top of the old accreted sediments at Sites C0002 and C0009 fluid source rocks must be older than Late Miocene age (Kinoshita et al. 2009; McNeill et al. 2010; Saffer et al. 2010). Although age models are apparently not available for the old accreted sediments, source rocks might be related to the Cretaceous to Tertiary Shimanto Belt (Taira et al. 1992).

7.1 Hydrocarbon Seepage and its Sources at Mud Volcanoes of the Kumano Forearc Basin
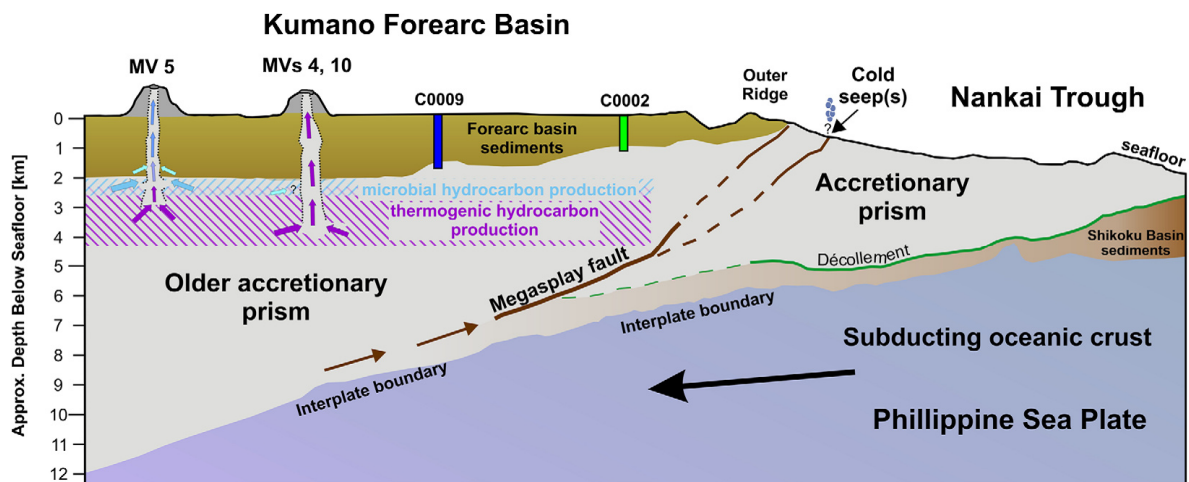
Figure 63: *Sketch illustrating origins and migration pathways of fluids in the Nankai Trough subduction zone (adapted from Park et al. 2002; Toki et al. 2004; Strasser et al. 2009; Saffer et al. 2010). Hydrocarbons expelled from MVs in the Kumano forearc basin originate from older accreted sediments below the forearc basin, whereas fluids generated at the interplate boundary are most likely transported along faults to seepage sites at the outer ridge. Note: Positions of MVs 5, 4, and 10 displayed as examples relative to IODP Sites C0009 and C0002 only. Horizontal distances not for scale.*

Gas Hydrates and Their Physical State

[26] Gas hydrates in general and specifically those associated to MVs are a dynamic methane reservoir (Dickens 2003; Feseker et al. 2009). The top of hydrates and also the top of the methane zone in MV deposits usually deepens with increasing distance to the MV conduit (Egorov et al. 1999; Castellini et al. 2006; Pape et al. 2011b). The presence of gas hydrates at MVs 2, 4, 5, and 10 (Table 16) demonstrates that upward methane flux was sufficient to induce hydrate formation at depths shallower than 3 mbsf in the recent past. However, in contrast to the massive, cm-sized and sometimes porous hydrates frequently collected at intense gas emission sites (Sassen et al. 1999; Suess et al. 1999; Torres et al. 2004), hydrate chips recovered from the Kumano basin MVs were dispersed and relatively small in size (Figures 58a and 58b). This, along with the virtual lack of free gas emissions (i.e. the absence of gas flares during hydroacoustic surveys), suggests that hydrate formation is not ongoing at present and that the hydrates found are subject to decomposition.

[27] It is known that warm (>20°C) fluids can be injected into near-surface deposits and induce thermal hydrate dissociation in case the hydrate dissociation temperature is surpassed (Feseker et al. 2009; Pape et al. 2011b; Römer et al. 2012). Because of the differences in the stability conditions between both crystallographic hydrate structures widespread in nature (sI and sII), the hydrate crystal structure has to be known for calculating actual hydrate dissociation temperatures. However, analysis of hydrate crystal structures has not been conducted for hydrates recovered during cruise SO-222, so far. The virtual absence of hydrocarbons > C_3 in hydrates recovered from MVs 2, 4, and 5 suggests that sI is the dominant hydrate phase at

these sites. In contrast, a prevalence of sII hydrates at MV 10 might be inferred from the presence of C_3 and C_4-isomers. Calculations of phase boundaries substantiate that both, sI and sII hydrates, would in principle be stable at the MVs in the Kumano basin investigated (Figure 64) and would start to decompose when sediment temperatures exceed ca. 16.7 to 17.6°C. During the time of investigation both, bottom water temperatures (ca. 1.7 to 2.1°C, Figure 64) and in situ temperatures in shallow sediments at MVs 2, 3, 4, 5, 10, and 13 (Kopf et al. 2013), were lower than the calculated hydrate dissociation temperatures of sI and sII hydrates. Exceptions were MVs 2 and 3 where sediment geothermal gradients were raised significantly above the background level and ranged between 0.03 and 0.06 °C/m. The bottom water temperatures measured matched those reported by Kinoshita et al. (2011) and annual temperature variations less than 0.2°C were stated for a time period of about 900 days (Hamamoto et al. 2011). Therefore, the assumed hydrate decay at MVs lacking elevated temperatures in uppermost sediments is likely caused by dissolution due to pore water methane undersaturation resulting from currently insufficient methane supply rather than by thermal dissociation. This might be supported by the presence of similar looking hydrates on the slopes of MVs 2 (cores GeoB16771-1 and -772-1) and 4 (-722-2) where the impact of heat impulses from below should be comparably low.

[28] Moreover, the stable carbon isotope signatures of hydrate-bound and dissolved methane at similar depth varied only slightly ($\delta^{13}C$ between −1.7‰ and +3.3‰, Table 15). In theory, matching $\delta^{13}C$ ratios of hydrate-bound methane and of methane dissolved in the immediate pore waters should either be found i) during phases of high MV activity, when methane concentrations in the pore water exceed solubility and hydrates form, or ii) during phases of low fluid flux from below, when hydrates decompose and substantial methane amounts are released. Considering our various observations (lack of seafloor gas emissions, sparse seafloor settlement by chemosynthesis-based organisms, dispersed state of hydrates recovered) we propose that similar $\delta^{13}C$ ratios of hydrate-bound methane and dissolved methane determined for our samples result from current hydrate dissolution.

[29] Considering the magnitude of dissolution rates (0.5 – 30 mm yr^{-1}) calculated for buried hydrates surrounded by methane-undersaturated pore water (Lapham et al. 2010), we propose that hydrate dissolution at MVs 2, 4, 5, and 10 was already ongoing for several months at least at the time of our investigation. Very low methane concentrations (<1 μmol L^{-1}) in the uppermost sediments demonstrate that methane released during hydrate decomposition is effectively consumed by AOM (Hoehler et al. 1994; Miyazaki et al. 2009) in overlying sediments (Figure 60). As exemplified for MV 10, where hydrates were found at shallow depth, methane concen-

trations at the seafloor are consequently too low to enable significant chemosynthesis-based benthic life at the time of sampling.
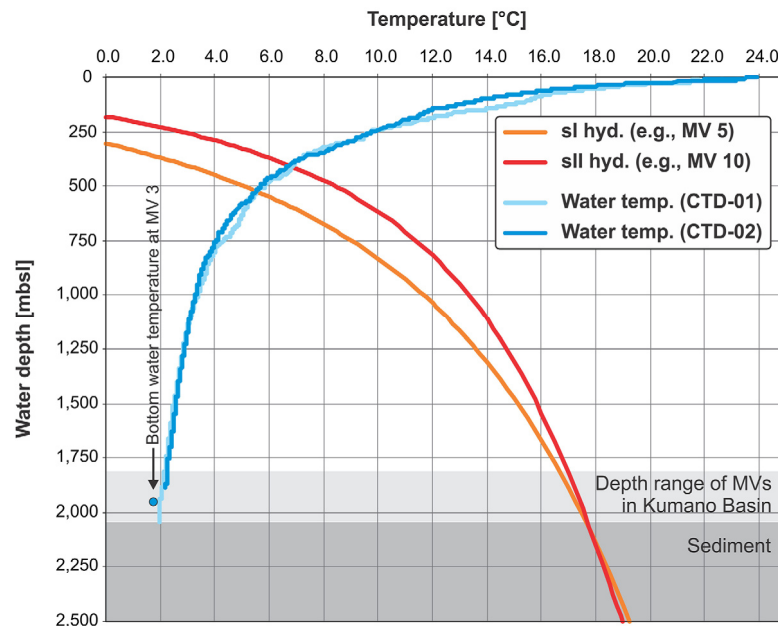
Figure 64*: Phase boundaries calculated for MV-associated gas hydrates in the Kumano basin using the HWHYD U.K. software (Masoudi and Tohidi 2005), molecular compositions of hydrate-bound gases determined for MV 5 and MV 10 (Table 15), and bottom water salinities of 34.59 PSU (CTD-02, GeoB16779-1 at 2.070 meters below sealevel). Those MVs were selected because different hydrate crystal structures were inferred from gas compositions. Calculated dissociation pressures at individual temperatures were converted into actual water depths considering algorithms given in the (Fofonoff and Millard 1983). Water temperatures were determined at stations CTD-01 (GeoB16701-1) ca. 4.4 km W of MV 9 and CTD-02 above MV 4. Bottom water temperatures at MV 3 were recorded during ROV dive GeoB16767-1.*

Current Activities of Individual MVs

[30] Active submarine mud volcanism is usually accompanied by flow of heat and fluids into shallow sediments and potentially also into bottom water. In general, an increase in methane concentration with increasing depth along with the top of the methane zone being positioned in the upper few meters is a significant feature of (sub-)recent hydrocarbon seepage activity (e.g. Borowski et al. 1996; Castellini et al. 2006; Wallmann et al. 2006; Coffin et al. 2008; Bhatnagar et al. 2011). In contrast, the SMI at non-seep sites is typically positioned at several tens of meters depth. In previous studies methane enrichments detected above MV 5 in 2004 were suggested to be caused by earthquake-induced mud volcanic activity (Tsunogai et al. 2012) and relatively high heat fluxes were measured at MV 8 (Hamamoto et al. 2011).

[31] Although we only achieved an incomplete water column and seafloor coverage during hydroacoustic surveys and seafloor inspections in this study, it seemed that emissions of significant amounts of free, bubble-forming methane from the MVs into the hydrosphere did not occur during our time of investigation. Support for this assumption comes from the relatively moderate to low fluxes of MV-associated fluids in shallow sediments as indicated by the virtual absence of

7.1 Hydrocarbon Seepage and its Sources at Mud Volcanoes of the Kumano Forearc Basin

dense microbial mats (e.g. Beggiatoa sp.), the sparse distribution of chemosynthesis-based clams, and the SMI being positioned deeper than approx. 1 meter in most cores investigated (Figure 60).

Table 16: Depths of the SMI and gas hydrate occurrences at individual MVs

MV #	No. of cores re-trieved from summit area	Estimated depth of SMI at summit [cmbsf]	Gas hydrates / Top of gas hydrates
2	3	20	Gas hydrates / ca. 50 cmbsf
4	2	65	Gas hydrates / ca. 145 cmbsf
5	1	15	Gas hydrates / ca. 75 cmbsf
10	1	115	Gas hydrates / n. doc.
3	2	120	
8	1	280	
9	2	255	
11	n. assign.	145 (?)	
12	n. assign.	265 (?)	
13	2	95	

n. doc. = not documented; n. assign. = not assigned

[32] However, the discovery of assemblages of living Calyptogena individuals substantiates that at the summit area of MV 2 (Figures 58c – 58d) fluids are present in amounts sufficient to nourish chemosynthesis-based macrofauna (e.g. Paull et al. 1995; Sahling et al. 2002). Furthermore, the presence of Calyptogena shells at the summits of MV 3 and 10 and accumulations of hydrates at MVs 2, 4, 5, and 10 signify that high methane concentrations must have existed in the recent past. In conclusion, compared to gas fluxes observed at MVs in other regions, where virulent gas emission from the seafloor was observed (e.g. Greinert et al. 2006; Sauter et al. 2006; Sahling et al. 2009) the Kumano basin MVs appear to be in comparably low-activity or even dormant phases at present.

[33] Comparison of dissolved methane concentration profiles from the summit areas and slopes of individual MVs (Figure 60) demonstrates that, similar to MVs in other regions, methane is principally provided through one or few conduits situated in the geographic center of the MV structure (Dimitrov, 2002; Kopf, 2002; Pape et al. 2011b). The depth of the SMI may spatially vary across the MV summit since for instance it is controlled by the number and capacity of fluid migration pathways, the thickness of mud deposited on top of the sediments during recent MV eruptions and the time elapsed since MV activities. Nevertheless, different depths of the SMI and shapes of methane concentration profiles along with the occurrence of shallow hydrates restricted to some MVs suggest that the structures investigated differ in their intensity of methane flux from below.

[34] In this study at least one gravity core was retrieved from the summit area of most of the investigated MVs (Appendix A.6 Table 15). Methane concentration profiles of these cores were

used for rough assignments of relative methane flux intensities (Table 16). The SMI was generally situated above ca. 3.5 m at most MVs studied except for MVs 6 and 7. This indicates that methane upward flux was still sufficient to hamper seawater-derived sulfate to penetrate deeper into the sediments at most MVs. The very shallow SMI (<1 mbsf) and highest concentrations of dissolved methane on the summits of MVs 2, 4, and 5 (Table 16) correspond to the findings of hydrate pieces at those MVs. In contrast, the fluid flux providing concentrations of dissolved methane <10 μmol L^{-1} at the summits of MVs 6 and 7 was too low to induce hydrate formation in the recent past.. Because of the virtual lack of bubble emissions it seems unlikely that a great portion of methane in the uppermost sediments was derived from gas migration through the GHSZ. Due to efficient AOM, methane concentrations in the immediate subsurface might be, at present, too low to sustain settlement by chemosynthesis-based organisms. Our classification of methane flux intensities in shallow sediments generally agrees with previous interpretations of MV activities at MVs 3, 4, 5, and 6 (Kuramoto et al. 2001; Morita et al. 2004; Tsunogai et al. 2012), but differs from observations at MV 8 where at its edge regions living Calyptogena colonies were observed in 2006 (Miyazaki et al. 2009) and steep thermal gradients were reported in 2011 (Hamamoto et al. 2011). Based on our results it appears that currently highest methane fluxes occur at MVs 2, 3, 4, 5, 10, and 13 located in the northern Kumano basin.

[35] The geological causes for varying methane fluxes at the individual MVs remains subject to future studies. Remarkably, subduction-related earthquakes are frequent in the region investigated (Ito and Obara 2006; Shelly et al. 2006; Moore et al. 2007; Obana and Kodaira 2009) and a coincidence of seismic events and hydrocarbon seepage activity has already been proposed for other regions, such as MVs in Azerbeijan (Mellors et al. 2007) and Indonesia (Mazzini et al. 2007), cold seeps off Pakistan (Fischer et al. 2013) and also for MV 5 in our study area (Tsunogai et al. 2012). Therefore, it is tempting to assume that seismic activity below the old accreted sediments affects or even triggers the MV activity in the Kumano basin. Long-term borehole observatories partly installed with the seafloor drill rig MeBo (Freudenthal and Wefer 2013; Kopf et al. 2013) at MVs 3 and 4 during cruise SO-222 will give information about the relationship between seismic activity at the seismogenic zone and MV activity in the overlying older accretionary prism.

CONCLUSION

[36] Twelve mud volcanoes (MVs) in the Kumano forearc basin close to the Nankai subduction zone off Japan were investigated with regard to origins and flux intensities of hydrocarbons expelled in 2012. These MVs are well located within the gas hydrate stability zone and disseminated hydrates were recovered from MVs 2, 4, 5, and 10.

[37] For hydrates from MVs 2, 4, and 10, significant amounts of C_{2+} hydrocarbons (C_1/C_2 ratios as low as 35) along with enrichments in $^{13}C_{CH4}$ ($\delta^{13}C_{CH4}$ ratios between –39.9‰ and –37.6‰ V-PDB) substantiate that upward migrating hydrocarbons are predominantly of thermogenic origin. Considering geothermal gradients established at the adjacent IODP Sites C0009 and C0002, thickness of basin sediments, and minimum depth of the plate boundary, those hydrocarbons are most probably generated in old accreted sediments between about 2,300 and 4,300 mbsf. Much higher C_1/C_2 ratios (ca. 1,600) of hydrate-bound hydrocarbons recovered from MV 5 hint to additional ascent of comparably methane-rich hydrocarbons potentially formed in the basin sediments overlying the accretionary prism. These results may help to elucidate the provenance of hydrocarbons expelled from mud volcanoes at other subduction zones worldwide.

[38] For all MVs investigated, steepest gradients in methane concentrations and shallowest depths (<1 mbsf) of the sulfate-methane interface, indicating present methane ascent, were found at MVs 2, 4, 5, and 13. Larger accumulations of alive chemosynthetic organisms diagnostic for ongoing fluid flow from below were only found at MV 2, while randomly distributed clam shells were found at MVs 2, 3, 4, and 10. With respect to the virtual lack of free gas emissions at any of the MVs and the comparably small size of recovered hydrates it is proposed that these are remnants of more intense MV activity in the past and subject to dissolution at present. Except for MVs 2 and 5, we consequently regard current MV activities in the Kumano basin as moderate to low if compared to former times or to fluid discharge intensities of submarine MVs in other regions.

7.1 Hydrocarbon Seepage and its Sources at Mud Volcanoes of the Kumano Forearc Basin

References

Baba T, Yamada Y (2004) BSRs and Associated Reflections as an Indicator of Gas Hydrate and Free Gas Accumulation : An Example of Accretionary Prism and Forearc Basin System along the Nankai Trough , off Central Japan. Resour Geol 54:11–24..

Barber AJ, Tjokrosapoetro S, Charlton TR (1986) Mud Volcanoes , Shale Diapirs , Wrench Faults , and Melanges in Accretionary Complexes , Eastern Indonesia. Am Assoc Pet Geol Bull 70:1729–1741.

Bhatnagar G, Chatterjee S, Chapman WG, Dugan B, Dickens GR, Hirasaki GJ (2011) Analytical theory relating the depth of the sulfate-methane transition to gas hydrate distribution and saturation. Geochemistry, Geophys Geosystems 12:Q03003. doi: 10.1029/2010GC003397

Bohrmann G, Heeschen K, Jung C, Weinrebe W, Baranov B, Cailleau B, Heath R, Hühnerbach V, Hort M, Masson D, Trummer I (2002) Widespread fluid expulsion along the seafloor of the Costa Rica convergent margin. Terra Nov 14:69–79. doi: 10.1046/j.1365-3121.2002.00400.x

Bohrmann G, Ivanov M, Foucher J-P, Spiess V, Bialas J, Greinert J, Weinrebe W, Abegg F, Aloisi G, Artemov Y, Blinova V, Drews M, Heidersdorf F, Krabbenhöft A, Klaucke I, Krastel S, Leder T, Polikarpov I, Saburova M, Schmale O, Seifert R, Volkonskaya A, Zillmer M (2003) Mud volcanoes and gas hydrates in the Black Sea: new data from Dvurechenskii and Odessa mud volcanoes. Geo-Marine Lett 23:239–249. doi: 10.1007/s00367-003-0157-7

Borowski WS, Paull CK, Ussler W (1996) Marine pore-water sulfate profiles indicate in situ methane flux from underlying gas hydrate. Geol 24 :655–658. doi: 10.1130/0091-7613(1996)024<0655:MPWSPI>2.3.CO;2

Camerlenghi A, Cita MB, Vedova BD, Fusi N, Mirabile L, Pellis G (1995) Geophysical evidence of mud diapirism on the Mediterranean Ridge accretionary complex. Mar Geophys Res 17:115–141. doi: 10.1007/BF01203423

Castellini D, Dickens G, Snyder G, Ruppel C (2006) Barium cycling in shallow sediment above active mud volcanoes in the Gulf of Mexico. Chem Geol 226:1–30. doi: 10.1016/j.chemgeo.2005.08.008

Claypool GE, Kvenvolden KA (1983) Methane and other Hydrocarbon Gases in Marine Sediment. Annu Rev Earth Planet Sci 11:299–327. doi: 10.1146/annurev.ea.11.050183.001503

Coffin R, Hamdan L, Plummer R, Smith J, Gardner J, Hagen R, Wood W (2008) Analysis of methane and sulfate flux in methane-charged sediments from the Mississippi Canyon, Gulf of Mexico. Mar Pet Geol 25:977–987. doi: 10.1016/j.marpetgeo.2008.01.014

Dickens GR (2003) Rethinking the global carbon cycle with a large, dynamic and microbially mediated gas hydrate capacitor. Earth Planet Sci Lett 213:169–183. doi: 10.1016/S0012-821X(03)00325-X

Dimitrov LI (2002) Mud volcanoes—the most important pathway for degassing deeply buried sediments. Earth-Science Rev 59:49–76. doi: http://dx.doi.org/10.1016/S0012-8252(02)00069-7

Duan Z, Mao S (2006) A thermodynamic model for calculating methane solubility, density and gas phase composition of methane-bearing aqueous fluids from 273 to 523K and from 1 to 2000bar. Geochim Cosmochim Acta 70:3369–3386. doi: 10.1016/j.gca.2006.03.018

Egorov A V, Crane K, Vogt PR, Rozhkov AN, Shirshov PP (1999) Gas hydrates that outcrop on the sea floor: stability models. Geo-Marine Lett 19:68–75. doi: 10.1007/s003670050094

Feseker T, Pape T, Wallmann K, Klapp SA, Schmidt-Schierhorn F, Bohrmann G (2009) The thermal structure of the Dvurechenskii mud volcano and its implications for gas hydrate stability and eruption dynamics. Mar Pet Geol 26:1812–1823. doi: 10.1016/j.marpetgeo.2009.01.021

Fischer D, Mogollon JM, Strasser M, Pape T, Bohrmann G, Fekete N, Spiess V, Kasten S (2013) Subduction zone earthquake as potential trigger of submarine hydrocarbon seepage. Nat Geosci 6:647–651.

Fofonoff NP, Millard RC (1983), Algorithms for computation of fundamental properties of seawater. UNESCO Technical Papers in Marine Sciences, 44.

Freudenthal T, Wefer G (2013) Drilling cores on the sea floor with the remote-controlled sea floor drilling rig MeBo. Geosci Instrum Method Data Syst 2:329–337. doi: 10.5194/gi-2-329-2013

Greinert J, Artemov Y, Egorov V, Debatist M, McGinnis D (2006) 1300-m-high rising bubbles from mud volcanoes at 2080m in the Black Sea: Hydroacoustic characteristics and temporal variability. Earth Planet Sci Lett 244:1–15. doi: 10.1016/j.epsl.2006.02.011

Gulick Bangs, N. L. B., Moore, G. F., Ashi, J., Martin, K. M., Sawyer, D. S., Tobin, H. J., Kuramoto, S. SPS, Taira A (2010) Rapid forearc basin uplift and megasplay fault development from 3D seismic images of Nankai Margin off Kii Peninsula, Japan. Earth Planet Sci Lett 300:55–62.

Hachikubo A, Kosaka T, Kida M, Krylov A, Sakagami H, Minami H, Takahashi N, Shoji H (2007) Isotopic fractionation of methane and ethane hydrates between gas and hydrate phases. Geophys Res Lett 34:L21502. doi: 10.1029/2007GL030557

Hamamoto H, Yamano M, Goto S, Kinoshita M, Fujino K, Wang K (2011) Heat flow distribution and thermal structure of the Nankai subduction zone off the Kii Peninsula. Geochemistry, Geophys Geosystems 12:Q0AD20. doi: 10.1029/2011GC003623

Harris RN, Schmidt-Schierhorn F, Spinelli G (2011) Heat flow along the NanTroSEIZE transect: Results from IODP Expeditions 315 and 316 offshore the Kii Peninsula, Japan. Geochemistry, Geophys Geosystems 12:Q0AD16. doi: 10.1029/2011GC003593

Hayman NW, Byrne TB, McNeill LC, Kanagawa K, Kanamatsu T, Browne CM, Schleicher AM, Huftile GJ (2012) Structural evolution of an inner accretionary wedge and forearc basin initiation, Nankai margin, Japan. Earth Planet Sci Lett 353–354:163–172.

Henry PT, Kanamatsu K, Kyaw Thu M, the Expedition 333 Scientists (2012) NanTroSEIZE Stage 2: Subduction Inputs 2 and Heat Flow. Proc IODP 333.

Hensen C, Nuzzo M, Hornibrook E, Pinheiro LM, Bock B, Magalhães VH, Brückmann W (2007) Sources of mud volcano fluids in the Gulf of Cadiz—indications for hydrothermal imprint. Geochim Cosmochim Acta 71:1232–1248. doi: 10.1016/j.gca.2006.11.022

Hill I, Taira AA, Firth JV, et al. (1993) Proc ODP 131, Sci Res 131. College Station, TX (Ocean Drilling Program). doi:10.2973/odp.proc.sr.131.1993

Hoehler TM, Alperin MJ, Albert DB, Martens CS (1994) Field and laboratory studies of methane oxidation in an anoxic marine sediment: Evidence for a methanogen-sulfate reducer consortium. Global Biogeochem Cycles 8:451–463. doi: 10.1029/94GB01800

Ito Y, Obara K (2006) Dynamic deformation of the accretionary prism excites very low frequency earthquakes. Geophys Res Lett 33:L02311. doi: 10.1029/2005gl025270

James AT, Burns BJ (1984) Microbial alteration of subsurface natural gas accumulations. Am Assoc Pet Geol Bull 68: 957-960.

Kinoshita, M. H. Tobin, J. Ashi, G. Kimura, S. Lallemant, E. J. Screaton, D. Curewitz, H. Masago, K. T. Moe, and the Expedition 314/315/316 Scientists (2009), NanTroSEIZE Stage 1: investigations of seismogenesis, Nankai Trough, Japan, Proc. IODP 314/315/316.

Kinoshita M, Moore GF, Kido YN (2011) Heat flow estimated from BSR and IODP borehole data: Implication of recent uplift and erosion of the imbricate thrust zone in the Nankai Trough off Kumano. Geochem Geophys Geosyst 12: Q0AD18, doi:10.1029/2011gc003609.

Kopf A, Araki E, Toczko S, Expedition 332 Scientists (2011) Proc IODP 332. doi:10.2204/iodp.proc.332.2011

Kopf A, et al. (2013) Report and preliminary results of RV Sonne cruise SO-222: MEMO - MeBo drilling and in situ long-term monitoring in the Nankai Trough accretionary complex, Japan. Berichte, MARUM – Zentrum für Marine Umweltwissenschaften, Fachbereich Geowissenschaften, Universität Bremen, 297: 121pp

Kopf A (1999) Fate of sediment during plate convergence at the Mediterranean Ridge accretionary complex: Volume balance of mud extrusion versus subduction and/or accretion. Geol 27 :87–90. doi: 10.1130/0091-7613(1999)027<0087:FOSDPC>2.3.CO;2

Kopf AJ (2002) Significance of mud volcanism. Rev Geophys 40:1005. doi: 10.1029/2000rg000093

Kuramoto S, Ashi J, Greinert J, Gulick S, Ishimura T, Morita S, Nakamura K, Okada M, Okamoto T, Rickert D, Saito S, Suess E, Tsunogai U, Tomosui T (2001) Surface Observations of Subduction Related Mud Volcanoes and Large Thrust Sheets in the Nankai Subduction Margin; Report on YK00-10 and YK01-04 Cruises. JAMSTEC J Deep Sea Res. 19: 131 - 139

Kvenvolden KA, McDonald TJ (1986) Organic Geochemistry on the Joides Resolution: An Assay. 147 pp.

Lapham LL, Chanton JP, Chapman R, Martens CS (2010) Methane under-saturated fluids in deep-sea sediments: Implications for gas hydrate stability and rates of dissolution. Earth Planet Sci Lett 298:275–285. doi: 10.1016/j.epsl.2010.07.016

Marcaillou B, Henry P, Kinoshita M, Kanamatsu T, Screaton E, Daigle H, Harcouët-Menou V, Lee Y, Matsubayashi O, Kyaw Thu M, Kodaira S, Yamano M, the Expedition 333 Scientific Party (2012) Seismogenic zone temperatures and heat-flow anomalies in the To-nankai margin segment based on temperature data from IODP expedition 333 and thermal model. Earth Planet Sci Lett 349-350:171–185. doi: 10.1016/j.epsl.2012.06.048

Masoudi R, Tohidi B (2005) Estimating the hydrate stability zone in the presence of salts and/or organic inhibitors using water partial pressure. J Pet Sci Eng 46:23–36. doi: 10.1016/j.petrol.2004.10.002

Mastalerz V, de Lange GJ, Dählmann A, Feseker T (2007) Active venting at the Isis mud volcano, offshore Egypt: Origin and migration of hydrocarbons. Chem Geol 246:87–106. doi: 10.1016/j.chemgeo.2007.09.005

Mazzini A, Svensen H, Akhmanov GG, Aloisi G, Planke S, Malthe-Sørenssen A, Istadi B (2007) Triggering and dynamic evolution of the LUSI mud volcano, Indonesia. Earth Planet Sci Lett 261:375–388. doi: 10.1016/j.epsl.2007.07.001

McNeil LC, Saffer D, Byrne T, Araki E, Toczko S, Eguchi N, Takahashi K (2010) Expedition 319 Scientists. 2010. IODP Expedition 319, NanTroSEIZE Stage 2: First IODP riser drilling operations and observatory installation towards understanding Subduction Zone seismogenesis. Sci Drill 10:4–13.

Mellors R, Kilb D, Aliyev A, Gasanov A, Yetirmishli G (2007) Correlations between earthquakes and large mud volcano eruptions. J Geophys Res 112:B04304. doi: 10.1029/2006jb004489

Mikada H, Moore GF, Taira A, Becker K, Moore JC, Klaus A (2005) Proc ODP 190/196, Sci Res: College Station, TX (Ocean Drilling Program). doi:10.2973/odp.proc.sr.190196.2005.

Milkov A V (2000) Worldwide distribution of submarine mud volcanoes and associated gas hydrates. Mar Geol 167:29–42.

Miyazaki J, Higa R, Toki T, Ashi J, Tsunogai U, Nunoura T, Imachi H, Takai K (2009) Molecular Characterization of Potential Nitrogen Fixation by Anaerobic Methane-Oxidizing Archaea in the Methane Seep Sediments at the Number 8 Kumano Knoll in the Kumano Basin, Offshore of Japan. Appl Environ Microbiol 75:7153–7162. doi: 10.1128/aem.01184-09

Moore GF, Kanagawa K, Strasser M, Dugan B, Maeda L, Toczko S, the Expedition 338 Scientists (2013) NanTroSEIZE Stage 3: NanTroSEIZE plate boundary deep riser 2. Proc IODP 338, Prel Rep. doi: doi:10.2204/iodp.pr.338.2013

Moore GF, Taira A, Klaus A, Becker L, Boeckel B, Cragg BA, Dean A, Fergusson CL, Henry P, Hirano S, Hisamitsu T, Hunze S, Kastner M, Maltman AJ, Morgan JK, Murakami Y, Saffer DM, Sánchez-Gómez M, Screaton EJ, Smith DC, Spivack AJ, Steurer J, Tobin HJ, Ujiie K, Underwood MB, Wilson M (2001) New insights into deformation and fluid flow processes in the Nankai Trough accretionary prism: Results of Ocean Drilling Program Leg 190. Geochemistry, Geophys Geosystems 2:1058. doi: 10.1029/2001GC000166

Moore GF, Bangs NL, Taira A, Kuramoto S, Pangborn E, Tobin HJ (2007) Three-Dimensional Splay Fault Geometry and Implications for Tsunami Generation. Science 318:1128–1131. doi: 10.1126/science.1147195

Moore JC, Vrolijk P (1992) Fluids in accretionary prisms. Rev Geophys 30:113–135. doi: 10.1029/92rg00201

Moore JC, Saffer D (2001) Updip limit of the seismogenic zone beneath the accretionary prism of southwest Japan: An effect of diagenetic to low-grade metamorphic processes and increasing effective stress. Geology 29:183–186. doi: 10.1130/0091-7613(2001)029<0183:ulotsz>2.0.co;2

Morita S, Ashi J, Aoike K, Kuramoto S (2004) Evolution of Kumano Basin and Sources of Clastic Ejecta and Pore Fluid in Kumano Mud Volcanoes, Eastern Nankai Trough. Int. Symp. Methane Hydrates Fluid Flow Up. Accretionary Prism.

Nikolovska A, Sahling H, Bohrmann G (2008) Hydroacoustic methodology for detection, localization, and quantification of gas bubbles rising from the seafloor at gas seeps from the eastern Black Sea. Geochemistry, Geophys Geosystems 9:Q10010. doi: 10.1029/2008GC002118

Obana K, Kodaira S (2009) Low-frequency tremors associated with reverse faults in a shallow accretionary prism. Earth Planet Sci Lett 287:168–174.

Orphan VJ, Taylor LT, Hafenbradl D, Delong EF (2000) Culture-Dependent and Culture-Independent Characterization of Microbial Assemblages Associated with High-Temperature Petroleum Reservoirs. Appl Environ Microbiol 66:700–711. doi: 10.1128/AEM.66.2.700-711.2000

Pape T, Bahr A, Rethemeyer J, Kessler JD, Sahling H, Hinrichs K-U, Klapp SA, Reeburgh WS, Bohrmann G (2010a) Molecular and isotopic partitioning of low-molecular-weight hydrocarbons during migration and gas hydrate

precipitation in deposits of a high-flux seepage site. Chem Geol 269:350–363. doi: 10.1016/j.chemgeo.2009.10.009

Pape T, Kasten S, Zabel M, Bahr A, Abegg F, Hohnberg H-J, Bohrmann G (2010b) Gas hydrates in shallow deposits of the Amsterdam mud volcano, Anaximander Mountains, Northeastern Mediterranean Sea. Geo-Marine Lett 30:187–206. doi: 10.1007/s00367-010-0197-8

Pape T, Bahr A, Klapp SA, Abegg F, Bohrmann G (2011a) High-intensity gas seepage causes rafting of shallow gas hydrates in the southeastern Black Sea. Earth Planet Sci Lett 307:35–46. doi: 10.1016/j.epsl.2011.04.030

Pape T, Feseker T, Kasten S, Fischer D, Bohrmann G (2011b) Distribution and abundance of gas hydrates in near-surface deposits of the Håkon Mosby Mud Volcano, SW Barents Sea. Geochemistry, Geophys Geosystems 12:Q09009. doi: 10.1029/2011GC003575

Park J-O, Tsuru T, Kodaira S, Cummins PR, Kaneda Y (2002) Splay Fault Branching Along the Nankai Subduction Zone. Science 297:1157–1160. doi: 10.1126/science.1074111

Paull CK, Ussler W, Borowski WS, Spiess FN (1995) Methane-rich plumes on the Carolina continental rise: Associations with gas hydrates. Geol 23 :89–92. doi: 10.1130/0091-7613(1995)023<0089:MRPOTC>2.3.CO;2

Römer M, Sahling H, Pape T, Bahr A, Feseker T, Wintersteller P, Bohrmann G (2012) Geological control and magnitude of methane ebullition from a high-flux seep area in the Black Sea—the Kerch seep area. Mar Geol 319-322:57–74. doi: 10.1016/j.margeo.2012.07.005

Saffer D, McNeill L, Byrne T, Araki E, Toczko S, Eguchi N, Takahashi K, the Expedition 319 Scientists (2010) NanTroSEIZE Stage 2: NanTroSEIZE Riser/Riserless Observatory. Proc IODP 319:83 pp.

Sahling H, Rickert D, Lee RW, Linke P, Suess E (2002) Macrofaunal community structure and sulfide flux at gas hydrate deposits from the Cascadia convergent margin, NE Pacific. Mar Ecol Prog Ser 231:121 – 138.

Sahling H, Bohrmann G, Artemov YG, Bahr A, Brüning M, Klapp SA, Klaucke I, Kozlova E, Nikolovska A, Pape T, Reitz A, Wallmann K (2009) Vodyanitskii mud volcano, Sorokin trough, Black Sea: Geological characterization and quantification of gas bubble streams. Mar Pet Geol 26:1799–1811. doi: 10.1016/j.marpetgeo.2009.01.010

Saito S, Underwood MB, Kubo Y, the Expedition 322 Scientists (2009) NanTroSEIZE Stage 2: Subduction Inputs. Proc IODP 322: Tokyo (Integrated Ocean Drilling Program Management International, Inc.). doi:10.2204/iodp.proc.322.2010

Sassen R, Joye S, Sweet ST, DeFreitas DA, Milkov A V, MacDonald IR (1999) Thermogenic gas hydrates and hydrocarbon gases in complex chemosynthetic communities, Gulf of Mexico continental slope. Org Geochem 30:485–497. doi: 10.1016/S0146-6380(99)00050-9

Sassen R, Sweet ST, DeFreitas DA, Milkov A V (2000) Exclusion of 2-methylbutane (isopentane) during crystallization of structure II gas hydrate in sea-floor sediment, Gulf of Mexico. Org Geochem 31:1257–1262. doi: 10.1016/S0146-6380(00)00144-3

Sauter EJ, Muyakshin SI, Charlou J-L, Schlüter M, Boetius A, Jerosch K, Damm E, Foucher J-P, Klages M (2006) Methane discharge from a deep-sea submarine mud volcano into the upper water column by gas hydrate-coated methane bubbles. Earth Planet Sci Lett 243:354–365. doi: 10.1016/j.epsl.2006.01.041

Schlüter HU, Prexl A, Gaedicke C, Roeser H, Reichert C, Meyer H, von Daniels C (2002) The Makran accretionary wedge: sediment thicknesses and ages and the origin of mud volcanoes. Mar Geol 185:219–232. doi: 10.1016/S0025-3227(02)00192-5

Screaton E, Kimura G, Curewitz D, Moore G, Chester F, Fabbri O, Fergusson C, Girault F, Goldsby D, Harris R, Inagaki F, Jiang T, Kitamura Y, Knuth M, Li CF, Liljedahl LC, Louis L, Milliken K, Nicholson U, Riedinger N, Sakaguchi A, Solomon E, Strasser M, Su X, Tsutsumi A, Yamaguchi A, Ujiee K, Zhao X (2009) Interactions between deformation and fluids in the frontal thrust region of the NanTroSEIZE transect offshore the Kii Peninsula, Japan: Results from IODP Expedition 316 Sites C0006 and C0007. Geochem Geophys Geosyst 10:Q0AD01. doi: 10.1029/2009gc002713

Selley RC (1998) Elements of petroleum geology, 2nd ed. 470 pp. Academic Press.

Seewald JS (2003) Organic-inorganic interactions in petroleum-producing sedimentary basins. Nature 426:327–333.

Shelly DR, Beroza GC, Ide S, Nakamula S (2006) Low-frequency earthquakes in Shikoku, Japan, and their relationship to episodic tremor and slip. Nature 442:188–191.

Sloan ED, Koh CA (2007) Clathrate hydrates of natural gases, 3rd ed. 752 pp. CRC Press, Boca Raton.

Strasser M, Moore GF, Kimura G, Kitamura Y, Kopf AJ, Lallemant S, Park J-O, Screaton EJ, Su X, Underwood MB, Zhao X (2009) Origin and evolution of a splay fault in the Nankai accretionary wedge. Nat Geosci 2:648–652. doi: 10.1038/ngeo609

Suess E, Torres ME, Bohrmann G, Collier RW, Greinert J, Linke P, Rehder G, Trehu A, Wallmann K, Winckler G, Zuleger E (1999) Gas hydrate destabilization: enhanced dewatering, benthic material turnover and large methane plumes at the Cascadia convergent margin. Earth Planet Sci Lett 170:1–15. doi: 10.1016/S0012-821X(99)00092-8

Taira A, Hill I, Firth J, Berner U, Brückmann W, Byrne T, Chabernaud T, Fisher A, Foucher J-P, Gamo T, Gieskes J, Hyndman R, Karig D, Kastner M, Kato Y, Lallemant S, Lu R, Maltman A, Moore G, Moran K, Olaffson G, Owens W, Pickering K, Siena F, Taylor E, Underwood M, Wilkinson C, Yamano M, Zhang J (1992) Sediment deformation and hydrogeology of the Nankai Trough accretionary prism: Synthesis of shipboard results of ODP Leg 131. Earth Planet Sci Lett 109:431–450. doi: 10.1016/0012-821X(92)90104-4

Tobin HJ, Kinoshita M (2006) NanTroSEIZE: The IODP Nankai Trough Seismogenic Zone Experiment. Sci Drill 2:23–27. doi: 10.2204/iodp.sd.2.06.2006

Tobin HJ, Saffer DM (2009) Elevated fluid pressure and extreme mechanical weakness of a plate boundary thrust, Nankai Trough subduction zone. Geology 37:679–682. doi: 10.1130/g25752a.1

Toki T, Tsunogai U, Gamo T, Kuramoto S, Ashi J (2004) Detection of low-chloride fluids beneath a cold seep field on the Nankai accretionary wedge off Kumano, south of Japan. Earth Planet Sci Lett 228:37–47.

Torres ME, Wallmann K, Tréhu AM, Bohrmann G, Borowski WS, Tomaru H (2004) Gas hydrate growth, methane transport, and chloride enrichment at the southern summit of Hydrate Ridge, Cascadia margin off Oregon. Earth Planet Sci Lett 226:225–241. doi: 10.1016/j.epsl.2004.07.029

Tsunogai U, Maegawa K, Sato S, Komatsu DD, Nakagawa F, Toki T, Ashi J (2012) Coseimic massive methane release from a submarine mud volcano. Earth Planet Sci Lett 341-344:79–85. doi: 10.1016/j.epsl.2012.06.004

Wallmann K, Drews M, Aloisi G, Bohrmann G (2006) Methane discharge into the Black Sea and the global ocean via fluid flow through submarine mud volcanoes. Earth Planet Sci Lett 248:545–560. doi: 10.1016/j.epsl.2006.06.026

Westbrook GK, Smith MJ (1983) Long decollements and mud volcanoes: Evidence from the Barbados Ridge Complex for the role of high pore-fluid pressure in the development of an accretionary complex. Geology 11:279–283. doi: 10.1130/0091-7613(1983)11<279:LDAMVE>2.0.CO;2

Whiticar MJ (1990) A geochemial perspective of natural gas and atmospheric methane. Org Geochem 16:531–547. doi: 10.1016/0146-6380(90)90068-B

CHAPTER 7.2 – MANUSCRIPT VIII

TEMPORAL AND SPATIAL VARIABILITY OF MUD VOLCANISM IN THE KUMANO FOREARC BASIN, SE JAPAN

Sebastian B. Hammerschmidt[1]*, Achim Kopf[1]

In preparation for submission to

Earth, Planets, Space

*corresponding author: shammerschmitd@marum.de

[1] MARUM, University of Bremen, Bremen, Germany

Abstract Mud volcanoes are one of the most prominent fluid escape structures worldwide. Mostly encountered at convergent margins, mud volcanism is commonly associated with seismogenesis. At the Nankai Trough subduction zone, offshore the eastern coast of SW Japan, earthquakes occur frequently and likely influence mud volcanism in the Kumano forearc basin. During MARUM expedition SO-222 with research vessel SONNE, thirteen of these mud volcanoes were mapped and cored to investigate temporal and spatial changes in mud volcanism. Most of the mud volcanoes were covered by hemipelagic background sediment with intercalations of ash layers and turbidites, indicating a currently dormant state. Samples for radiocarbon dating were taken beneath the turbidites and ash layers, and at the transition between background sediment and mud breccia. Preliminary results indicate ages of 4427 – 30391 yr cal. BP. Five mud volcanoes in the centre of the basin are assumed to have been inactive for at least 22000 yr cal. BP. One mud volcano in the eastern part of the basin may have been in a dormant state for at least 28000 yr cal. BP. An ash layer detected in cores from individual mud volcanoes was dated to be ca. 20000 yr cal. BP. The ash layer further correlates with a sequence of abundant, wood-rich turbidites. Our preliminary results suggest a NW-SE increase in mud volcanism over time. Turbidites overlying the inactive mud volcanoes are probably derived from currents migrating along the Shingu Submarine Canyon. Whether the turbidites were triggered by floods, storms, earthquakes, or other natural effects remains unclear at this point. Future work will include the radiocarbon dating of additional 13 samples from cored material. Moreover, background sediment close to the ash layers at another three mud volcanoes will be sampled and dated to further constrain our previous age estimations. The additional data will improve our understanding of mud and fluid expulsion in the Kumano forearc basin, and its changes in space and time.

INTRODUCTION

[1] At the Nankai Trough subduction zone, SE offshore the Japanese Kii Peninsula, two M8+ ruptures have occurred in the last century: the 1944 Tonankai earthquake and the 1946 Nankaido earthquake (e.g. Ando 1975; Satake 1993; Ichinose et al. 2003). In natural formations, strain caused by seismic waves triggers dynamic and static changes in the pore fluid pressure (Davis et al. 2013; Elkhoury et al. 2006, 2011; Manga et al. 2012), which in turn can influence the seismo-tectonic behaviour of fault zones (e.g. Saffer and Tobin 2011).

[2] Changes in pore pressure in the subsurface can further lead to the activation of fluid escape structures, such as mud volcanoes (e.g. Kopf, 2002; Tsunogai et al. 2012; Lupi et al. 2013). MVs are a common feature at convergent margins, e.g. at the Makran accretionary wedge (Schlüter et al. 2002), the Mediterranean accretionary wedge (Kopf et al. 1998; Kopf and Behrmann 2000), the Costa Rica margin (e.g. Tryon et al. 2010) and the Nankai accretionary prism (Kuramoto et al. 2001; Morita et al. 2004; Tsunogai et al. 2012). MVs form as a consequence of fluid overpressure and density inversion in the subsurface, leading to focused expulsion of fluids, fluidized mud and clasts from the parent bed and overlying formations (Dimitrov 2002; Kopf 2002). At subduction zones, fluid overpressure and density inversion are facilitated by rapid subduction of unconsolidated sediment, lateral and vertical compaction, mineral dehydration, organic decomposition and low-grade metamorphic reactions (Seewald 2003; Saffer and Tobin 2011, and references therein).

[3] At the Nankai Trough subduction zone, a total of thirteen MVs in the Kumano forearc basin were investigated and mapped during MARUM (Centre for Marine Environmental Sciences) expedition SO-222 with research vessel *SONNE*. Post-cruise analyses on gases escaping from the

MVs indicate a reservoir between 2.3 and 4.3 km depth, i.e. in accreted material of the Tertiary to Cretaceous Shimanto belt underlying the Kumano basin (Pape et al. 2014). However, despite the vast variety of scientific studies conducted at the Nankai Trough, and particularly in the Kumano basin, little is known about episodic activity of the MVs. Coseismic expulsion of fluids and solids at MVs is observed worldwide (e.g., Manga and Brodsky 2006). For the Kumano forearc basin, Tsunogai et al. (2012) found two prominent methane plumes that were ejected by single MV as consequence of an M7.5 earthquake in 2004. Other MVs in the Kumano forearc basin are covered by hemipelagic background sediments, with intercalations of turbidites and ash layers (Kopf et al. 2013), and thus, seem to be dormant. Heezen and Ewing (1952) found that earthquakes are the main mechanism causing turbidite currents, but subsequent studies identified several other triggers, including storm wave and sediment loading, tsunamis, aseismic slip, hyperpycnal flow and gas hydrate dissociation (e.g. Adams 1990; Hampton et al. 1996; Goldfinger et al. 2003; Lee et al. 2007, and references therein).

[4] In the present study we evaluate the activity of the MVs based on sedimentological descriptions of shallow cores from the Kumano forearc basin and by radiocarbon dating of hemipelagic background sediments overlying mud breccia, and of background sediments, which underlie turbidites and ash layers. We identify an ash layer, which is traceable through the basin, and discuss possible processes leading to turbidite generation. Undisturbed deposition of turbidites and ash layers on top of MVs constrains minimum ages of MV activity and thus helps to elucidate the current state of fluid expulsion in the Kumano forearc basin.

GEOLOGICAL SETTING

[5] The Kumano forearc basin is located landward of the Nankai Trough subduction zone, SE offshore the Kii Peninsula, Japan. It opened during the late Miocene following subduction of the Philippine Sea Plate beneath the Eurasian Plate, which commenced around 15 Ma (Taira 2001). Currently, the plate convergence rate is 4 – 6.5 cm/yr with an azimuth of 300°- 315°N (Seno et al. 1993; Miyazaki and Heki 2001). Beneath the Kumano basin, the subducting plate boundary is between 10 and 20 km depth (Moore and Saffer 2001; Marcaillou et al. 2012). The up to ~2000 m thick Kumano basin fill is mainly composed of hemipelagic sediments with intercalations of sandy turbidites and ash layers (Expedition 315 Scientists 2009; Expedition 319 Scientists 2010; Kopf et al. 2013; Strasser et al. 2014). Sedimentation rate increased between 1.67 and 1.56 Ma during and episode of activity of a splay fault system in the accretionary prism (Strasser et al. 2009), and on average, is estimated to be $\geq$ 800 m Ma^{-1} (i.e. 0.8 m ka^{-1}; Tobin et al. 2009). The Kumano forearc basin overlies the landward succession of the former prism toe, which includes

Miocene to Cretaceous rocks from the subducted Shikoku basin sediments and Shimanto Belt, respectively (Taira et al. 1992; Expedition 348 Scientists and Scientific Participants 2014).

[6] During MARUM Expedition SO-222 with R/V SONNE, 13 MVs were mapped and investigated (Kopf et al. 2013; Pape et al. 2014; Figure 65). The MVs have basal diameters of up to 2 km, and can be easily identified based on their conically-shaped domes which can reach heights > 100 m (Kuramoto et al. 2001; Kopf 2002; Morita et al. 2004). The ejecta of the MVs include low viscosity mud and clasts, which are derived from upper and lower Miocene to late Pliocene parent beds (Sawada et al. 2002; Morita et al. 2004). Morita et al. (2004) carried out seismic reflection studies in the Kumano basin, and found that the MVs overlie anticlines, which can promote fluid accumulation and lateral migration (e.g. Gluyas and Swarbrick 2009; Figure 65).
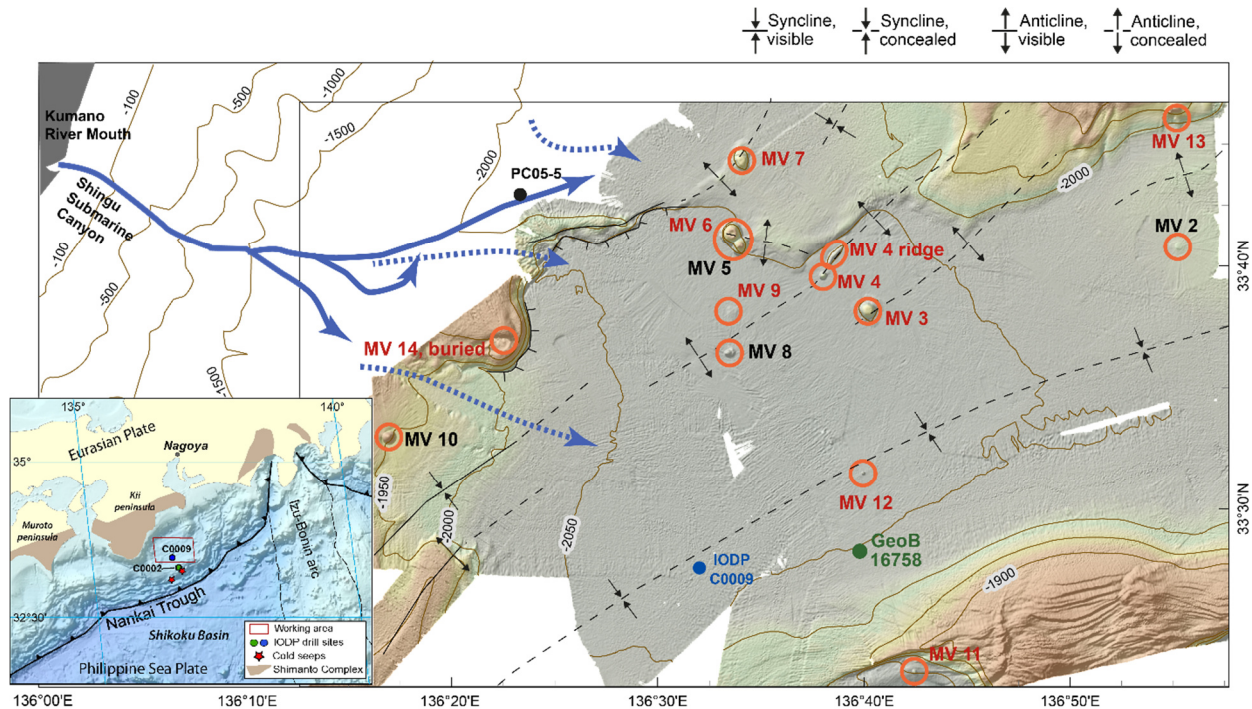
Figure 65: *Bathymetric and relief map of the Kumano forearc basin (modified from Pape et al. 2014). The map shows 13 mud volcanoes (MV), of which MV 2 and MV 3 exhibit recent activity. Anti- and synclines are taken from Morita et al. (2004). Separately shown is the background core GeoB16758. The map was extended with bathymetric information and estimated directions of turbidite currents following Shirai et al. (2010) (solid blue arrows) and Arita and Kinoshita (1988) (broken blue arrows). The inlay gives a regional tectonic overview, including IODP Sites C0002 and C0009. PC05-5 denotes the location of a piston core taken by Shirai et al. (2010). Red-labelled MVs were sampled for radiocarbon dating.*

[7] Nakamura et al. (2005, 2007) presented 3D seismic reflection data from MVs 3, 5, and 6, and based on discontinuous bottom simulating reflectors, concluded that MV 5 was active, while MVs 3 and 6 were in a dormant state. These conclusions support the findings of Sawada et al. (2002), who dated the dormant state of MV 6 to 22000 yr BP. During Exp. SO-222, based on heat flow measurements, Kopf et al. (2013) found only two recently active mud volcanos (i.e. MVs 2, 3). In a subsequent study, at MVs 2, 3 and 10, Pape et al. (2014) identified thermogenic gases, which

probably originated from 2.3 – 4.3 km depths, but they concluded that these gases were derived from dissociation of gas hydrates that formed earlier during times of higher fluid flow activity, rather than recent fluid flow from depth. Preceding studies have highlighted episodic activity of mud volcanoes in the Kumano basin, which was related to seismic activity, e.g. the M7.5 earthquake in 2004 (Tsunogai et al. 2012).

MATERIAL AND METHODS

Visual Core Description

[8] 13 gravity cores from mud volcanoes 3, 4, 6, 7, 9, 11, 12 and 13 are presented in this study (Table 17). A detailed description of the cores is given in Kopf et al. (2013) and will be briefly reviewed here. The main lithologies detected in the gravity cores were: (1) dark grey – olive grey mud breccia with mm – cm sized, semi-lithified mud-, silt- and sandstone clasts, and (2) dark green hemipelagic background sediment, including shell fragments and various calcareous and siliciclastic nanno- and microfossils, such as foraminifera and diatoms (see Appendix A.7, Figure S.22). The background sediment had intercalations of darker layers with varying grain size, which exhibited upwared-fining indicative of turbidites (Kopf et al. 2013). In core GeoB16758 turbidites were characterized by high wood content. Ash layers and clasts in background sediment were sparse. Cores taken at MV 3 and 4 were dominated by mud breccia in the caldera. By contrast, on the flanks, mud breccia alternates with background sediments. At the northern flank of MV 4 (core GeoB16728) unusual lithologies were detected. Between 700 and 1600 cmbsf (centimetre below seafloor) black clay and sands, partly enriched with mica and disturbed by mass wasting deposits, were present. MVs 6, 7, 9, 13 and 14 are covered by background sediments, including intercalations of turbidites and ash layers (see Appendix A.7, Figure S.22). GeoB16721, taken at the crest of MV 9, shows an exceptional amount of layers signalling discrete events, with 29 turbidites and 1 ash layer. At MV 12, mud breccia was found at the crest, while at the flanks, mud breccia was covered with background sediments.

Radiocarbon Dating

[9] In total, 54 samples taken from gravity cores were subject to age determination, which was based on planktonic foraminifera present in the samples. All radiocarbon analyses were carried out at the "Conventional Radiocarbon dating service laboratory" of the Institute of Hygiene and Medical Ecology in Kiev. Radiocarbon (^{14}C) dating (Libby and Johnson 1955) is based on the concept that ^{14}C in living tissue is always in equilibrium with atmospheric concentrations, while in dead organisms, ^{14}C decays with a half-life time of 5730 ± 40 years (Godwin 1962; Taylor 1997).

Table 17: *Overview of results for radiocarbon measurements and spatial information of individual stations. BG = background. MV = mud volcano. TBD = to be determined. mbsl = meter below sea level. cmbsf = cm below seafloor. ** low amount of datable ^{14}C*

Latitude	Longitude	Depth [mbsl]	Station [GeoB]	Core Depth [cmbsf]	ID	Age [yr cal. BP]	+/-	MV	Taken Below
33°28.113' N	136°39.978' E	2040	16758	236	30	20502	448	BG	turbidite
33°28.113' N	136°39.978' E	2040	16758	296	32	20932	454	BG	turbidite
33°28.113' N	136°39.978' E	2040	16758	309	31	19412	523	BG	turbidite
33°38.200' N	136°40.480' E	2025	16732	1237	53	TBD	TBD	3, NE flank	base of mud breccia, transition to background
33°38.200' N	136°40.480' E	2025	16732	2528	54	TBD	TBD	3, NE flank	base of mud breccia, transition to background
33°39.503' N	136°38.017' E	2061	16723	148	1	20567	513	4, NE flank	background, clast-rich interval
33°40.212' N	136°38.584' E	2007	16727	158	43	TBD	TBD	4 ridge	ash layer
33°39.560' N	136°38.040' E	2062	16728	191	44	TBD	TBD	4, N flank	background
33°39.560' N	136°38.040' E	2062	16728	317	45	TBD**	TBD	4, N flank	background
33°39.560' N	136°38.040' E	2062	16728	529	46	22242	413	4, N flank	background, above fault
33°39.560' N	136°38.040' E	2062	16728	1009	47	TBD	TBD	4, N flank	background
33°39.560' N	136°38.040' E	2062	16728	1049	48	TBD	TBD	4, N flank	turbidite
33°39.560' N	136°38.040' E	2062	16728	1070	49	TBD	TBD	4, N flank	turbidite
33°39.560' N	136°38.040' E	2062	16728	1105	50	TBD	TBD	4, N flank	turbidite
33°39.560' N	136°38.040' E	2062	16728	1221	51	TBD	TBD	4, N flank	brecciated material
33°39.560' N	136°38.040' E	2062	16728	1522	52	TBD	TBD	4, N flank	massive sand layer, rich in mica
33°41.093' N	136°33.571' E	1920	16750	67	55	4427	172	6	background
33°41.093' N	136°33.571' E	1920	16750	153	56	7968	155	6	background
33°41.093' N	136°33.571' E	1920	16750	221	57	13276	261	6	background
33°44.127' N	136°34.046' E	1950	16751	114	58	19794	311	7	ash layer
33°44.127' N	136°34.046' E	1950	16751	130	59	22953	402	7	turbidite
33°44.127' N	136°34.046' E	1950	16751	185	18	21665	1172	7	turbitide
33°36.194' N	136°33.453' E	2020	16720	170	40	TBD	TBD	8	background
33°37.426' N	136°33.519' E	2050	16721	131	41	11304	324	9	background
33°37.426' N	136°33.519' E	2050	16721	171	42	13267	210	9	background
33°37.426' N	136°33.519' E	2050	16721	183	5	14855	676	9	turbidite
33°37.426' N	136°33.519' E	2050	16721	210	28	14897	620	9	turbidite
33°37.426' N	136°33.519' E	2050	16721	260	3	16286	740	9	turbidite
33°37.426' N	136°33.519' E	2050	16721	291	12	18225	393	9	turbidite
33°37.426' N	136°33.519' E	2050	16721	312	4	17099	659	9	turbidite
33°37.426' N	136°33.519' E	2050	16721	337	23	19407	977	9	turbidite
33°37.426' N	136°33.519' E	2050	16721	357	13	18923	463	9	turbidite
33°37.426' N	136°33.519' E	2050	16721	415	19	17769	1176	9	turbidite
33°37.426' N	136°33.519' E	2050	16721	432	22	20081	561	9	ash layer
33°37.426' N	136°33.519' E	2050	16721	452	2	19706	480	9	turbidite
33°37.426' N	136°33.519' E	2050	16721	467	10	21768	420	9	turbidite
33°37.426' N	136°33.519' E	2050	16721	482	21	21422	610	9	turbidite
33°37.426' N	136°33.519' E	2050	16721	497	11	21315	670	9	turbidite
33°37.426' N	136°33.519' E	2050	16721	508	27	24258	564	9	turbidite
33°37.426' N	136°33.519' E	2050	16721	523	7	22382	604	9	turbidite

Latitude	Longitude	Depth [mbsl]	Station [GeoB]	Core Depth [cmbsf]	ID	Age [yr cal. BP]	+/-	MV	Taken Below
33°37.426' N	136°33.519' E	2050	16721	536	14	22625	533	9	turbidite
33°37.426' N	136°33.519' E	2050	16721	557	16	22250	543	9	turbidite
33°23.272' N	136°42.432' E	2010	16756	181	60	28051**	574	11	turbidite
33°23.272' N	136°42.432' E	2010	16756	281	61	18893**	286	11	turbidite
33°23.272' N	136°42.432' E	2010	16756	380	15	21323	730	11	background
33°31.326' N	136°39.885' E	2050	16759	140	62	6545	168	12	background
33°31.326' N	136°39.885' E	2050	16759	245	63	12560	252	12	background
33°31.326' N	136°39.885' E	2050	16759	340	64	15196	406	12	turbidite
33°31.326' N	136°39.885' E	2050	16759	538	24	18224	457	12	turbidite
33°46.105' N	136°54.865' E	1880	16781	124	65	TBD	TBD	13	base of background, transition to mud breccia
33°46.105' N	136°54.865' E	1880	16781	128	34	22139	1176	13	base of background, transition to mud breccia
33°46.105' N	136°54.865' E	1880	16781	192	35	30391	480	13	mollusc shell
33°40.665' N	136°25.128' E	2000	16791	153	66	TBD	TBD	14, buried	turbidite
33°40.665' N	136°25.128' E	2000	16791	441	67	TBD	TBD	14, buried	background
33°40.665' N	136°25.128' E	2000	16791	450	26	28375	760	14, buried	background

The relative proportion of ^{14}C is compared with the stable isotopes ^{12}C and ^{13}C, assuming that: (1) atmospheric ^{14}C concentrations remained relatively constant over the ^{14}C time scale (i.e. up to 60000 BP), (2) ^{14}C mixing took place rapidly and completely in all carbon reservoirs in the world, (3) carbon isotope ratios the dead tissue were only affected by decay of ^{14}C, (4) the half-life of ^{14}C is constant, and finally (5) the technique and instruments used for determination of ^{14}C have the appropriate accuracy and precision (Taylor 1997).

[10] The Kiev laboratory used accelerator-based mass-spectrometric (AMS) techniques, which allow dating of small amounts (mg-scale) of organic carbon. Samples were prepared using an ethanol-benzene-mixture following Arslanov (1987), including purification of benzene (Buzinny et al. 1998). This is followed by liquid scintillation (LS) counting which was applied with a Perkin Elmer Quantulus LS spectrometer 1220. This ultra-low level counter uses PPO and POPOP as scintillators and 7 ml, 3 ml, and 0.8 ml aluminium Teflon and copper Teflon vials (Buzinny and Skripkin 1995; Buzinny et al. 1995, 1998). All vials were calibrated using quench-curve fitting, and fractionation effects were removed from the results (Buzinny et al. 1995 1998). The resulting ages are related to BP (before present, i.e. number of radiocarbon years before 1950). The values reported here were corrected for natural variations of ^{14}C over time, including changes in climate, spatial variations in the marine reservoir, as well as temporal variations of the magnetic field of the earth or the intensity of cosmic storms (e.g. de Vries 1958; Stuiver 1961; Stuiver and Suess 1966; Stuiver and Braziunas 1993a, b; Voelker et al. 1998, 2000). The raw ages were corrected

using the program OxCal v4.2 by Bronk Ramsey and colleagues (Bronk Ramsey 1995, 2009; Bronk Ramsey and Lee 2013), and the implemented Marine13 calibration curve (Reimer et al. 2013). Local marine reservoir corrections of ^{14}C for south-east Japan were obtained from the 14CHRONO group (Queen's University Belfast, UK; http://calib.qub.ac.uk/marine/) and are based on Shishikura et al. (2007). Subsequent results are reported in calibrated BP (cal. BP).
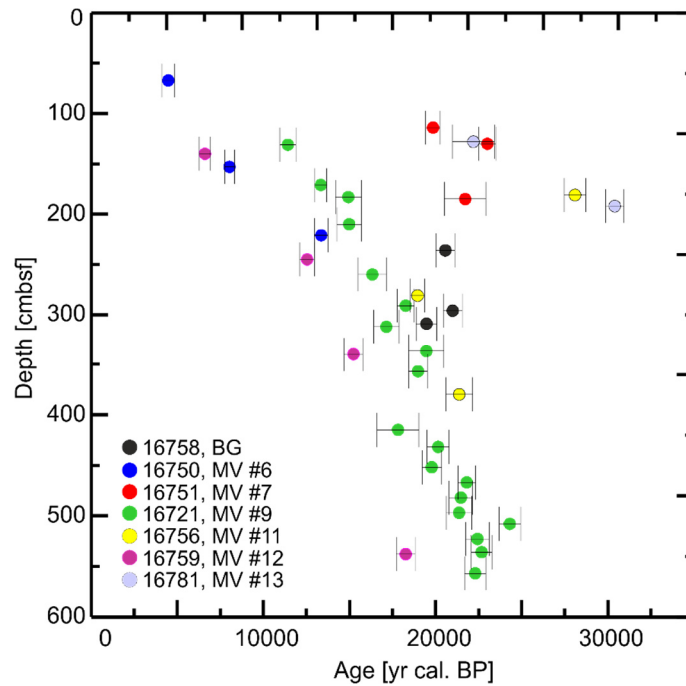
Figure 66: *Results of radiocarbon dating. No age reversal occurs before 17000 yr cal. BP. Sample from MVs 6 and 12 show no age reversals. The oldest sample from MV 13 was a mollusc shell found in a mud breccia, and therefore, gives no information about the true age of the formation. MV = mud volcano. BG = background.*

PRELIMINARY RESULTS

[11] Preliminary results of radiocarbon dating are displayed in Fig. 66 and Table 17. For the cores in this study, ages range from 4427 to 30391 yr cal. BP. The oldest sample (HB 13) was found at MV 13 at 192 cmbsf, while the two deepest samples at 538 (HB 24) and 557 cmbsf (HB 16) had an age of only 18224 ± 457 and 22250 ± 543 yr cal. BP. However, the oldest sample was a mollusc shell, which was found in mud breccia. It is assumed that the shell was transported from deeper intervals during times of active mud volcanism and therefore does not represent the age of the formation. For periods younger than 17000 yr cal. BP no processes occurred that caused age reversals. Disregarding earlier age reversals, cores from MVs 7, 9, 11, and 13 exhibit similar minimum ages, while at MV 14, the deepest sample gives a minimum age of 28375 ± 760 yr cal. BP (Table 17). At MV 13, in core GeoB16781, the transition from background sediments to mud breccia at 128 cmbsf was dated with 22139 ± 1176 yr cal. BP. Sedimentary material directly beneath ash layers at MVs 7 and 9 has an age of around 20000 yr cal. BP. Background sediments

sampled directly beneath turbidites have ages between 11304 ± 324 yr cal. BP and 24258 ± 273 yr cal. BP.

PRELIMINARY INTERPRETATION AND DISCUSSION

[12] Our analyses revealed significantly older radiocarbon ages than comparable studies. Shirai et al. (2010) recovered one piston core of roughly 4 m length at a position 20 km north-east of MV 6 (Figure 65, station PC05-5), and radiocarbon dating of their deepest sample at 360 cmbsf gave only 4670 – 4820 yr cal. BP. At MV 6, we found similar ages already at 67 cmbsf, which may be a consequence of limited sedimentation on top of MV 6. Alternatively, at around 4500 yr cal. BP, the cone of MV 6 may have been poorly developed and could be buried by hemipelagic background sediments. Over time, however, growth of the mud cone to ca. 80 m (Kuramoto et al. 2001), may have caused enhanced erosion or unroofing by slumping at its crest. Such relatively high-relief features are also less susceptible to deposition of turbidites. The fact that no mud breccia was found implies that beneath MV 6, the cone grew by updoming due to upward migration of a mud diatreme or diapir, but not from fluid and mud expulsion. It is possible that adjacent structural or lithological features provided easier fluid escape pathways, which led to the formation and growth of MV 5. However, without further seismic imaging, sedimentological studies and dating of material from MV 5, this hypothesis remains highly speculative.

[13] It is unclear what caused the 20000 yr cal. BP old ash layer, but for Japan, statistical analyses suggest a relationship between volcanic eruptions and earthquakes as trigger mechanism (Yamashina and Nakamura 1978; Eggert and Walter 2009). While the volcanic activity and subsequent pyroclastic fallout were probably related to an earthquake, most of the mud volcanoes covered by the ash layer remained dormant. In fact, the fallout occurred around 2000 yr after the estimated last activity of MV 6 (Sawada et al. 2002) and the estimated minimum periods of quiescence for MVs 7, 9, 11, and 13. That no MVs were reactivated during the 1944 Tonankai and 1946 Nankaido earthquakes implies that the reservoirs beneath the mud volcanoes are depleted with respect to fluidized mud and fluids, or that conduits are clogged. The longest inactivity is reported for MV 14, and with MVs 2, 3 and 5 being most recently active (Tsunogai et al. 2012; Kopf et al. 2013) and MV 10 being covered by mud breccia (Kopf et al. 2013). The timing of MV activity suggests a NW-SE migration of active mud volcanism in the Kumano basin. The reason for this apparent trend remains unclear at this point, but might be related to changes in the local stress field, or the corresponding decrease in age of the underlying accretionary prism.

[14] The turbidite layers are of varying thickness and are not equally distributed within the basin. For instance, the large amount of turbidites deposited on top of MV 9, the flank of MV 12 and the Kumano basin floor (core GeoB16758 were not encountered at the other locations. While this is

not surprising giving the bathymetric differences of several 10s of m between the different coring locations and between the top of MVs and their flanks, it makes a basin-wide correlation difficult. Most turbidites are probably derived by turbidite currents originating from the Kumano River mouth and travelling along the steep Shingu Canyon (Figure 65; Arita and Kinoshita 1988; Shirai et al. 2010). Distinguishing between turbidity triggering mechanisms, however, is difficult. Turbidites can be caused by low pressure weather systems/typhoons, flood events, tsunamis and earthquakes (e.g. Adams 1990; Hampton et al. 1996; Goldfinger et al. 2003; Lee et al. 2007, and reference therein), all of which are common in SW Japan. For instance, in core GeoB16758, the turbidites between 236 and 309 cmbsf are of similar age (Table 17), with an error-weighted average of 20361 ± 273 yr cal. BP. The ash layers and the turbidites in core GeoB16758 are also of similar age, and both might be related to the same earthquake. Moreover, the abundance and high wood content of the turbidites in GeoB16758 (Kopf et al. 2013) is indicative of seismically-induced slope failure of the Kumano River mouth (Figure 65; Shirai et al. 2010). However, their areal distribution is inconsistent for seismoturbidity. Only core GeoB16758 was affected, although other locations (e.g. MV 9, flank of MV 12) are located at similar depths and are closer to the estimated turbidite flow pathways (Figure 65).

PRELIMINARY CONCLUSION AND OUTLOOK

[15] Based on the radiocarbon dating, we suggest that MVs 6, 7, 9, 11, and 13 are in a dormant state for at least ca. 22000 yr cal. BP. An apparent NW-SE gradient of MV activity is observed, with generally dormant MVs to the NW. Turbidite layers found on top of these inactive features were probably derived by turbidity currents along Shingu Submarine Canyon. At least one turbidite sequence in core GeoB16758 shows ages similar to an ash layer that covers MVs 4 (ridge), 6, 7, 8, 9, and 11, and which might be related to seismogenesis at ca. 20000 yr cal. BP. Distinguishing between turbidite currents caused by storms, floods, earthquakes and tsunamis is not possible with the data considered here.

[16] This work will be advanced using the results of radiocarbon dating for the remaining 13 samples. So far, we have only obtained two ages for the ash layer. Therefore, to further constrain its depositional age, the background material close to the ash layers at MVs 6, 8 and 11 will be sampled and dated as well. Similarly, the transition between mud breccia and background sediments sampled at MVs 3 and 13 will constrain the timing of the termination of fluid and mud expulsion. This will help to rigorously test the hypothesis of a NW-SW gradient in mud volcanism. The bathymetric map shown in Fig. 65 will be improved with additional multibeam data to further identify possible pathways for turbidite currents. The timing of onset and termination of mud and fluid expulsion will help to further elucidate spatial and temporal patterns of fluid escape in the Kumano forearc basin.

Acknowledgments

References

Adams J (1990) Paleoseismicity of the Cascadia Subduction Zone: Evidence from turbidites off the Oregon-Washington Margin. Tectonics 9:569–583. doi: 10.1029/TC009i004p00569

Ando M (1975). Source mechanisms and tectonic significance of historical earthquakes along the Nankai Trough, Japan. Tectonophysics 27, 119-140.

Arita M, Kinoshita Y (1988) Explanatory notes of sedimentologicalmap of Kumano Nada 1:200000. Mar Geol Map Ser 32:26 pp.

Arslanov KA (1987) Radiocarbon: Geochemistry and Geochronology (in Russian). Leningrad, Leningrad University Press: 300pp.

Bronk Ramsey C (1995) Radiocarbon calibration and analysis of stratigraphy : The OxCal Program. Radiocarbon 37:425–430.

Bronk Ramsey C (2009) Bayesian analysis of radiocarbon dates. Radiocarbon 51:337–360.

Bronk Ramsey C, Lee S (2013) Recent and Planned Developments of the Program OxCal. Radiocarbon 55:

Buzinny M, Skripkin V (1995) Newly Designed 0.8-ML Teflon® Vial for Microvolume Radiocarbon Dating. Radiocarbon 37:743 – 747.

Buzinny M, Kovalyukh N, Likhtarjov I, Los I, Nesvetajlo V, Pazdur MF, Skripkin V, Shkvorets O, Sobotovich E (1995) Ecological Chronology of Nuclear Fuel Cycle Sites. Radiocarbon 37:469 – 473.

Buzinny M, Likhtarev I, Talerko N (1998) The vicinity of the chernobyl npp. Radiocarbon 40:373–379.

Davis E, Kinoshita M, Becker K, Wang K, Asano Y, Ito Y (2013) Episodic deformation and inferred slow slip at the Nankai subduction zone during the first decade of CORK borehole pressure and VLFE monitoring. Earth Planet Sci Lett 368:110–118. doi: http://dx.doi.org/10.1016/j.epsl.2013.03.009

De Vries H (1958) Variation in concentration of radiocarbon with time and location on earth. Akademie Van Wet

Dimitrov LI (2002) Mud volcanoes—the most important pathway for degassing deeply buried sediments. Earth-Science Rev 59:49–76. doi: 10.1016/S0012-8252(02)00069-7

Eggert S, Walter TR (2009) Volcanic activity before and after large tectonic earthquakes: Observations and statistical significance. Tectonophysics 471:14–26. doi: 10.1016/j.tecto.2008.10.003

Elkhoury JE, Brodsky EE, Agnew DC (2006) Seismic waves increase permeability. Nature 441:1135–1138. doi: http://www.nature.com/nature/journal/v441/n7097/suppinfo/nature04798_S1.html

Elkhoury JE, Niemeijer A, Brodsky EE, Marone C (2011) Laboratory observations of permeability enhancement by fluid pressure oscillation of in situ fractured rock. J Geophys Res 116:B02311. doi: 10.1029/2010jb007759

Expedition 315 Scientists (2009) Site C0002. In: Kinoshita M, Tobin H, Ashi J, Kimura G, Lallemant S, Screaton EJ, Curewitz D, Masago H, Moe KT, the Expedition 314/315/316 Scientists (eds) Proc IODP 315. Integrated Ocean Drilling Program Management International, Inc., Washington D.C. doi:10.2204/iodp.proc.314315316.124.2009

Expedition 319 Scientists (2010) Site C0009. In: Saffer D, McNeill L, Byrne T, Araki E, Toczko S, Eguchi N, Takahashi K, Expedition 319 Scientists (eds) Proc IODP 319. Integrated Ocean Drilling Program Management International, Tokyo. doi:10.2204/iodp.proc.319.103.2010

Expedition 348 Scientists and Scientific Participants (2014) Expedition 348 Preliminary Report NanTroSEIZE Stage 3 : NanTroSEIZE plate boundary deep riser 3. IODP Prelim Rep 348:71. doi: 10.2204/iodp.pr.348.2014

Gluyas J, Swarbrick R (2009) Petroleum Geoscience. John Wiley & Sons

Godwin H (1962) Half-life of Radiocarbon. Nature 195:984.

Goldfinger C, Nelson CH, Johnson JE (2003) Holocene earthquake records from the Cascadia subduction zone and northern San Andreas Fault based on precise dating of offshore turbidites. Annu Rev Earth Planet Sci 31:555–577. doi: 10.1146/annurev.earth.31.100901.141246

Hampton MA, Lee HJ, Locat J (1996) Submarine landslides. Rev Geophys 34:33–59. doi: 10.1029/95RG03287

Heezen BC, Ewing WM (1952) Turbidity currents and submarine slumps, and the 1929 Grand Banks [Newfoundland] earthquake. Am J Sci 250 :849–873. doi: 10.2475/ajs.250.12.849

Ichinose GA., Thio HK, Somerville PG, Sato T, Ishii T (2003). Rupture process of the 1944 Tonankai earthquake (M s 8.1) from the inversion of teleseismic and regional seismograms. J Geophys Res 108, 2497.

Kopf AJ (2002) Significance of mud volcanism. Rev Geophys 40:1005. doi: 10.1029/2000rg000093

Kopf A, Behrmann JH (2000) Extrusion dynamics of mud volcanoes on the Mediterranean Ridge accretionary complex. Geol Soc London, Spec Publ 174:169–204. doi: 10.1144/gsl.sp.1999.174.01.10

Kopf A, Robertson AHF, Clennell MB, Flecker R (1998) Mechanisms of mud extrusion on the Mediterranean Ridge Accretionary Complex. Geo-Marine Lett 18:97–114. doi: 10.1007/s003670050058

Kopf A, et al. (2013) Report and Preliminary Results of R/V SONNE Cruise SO222. Berichte, MARUM – Zent für Mar Umweltwissenschaften, Fachbereich Geowissenschaften, Univ Bremen 297:121.

Kuramoto S, Ashi J, Greinert J, Gulick S, Ishimura T, Morita S, Nakamura K, Okada M, Okamoto T, Rickert D, Saito S, Suess E, Tsunogai U, Tomosui T (2001) Surface Observations of Subduction Related Mud Volcanoes and Large Thrust Sheets in the Nankai Subduction Margin; Report on YK00-10 and YK01-04 Cruises. JAMSTEC J. Deep Sea Res. 19: 131 – 139

Lee HJ, Locat J, Desgagnés P, Parsons JD, McAdoo BG, Orange DL, Puig P, Wong FL, Dartnell P, Boulanger E (2007) Submarine Mass Movements on Continental Margins. Cont. Margin Sediment. Blackwell Publishing Ltd., pp 213–274

Libby WF, Johnson F (1955) Radiocarbon dating. University of Chicago Press, Chicago

Lupi M, Saenger EH, Fuchs F, Miller SA (2013) Lusi mud eruption triggered by geometric focusing of seismic waves. Nat Geosci 6:642–646.

Manga M, Brodsky E (2006) Seismic Triggering of Eruptions in the Far Field: Volcanoes and Geysers. Annu Rev Earth Planet Sci 34:263–291. doi: 10.1146/annurev.earth.34.031405.125125

Manga M, Beresnev I, Brodsky EE, Elkhoury JE, Elsworth D, Ingebritsen SE, Mays DC, Wang C-Y (2012) Changes in permeability caused by transient stresses: Field observations, experiments, and mechanisms. Rev Geophys 50:RG2004. doi: 10.1029/2011RG000382

Marcaillou B, Henry P, Kinoshita M, Kanamatsu T, Screaton E, Daigle H, Harcouët-Menou V, Lee Y, Matsubayashi O, Kyaw Thu M, Kodaira S, Yamano M, the Expedition 333 Scientists (2012) Seismogenic zone temperatures and heat-flow anomalies in the To-nankai margin segment based on temperature data from IODP expedition 333 and thermal model. Earth Planet Sci Lett 349-350:171–185. doi: 10.1016/j.epsl.2012.06.048

Miyazaki S, Heki K (2001) Crustal velocity field of southwest Japan: Subduction and arc-arc collision. J Geophys Res 106:4305–4326. doi: 10.1029/2000jb900312

Moore JC, Saffer D (2001) Updip limit of the seismogenic zone beneath the accretionary prism of southwest Japan: An effect of diagenetic to low-grade metamorphic processes and increasing effective stress. Geology 29:183–186. doi: 10.1130/0091-7613(2001)029<0183:ulotsz>2.0.co;2

Morita S, Ashi J, Aoike K, Kuramoto S (2004) Evolution of Kumano Basin and Sources of Clastic Ejecta and Pore Fluid in Kumano Mud Volcanoes, Eastern Nankai Trough. Int. Symp. on Methane Hydrates and Fluid Flow in Upper Accretionary Prisms.

Nakamura Y, Ashi J, Morita S, Mochizuki K (2005) Detailed Seismic Image of Mud Volcones in Kumano Basin. AGU Fall Meet 2005, Abstr T13B-0457

Nakamura Y, Morita S, Ashi J (2007) Mini 3D seismic surveys of mud volcanoes in the Kumano Basin. AGU Fall Meet 2007, Abstr V13B–1352

Pape T, Geprägs P, Hammerschmidt S, Wintersteller P, Wei J, Fleischmann T, Bohrmann G, Kopf AJ (2014) Hydrocarbon seepage and its sources at mud volcanoes of the Kumano forearc basin, Nankai Trough subduction zone. Geochemistry, Geophys Geosystems 15:2180–2194. doi: 10.1002/2013GC005057

Reimer PJ, Bard E, Bayliss A, Beck JW, Blackwell PG, Bronk Ramsey C, Buck CE, Cheng H, Edwards RL, Friedrich M, Grootes PM, Guilderson TP, Haflidason H, Hajdas I, Hatté C, Heaton TJ, Hoffmann DL, Hogg AG, Hughen KA, Kaiser KF, Kromer B, Manning SW, Niu M, Reimer RW, Richards DA, Scott EM, Southon JR, Staff RA, Turney CSM, van der Plicht J (2013) IntCal13 and Marine13 Radiocarbon Age Calibration Curves 0–50,000 Years cal BP. Radiocarbon 55:1869 – 1887. doi: 10.2458/azu_js_rc.55.16947

Saffer DM, Tobin HJ (2011) Hydrogeology and Mechanics of Subduction Zone Forearcs: Fluid Flow and Pore Pressure. Annu Rev Earth Planet Sci 39:157–186. doi: doi:10.1146/annurev-earth-040610-133408

Satake, K., 1993. Depth Distribution of Coseismic Slip Along the Nankai Trough, Japan, From Joint Inversion of Geodetic and Tsunami Data. J. Geophys. Res. 98, 4553-4565.

Sawada T, Ashi J, Murayama M, Aoike K, Ujiie Y, Kuramoto S, Kinoshita M, Tokuyama H (2002) Surface Geology and History of Mud Volcanoes in the Kumano Trough Based on Analysis of Piston Cores. AGU Fall Meet 2002, Abstr. T11B-1249

Schlüter HU, Prexl A, Gaedicke C, Roeser H, Reichert C, Meyer H, von Daniels C (2002) The Makran accretionary wedge: sediment thicknesses and ages and the origin of mud volcanoes. Mar Geol 185:219–232. doi: 10.1016/S0025-3227(02)00192-5

Seewald JS (2003) Organic-inorganic interactions in petroleum-producing sedimentary basins. Nature 426:327–333.

Seno T, Stein S, Gripp AE (1993) A model for the motion of the Philippine Sea plate consistent with NUVEL-1 and geological data. J Geophys Res 98:17941–17948.

Shirai M, Omura A, Wakabayashi T, Uchida J, Ogami T (2010) Depositional age and triggering event of turbidites in the western Kumano Trough, central Japan during the last ca. 100years. Mar Geol 271:225–235. doi: 10.1016/j.margeo.2010.02.015

Shishikura M, Echigo T, Kaneda H (2007) Marine reservoir correction for the Pacific coast of central Japan using 14C ages of marine mollusks uplifted during historical earthquakes. Quat Res 67:286–291. doi: 10.1016/j.yqres.2006.09.003

Strasser M, Moore GF, Kimura G, Kitamura Y, Kopf AJ, Lallemant S, Park J-O, Screaton EJ, Su X, Underwood MB, Zhao X (2009) Origin and evolution of a splay fault in the Nankai accretionary wedge. Nat Geosci 2:648–652. doi: 10.1038/ngeo609

Strasser M, Dugan B, Kanagawa K, Moore GF, Toczko S, Maeda L, Kido Y, Moe KT, Sanada Y, Esteban L, Fabbri O, Geersen J, Hammerschmidt S, Hayashi H, Heirman K, Hüpers A, Jurado MJ, Kameo K, Kanamatsu T, Kitajima H, Masuda H, Milliken K, Mishra R, Motoyama I, Olcott K, Oohashi K, Pickering KT, Ramirez SG, Rashid H, Sawyer D, Schleicher A, Shan Y, Skarbek R, Song I, Takeshita T, Toki T, Tudge J, Webb S, Wilson DJ, Wu H, Yamaguchi A (2014) Site C0002. In: Strasser et al. (eds) IODP Proc 338:248. doi: 10.2204/iodp.proc.338.103.2014

Stuiver M (1961) Variations in radiocarbon concentration and sunspot activity. J Geophys Res 66:273–276. doi: 10.1029/JZ066i001p00273

Stuiver M, Suess HE (1966) On the relationship between radiocarbon dates and true sample ages. Radiocarbon 8:534 – 540.

Stuiver M, Braziunas TF (1993a) Modeling Atmospheric ^{14}C Influences and ^{14}C Ages of Marine Samples to 10 000 BC. Radiocarbon 35:137–189.

Stuiver M, Braziunas TF (1993b) Sun, ocean, climate and atmospheric $^{14}CO_2$: an evaluation of causal and spectral relationships. The Holocene 3:289–305. doi: 10.1177/095968369300300401

Taira A (2001) Tectonic Evolution of the Japanese Arc System. Annu Rev Earth Planet Sci 29:109–134. doi: 10.1146/annurev.earth.29.1.109

Taira A, Byrne TB, Ashi J (1992) Photographic atlas of an accretionary prism: Geologic structures of the Shimanto Belt, Japan. Springer

Taylor RE (1997) Radiocarbon Dating. In: Taylor RE, Aitken M (eds) Chronom. Dating Archaeol. Springer US, pp 65–96

Tobin H, Kinoshita M, Ashi J, Lallemant S, Kimura G, Screaton E, Thu M, Masago H, Curewitz D, IODP Expeditions 314/315/316 Scientific Party (2009) NanTroSEIZE Stage 1 Expeditions 314, 315, and 316: First Drilling Proram of the Nankai Trough Seismogenic Zone Experiment. Sci Drill 1:4–17. doi: 10.2204/iodp.sd.8.01.2009

Tryon MD, Wheat CG, Hilton DR (2010) Fluid sources and pathways of the Costa Rica erosional convergent margin. Geochem Geophys Geosyst 11:Q04S22. doi: 10.1029/2009gc002818

Tsunogai U, Maegawa K, Sato S, Komatsu DD, Nakagawa F, Toki T, Ashi J (2012) Coseimic massive methane release from a submarine mud volcano. Earth Planet Sci Lett 341-344:79–85. doi: 10.1016/j.epsl.2012.06.004

Voelker AL, Sarnthein M, Grootes PM, Erlenkeuser H, Laj C, Mazaud A, Nadeau MJ, Schleicher M (1998) Correlation of marine (super 14) C ages from the Nordic Seas with the GISP2 isotope record; implications for (super 14) C calibration beyond 25 ka BP. Radiocarbon 40:517 – 534.

Voelker AHL, Grootes PM, Nadeau M-J, Sarnthein M (2000) Radiocarbon levels in the Iceland sea from 25-53 kyr and their link to the earth's magnetic field intensity. Radiocarbon 42:437–452.

Yamashina K, Nakamura K (1978) Correlations between tectonic earthquakes and volcanic activity of izu-oshima volcano, japan. J Volcanol Geotherm Res 4:233–250. doi: 10.1016/0377-0273(78)90015-X

CHAPTER 7.3 – MANUSCRIPT IX

ELUCIDATING MUD ASCENT IN THE KUMANO FOREARC BASIN, SE JAPAN

Sebastian B. Hammerschmidt[1]*, Achim Kopf[1]

In preparation for submission to

Earth, Planets, Space

* shammerschmidt@marum.de

[1] MARUM, University of Bremen, Bremen, Germany

Abstract Submarine mud volcanism is a common feature at convergent margins worldwide. In the Kumano forearc basin, SE offshore Japan, seven established and seven newly discovered mud volcanoes were investigated during MARUM Expedition SO-222 by bathymetric mapping and coring. Cores were sampled for X-ray diffraction (XRD) and illite crystallinity (IC) analyses, and clasts found in the mud breccia were petrographically analysed. IC values ranged from $0.271 - 0.382$ $\Delta°2\theta$ for the mud breccia, and $0.225 - 0.345$ $\Delta°2\theta$ for the background sediments. XRD analyses revealed the overall dominance of quartz, plagioclase and illite. Clasts in the mud breccia are composed of mud-, silt and sandstone, which showed neomorphism of calcareous nannofossils, moldic porosity, pressure solution, as well as quartz and calcite cementation. Therefore, all clasts show evidence of marine burial diagenesis at temperatures $> 70 - 80°C$. Based on the IC of the mud breccia matrix, an empirical temperature-IC-relationship, and a constant temperature gradient of $43°C/km$, we estimate that the mud originated from ~6-7 km depth. Significant amounts of hydrocarbon gases are present but were not introduced into the mud deeper than 4.3 km below seafloor (kmbsf). The first clasts are not introduced deeper than 3 kmbsf. IC values of the hemipelagic background sediments show values similar to the mud breccia matrix, most likely reflecting terrigenous input of the Miocene Kumano/Tanabe group, the Cretaceous Shimanto supergroup and the metamorphic Sanbagawa belt onshore the Kii peninsula. Future analyses will focus on minerals in thin sections and $\delta^{18}O$ and $\delta^{13}C$ values of carbonate cements in order to further constrain the parent units and the source depth. The similarity between the background sediments and mud breccia requires further investigation as well.

INTRODUCTION

[1] Mud volcanism is a globally observed phenomenon (e.g. Milkov 2000; Dimitrov 2002; Kopf 2002). Although mud volcanism occurs on a wide range of geological and tectonic settings, it is commonly observed at active convergent margins (e.g. Kopf et al. 1998; Kopf and Behrmann 2000; Kuramoto et al. 2001; Morita et al. 2004; Schlüter et al. 2002; Tryon et al. 2010; Tsunogai et al. 2012). At accretion-dominated subduction zones, mud volcanoes (MVs) can occur along the entire width of the subduction complex, including the frontal part of the accretionary prism (e.g. Henry et al. 1996), the forearc basin (e.g. Morita et al. 2004), and the back-arc basin (e.g. Limonov et al. 1994). The primary driving mechanism for mud volcanism is density inversion (Kopf 2002), which, at subduction zones, is easily triggered by accelerated burial of the incoming sediment. Subsequent dewatering of the sediments, coupled with early metamorphic reactions and hydrocarbon generation, provides the fluid sources that facilitate mud volcanism (Kopf 2002; Seewald 2003; Saffer and Tobin 2011).

[2] In the Kumano forearc basin, which belongs to the Nankai Trough subduction complex SE offshore Japan, mud volcanism was detected and investigated in several previous studies (Kuramoto et al. 2001; Sawada et al. 2002; Morita et al. 2004; Nakamura et al. 2005, 2007; Kasaya et al. 2011; Tsunogai et al. 2012). In total, 11 mud volcanoes have been identified: seven in the southern part and four in the northern part of the basin. During MARUM (Centre for Marine Environmental Sciences) expedition SO-222 with research vessel *SONNE*, in the southern Kumano basin, seven additional MVs were identified (Kopf et al. 2013; Fig. 66). Thirteen of the 14 total MVs were mapped and cored, and subject to post-cruise analyses including gas composition (Pape et al. 2014; cf. chapter 7.1 in this thesis) and radiocarbon dating (Hammerschmidt and

Kopf, in preparation; cf. chapter 7.2 in this thesis). While the latter focuses on the temporal and spatial variability of mud expulsion, Pape et al. (2014) investigated the source depth of hydrocarbon gases that formed gas hydrates beneath the MVs. They concluded that the gases must originate from depths between 2.3 and 4.3 kmbsf (km below seafloor), i.e. the Tertiary to Cretaceous part of the accretionary prism, which is mainly composed of rocks from the Shimanto belt. Morita et al. (2004) investigated the hydrocarbon gas potential of clasts found in the MVs and found that the organic content in the rocks was too immature to have originated at the same depth as thermogenic gases, and thus concluded that the hydrocarbon gases and clastic ejecta are derived from different source depths. So far, no analyses were carried out regarding the source depth of the mud breccia.

[3] In this study, the possible source depth of volcanic ejecta at the Nankai Trough is further investigated. Samples of mud breccia and hemipelagic background sediments were subject to X-ray diffraction (XRD) and illite crystallinity (IC) analyses. In addition, clasts were analysed petrographically for diagenetic features.

GEOLOGICAL SETTING

[4] The Kumano forearc basin, located between the Kii peninsula to the north-west and the Nankai Trough in the south-east, formed in the late Miocene as consequence of ongoing subduction of the Philippine Sea Plate beneath the Eurasian Plate. Subduction started around 15 Ma (Taira 2001), and today takes place at a rate of 4.1 – 6.5 cm/yr with an azimuth of 300°- 315°N (Seno et al. 1993; Miyazaki and Heki 2001). The Kumano basin covers an area of 70000 km^2, and the boundary between basin sediments and accretionary prism can reach depths of up to 2000 mbsf. The accretionary prism beneath the Kumano basin consists of folded and imbricated rocks from the subducting Shikoku basin (Miocene) and the Shimanto belt (Cretaceous) (Taira et al. 1992; Expedition 348 Scientists and Scientific Participants 2014). The plate boundary thrust is located between 10 and 20 km depth (Moore and Saffer 2001; Marcaillou et al. 2012). The basin infill is characterized by hemipelagic sediments intercalated with sandy turbidites and ash layers (Expedition 315 Scientists 2009; Expedition 319 Scientists 2010; Kopf et al. 2013; Strasser et al. 2014). Between 1.67 and 1.56 Ma, a temporarily active splay fault system in the frontal part of the accretionary prism is assumed to have increased sedimentation in the Kumano basin (Strasser et al. 2009). The presumed average sedimentation rate is $\geq$ 800 m Ma^{-1} (i.e. 0.8 m ka^{-1}; Tobin et al. 2009), and the basin fill of the Kumano basin is dominated by a submarine fan system. Via this system, eroded material from the Tertiary to Cretaceous Shimanto Belt, the Miocene forearc sediments of the Kumano, Owase, and Tanabe groups, and the igneous rocks from the Miocene

Kumano Group, Omine Group and the Shionomisaki complex on the Kii peninsula are deposited in the Kumano basin (Choi et al. 2011; Takano et al. 2013).

[5] During MARUM Expedition SO-222 with *R/V SONNE*, thirteen MVs were subject to mapping and coring (Kopf et al. 2013; Pape et al. 2014). The MVs have conically-shaped domes with basal diameters of up to 2 km and heights greater 100 m (Kuramoto et al. 2001; Kopf 2002; Morita et al. 2004). Seismic studies revealed that most of the MVs overly anticlines (Figure 67; Morita et al. 2004). Solid components ejected via the MVs include low viscosity mud and clasts of Miocene to Pliocene age (Sawada et al. 2002; Morita et al. 2004).
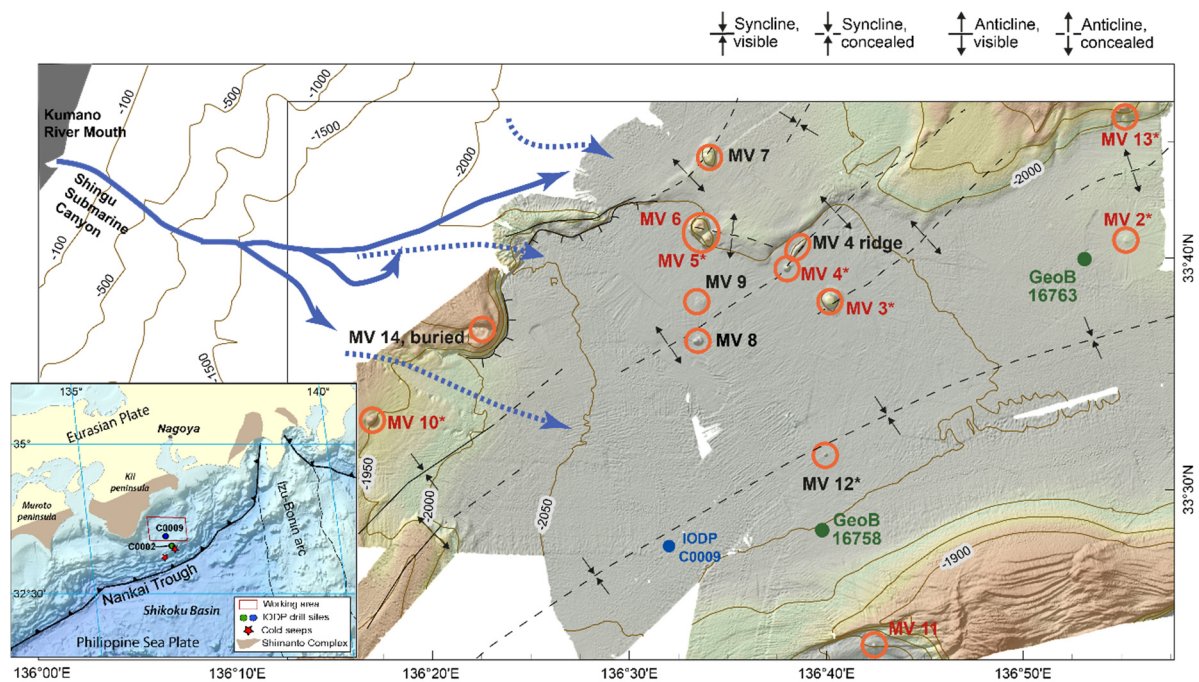
Figure 67: *Bathymetric map of the study area in the Kumano forearc basin (modified from Pape et al. 2014). The map comprises 13 mud volcanoes (MV) mapped during SO-222 and anti- and synclines (from Morita et al. 2004). Separately shown are background cores GeoB16758 and GeoB16763. The map was extended following Shirai et al. (2010). Solid and broken blue arrows show directions of turbidite currents suggested by Shirai et al. (2010) and Arita and Kinoshita (1988), respectively. The inlay gives a regional tectonic overview, including IODP Sites C0002 and C0009. Cores from red-labelled MVs were sampled for XRD and IC analyses. Locations with stars indicate the origin of clasts that were subject to thin section analyses.*

[6] Based on radiocarbon dating and tephrachronology, Sawada et al. (2002) concluded that MV 6 has been dormant since at least 22000 yr BP. This is supported by 3D seismic reflection studies of Nakamura et al. (2005, 2007) who investigated the continuity of bottom simulating reflectors (BSR) beneath the MVs. BSR can be interrupted by ascend of warm fluids as consequence of mud volcanism. Nakamura et al. (2005, 2007) concluded that MVs 3 and 6 are inactive, while MV 5 shows signs of ongoing eruption. MV 5 showed also coseismic activity as consequence of an M7.5 earthquake that occurred in 2004 (Tsunogai et al. 2012). Based on heat flow measurements by Kopf et al. (2013), only two mud volcanos (i.e. MVs 2, 3) were found to be

recently active. At MVs 2, 3 and 10, Pape et al. (2014) reported escaping thermogenic hydrocarbon gases. They suggested that these gases are derived from dissociating gas hydrates that formed during active migration of hydrocarbon gases from 2.3 – 4.3 km depth.

MATERIAL AND METHODS

Visual Core Description and Thin Section Analyses

[7] Overall, 16 gravity cores from mud volcanoes 2, 3, 4, 5, 6, 10 and 13, and 2 gravity cores from hemipelagic basin sediments were sampled for XRD and thin section analyses (Table 18). Detailed visual core description is given in Kopf et al. (2013) and briefly summarized here.

[8] Cores from mud volcanoes are dominated either by dark grey – olive grey mud breccia or dark green hemipelagic background sediment. The mud breccia comprised mm – cm sized, semi-lithified mud-, silt- and sandstone clasts. The background sediment was characterized by shell fragments and calcareous and siliciclastic nanno- and microfossils. Cores taken from hemipelagic basin sediments comprised only background sediments. In all cores, background material had interlayers of silty to sandy material showing a fining upward behaviour. Background sediments rarely hosted ash layers and clasts. Cores taken at the crest of MV 2, 3, 4, 5 and 10 consisted of mud breccia solely. At the flanks of MVs 3 and 4, mud breccia was disrupted by hemipelagic background sediments. In core GeoB16728, which was taken at the northern flank of MV 4, black clay and sands, partly enriched with mica and disturbed by mass wasting deposits, were encountered between 700 and 1600 cmbsf (centimetre below seafloor). MVs 6, 10, and 13 are covered by background sediments, including intercalations of turbidites and ash layers. Mud breccia was found on top of MV 12, but at its flank, hemipelagic background sediments overlaid mud breccia.

[9] Thin sections were prepared from 29 individual clasts in the laboratories of MKfactory in Potsdam, Germany (www.mkfactory.de/). Thin section analyses were performed using cross polarized transmitted and reflected light microscopy.

XRD and Illite Crystallinity

[10] XRD analyses were performed at the "Central Laboratory for Crystallography and Applied Material Sciences" (ZEKAM) at Department 5, University of Bremen. Measurements were carried out with a Phillips X'Pert Pro MD X-ray diffractometer equipped with a Cu tube Kα, λ 1.541), a fixed divergence slit ($\frac{1}{4}°2\theta$), a 15-sample changer, a secondary monochromator, and the X'Celerator detector system (Vogt 2009). After grinding the samples with a mortar and pestle to a grain size < 20 μm, the Philips/Panalytical backloading system was used to randomly distribute the particles. Standard measurements are made from 3° to 85°2θ, with a calculated step size of 0.016°2θ. Mineral identification and semi-quantification was done graphically with the program

MacDiff (Petschick 2001). The Philips/Panalytical software X'Pert HighScore was used to identify mineral phases. This was followed by full quantification of mineral assemblage of the bulk fraction via the QUAX full pattern method (c.f, Vogt et al. 2002). Relative errors for quartz, calcite, dolomite and NaCl are 1 wt%, for other carbonates the error is 2 – 3 wt%, for clay minerals, feldspars, mica and Fe-oxides it ranges from 5 to 10 wt%, and for all other minerals the relative error is 2 – 5 wt% (Vogt et al. 2002).

[11] Illite crystallinity is defined as the full half width at half maximum of the first illite diffraction peak (Kübler and Jaboyedoff 2000). The divergence slit remains fixed, and clay-sized particles were oriented. Illite crystallinity is reported in $\Delta°2\theta$, and following the original definition of Kübler (1967), IC can be used to define a transition between diagenesis and anchimetamorphism (i.e. greenschist metamorphism). The boundaries between diagenesis and anchizone are set at an IC value of 0.42 $\Delta°2\theta$ and between anchi- und epizone at an IC value of 0.25 $\Delta°2\theta$ (e.g. Blenkinsop 1988; Kisch 1990; Robinson et al. 1990). In terms of temperature, Kisch (1987) proposed that anchizone and epizone start at ca. 200°C and 300°C, respectively.
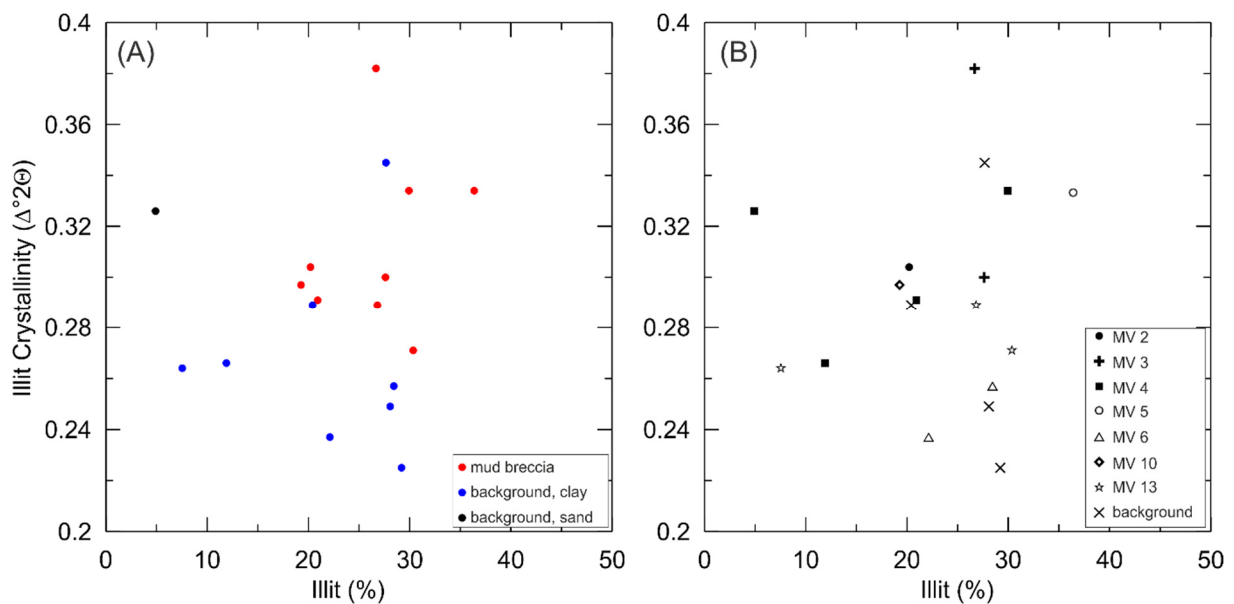
Figure 68: *Illite crystallinity plotted against illite concentrations. (A) Data points colored for lithology (B) Data points appointed to individual MVs*

PRELIMINARY RESULTS

XRD and Illite Crystallinity

[12] In total, 18 samples were subject to XRD and illite crystallinity (IC) analyses, of which 9 samples were taken from mud breccia and another 9 samples of hemipelagic background sediment were taken from both on and off mud volcanoes (Table 18; Fig. 66). XRD analyses revealed that all samples are dominated by quartz and plagioclase. Illite was present as major constituent (i.e. concentration > 10%) in all samples except the sandstone found at MV 4 (core GeoB16728), and

Table 18: *Overview of the results of XRD and illite crystallinity (IC) analyses. Minor constituents were often within the range of uncertainty and/or close the detection limit.*

Longi-tude	Latitude	Depth [mbsl]	Core GeoB	MV	Sampled from	Core Depth [cmbsf]	IC	Major Const. [>10%]	Minor Const. [1 - 10 %]
33°40.518' N	136°55.195' E	2000	16772	2	mud breccia	106	0.304	Qtz, Plg, Ill	Kfs, Calc, Mom, Kao, Chl, Zrk, Bt, Gk
33°38.039' N	136°40.244' E	1800	16709	3, N flank	mud breccia	1982	0.382	Qtz, Plg, Ill	Kfs, Calc, Kao, Chl
33°38.200' N	136°40.480' E	2025	16732	3, NE flank	mud breccia	67	0.300	Qtz, Plg, Ill	Kfs, Calc, Kao, Chl, Zeo, Sill
33°39.503' N	136°38.017' E	2061	16723	4, NE flank	mud breccia	245	0.291	Qtz, Plg, Kfs, Calc, Ill	Mom, Kao, Chl, Zeo
33°39.489' N	136°38.038' E	2030	16754	4, N flank	mud breccia	100	0.334	Qtz, Plg, Ill	Kfs, Calc, Mom, Kao, Chl, Opx
33°39.560' N	136°38.040' E	2062	16728	4, N flank	dark grey clay	1077	0.266	Qtz, Plg, Kfs, Ill	Calc, Kao, Chl, Cpx, Chd, Pyr, Fe-Ox
33°39.560' N	136°38.040' E	2063	16728	4, N flank	dark grey sandstone, un-consolidated	1505	0.326	Qtz, Plg, Kfs	Ill, Sm, Kao, Chl, Cpx, Musc
33°40.593' N	136°34.002' E	1900	16746	5	mud breccia	132	0.334	Qtz, Plg, Kfs, Ill	Calc, Mom, Kao, Chl, Zeo
33°41.093' N	136°33.571' E	1920	16750	6	background	76	0.257	Qtz, Plg, Calc, Ill	Kfs, Kao, Chl, NaCl, Cpx, Fe-Ox
33°41.093' N	136°33.571' E	1920	16750	6	background	286	0.237	Qtz, Plg, Calc, Ill	Kfs, Kao, Chl, NaCl
33°32.824' N	136°16.880' E	1885	16716-2	10	mud breccia	14	0.297	Qtz, Plg, Kfs, Ill	Calc, Kao, Chl, NaCl
33°46.105' N	136°54.865' E	1880	16781-1	13	background	46	0.264	Qtz, Plg, Kfs, Calc	Ill, Sm, Kao, Chl, Epi, Zeo, Musc
33°46.105' N	136°54.865' E	1880	16781-1	13	mud breccia	259	0.271	Qtz, Plg, Calc, Ill	Kfs, Kao, Chl
33°46.100' N	136°54.775' E	1891	16782-2	13	mud breccia	161	0.289	Qtz, Plg, Kfs, Ill	Calc, Mom, Kao, Chl
33°39.995' N	136°53.012' E	2012	16763	back-ground	background	35	0.345	Qtz, Plg, Ill	Kfs, Calc, Mom, Kao, Chl, Cpx, Pyr
33°28.113' N	136°39.978' E	2040	16758	back-ground	background	78	0.289	Qtz, Plg, Calc, Ill	Kfs, Kao, Chl, NaCl
33°28.113' N	136°39.978' E	2040	16758	back-ground	background	175	0.225	Qtz, Plg, Ill	Kfs, Calc, Mom, Kao, Chl
33°28.113' N	136°39.978' E	2040	16758	back-ground	background	378	0.249	Qtz, Plg, Calc, Ill	Kfs, Mom, Kao, Chl, Cpx, NaCl

Note: Bt = biotite, Calc = calcite, Chd = chloritoid, Chl = chlorite, Cpx/Opx = clino-/orthopyroxene, Epi = epidote, Fe-Ox = iron oxide, Gk = glauconite, Ill = illites, Kfs = K-feldspar, Kao = kaolinite, Mom = montmorillonites, Musc = muscovite, Plg = plagioclase, Pyr = pyrite, Qtz = quartz, Sill = sillimanite, Sm = smectite, Zeo = zeolite, Zrk = zircon

in hemipelagic background material on top of MV 13 (GeoB16781; Table 18). Other major constituents include illites, K-feldspar, and calcite.

[13] IC values range from 0.271 to 0.382 $\Delta°2\theta$ with an average of 0.311 $\Delta°2\theta$ for the mud breccia, while the background sediments exhibit 0.225 – 0.345 $\Delta°2\theta$ with an average of 0.273 $\Delta°2\theta$. Changes in the IC values are independent of sampling depth or location. IC values in background sediments show a higher diversity, which is also indicated when plotting IC values against illite content (Figure 68). Mud breccia show no positive trend with illite content (Figure 68a), while the hemipelagic background sediment even suggests a negative relationship between IC and illite concentration. As expected, the one sample of background sediment dominated by sand has the lowest illite concentration, but surprisingly also one of the highest IC values (0.326 $\Delta°2\theta$) . Correlation of IC with illite content for individual mud volcanoes is difficult to identify (Figure 68b).

Thin Section Analyses

[14] Most of the cores taken directly from mud volcanoes were dominated lithologically by mud breccia (Kopf et al. 2013). Clasts ranged from semi-lithified claystones and silty claystones to lithified silt- and sandstones. Some clasts showed a variety of veins filled with quartz or calcite cement.

[15] From the 29 clasts that were petrographically analysed, two examples are shown from MV 3 (Plates 1) and MV 10 (Plate 2). Clasts found in cores taken from the crest of MV 3 showed signs of previously deep burial. Porosity was low, and fractures were filled with polycrystalline quartz (Plates 1C). Secondary, mainly moldic pores were found in fossils of planktontic and benthic foraminifera, of which some showed neomorphosis (Plates 1A, B, D). Almost all pores were filled with calcite cement (Plates 1B, F) and/or black, possibly organic material or pyrite (Plates 1F). Clasts found in the upper 100 cmbsf at the NE flank of MV 3 showed strong evidence of deformation. Polycrystalline quartz was common, as well as stylolites and micritic contact rims around grains (Plates 1E, G, H). One clast was characterized by a matrix solely of polycrystalline quartz and nearly zero porosity (Plates 1E), another clast showed intercrystalline porosity between obviously reworked polycrystalline, angular quartz grains with micritic rims and internal stylolites (Plates 1G, H). The second clast had fractures that were partly or completely filled with blocky calcite (Plates 1B). At depths greater 100 cmbsf, clasts found at the NE flank of MV 3 resemble the previously described clasts found at more shallow depths and at the top of MV 3, but are also characterized by a relatively higher amount of black, organic material in fractures and secondary porosity (Plates 1F). Besides blocky calcite, high-Mg calcite is observed as well (Plates 1F).

[16] At MV 10 (Plate 2), compared to MV 3, similar features were found. Cores from the crest hosted clasts which showed strong deformation features, including intracrystalline deformation

7.3 Elucidating Mud Ascent in the Kumano Forearc Basin, SE Japan
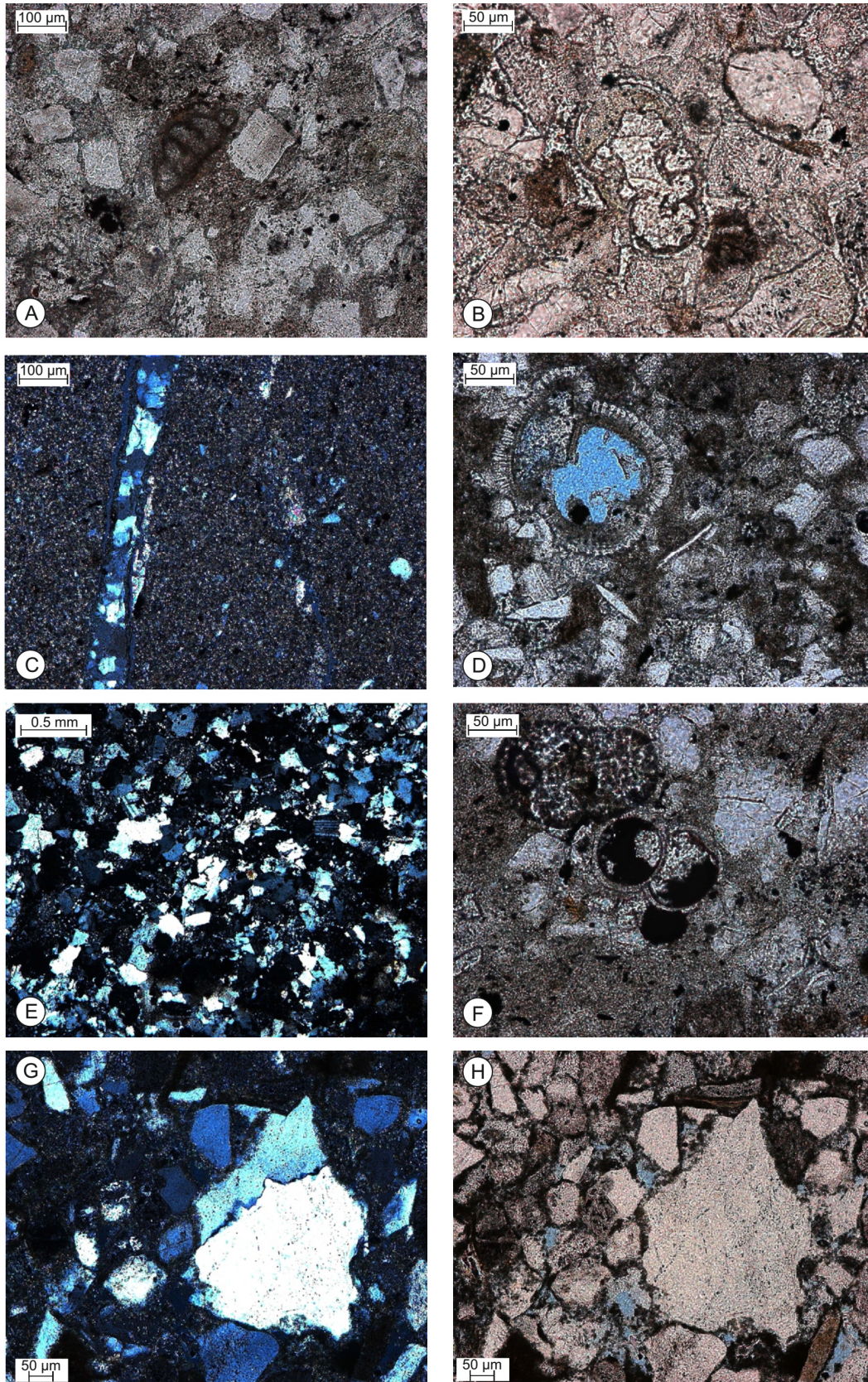
Plate 1: *Thin sections made from clasts found at MV 3.* **(A), (B)** *Examples for neomorphism visible in PPL in planctic foraminifera* **(C)** *fracture filled with polycrystalline quartz, XPL* **(D)** *moldic porosity, XPL (light blue colour)* **(E)** *matrix of polycrystalline quartz, XPL* **(F)** *foraminifera filled with organic matter or pyrite, PPL* **(G)** *stylolite encountered between to quartz grains* **(H)** *same as (G) but under PPL. The bright yellow spots indicate open pore space.*

and brecciation, and stylolites (Plate 2A, B). Black micritc rims occur at grain-grain contacts and only minor secondary porosity is observed (Plate 2C). One unusual clast hosted several large feldspar grains, clearly visible based on their zonation and twinning (Plate 2D). While deformation is minor (rare occurrence of stylolites), the feldspars were affected by dissolution, and are embedded in kaolinitc ground mass what may be kaolinite. This is also the only clast which showed significant secondary porosity.
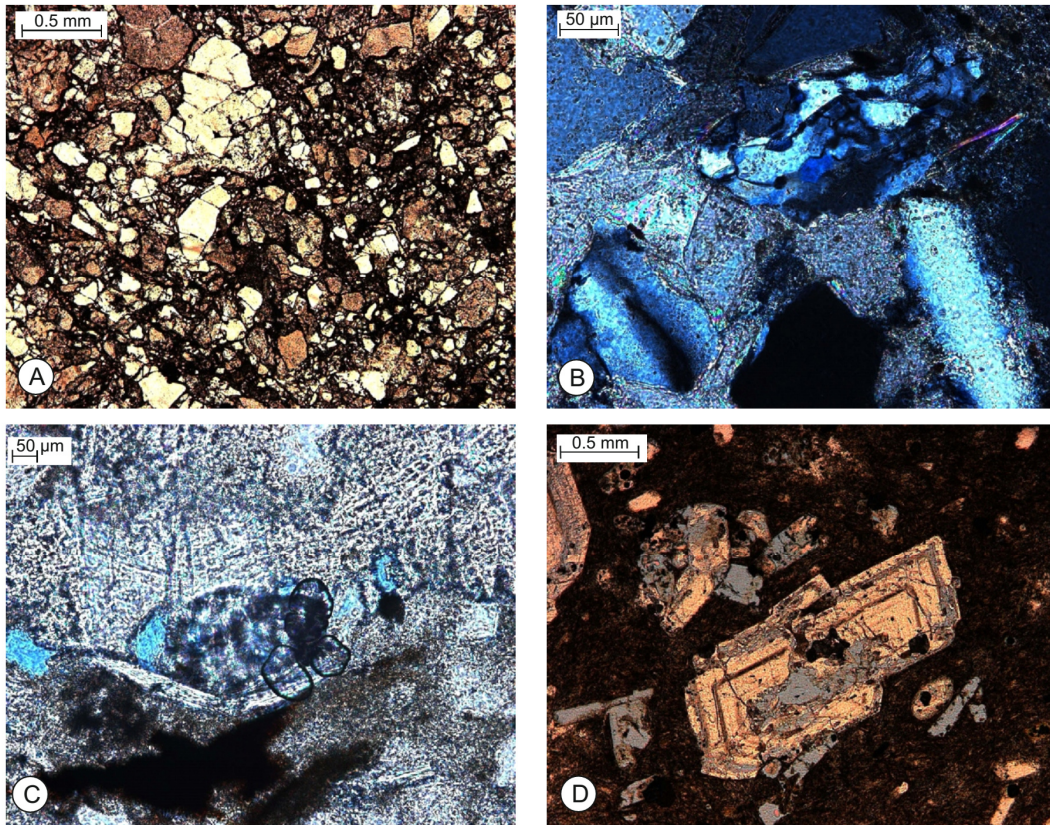
Plate 2: *Thin sections made from clasts found at MV 10.* **(A)** *Example for brecciated grains with black, micritic rims, PPL* **(B)** *internally deformed quartz grain and stylolites, XPL* **(C)** *secondary porosity, indicated by blue staining of open pore space, XPL* **(D)** *feldspar grains, visible by zonation and twinning, strongly affected by dissolution in clay matrix, probably mainly kaolinite, XPL.*

PRELIMINARY INTERPRETATION AND DISCUSSION

[17] Underwood et al. (1993) used an observed empirical relationship between vitrinite reflectivity and IC together with an empirical temperature-vitrinite reflectivity relationship given by Barker (1988) to derive the following equation:

$$IC = 1.197 - 0.0029(T°C) \qquad (26)$$

Following the generally accepted boundaries for the onset of the anchi- and epizone at 0.45 $\Delta°2\theta$ and 0.25 $\Delta°2\theta$, respectively (Blenkinsop 1988), the corresponding temperature limits for the anchizone are 270°C and 330°C. Underwood et al. (1993) emphasized that equation (26) holds an uncertainty of ± 50°C, and since it was determined from samples of the Tertiary Shimanto Belt,

Muroto Peninsula, SE Japan it may be of limited applicability for other locations. However, the Kumano basin fill is most likely underlain by rocks of the Cretaceous and Tertiary Shimanto Belt (Taira et al. 1992), which is the likely source of ejecta from MVs in the Kumano Basin (Pape et al. 2014). Therefore, we assume that equation (26) can also be applied to the samples in this study. The results imply that the mud breccia samples experienced temperatures between 281°C and 319°C, well within the boundaries of the anchizone (Table 19 and Fig. 68). Harris et al. (2011) estimated a temperature gradient of 43°C/km for the Kumano forearc basin that included corrections for subsidence and sedimentation rate. Assuming that this temperature gradient is constant sets the anchizone at a depth of 6.2 – 7.6 km, and the source depth of the mud breccia to 6.5 – 7.4 km. In general, the transition from diagenesis to anchimetamorphism coincides with the transition from the dry-gas phase of hydrocarbons to unproductive rocks, i.e. the depth at which hydrocarbons are not significant (Kübler and Jaboyedoff 2000). The results of Pape et al. (2014) imply that the source depth for thermogenic hydrocarbon gases is shallower than 4.3 kmbsf, therefore it makes sense that the hydrocarbon gases expelled at the mud volcanoes are derived from depths shallower than the fluidized mud. This is also apparent when estimating vitrinite reflectivity using the following empirical relationship between vitrinite reflectivity and IC (Underwood et al. 1992):

$$\%R_o = 0.57 - 5.99 \log(IC) \tag{27}$$

where IC is the illite crystallinity and R_o is the vitrinite reflectivity. Applying this formula to the IC values presented here gives R_o concentrations between 3.1% and 4.0%, which imply a supermature regime where hydrocarbon gas production ceased (e.g. Kübler and Jaboyedoff, 2000). This suggests that the hydrocarbon gases certainly contribute to, but do not initiate mud ascent.

[18] Major mineral constituents reveal that material from the deep diagenetic zone was also incorporated in the mud breccia during mud ascent (Table 18). All samples from mud breccia are dominated by quartz and illite, both of which are generated by the dissolution of kaolinite and its reaction with K-feldspar or any other potassium-rich agent at temperatures > 130°C (i.e. ca. 3 km depth; Bjørlykke 2014). Evidence of K-feldspar dissolution clearly indicated by the corroded K-feldspars in the thin section of a mud clast found at MV 10. The presence of stylolites and polycrystalline quartz, sometimes accompanied by calcite cement, further indicates that the clasts are derived from the deep burial diagenetic regime (e.g. Choquette and James 1990), i.e. from intervals where temperatures are > 70 – 80°C (Worden and Morad 2000; Bjørlykke and Jahren 2012; Bjørlykke 2014) which correspond to depths > 1.8 km. No anchimetamorphism (i.e. greenschist facies mineral assemblages) were found in the clasts, therefore, the clasts are probably not derived from depths > 6.2 kmbsf. Clasts with calcareous nannofossils are partly filled

Table 19: *Estimated temperature, source depth and vitrinite reflectivity R₀ based on IC values (after Underwood et al. 1992, 1993)*

Longitude	Latitude	Depth [mbsl]	Core GeoB	MV #	Sampled from	Core Depth [cmbsf]	IC	Temp. [°C]	Source Depth, 43°C/km [km]	R_o [%]
33°40.518' N	136°55.195' E	2000	16772	2	mud breccia	106	0.304	307.93	7.2	3.7
33°38.039' N	136°40.244' E	1800	16709	3, N flank	mud breccia	1982	0.382	281.03	6.5	3.1
33°38.200' N	136°40.480' E	2025	16732	3, NE flank	mud breccia	67	0.300	309.31	7.2	3.7
33°39.503' N	136°38.017' E	2061	16723	4, NE flank	mud breccia	245	0.291	312.41	7.3	3.8
33°39.489' N	136°38.038' E	2030	16754	4, N flank	mud breccia	100	0.334	297.59	6.9	3.4
33°39.560' N	136°38.040' E	2062	16728	4, N flank	dark grey clay	1077	0.266	321.03	7.5	3.5
33°39.560' N	136°38.040' E	2063	16728	4, N flank	dark grey sandstone, unconsolidated	1505	0.326	300.34	7.0	4.0
33°40.593' N	136°34.002' E	1900	16746	5	mud breccia	132	0.334	297.59	6.9	3.4
33°41.093' N	136°33.571' E	1920	16750	6	background	76	0.257	324.14	7.5	4.3
33°41.093' N	136°33.571' E	1920	16750	6	background	286	0.237	331.03	7.7	4.1
33°32.824' N	136°16.880' E	1885	16716-2	10	mud breccia	14	0.297	310.34	7.2	3.7
33°46.105' N	136°54.865' E	1880	16781-1	13	background	46	0.264	321.72	7.5	4.0
33°46.105' N	136°54.865' E	1880	16781-1	13	mud breccia	259	0.271	319.31	7.4	4.0
33°46.100' N	136°54.775' E	1891	16782-2	13	mud breccia	161	0.289	313.10	7.3	3.8
33°39.995' N	136°53.012' E	2012	16763	background	background	35	0.345	293.79	6.8	3.3
33°28.113' N	136°39.978' E	2040	16758	background	background	78	0.289	313.10	7.3	3.7
33°28.113' N	136°39.978' E	2040	16758	background	background	175	0.225	335.17	7.8	4.5
33°28.113' N	136°39.978' E	2040	16758	background	background	378	0.249	326.90	7.6	4.2

with calcite cement and/or pyrite and probably derived from < 1.8 kmbsf, because neomorphism, moldic porosity and pyrite precipitation imply marine burial diagenesis (e.g. Melim et al. 1995, 2002, Vanneste et al. 2012). Pyrite precipitation requires decomposable organic matter, dissolved

sulphide and reactive detrital iron minerals (Berner 1970, 1984). It is further associated with anaerobic oxidation of bacterial methane (AOM), which occurs up to depths > 100 m (Regnier et al. 2011). Consequently, we infer that methane seepage caused authigenic carbonate cement to form, and ongoing AOM-generated hydrogen sulphide, promoted pyrite formation. During times of active mud volcanism, these carbonates were broken apart. A similar mechanism has been proposed for the Darwin MV at the Gulf of Cadiz (Vanneste et al. 2012).

[19] We infer that fluidized mud, hydrocarbon gas, and the ejected clasts are all derived from different stratigraphic levels. Mud ascent originates in the anchizone between 6.2 and 7.6 km depth. Most likely, early metamorphism, rapid lateral loading and imbricate thrusting in the accretionary prism led to fluid release, followed by undercompaction, density inversion and subsequent mud ascent (e.g. Kopf 2002). Mixing with hydrocarbon gases at 4.3 kmbsf further promoted mud ascent. Clasts were incorporated throughout mud ascent from 6.2 kmbsf, which correspond to rocks of Miocene to Cretaceous age (Expedition 348 Scientists and Scientific Participants 2014; Pape et al. 2014). Equivalent onshore strata on the Kii peninsula are the Miocene Kumano and Tanabe Groups, both which are ancient forearc basins, and the Cretaceous to Tertiary Shimanto Belt which extends beneath the Kumano Basin (Morita et al. 2004).

[20] However, this interpretation is limited by the assumptions that: (1) the temperature gradient is constant with depth, and (2) the bulk IC is not biased by shallower sediments that were incorporated in the mud breccia during upward migration. The second point is important considering the high variability and the generally lower IC values in hemipelagic background sediments, and that almost all samples (except for the dark sandstone in GeoB16728 and the background material in GeoB16781) have similar major mineral constituents. The Pliocene to Pleistocene basin fill of the Kumano basin is controlled by submarine fan turbidite systems (Takano et al. 2013). The material for these systems is mainly derived from terrigenous Kii Peninsula sediment from the Kumano/Kinokawa Rivers and submarine canyons, e.g. the Shingu canyon (Shirai et al. 2010; Takano et al. 2013; Usman et al. 2014) (Figure 67). Catchment areas are characterized by rocks from the Miocene Kumano/Tanabe group, the Cretaceous Shimanto Supergroup and the metamorphic Sanbagawa belt (Morita et al. 2004; Choi et al. 2011; Kasaya et al. 2011; Usman et al. 2014). Here, we suggest that the background material reflects the input from this catchment area, which would explain the generally low IC values, its large variability and similar major mineral assemblages (Figures 67, 68).

[21] It is likely that during mud ascent, background material was incorporated and that the measured IC values underestimate the true IC values. However, given the small variability of the samples from mud breccias, we infer that the influence of background sediments was small.
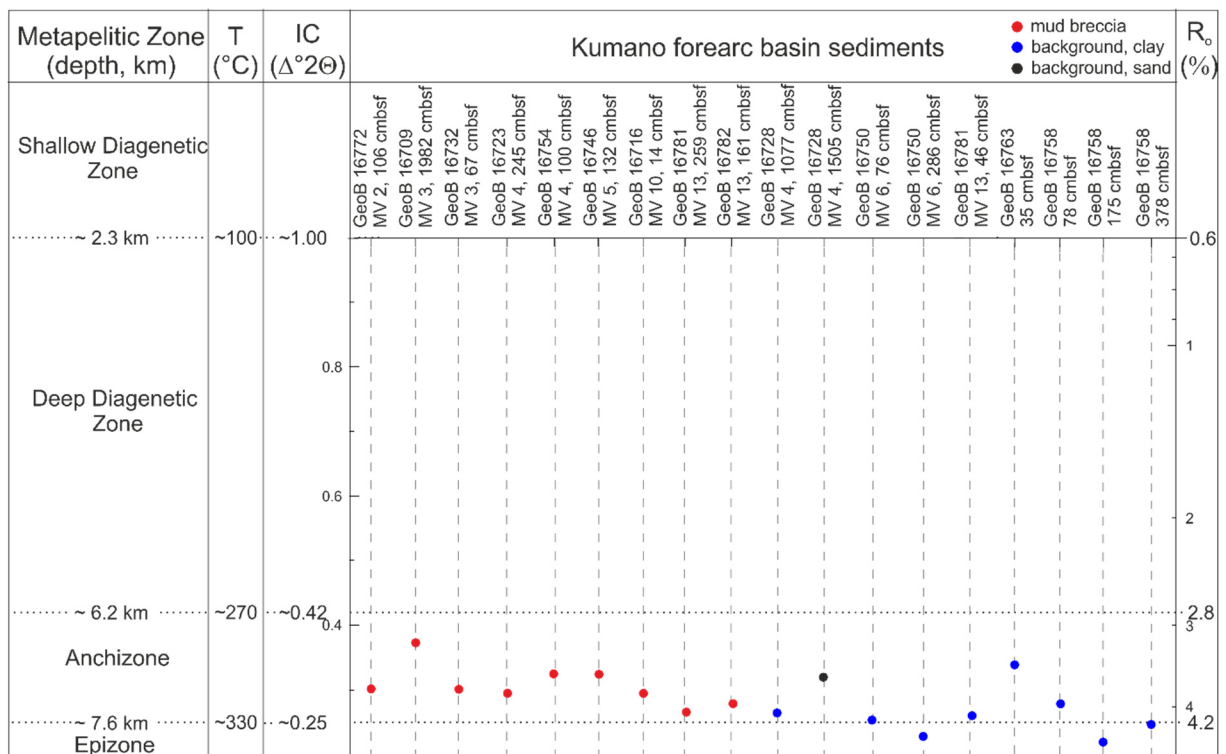
Figure 69: *Overview of illite crystallinity IC found in the samples investigate here. Depths are estimated based on a constant temperature gradient of 43°C/km. Boundaries for diagenetic, anchi- and epizone from Kübler and Jaboyedoff (2000). Temperature estimations are based on equation (26) (from Underwood et al.1993). Vitrinite reflectivity R_o was estimated using equation (27) (from Underwood et al. 1992).*

PRELIMINARY CONCLUSION AND OUTLOOK

[22] This work focused on XRD and IC analyses on samples of mud breccia and hemipelagic background sediments from the Kumano forearc basin, and thin section analyses on clasts found in the mud breccia. Preliminary results suggest that the mud ascent starts in the anchizone at depths of 6.2 – 7.6 km, based on an empirical temperature-IC-relationship and a constant temperature gradient of 43°C/km. Most likely, the mud ascent was assisted by hydrocarbon gases starting at 4.3 kmbsf, whereas incorporation of clasts commenced probably between 3 and 6.2 kmbsf. The overall low IC values and the high variability in background sediments are explained by the basin fill being controlled by a submarine canyon-fan system, which leads to the predominance of material from the Miocene Kumano/Tanabe group, the Cretaceous Shimanto super-group and the metamorphic Sanbagawa belt.

[23] Future analyses will include a re-evaluation of the thin sections to identify key minerals, which might give more information about the provenance of the clasts. In addition, $\delta^{18}O$ and $\delta^{13}C$ values of carbonate cements that were found in clasts will be used to further constrain the source temperatures. Also, additional research will be necessary to explain the striking similarity between background sediments and mud breccia regarding their IC and mineral constituents. Last but not least, particular focus will be lain on the geothermal gradient that was used for estimating the

depth of the anchi- and epizones. At the Nankai trough, it is suggested that fluid flow through the oceanic crust significantly reduces *in situ* temperatures (Rotman and Spinelli 2013). Indeed, recent geothermal models imply temperatures of ca. 150°C at around 7 km depth and 300°C at around 15 km depth, close to the location of the thrust fault boundary (e.g. Li 2011). This would change the interpretation substantially. For instance, if the anchizone is close to the thrust fault boundary, mud volcanism might be closely related to tectonic processes. Alternatively, mud ascend could also start at more shallow levels, but then the IC is controlled by input from terrigenous material. Upcoming work needs to address this issue.

Acknowledgments

References

Arita M, Kinoshita Y (1988) Explanatory notes of sedimentologicalmap of Kumano Nada 1:200000. Mar Geol Map Ser 32:26 pp.

Barker CE (1988) Geothermics of petroleum systems: implications of the stabilization of kerogen thermal maturation after a geologically brief heating duration at peak temperature. Pet Syst United States US Geol Surv Bull 1870:26–29.

Berner RA (1970) Sedimentary pyrite formation. Am J Sci 268 :1–23. doi: 10.2475/ajs.268.1.1

Berner RA (1984) Sedimentary pyrite formation: An update. Geochim Cosmochim Acta 48:605–615. doi: 10.1016/0016-7037(84)90089-9

Bjørlykke K (2014) Relationships between depositional environments, burial history and rock properties. Some principal aspects of diagenetic process in sedimentary basins. Sediment Geol 301:1–14. doi: 10.1016/j.sedgeo.2013.12.002

Bjørlykke K, Jahren J (2012) Open or closed geochemical systems during diagenesis in sedimentary basins: Constraints on mass transfer during diagenesis and the prediction of porosity in sandstone and carbonate reservoirs. Am Assoc Pet Geol Bull 96:2193–2214. doi: 10.1306/04301211139

Blenkinsop TG (1988) Definition of low-grade metamorphic zones using illite crystallinity. J Metamorph Geol 6:623–636. doi: 10.1111/j.1525-1314.1988.tb00444.x

Choi P-Y, Nakae S, Kim H (2011) Fault tectonic analysis of Kii peninsula, Southwest Japan: Preliminary approach to Neogene paleostress sequence near the Nankai subduction zone. Isl Arc 20:455–476. doi: 10.1111/j.1440-1738.2011.00779.x

Choquette PW, James NP (1990) Limestones—the burial diagenetic environment. Diagenes Geosci Canada, Repr Ser 4:75–111.

Dimitrov LI (2002) Mud volcanoes—the most important pathway for degassing deeply buried sediments. Earth-Science Rev 59:49–76. doi: http://dx.doi.org/10.1016/S0012-8252(02)00069-7

Expedition 315 Scientists (2009) Site C0002. In: Kinoshita M, Tobin H, Ashi J, Kimura G, Lallemant S, Screaton EJ, Curewitz D, Masago H, Moe KT, the Expedition 314/315/316 Scientists (eds) Proc IODP 315. Integrated Ocean Drilling Program Management International, Inc., Washington D.C. doi:10.2204/iodp.proc.314315316.124.2009

Expedition 319 Scientists (2010) Site C0009. In: Saffer D, McNeill L, Byrne T, Araki E, Toczko S, Eguchi N, Takahashi K, Expedition 319 Scientists (eds) Proc IODP 319. Integrated Ocean Drilling Program Management International, Tokyo. doi:10.2204/iodp.proc.319.103.2010

Expedition 348 Scientists, Scientific Participants (2014) Expedition 348 Preliminary Report NanTroSEIZE Stage 3 : NanTroSEIZE plate boundary deep riser 3. IODP Prelim Rep 348:71. doi: 10.2204/iodp.pr.348.2014

Harris RN, Schmidt-Schierhorn F, Spinelli G (2011) Heat flow along the NanTroSEIZE transect: Results from IODP Expeditions 315 and 316 offshore the Kii Peninsula, Japan. Geochemistry, Geophys Geosystems 12:Q0AD16. doi: 10.1029/2011GC003593

Henry P, Le Pichon X, Lallemant S, Lance S, Martin JB, Foucher J-P, Fiala-Médioni A, Rostek F, Guilhaumou N, Pranal V, Castrec M (1996) Fluid flow in and around a mud volcano field seaward of the Barbados accretionary wedge: Results from Manon cruise. J Geophys Res Solid Earth 101:20297–20323. doi: 10.1029/96JB00953

Kasaya T, Kanamatsu T, Sawa T, Kinosita M, Tukioka S, Yamamoto F (2011) Acoustic images of the submarine fan system of the northern Kumano basin obtained during the experimental dives of the Deep Sea AUV URASHIMA. Copublished in Explor Geophys, Butsuri-Tansa and Jigu-Mulli-wa-Mulli-Tamsa 42:80–87.

Kisch HJ (1987) Correlation between indicators of very-low-grade metamorphism, in Frey, M., ed., Low temperature metamorphism: Glasgow, Blackie and Son, p. 228-300.

Kisch HJ (1990) Calibration of the anchizone: a critical comparison of illite "crystallinity"scales used for definition. J Metamorph Geol 8:31–46. doi: 10.1111/j.1525-1314.1990.tb00455.x

Kopf AJ (2002) Significance of mud volcanism. Rev Geophys 40:1005. doi: 10.1029/2000rg000093

Kopf A, Behrmann JH (2000) Extrusion dynamics of mud volcanoes on the Mediterranean Ridge accretionary complex. Geol Soc London, Spec Publ 174:169–204. doi: 10.1144/gsl.sp.1999.174.01.10

Kopf A, Robertson AHF, Clennell MB, Flecker R (1998) Mechanisms of mud extrusion on the Mediterranean Ridge Accretionary Complex. Geo-Marine Lett 18:97–114. doi: 10.1007/s003670050058

Kopf A, et al. (2013) Report and Preliminary Results of R/V SONNE Cruise SO222. Berichte, MARUM – Zent für Mar Umweltwissenschaften, Fachbereich Geowissenschaften, Univ Bremen 297:121.

Kübler B (1967) La cristallinité de l'illite et les zones tout à fait supérieures de métamorphisme. In: Schaer J (ed) Colloq. sur les étages tectoniques. À la Baconnière, Neuchâtel, pp 105 – 122

Kübler B, Jaboyedoff M (2000) Illite crystallinity. Comptes Rendus l'Académie des Sci - Ser IIA - Earth Planet Sci 331:75–89. doi: 10.1016/S1251-8050(00)01395-1

Kuramoto S, Ashi J, Greinert J, Gulick S, Ishimura T, Morita S, Nakamura K, Okada M, Okamoto T, Rickert D, Saito S, Suess E, Tsunogai U, Tomosui T (2001) Surface Observations of Subduction Related Mud Volcanoes and Large Thrust Sheets in the Nankai Subduction Margin; Report on YK00-10 and YK01-04 Cruises. JAMSTEC J Deep Sea Res 19:131 – 139.

Li C-F (2011) An integrated geodynamic model of the Nankai subduction zone and neighboring regions from geophysical inversion and modeling. J Geodyn 51:64–80. doi: 10.1016/j.jog.2010.08.003

Limonov AF, Woodside JM, Ivanov MK (1994) Mud volcanism in the Mediterranean and Black seas and shallow structure of the Eratosthenes Seamount. Initial results Geol Geophys Investig Dur third "'Training-through-Research'"Cruise R/N Gelendzhik 64:173.

Marcaillou B, Henry P, Kinoshita M, Kanamatsu T, Screaton E, Daigle H, Harcouët-Menou V, Lee Y, Matsubayashi O, Kyaw Thu M, Kodaira S, Yamano M, the Expedition 333 Scientific Party (2012) Seismogenic zone temperatures and heat-flow anomalies in the To-nankai margin segment based on temperature data from IODP expedition 333 and thermal model. Earth Planet Sci Lett 349-350:171–185. doi: 10.1016/j.epsl.2012.06.048

Melim LA, Swart PK, Maliva RG (1995) Meteoric-like fabrics forming in marine waters: Implications for the use of petrography to identify diagenetic environments. Geol 23 :755–758. doi: 10.1130/0091-7613(1995)023<0755:MLFFIM>2.3.CO;2

Melim LA, Westphal H, Swart PK, Eberli GP, Munnecke A (2002) Questioning carbonate diagenetic paradigms : evidence from the Neogene of the Bahamas. Mar Geol 185:27 – 53.

Milkov A V (2000) Worldwide distribution of submarine mud volcanoes and associated gas hydrates. Mar Geol 167:29–42.

Miyazaki S, Heki K (2001) Crustal velocity field of southwest Japan: Subduction and arc-arc collision. J Geophys Res 106:4305–4326. doi: 10.1029/2000jb900312

Moore JC, Saffer D (2001) Updip limit of the seismogenic zone beneath the accretionary prism of southwest Japan: An effect of diagenetic to low-grade metamorphic processes and increasing effective stress. Geology 29:183–186. doi: 10.1130/0091-7613(2001)029<0183:ulotsz>2.0.co;2

Morita S, Ashi J, Aoike K, Kuramoto S (2004) Evolution of Kumano basin and Sources of Clastic Ejecta and Pore Fluid in Kumano Mud Volcanoes, Eastern Nankai Trough. Int. Symp. on Methane Hydrates and Fluid Flow in Upper Accretionary Prisms.

Nakamura Y, Ashi J, Morita S, Mochizuki K (2005) Detailed Seismic Image of Mud Volcones in Kumano basin. AGU Fall Meet 2005, Abstr T13B-0457

Nakamura Y, Morita S, Ashi J (2007) Mini 3D seismic surveys of mud volcanoes in the Kumano basin. AGU Fall Meet 2007, Abstr V13B–1352

Pape T, Geprägs P, Hammerschmidt S, Wintersteller P, Wei J, Fleischmann T, Bohrmann G, Kopf AJ (2014) Hydrocarbon seepage and its sources at mud volcanoes of the Kumano forearc basin, Nankai Trough subduction zone. Geochemistry, Geophys Geosystems 15:2180–2194. doi: 10.1002/2013GC005057

Petschick R (2001) MacDiff–The user-friendly X-ray powder diffractometry analysis tool for Macintosh computers.

Regnier P, Dale AW, Arndt S, LaRowe DE, Mogollón J, Van Cappellen P (2011) Quantitative analysis of anaerobic oxidation of methane (AOM) in marine sediments: A modeling perspective. Earth-Science Rev 106:105–130. doi: 10.1016/j.earscirev.2011.01.002

Robinson D, Warr LN, Bevins RE (1990) The illite "crystallinity" technique: a critical appraisal of its precision. J Metamorph Geol 8:333–344. doi: 10.1111/j.1525-1314.1990.tb00476.x

Rotman HMM, Spinelli GA (2013) Global analysis of the effect of fluid flow on subduction zone temperatures. Geochemistry, Geophys Geosystems 14:3268–3281. doi: 10.1002/ggge.20205

Saffer DM, Tobin HJ (2011) Hydrogeology and Mechanics of Subduction Zone Forearcs: Fluid Flow and Pore Pressure. Annu Rev Earth Planet Sci 39:157–186. doi: doi:10.1146/annurev-earth-040610-133408

Sawada T, Ashi J, Murayama M, Aoike K, Ujiie Y, Kuramoto S, Kinoshita M, Tokuyama H (2002) Surface Geology and History of Mud Volcanoes in the Kumano Trough Based on Analysis of Piston Cores. AGU Fall Meet 2002, Abstr. T11B-1249

Schlüter HU, Prexl A, Gaedicke C, Roeser H, Reichert C, Meyer H, von Daniels C (2002) The Makran accretionary wedge: sediment thicknesses and ages and the origin of mud volcanoes. Mar Geol 185:219–232. doi: 10.1016/S0025-3227(02)00192-5

Seewald JS (2003) Organic-inorganic interactions in petroleum-producing sedimentary basins. Nature 426:327–333.

Seno T, Stein S, Gripp AE (1993) A model for the motion of the Philippine Sea plate consistent with NUVEL-1 and geological data. J Geophys Res 98:17941–17948.

Shirai M, Omura A, Wakabayashi T, Uchida J, Ogami T (2010) Depositional age and triggering event of turbidites in the western Kumano Trough, central Japan during the last ca. 100years. Mar Geol 271:225–235. doi: 10.1016/j.margeo.2010.02.015

Strasser M, Moore GF, Kimura G, Kitamura Y, Kopf AJ, Lallemant S, Park J-O, Screaton EJ, Su X, Underwood MB, Zhao X (2009) Origin and evolution of a splay fault in the Nankai accretionary wedge. Nat Geosci 2:648–652. doi: 10.1038/ngeo609

Strasser M, Dugan B, Kanagawa K, Moore GF, Toczko S, Maeda L, Kido Y, Moe KT, Sanada Y, Esteban L, Fabbri O, Geersen J, Hammerschmidt S, Hayashi H, Heirman K, Hüpers A, Jurado MJ, Kameo K, Kanamatsu T, Kitajima H, Masuda H, Milliken K, Mishra R, Motoyama I, Olcott K, Oohashi K, Pickering KT, Ramirez SG, Rashid H, Sawyer D, Schleicher A, Shan Y, Skarbek R, Song I, Takeshita T, Toki T, Tudge J, Webb S, Wilson DJ, Wu H, Yamaguchi A (2014) Site C0002. In: Strasser et al. (eds) IODP Proc 338:248. doi: 10.2204/iodp.proc.338.103.2014

Taira A (2001) Tectonic Evolution of the Japanese Arc System. Annu Rev Earth Planet Sci 29:109–134. doi: 10.1146/annurev.earth.29.1.109

Taira A, Byrne TB, Ashi J (1992) Photographic atlas of an accretionary prism: Geologic structures of the Shimanto Belt, Japan. Springer

Takano O, Itoh Y, Kusumoto S (2013) Variation in Forearc Basin Configuration and Basin- filling Depositional Systems as a Function of Trench Slope Break Development and Strike-Slip Movement : Examples from the Cenozoic Ishikari – Sanriku-Oki and Tokai-oki Kumano-nada Forearc Basins. In: Itoh Y (ed) Mech. Sediment. Basin Form. - Multidiscip. Approach Act. Plate Margins. pp 3–26

Tobin H, Kinoshita M, Ashi J, Lallemant S, Kimura G, Screaton E, Thu M, Masago H, Curewitz D, IODP Expeditions 314/315/316 Scientific Party (2009) NanTroSEIZE Stage 1 Expeditions 314, 315, and 316: First Drilling Proram of the Nankai Trough Seismogenic Zone Experiment. Sci Drill 1:4–17. doi: 10.2204/iodp.sd.8.01.2009

Tryon MD, Wheat CG, Hilton DR (2010) Fluid sources and pathways of the Costa Rica erosional convergent margin. Geochem Geophys Geosyst 11:Q04S22. doi: 10.1029/2009gc002818

Tsunogai U, Maegawa K, Sato S, Komatsu DD, Nakagawa F, Toki T, Ashi J (2012) Coseimic massive methane release from a submarine mud volcano. Earth Planet Sci Lett 341-344:79–85. doi: 10.1016/j.epsl.2012.06.004

Underwood MB, Laughland MM, Byrne T, Hibbard JP, DiTullio L (1992) Thermal evolution of the Tertiary Shimanto Belt, Muroto Peninsula, Shikoku, Japan. Isl Arc 1:116–132. doi: 10.1111/j.1440-1738.1992.tb00064.x

Underwood MB, Laughland MM, Kang SM (1993) A comparison among organic and inorganic indicators of diagenesis and low-temperature metamorphism, Tertiary Shimanto Belt, Shikoku, Japan. Geol Soc Am Spec Pap 273:45 – 62. doi: 10.1130/SPE273-p45

Usman MO, Masago H, Winkler W, Strasser M (2014) Mid-Quaternary decoupling of sediment routing in the Nankai Forearc revealed by provenance analysis of turbiditic sands. Int J Earth Sci 103:1141–1161. doi: 10.1007/s00531-014-1011-z

Vanneste H, Kastner M, James RH, Connelly DP, Fisher RE, Kelly-Gerreyn BA, Heeschen K, Haeckel M, Mills RA (2012) Authigenic carbonates from the Darwin Mud Volcano, Gulf of Cadiz: A record of palaeo-seepage of hydrocarbon bearing fluids. Chem Geol 300-301:24–39. doi: 10.1016/j.chemgeo.2012.01.006

Vogt C, Lauterjung J, Fischer RX (2002) Investigation of the Clay Fraction ($<2 \mu$m) of the Clay Minerals Society Reference Clays. Clays Clay Miner 50:388–400.

Vogt C (2009) Data report: semiquantitative determination of detrital input to ACEX sites based on bulk sample X-ray diffraction data. In: Backman J, Moran K, McInroy DB, Mayer LA, the Expedition 302 Scientists, Proc IODP 302: Edinburgh (Integrated Ocean Drilling Program Management International, Inc.). doi:10.2204/iodp.proc.302.203.2009

Worden RH, Morad S (2000) Quartz cementation in oil field sandstones: a review of the key controversies. Quartz Cem sandstones 29:1–20.

CHAPTER 8

Conclusion & Outlook

SUMMARY

[1] The cumulative dissertation presented here aimed at understanding fluid generation, migration, and fluid response to seismo-tectonic events in the Nankai Trough subduction complex. The thesis is based on data obtained by long-term and real-time monitoring instruments, and coring of fluid escape structures (i.e. mud volcanoes) in the Kumano forearc basin. Each method covered individual objectives, which were as follows: (i) long-term borehole pressure and temperature monitoring at the Megasplay fault to investigate possible coseismic activity, fluid migration at and hydrogeological properties of the fault zone (in combination with laboratory experiments), and evaluation of the fidelity of the SmartPlug borehole observatory (ii) real-time drilling mud gas monitoring starting at the transition between accretionary prism and Kumano forearc basin to estimate the gas composition at depth, possible migration of deep gas, *in situ* generation of hydrocarbons, and evaluation of the fidelity of the newly installed drilling mud gas monitoring system onboard *D/V Chikyu* and (iii) investigation of past and recent fluid migration, source depth and coseismic activity of mud volcanoes in the Kumano forearc basin by analyzing their ejecta.

[2] Although deployment, recovery, and data analyses proved that the SmartPlug borehole observatory was a great success, the role of the Megasplay fault in terms of fluid migration remains still unresolved. The pressure readings of the SmartPlug gave no hint for strain or fluid migration related to fault slip, or permanent deformation of the formation surrounding the borehole. This is most likely a combination of the strain sensitivity of the formation and the disability of the SmartPlug to monitor strain $\leq 10^{-10}$. Although the data point to the presence of a damage zone that sets the lower limit of bulk hydraulic diffusivity to 10^{-5} m^2 s^{-1}, the possibility of fluid migration along or across the fault, including spatial and temporal changes in the hydrogeological setting, remains unclear. What became apparent is the susceptibility of the fluid pressure to seismic waves, microseism, tidal signals and tsunami waves. Dynamic pressure oscillations can affect the permeability in fault zones (e.g. Elkhoury et al. 2006, 2011), thus the abovementioned natural signals might influence the hydraulic properties of the Megasplay fault zone over time.

[3] While fluid migration at the Megasplay fault zone remains unclear, mixing of deep fluids with shallow fluids generated *in situ* were well documented in the accretionary prism beneath the Kumano forearc basin. This is supported by the elevated ^{222}Rn and ^{3}He/^{4}He values at depths as shallow as 950 mbsf, where hydrocarbon gases are missing any thermogenic influence. Starting with 1700 mbsf, the hydrocarbon gas composition of the drilling mud gas encountered during Exp. 338 and 348 clearly imply mixing of bacterial with thermogenic components. Assuming a temperature gradient of ca. 41°C/km and based on a time-temperature index model, thermogenic cracking of hydrocarbons does not start at depths shallower than 2000 mbsf. Based on the measured ^{3}He/^{4}He isotope ratios, steady-state flow of deep, probably primordial fluids was estimated

to have a maximum velocity of 3.5 mm/yr. However, given the elevated ^{222}Rn and ^{3}He/^{4}He isotope values in the shallowest sample, the half-life time of ^{222}Rn, and the positive correlation with He concentration and ^{3}He/^{4}He isotope ratios, this velocity estimate seems unlikely. Moreover, high concentrations at depths shallower 1000 mbsf were only found during IODP Exp. 338. Therefore, it is further suggested that episodic fluid flow, possibly triggered by local and/or regional earthquakes, contributed significantly to the gas concentrations.

[4] These conclusions are complemented by the observations of Pape et al. (2014), who investigated fluid dynamics and origins of the hydrocarbon gases escaping mud volcanoes in the Kumano forearc basin. Pape et al. (2014) clearly identified three mud volcanoes, where remnants of gas hydrates were present and where thermogenic hydrocarbon gas is escaping. The hydrates formed during times of higher volcanic activity, and are sourced by hydrocarbon gas from 2.3 – 4.3 km depth. At the time of sampling and coring, however, the gaseous components escaping the mud volcanoes are more likely to be fuelled by the dissociation of gas hydrates rather than an active migration of deep thermogenic gas. Similar conclusions can be drawn following core description and radiocarbon dating of background sediments at the transition to mud breccia and beneath turbidites and ash layers overlying mud volcanoes. The results suggest an NW-SE gradient of dormant mud volcanoes in the Kumano forearc basin. Inactivity can be dated back to at least ca. 28000 years. Although mud volcanism generally correlates with earthquakes (e.g. Manga et al. 2009; Lupi et al. 2013), it seems that at Nankai, mud volcanoes are (re-)activated by earthquakes only if a distinct, strain-related, threshold pressure at depth is exceeded. It is further suggested that for mud volcanism, not only fluid migration and accumulation, but the general presence of fluidized mud is of great importance. Preliminary results for illite crystallinity implied source depths within the Anchizone, i.e. between 6.3 and 7.2 km. At the same time, thin section analyses from clasts found in mud breccia point to source depths between 6.3 kmbsf (i.e. the onset of anchimetamorphism) and 3 kmbsf, while the oil and gas window is not reached before 4.3 kmbsf (Pape et al. 2014). However, these depths are calculated based on a constant temperature gradient of 43°C/km. Most likely, the temperature gradient is lower, which would shift our assumptions for source depths to deeper stratigraphic levels. Unaffected by the temperature estimation is the conclusion that the ejecta are all originating from different stratigraphic levels. Mud ascent started as a consequence of density inversion in the anchizone, and got further promoted within the oil and gas window.

[5] In conclusion, this dissertation clearly shows that fluid migration from deep levels of the accretionary prism to higher stratigraphic intervals is possible and active. Mud volcanoes as prominent fluid escape structures are dormant at the moment, but remnants of gas hydrates highlight the presence of thermogenic hydrocarbons derived from depths greater 2.3 km. At the same

time, no clear conclusion can be drawn regarding the migration pathways. Long-term borehole monitoring at the Megasplay fault provided some interesting insight of small scale, dynamic fluid pressure oscillation as response to natural signals, but no large-scale fluid migration was indicated by the SmartPlug data. It remains also unclear whether fluids flow along focused pathways, or migrate via diffusive flow. Most likely, it is a combination of both (e.g. Yamada et al. 2014), but the temporal and spatial limitations of the applied methods make it impossible to depict a clear mechanism. The role of local, regional and distant earthquakes and associated seismic waves remains puzzling at well.

OUTLOOK

[6] As abovementioned, this PhD thesis elucidates, but does not satisfactorily answer the fate of fluids in the Nankai Trough subduction complex. Three manuscripts, namely chapters 6.2, 7.2 and 7.3 are still in preparation. These manuscripts are still subject to ongoing research, including modelling of fluid-associated heat transfer in the accretionary prism, and calculation of peak-ground velocity and peak-ground acceleration to estimate the likelihood of earthquake-induced episodic fluid flow (chapter 6.2, section "Preliminary Conclusion and Outlook"). It will be further necessary to re-evaluate available and to include new datasets that will help to depict spatial and temporal variations of mud volcano activity and the source depth of mud ascent beneath the Kumano forearc basin (chapters 7.2, 7.3, section "Preliminary Conclusion and Outlook"). At the same time, the geothermal model for estimating the source depth needs to be reconsidered.
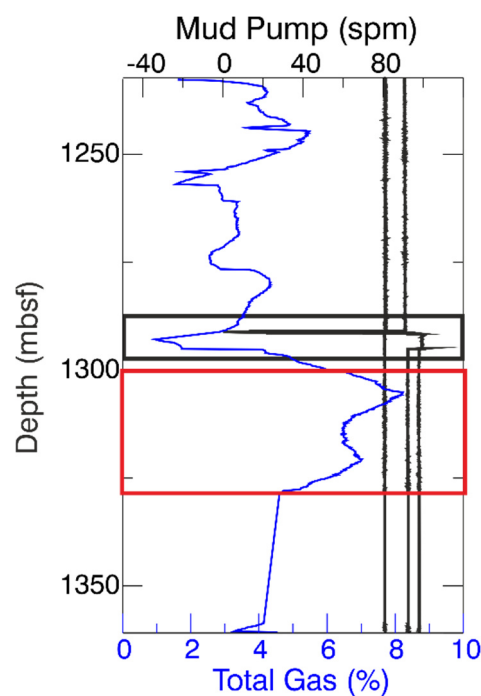
Figure 70: *Total gas concentration in response to mud pump activity. When the mud pumps stopped working, drilling mud circulation ceased. This is accompanied with a drop in total gas concentration in the drilling mud (black box). The red box highlights a period where total gas concentration suddenly increased due to swabbing.*

[7] When it comes to the origin of fluids, a qualitative assessment based on drilling mud gas data is possible, but it is still not completely resolved to what extend the drilling parameters influence the drilling mud gas composition. That this is one of the emerging issues became apparent during analyses of hydrocarbon and noble gas concentrations in drilling mud gas samples from IODP Exp. 338 and 348 (cf. chapter 6).

[8] Two examples of drilling-related artifacts are shown in Figs. 70 and 71. At ca. 1320 mbsf, a prominent gas peak correspond to a time when the drill string was moved up- and downwards several times (red box in Figure 70), and thus are interpreted as "trip gas" or "swab gas" rather than a true increase in formation gas concentration. An example of swab gas is also visible from 30 Dec 2013 – 01 Jan 2014 (Figure 71). While swabbing between ca. 4916.0 and 5010.7 mBRT, gas concentrations in drilling mud increased abruptly (total gas > 3.5 % and methane > 28000 ppmv). This is explained by rapid or large upward movement of the drill string, which reduces the hydrostatic pressure in borehole temporarily. If the hydrostatic pressure falls below the formation pressure of a gas bearing formation, gas is introduced into the borehole. Breakouts, possibly caused by temporary underpressure in the borehole, were also suggested by the presence of "pressure cuttings" (Expedition 348 Scientists, in preparation).
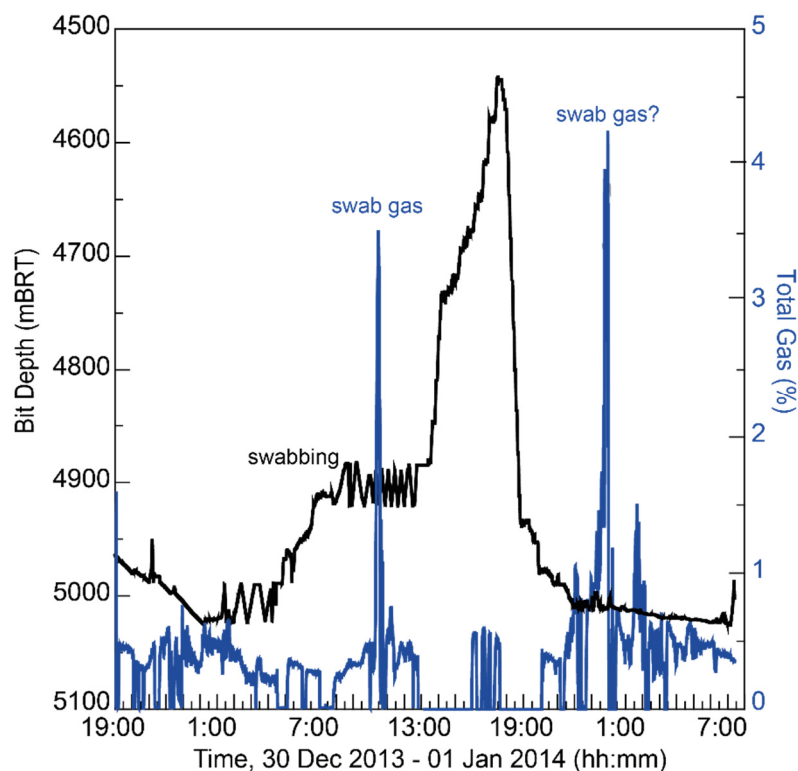
Figure 71: *Overview of the period from 30 Dec 2013 – 01 Jan 2014 during IODP Exp. 348, when swabbing caused gas kicks >4%. Black lines denote the bit depth in meter below rotary table (mBRT), the blue line indicates total gas in %. The second gas kick cannot be simply explained by swabbing.*

[9] Other than the drilling operation, the degasser configuration influences the gas concentrations as well. For instance, degassing is less effective when the mud level below the degasser (i.e. the mud level in the mud trough) drops. As a result, during IODP Expeditions 338 and 348, gas concentrations declined as soon as the mud pumps stopped working (e.g., black box in Figure 70). Another example is the obvious difference between concentrations of hydrocarbon gases in the drilling mud gas data with the concentrations found during coring the same section in Hole C0002P (Figure 72). Methane in drilling mud gas from Hole C0002P was up to one order of magnitude lower compared to concentrations encountered during drilling. Reasons for this discrepancy are manifold, including the use of a higher mud weight in Hole C0002P and changing degasser efficiency (i.e. how much gas could be extracted from the drilling mud). A higher mud density would reduce the intake of higher hydrocarbons, and at the surface, hydrocarbons are likely to be retained in the cold, dense drilling mud (Ablard et al. 2012).

[10] The relationship between drilling operation and drilling mud gas concentrations will be further explored in collaboration with experts from the Japan Agency for Marine-Earth Science and Technology (JAMSTEC), and together with the three manuscripts that are still in preparation, namely chapters 6.2, 7.2 and 7.3, finished and submitted until the end of 2014. Funding is granted by MARUM within the "Conclusion of Manuscripts" program.
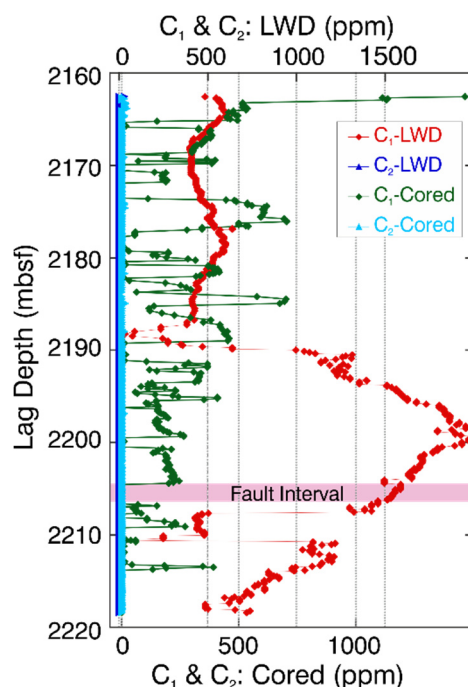
Figure 72: *Drilling mud gas data for methane (C_1) and ethane (C_2) found during coring and drilling with (logging-while-drilling, LWD) of Hole C0002P (from Hammerschmidt et al. 2014). Gas concentrations for the cored and drilled interval are shown on the bottom and top x-axis, respectively.*

PERSPECTIVES

[11] To really understand the role of fault zones for fluid flow in accretionary prisms, it would be necessary to build a vast array of monitoring instruments, which cover a wide area of the fault zone to be investigated, along-dip and along-strike. A prerequisite for establishing such a network is the need for improving the individual instruments. Nowadays, data storage is no issue, but CORK systems like the SmartPlug are limited by power supply, sampling frequency, and opportunities for data download and maintenance. Increasing the sampling frequency would decrease the life time of the batteries installed at the CORK head, and thus, additional offshore dive expeditions would be necessary (which in turn requires additional funding). Recently, a way to overcome these obstacles was realized with the LTBMS installed at NanTroSEIZE Site C0002 (Kopf et al. 2011). In 2011, the instrument started monitoring autonomously, but since January 2013, the LTBMS is connected to the DONET, which provides unlimited power supply and real-time monitoring of the formation parameters. Terminating the dependence on batteries resulted in an increase of the sampling frequency from 1 min^{-1} to 1 s^{-1}. A network of instruments with similar configurations covering a wide part of a fault zone might give valuable insights in fault dynamics, fluid migration, and most importantly, the fault response to dynamic pore pressure oscillations. Based on the calculations presented in Hammerschmidt et al. (2013), estimating the fault zone properties, including spatial and temporal variations, would provide the basic parameters to model a threshold value of dynamic oscillations that would be necessary to increase the permeability and to initiate fluid migration. In a next step, it would be interesting to know at what permeability the fault weakens, and how thermal pressurization and dilatancy hardening are influencing this behaviour.

[12] For the real-time drilling mud gas monitoring, degassing efficiency onboard *D/V Chikyu* is a crucial issue, and further technical improvements are required for a quantitative assessment of drilling mud gas. Recently, Schlumberger Ltd. Introduced the FLAIR system, which enhances liberation of gas components from the drilling mud by heating of the drilling mud during gas extraction. This allows quantification of lower hydrocarbons ($C_1 – C_5$), and subsequent carbon isotope analyses. In a next step, in would be possible to further depict secondary mechanisms like oxidation, mixing, and further constrain estimations on *in situ* temperature. At the same time, contamination with atmospheric gases would be minimized, which would improve noble gas analyses. Consequently, analyses including fluid migration, heat flow and pressurization of the fault zone based on noble gas data would lead to more reliable results.

[13] Fluid expulsion at mud volcanoes further depicts the chance to estimate the depth of origin of the primary fluids escaping the accretionary prism and the forearc basin. If we can combine long-term monitoring and fluid sampling at mud volcanoes in the Kumano forearc basin, a direct

connection between seismo-tectonic processes, source depth of fluids and solids, and fluid flow rates could be drawn. A first step in this direction is the development and application of borehole observatories that were designed for installation with the MARUM MeBo (Meereseboden-Borhgerät, cf. Appendix B), including MeBoCORKs (cf. chapter 4.1). Further development of these instruments and wide-spread usage would elucidate fluid and heat flow, geochemical cycling, spatial and temporal variations, and changes with seismic events. It would be possible to see the spatial distribution of deformation (horizontally and vertically), and subsequent stress-strain modelling could point to areas or fault segments that are likely to rupture in the future (Ando 1975), leading to a risk map of the Nankai subduction complex.

References

Ablard P, Bell C, Cook D, Fornasier I, Poyet J-P, Sharma S, Fielding K, Lawton G, Haines G, Herkommer MA, Mccarthy K, Radakovic M, Umar L (2012) The Expanding Role of Mud Logging. Oilf Rev 24:24–41.

Ando M (1975) Source Mechanisms and Tectonic Significance of Historical Earthquakes along the Nankai Trough, Japan. Tectonophysics 27:119 – 140.

Elkhoury JE, Brodsky EE, Agnew DC (2006) Seismic waves increase permeability. Nature 441:1135–1138.

Elkhoury JE, Niemeijer A, Brodsky EE, Marone C (2011) Laboratory observations of permeability enhancement by fluid pressure oscillation of in situ fractured rock. J Geophys Res 116:B02311. doi: 10.1029/2010jb007759

Hammerschmidt SB, Davis EE, Hüpers A, Kopf A (2013) Limitation of fluid flow at the Nankai Trough megasplay fault zone. Geo-Marine Lett 33:405–418. doi: 10.1007/s00367-013-0337-z

Hammerschmidt S, Toczko S, Kubo Y, Wiersberg T, Fuchida S, Kopf A, Hirose T, Saffer D, Tobin H, the Expedition 348 Scientists (2014) Influence of drilling operations on drilling mud gas monitoring during IODP Exp. 338 and 348 [abstract], EGU General Assembly 2014, abstract # EGU2014-5904

Kopf A, Saffer DM, Davis EE, Hammerschmidt S, LaBonte A, Meldrum R, Toczko S, Lauer R, Heesemann M, Macdonald R, Wheat CG, Jannasch HW, Edwards K, Orcutt B, Haddad A, Villinger H, Araki E, Kitada K, Kimura T, Kido Y (2011) The SmartPlug and GeniusPlug: simple retrievable observatory systems for NanTroSEIZE borehole monitoring. In: Kopf A, Araki E, Toczko S, Expedition 332 Scientists, Proc IODP 332. doi:10.2204/iodp.proc.332.105.2011

Lupi M, Saenger EH, Fuchs F, Miller SA (2013) Lusi mud eruption triggered by geometric focusing of seismic waves. Nat Geosci 6:642–646.

Manga M, Brumm M, Rudolph ML (2009) Earthquake triggering of mud volcanoes. Mar Pet Geol 26:1785–1798.

Pape T, Geprägs P, Hammerschmidt S, Wintersteller P, Wei J, Fleischmann T, Bohrmann G, Kopf AJ (2014) Hydrocarbon seepage and its sources at mud volcanoes of the Kumano forearc basin, Nankai Trough subduction zone. Geochemistry, Geophys Geosystems 15:2180–2194. doi: 10.1002/2013GC005057

Yamada Y, Baba K, Miyakawa A, Matsuoka T (2014) Granular experiments of thrust wedges: Insights relevant to methane hydrate exploration at the Nankai accretionary prism. Mar Pet Geol 51:34–48. doi: 10.1016/j.marpetgeo.2013.11.008

Acknowledgements

ACKNOWLEDGEMENTS

Writing this thesis would have been much harder without the aid of individual people, of which several are mentioned in this chapter. Of course, there were a lot of people on this way who helped me with small but essential things and whom I might have forgotten – I want to thank them no less even if their name does not appear here.

Supervision and Advice

First of all, I want to thank my supervisor Prof. Dr. Achim Kopf who gave me this position in the first place. He was of tremendous help to realize my scientific ideas within the individual research projects. I greatly appreciated his advice, and I am very grateful that he governed me the scientific freedom to follow the tracks I was most interested in.

I also would like to thank Wolfgang Bach, who not only participated actively in my thesis committee, but who also acted as second reviewer for my PhD thesis. During the last three years, he showed great interest in my work, and provided valuable feedback.

Heinrich Villinger, Andre Hüpers, and Eiichiro Araki are as well gratefully acknowledged for taking part in my thesis committee. Their feedback helped me to sort out ideas and their input was of great help in planning the individual steps of my thesis. Eiichiro Araki further provided access to the DONET seismological network and was of great help in data evaluation and discussion.

For their (lab) support, advice, review, and/or valuable technical discussions, I would like to thank (without order): Demian Saffer, Matt Ikari, Thomas Wiersberg, Verena Heuer, Sean Toczko, Ana Maia, Andre Hüpers, Enzio Schnabel, Samuel Niedermann, Jörg Erzinger, Michael Strasser, Matthias Lange, Christian Zöllner, Timo Fleischmann, and Petra Renken.

Funding Agencies

Friends, Colleagues and Family

Working on drilling vessels like *Chikyu* or research vessels like *SONNE* can be very tough. Working days > 12 hours are common, and can be very intense if experienced for months in a confined environment like a ship. I think without the wonderful people I met on Exps. SO-222, 338 and 348, these experiences would have been not as great. For the fun and the support during these expeditions, I would like to thank all my colleagues and the crew who participated. In particular, I want to thank (without order, but some are already mentioned elsewhere): Hiroko Kitajima, Sean Toczko, Maximilian Vahlenkamp, Katelyn Huffman, Susanna Webb, Anja Schleicher, Andre Hüpers, Matt Ikari, Michael Strasser, Emilie Even, Brian Boston, Ana Maia, Patrizia Geprägs, Eri Amsler, Timo Fleischmann, Kazuya Kitada and Maria José Jurado Rodriguez.

I would also like to thank my office mates Frank Ohnemueller, Lera Kirillova, Timo Fleischmann, and Rieke Wielkens, as well as Lea Weiß, Jens Fischer, Katja Hockun, Sebastian Schlenzeck, Kevin Becker, Nicole Syring, Jonathan Lavi, Vasily Alekseev, Ursula Marciniak, Max Vahlenkamp, and Patrizia Geprägs for the fun time inside and outside the office. Without them, the last three years would have been not as great, and finishing up the PhD thesis would have been much tougher.

Last but not least, I would like to thank my family, who served as great role models. Thanks to them I developed inner strength and ambition, two characteristics which helped me enormously to accomplish the goals I set for myself, including this dissertation.

APPENDIX A

Supplementary Material

<div align="center">

CHAPTER A.1

APPENDIX FOR MANUSCRIPT II –

LIMITATION OF FLUID FLOW AT THE NANKAI TROUGH MEGASPLAY FAULT ZONE

</div>

TIDAL RESPONSE MODEL

[1] Pressure in the formation is described via the non-dimensionalized cylindrical flow equation (Sawyer et al. 2008):

$$\frac{\delta P_D}{\delta t_D} = \frac{\delta^2 P_D}{\delta r_D^2} + \frac{1}{r_D}\frac{\delta P_D}{\delta r_D} + \Xi_D(t_D) \tag{S.1}$$

with P_D being the dimensionless pressure, r_D is the dimensionless radius, and t_D is the dimensionless time. The source term Ξ_D is necessary to describe the sinusoidal changes in the formation pressure and is defined as:

$$\Xi_D(t_D) = \omega_D \cos(\omega_D t_D) \tag{S.2}$$

with ω_D being the dimensionless frequency which can be derived by:

$$\omega_D = \frac{a^2\omega}{c} = \frac{a^2 2\pi}{tc} \tag{S.3}$$

where a is the screen radius, c is the hydraulic diffusivity and t is the period of a diurnal tidal frequency; here, 24 h (i.e. S_1 or "solar diurnal") was taken.

[2] Since Ξ_D describes a propagating sinusoidal wave, the problem can be fundamentally solved by using Kelvin functions (i.e. modified Bessel functions of the first and second kind). Based on the solutions of Sawyer et al. (2008) and Hsieh et al. (1987), the amplitude response A and the phase shift ϕ can then be determined by:

$$A = \frac{1}{\sqrt{E^2 + F^2}} \tag{S.4}$$

$$\phi = -\operatorname{atan}\frac{F}{E} \tag{S.5}$$

The imaginary parts E and F are defined as:

$$E = 1 - \frac{\omega_\mathrm{D}}{\beta_\mathrm{D}} [\Psi \mathrm{Ker}(\sqrt{\omega_\mathrm{D}}) + \Phi \mathrm{Kei}(\sqrt{\omega_\mathrm{D}})] \qquad \text{(S.6)}$$

$$F = \frac{\omega_\mathrm{D}}{\beta_\mathrm{D}} [\Phi \mathrm{Ker}(\sqrt{\omega_\mathrm{D}}) + \Psi \mathrm{Kei}(\sqrt{\omega_\mathrm{D}})] \qquad \text{(S.7)}$$

with

$$\Phi = \frac{-\mathrm{Ker}_1(\sqrt{\omega_\mathrm{D}}) + \mathrm{Kei}_1(\sqrt{\omega_\mathrm{D}})}{\sqrt{2\omega_\mathrm{D}}\mathrm{Ker}_1^2(\sqrt{\omega_\mathrm{D}}) + \mathrm{Kei}_1^2(\sqrt{\omega_\mathrm{D}})} \qquad \text{(S.8)}$$

$$\Psi = \frac{-\mathrm{Ker}_1(\sqrt{\omega_\mathrm{D}}) - \mathrm{Kei}_1(\sqrt{\omega_\mathrm{D}})}{\sqrt{2\omega_\mathrm{D}}\mathrm{Ker}_1^2(\sqrt{\omega_\mathrm{D}}) + \mathrm{Kei}_1^2(\sqrt{\omega_\mathrm{D}})} \qquad \text{(S.9)}$$

Ker(x) and Kei(x) are the real and imaginary part of Kelvin functions of order 0, whereas Ker$_1(x)$ and Kei$_1(x)$ are the real and imaginary part of Kelvin functions of order 1. Modelling took place for compliance ratios in the order of $10^{-4} - 10^4$ and hydraulic diffusivities in the range of $10^{-10} - 10^{-2}$ m^{2}s^{-1}.

[3] Beside the modelling approach it is possible to generate an estimation of the amplitude and phase response based on SmartPlug instrument specifications and the borehole dimensions (Sawyer et al. 2008). Therefore it is first necessary to compute the system compressibility β of the instrument which is here simply the sum of β_w and β_steel, i.e. the fluid and steel compressibility, respectively:

$$\beta = \beta_\mathrm{w} + \beta_\mathrm{steel} \left[\frac{r_\mathrm{to}}{(r_\mathrm{to} - r_\mathrm{ti})} + \frac{r_\mathrm{co}}{(r_\mathrm{co} - r_\mathrm{ci})} + \frac{r_\mathrm{so}}{(r_\mathrm{so} - r_\mathrm{si})} \right] \qquad \text{(S.10)}$$

where r_to and r_ti are the outer and inner radius of the hydraulic tubing, r_co and r_ci are the outer and inner radius of the casing and r_so and r_si are the outer and inner radius of the screens. The relationship between formation compressibility m_f and the system compressibility β is then represented by the formation-instrument compliance ratio β_D:

$$\beta_\mathrm{D} = \frac{2\pi r_\mathrm{so}^2 h m_\mathrm{f}}{\beta V} \qquad \text{(S.11)}$$

with

$$V = \pi(r_\mathrm{so}^2 - r_\mathrm{si}^2)h + \pi r_\mathrm{ti}^2 L_\mathrm{t} \qquad \text{(S.12)}$$

[4] Following Sawyer et al. (2008), the volume V is the sum of the screen volume (first term) and the volume of the hydraulic tubing (second term). The variables h and βV are the screen height and the wellbore storage, r_{so}, r_{si} and r_{ti} are the outer screen, inner screen and inner tubing radii respectively, and L_t is the length of the hydraulic tubing. The defined variables are listed in Table S.1 of the supplementary material.

PERMEABILITY MEASUREMENTS

[5] The pressure permeameter set-up is displayed in Fig. S.2 of the supplementary material, and consists of a test cell, which hosts the sample specimen. The cell is filled with de-aired water, and connected to one headwater and one tailwater burette, which are filled with de-aired, de-ionized water, via seawater/de-ionized water medium decollators. Confining pressure inside the test cell is build up and independently, a pressure gradient was applied to the sample. The pressure gradient was applied via 2-channel pressure regulators, which control the pressure in the burettes. The pressure is forwarded in the chamber with de-ionized water in the medium decollator, which causes the membrane that separates the de-ionized water from the seawater to expand. Consequently, the pressure in the chamber filled with seawater is increased, forcing seawater to migrate through the specimen. This is essential due to the clayey nature of the samples. If de-ionized water would migrate through the latter, weakly bound ions are leached off the clay minerals, leading to an increase in thickness of the viscous bound water layer and thus to an artificial decrease in permeability (Olsen and Daniel 1981). Water exchange between the specimen and the de-ionized water in the test cell is hindered by a rubber membrane surrounding the specimen and the filters as well as by the upper pore pressure cap which sits on top of the specimen.

[6] Flow-through experiments were conducted under effective stresses of 0.5 MPa, 1.0 MPa and 1.5 MPa. The permeability is then calculated based on the volume change in the head- and tailwater burettes, which allows the determination of the flow rate. The latter together with the cross-sectional area of the sample and the applied pressure gradient allowed the calculation of the hydraulic conductivity using Darcy's law (e.g. Rowe et al. 2011, see below).

[7] Intrinsic permeability is defined by rock properties alone, whereas hydraulic conductivity accounts also for the fluid properties. To a smaller or greater extent, both parameters have certain weaknesses in adequately reflecting the hydrogeological response of a formation, because flow and transport connectivity can be established although high permeability structures may be absent (Sánchez-Vila et al. 1996; Fogg et al. 2000; Knudby and Carrera 2006). Based on Knudby and Carrera (2006), the hydraulic diffusivity was chosen in the present case (cf. below).

[8] After determination of the volume change in the head- and tailwater burettes, the flow rate can be calculated. The latter together with the cross-sectional area of the sample and the applied pressure gradient allowed the calculation of the hydraulic conductivity using Darcy's law (e.g. Rowe et al. 2011):

$$K = -\frac{Q\Delta L}{A\Delta h}$$

(S.13)

where Q is the measured flow rate in $m^3\,s^{-1}$, K is the hydraulic conductivity in $m\,s^{-1}$, A is the cross-sectional area, Δh is the difference in head across the sample in meters and ΔL is the length of the sample in meters. The difference in head is related to the pressure difference ΔP by:

$$\Delta h = \Delta z + \frac{\Delta P}{\rho g}$$

(S.14)

with ρ being the fluid density, g being the gravitational constant (i.e. 9.81 m s^{-2}) and Δz being the elevation difference between sample input and output locations (thus, here, $\Delta z = \Delta L$). Following the assumptions of Rowe et al. (2011), the volume and density change caused by the applied pressure itself is below 0.1 % and therefore, it can be neglected. The intrinsic permeability k is then derived by:

$$k = \frac{K\mu}{\rho g}$$

(S.15)

where μ is the dynamic fluid viscosity for water with a temperature of 20 °C and a salinity of 35 kg m^{-3}, i.e. 0.0010432 Ns m^{-2} (Kestin et al. 1981). The hydraulic diffusivity was calculated by means of Eq. 7 given in sub-chapter "Determining the Tidal Loading Efficiency and Formation Properties" of the main article.

SUPPLEMENTARY FIGURES
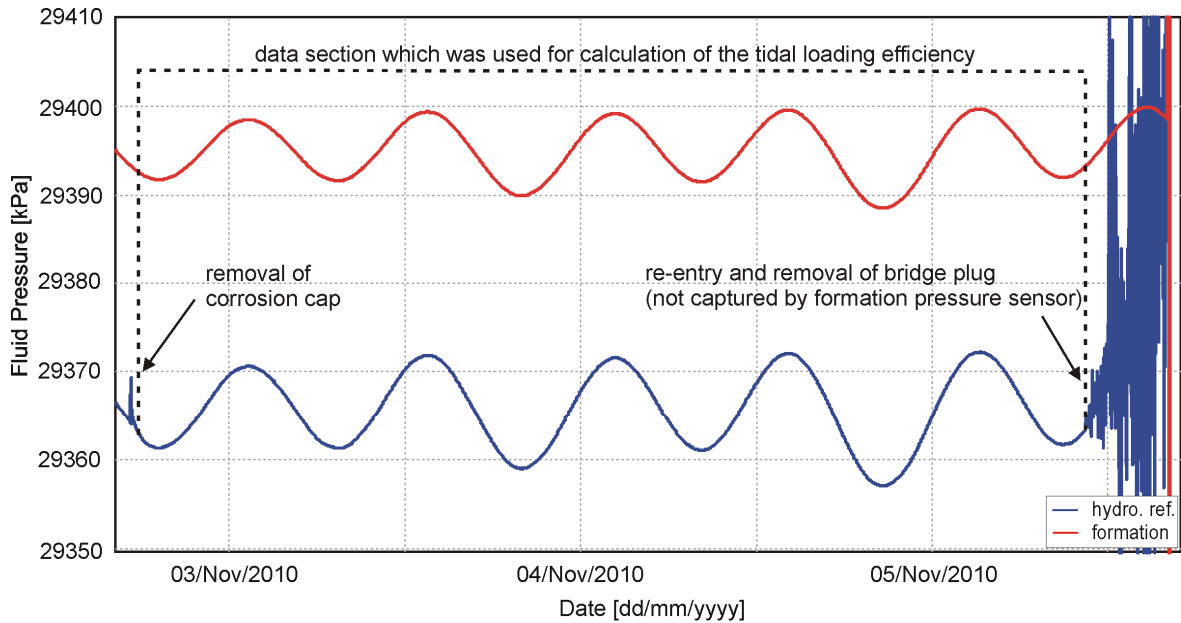
Figure S.1: Section of the fluid pressure data monitored by the SmartPlug borehole observatory (modified from Hammerschmidt et al. 2013). For calculation of the tidal loading efficiency, the time period between corrosion cap removal and removal of the bridge plug was chosen. The sinusiodal variations in the pressure data indicate the influence of (semi-)diurnal tidal signals.
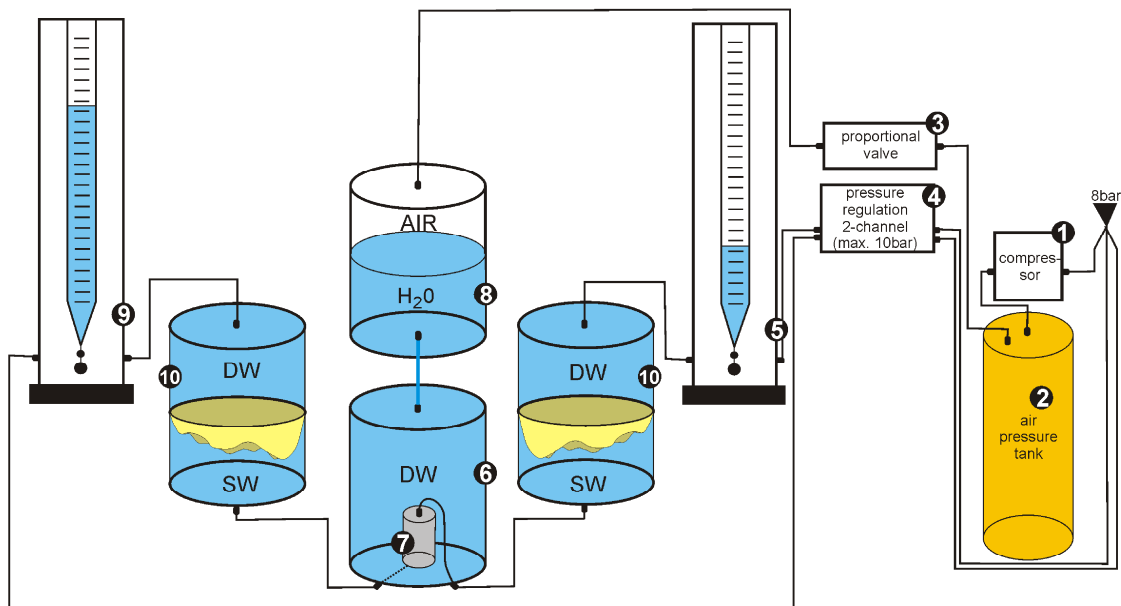
Figure S.2: Schematic of the high-pressure permeability test. (1) Air pressure booster x4 (2) Air pressure tank (3) Air pressure regulating proportional valve, 1-channel (4) Air pressure regulator, 2-channels (5) Tailwater burette (6) Test cell (7) Test specimen inside flexible membrane (8) Medium decollator (air/water) (9) Headwater burette (10) Medium decollator (de-ionized and de-aired water (DW)/seawater (SW)) (modified from Anna Reusch, Geological Institute, ETH Zurich, personal communication, 2012)
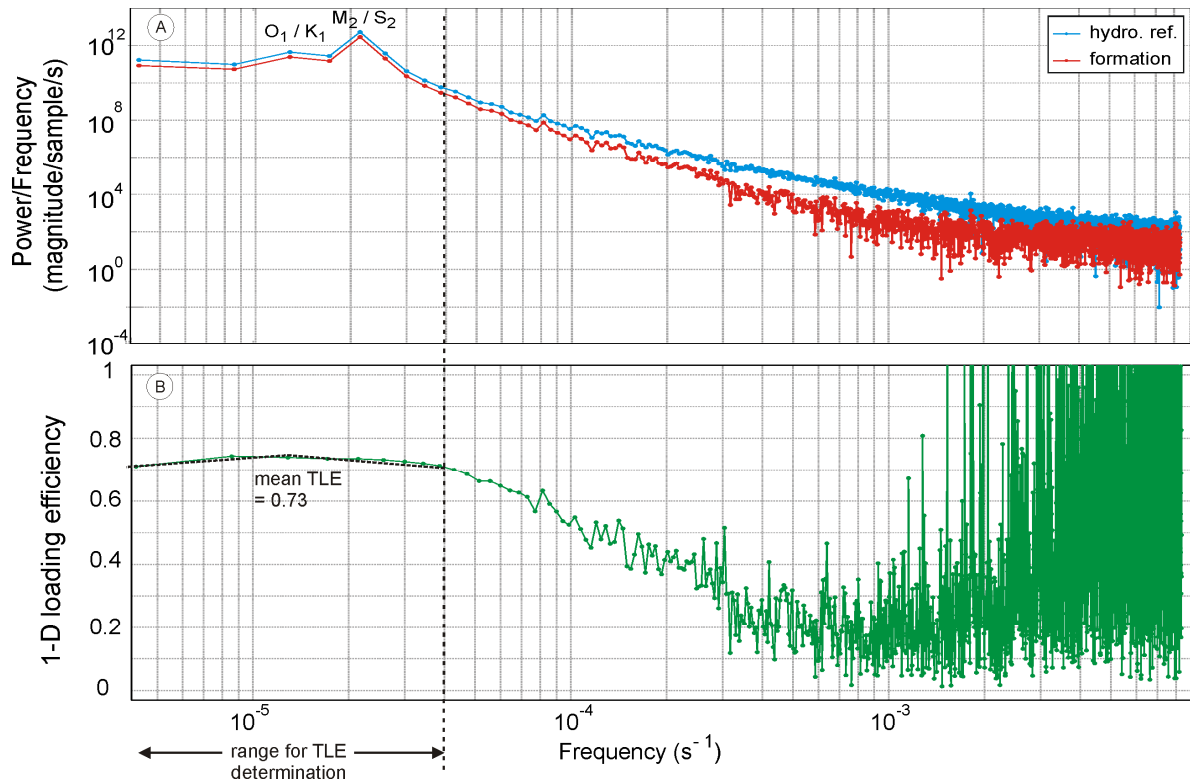
Figure S.3: *(A) Power spectral density (PSD) for the unprocessed SmartPlug fluid pressure data from 02 November - 05 November 2010. The blue and red lines indicate the PSD for the hydrostatic reference and formation pressures respectively. The diurnal (O_1, K_1) and semidiurnal (S_2, M_2) frequencies have the highest energy, whereas for higher frequencies the noise is steadily increasing and the power is decreasing (see the main text, sub-chapter "Formation properties at Site C0010", for further explanations). However, the diurnal frequencies have only a small magnitude due to the short time period. Also, a clear distinction between the diurnal and semidiurnal frequencies themselves is not possible due to the low sampling frequency of the SmartPlug. (B) Tidal loading efficiency (TLE) for the unprocessed SmartPlug fluid pressure data for 02 November - 05 November 2010. For determination of the TLE, only frequencies smaller or equal to 4×10^{-5} s^{-1} were considered*

SUPPLEMENTARY TABLES

Table S.1: *Overview of SmartPlug engineering specifications and constants for calculation of the formation instrument compliance ratio and the hydrogeologic and poroelastic properties*

Variable	Definition	Dimension
r_{to}	tubing outer radius	0.0032 m
r_{ti}	tubing inner radius	0.0023 m
r_{ci}	casing inner radius	0.1122 m
r_{co}	casing outer radius	0.1222 m
r_{si}	screens inner radius	0.1222 m
r_{so}	screens outer radius	0.1422 m
L_t	tubing length	1.30 m
h	screen height	18.4 m
β_w	fluid compressibility	4.0×10^{-10} Pa^{-1}
β_{steel}	steel compressibility	5.0×10^{-12} Pa^{-1}
β_s	grain compressibility	2.0×10^{-11} Pa^{-1}
T	borehole temperature	18.9 °C
ρ	fluid density	1024 kg m^{-3}
n	formation porosity	0.38
v	Poisson's ratio	0.1

Table S.2: *Overview of the results for the permeability (variable k) measurements and corresponding hydraulic conductivity (variable K) and hydraulic diffusivity (variable c).*

Sample	Depth [mbsf]	Orientation	Effective Stress [MPa]	k [m^2]	K [m s^{-1}]	c [m^2 s^{-1}]
C0004D-54R-2 W	388.070	vertical	0.5	5.9×10^{-17}	5.6×10^{-10}	3.7×10^{-5}
			1.0	7.3×10^{-17}	6.9×10^{-10}	4.6×10^{-5}
			1.5	6.2×10^{-17}	5.8×10^{-10}	3.9×10^{-5}
	388.255	horizontal	0.5	1.9×10^{-15}	1.8×10^{-8}	1.2×10^{-3}
			1.0	2.5×10^{-16}	2.5×10^{-9}	1.7×10^{-4}
			1.5	1.2×10^{-16}	1.2×10^{-9}	7.7×10^{-5}
C0004D-54R-2 W	389.020	vertical	0.5	2.4×10^{-17}	2.2×10^{-10}	1.5×10^{-5}
			1.0	3.4×10^{-17}	3.2×10^{-10}	2.2×10^{-5}
			1.5	2.6×10^{-17}	2.4×10^{-10}	1.6×10^{-5}
		horizontal	0.5	1.1×10^{-16}	9.9×10^{-10}	6.6×10^{-5}
			1.0	1.2×10^{-16}	1.2×10^{-09}	7.7×10^{-5}
			1.5	9.3×10^{-17}	8.8×10^{-10}	5.9×10^{-5}
C0006E-37X-2 W	288.435	vertical	0.5	1.6×10^{-17}	1.5×10^{-10}	1.0×10^{-5}
			1.0	1.4×10^{-17}	1.3×10^{-10}	8.5×10^{-6}
			1.5	1.6×10^{-17}	1.5×10^{-10}	9.9×10^{-6}
		horizontal	0.5	3.1×10^{-17}	2.9×10^{-10}	2.0×10^{-5}
			1.0	1.9×10^{-17}	1.9×10^{-10}	1.2×10^{-5}
			1.5	2.2×10^{-17}	2.1×10^{-10}	1.4×10^{-5}
C0006E-42X-2 W	337.245	vertical	0.5	2.3×10^{-17}	2.1×10^{-10}	1.4×10^{-5}
			1.0	1.8×10^{-17}	1.7×10^{-10}	1.1×10^{-5}
			1.5	2.0×10^{-17}	1.9×10^{-10}	1.3×10^{-5}
		horizontal	0.5	5.6×10^{-17}	5.3×10^{-10}	3.5×10^{-5}
			1.0	4.6×10^{-17}	4.3×10^{-10}	2.9×10^{-5}
			1.5	4.3×10^{-17}	2.1×10^{-10}	2.7×10^{-5}
C0006E-46X-4 W	376.770	vertical	0.5	1.2×10^{-17}	1.1×10^{-10}	7.3×10^{-6}
			1.0	8.2×10^{-18}	7.7×10^{-11}	5.1×10^{-6}
			1.5	9.5×10^{-18}	9.0×10^{-11}	6.0×10^{-6}
		horizontal	0.5	5.8×10^{-17}	5.5×10^{-10}	3.6×10^{-5}
			1.0	4.4×10^{-17}	4.1×10^{-11}	2.8×10^{-5}
			1.5	3.3×10^{-17}	3.1×10^{-11}	2.0×10^{-5}
C0006E-47X-4 W	386.405	vertical	0.5	4.0×10^{-17}	3.8×10^{-10}	2.5×10^{-5}
			1.0	2.9×10^{-17}	7.7×10^{-11}	1.8×10^{-5}
			1.5	2.6×10^{-17}	2.5×10^{-10}	1.7×10^{-5}
		horizontal	0.5	1.1×10^{-16}	9.8×10^{-10}	6.6×10^{-5}
			1.0	5.1×10^{-17}	4.8×10^{-10}	3.2×10^{-5}
			1.5	3.4×10^{-17}	3.2×10^{-10}	1.2×10^{-5}
C0006E-49X-1 W	401.370	vertical	0.5	3.3×10^{-18}	3.1×10^{-11}	2.1×10^{-6}
			1.0	1.8×10^{-17}	1.7×10^{-10}	1.1×10^{-5}
			1.5	4.7×10^{-18}	4.4×10^{-11}	3.0×10^{-6}
		horizontal	0.5	3.9×10^{-17}	3.7×10^{-10}	2.4×10^{-5}
			1.0	2.7×10^{-16}	2.5×10^{-10}	1.7×10^{-4}
			1.5	1.5×10^{-17}	1.4×10^{-10}	9.3×10^{-6}
C0006F-09R-1 W	466.670	vertical	0.5	2.8×10^{-17}	2.6×10^{-10}	1.7×10^{-5}
			1.0	2.0×10^{-17}	1.9×10^{-10}	1.2×10^{-5}
			1.5	2.1×10^{-17}	2.0×10^{-10}	1.3×10^{-5}
		horizontal	0.5	1.4×10^{-17}	1.4×10^{-10}	9.0×10^{-6}
			1.0	2.2×10^{-17}	2.0×10^{-10}	1.4×10^{-4}
			1.5	1.5×10^{-17}	1.4×10^{-10}	9.5×10^{-6}
C0006F-11R-1 W	485.650	vertical	0.5	1.2×10^{-15}	1.1×10^{-8}	7.4×10^{-4}
		horizontal	0.5	8.8×10^{-18}	8.6×10^{-11}	5.8×10^{-5}
			1.0	2.0×10^{-17}	1.9×10^{-10}	1.3×10^{-5}
			1.5	1.9×10^{-17}	1.8×10^{-10}	1.2×10^{-5}
C0006F-18R-1 W	552.310	vertical	0.5	1.2×10^{-17}	1.1×10^{-10}	7.6×10^{-6}
			1.0	4.7×10^{-18}	4.4×10^{-11}	3.0×10^{-6}
			1.5	4.1×10^{-18}	3.9×10^{-11}	2.6×10^{-6}

References

Fogg GE, Carle SF, Green C (2000) Connected-network paradigm for the alluvial aquifer system. In: Zhang D, Winter CL (Eds.), Theory, Modelling, and Field Investigation in Hydrogeology: A Special Volume in Honor of Shlomo P. Neuman's 60th Birthday, Boulder, Colorado, GSA Special Paper 348: 25 - 42

Hammerschmidt S, Davis EE, Kopf A (2013) Fluid pressure and temperature transients detected at the Nankai Trough Megasplay Fault: Results from the SmartPlug borehole observatory. Tectonophysics 600:116 – 133. doi: 10.1016/j.tecto.2013.02.010

Hsieh PA, Bredehoeft JD, Farr JM (1987) Determination of aquifer transmissivity from Earth tide analysis. Water Resour Res 23: 1824-1832

Kestin J, Khalifa HE, Correia RJ (1981) Tables of the dynamic and kinematic viscosity of aqueous NaCl solutions in the temperature range 20-150 °C and the pressure range 0.1-35 MPa. Journal of Physical and Chemical Reference Data 10: 71-88

Knudby C, Carrera J (2006) On the use of apparent hydraulic diffusivity as an indicator of connectivity. J Hydrol 329: 377-389

Olsen RE, Daniel DE (1981) Measurement of the Hydraulic Conductivity of Fine-Grained Soils. In: Zimmie TF, Riggs CO (eds) Permeability and Groundwater Contaminant Transport. American Society for Testing of Materials, STP, pp 18 - 64

Rowe K, Screaton, E. Guo, J. Underwood MB (2011) Data report: permeabilities of sediments from the Kumano Basin transect off Kii Peninsula, Japan. In: Kinoshita M, Tobin H, Ashi J, Kimura G, Lallemant S, Screaton EJ, Curewitz D, Masago H, Moe KT, Expedition 314/315/316 Scientists, Proc IODP 314/315/316. Integrated Ocean Drilling Program Management International, Washington, DC. doi: 10.2204/iodp.proc.314315316.211.2011

Sánchez-Vila X, Carrera J, Girardi JP (1996) Scale effects in transmissivity. J Hydrol 183: 1-22

Sawyer AH, Flemings P, Elsworth D, Kinoshita M (2008) Response of submarine hydrologic monitoring instruments to formation pressure changes: Theory and application to Nankai advanced CORKs. J Geophys Res 113: B01102. doi: 10.1029/2007jb005132

CHAPTER A.2

APPENDIX FOR MANUSCRIPT III –
BOREHOLE FLUID PRESSURE RESPONSE TO NON-VOLCANIC TREMOR

LFE LOCALIZATION

[1] LFE were localized using the envelope correlation method (Obara 2002; Obara et al. 2004; Maeda and Obara 2009; Obana and Kodaira 2009). After filtering of the waveforms and calculating an envelope using an Hilbert transform, the following two steps were carried out (Figures S.4 – S.12): (1) during every tremor and for each station pair, an arrow was drawn, pointing to the station where the LFE arrived first, and (2) σ_t^2 was determined for every station pair at every grid point, and where more than three station pairs had $\sigma_t^2 \leq 0.5$, the potential epicenter was plotted. Possible epicenters were further investigated by the "weighted density", ρ_w. This weighing factor was determined by dividing the study area into equally spaced rectangles of 0.2° spacing, and for each rectangular, the incidence of epicenters with ≥ 3 was counted. Epicenters supported by more than three station pairs were given a greater weight by multiplying them with absolute values (Table S.3). Here, ρ_w is then defined as the total (weighted) number of epicenters per rectangular. Hypocenter determination is not possible with the method used here.

Table S.3 : Calculation of weighted density

Number of station pairs with $\sigma_t^2 \leq 0.5$	Count Added to Total Number of Stations
3	1
4	2
5	3
6	4
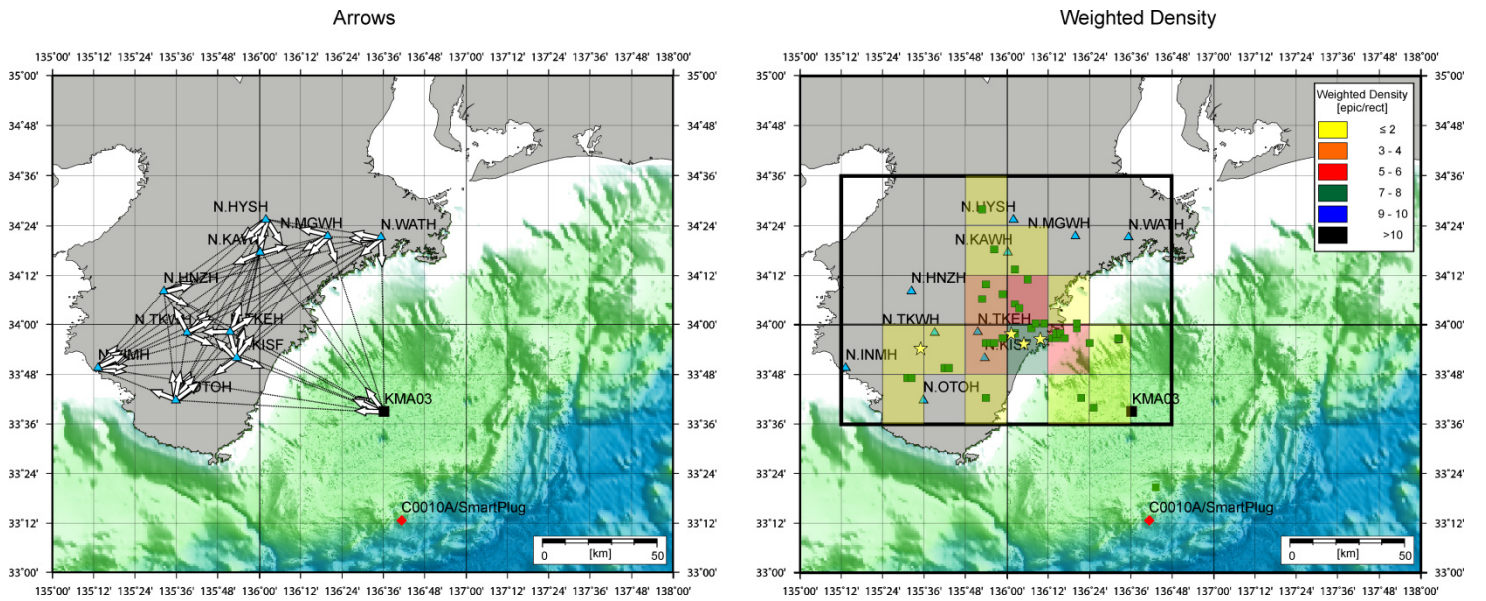
Figure S.4*: Localization of low-frequency earthquake which occurred on 14 Aug 2010, 00:23 – 00:25.* ***Left:*** *Map showing the localization carried out graphically by arrows drawn for individual station pairs. The arrow points to the station where the LFE was visible first.* ***Right:*** *weighted density for patches of 0.2° spacing. Darker colors indicate higher weighted density. Green rectangles: number of successful localizations = 3; yellow stars: number of successful localizations = 4; blue stars: number of successful localizations ≥ 5.*
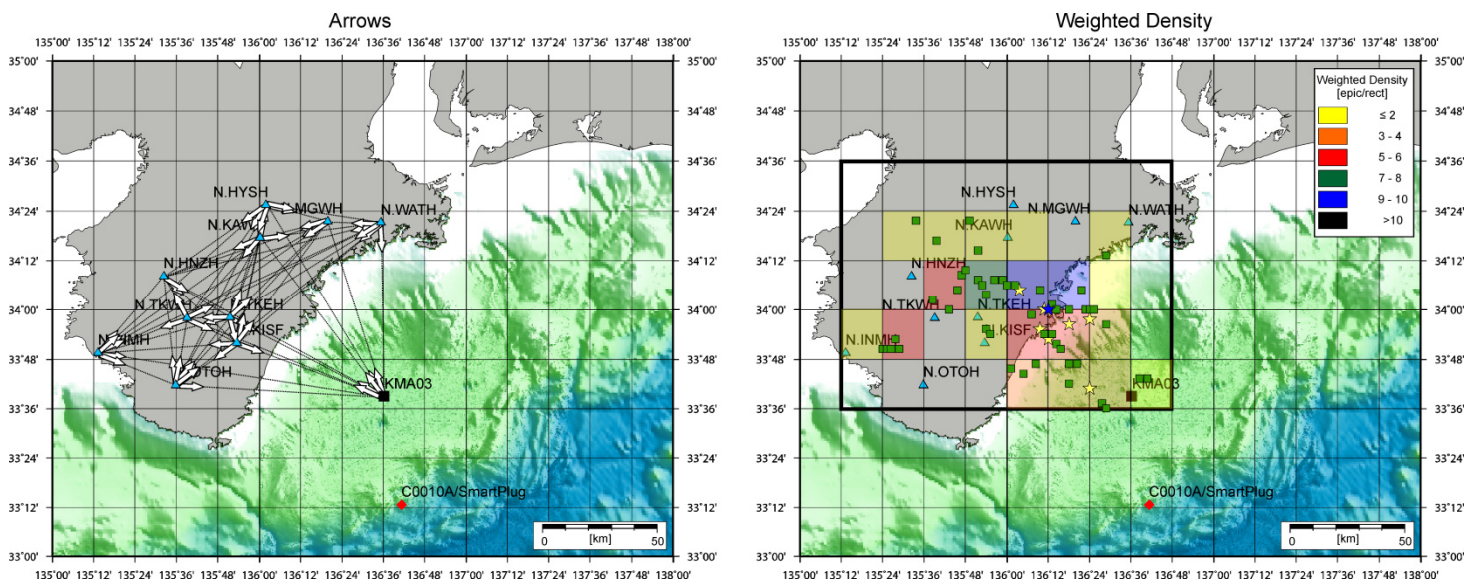
Figure S.5*: Localization of low-frequency earthquake which occurred on 14 Aug 2010, 00:31 – 00:34.* ***Left:*** *Map showing the localization carried out graphically by arrows drawn for individual station pairs. The arrow points to the station where the LFE was visible first.* ***Right:*** *weighted density for patches of 0.2° spacing. Darker colors indicate higher weighted density. Green rectangles: number of successful localizations = 3; yellow stars: number of successful localizations = 4; blue stars: number of successful localizations ≥ 5.*

Figure S.6*: Localization of low-frequency earthquake which occurred on 14 Aug 2010, 00:43 – 00:46. **Left:** Map showing the localization carried out graphically by arrows drawn for individual station pairs. The arrow points to the station where the LFE was visible first. **Right:** weighted density for patches of 0.2° spacing. Darker colors indicate higher weighted density. Green rectangles: number of successful localizations = 3; yellow stars: number of successful localizations = 4; blue stars: number of successful localizations ≥ 5.*

Figure S.7*: Localization of low-frequency earthquake which occurred on 14 Aug 2010, 00:51 – 00:53. **Left:** Map showing the localization carried out graphically by arrows drawn for individual station pairs. The arrow points to the station where the LFE was visible first. **Right:** weighted density for patches of 0.2° spacing. Darker colors indicate higher weighted density. Green rectangles: number of successful localizations = 3; yellow stars: number of successful localizations = 4; blue stars: number of successful localizations ≥ 5.*

Figure S.8: *Localization of low-frequency earthquake which occurred on 14 Aug 2010, 00:53 – 00:56. **Left:** Map showing the localization carried out graphically by arrows drawn for individual station pairs. The arrow points to the station where the LFE was visible first. **Right:** weighted density for patches of 0.2° spacing. Darker colors indicate higher weighted density. Green rectangles: number of successful localizations = 3; yellow stars: number of successful localizations = 4; blue stars: number of successful localizations ≥ 5.*
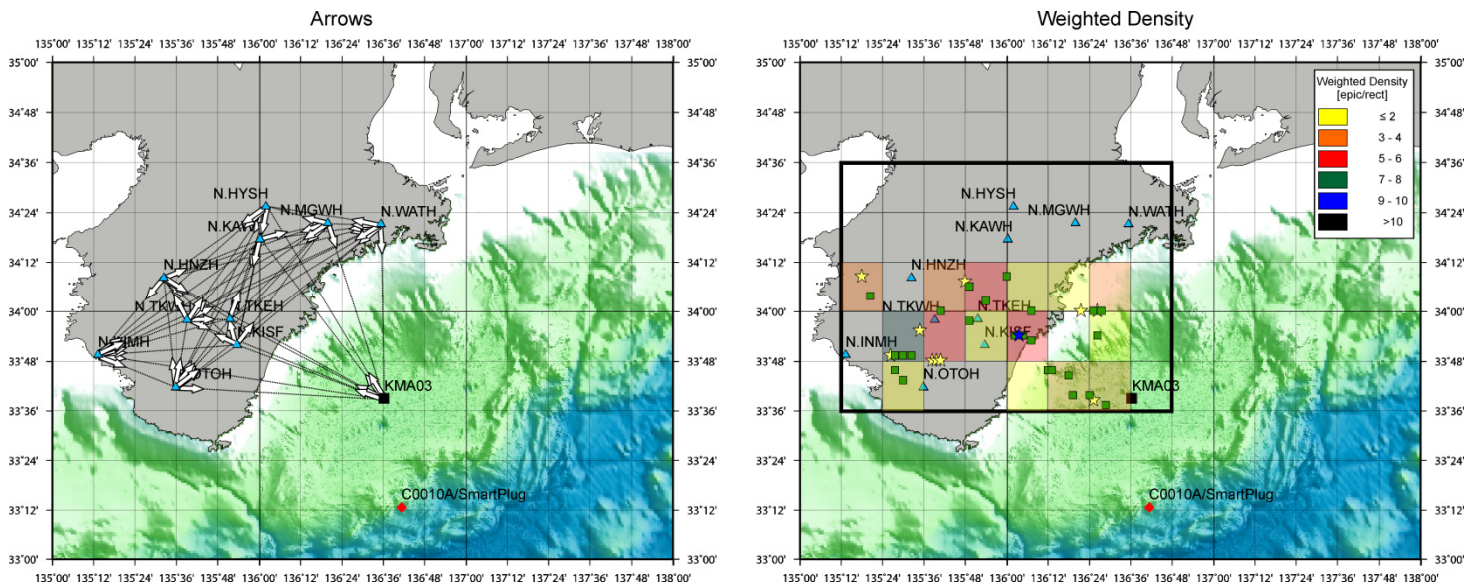

Figure S.9 : *Localization of low-frequency earthquake which occurred on 14 Aug 2010, 00:56 – 00:59. **Left:** Map showing the localization carried out graphically by arrows drawn for individual station pairs. The arrow points to the station where the LFE was visible first. **Right:** weighted density for patches of 0.2° spacing. Darker colors indicate higher weighted density. Green rectangles: number of successful localizations = 3; yellow stars: number of successful localizations = 4; blue stars: number of successful localizations ≥ 5.*
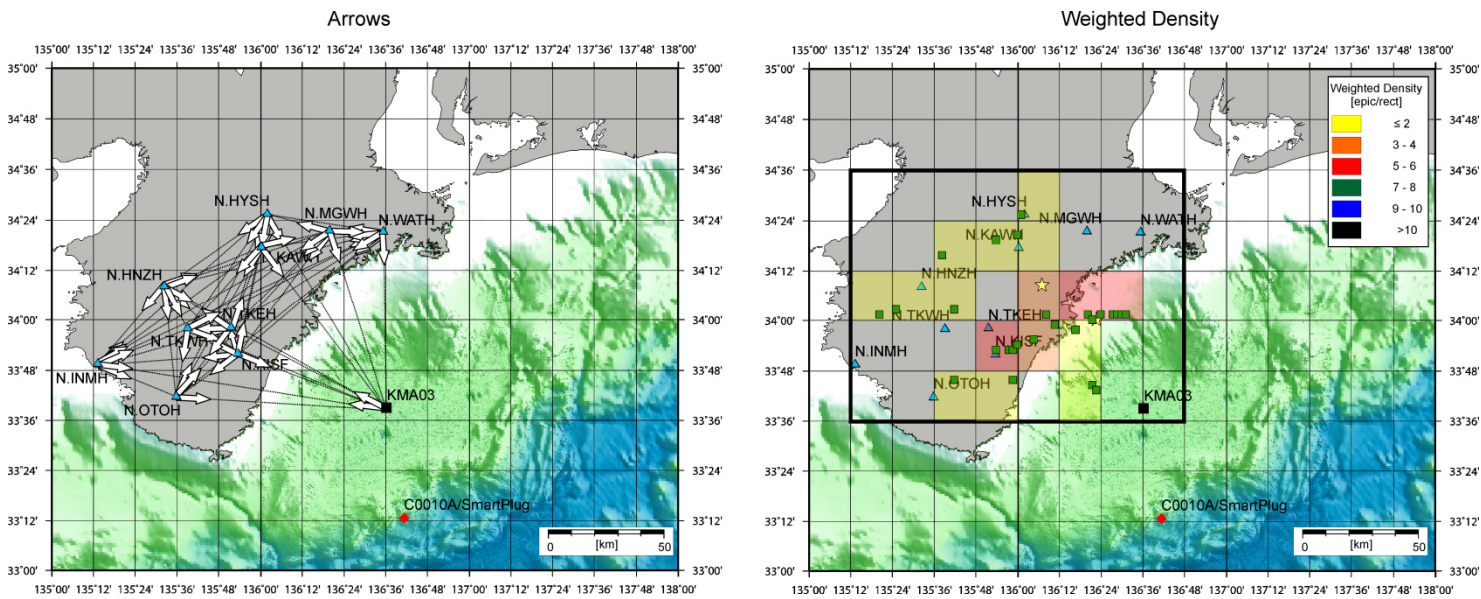
Figure S.10 *: Localization of low-frequency earthquake which occurred on 14 Aug 2010, 01:01 – 01:03.* **Left:** *Map showing the localization carried out graphically by arrows drawn for individual station pairs. The arrow points to the station where the LFE was visible first.* **Right:** *weighted density for patches of 0.2° spacing. Darker colors indicate higher weighted density. Green rectangles: number of successful localizations = 3; yellow stars: number of successful localizations = 4; blue stars: number of successful localizations ≥ 5.*
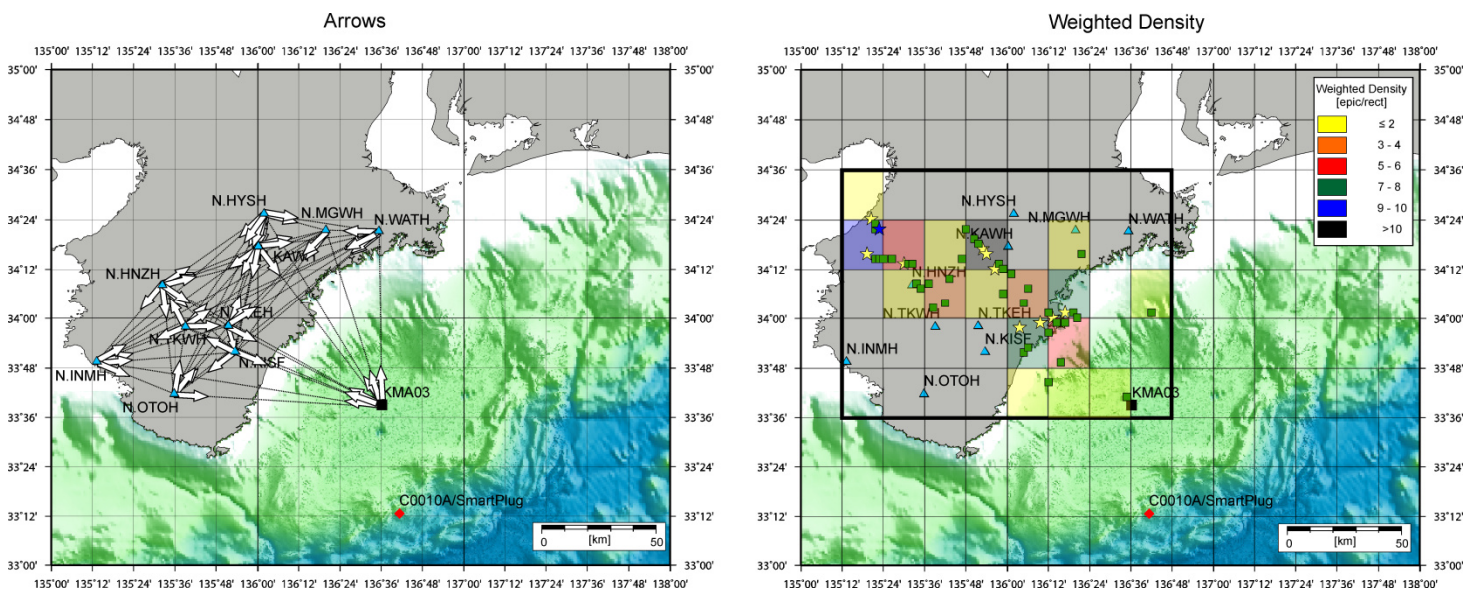
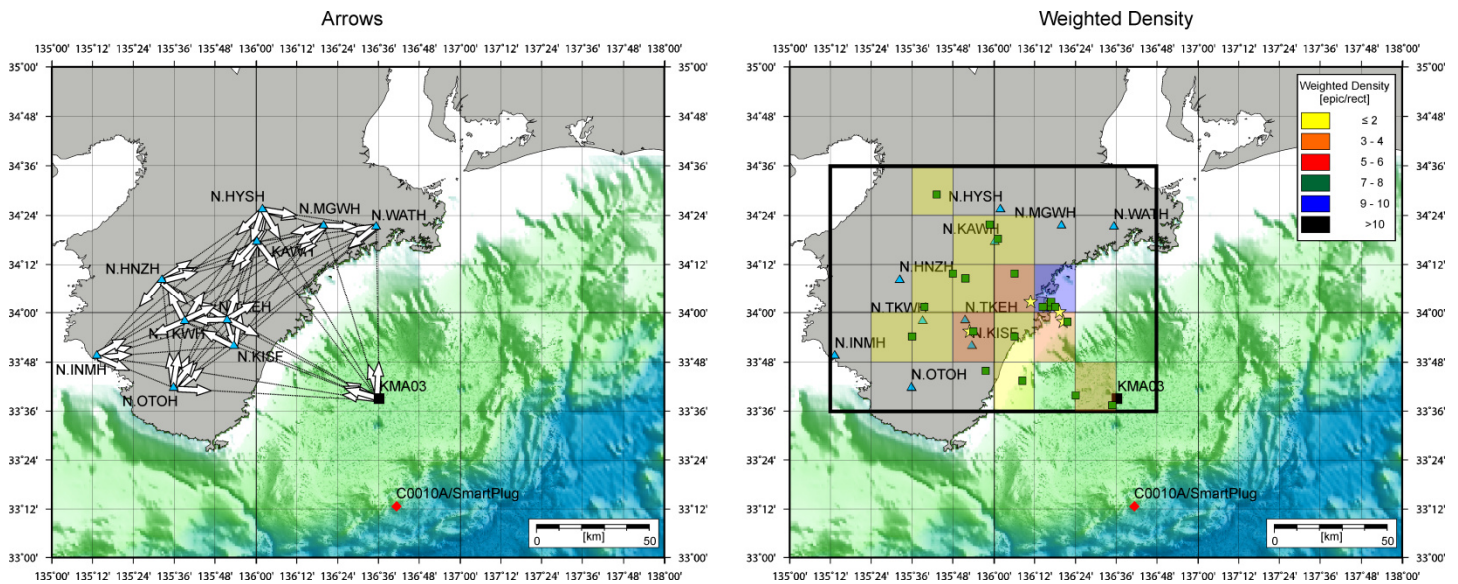***Figure S.11****: Localization of low-frequency earthquake which occurred on 14 Aug 2010, 01:03 – 01:05.* **Left:** *Map showing the localization carried out graphically by arrows drawn for individual station pairs. The arrow points to the station where the LFE was visible first.* **Right:** *weighted density for patches of 0.2° spacing. Darker colors indicate higher weighted density. Green rectangles: number of successful localizations = 3; yellow stars: number of successful localizations = 4; blue stars: number of successful localizations ≥ 5.*
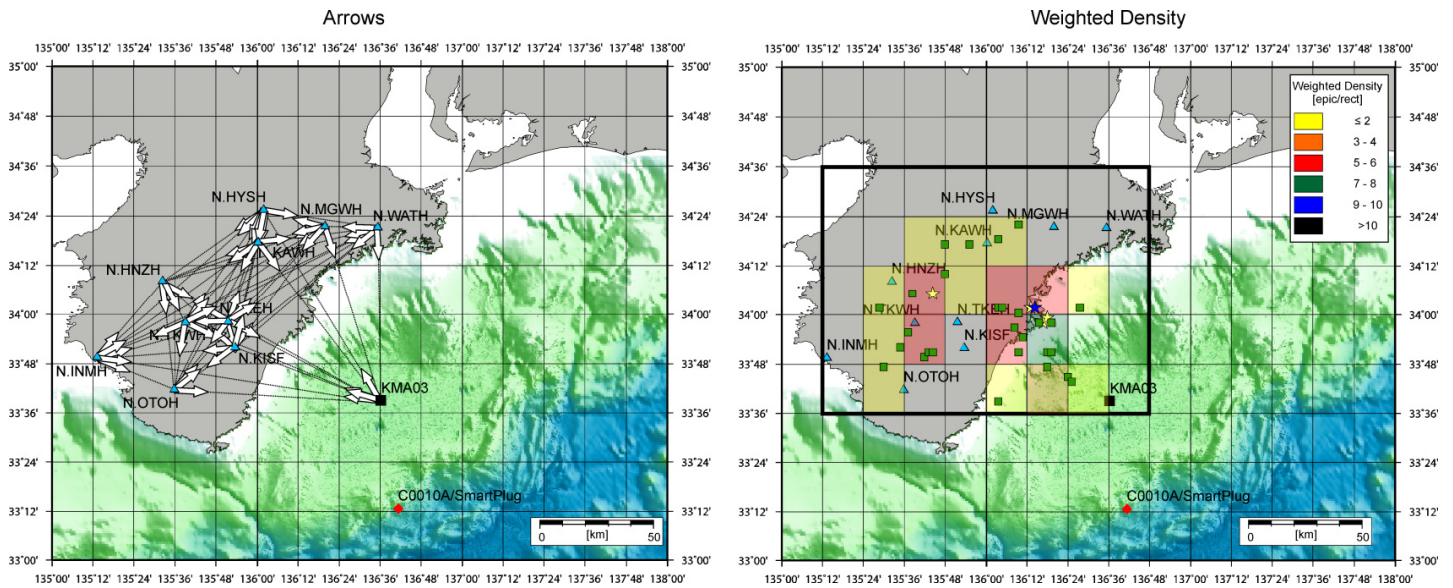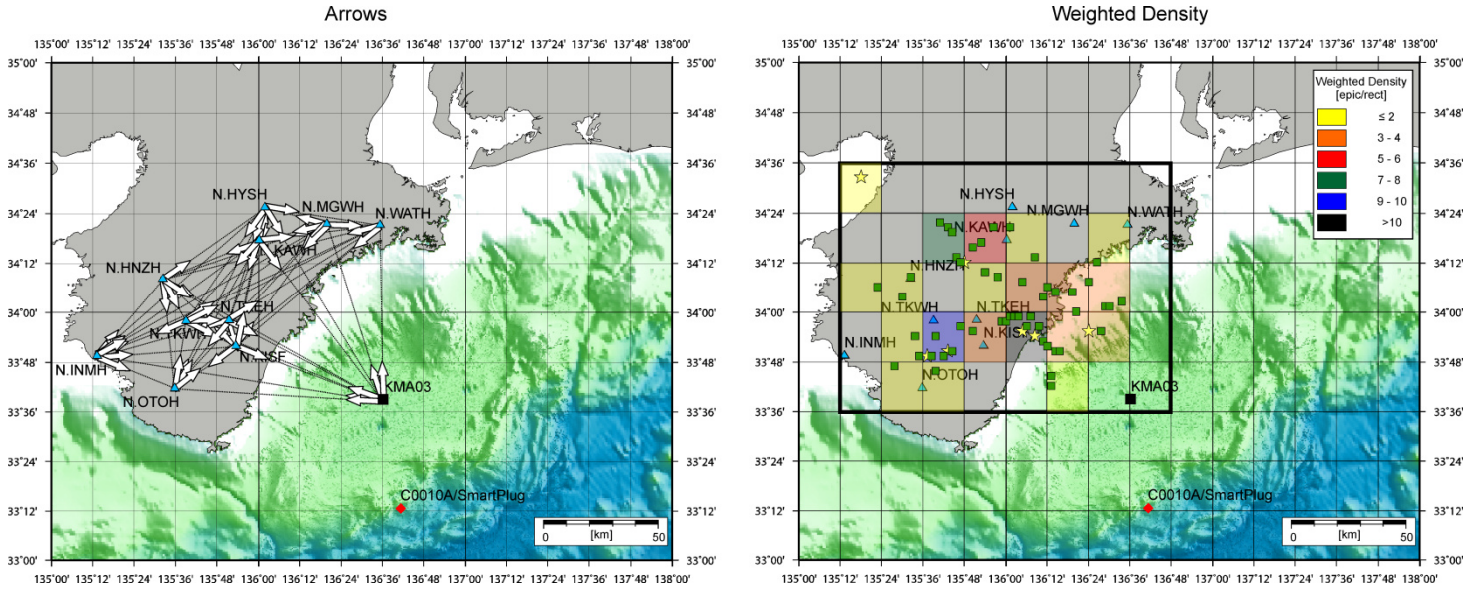
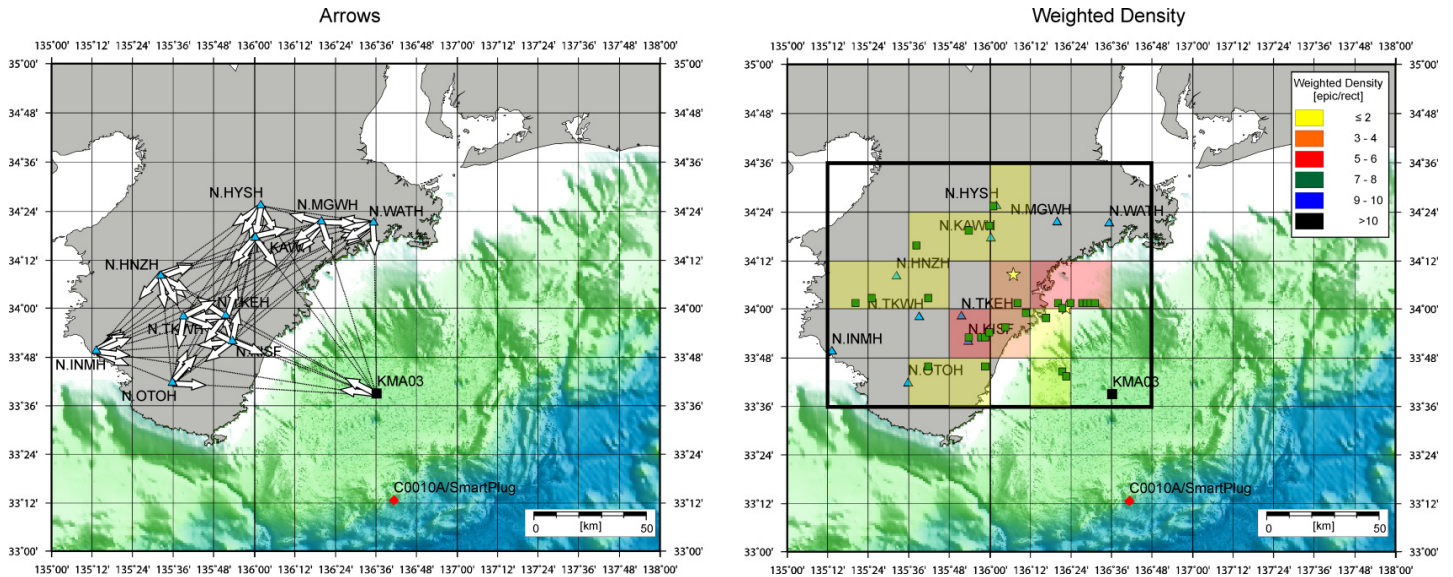**Figure S.12**: *Localization of low-frequency earthquake which occurred on 14 Aug 2010, 01:25 – 01:27.* **Left:** *Map showing the localization carried out graphically by arrows drawn for individual station pairs. The arrow points to the station where the LFE was visible first.* **Right:** *weighted density for patches of 0.2° spacing. Darker colors indicate higher weighted density. Green rectangles: number of successful localizations = 3; yellow stars: number of successful localizations = 4; blue stars: number of successful localizations ≥ 5.*

## FIRST ORDER MODELING OF CRUSTAL DEFORMATION

[2] Strain following small-scale slip was estimated using a simple first-order model for crustal deformation based on the work of Cohen (1996, 1999):

$$\theta = \frac{\Delta u \cos(\alpha)}{\pi} \frac{[2D(x - x_D)(x - x_P)]}{[(x - x_D)^2 + D^2]^2} \tag{S.16}$$

with

$$x_D = \frac{D}{\tan \alpha} \tag{S.17}$$

and

$$x_P = \frac{2D}{\sin(2\alpha)} \tag{S.18}$$

where θ is horizontal surface strain, α is dip, D denotes depth of faulting, x_D and x_P are the surface positions directly above and perpendicular to the down-dip end of the fault, respectively, and Δu is slip (Figure S.13). Slip is assumed to be uniform, and takes place along a rectangular fault patch in a homogenous elastic half space (Cohen 1996). For Nankai, a dip angle of 40° was estimated (Saiga et al. 2013). A slip of 10 cm was modelled, which is suitable to displacements following slow-slip events found at Nankai (Nishimura et al. 2013) and Cascadia (Dragert et al. 2001; Rogers and Dragert 2003).
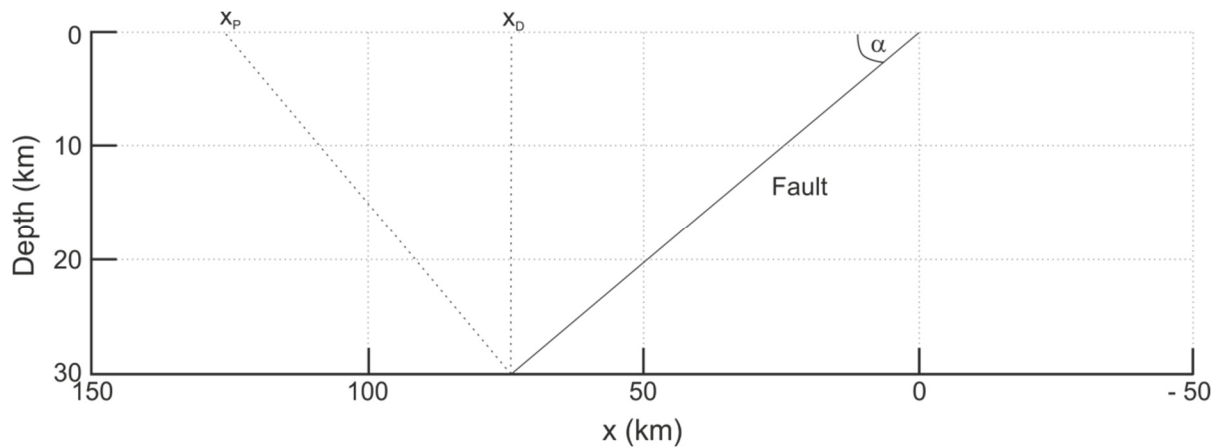
Figure S.13: *Simple first-order model for crustal deformation following fault slip (after and modified from Cohen, 1996, 1999). The zero-point denotes the onset of prism toe*

RELATIONSHIP DISTANCE – PRESSURE TRANSIENTS

[3] As was mentioned in the discussion chapter in the main part of the manuscript, most of the non-volcanic tremor (NVT) occurring during the monitoring period of the SmartPlug remained undetected. As an example, three ATMOS maps with NVT epi- and hypocenters for the period from 14 – 16 August 2010 are shown. Hypocentral depth was up to 60 km, and while most of the NVT occurred onshore the Kii peninsula, at least one NVT originated offshore. However, only one NVT corresponds with the pressure transients in the SmartPlug data. Following the discussion in the main part of the manuscript, we believe that neither the (tectonically or seismic wave-) induced strain nor the strain rate exceeded the threshold limit of 10^{-10} and 10^{-10} min^{-1}, respectively, of the borehole configuration (incl. formation and instrument specifications).
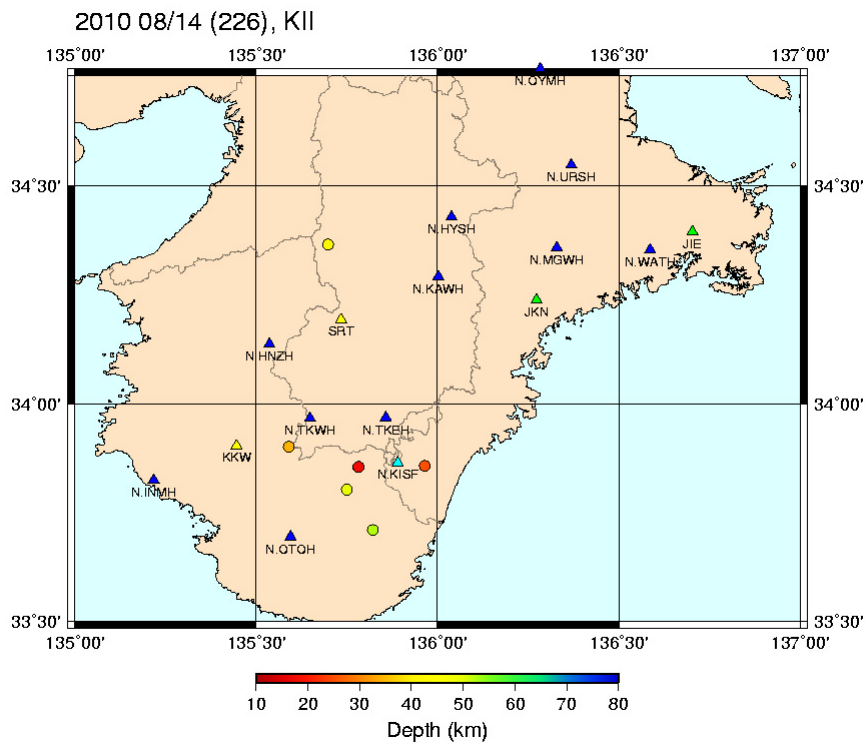
Figure S.14: *Overview of non-volcanic tremor epi- and hypocenters found by ATMOS on 14 August 2010 (Japanese Standard Time; from http://tremor.geol.sci.hiroshima-u.ac.jp/). Blue, light blue, green and yellow triangles indicate Hi-Net, F-Net, University of Tokyo and Japanese Meteorological Agency stations, respectively. Circles indicate the epicenter, the color the hypocentral depth.*
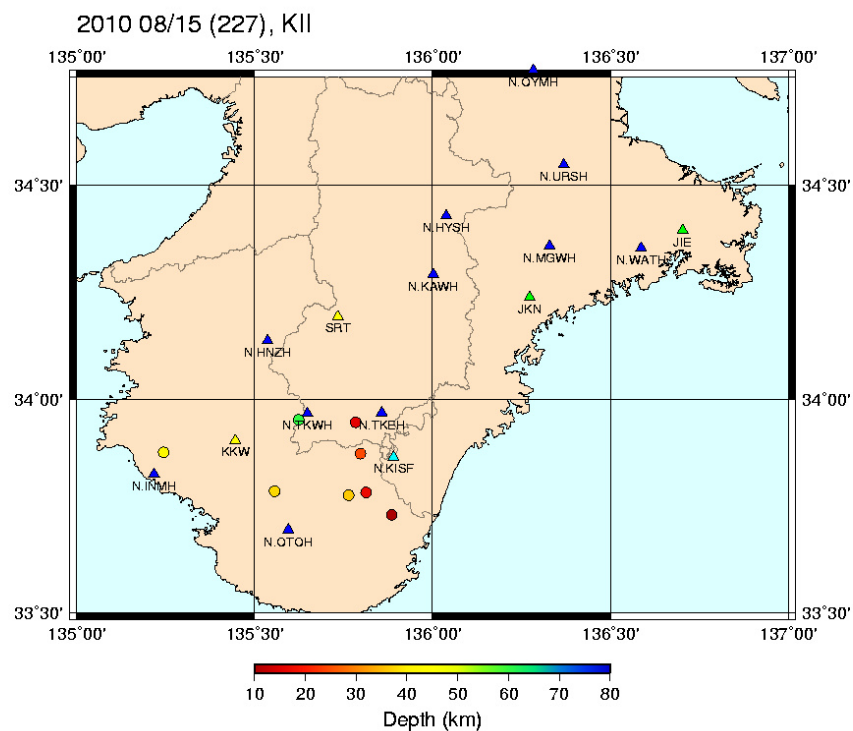
Figure S.15: *Overview of non-volcanic tremor epi- and hypocenters found by ATMOS on 15 August 2010 (Japanese Standard Time; from http://tremor.geol.sci.hiroshima-u.ac.jp/). Blue, light blue, green and yellow triangles indicate Hi-Net, F-Net, University of Tokyo and Japanese Meteorological Agency stations, respectively. Circles indicate the epicenter, the color the hypocentral depth.*
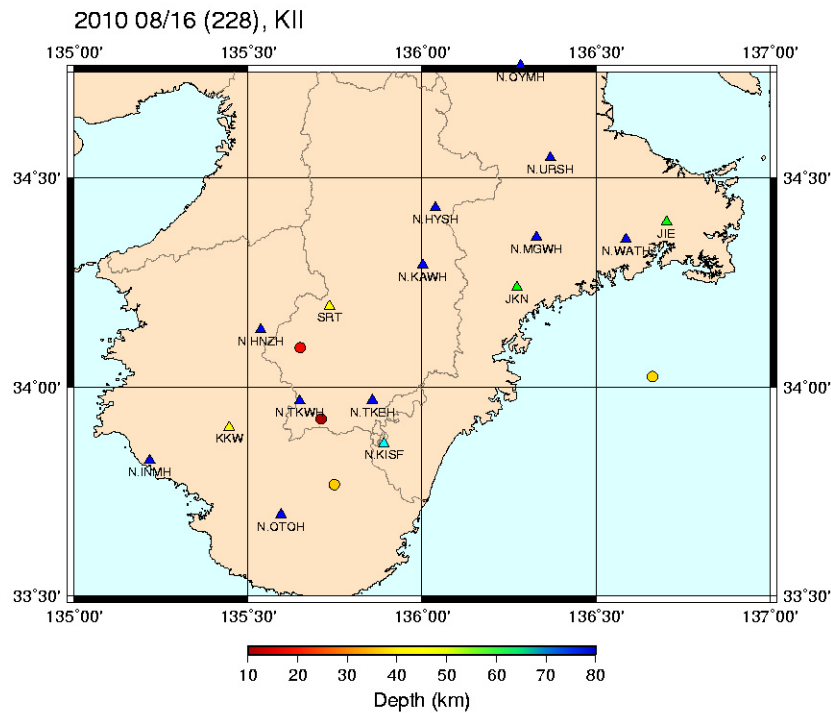
Figure S.16: *Overview of non-volcanic tremor epi- and hypocenters found by ATMOS on 16 August 2010 (Japanese Standard Time; from http://tremor.geol.sci.hiroshima-u.ac.jp/). Blue, light blue, green and yellow triangles indicate Hi-Net, F-Net, University of Tokyo and Japanese Meteorological Agency stations, respectively. Circles indicate the epicenter, the color the hypocentral depth.*

SUPPLEMENTARY TABLES

Table S.4: *Overview of normal earthquakes found in the SmartPlug data and theoretical seismic energy density "e" at Site C0010 induced by these earthquakes (modified from Hammerschmidt et al. 2013a)*

[please see File "Table S.4.xlsx" on the attached CD, Folder APPENDIX A.2]

References

Cohen SC (1996) Convenient Formulas for Determining Dip-Slip Fault Parameters from Geophysical Observables. Bull Seismol Soc Am 86:1642–1644.

Cohen SC (1999) Numerical Models of Crustal Deformation in Seismic Zones. Adv Geophys 41:133 – 231.

Dragert H, Wang K, Rogers G (2004) Geodetic and seismic signatures of episodic tremor and slip in the northern Cascadia subduction zone. Earth Planets Sp 52:1143–1150.

Maeda T, Obara K (2009) Spatiotemporal distribution of seismic energy radiation from low-frequency tremor in western Shikoku, Japan. J Geophys Res Solid Earth 114:B00A09. doi: 10.1029/2008JB006043

Nishimura T, Matsuzawa T, Obara K (2013) Detection of short-term slow slip events along the Nankai Trough, southwest Japan, using GNSS data. J Geophys Res Solid Earth 118:3112–3125. doi: 10.1002/jgrb.50222

Obara K (2002) Nonvolcanic Deep Tremor Associated with Subduction in Southwest Japan. Science 296:1679–1681. doi: 10.1126/science.1070378

Obara K, Hirose H, Yamamizu F, Kasahara K (2004) Episodic slow slip events accompanied by non-volcanic tremors in southwest Japan subduction zone. Geophys Res Lett 31:L23602. doi: 10.1029/2004gl020848

Obana K, Kodaira S (2009) Low-frequency tremors associated with reverse faults in a shallow accretionary prism. Earth Planet Sci Lett 287:168–174. doi: http://dx.doi.org/10.1016/j.epsl.2009.08.005

Rogers G, Dragert H (2003) Episodic Tremor and Slip on the Cascadia Subduction Zone: The Chatter of Silent Slip. Science 300:1942–1943. doi: 10.1126/science.1084783

Saiga A, Kato A, Kurashimo E, Iidaka T, Okubo M, Tsumura N, Iwasaki T, Sakai S, Hirata N (2013) Anisotropic structures of oceanic slab and mantle wedge in a deep low-frequency tremor zone beneath the Kii Peninsula, SW Japan. J Geophys Res Solid Earth 118:1091–1097. doi: 10.1002/jgrb.50069

APPENDIX A.3

APPENDIX FOR MANUSCRIPT IV –

BOREHOLE FLUID PRESSURE ARTIFACTS STIMULATED BY SEISMIC WAVES

ATTENUATION AT CASING SCREENS

[1] The attenuation Q of seismic wave modes inside the borehole is calculated following the work of Rubino et al. (2008) and Rubino and Holliger (2013). We assume that at the casing screens, dynamic oscillations initiated by seismic waves force fluid out of the borehole. Eventually, this leads to energy loss due to the interaction between the fluid and solid rock mass (Norris 1993).

Table S.5: Material properties of the formation and the SmartPlug (based on Hammerschmidt et al. 2013; Rubino and Holliger 2009)

Variable	Description	Value
K_w	bulk modulus water [Pa]	1.25×10^9
K_m	bulk modulus formation matrix [Pa]	1.00×10^9
K_b	high pressure bulk rock modulus [Pa]	1.16×10^9
K_s	bulk modulus of grains [Pa]	50.0×10^9
K_{instr}	bulk modulus instrument [Pa]	200.0×10^9
K_{binstr}	high pressure bulk instrument modulus [Pa]	222.3×10^9
v	Poisson's Ratio	0.1
v_{steel}	Poisson's Ratio casing	0.5
ρ_w	density of seawater [kg/m³]	1025
ρ_b	average density of bulk rock [kg/m³]	2650
η_w	fluid viscosity at 18.9°C [Pa s]	1.2×10^{-3}
n	porosity	0.38
n_{steel}	estimated porosity casing	0.05
k	intrinsic permeability [m²]	2.1×10^{-17}
R	aspect ratio pore space	1.3×10^{-3}

We start by calculating the effective bulk modulus of the fluid saturating the soft pores, K_f (Rubino and Holliger 2013):

$$K_f = \frac{3}{2} + \frac{\sqrt{-1}\omega\eta}{R^2}$$

(S. 19)

The variable R denotes the aspect ratio of the pores, $\omega = 2\pi f$ is the angular frequency, and η is the fluid viscosity (see also Table S.5). The complex valued bulk modulus $K(\omega)$ is then a function of the compliant porosity n_c (Gurevich et al. 2010), and K_m, K_b, K_f and K_s , i.e. the bulk modulus of formation matrix, high-pressure rock bulk modulus, the frequency-dependent bulk modulus and the water bulk modulus:

$$K(\omega) = \left[\frac{1}{K_b} + \left(\left(\left(\frac{1}{K_m} - \frac{1}{K_b} \right)^{-1} \right) \left(\frac{1}{n_c} \left(\frac{1}{K_f} - \frac{1}{K_s} \right)^{-1} \right) \right)^{-1} \right]^{-1}$$ (S. 20)

Now, we can compute the effective stress coefficient α as well as the shear modulus μ:

$$\alpha = 1 - \frac{K(\omega)}{K_s}$$ (S.21)

$$\mu = \left(\frac{1}{\mu_M} - \frac{4}{15} \left(\frac{1}{K_m} - \frac{1}{K(\omega)} \right) \right)^{-1}$$ (S.22)

with μ_M being the static shear modulus, which is defined as:

$$\mu_M = \frac{K_m}{2(1 + v)}$$ (S.23)

where v denotes Poisson's ratio. The complex compressional velocity is then derived by (Carcione 2001):

$$V_p = \frac{1}{Re \left(\frac{1}{V_{pc}} \right)}$$ (S.24)

with

$$V_{pc} = \sqrt{\frac{M_c(\omega)}{\rho_b}}$$ (S.25)

where ρ_b is the average bulk density, $M_c = \lambda_c + 2\mu$ is the complex plane-wave modulus and

$$\lambda_c = K_c - \frac{2}{3}\mu$$ (S.26)

$$K_c = K_w + K_{av}\alpha^2$$ (S.27)

$$K_{av} = \left(\frac{\alpha - n}{K_s} + \frac{n}{K_f} \right)^{-1}$$ (S.28)

Finally, the inverse quality factor, i.e., the attenuation, is given by Carcione (2001):

$$\frac{1}{Q_P(\omega)} = \frac{Im\ (V_{pc})^2}{Re\ (V_{pc})^2} \tag{S.29}$$

References

Carcione JM (2001) Energy Balance and Fundamental Relations in Dynamic Anisotropic Poro-Viscoelasticity. Proc Math Phys Eng Sci 457:331–348. doi: 10.2307/3067204

Gurevich B, Makarynska D, de Paula O, Pervukhina M (2010) A simple model for squirt-flow dispersion and attenuation in fluid-saturated granular rocks. Geophysics 75:N109–N120. doi: 10.1190/1.3509782

Hammerschmidt SB, Davis EE, Hüpers A, Kopf A (2013) Limitation of fluid flow at the Nankai Trough megasplay fault zone. Geo-Marine Lett 33:405–418. doi: 10.1007/s00367-013-0337-z

Norris AN (1993) Low-frequency dispersion and attenuation in partially saturated rocks. J Acoust Soc Am 94:359 – 370. doi: 10.1121/1.407101

Rubino JG, Holliger K (2013) Research note: Seismic attenuation due to wave-induced fluid flow at microscopic and mesoscopic scales. Geophys Prospect 61:882–889. doi: 10.1111/1365-2478.12009

Rubino J, Ravazzoli C, Santos J (2008) Equivalent viscoelastic solids for heterogeneous fluid-saturated porous rocks. Geophysics 74:N1–N13. doi: 10.1190/1.3008544

APPENDIX A.4

APPENDIX FOR MANUSCRIPT V –

REAL-TIME DRILLING MUD GAS MONITORING FOR QUALITATIVE EVALUATION OF SUBSURFACE HYDROCARBON GAS COMPOSITION

SUPPLEMENTARY FIGURES
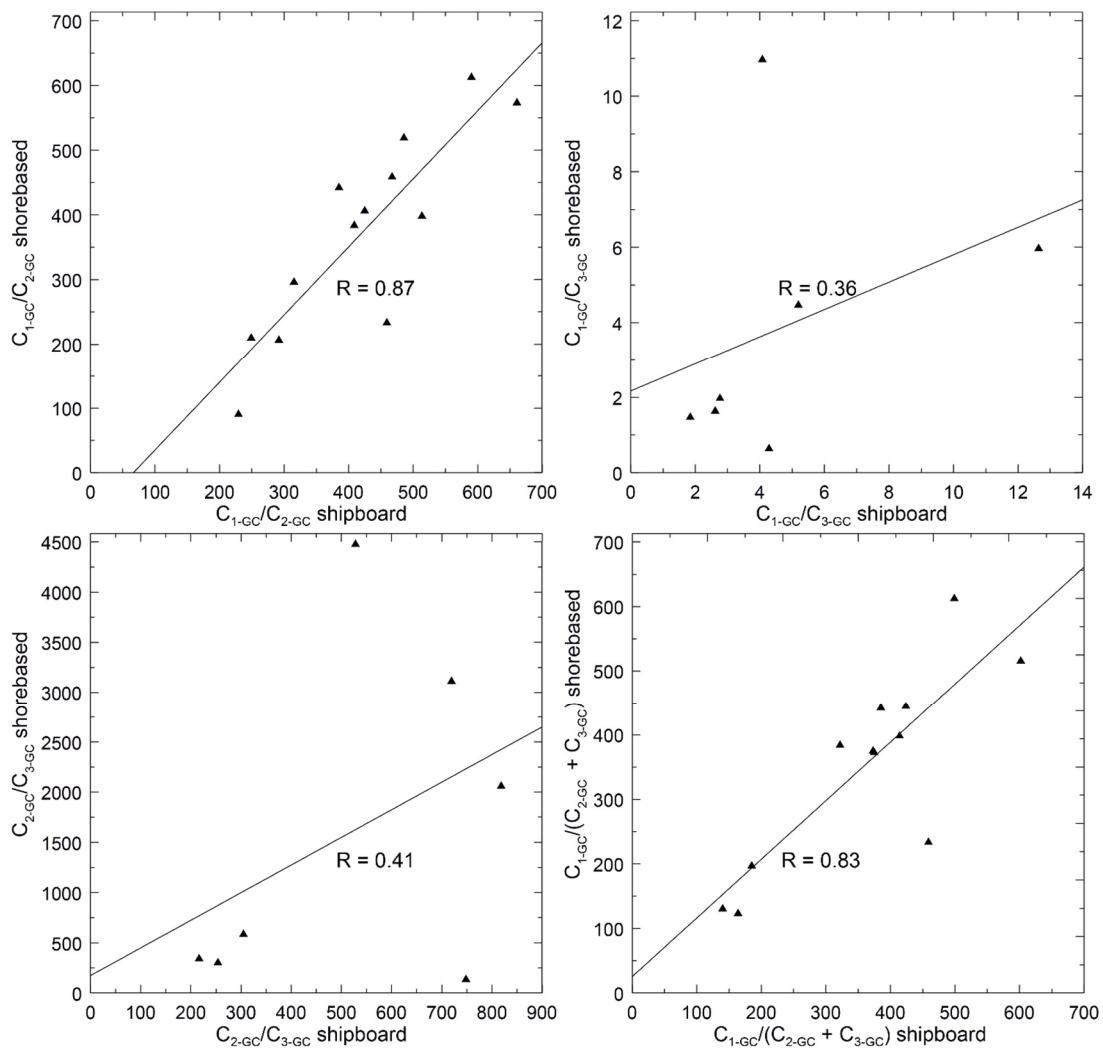
Figure S.17: *Correlation of SciGas shipboard and shorebased gas ratios. While the C_1/C_2 ratios and the Bernard parameters show a good correspondence, the data scatter of the C_2/C_3 ratios and C_1/C_3 ratios preclude any clear correlation.*

Appendix A.4

Figure S.18: *Correlation Fluid of SciGas shipboard and shorebased data with the dataset generated by Geoservices ("GEO") during Exp. 338 (Expedition 338 Scientists, 2014a). Shown are the C_1/C_2, C_2/C_3 and C_1/C_3 ratios. "Shipboard" refers to the data obtained simultaneously with Geoservices data. "Shorebased" refers to the data gained by onshore analyses of samples taken from the SciGas system during IODP Exp. 338.*
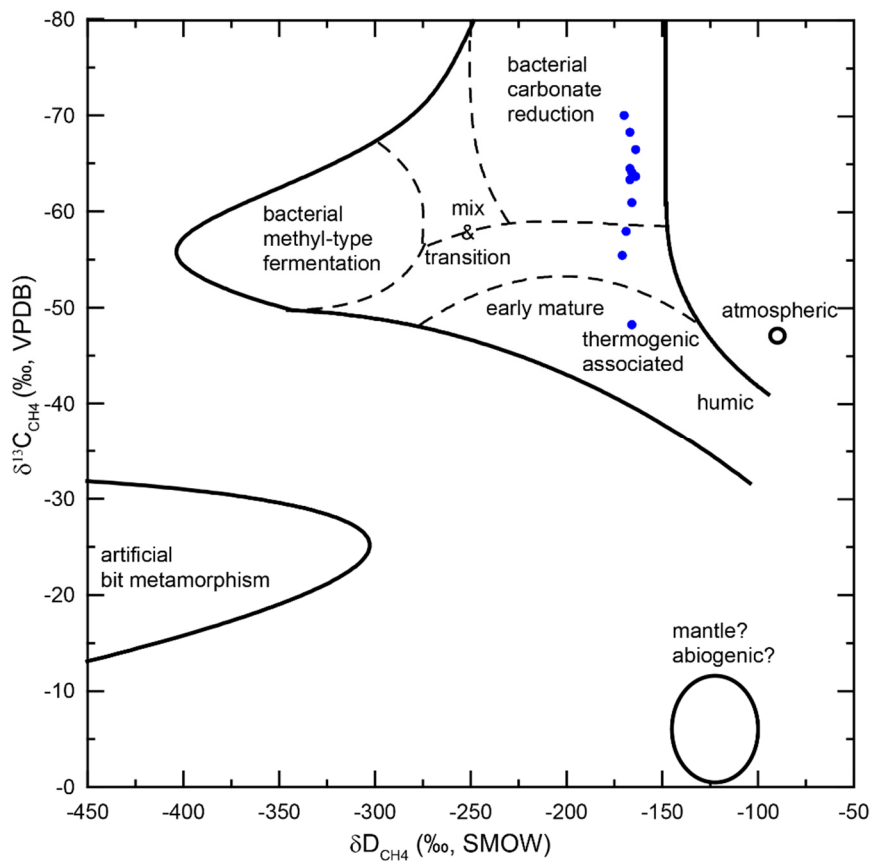
Figure S.19: *Shorebased δD$_{CH4}$ values plotted against shipboard δ^{13}C$_{CH4}$ data (diagram modified from Whiticar 1999). The sampled methane is derived by bacterial carbonate reduction, and gets a more thermogenic signature with depth.*
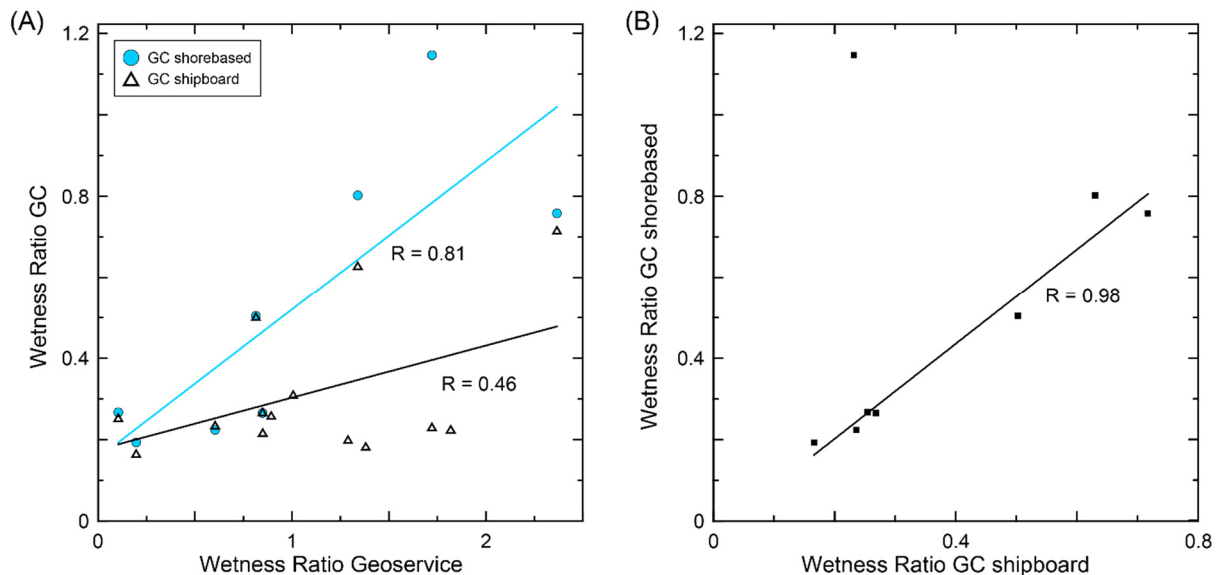
Figure S.20: *Correlation between the different total wet gas ratios.* **(A)** *The panel shows a relatively good correlation of the shorebased SciGas data with the data from Geoservices (blue circles, R = 0.81), while the two shipboard datasets reveal a larger scatter (triangles; R = 0.46).* **(B)** *Neglecting the outlier at ca. 1600 mbsf, the total wet gas ratios of both GC datasets correspond well with R = 0.98.*
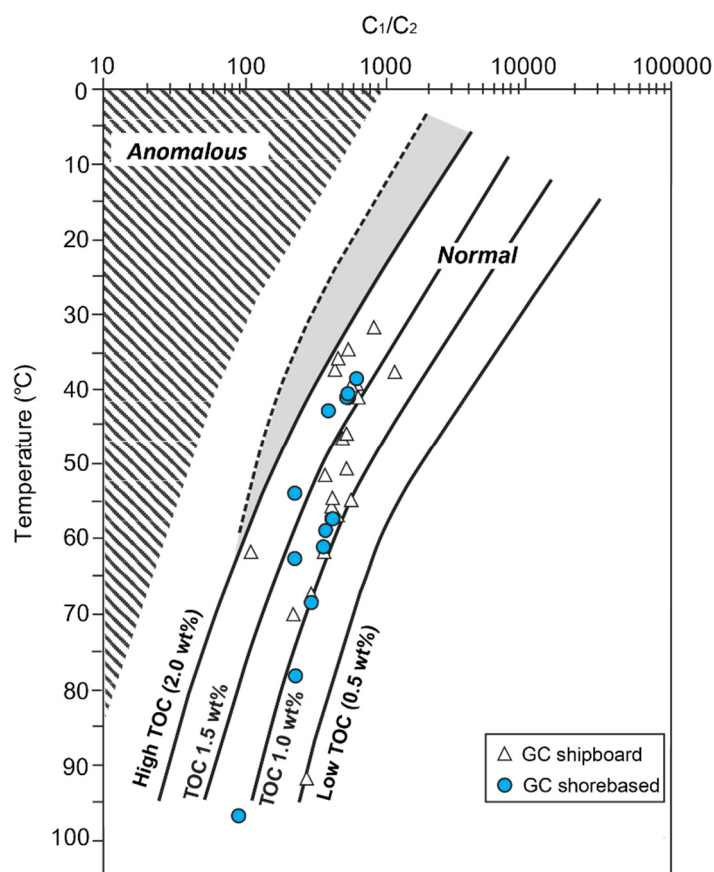
Figure S.21: C_1/C_2-Temperature-TOC diagram following the empirical relationship compiled by JOIDES PPSP (1992). Shipboard TOC data from IODP Expedition 338 (Strasser et al. 2014) was used to associate the SciGas shipboard (white points; Expedition 338 Scientists 2014a) and the onshore GC data (blue points) to appropriate temperatures. The temperature estimations are given in Figure 52 in the main text.

SUPPLEMENTARY TABLES

Table S.6: Overview of the different gas ratios. GEO = shipboard data generated by Geoservices, GC = data generated using a gas chromatograph, TWG = total wet gas ratio, R_0 = vitrinite reflectance.

[please see File "Table S.6.xlsx" on the attached DVD, Folder APPENDIX A.4]

References

Strasser M, Dugan B, Kanagawa K, Moore GF, Toczko S, Maeda L, Kido Y, Moe KT, Sanada Y, Esteban L, Fabbri O, Geersen J, Hammerschmidt S, Hayashi H, Heirman K, Hüpers A, Jurado Rodriguez MJ, Kameo K, Kanamatsu T, Kitajima H, Masuda H, Milliken K, Mishra R, Motoyama I, Olcott K, K. O, Pickering KT, Ramirez SG, Rashid H, Sawyer D, Schleicher A, Shan Y, Skarbek R, Song I, Takeshita T, Toki T, Tudge J, Webb S, Wilson DJ, Wu H-Y, Yamaguchi A (2014) Site C0002. In: Strasser et al. (eds) IODP Proc 338:92. doi: 10.2204/iodp.proc.338.102.2014

JOIDES PPSP (1992) Ocean Drilling Guidelines for Pollution Prevention and Safety. JOIDES J 18

Whiticar MJ (1999) Carbon and hydrogen isotope systematics of bacterial formation and oxidation of methane. Chem Geol 161:291 – 314.

APPENDIX A.5

APPENDIX FOR MANUSCRIPT VI –
GAS MIGRATION IN THE NANKAI TROUGH ACCRETIONARY PRISM

ADDITIONAL TABLES

[1] Table S.7 on the following page shows the results of the noble gas analyses outlined in the main text.

References

Lee J-Y, Marti K, Severinghaus JP, Kawamura K, Yoo H-S, Lee JB, Kim JS (2006) A redetermination of the isotopic abundances of atmospheric Ar. Geochim Cosmochim Acta 70:4507–4512. doi: 10.1016/j.gca.2006.06.1563

Porcelli D, Ballentine CJ, Wieler R (2002) An Overview of Noble Gas Geochemistry and Cosmochemistry. Rev Mineral Geochemistry 47 :1–19. doi: 10.2138/rmg.2002.47.1

Table S.7: Results for noble gas analyses on drilling mud gas samples collected during IODP Expeditions 338 and 348.

Depth (mbsf)	Messfile	^{4}He (mbar)	^{20}Ne (mbar)	^{40}Ar (mbar)	^{84}Kr (mbar)	^{132}Xe (mbar)	^{3}He/^{4}He (Ra)	^{20}Ne/^{22}Ne	^{21}Ne/^{22}Ne	^{40}Ar/^{36}Ar	^{38}Ar/^{36}Ar	^{4}He/^{20}Ne
950	M461A	0,00515 ±0,00026	0,01367 ±0,00068	7,75 ±0,39	0,000544 ±0,000027	0,0000229 ±0,0000014	1,348 ±0,041	9,798 ±0,010	0.02896 ±0.00024	296,9 ±1,6	0.18707 ±0.00094	0,3770 ±0,0029
1400	M460A	0,00531 ±0,00027	0,01446 ±0,00072	7,47 ±0,37	0,000495 ±0,000025	0,0000185 ±0,0000013	1,044 ±0,045	9,8331 ±0,0088	0.02900 ±0.00025	294,7 ±1,4	0,1882 ±0,0012	0,3675 ±0,0029
1700	M462A	0,00539 ±0,00027	0,01559 ±0,00078	8,43 ±0,42	0,000557 ±0,000028	0,0000210 ±0,0000015	1,114 ±0,037	9,832 ±0,010	0.02900 ±0.00025	294,8 ±1,3	0,1878 ±0,0011	0,3460 ±0,0027
1800	M458A	0,00553 ±0,00028	0,01482 ±0,00074	8,07 ±0,40	0,000552 ±0,000029	0,0000215 ±0,0000015	0,919 ±0,034	9,8109 ±0,0090	0.02896 ±0.00043	n.d.	n.d.	0,3731 ±0,0029
1850	M459A	0,00538 ±0,00027	0,01617 ±0,00081	9,03 ±0,45	0,000643 ±0,000033	0,0000233 ±0,0000015	1,067 ±0,031	9,7926 ±0,0082	0.02894 ±0.00024	296,6 ±1,4	0,1884 ±0,0011	0,3330 ±0,0026
air (1013mbar)		0,00531	0,0167	9,42	0,000658	0,0000237	1	9,80	0,0290	298,6*	0,1885*	0,319
2050	M480A	0,00702 ±0,00035	0,0200 ±0,0010	10,31 ±0,52	0,000757 ±0,000038	0,0000291 ±0,0000021	1,055 ±0,046	9,8100 ±0,0087	0.02899 ±0.00027	297,2 ±1,4	0,1889 ±0,0011	0,3535 ±0,0055
2050	M480B	0,00614 ±0,00031	0,01870 ±0,00093	10,78 ±0,54	0,000761 ±0,000038	0,0000309 ±0,0000019	1,034 ±0,046	9,7930 ±0,0089	0.02895 ±0.00027	295,9 ±1,3	0,1884 ±0,0011	0,3304 ±0,0026
2200	M484A	0,00632 ±0,00032	0,01900 ±0,00095	10,33 ±0,52	0,000718 ±0,000036	0,0000305 ±0,0000064	1,054 ±0,045	9,7977 ±0,0089	0.02897 ±0.00027	297,5 ±1,4	0,1884 ±0,0013	0,3345 ±0,0027
2349.5	M482A	0,00608 ±0,00030	0,01769 ±0,00088	9,93 ±0,50	0,000717 ±0,000036	0,0000264 ±0,0000018	1,100 ±0,036	9,7904 ±0,0087	0.02897 ±0.00028	295,2 ±1,4	0,1882 ±0,0011	0,3457 ±0,0027
2349.5	M486A	0,00627 ±0,00031	0,01889 ±0,00094	10,79 ±0,54	0,000750 ±0,000038	0,0000275 ±0,0000057	1,033 ±0,035	9,8013 ±0,0089	0.02900 ±0.00027	296,6 ±1,5	0,1883 ±0,0012	0,3338 ±0,0027
2850	M481A	0,00672 ±0,00034	0,01977 ±0,00099	11,24 ±0,56	0,000794 ±0,000040	0,0000288 ±0,0000060	1,090 ±0,034	9,7987 ±0,0090	0.02897 ±0.00027	295,9 ±1,3	0,1883 ±0,0011	0,3421 ±0,0027
2968.5	M479A	0,00800 ±0,00040	0,01610 ±0,00081	9,48 ±0,47	0,000674 ±0,000034	0,0000243 ±0,0000050	1,522 ±0,039	9,798 ±0,017	0.02899 ±0.00028	296,4 ±1,6	0.1884 ±0.0013	0,5000 ±0,0040
3050	M485A	0,00655 ±0,00033	0,01952 ±0,00098	10,98 ±0,55	0,000763 ±0,000039	0,0000307 ±0,0000063	1,048 ±0,030	9,7966 ±0,0092	0.02897 ±0.00027	296,3 ±1,6	0,1886 ±0,0010	0,3375 ±0,0027
air (1013mbar)		0,00531	0,0167	9,42	0,000658	0,0000237	1	9,80	0,0290	298,6*	0,1885*	0,319

Air composition following Porcelli et al. (2002), p. 3 except * Lee et al. (2006)

n.d. not determined

all errors: 2sigma

APPENDIX A.6

APPENDIX FOR MANUSCRIPT VII –

HYDROCARBON SEEPAGE AND ITS SOURCES AT MUD VOLCANOES OF THE KUMANO FOREARC BASIN

ADDITIONAL INFORMATION ON MATERIAL AND METHODS

[1] During an expedition with the German research vessel 'SONNE' (SO-222, Legs A and B) in summer 2012, twelve MVs (Figures 57 and 58; Table S.8) in the Kumano forearc basin were inspected by means of hydroacoustic surveys, visual seafloor inspections and groundtruthing (Kopf et al. 2013).

Seafloor inspection, sampling and sample preparation

[2] Bathymetric mapping was conducted with the hull-mounted Kongsberg EM120 multibeam echosounder. A TV-grab equipped with a b/w camera and a color camera was used for on-line seafloor inspection and sampling of near-surface sediments. The TV-grab was deployed at MVs 2, 3, 4, and 10 at a ship velocity of less than 0.3 knots. Additional seafloor inspections and hydroacoustic bottom water investigations were carried out during two dives with the remotely operated vehicle (ROV) 'QUEST4000m' (MARUM) at MV 3 and MV 4. For possible detection of gas bubbles ascending from the seafloor, the ROV's forward-looking sonar was used (Nikolovska et al. 2008).

[3] Shallow sediment was sampled by gravity coring. The 6m-cutting barrel was equipped either with a PVC-liner for the recovery of sediments or a plastic foil for rapid access to gas hydrates. In total, 34 gravity cores from twelve MVs were investigated in this study (Table S.8).

[4] A single core (GeoB16763-1) was taken from basin sediments distant to MVs as background reference. For preparation of hydrate-bound gas, hydrate pieces were thoroughly cleaned in ice-cooled water in order to remove sediment particles and, then, the pure gas hydrate pieces were inserted into 10 ml-plastic syringes for dissociation at ambient temperature (Pape et al. 2010). The evolving hydrate-bound gas was left to escape the syringe via the canule adaptor for a while, and, having removed residual air from the syringe, injected into 20 ml-glass serum vials prefilled with saturated NaCl solution (6.12 M). Finally, about 17 ml of gas and 3 ml of NaCl solution were stored in the vial until analysis.

Table S.8: *Positions of gravity cores taken at mud volcanoes (MV) in the Kumano forearc basin.*

GeoB	Site	Latitude [N]	Longitude [E]	Water Depth [mbsl]	Location of core at MV
16764-1	MV #2	33°40.548	136°55.334	1,988	summit
16771-1	MV #2	33°40.496	136°55.409	2,000	slope
16772-1	MV #2	33°40.518	136°55.195	2,000	slope
16788-1	MV #2	33°40.515	136°55.335	1,992	summit
16788-2	MV #2	33°40.525	136°55.264	1,993	summit
16703-1	MV #3	33°37.990	136°40.219	1,945	summit
16704-1	MV #3	33°38.225	136°40.469	2,017	slope
16712-1	MV #3	33°38.039	136°40.244	1,942	summit
16735-1	MV #3	33°38.242	136°40.437	1,800	slope
16785-2	MV #3	33°38.213	136°40.427	2,018	slope
16722-2	MV #4	33°39.428	136°37.988	1,991	slope
16723-5	MV #4	33°39.503	136°38.017	2,061	slope
16725-1	MV #4	33°39.328	136°38.051	1,970	summit
16726-8	MV #4	33°39.538	136°38.033	2,052	slope
16736-1	MV #4	33°39.348	136°38.024	1,800	summit
16754-2	MV #4	33°39.489	136°38.038	2,030	slope
16746-1	MV #5	33°40.593	136°34.002	1,900	summit
16747-5	MV #5	33°40.673	136°34.015	1,900	slope
16748-1	MV #5	33°40.492	136°33.916	1,920	slope
16749-1	MV #6	33°41.037	136°33.669	1,920	
16750-1	MV #6	33°41.093	136°33.571	1,920	
16751-1	MV #7	33°44.127	136°34.046	1,950	
16707-1	MV #8	33°36.272	136°33.363	2,025	
16720-1	MV #8	33°36.144	136°33.453	2,020	
16708-1	MV #9	33°37.989	136°33.439	2,044	
16721-1	MV #9	33°37.926	136°33.519	2,050	
16716-2	MV #10	33°32.824	136°16.880	1,850	summit
16742-1	MV #10	33°32.917	136°17.025	1,850	summit
16756-1	MV #11	33°23.272	136°42.431	2,010	summit
16757-1	MV #11	33°23.292	136°42.389	2,000	slope
16759-3	MV #12	33°31.326	136°39.885	2,050	
16780-1	MV #13	33°46.115	136°54.886	1,870	slope
16781-1	MV #13	33°46.105	136°54.865	1,880	summit
16782-2	MV #13	33°46.118	136°54.769	1,890	slope
16763-1	reference site	33°39.995	136°53.012	2,012	

[5] For vertical profiling of methane concentrations in non-pressurized gravity cores recovered with PVC liner, a modified headspace technique (Kvenvolden and McDonald 1986) was used. 3 ml of sediment were taken with cut-off syringes immediately after core recovery, when concentrations of light hydrocarbons in lower sediment intervals have still not equilibrated to atmospheric pressure, at defined depths and transferred into 20 ml glass vials prefilled with 5 ml of 1 M NaOH. The samples were stored at +4°C until analysis onshore.

Analytical methods

[6] Gas samples were analyzed for their molecular compositions and methane concentrations by gas chromatography (GC) (Pape et al. 2010). Calibrations and performance checks were conducted regularly using commercial pure gas standards and gas mixtures. The coefficient of variation determined for the analytical procedure was less than 2%. Concentrations were corrected with regard to compound-specific solubilities (CH_4, C_2H_6, and CO_2) in saturated NaCl solution according to Duan and Sun (2003), Duan and Mao (2006), and Mao et al. (2005).

[7] Stable carbon isotope ratios ($^{13}C/^{12}C$) of CH_4 in hydrate-bound and dissolved gas were determined by GC–isotope ratio mass spectrometry (GC–IRMS). For this, a Trace Ultra-GC IsoLink connected to a MAT 253 isotope ratio mass spectrometer via a ConFlo IV interface (all components Thermo Fisher Scientific Inc.) was used. For separation of CH_4, a CARBOXEN-1006 PLOT capillary column (Supelco Inc.) was used. Chromatography and reproducibility were checked daily using commercial methane standards (Air Liquide GmbH, Germany). The reproducibility is estimated at ± 0.3‰ for $\delta^{13}C$. The system offset was determined by correcting analyzed isotope ratios against two commercial standards (Isometric Instruments, Canada, and Biogeochemical Laboratories, Indiana University) certified for stable C-isotope signatures of CH_4. Carbon isotopic ratios are arithmetic mean values from triplicate measurements and are reported in δ-notation in parts permil (‰), relative to the Vienna PeeDee Belemnite (V-PDB).

References

Duan Z, Mao S (2006) A thermodynamic model for calculating methane solubility, density and gas phase composition of methane-bearing aqueous fluids from 273 to 523K and from 1 to 2000bar. Geochim Cosmochim Acta 70:3369–3386. doi: 10.1016/j.gca.2006.03.018

Duan Z, Sun R (2003) An improved model calculating CO2 solubility in pure water and aqueous NaCl solutions from 273 to 533 K and from 0 to 2000 bar. Chem Geol 193:257–271. doi: 10.1016/S0009-2541(02)00263-2

Kopf A, et al. (2013) Report and preliminary results of RV Sonne cruise SO222: MEMO - MeBo drilling and in situ long-term monitoring in the Nankai Trough accretionary complex, Japan. Berichte, MARUM – Zentrum für Marine Umweltwissenschaften, FB Geow Univ Bremen, 297: 121pp.

Kvenvolden KA, McDonald TJ (1986) Organic geochemistry on the Joides Resolution - An Assay. ODP Texas A&M University, Technical Note 6: 147pp.

Mao S, Zhang Z, Hu J, Sun R, Duan Z (2005) An accurate model for calculating C2H6 solubility in pure water and aqueous NaCl solutions. Fluid Phase Equilib 238:77–86. doi: 10.1016/j.fluid.2005.09.014

Nikolovska A, Sahling H, Bohrmann G (2008) Hydroacoustic methodology for detection, localization, and quantification of gas bubbles rising from the seafloor at gas seeps from the eastern Black Sea. Geochemistry, Geophys Geosystems 9:Q10010. doi: 10.1029/2008GC002118

Pape T, Bahr A, Rethemeyer J, Kessler JD, Sahling H, Hinrichs K-U, Klapp SA, Reeburgh WS, Bohrmann G (2010) Molecular and isotopic partitioning of low-molecular-weight hydrocarbons during migration and gas hydrate precipitation in deposits of a high-flux seepage site. Chem Geol 269:350–363. doi: 10.1016/j.chemgeo.2009.10.009

APPENDIX A.7

APPENDIX FOR MANUSCRIPT VIII –

TEMPORAL AND SPATIAL VARIABILITY OF MUD VOLCANISM IN THE KUMANO FOREARC BASIN, SE JAPAN

ADDITIONAL FIGURES
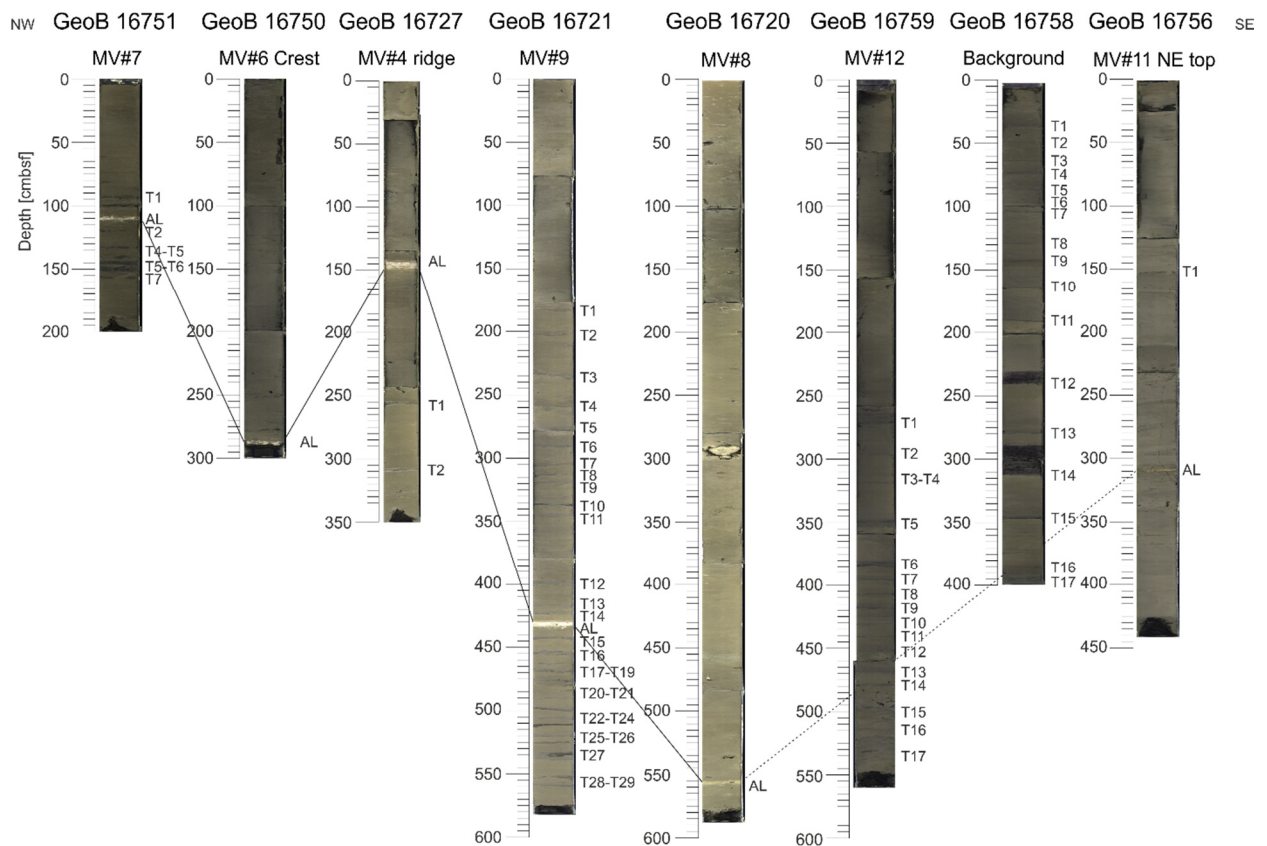
Figure S.22: *NW-SE transect of cores taken at mud volcanoes in the Kumano forearc basin during expedition SO-222. One ash layer (AL) can be traced, although it is absent in cores GeoB16720 and GeoB16758. Abundant, wood-rich turbidites were only encountered in GeoB16758.*

APPENDIX B

MeBoCORK, MeBoPLUG, and MeBoPUPPI

CHAPTER B.1

SIMPLE, AFFORDABLE AND SUSTAINABLE BOREHOLE OBSERVA-TORIES FOR COMPLEX MONITORING OBJECTIVES

A. Kopf[1]*, T. Freudenthal[1], V. Ratmeyer[1], M. Bergenthal[1], M. Lange[1], T. Fleischmann[1],

S.B. Hammerschmidt[1], C. Seiter[1], and G. Weger[1]

Ready for submission to

Geoscientific Instrumentation, Methods and Data Systems

* corresponding author: akopf@marum.de

[1] MARUM, University of Bremen, Bremen, Germany

Abstract Seafloor drill rigs are remotely operated systems that provide a cost effective means to recover sedimentary records of the upper sub-seafloor deposits. Recent increases in their payload included down-hole logging tools or autoclave coring systems. We here report on another milestone in using seafloor rigs: The development and installation of shallow borehole observatories. Three different systems have been developed for the MARUM-MeBo seafloor drill, which is operated by MARUM, Univ. Bremen, Germany. A simple design, the MeBoPLUG, separates the inner borehole from the overlying ocean by using o-ring seals at the conical threads of the drill pipe. The systems are self-contained and include data loggers, batteries, thermistors and a differential pressure sensor. A second design, the so-called MeBoCORK, is more sophisticated and also hosts an acoustic modem for data transfer and, if desired, fluid sampling capability using osmotic pumps. Of these MeBoCORKs, two systems have to be distinguished: The CORK-A (A = autonomous) can be installed by the MeBo alone and monitors pressure and temperature inside and above the borehole (the latter for reference). The CORK-B (B = bottom) has a higher payload and can additionally be equipped with geochemical, biological or other physical components. Owing to its larger size, it is installed by ROV and utilises a hotstab connection in the upper portion of the drill string. Either design relies on a hotstab connection from beneath which coiled tubing with a conical drop weight is lowered to couple to the formation. These tubes are fluid-saturated and either serve to transmit pore pressure signals or collect pore water in the OsmoSampler. The third design, the MeBoPUPPI (Pop-Up Pore Pressure Instrument), is similar to the MeBoCORK-A and monitors pore pressure and temperature in a self-contained manner. Instead of transferring data upon command using an acoustic modem, the MeBoPUPPI contains a pop-up telemetry with Iridium link. After a predefined period, the data unit with satellite link is released, ascends to the sea surface, and remains there for up to two weeks while sending the long-term data sets to shore. In summer 2012, two MeBoPLUGs, one MeBoCORK-A and one MeBoCORK-B were installed with MeBo on German *R/V Sonne* in the Nankai Trough area, Japan. We have successfully downloaded data from the CORKs, attesting that coupling to the formation worked and pressure records were elevated relative to the seafloor reference. In the near future, we will further deploy the first two MeBoPUPPIs. Recovery of all monitoring systems by ROV is planned for 2016.

INTRODUCTION

[1] Around 20 years ago, the scientific community started to use borehole observatories, so-called CORKs (Circulation Obviation Retrofit Kits), which are installed inside submarine boreholes, and which allow the re-establishment and monitoring of *in situ* conditions (see summary in Davis and Becker 2001). The key principle as well as the main objective is to provide a hydraulic seal between the borehole environment and the overlying ocean water body (Figure S.23). Based on this principle, various types of instruments with different capabilities have been developed over the past decades, the majority of those with scientific purposes within the Ocean Drilling Program (ODP) and the Integrated Ocean Drilling Program (IODP; see review by Becker and Davis 2005).

[2] From the first CORKs, which allowed only rudimentary fluid pressure and temperature measurements, the instruments evolved to multi-functional and multi-level subseafloor laboratories, including, for example, hydrologically isolated zones with casing screens (e.g. Davis et al. 2006), thermistor strings (e.g. Davis and Villinger 2006), long-term fluid sampling devices (Evans et al. 2009), *in situ* microbiological experiments (Orcutt et al. 2010), or strainmeter (Kopf et al. 2011a). The advantages of long-term monitoring are the ability to obtain: (1) reliable measurement of ambient pore pressure (this measurement often requires significant time after drilling to re-equil-

ibrate to original *in situ* conditions and usually cannot be obtained by downhole tools); (2) formation elastic and hydrologic properties determined from the response to tidal and seismic loading (e.g. Wang and Davis 1996; Davis et al. 2004); (3) records of hydraulic transients associated with e.g. seismic and aseismic slip, fluid flow events, and possible precursory phenomena, over a wide range of timescales and rates (e.g. Davis et al. 2001, 2006); (4) temperature anomalies associated with fluid flow episodes (Davis and Villinger 2006) or as precursors to earthquakes (Johnson et al. 2000); and (5) transient changes in chemical composition or seepage rate (Brown et al. 2005). The phenomena have in common that they are episodic in nature, and time series data are the only feasible way of increasing our understanding of them.
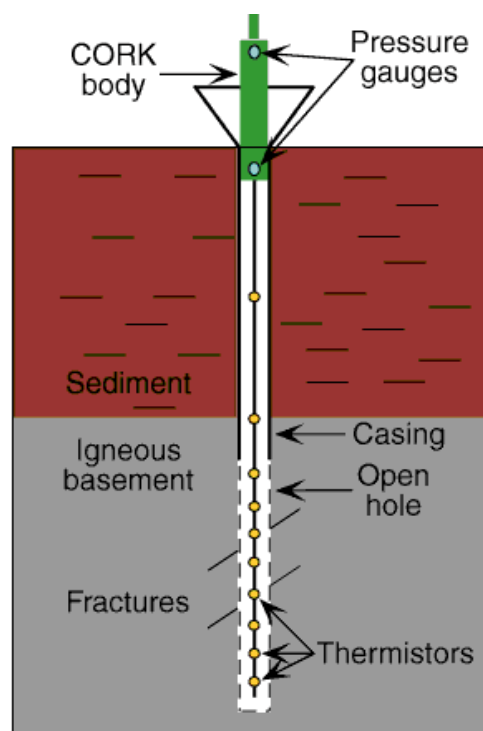
Figure S.23*: Schematic of a CORK observatory's main components: Here an example in sediment-laden oceanic crust and a simple CORK head with seal and P transducers (green unit with light blue sensors) plus a thermistor string (self contained; see yellow circles). From Becker and Davis (2005).*

[3] Nonetheless, most boreholes are still left uninstrumented, which is a major loss for the scientific community. Installation of CORKs usually requires a drillship, which is a major logistic and financial effort. Moreover, the increasing complexity of the CORK systems increased not only the expenses but led also to longer installation times and a higher sensitivity of the instruments to environmental constraints.

[4] An affordable alternative to the drill ships is currently seen in the seafloor drills, which are tethered, remotely controlled devices that can be run from ships of opportunity provided they offer sufficient space and a strong enough A-frame. One such seafloor drill is the MARUM-MeBo

(<u>Me</u>eresboden-<u>Bo</u>hrgerät), which has recently been developed at MARUM, Univ. Bremen (Germany) (see details in Freudenthal and Wefer 2013). The MeBo can be operated from any research vessel and allows coring to a depth of 70 m in either push coring mode for soft sediments or rotary coring mode for hard rock drilling. A second device is currently under implementation (sea trials anticipated in fall 2014) and will core to 200 m below seafloor with the majortity of the other parameters similar to the first one.

[5] In this manuscript we describe our main objectives in implementing observatories into MeBo boreholes. Foremost, this is the efficiency of a single round-trip of the seafloor drill and observatory unit (whereas drill ships always need a second round-trip by pipe or wire in order to deploy the borehole instrument). Secondly, the rather generic and modular design is a second objective so that a wealth of parameters may be monitored in a variety of settings. In the following, we present three types of miniature borehole observatories, which on one hand have evolved back to more simple systems when compared to ODP/IODP CORKs, but which on the other hand provide a wide range of possible *in situ* measurements. In addition to the technological concept, we report on the first installation of such MeBo observatories in the Nankai Trough area offshore Japan, this way providing a proof-of-concept.

STATE-OF-THE-ART: SEAFLOOR DRILLS

[6] Seafloor robotic drills bridge the gap between conventional seabed sampling techniques from multi-purpose research vessels (like gravity coring or dredging) and dedicated drilling vessels. Working from a stable platform at the seabed, which is not affected by ship movements due to wave heave or currents, ensures optimized control on the drilling process. As consequence of the increasing demand of core drillings in the range of 10-200 m for geotechnical site investigation, mineral ore exploration a variety of seabed drill rigs have been developed within the last decade (McGinnis 2009). They are, however, more or less all in prototype status, with the MARUM MeBo being one of the most mature systems (see review in Freudenthal and Wefer, 2013).

The MeBo Seafloor Drill Rig

[7] MeBo (<u>Me</u>eresboden-<u>Bo</u>hrgerät, the German term for seafloor drill rig) is a robotic drill that is deployed on the seabed and remotely controlled from the vessel. The complete MeBo-system, including drill, winch, launch and recovery system, control unit, as well as workshop and spare drill tools is shipped within six 20' containers (one of which being the MeBo drill itself; Figure S.24). A steel armoured umbilical with a diameter of 32 mm is used to lower the 10-tons heavy device to the seabed where four legs are being armed out in order to increase the stability of the rig. Copper wires and fibre optic cables within the umbilical are used for energy supply from the

vessel and for communication between the MeBo and the control unit on the deck of the vessel. The maximum deployment depth in the current configuration is ~2000 m.

[8] The mast with the feeding system forms the central part of the drill rig. The drill head provides the required torque and rotary speed for rock drilling and is mounted on a guide carriage that moves up and down the mast with a maximum push force of 4 tons. A water pump provides sea water for flushing the drill string for cooling of the drill bit and for removing the drill cuttings. Core barrels and rods are stored on two magazines on the drill rig. Wire-line core barrels (HQ) and hard metal drill bits with 55 mm core diameter (push coring) are usually used in soft marine deposits. The stroke length was 2.35 m each. With complete loading of the magazines a maximum coring depth of more than 70 m can be reached. Station time can reach more than 24 hrs per deployment. For a more detailed description of the MeBo refer to Freudenthal and Wefer (2009, 2013).
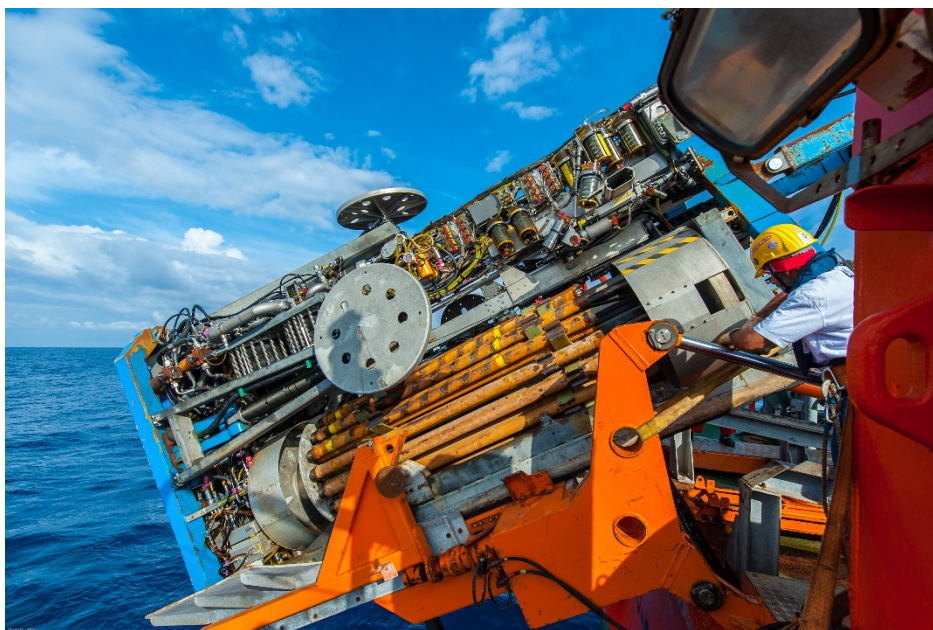
Figure S.24: *MARUM-MeBo drill rig during launch on the aft deck of R/V Sonne*

METHODOLOGY

Methodological objectives

[9] Among the tasks we try to achieve with the MeBo borehole observatories, there are four fundamental ones:

1) seal the borehole,

2) collect data over long periods of time,

3) transfer data to the scientist/end user, and

4) increase capability by adding payload.

[10] Our concept is very generic. Tasks 1 and 2 are mandatory and realised in all three MeBo observatory systems, whereas tasks 3 and 4 provide a suite of options that can be tailored to the needs of an individual campaign.

Borehole Seal

[11] The MeBo seafloor drill uses H-size HQ wireline coring tools. The outer diameter of the drill rods is 98 mm. During the routine drilling operations, these pipes are used to extend the drill string downhole, and are recovered once terminal depth of a given hole is reached (Freudenthal and Wefer 2013). Each HQ rod has a male end with a conical thread at the base and a female conical thread at the top end.

[12] If an observatory is to be set with MeBo, procedures change in the sense that some drill pipe (i.e. several of the 2.35 m-long rods) remain in the ground and serve as casing to stabilise the upper portion of the hole where the soft sediments would otherwise close in. The final, uppermost drill rod is then prepared to provide the borehole seal. In addition, this rod has a widened outer diameter to that it will facilitate seal at the seafloor where the drilling operation may have excavated the ground.

[13] The two main principles to have a sealed upper rod are to screw in an instrumented plug having the shape of the conical thread and additional o-ring seals, or to prepare an entirely new instrumented rod of up to 2.35 m length with a hotstab seal in the middle. These two principles have been used in designs of the so-called MeBoPLUG and the MeBoCORK-A and –B, respectively (see section *Implementation* below).

Data Mining

[14] In addition to the borehole seal, data mining in the borehole and/or formation ia a pre-requisite for the instrumented drilling rods. If the inner volume of the "casing" (i.e. MeBo drill pipes in the ground) is the target, a simple plug with a data logger and transducers is sufficient to monitor e.g. the equilibration of the hole and ambient values thereafter. If, however, coupling to the formation is desired, a mechanism is needed that couples the transducers to the open hole formation. For this purpose, we designed a small device at the base of the instrumented uppermost drill rod that has a small coil with PVC tubing (1 mm inner diameter) which can be unrolled via an electrical motor upon command (acoustic signal or timer with pre-set date/time for lowering). At the tip of the tubing there is a stainless steel conical drop weight with a boring that will then provide access to the sediment at the base of the hole. The tubing may then serve to get ambient pore pressure readings, or extract pore water samples (in case OsmoSampler is hooked to it at

the seafloor). We have realised designs of both in the MeBoPLUG and the MeBoCORK-A and – B, respectively (see section *Implementation* below).

Data Transfer

[15] Retrieval of CORK data has always been a crucial issue in the past, with all ODP- and IODP-CORKs relying on ROV visits during regular 3rd party cruises in the years after deployment. This is a costly endeavour and further bears the difficulty of vagueness in planning because of dependency on weather, shiptime providers, etc. One of the key requirements in developing MeBo observatories was hence to start with a simple instrument to be recovered by ROV and then evolve to systems which make ROV visits or even visits of a vessel obsolete.

[16] As a consequence, the MeBoCORK systems aimed at including acoustic modems so that the successful deployment and health of the system after the MeBo took off can be attested. Data transfer is moderately fast, so that practically, only limited data sets are to be downloaded that way while a final visit to recover the instruments by ROV seems still advisable. In case the deployments take place in an area where a return cruise is not anticipated for longer periods of time, it may be better to release a pop-up unit with a mirror data set of the main data logger as well as an iridium telemetry to transfer the data without the necessity to retrieve the instrument. If the latter is sufficiently cheap, net cost may be saved since ship time is also precious. We have realised designs of both in the MeBoCORK-A and –B and the MeBoPUPPI, respectively (see section *Implementation* below).

Increased Payload

[17] Given the wealth of critical parameters that govern seafloor processes, scientist desire to deploy multi-sensor instruments that often consume considerable energy. One main objective in MeBo-corking was hence to have a modular seafloor unit where space for additional devices and batteries play a minor role. Such a unit has to exchange the initial MeBoCORK instrument (with a limited lifetime) without affecting the borehole seal. This was achieved by an hotstab connector that can transport fluids, power, or both. At the seafloor end, capabilities may be increased by adding OsmoSamplers with long tubing coils for fluid sampling over 24 months and longer, but also to provide power for energy-demanding systems such as geophones, etc. We have realised this by inventing the MeBoCORK-B (see section *Implementation* below).

[18] In the next section we will introduce three general instruments of the MeBo observatory family: the PLUGs, CORKs and PUPPIs. Each of them is employing several (if not all) of the tasks listed above. In addition to those observatory instruments realised, many other combinations of transducers and data transfer principles, but also implementation of new transducers. This could

be either in the instrumented drill pipe (if sufficiently slim) or inside the seafloor unit. With its generic and modular design MeBo observatories may become a versatile and affordable way to monitor hydrogeochemical and geological processes in the shallow sub-seafloor (<200 m).

Implementation

MeBoPLUG Borehole Observatories

[19] In regular-size industry boreholes, the casing of the upper portion on the well is a couple of decimetres, and re-entry into the hole is facilitated by a conical seafloor structure, often complemented by a platform to land a ROV. For the seafloor drill holes, all this is miniaturized and in case of MeBo a diameter of only 98-110 mm is available. Space is hence most seriously governing the design of the MeBo observatories, and re-entry is not feasible in such narrow drill pipes. In essence, the entire hole completion was initially designed as a stand-alone instrument, which does not differ from the geometry of a standard MeBo drill pipe (appx. 235 cm long and 10 cm in diameter).

[20] The name of the instrument is leaned from the SmartPlug and GeniusPlug observatories, which also represent simple types of CORKs designed as extension to mechanical bridge plugs, but IODP drillhole-sized (Kopf et al. 2001b). Instead of a bridge plug or CORK seal, we make use of the conical threads of the MeBo drill pipes and seal the pipe with a pair of additional o-rings (Figure S.25). The pressure housing is machined from a thermoplastic synthetic polymer, polyoxymethylene (POM), which tolerates moderate P and T and has successfully been used to 25 MPa confining pressure. At the top, a handle designed to specification of the ROV *MARUM-Quest* manipulator was added. In the borehole-facing section, a thermistor as well as the downward-looking P port are situated (Figure S.25, inset on right).

[21] Inside the housing we hosted standard RBR data loggers with Keller differential pressure transducers for monitoring P transients in the boreholes (as a proxy for strain; Davis et al. 2006) relative to the seafloor P signal. With this approach we omit de-tiding of our data because all signals from wave action, etc. occur more or less simultaneously at the seafloor and in the shallow sub-seafloor formation. Given that only one thermistor was fitted into the so-called MeBoPlugs, we are lacking a temperature record from the seafloor (i.e. upward-looking side of the MeBoPlug; see Figure S.25). In order to overcome this shortcoming, a simple self-contained device for sea bottom T monitoring, a so-called MTL (Miniature Temperature Logger by Antares; Pfender and Villinger 2002) was deployed by ROV next to the MeBoPlug (see next section). The sampling rate of the MeBoPlugs was set to 10 s on the RBR data loggers, which is providing them with an estimated lifespan of about 4 years (anticipated end of recording is February 2016).

Figure S.25: Left: *MeBoPlug prior to being screwed into a MeBo drill pipe* ***Right:*** *bottom view into the borehole with ports for P [hole at left] and T [little pin at right] monitoring. See text.*

MeBoCORK Borehole Observatories

[22] The two versions of the MeBoCORK, as seen in Figs. 4, 5, 6 and 7, are both self-contained with power, data logging, data transmission and transducers. They are recoverable at all times and hence minimize the risk of losing the investment. In the following paragraphs, the deployment mechanism is explained in some detail. First, the MeBo hole has to be prepared for long-term instrumentation after coring is completed. This is achieved by leaving several pieces of MeBo outer drilling rods in the ground after wireline core retrieval. These rods, appx. 30-40 m in total length, act as a casing and stabilize the upper subseafloor portion where the deposits are poorly consolidated and otherwise may close in. Only the lowermost part of the hole is free of "casing" and provides direct access to the formation. The first prerequisite to keep the MeBo CORK simple follows the first hydrological observatory in ODP: only hydraulic tubing is lowered into the hole to access fluid pressure (or fluids) at depth (Wheat et al. 2011), and all electronics remain at the wellhead. For MeBo, a string of 2 armoured PTFE tubes is coiled up in the lower part of the MeBo-set observatory unit (termed MeBoCORK-A, where A stands for "autonomous", i.e. MeBo by itself is capable of placing a stand-alone observatory), namely in the lower portion of the "adapter" hosting the receptacle for the hotstab. Once the drilling device has set this piece, the coil of tubing is unlocked and a dead weight favours the tubing's descent towards terminal depth where the hole is open. The upper end each individual tubing connects to borings of the hotstab receptacle. The lower unit also hosts battery packs.
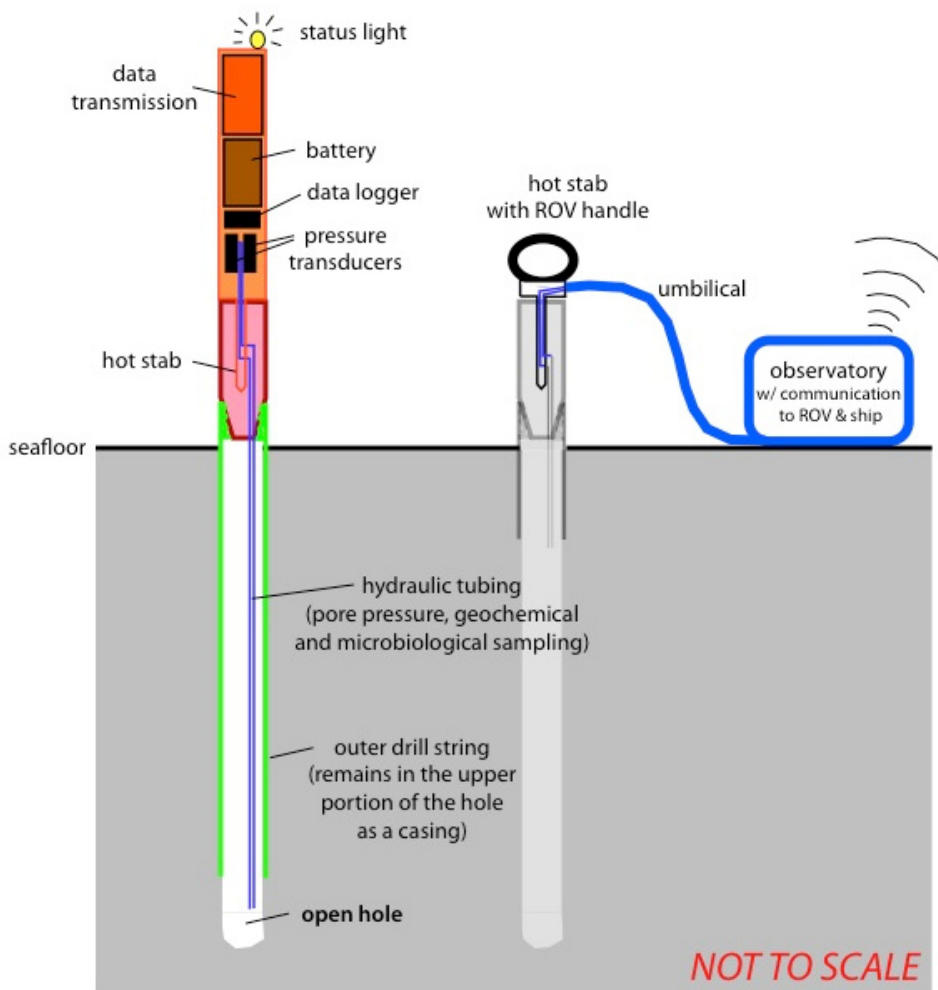
Figure S.26: *Schematic diagram of MeBoCORK-A **(left)** and MeBoCORK-B **(right)***

[23] The upper portion of the MeBoCORK-A hosts the data transmission unit, data logger and transducers, the latter of which are connected to the borings of the male hotstab end (Figures S.26 (left), S.27). The hotstab is mated with its female counterpart, and the two halves of CORK-A are further secured by a bayonet connector that allows coupling of the MeBo top drive and hence torque being transmitted (in clockwise direction only!). During installation MeBo fully srews in the entire CORK instrument, which in total is the exact length of a regular MeBo drill rod and which sits on the magazine with the other rods. Once this piece is properly set, MeBo pushes the unit to a depth so that only the titanium part (ca 70 cm long) sticks out of the seafloor and then takes off. In the initial design, this simple, MeBo-set CORK monitors pressure and temperature, which are both indicators for deep-seated fluid flow; pore pressure is additionally valuable as strain proxy (see above). Depending on the sampling rate, the batteries will allow monitoring for many months to a few years (in case of the system deployed during leg SO-222A = 7 months).
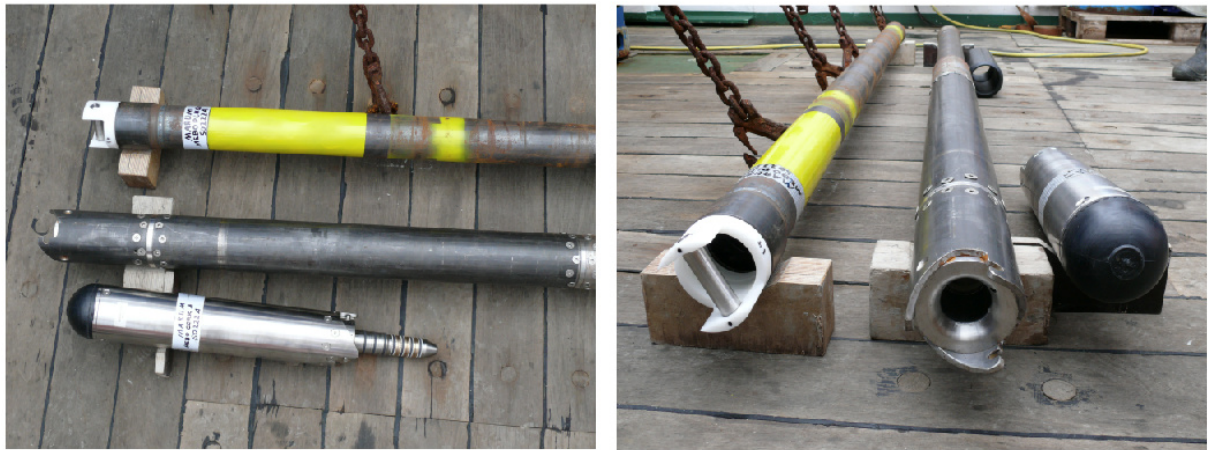
Figure S.27: *MeBoCORK A (=autonomous) as well as MeBoPlug for comparison. See text.*

[24] If monitoring or parameters other than pressure and temperature is desired, the instrumented MeBo rod (CORK-A) is too small and an ROV dive is required to recover the CORK-A and deploy an external, more sophisticated observatory unit (Figures S.26 (right), S.28). Since the ROV dives to the seafloor and connects a seafloor (0sea bottom) unit to the MeBo rod with Hotstab receptacle, this system was termed MeBoCORK-B (=bottom). The ROV is able to un-latch the bayonet connector in counter-clockwise direction and can transport the MeBo-set CORK back to the ship, because its weight is low and the diameter is suitable for the manipulator claw. Before this, a seafloor unit will be placed next to the MeBo drillsite (Figure S.28). This system contains of a pressure housing with an attached hood in which a male hotstab adapter plus the umbilical of armoured tubing strings is coiled up. The ROV takes the hotstab and places it into the lower portion of the MeBoCORK, which is remaining connected to the outer drillstring at all times. This operation is straightforward and has been done in a similar way when pressure units from ODP or IODP CORKs got replaced. The pressure housing at the seafloor can be equipped to the mission's/scientists' specifications, and in the case of this proposal will host the P and T transducers (same as in the instrumented rod) plus an OsmoSampler (Figure S.29; see also Jannasch et al. 2003).
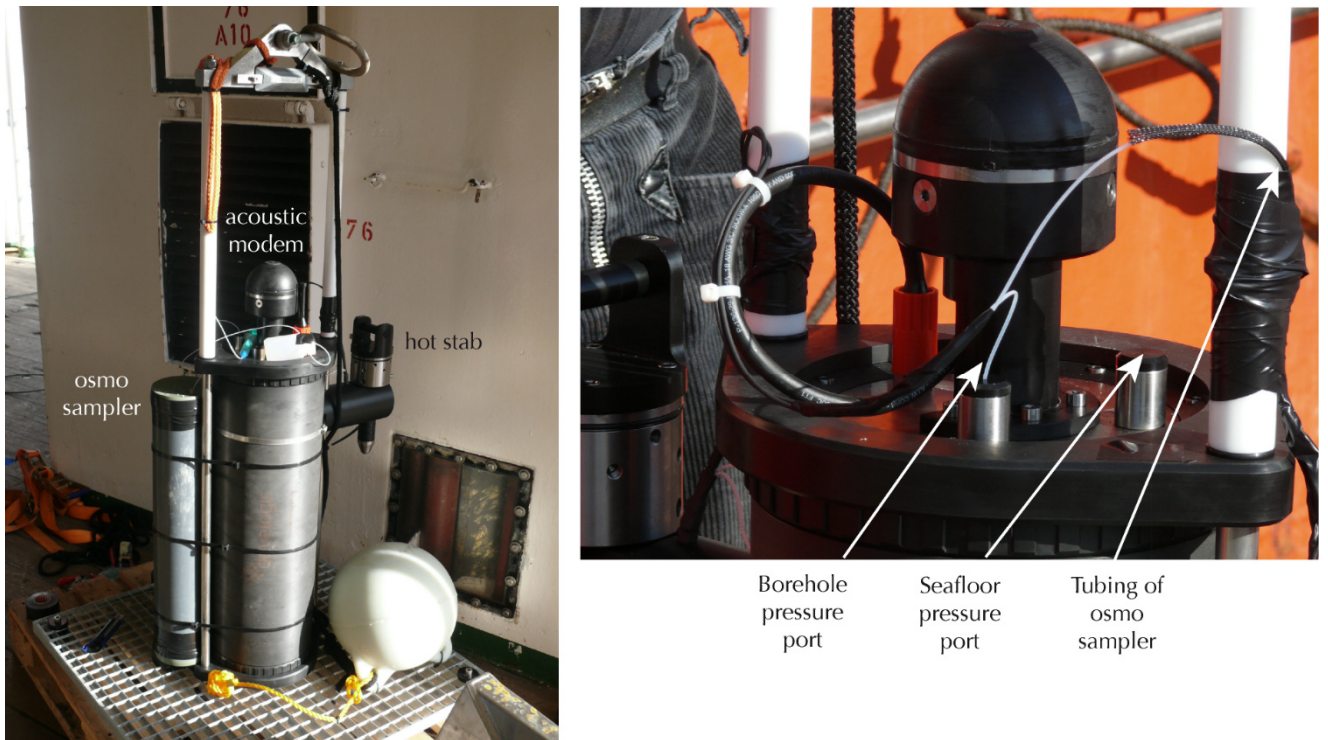
Figure S.28: *MeBoCORK B (=bottom) unit containing a pressure housing, acoustic modem, attached Os-moSampler, and the hot stab connector to couple to the drill pipe. Left photo shows overall unit, right photo contains detail with layout of tubings. See text.*

[25] Both MeBoCORK instruments are programmed to measure the pressure for a period of 30 s and then record the average P value. Seafloor reference and borehole P are offset by 15 s, so that the data are written to the disk alternately.

Figure S.29: *OsmoSampler (tubing coil [top] and pumps [below]) that are hosted in a PVC tube attached to MeBoCORK-B.*

MeBoPUPPI Borehole Observatories

[26] In a recent effort, we have taken the MeBo long-term borehole observatory science to the next level and build pop-up borehole instruments that can be released from the casing string after a predefined period. An underwater mateable connector further enables the user to also „manually" release the unit by ROV. Once the unit has ascended to sea level, the popup unit (Figure S.30) send their data via satellite link, rendering a second visit and additional shiptime unnecessary. Such instruments would in a first iteration monitor pressure and temperature, but could be equipped with geophones, seismometers and other components depending on the scientific demands of a given mission, the duration of monitoring, the amount of time series data, etc..

Figure S.30: *Schematic diagram **(left)** and photograph **(right)** of MeBoPUPPI observatory*

[27] In contrast to the MeBoCORK systems, the MeBoPUPPIs do not rely on a hotstab connector and tubing that is lowered towards terminal depth of the borehole where direct access to the formation exists. Instead, the monitoring is restricted to P and T inside and outside of the borehole as well as tilt using a triaxial array of accelerometers. If desired, an additional unit that samples simultaneously one hydrophone and three geophone channels (type SM6, with 4.5 Hz lower frequency band, but no mechanical gimbaling system) can be mounted. Either sensing package has to remain in the borehole string for reasons of limited space and weight of the popup unit. This may be equally the case for part of the battery packs when very long monitoring periods are desired. In these cases, almost all of the total of 235 cm length of a MeBo drill rod segment, excluding a 53 cm-long adapter to protect the glass dome (Figure S.30, righthand side drawing) are available.

RESULTS

[28] During cruise SO-222 on *R/V Sonne*, the MeBo was deployed 6 times in water depth between 1900 m and 2050 m. The main objective of this cruise was to install borehole observatories with the MeBo, so holes were only drilled down to 35 mbsf (meters below seafloor) or shallower. As explained before, the drilling procedure in observatory installations encompasses that only a few drill pipes are recovered to create open hole conditions at the base, and that a drill pipe that already included either a MeBoPLUG or a MeBoCORK-A is added to terminate the hole near the seafloor. Once that final rod was set the MeBo took of vertically while being assisted by the winch, and was then recovered on deck.

[29] As explained in more detail in Kopf et al. (2013), a total of four observatories were set with MeBo during cruise SO-222 with *R/V Sonne*, and in case of MeBoCORK-B assisted by ROV. In general, operations were effortlessly carried out, in particular for MeBoPlug #1 and MeBoCORK-A. Both systems were pre-installed on the uppermost, final drill rod, which was pushed down into the seafloor so that only appx. 70-80 cm stuck out into the water column. Fig. S.31 (A, B) illustrates how the situation looked like before MeBo took off.

[30] When installing MeBoPlug #2 in the Kumano Basin, we encountered some problems with drilling progress when hitting several indurated sand layers at appx. 17 mbsf. Despite efforts to clean the hole with pressurized fluid, the string did not progress any deeper, so that the only option to install MeBoPlug #2 was to screw on the drill pipe section that hosted the MeBoPlug and leave it sticking out of the seafloor by appx. 2.5 meters. Despite this fragile pipe representing an obstacle, the MeBo take-off went well and the pipe was not bend or damaged.

[31] The majority of the other installations were also successful, e.g. for the autonomous CORK-A (Figure S.31C), the CORK-B downhole assembly with endcap protecting the female hotstab end (Figure S.31B), as sighted later on by ROV. In particular the latter example demonstrates that the black end cap on the female hotstab connector (Figure S.31B) can easily be replaced with a hotstab on an umbilical that is connected to P transducers and OsmoSamplers (Figure S.29), which are hosted in a pressure housing together with the data logger, acoustic data transmission and other electronics (Figure S.31D).

[32] During the installation of MeBoCORK-A at the crest of Kumano Basin mud volcano #4 (Kopf et al. 2013) we encountered no problems, and once the MeBo had taken off, we sent an acoustic signal to unlatch the drop weight and lower the coiled pore pressure tubing into the open bottom end of the otherwise cased drill hole. This process is controlled by an electrical motor which operates in either "command-mode" (triggered acoustically) or "timer-mode" (veering of tubing

starts at a pre-programmed date and time). As can be seen from one of the first data sets downloaded from the CORK-A via acoustic communication by *develogic*, the borehole pressure shows appx. 18 m higher pressure values than its seafloor counterpart (Figure S.32), which is in good agreement with the terminal depth of appx. 19 mbsf at this drill site. It can further be observed that the borehole temperature is appx. 1.1°C warmer than the bottom water temperature (blue vs. turquoise data in Figure S.32).
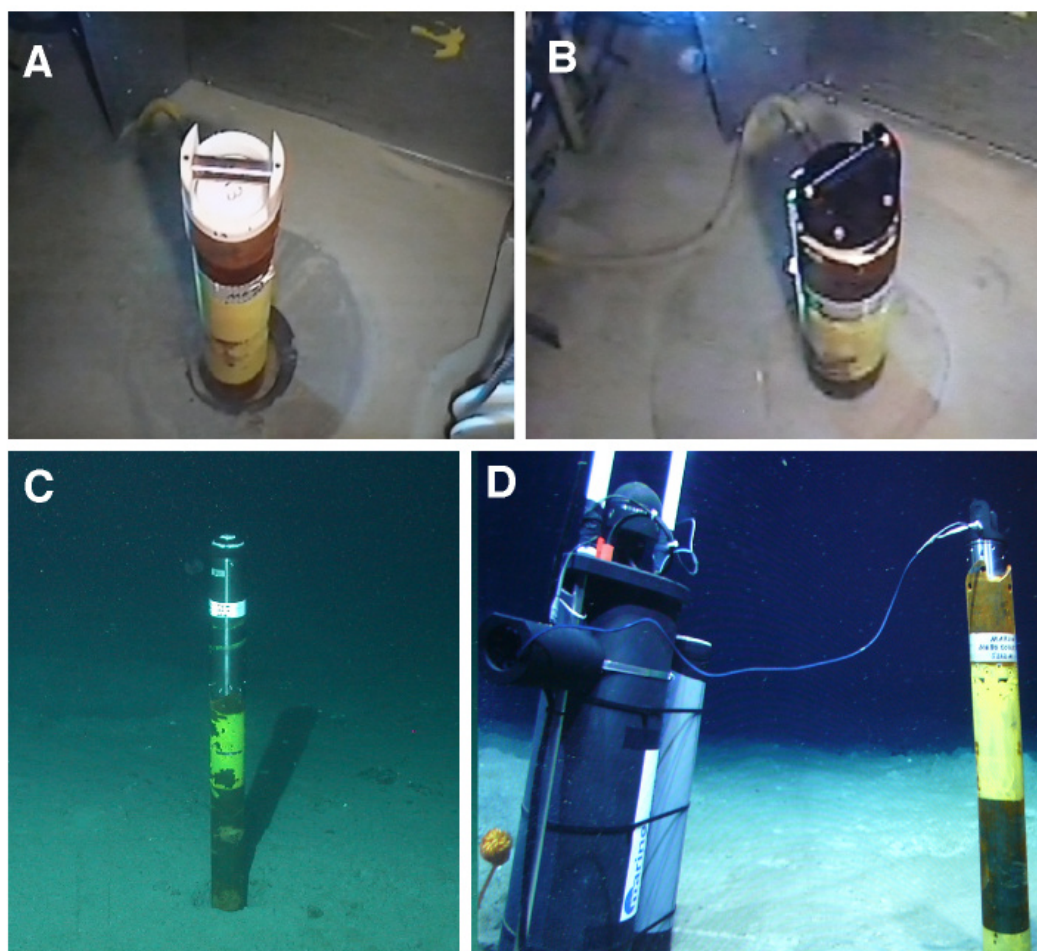
Figure S.31: (A) *MeBoPlug and* **(B)** *MeBoCORK-B top hole assembly with black endcap after installation with MeBo. Photos were taken immediately before the seafloor drill rig takes off the ground.* **(C)** *MeBoCORK-A and* **(D)** *MeBoCORK-B with seafloor unit. Photos were taken during subsequent ROV visits. See text.*

[33] At a neighbouring mud volcano, MV#3, we had at first no problem untangling the hotstab of the seafloor unit of MeBoCORK-B, take it to the MeBo drill rod, and plug the hotstab into its female counterpart (Figure S.31D). However, there was some uncertainty that the tubing got caught and pinched during this operation, so that we unplugged the hotstab again and pushed it back in more safely a second time. The P records of seafloor reference and downward-looking (=borehole) P are shown in Fig. S.33. It can be seen that the differential pressures do not change much over the time of installation, which is unexpected given that the borehole terminates 33 mbsf and

the drop weight should sit near terminal depth of this hole. The only explanation for the P record measured is a leak somewhere inside the upper end of the female hotstab end of the drill string; all other sources of error, including the entire bottom unit, umbilical with tubes to hotstab and OsmoSampler, as well as the hotstab connector itself, are flawless.
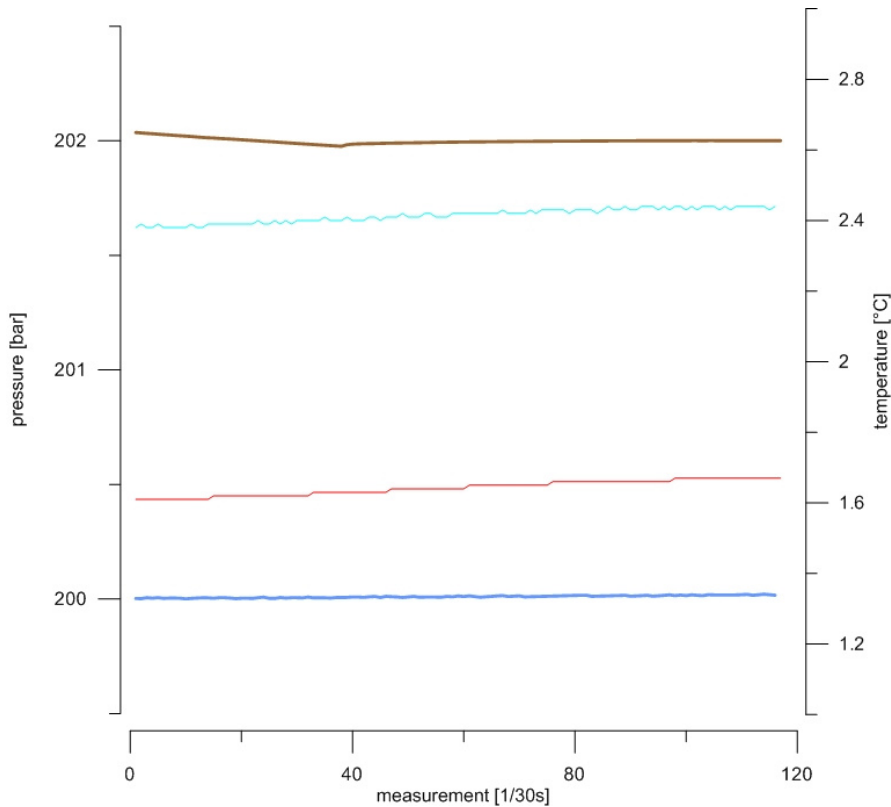
Figure S.32: *First data sets from MeBoCORK-A as recovered by acoustic data transmission. Pressure curves are blue/turquoise colours, T curves are red/brown colours (seafloor/borehole in either case). The x-axis represents the time over 60 minutes, in which data are integrated over 30 s each. Note the offset in borehole vs. reference pressure, which attests the successful deployment of the drop weight and coiled tubing and access to the open hole formation.*

DISCUSSION, CONCLUSION & OUTLOOK

[34] In summary, the "MeBoCORK concept" with its three versions (MeBoPLUG, -CORK and -PUPPI) aimed at a smart approach where an observatory can either be set by MeBo alone, or in combination of MeBo and ROV. The designs represented a compromise scientifically since a limited set of parameters is monitored, however, this has not been any different when the first full-size ODP-CORKs were deployed (Becker and Davis 2005). However, the three approaches taken appear extremely valuable at this stage and the future will likely provide opportunities for payload being added onto either observatory unit.

[35] In the pilot study off Japan, we demonstrated that one MeBoCORK-A and one MeBoCORK-B as well as two MeBoPLUGs can successfully be deployed. This meant that 4 out of a total of 6 MeBo holes drilled during a 2-week expedition got instrumented. For the MeBoPUPPIs, we are

currently in the phase of long-term performance tests in the pool before taking them into the natural environment.
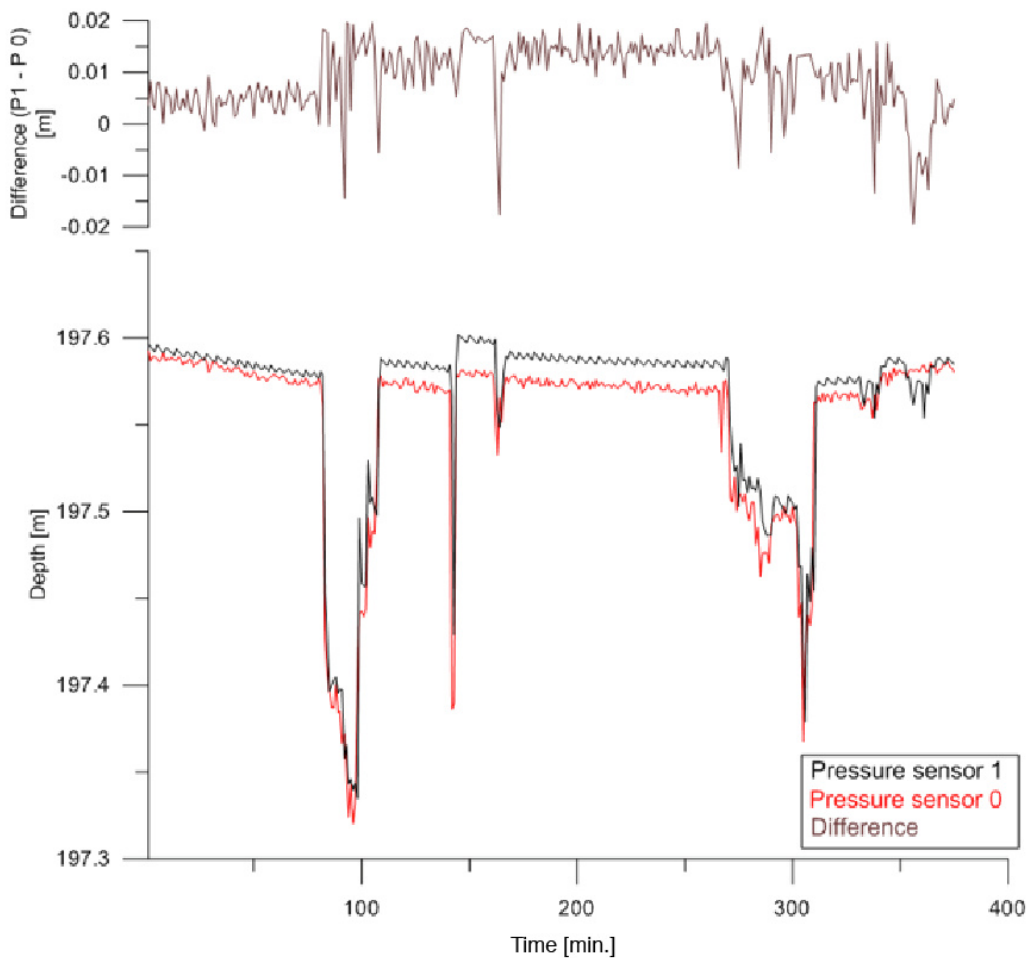
Figure S.33: *Data set covering the connection of MeBoCORK B with ROV Quest. For reasons to be explored, the borehole pressure is not any higher than the seafloor reference, suggesting a problem with the hotstab connection. Note that the vertical scale is in m * 10¹ and that the horizontal unit is minutes.*

[36] Of course, the MARUM-MeBo borehole observatories are limited and high performance seismometers or strainmeters may turn out impossible to be installed because of both their size and energy consumption. However, it appears that future scientific ocean drilling may have to cope with such a mission-specific approach from ships of opportunity. In addition to it being most affordable, there are associated advantages such as absent heave on the system during installation (i.e. no danger of destroying the instruments). Future avenues to increase the payload of the MeBoPLUGs and -CORKs are miniaturisation of transducers and optimisation of power consumption of the components, potentially combined with new ocean bottom fuel-cell technologies.

Acknowledgements

References

Becker K, Davis EE (2005) A review of CORK designs and operations during the Ocean Drilling Program. Proc Integr Ocean Drill Progr 301

Davis EE, Becker K (2001) Using ODP boreholes for studying subseafloor hydrogeology: Results from the first decade of CORK observations. Geosci Can 28:171-178.

Davis EE, Villinger HW (2006) Transient formation fluid pressures and temperatures in the Costa Rica forearc prism and subducting oceanic basement: CORK monitoring at ODP Sites 1253 and 1255. Earth Planet Sci Lett 245:232–244.

Davis EE, Becker K, Wang K, Obara K, Ito Y, Kinoshita M (2006) A discrete episode of seismic and aseismic deformation of the Nankai trough subduction zone accretionary prism and incoming Philippine Sea plate. Earth Planet Sci Lett 242:73–84.

Freudenthal T, Wefer G (2009) Shallow drilling in the deep sea: The sea floor drill rig MeBo. Ocean. 2009 – Eur: 1–4

Freudenthal T, Wefer G (2013) Drilling cores on the sea floor with the remote-controlled sea floor drilling rig MeBo. Geosci Instrum Method Data Syst 2:329–337. doi: 10.5194/gi-2-329-2013

Jannasch HW, Davis EE, Kastner M, Morris J, Pettigrew T, Plant JN, Solomon E, Villinger H, Wheat CG (2003) CORK-II: long-term monitoring of fluid chemistry, fluxes, and hydrology in instrumented boreholes at the Costa Rica subduction zone. Proc Ocean Drill Program, Initial Reports 205

Kopf A, Araki E, Toczko S, the Expedition 332 Scientists (2011a). NanTroSEIZE Stage 2: Riserless Observatory. IODP Prel Rep 332.

Kopf A, Saffer DM, Davis EE, Hammerschmidt S, LaBonte A, Meldrum R, Toczko S, Lauer R, Heesemann M, Macdonald R, Wheat CG, Jannasch HW, Edwards K, Orcutt B, Haddad A, Villinger H, Araki E, Kitada K, Kimura T, Kido Y (2011b). The SmartPlug and GeniusPlug: Simple retrievable observatory systems for NanTroSEIZE borehole monitoring. In: Kopf A, Araki E, Toczko S, the Expedition 332 Scientists (eds) Proc IODP, 332: Tokyo (Integrated Ocean Drilling Program Management International, Inc.).

McGinnis T (2009) Seafloor Drilling. In: Bar-Cohen Y, Zacny K (eds.) Drilling in Extreme Environments. Wiley, 309-345

Orcutt B, Wheat CG, Edwards KJ (2010) Subseafloor Ocean Crust Microbial Observatories: Development of FLOCS (FLow-through Osmo Colonization System) and Evaluation of Borehole Construction Materials. Geomicrobiol J 27:143–157.

Pfender M, Villinger H (2002) Miniaturized data loggers for deep sea sediment temperature gradient measurements. Mar Geol 186:557–570. doi: 10.1016/S0025-3227(02)00213-X

Schultheiss, P.J. McPhail, S.D. 1986. Schultheiss PJ, McPhail SD (1986) Direct indication of pore-water advection from pore pressure measurements in Madeira Abyssal Plain sediments. Nature 320:348–350.

Wheat CG, Jannasch HW, Kastner M, Hulme S, Cowen J, Edwards K, Orcutt BN, Glazer B (2011) Fluid Sampling from Oceanic Borehole Observatories: Design and Methods for CORK Activities (1990-2010). Proc ODP 327

APPENDIX C

Contributions to Conferences

APPENDIX C.1

CONTRIBUTIONS TO CONFERENCES: ORAL

The Easy Way of Monitoring Geohazards: MeBo-CORK the Easy Way of Monitoring Geohazards: MeBo-CORK as an Affordable Alternative to IODP Borehole Observatories

S. B. Hammerschmidt[1]*, A. Kopf[1], T. Freudenthal[1], V. Ratmeyer[1], M. Bergenthal[1], J. Renken[1], G. Wefer[1]

* corresponding author: hammerschmidt@uni-bremen.de
[1] MARUM Research Center, Marine Geotechnics, University of Bremen, Bremen, Germany

Borehole observatories (or circulation obviation retrofit kits, CORKs) are reliable instruments to obtain long-term *in situ* measurements of various parameters, with pressure and temperature being the most rudimentary. In the last 20 years, CORKs evolved from simple observatories to multifunctional sub-seafloor laboratories encompassing strainmeters, seismometers, geochemical samplers or microbiological chambers. Unfortunately, for installation and recovery a drillship is usually required, which is rarely available and expensive, and limited in the area of operation. Here, an affordable and more independent alternative is presented for shallow boreholes made by seafloor drills: the "MeBo-CORK.

Long-term data gathered by the MeBo-CORKs will help understanding strain and fault slip at plate boundaries as well as the mechanisms governing thermal anomalies or changes in fluid chemistry. Subsequently, the potential for fluid flow processes and geohazards (e.g. landslides, earthquakes) can be evaluated.

MeBo-CORKs were designed for the seafloor drill rig MeBo developed at MARUM Bremen. Two different MeBo-CORK designs are available, which both rely on casing in the upper part and a hotstab to connect the instrument to hydraulic tubing being dropped into the open hole at depth where fluid sampling and pressure monitoring take place. The first design is set by MeBo alone and comprises *in situ* pressure and temperature measurement. The second design also latches at the hotstab, but replaces the initially set MeBo-CORK with a seafloor unit with additional payload (i.e. mission specific sensors or sampling units for e.g., geochemistry, microbiology, etc.).

Recent studies highlighted the relationships between fluid pressure transients, strain accumulation and co- and aseismic deformation. Pressure and temperature transients in CORKs can also be caused by seismic and/or tsunami waves, storm events and tides, groundwater flow or gas hydrate dissociation.

MeBo-CORKs provide the same possibilities as conventional CORKs, and therefore represent an affordable yet more independent alternative. In summer 2012, a first field test is envisaged at the Nankai Trough, Japan. There, MeBo-CORKs will be installed in gas hydrate-bearing mud volcanoes to monitor *in situ* pressure and temperature in an active subduction zone.

Long-term Borehole Monitoring at the Nankai Trough: Fluid Pressure Data as Proxy for Formation Properties and Seismo-tectonic Processes

S. B. Hammerschmidt[1]*, E.E. Davis[2], A. Hüpers[1], E. Araki[1], A. Kopf[1]

*corresponding author: hammerschmidt@uni-bremen.de
[1] MARUM Research Center, Marine Geotechnics, University of Bremen, Bremen, Germany
[2] Pacific Geoscience Center, Geological Survey of Canada, Sidney, B.C., Canada
[3] Japan Agency for Earth-Science and Technology, DONET Research Group, Yokosuka, Japan

The Nankai Trough subduction zone, SE offshore Japan, is one of the most earthquake prone areas in the world. Besides normal earthquakes, the last decade revealed the existence of slow earthquakes, including episodic tremor and slip. Fluid migration along or across a giant out-of-sequence thrust fault, termed "megasplay fault", was repeatedly discussed to be important for subduction-related seismogenesis and tsunamigenesis. To investigate the existence, role and possibility of fluid flow, a SmartPlug borehole observatory was installed in IODP (Integrated Ocean Drilling Program) Hole C0010A, where a shallow branch of the splay fault is penetrated. At around 370 mbsf, *in situ* fluid pressure was monitored from August 2009 - November 2010.

The pressure data were heavily influenced by tidal noise, which allowed determination of the poroelastic and hydrological properties of the monitored formation by modeling pressure and amplitude response. After validating the model with laboratory permeability and logging-while-drilling data, it became clear that the splay fault zone has a hydraulic diffusivity too high for its porosity. Enhancement of hydraulic diffusivity is explained by the presence of fractures, particularly in close proximity to the casing screens. No recent fluid flow was observed, nor is it possible to estimate the connectivity of the fracture network.

After de-tiding and filtering of the pressure data, several transients were detected. These are explained by tsunami waves, local and distant storm-induced microseism and seismic waves triggered by normal earthquakes. Strain in the rock matrix caused by the arrival of seismic waves reached values of up to 10^{-7}, and was at least once followed by a drop in formation pressure, which is interpreted as temporary increase in permeability. Anomalous pressure transients (APTs) were found as well and compared with seismic waveform data from the Japanese DONET (Dense Ocean Floor Network for Earthquakes and Tsunamis). After processing of both datasets, most of the APTs corresponded again to microseism and seismic waves. Refraction and amplification of seismic waves led to discrete pressure anomalies in the upper cased and sealed borehole interval. One four-hour APT correlates with the onset of non-volcanic tremor, and manifests in the pressure data rather due to arriving seismic waves than by tectonic deformation of the formation. Also, the APT is more prominent than transients triggered by normal earthquakes, which suggest that trapped and amplified seismic wave modes are accountable. The tremor hypocenter and missing tectonic strain suggests that slip occurred on one deep fault patch, without migration to neighboring patches. Consequently, deep non-volcanic tremor might lead to stress accumulation at the locked seismogenic zone beneath the accretionary prism, increasing the likelihood of sudden stress release by a dynamic rupture in the future.

Consequently, the SmartPlug borehole observatory, which is attached to a mechanically set and retrievable Baker Hughes bridge plug, is a reliable instrument for monitoring of the borehole environment and surrounding formation. Beside elastic and hydrological properties of the formation, it is valuable for assessing tectonic processes. Future studies will focus on an enhanced version of the SmartPlug, which allows geochemical investigation of the fluids during the whole monitoring period. Recovery is envisaged for 2014, and will provide valuable insights into seismo-tectonic mechanisms.

APPENDIX C.2

CONTRIBUTIONS TO CONFERENCES: POSTER

Fluid Pressure and Temperature Response at the Nankai Trough Megasplay **Fault: Initial Results of the SmartPlug Borehole Observatory**

Hammerschmidt, S.[1]*, Kopf, A.[2], and the IODP Expedition 332 Scientists[3]

*corresponding author: hammerschmidt@uni-bremen.de
[1]University of Bremen, Department Geosciences, Germany
[2]MARUM, University of Bremen, Germany
[3] D/V Chikyu, Site C0010, SE offshore Japan

The SmartPlug is the first borehole observatory in the IODP Nankai Trough Seismogenic Zone Experiment (NanTroSEIZE). It was installed at Site C0010 where it penetrates one of the shallow branches of the Megasplay fault to obtain pressure and temperature data from the fault and from a hydrostatic reference section. Here, a 15 months-lasting pore pressure and temperature record collected by the SmartPlug is evaluated. The main objective of this work was to clarify the origin of transients in the data and its possible relationship to natural processes such as earthquakes, tectonic deformation or splay fault activity, as well as storms or low-pressure weather systems.

After pressure and temperature data were processed properly, comparisons were made using seismic data from the Japanese F-Net and Hi-Net, theoretical travel time calculations provided by the USGS as well as earthquake lists from the ISC. Additionally, meteorological data provided by the JMA and the U.S. COAPS as well as theoretical travel time calculations for tsunamis from the U.S. NGDC were used.

It can be shown that pulse-like pressure transients are related to regional/teleseismic earthquakes, originating mainly from the "Pacific Ring of Fire", from various depths and with diverse focal mechanisms. Approaching seismic waves of at least one regional earthquake led to a significant drop in the formation pressure, which is interpreted as a seismic wave-induced increase in permeability. The arrival of Rayleigh waves caused amplification of the borehole pressure, probably due to induced fluid flow. Tremor-like pressure transients are interpreted to be microseism, which is, based on pressure transient characteristics, triggered by storms or low-pressure weather systems on the open ocean. Approaching tsunamis look similar but caused longer period oscillations in the pressure record. Mainly in the seafloor pressure data distinct peaks are visible, some of which look similar to distinct peaks in the temperature data suggesting the same, so far unresolved triggering mechanism. The reason for the other distinct peaks remains unclear at this point.

Regarding the long-term and medium-term transients in the pressure and temperature data, respectively, no satisfying explanations were found. For the pressure transients, due to the similar characteristics, related mechanisms can be suggested. The results obtained so far exclude any seismogenic event at the Megasplay Fault or within the accretionary prism to be responsible for the observed pore pressure and temperature variations.

After the 15-months deployment, the SmartPlug temporary borehole observatory got replaced with an extended GeniusPlug, which also represents an instrumented bridge plug in the cased borehole. In addition to monitoring pressure and temperature, the GeniusPlug also contains a 30cm-long unit hosting an osmotically driven geochemical fluid sampler as well as chambers for microbiological experiments under *in situ* conditions. The instrument is designed to give a full 2-year record of pressure and temperature data and material for geochemical and biological analysis. Recovery with D\V Chikyu is envisaged for 2012.

The Advantage of Evolving Backwards: Simple CORKs for Beneficial Long-Term Borehole Monitoring at the Nankai Margin

S. B. Hammerschmidt[1]*, A. Kopf[1], E.E. Davis[3], D. Saffer[4], C.G. Wheat[5], A. LaBonte[3], R. Meldrum[3], M. Heesemann[3], R. MacDonald[3], H. Villinger[2], T. Freudenthal[1], V. Ratmeyer[1], M. Bergenthal[1], J. Renken[1], G. Wefer[1]

Presented at the *International Conference on a New Perspective of Great Earthquakes along Subduction Zones,* 28 February – 01 March 2012, Kochi, Japan

* corresponding author: hammerschmidt@uni-bremen.de
[1] MARUM Research Center, Marine Geotechnics, University of Bremen, Bremen, Germany
[2] Department of Geosciences, University of Bremen, Bremen, Germany
[3] Pacific Geoscience Centre, Geological Survey of Canada, British Columbia, Canada
[4] Department of Geosciences, Pennsylvania State University, Pennsylvania, USA
[5] Global Undersea Research Unit, University of Alaska Fairbanks, Alaska, USA

Nowadays, borehole observatories, termed Circulation Obviation Retrofit Kits or CORKs, are an inherent part of ocean science, and allow constant *in situ* monitoring of various poroelastic and petrophysical parameters. Beginning with a first simple sketch on a dinner napkin almost 20 years ago, CORKs evolved from rudimentary installations consisting mainly of pressure and temperature sensors to multifunctional borehole laboratories. The latter are usually adjustable to the diverse geoscientific objectives, including e.g. strainmeter, microbiological chambers (i.e. FLOCS) and fluid sampling units (i.e. OsmoSampler). In addition to that, packers can be located along the borehole instrument string, separating the up to several 100 m deep boreholes into individual hydrological regimes where different *in situ* measurements can take place.

Although the scientific outcome of borehole observatories is vital, the majority of boreholes across the oceans remained uninstrumented in the past, which is a major loss for the scientific community. The use of CORKs is the result of the logistic effort and associated with this, also a major financial one. Most CORKs require a drillship for installation, and subsequent ROV assignments for downloading of the data and maintenance of the instruments. In addition to that, the instruments are, with increasing complexity, more expensive and require a longer installation time, making the deployment more sensitive to weather conditions during installation and the installation procedure itself.

Here we present three types of Mini-CORKs, which contradict the evolution to more complex systems yet providing a diverse range of sensors for long-term monitoring of *in situ* parameters. The regional example chosen is the Nankai Trough, which is prone to repeated subduction megathrust earthquakes of M8 and larger. The area has been visited during several DSDP, ODP and IODP expedition, many of which had long-term observatories as a key scientific objective on their agenda. In fact, two of the most complex multi-level CORK systems are currently installed in Nankai: The A-CORK (Advanced CORK) along the Muroto transect (see Proceedings of ODP Legs 190 and 196 for reference), and the Seismo-CORK (or LTBMS, Long-term Borehole Monitoring System, which got recently successfully deployed with D/V Chikyu; see IODP Exp. 332 Proceedings). At the same time, problems occurred during some of the more complicated CORK systems and not all components showed full functionality after their deployment. Also, increased cost for ship time has forced IODP into a situation where the observatory has to be provided in large parts by third party funds. As a consequence, a need for affordable CORKs has emerged. We here want to introduce three types of Mini-CORKs, which got recently developed for monitoring EQ-related changes in physical parameters at the Nankai Margin.

The first type, called SmartPlug or mini-CORK, is a very simple system consisting only of two pressure transducers and four temperature sensors. The SmartPlug is attached to a retrievable bridge plug, at which, once lowered down into the borehole, a packer is set to isolate the section below the SmartPlug for *in situ* measurements of pressure and temperature. For comparison, a simultaneous monitoring of hydrostatic reference pressure and temperature is possible by one pressure and three temperature sensors (one in

the pressure sensor, one in the data logger housing and one stand-alone miniature temperature logger) being located inside the SmartPlug casing. Although a drillship is required for installation and recovery of the SmartPlug, its low overall cost and small size of c. 1.3m allows a fast and variable placement even within shallow boreholes. During IODP Exp. 319, such a Mini-CORK was successfully installed in the Nankai accretionary prism, where a shallow branch of a giant out-of-sequence thrust fault was penetrated and subsequently monitored. After recovery during IODP Exp. 332, the SmartPlug provided a 15-months lasting pressure and temperature dataset, which proved to be reliable in detecting incoming seismic and tsunami waves as well as low-pressure weather systems. Moreover, important assumptions could be made regarding the poroelastic properties of the surrounding formation.

The SmartPlug got replaced by a more advanced version, the GeniusPlug, which has a bulkhead extension at its lower part, including an OsmoSampler and FLOCS microbiological chambers, allowing *in situ* fluid sampling and microbiological experiments during the monitoring period. Like the SmartPlug, the GeniusPlug requires a drillship for installation and recovery, but its simple design allows a fairly fast and easy installation in nearly every borehole and at variable depths.

Going one step further in simplicity, a Mini-CORK has recently developed for installation without a drillship. The so-called MeBo-CORK was designed for the portable seafloor drill rig MeBo (MARUM, Univ. Bremen, Germany). The latter can be operated from any research vessel and allows coring to a depth of 70 m, which may be followed by instrumentation of the borehole with the MeBo-CORK. Two designs are available, which both need casing at the upper part of the borehole and a hotstab to connect the instrument to the sensor strings within the borehole where fluid sampling, pressure and temperature monitoring take place. The first design is installed by the MeBo, and allows *in situ* measurement of pressure and temperature solely. By using a ROV, the initial MeBo-CORK can be replaced by the second design, where a seafloor unit including additional mission specific sensors is attached to the hotstab. Telemetric data submission makes costly and time-consuming recovery operations obsolete. A first field test for the MeBo-CORKs into mud volcanoes in the Kumano forearc basin is envisaged for summer 2012.

Extending NanTroSEIZE landwards: Long-term observatories in the Kumano Basin active mud volcanoes to monitor EQ precursors!?

Kopf, A.*[1], S. Hammerschmidt[1], T. Freudenthal[1], V. Ratmeyer[1], M. Tryon[2], S. Toczko[3], Y. Ashi[4]

*corresponding author: akopf@uni-bremen.de

[1] MARUM Research Center, University of Bremen, Bremen, Germany

[2] SCRIPPS Institution of Oceanography, University of California San Diego, La Jolla, USA

[3] CDEX, Yokohama, Japan

[4] ORI, University of Tokyo, Tokyo, Japan

Approximately 90% of the seismic moment on Earth is released in often devastating subduction zone earthquakes (EQs). The Nankai Trough area, offshore Japan, is one of such subduction zones prone to repeated subduction megathrust earthquakes of M8 and larger. The area has been visited during several DSDP, ODP and IODP expeditions, many of which had long-term observatories as a key scientific objective on their agenda.

In the Integrated Ocean Drilling Program (IODP), the study of seismogenesis along an active convergent margin plays a key role in the form of a multi-expedition effort named "NanTroSEIZE" (Nankai Trough Seismogenic Zone Experiment). To date, eight expeditions (IODP Expeditions 314-316, 319, 322, 326, 332-333) drilled 12 sites along a transect from the incoming plate across the frontal accretionary prism to the forearc basin. In the near future, the deepest hole will tap into the seismogenic portion of the subduction megathrust using Riser drilling. Among the main results, one of the most astonishing ones is the lack of deep-seated fluids along any of the main faults penetrated during NanTroSEIZE, including the décollement and a number of branches of the mega-splay fault cutting the Nankai forearc.

At the same time, deep-seated fluid geochemistry is a powerful tool to shed light on the physico-chemical processes governing subduction zone dynamics at moderate PT conditions. Those fluids may ascend along fault zones or conduits of mud domes from depths of many kilometres to the seafloor at very high rates. Mobile element concentrations and isotope signatures of aqueous and gaseous fluids are hence nearly unchanged compared to their depth of origin, and hence may give hints regarding the in situ processes at depth. Onshore, earlier studies have attested that the geochemical composition of both waters and gas emitted during mud volcanic eruptions prior to large EQs show profound changes compared to background values. Those discrepancies may be associated with fluid pathways related to pre-seismic stress changes at depth and provide insight into the depth of origin (e.g. crustal fluids, etc.). For Nankai, such phenomena may be important to (i) identify a deep fluid source, possible taking the „short-cut" from seismogenic depth to the Kumano forearc seafloor along out-of-sequence faults feeding the mud volcanoes, and (ii) to associate fluid geochemical transients with certain seismic events from DONET or other long-term seismometers.

In a future seagoing expedition with German RV SONNE (June/July 2012), several of the Kumano Basin mud volcanoes will be drilled using the portable seafloor drill rig MeBo by MARUM, Univ. Bremen, Germany. One location will be a reconnaissance study from CHIKYU cruise 903 into that area. The mud domes have been shown to be active (e.g. interrupted BSRs in pseudo-3D seismic lines, seepage on the crest, etc.), emitting thermogenic methane and sporting gas hydrates and clasts mobilised within the accretionary complex underneath. The drill holes will be fully cored to max 70 mbsf, cased and then instrumented with a simple, slim "MeBo-CORK". Two designs are available, which both rely on a hotstab-connection completing the casing string and isolating it from the overlying ocean body. At its lower end, the hotstab is connected to coiled tubing, which extends into the open hole near terminal drilling depth. The first design is installed by the MeBo and comprises a self-contained unit measuring pressure and

temperature and sending acoustic data on demand (i.e. it is an instrumented MeBo drill rod). By using a ROV, the initial MeBo-CORK can be replaced at a later visit by the second design, where a seafloor unit including additional mission-specific payload is attached to the hotstab. This second seafloor-based unit is connected to the hotstab via an umbilical, and may host osmo-samplers, FLOCS units, etc. – it will be replaced as a whole with an identical seafloor unit by ROV once the tubing of the osmo-sampler reaches its limit every approx. 2 years. Otherwise, data can be downloaded at any time via ship of opportunity in the area, and can be correlated to seafloor stations such as those from DONET, temporary arrays, etc. With the current design of the MeBo-CORKs deployed at the Kumano mud volcanoes, we hope to establish tools that monitor EQ precursor phenomena related to stress changes, i.e. pore P transients, geochemical changes and maybe T variations. If tied to real-time networks such as DONET, such information may turn out to be useful to mitigate geohazards and provide society with means of earthquake warning systems. Last but not least, the geochemical transients will further illuminate physico-chemical constraints at seismogenic depth, which may turn out to be helpful in explaining the stress-heat flow paradox (e.g. by attesting certain chemical and mineralogical processes, authigenic precipitation reactions, etc.).

A Wealth of Signals from the Nankai Trough Megasplay Fault as Indicated by Long-term SmartPlug Borehole Observatory Data

S. Hammerschmidt[1]*, A. Kopf[1]

Presented at the *IODP/ICDP Kolloquium*,
07 – 09 March 2012, Kiel, Germany

*corresponding author: shammerschmidt@marum.de
[1] MARUM Research Center, University of Bremen, Bremen, Germany

Almost 20 years ago, the scientific community working in the marine realm started to use borehole observatories to monitor the re-establishment of *in* situ conditions inside a borehole and their consequent response to tectonic, hydrogeologic and/or atmospheric events. In the IODP Nankai Trough Seismogenic Zone Experiment (NanTroSEIZE), the first borehole observatory, the so-called SmartPlug, was installed during IODP Exp. 319, and after 15 months, got recovered on IODP Exp. 332. It penetrated one of the shallow branches of a giant out-of-sequence splay fault system (OOSS), the so-called megasplay fault, which separates the Nankai Trough accretionary prism into an inner and an outer part. The OOSS might have shown coseismic activity during the 1944 Tonankai M8.1 earthquake, and is thought to act as potential pathway for upward migrating fluids, which subsequently would also affect the seismogenic potential of the underlying thrust fault. Thus potential activity of the megasplay fault could be indicated by pressure and temperature transients in the SmartPlug dataset. Moreover, deformational events or even anomalous events like very-low frequency earthquakes, slow-slip events or seismic tremor (which could "load" the seismogenic zone) could be seen in the data. However, transients can also be caused by the arrival of seismic and tsunami waves radiated form regional/farfield earthquakes, by low-pressure weather systems, mass wasting processes and internal waves and/or simply represent sensor artifacts. Therefore, the aim of this work was the evaluation of the 15-month lasting SmartPlug data regarding the triggering mechanisms for the observed temperature and fluid pressure oscillations.

The SmartPlug is instrumented with two Paroscientific pressure transducers, one monitoring the pressure at the megasplay fault zone and one measuring the hydrostatic reference pressure, hereafter termed formation and HR pressure, respectively. Temperature is monitored by these sensors, and by a sensor located in the data logger housing. An autonomous temperature measurement was made by an ANTARES miniature temperature logger (MTL), which is, together with the data logger housing, situated in the hydrostatic reference section.

It was necessary to de-tide the pressure data using the approach of Pawlowicz et al. (2002), which was followed by high-pass butterworth filtering with a cut-off frequency of 0.002 Hz. Pressure and temperature transients were compared using global and Japanese earthquake catalogues, meteorological data from the U.S. COAPS and theoretical travel time calculations for seismic and tsunami waves provided by the USGS and the U.S. NGDC, respectively. The detected transients were separated in (a) short-term, (b) medium-term and (c) long-term anomalies:

(a) The short-term anomalies include pulse-like pressure transients, step-like pressure transients, and distinct peaks in the HR pressure and the temperature. Pulse-like transients look similar to common seismograms and can be clearly attributed to the arrival of seismic waves originating from regional or farfield earthquakes within the "Pacific Ring of Fire". Often observed is an amplified formation pressure compared to the HR pressure when Rayleigh waves approach Site C0010; this is interpreted to be caused by seismic wave induced strain and subsequent dewatering of the material close to the casing screens. Step-like transients are rare in the dataset. However, at least one sudden pressure drop can be correlated to the arrival of seismic waves from a regional M6.2 earthquake, which is explained by seismic wave-induced increase in permeability. Still unresolved is the origin of the distinct peaks in the HR pressure data. These anomalies occur also in the raw data, thus filter effects can be excluded. The short duration of 3-4 minutes also excludes tectonic deformational processes to be responsible. Possible triggering

mechanisms might be internal waves or mass wasting processes. However, the SmartPlug was probably protected from these effects by a 200kg heavy corrosion cap, which was set at the wellhead directly after the installation. These anomalies look similar to distinct peaks in the temperature data suggesting the same unresolved triggering mechanism.

(b) Two types of medium-term pressure transients were detected: short-period anomalies, with periods of up to 3 minutes, and long-period anomalies, with less pronounced envelopes and periods of up to 10 minutes. The former can clearly be attributed to the arrival of low pressure weather systems or storms, which subsequently cause microseism which influences the pressure data. This is supported by waveform data from the Japanese F-Net, which show a simultaneous increase in the frequency range of 0.1 – 0.25 Hz. By contrast. long-period anomalies are related to the arrival of tsunami waves, which is supported by theoretical travel time calculations by the U.S. NGDC. Tsunami waves are in the infragravity frequency range, thus leading to longer-period oscillations. The medium-term temperature transients remain puzzling, due to their contrasting anomalies in the HR section, which surprisingly sometimes correspond with anomalies in the formation section, as well as a missing correlation with pressure, seismic and meteorological data.

(c) Whereas the long-term temperature evolution clearly shows a re-establishment of *in situ* conditions, the long-term pressure transients are also still unresolved. Deformational events in the accretionary prism, subsidence, sensor errors and ocean bottom currents could be possible triggering mechanisms, but based on the curve progressions and anomaly characteristics these can be all excluded. Regarding the long-term pressure transients, sensor drift would be a possible explanation However, the here calculated apparent drift led to an excess fluid pressure of almost 20 kPa at the end of the monitoring period, which is not supported by the hydrostatic checks made during the deployment and recovery of the SmartPlug. These indicated only a difference of 0.2 kPa, which is in the range of sensor drift published for the Paroscientific sensors.

Consequently, our observations so far exclude any seismogenic event at the Megasplay Fault or within the accretionary prism to be responsible for the observed fluid pressure and temperature variations. However, this does not mean that the megasplay could not be reactivated in case of an earthquake at seismogenic depth.

References

Amante, C., and B. W. Ealkins (2009), ETOPO1 1 Arc-Minute Global Relief Model: Procedures, Data Sources and Analysis, *NOAA Technial Memorandum NESDIS*, *NGDC-24*, 19 pp.

Pawlowicz, R., B. Bearsley, and S. Lentz (2002), Classical Tidal Harmonic Analysis Including Error Estimates in MATLAB using T_TIDE, *Computers & Geosciences*, *28*, 929 - 937.

Wessel, P., and W. H. F. Smith (1991), Free software helps map and display data, *Eos Trans. AGU*, *72*(441).

The Era of Mini-CORKS: Affordable Yet Fully Equipped Borehole Observatories for Long-term Monitoring of Geohazards

A. Kopf[1], S.Hammerschmidt[1] , E.E. Davis[3], D. Saffer[4], C.G. Wheat[5], A. LaBonte[3], R. Meldrum[3], M. Heesemann[3], R. MacDonald[3], H. Villinger[2], T. Freudenthal[1], V. Ratmeyer[1], M. Bergenthal[1], J. Renken[1], G. Wefer[1]

*corresponding author: akopf@uni-bremen.de
[1] MARUM Research Center, University of Bremen, Bremen, Germany
[2] Department of Geosciences, University of Bremen, Bremen, Germany
[3] Pacific Geoscience Centre, Geological Survey of Canada, British Columbia, Canada
[4] Department of Geosciences, Pennsylvania State University, Pennsylvania, USA
[5] Global Undersea Research Unit, University of Alaska Fairbanks, Alaska, USA

Borehole Observatories, so-called Circulation Obviation Retrofit Kits or CORKs, are a profound way to allow the re-establishment of *in situ* conditions in submarine boreholes and their subsequent monitoring for several months or even years. Since the first CORKs were installed almost 20 years ago, borehole observatories evolved from simple instruments providing only pressure and temperature sensors to multifunctional, interdisciplinary subseafloor laboratories, including fluid sampling devices (i.e. OsmoSampler, Jannasch et al., 2003), microbiological chambers (i.e. FLOCS, Orcutt et al., 2010) or strainmeter (e.g. Kopf et al., 2011). The scientific outcome, even of the more simple CORKs, is enormous. Recent studies showed that seismogenic activity at convergent margins, e.g. at the Nankai Trough, can be clearly correlated with pressure transients detected by borehole observatories (e.g. Davis et al., 2006; Davis et al., 2009). By monitoring *in situ* pressure, temperature and geochemistry over months or even years, it is generally possible to detect distinct changes in geochemical and isotope composition as well as strain (Bredehoeft, 1967; Davis et al., 2004) and relate these to seismogenic processes by comparing the data with volumetric strainmeter measurements or deformational events identified via GPS data (e.g. Solomon et al., 2009).

Unfortunately, despite their potential vital scientific outcome, several boreholes remained uninstrumented in the past, and were abandoned after drilling and coring were completed. This has several reasons: first of all, CORKs usually require a drillship for installation and subsequent ROV assignments for instrument maintenance and data download, which is not only a logistic but also a great financial effort. In addition to that, the increasing complexity of CORKs made them more affected by environmental constraints during and after the installation and by the installation procedure itself, which became noticeable in longer ship time and subsequently, again, in increased financial and logistic expenses.

Here we present three types if Mini-CORKs, which, instead of representing one step further to more complexity and higher expenses, are simpler yet provide a comprehensive set of measurements. As a regional example, the Nankai Trough accretionary prism is chosen, which started to form around 2.8 Ma years ago by subduction of the Philippine Sea Plate beneath the Eurasian Plate. In the past this led to repeated subduction thrust earthquakes of M8+, therefore this area was already chosen by the Deep Sea Drilling Project (DSDP), Ocean Drilling Project (ODP) and Integrated Ocean Drilling Project (IODP) for investigating the processes influencing the seismogenic activity. For this purpose, highly sophisticated CORKs were already installed, for instance the Advanced-CORK or the Seismo-CORK. Unfortunately, due to their complexity and the need for more ship time, IODP was forced to rely on third party funding. At the same time, not all sensors of the CORKs worked properly after the installation was completed. Consequently, the need for less complex and less expensive yet sufficiently equipped CORKs arose, which may be satisfied by the here presented alternatives.

One simple Mini-CORK is called the SmartPlug, which consists solely of two Paroscientific pressure and temperature sensors, one additional temperature sensor in the data logger housing and one autonomous

ANTARES miniature temperature logger. The instrument is attached to a retrievable bridge plug, which seals the borehole and isolates the zone of interest from the overlying water column. Pressure and temperature measurements take place in a hydrostatic reference section and in the zone of interest, where the sensors are connected to the formation via perforated casing screens. The SmartPlug was already installed at IODP Site C0010 during IODP Exp. 319 (Saffer et al., 2009), and after 15 months, got recovered during IODP Exp. 332 (Kopf et al., 2011). The data proved to be reliable in detecting incoming seismic and tsunami waves as well as low-pressure weather systems. Moreover, important assumptions could be made regarding the poroelastic properties of the surrounding formation.

The SmartPlug got replaced by a second, slightly advanced MiniCORK, the so-called GeniusPlug. It has the same simple design, but has a bulkhead extension at its lower part where an OsmoSampler and a FLOCS microbiological chamber are incorporated. Recovery is planned for 2012 or 2013 (associated with Exp 338).

Even simpler is the so-called MeBo-CORK, which was designed especially for the portable MARUM drill rig MeBo. The latter can drill to depths of up to 70 m and can be operated from any ship of opportunity. After coring, the upper part of the borehole remains cased, and is hydraulically sealed by an adapter which contains a hotstab hydraulic connection and an electrical connection. From this seal, pressure and temperature sensors are let down inside the borehole, where they monitor *in situ* pressure and temperature development. The MeBo-CORKs connect to these sensors via the hotstab connection, and can transmit the data via a telemetric unit, making time-consuming and costly recovery operations obsolete. Two MeBo-CORK designs will be available, one which can be installed directly by the MeBo, and one which replaces the first one and has to be installed by an ROV. At the same time, the second design consists of a seafloor unit, which has also the telemetric unit, battery packs, data logger and pressure transducers, but which allows adding further mission specific sensors and devices.

A first field test is envisaged for an expedition with R/V Sonne (SO-222) at the Nankai Trough in 2012, where the MeBo will drill into mud volcanoes piercing the Kumano forearc basin. These boreholes will be instrumented by MeBo-CORKs, thus allowing to observe pressure and temperature as well as fluid sampling over the whole monitoring period. Since mud volcanoes can serve as window to depth this may provide valuable insights into seismogenic processes of the underlying splay fault system or even the plate boundary megathrust.

References

Bredehoeft, J. D. (1967), Response of Well-Aquifer Systems to Earth Tides, *J. Geophys. Res.*, *72*(12), 3075-3087.

Davis, E., K. Becker, R. Dziak, J. Cassidy, K. Wang, and M. Lilley (2004), Hydrological response to a seafloor spreading episode on the Juan de Fuca ridge, *Nature*, *430*(6997), 335-338.

Davis, E. E., K. Becker, K. Wang, K. Obara, Y. Ito, and M. Kinoshita (2006), A discrete episode of seismic and aseismic deformation of the Nankai trough subduction zone accretionary prism and incoming Philippine Sea plate, *Earth and Planetary Science Letters*, *242*(1-2), 73-84.

Davis, E., K. Becker, K. Wang, and M. Kinoshita (2009), Co-seismic and post-seismic pore-fluid pressure changes in the Philippine Sea plate and Nankai decollement in response to a seismogenic strain event off Kii Peninsula, Japan, *Earth, Planets and Space*, *61*(6), 9.

Jannasch, H., E.E. Davis,, M. Kastner, J. Morris, T. Pettigrew, J.N. Plant, E. Solomon, H. Villinger, and C.G. Wheat, (2003), *CORK-II: long-term monitoring of fluid chemistry, fluxes, and hydrology in instrumented boreholes at the Costa Rica subduction zone.*, paper presented at Proceedings of the Ocean Drilling Program, Initial Reports, 205.

Kopf, A., E. Araki, S. Toczko, and the Expedition 332 Scientists (2011), NanTroSEIZE Stage 2: Riserless Observatory, Proceedings IODP , Exp 332: http://publications.iodp.org/proceedings/332/332title.htm

Orcutt, B., C. G. Wheat, and K. J. Edwards (2010), Subseafloor Ocean Crust Microbial Observatories: Development of FLOCS (FLow-through Osmo Colonization System) and Evaluation of Borehole Construction Materials, *Geomicrobiology Journal*, *27*(2), 143 - 157.

Saffer, D., L. McNeill, E. Araki, T. Byrne, N. Eguchi, S. Toczko, K. Takahashi and the Expedition 319 Scientists (2009), NanTroSEIZE Stage 2: NanTroSEIZE Riser/Riserless Observatory, *IODP Preliminary Report*, *319*, 83 pp.

Solomon, E. A., M. Kastner, C. G. Wheat, H. Jannasch, G. Robertson, E. E. Davis, and J. D. Morris (2009), Long-term hydrogeochemical records in the oceanic basement and forearc prism at the Costa Rica subduction zone, *Earth and Planetary Science Letters*, *282*(1-4), 240-251.

Implications for Petrophysical and Hydrological Properties of the Nankai Trough Megasplay Fault Based on SmartPlug Borehole Observatory Data

S.Hammerschmidt[1]* , E.E. Davis[2], A. Kopf[1]

*corresponding author: shammerschmidt@marum.de
[1] MARUM Research Center, University of Bremen, Bremen, Germany
[2] Pacific Geoscience Centre, Geological Survey of Canada, British Columbia, Canada

The SmartPlug is the first borehole observatory in the IODP Nankai Trough Seismogenic Zone Experiment (NanTroSEIZE). It was installed in the Nankai Trough accretionary prism where Hole C0010 penetrates one of the shallow branches of a giant out-of-sequence splay fault system (OOSS), the so-called megasplay fault. The main objectives were to monitor *in situ* fluid pressure and temperature from the fault zone via casing screens and compare them to a hydrostatic reference section. The OOSS may be connected to the seismogenic part of the underlying thrust fault boundary and is thought to act as potential pathway for upward migrating fluids, which subsequently would affect the seismogenic potential of the thrust fault. Moreover, the OOSS is inferred to have shown coseismic rupture during the 1944 Tonankai M8.1 earthquake, which may be supported by potential along-fault flow and elevated fluid pressure in the fault zone. Investigations regarding the petrophysical and hydrogeological characteristics of the OOSS are rare; the SmartPlug pressure dataset helps to overcome this information gap.

The 15 month-lasting record is heavily affected by tidal signals, which are usually removed to allow a proper investigation of anomalies. However, here the tidal noise itself was investigated, because it reveals important hydrogeological characteristics of the megasplay fault zone. The main objective of this work was to determine the tidal loading efficiency, and place bounds on elastic properties, permeability and hydraulic diffusivity. It was also possible to define an instrument compliance ratio from tidal and instrument response analysis, and to estimate the permeability of the damage zone surrounding the casing screens.

A mean tidal loading efficiency of 0.82 was obtained, which is similar to published results for samples from convergent margins of similar porosity. The instrument compliance ratio ranges from ca. 60 to values of up to 10^4 for calculations based on instrument specifications and tidal response analysis, respectively. This together with the low wellbore storage of around $10^{-10} - 10^{-12}$ m^3 Pa^{-1}, the absence of any phase shift and the low amplitude damping of 0.7% allows the assumption that the SmartPlug is a stiff instrument, surrounded by a sufficiently high permeable material. However, it is suggested that the apparently high permeability is owed to a drilling-induced damage zone surrounding the casing, which allows a good hydraulic connection to the fault zone. At the same time, based on porosity-permeability relationships, a permeability of only 7.5 x 10^{-18} m^2 was estimated, which led to a hydraulic diffusivity of only 2.6 x 10^{-13} m^2 s^{-1} (calculated using elastic properties inferred from the tidal loading efficiency and under the assumption that the material at the casing screens is homogeneous). Ultimately, it is unlikely that the megasplay fault can act as fluid pathway.

In summary, our work shows that semi-quantitave estimates of the petrophysical and hydrogeologic parameters are possible with pressure data from the SmartPlug borehole observatory, a self-contained instrument of only a little more than 1 m length, compatible with standard industry bridge plugs, and having simple, robust electronics that have a monitoring lifetime of 10 years.

Using tidal noise in long-term fluid pressure data: an example from the SmartPlug borehole observatory

S.Hammerschmidt[1]* , E.E. Davis[2], A. Kopf[1]

*corresponding author: shammerschmidt@marum.de
[1] MARUM Research Center, University of Bremen, Bremen, Germany
[2] Pacific Geoscience Centre, Geological Survey of Canada, British Columbia, Canada

During the last two decades, borehole observatories or CORKs (Circulating Obviation Retrofit Kits) proved to be reliable systems for monitoring *in situ* properties like pressure, temperature and or the geochemistry of the fluids. The scientific outcome is vital, not only for understanding the hydrogeology of the oceanic crust, including the global transport of solutes and heat flow budgets, but also in shedding light on seismogenic processes at convergent margins.

Here, a very simple CORK system, the SmartPlug, was installed in the Nankai Trough accretionary prism, SE Japan, where it crosscuts a shallow branch of a giant splay fault system showing a co-seismic potential. The 15-months lasting record was heavily influenced by tidal noise, which can be dealt with by two ways: (1) by conducting a fast fourier transformation and by calculating the power spectral density, the so-called "tidal loading efficiency" can be obtained, i.e. the total fraction of a pressure change caused by tidal signals which is elastically taken up by the fluid. The tidal loading efficiency can be used to infer hydrogeologic and poroelastic properties of the splay fault system, and subsequently, to shed light on its mechanical properties and the possibility of fluid migration. Consequently, using the tidal noise in the fluid pressure data improves our understanding of the co-seismic potential of the splay fault system. (2) The tidal noise was removed, and the pressure data was evaluated for co-seismic transients.

Report from IODP Expedition 338: Nankai Trough Seismogenic Zone Experiment Stage 3 - Plate Boundary Deep Riser 2

A. Hüpers[1]*, S.Hammerschmidt[1], and the IODP Expedition 338 Scientists

Presented at the *IODP/ICDP Kolloquium*, 25 – 27 March 2013, Freiberg, Germany

*corresponding author: ahuepers@marum.de

[1] MARUM Research Center, University of Bremen, Bremen, Germany

The Nankai Trough Seismogenic Zone Experiment (NanTroSEIZE) is a multistage drilling project of the Integrated Ocean Drilling Program (IODP). NanTroSEIZE comprises interdisciplinary approaches including direct sampling, *in situ* measurements, and long-term monitoring of the Nankai subduction system off Kii peninsula (SW Japan) to investigate fault mechanics and seismogenesis along a subduction megathrust. The offshore expeditions and associated core and log data are complemented by shore-based research such as laboratory experiments and numerical modeling. The primary goals of IODP Expedition 338 with D/V *Chikyu* (1 October 2012 - 13 January 2013) were to deepen Site C0002 above the presumably locked portion of the megathrust from 856 meters below the sea floor (mbsf) with riser drilling, analyse cuttings and limited cores (100 m from 2300 – 2400 mbsf), conduct logging-while-drilling (LWD), and eventually case the hole to the target depth of 3600 mbsf. However, rough sea conditions along with the strong Kuroshio Current on November 17 caused damage to part of the riser pipe. As a result further riser drilling operations were abandoned and the hole was suspended at 2005 mbsf but left for future re-entry. Drilling operations were revised to LWD and coring with riserless drilling at important sites for NanTroSEIZE. The aim of the contingency plan included a comprehensive characterization of the alteration stage of the oceanic basement seaward of the subduction zone (Site C0012), investigation of the early stage evolution of the Kumano Basin (Site C0002), assessment of recent activity of the shallow megasplay fault zone system (Site C0022), and mechanics of submarine landslides (Sites C0018, C0021).

At Site C0002, Expedition 338 successfully conducted LWD, mud gas monitoring, and cuttings analyses while riser drilling to 2005 mbsf (Hole C0002F) and also recovered cores from 200-505 mbsf (C0002K, C0002L), 900-920 mbsf (C0002H) and 1100-1120 mbsf (C0002J) during riserless operation. Preliminary results give evidence for syn-depositonal erosional processes in the lower part of Kumano forearc basin (Unit III) and provide new insights on the debatable unconformity between forearc basin sediments and the accretionary prism. The lithology of the accretionary prism sediments is composed of silty claystone with sandstone as a minor lithology. Two lithological units (Unit IV and V) can be distinguished in the wedge that are separated by a major fault zone at 1640 mbsf. The upper section of Unit IV is composed of accreted slope basin sediments while the underlying sediments represent probably deposits from the trench, accretionary prism slope basin or Shikoku Basin submarine fan. Unit V is dominanted by a greenish-gray silty claystone. Downhole increase of thermogenically formed gas and evidence for mechanical compaction and cementation provide constraints on physical properties and insights in processes in the unknown deeper part of the accretionary prism.

Results from riserless drilling at Site C0012 include a comprehensive LWD characterization and allow a detailed core-log-seismic integration of the subduction inputs. The sediment/basement contact was penetrated at ~530msbf. The underlying oceanic crust consists of a 100 m thick zone of altered pillow basalts and sheet flow deposits. Fluctuations in gamma ray values may reflect a changing volume of sediment within the basement. Below 626 mbsf logging data suggests a less altered basement without evidence for interlayered sediment horizons. The hole was abandonded when the target depth of 709 mbsf was reached.

Expedition 338 collected LWD logs in Holes C0018B and C0021A and cores in C0021B in the slope basin seaward of the megasplay fault. Maximum target depth for these holes was 420 mbsf. The LWD data provides new constraints to characterize *in situ* internal structures and properties of mass-transport

deposits and to improve our understanding of submarine landslides in the slope basins seaward of the splay fault. In addition, low angle faults identified in X-ray Computed Tomography scans of cores from Site C0021 suggest a splay-fault-related, out-of-sequence thrust within slope basin sediments and shed new light on recent activity of the megasplay. At Site C0022B the megasplay fault is probably located within an interval of 100-101 mbsf. Several observations are in favor for this interval which is characterized by an increase in bedding dips in the vicinity of this interval, a higher density of minor faults 15-20 m above the interval and the presence of three 2 cm-thick intervals of claystone showing planar fabrics never encountered elsewhere at Hole C0022B. The hole was terminated at 416 mbsf.

In conclusion, Expedition 338 results provide new insights into the Nankai subduction system. Numerous whole-round and cuttings samples were taken for further on-shore laboratory investigations of composition, microstructures, frictional properties, and porosity/permeability.

Influence of drilling operations on drilling mud gas monitoring during IODP Exp. 338 and 348

S.Hammerschmidt[1]*, S. Toczko[2], Y. Kubo[2], S. Fuchida[3], T. Wiersberg[4], A. Kopf[1], T. Hirose[5], D. Saffer[6], H. Tobin[7], and the Expedition 348 Scientists

*corresponding author: shammerschmidt@marum.de
[1] MARUM Research Center, University of Bremen, Bremen, Germany
[2] JAMSTEC, Yokohama, Japan
[3] Scientific Drilling, GFZ German Research Centre for Geosciences, Potsdam, Gemany
[4] Osaka City University, Osaka, Japan
[5] JAMSTEC, Kochi, Japan
[6] The Pennsylvania State University, University Park, USA
[7] University of Wisconsin-Madison, Madison, USA

The history of scientific ocean drilling has developed some new techniques and technologies for drilling science, dynamic positioning being one of the most famous. However, while industry has developed newer tools and techniques, only some of these have been used in scientific ocean drilling. The introduction of riser-drilling, which recirculates the drilling mud and returns to the platform solids and gases from the formation, to the International Ocean Drilling Program (IODP) through the launch of the Japan Agency of Marine Earth-Science and Technology (JAMSTEC) riser-drilling vessel D/V Chikyu, has made some of these techniques available to science. IODP Expedition 319 (NanTroSEIZE Stage 2: riser/riserless observatory) was the first such attempt, and among the tools and techniques used was drilling mud gas analysis.

While industry regularly conducts drilling mud gas logging for safety concerns and reservoir evaluation, science is more interested in other components (e.g He, ^{222}Rn) that are beyond the scope of typical mud logging services. Drilling mud gas logging simply examines the gases released into the drilling mud as part of the drilling process; the bit breaks and grinds the formation, releasing any trapped gases. These then circulate within the "closed circuit" mud-flow back to the drilling rig, where a degasser extracts these gases and passes them on to a dedicated mud gas logging unit. The unit contains gas chromatographs, mass spectrometers, spectral analyzers, radon gas analyzers, and a methane carbon isotope analyzer. Data are collected and stored in a database, together with several drilling parameters (rate of penetration, mud density, etc.). This initial attempt was further refined during IODP Expeditions 337 (Deep Coalbed Biosphere off Shimokita), 338 (NanTroSEIZE Stage 3: NanTroSEIZE Plate Boundary Deep Riser 2) and finally 348 (NanTroSEIZE Stage 3: NanTroSEIZE Plate Boundary Deep Riser 3). Although still in its development stage for scientific application, this technique can provide a valuable suite of measurements to complement more traditional IODP shipboard measurements. Here we present unpublished data from IODP Expeditions 338 and 348, penetrating the Nankai Accretionary wedge to 3058.5 meters below seafloor. Increasing mud density decreased degasser efficiency, especially for higher hydrocarbons. Blurring of the relative variations in total gas by depth was observed, and confirmed with comparison to headspace gas concentrations from the cored interval. Theoretically, overpressured zones in the formation can be identified through C2/C3 ratios, but these ratios are highly affected by changing drilling parameters. Proper mud gas evaluations will need to carefully consider the effects of variable drilling parameters when designing experiments and interpreting the data.

Episodic Deep Fluid Expulsion at Mud Volcanoes in the Kumano Forearc Basin, SE offshore Japan

S.Hammerschmidt[1]*, A. Kopf[1]

*corresponding author: shammerschmidt@marum.de
[1] MARUM Research Centre, University of Bremen, Bremen, Germany

Compressional forces at convergent margins govern a variety of processes, most prominently earthquakes, landslides and mud volcanoes in the forearc. Although all seem related to fluid pressure changes, mud volcanoes are not only characterized by expulsion of fluids, but also fluidized mud and clasts that got ripped-up during mud ascension. They hence provide information regarding mobilization depth, diagenetic overprint, and geodynamic pathways.

At the Nankai Trough subduction zone, SE offshore Japan, mud volcanism id common and supposed to be related to seismogenic processes. During MARUM Expedition SO-222 with R/V SONNE, mud volcanoes in the Kumano forearc basin were mapped, cored and sampled. By extending the Integrated Ocean Drilling Program (IODP) Kumano transect landwards, 5 new mud volcanoes were identified by multibeam mapping. Cores revealed mud breccia with semi-consolidated silt- to claystone clasts and gaseous fluid escape structures, while the hemipelagic background sediments are characterized by intercalations of turbidites, ash layers and calcareous fossils. Clasts were subject to thin-section analyses, and the cores were sampled for XRD analyses and radiocarbon dating. Clasts showed prominent deformation structures, neomorphism and pores and fractures filled with polycrystalline quartz and/or calcite cement, probably formed during deep burial and early metamorphosis. Illite crystallinity based on XRD measurements varies between 0.24 and 0.38, which implies that the material originates from the Anchizone at depths $\geq$ 4 km. Radiocarbon dating revealed ages between 4450 and 30300 yr cal. BP, with age reversals occurring not earlier than 17000 yr cal. BP. Radiocarbon dating beneath turbidites and ash layers found at mud volcano #9 points to an episodic occurrence of these earthquake-related features in intervals of ca. 620 yr, while the mud volcano itself remained inactive.

In summary, the preliminary results suggest that the mud volcanoes are nurtured from a reservoir within the older part of the accretionary prism, but that mud volcanic activity is less frequent than major earthquakes. Future models will focus on source depth and temperature, and might elucidate the prerequisites for fluid migration and its role in seismogenesis at the Nankai Trough subduction zone.

APPENDIX C.3

CONTRIBUTIONS TO CONFERENCES: ABSTRACT ONLY

Report from IODP Expedition 348: Nankai Trough Seismogenic Zone Experiment Stage 3 - Plate Boundary Deep Riser 3

S.Hammerschmidt[1]*, H. Sone[2], and the IODP Expedition 348 Scientists

*corresponding author: shammerschmidt@marum.de
[1] MARUM Research Centre, University of Bremen, Bremen, Germany
[2] GFZ German Research Centre for Geosciences, Helmholtz Centre Potsdam, Potsdam, Germany

The Integrated Ocean Discovery Program (IODP) Nankai Trough Seismogenic Zone Experiment (NanTroSEIZE) is an international drilling project targeting the Nankai Trough subduction complex, SE offshore Japan. While Stage 1 of NanTroSEIZE focused on intense coring and logging-while-drilling (LWD) of the Kumano transect, Stage 2 added *in situ* long-term monitoring and riser drilling. The latter is essential for accomplishing deep drilling, and therefore, riser drilling was again the method of choice during Stage 3. Starting with IODP Exp. 326, riser drilling at Site C0002 above a presumably locked portion of an out-of-sequence splay fault system allowed deepening Hole C0002F from 856 meters below seafloor (mbsf) to 2005 mbsf. As a follow-up, the primary goals of IODP Expedition 348 with D/V *Chikyu* (14 September 2013 - 31 January 2014) were to further deepen the hole to 3600 mbsf using riser drilling technology, including LWD, lithological/structural description of cuttings, drilling mud gas monitoring, and coring from 2300 to 2400 mbsf. Prior to riser drilling, a new coring tool was tested by drilling and coring Hole C0002M to a depth of ca. 513 mbsf. After re-entering Hole C0002F, sidetracking at ca. 850 mbsf commenced for Hole C0002N, which was drilled to 2330 mbsf. Unfortunately, borehole conditions required again sidetracking at ca. 1950 mbsf, leading to a new borehole (C0002P). Drilling stopped at 2163 mbsf, and after coring from 2163 mbsf to 2218.5 mbsf, drilling continued smoothly to ca. 3060 mbsf. At that point, borehole conditions and time constraints made it necessary to complete the borehole and to make it ready for re-entry on upcoming IODP expeditions.

In total, preliminary results from both Hole C0002M and C0002N confirmed interpretations and unit boundaries from previous expeditions. In Hole C0002M, Unit II was encountered from 475 – 512.5 mbsf, and based on the predominance of hemipelagic mud with intercalations of turbidites, was again interpreted as lower Kumano forearc basin sediment. Biostratigraphic ages confirms a Pleistocene age. LWD and lithological data from Hole C0002N correspond to data from IODP Exp. 338, which point to syn-depositional erosional processes in the lower part of Kumano forearc basin (Unit III). The unconformity between forearc basin sediments and the upper accretionary prism was defined at 915.0 mbsf based on changes in gamma ray response seen in the LWD data and 975.5 mbsf based on a sudden change from mainly silty-claystone to a more sand-dominated lithology observed in the cuttings. Calcareous assemblages point to Pliocene to Miocene age. The LWD gamma ray response and the cuttings-based sand content was used to further

divide Unit IV into five different subunits, following those identified in Hole C0002F (Exp. 338) at overlapping depth ranges. The increase in LWD gamma ray at 1656.3 mbsf marks the start of Univ V in Hole C0002N, consistent with LWD responses observed in Hole C0002F. The distinct decrease in sand-content and dominance of (fine silty) claystone observed from cuttings collected below 1665.5 mbsf is consistent with the gamma ray increase, thus Unit V is interpreted as trench or Shikoku basin hemipelagic deposits of Miocene age, and can be correlated with Unit III at Sites C0011 and C0012 on the Phillippine Sea Plate. LWD data and cuttings lithology observations from the remaining deeper portions of Hole C0002N and Hole C0002P indicate that in general only a gradual increase in gamma ray or fining of claystones is observed further below, suggesting possible continuation of hemipelagic deposits.

Evidence for mechanical deformation and compaction was observed through structural observations and physical properties measurement of cuttings and core material. Only preliminary insights are currently available as interpretation and confirmation of these results requires comparison with detailed examination of sonic and borehole image log data which only became available after the Expedition. In addition to the deformational structures observed in the drilling cuttings, fault-related rocks associated with a brittle fault zone were encountered in the core recovered from Hole C0002P. The frequency of the occurrence of such major structures outside of the cored interval is unclear and awaits results from borehole image analyses. While onboard density measurements of hand-picked cuttings suggest porosity loss and mechanical compaction with depth, compressional wave velocity from the LWD data in Hole C0002P so far does not show an obvious increasing trend associated with sediment compaction. Whether this suggests abnormally high pore pressure or not shall be investigated together with further log data analyses and core laboratory measurement studies.

For all boreholes, TOC/TN ratios point to a dominance of marine organic matter. Methane predominated headspace gas samples from cores in Hole C0002M and C0002P. Concentrations found in headspace gas samples were up to two orders of magnitude higher than the drilling mud gas samples from the same interval, indicating an underestimation of hydrocarbons by real-time monitoring. The Bernard parameter and $\delta^{13}C_{CH4}$ of the drilling mud gas indicated a shift to a thermogenic regime at depths greater 1700 mbsf. Non-hydrocarbon gases showed mainly an atmospheric composition.

In conclusion, Expedition 348 results provide new insights into the Nankai subduction system. LWD data, core, cuttings, pore water and drilling mud gas were successfully collected, and will be subject to later onshore analysis for composition, geochemistry, microstructures, transport properties, and mechanical properties.

Episodic Deep Fluid Expulsion at Mud Volcanoes in the Kumano forearc basin, SE offshore Japan

S.Hammerschmidt[1]*, A. Kopf[1]

*corresponding author: shammerschmidt@marum.de
[1] MARUM Research Centre, University of Bremen, Bremen, Germany

Compressive forces at convergent margins promote a diverse range of processes, with the most prominent being earthquakes, and volcanism. The latter includes not only magmatic eruptions, but also mud volcanism, which is characterized by expulsion of fluids, fluidized mud and clasts that were ripped-up during mud ascension. At the Nankai Trough subduction zone, SE offshore Japan, mud volcanism was repeatedly reported, and activity is supposed to be related to seismogenic processes. During MARUM Expedition SO-222 with *R/V SONNE*, mud volcanoes in the Kumano forearc basin were mapped, cored and sampled. By extending the Integrated Ocean Drilling Program (IODP) Kumano transect landwards, 5 new mud volcanoes were identified by multibeam mapping. Cores taken from the mud volcanoes and the background sediment revealed mud breccia with semi-consolidated silt- to claystone clasts and gaseous fluid escape structures, while the hemipelagic background sediments are characterized by intercalations of turbidites, ash layers and calcareous fossils. Clasts were subject to thin-section analyses, and the cores were sampled for XRD analyses and radiocarbon dating. Clasts showed prominent deformation structures, neomorphism and pores and fractures filled with polycrystalline quartz and/or calcite cement, probably formed during deep burial and early metamorphosis. Illite crystallinity based on XRD measurements varies between 0.24 and 0.38, which implies that the material originates from the Anchizone at depths $\geq$ 4 km. Radiocarbon dating revealed ages between 4450 and 30300 yr cal. BP, with age reversals occurring not earlier than 17000 yr cal. BP. Radiocarbon dating beneath turbidites and ash layers found at mud volcano #9 points to an episodic occurrence of these earthquake-related features in intervals of ca. 620 yr, while the mud volcano itself remained inactive. In summary, the preliminary results suggest that the mud volcanoes are nurtured from a reservoir within the older part of the accretionary prism, but that volcanic activity is not necessarily related to seismogenic processes. Based on these results, future models will focus on source depth and temperature, and might elucidate the prerequisites for fluid migration and its role in seismogenesis at the Nankai Trough subduction zone.

APPENDIX D

Overview of Research Expeditions and Reports

Appendix D

The following table gives an overview of expeditions where participation was necessary during the PhD thesis. I contributed to every of the listed cruise reports. Except for the SmartPlug and DONET data, all samples and datasets presented in this thesis are based on these expeditions (Table S.9).

Table S.9: Overview of research expeditions that took place during the PhD thesis

Time	Expedition	(Co-)Chief Scientists	Expedition Project Manager	Tasks	Associated Cruise Report(s)
11.2013 - 01.2014	IODP Expedition 348 "NanTroSEIZE Stage 3: NanTroSEIZE Plate Boundary Deep Riser 3" with D/V Chikyu	Harold Tobin Demian Saffer Takehiro Hirose	Nobu Eguchi Sean Toczko Lena Maeda Yusuke Kubo	Head of the gaschemistry group and drilling mud gas specialist, responsible for real-time drilling mud gas monitoring and data evaluation as well as coordination of drilling mud gas sampling	Expedition 348 Scientists and Scientific Participants 2014
10.2012 - 12.2012	IODP Expedition 338 "NanTroSEIZE Stage 3: NanTroSEIZE Plate Boundary Deep Riser 2" with D/V Chikyu	Brandon Dugan Kyu Kanagawa Gregory Moore Michael Strasser	Nobu Eguchi Sean Toczko Lena Maeda	Head of the geochemistry group and gas/porewater chemistry specialist, responsible for real-time drilling mud gas monitoring and data evaluation as well as coordination of drilling mud gas and porewater sampling	Moore et al. 2013 Strasser et al. 2014
06.2012 - 07.2012	MARUM Expedition SO-222 "Project MeMo - MeBo drilling & long-term Monitoring offshore Japan (Nankai Trough Accretionary Prism)" with R/V Sonne	Achim Kopf	Achim Kopf	Visual core description, physical properties, observatories, logistics (commissioner for dangerous goods)	Kopf et al. 2013

References

Expedition 348 Scientists, Scientific Participants (2014) Expedition 348 Preliminary Report NanTroSEIZE Stage 3: NanTroSEIZE plate boundary deep riser 3. IODP Prelim Rep 348:71. doi: 10.2204/iodp.pr.348.2014

Kopf A, et al. (2013) Report and Preliminary Results of R/V SONNE Cruise SO222. Berichte, MARUM – Zent für Mar Umweltwissenschaften, Fachbereich Geowissenschaften, Univ Bremen 297:121.

Moore G, Kanagawa K, Strasser M, Dugan B, Maeda L, Toczko S, the Expedition 338 Scientists (2013) NanTroSEIZE Stage 3: NanTroSEIZE Plate Boundary Deep Riser. IODP Prelim Rep 338. doi:10.2204/iodp.pr.338.2013

Strasser M, Dugan B, Kanagawa K, Moore GF, Toczko S, Maeda L, Kido Y, Moe KT, Sanada Y, Esteban L, Fabbri O, Geersen J, Hammerschmidt S, Hayashi H, Heirman K, Hüpers A, Jurado MJ, Kameo K, Kanamatsu T, Kitajima H, Masuda H, Milliken K, Mishra R, Motoyama I, Olcott K, Oohashi K, Pickering KT, Ramirez SG, Rashid H, Sawyer D, Schleicher A, Shan Y, Skarbek R, Song I, Takeshita T, Toki T, Tudge J, Webb S, Wilson DJ, Wu H, Yamaguchi A (2014) IODP Proc 338,Yokohama, (Integrated Ocean Drilling Program). doi: 10.2204/iodp.proc.338.2014